TECHNICAL PAPERS

(Contents Continued)

TECHNICAL BRIEFS

ANNOUNCEMENTS

R. Henry

Maitre-Assistant.

G. Ferraris

Ingenieur de Recherche.

Laboratoire de Mecanique des Structures,
CNRS ERA 911
Institut National des Sciences Appliquees,
69621 Villeurbanne, France

Substructuring and Wave Propagation: An Efficient Technique for Impeller Dynamic Analysis

This paper is of particular interest of gas turbine designers because it proposes an efficient method for dynamic analysis of rotationally periodic structures encountered in turbomachines. It combines the advantages of a substructure technique and that of wave propagation in periodic systems. The mode shapes and frequencies are obtained from the analysis of a single repetitive sector of the whole structure. The finite element method is the numerical method used. A detailed application of the method to a centrifugal compressor impeller is reported along with experimental verification of the computed results.

Introduction

Today, the rotating parts of turbomachines such as those of gas turbines and jet engines are subjected to highly hostile working conditions. The manufacturer is greatly concerned with any improvement in performance, life, and weight reduction without loss of reliability. The possibilities of excitation by forces or imposed displacements are numerous and, an appreciation of the life of structural components is linked to an accurate dynamic analysis. Therefore, it is worthwhile to carefully estimate the dynamic behavior of rotating parts in order to improve the geometry or eventually modify the design if an unacceptable dynamic response is detected. This goal cannot be acheived without effective and constant development of specific methods and corresponding computer programs to be used by engineers for their calculations. The design of a turbomachine often results in a compromise between the needs of aerodynamics and thermodynamics (for performance) and that of solid mechanics (for strength). In this paper, we are concerned with the dynamic analysis of rotating components and particularly with bladed disk assemblies.

State-of-the Art Survey

The relative stiffness of the disk to that of the blades is of importance for the mechanical modeling of the system. As a matter of fact, if the disk is very stiff, then the blade is essentially clamped. If the disk and blade stiffnesses are comparable, their motions are strongly coupled, and, in-dependant calculation is not permitted. Neither of the well-

known methods of blade analysis [1–3], nor the coupled blade-disk-rotor problems [4] will be considered here.

Bladed disk assemblies can be classified in two groups according to their dynamic behavior: first, those having a mostly axisymmetric behavior (nodal lines being diameters and/or circles) and, second, all the remaining cases.

The first group contains assemblies characterized by a large number of radial blades mounted on a thin disk, for example, turbine wheels of jet engines. The second one contains rotationally periodic structures (cyclic symmetry) such as centrifugal impellers with or without casing.

Axisymmetric Bladed Disks. As far as we known, Jäger [5] in 1962 is the first author to propose a numerical technique (I.B.M. 650) to determine frequencies and mode shapes of coupled blade-disk systems. The disk and the blades were modeled with transfer matrices; some rotation effects are taken into account. A practical application is reported and theoretical-experimental comparison done. Kirkhope and Wilson [6] in 1970 solved the same problem with finite elements. Trompette [7] studied the subject thoroughly and set clear limits to the hypothesis of axisymmetric behavior. It can be used only for thin disks with blades modeled as beam elements (1 mode per junction) [8] and some thick disks which have blades connected in a radial plane.

Rotationally Periodic Structures. As long as the mode shapes are not roughly axisymmetric (diameters and/or circles for nodal lines), the previous hypothesis is no longer permitted and one has to introduce methods using cyclic symmetry. A lot of methods have already been proposed to simplify complex bladed-disk dynamic calculations. Two series exist:
- All types of substructure methods using free, constrained, or other modes to reduce the structural degrees of freedom, reviewed in detail by Dickens [9].

• The methods using explicitly or implicitly the wave propagation concept.

• Modeling of the complete structure with large computer codes is not considered because of its high cost.

In 1975, Mak and Botman [10] used the modal synthesis technique proposed by Hurty [11] to analyze a 32 blade impeller composed of 16 repetitive sectors. The results were compared with holographic test data. In 1979, Michimura et al. [12] proposed a method called "reduced impedance method." Frequencies and mode shapes were obtained from calculating the zeros of a determinant. The size of the problem was determined by the number of attachment D.O.F. (degrees of freedom) between the substructures. The method was applied to two impellers having 6 and 8 repetitive sectors. The four lowest theoretical frequencies were calculated and compared to experiment. Good accuracy was achieved. Other substructure method such as [13] could be considered; however, most of them lead to large eigenvalue problems. In most cases all sectors have to be modeled and all desired frequencies have to be calculated at one time. Mak and Botman [10] tried to reduce the size of the problem by imposing some special conditions at the repetitive sector boundaries in order to "force" the desired modes. After some tests, this method appears to be cumbersome and yields doubtful results; therefore it should never be used.

On the other hand, in 1973, MacNeal et al. [14] developed a method taking into account cyclic symmetry by decomposition of displacements in a "finite Fourier transformation." Application was performed recently by Kuo [15, 16] with reasonable success. In 1979, Thomas [17] described the same technique using complex arithmetic. It was illustrated by analyses of an alternator end winding, a cooling tower with legs, and a turbine wheel with blades modeled by a single blade clamped on the rigid disk and coupled at the tip. The key advantage of these methods is that it is possible to analyze the complete structure by considering only one repetitive substructure. However, in practice, the reduction is not sufficient and a modal condensation technique has to be used – Guyan reduction |18| for example. This procedure leads to the treatment of full mass and stiffness matrices and requires user "know how." It was not considered in this work.

The fundamental principle of wave propagation in periodic structures has been studied for many years, as Brillouin has pointed out in his classical work [19]. Physicist and electrical engineers have developed these concepts over the years in relation to crystals, optics, electrical transmission lines, etc.

The subject has been reviewed by Sen Gupta [20] in 1980. Concerning mechanical structures Mead [21] presented a general theory of harmonic wave propagation in periodic systems with multiple coupling between adjacent periodic elements. The finite element technique was introduced by Orris and Petyt [22], and Thomas [23]. It should be noted that the Mac Neal method implemented in NASTRAN [14] is no more than the implicit use of the wave propagation relations of [19] and [21]. The first dynamic analysis of bladed disks by wave propagation and finite element techniques was performed by Salama et al. [24] in 1976. Frequencies and modes of 20, 36, and 60 bladed disk models were calculated and compared to the results of Kirkhope and Wilson [6]. Unfortunately, the previous applications are not very significant because the test structures are relevant for the axisymmetric assumptions of the first group. The same remarks apply to [25]. In our opinion, the wave propagation method is the best for calculation of rotationally periodic structures because it uses not only repetitive geometry, as substructure methods do, but also repetitive mechanical behavior. Nevertheless, for industrial structures such as centrifugal impellers, the improvement is still not sufficient because of the large remaining number of DOF. A detailed study [26] has recently been made to develop, apply, and check a mixed method for finite element analysis of rotationally periodic structures. This method, first presented in [27], combines the advantages of a substructure technique and that of wave propagation in periodic systems. It is demonstrated in [28]. The next stage of the work, reported in this paper, was to apply the technique developed in the foregoing studies to predict the vibration modes and frequencies of an existing industrial structure. The first stage impeller of a Fives Cail-Babcock centrifugal compressor, Fig. 1.

Previous Studies and Papers

Method of Analysis. Rotationally periodic structures often have complicated geometry. The repetitive sector can be made up of thin (blades, periphery of the disk) and thick (the hub) parts, Fig. 1. The total number of DOF is then of great importance, especially if three dimensional finite elements are used. The method is summarized as follows: (see Fig. 2 and the Appendix for details).

1 The computation of the complete structure, composed of N identical sectors, requires only a model of a single sector, (basic sector), of arbitrary shape—provided that it is repetitive.

―――― Nomenclature ――――――――――――――――――――――

N = number of repetitive sectors
N_s = number of substructures for a repetitive sector
δ_{cd}, δ_{cg} = propagation degrees of freedom (DOF) of the right and left connection boundary nodes
F_{cd}, F_{cg} = forces related to δ_{cd} and δ_{cg}
n_p = number of δ_{cd} or number of δ_{cg}
δ_{ci} = substructure interior connection DOF
n_{ci} = number of δ_{ci}
δ_i = interior DOF of the sector substructures
n_i = number of δ_i
ϕ_n = constrained dynamic normal modes
p_n = modal coordinate
n_m = number of ϕ_n or p_n
ϕ_c = constrained static modes
n_c = number of ϕ_c
T, U = kinetic and potential energies
μ = propagation constant
β = phase angle
M, K = mass and stiffness matrices

ω = natural frequency, rd/s
Δ = Ritz reduction matrix
ND,NC = number of diameters and circles, axisymmetric nodal lines
NT = total number of DOF for the complete rotationally periodic structure
NP,GP = number of DOF and gain for the wave propagation method (WPM)
NS,GS = number of DOF and gain for the Craig and Bampton substructure method (CBM)
NM,GM = number of DOF and gain for the present method

Subscripts and Superscripts

R,I = real and imaginary part of a complex number
t = matrix transposition symbol
n = nth repetitive sector
s = sth substructure of the basic repetitive sector
T = complete structure
I = basic repetitive sector, (first sector)
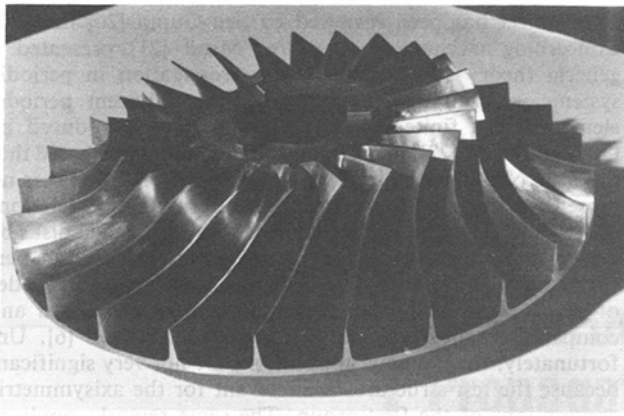
Fig. 1 Centrifugal compressor impeller
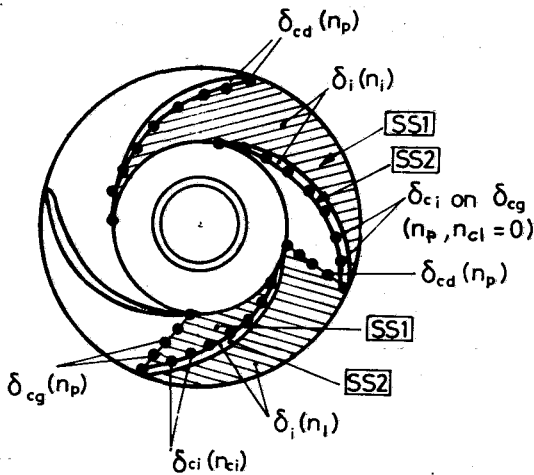
Fig. 2 Two different basic repetitive sectors with substructure possible arrangement

2 Finite element modeling of the Ns substructures composing the basic sector requires the following steps:

- Mass, stiffness matrices furnished by any finite element program including nonlinear geometric capability (for centrifugal effects).
- Calculation of the n_c^s static modes (ϕ_c^s) and n_m^s dynamic modes (ϕ_n^s).
- Ritz reduction.
- Assembly of the substructures if necessary ($N_s > 1$).

The number of DOF decreases from $2n_p + n_{ci} + n_i$ to $2n_p + n_{ci} + n_m$ where $n_m << n_i$.

3 Application of the wave propagation equations permits cancellation of the propagation DOF of the sector right boundary (δ_{cd}).

This leads to $n_p + n_{ci} + n_m$ complex equations.

4 Solution of the double real symmetric eigenproblem for each value of the phase angle β.

The number of equations becomes $2(n_p + n_{ci} + n_m)$.

It is noteworthy that the number n_{ci} of connection DOF (δ_{ci}) not involved with propagation can be considerably reduced if the basic sector and its substructures are chosen in a way that DOF δ_{ci} coincide with some δ_{cd} or δ_{cg}, then $n_{ci} \rightarrow 0$. Finally, the $N(n_p + n_{ci} + n_i)$ DOF of the complete structure are reduced to $2(n_p + n_{ci} + n_m)$ DOF, remembering that $n_{ci} + n_m << n_i$.

Summary of Results. The foregoing method was programmed in Fortran IV on a CDC 6600 computer and checked on various test structures. Preliminary tests were performed, and results compared to analytical results and/or a complete structural finite element model. Some useful conclusions for the analyses of the industrial structure presented herein have been derived [26, 27].

Any complex rotationally periodic structure is conveniently analyzed if a specific method is used: "Forced" boundary conditions or any axisymmetric model would lead to highly inaccurate results.

Modeling a single sector gives the same results as modeling the complete structure (other things being equal, the number of DOF per sector, types of finite elements, etc.).

The accuracy obtained for an axisymmetric structure (circular plate) calculated by the present method (with plate elements) and an axisymmetric one (thin shell elements) when compared to analytical results is the same, provided the number of nodes is identical on the boundary.

The Ritz reduction of interior DOF (δ_i) preserves the accuracy in the same way as Craig and Bampton substructure method does on the same structure.

The basic sector shape is of no importance provided it is repetitive.

Frequencies of the substructures partial modes have no influence on the final results. Only the mode shapes are important.

Provided the finite element mesh is equivalent, modeling the basic sector by one or several substructures does not modify the results.

The computer program capability of doing the computations in successive steps allows partial checking and makes any modification of any substructure easier – a noticeable improvement for the designer.

G is defined as the ratio of the total number, NT, of DOF, modeling the complete structure to that necessary for another method (other things being equal), say, NP for the wave propagation method (WPM) without Guyan reduction; NS, for the Craig and Bampton substructure method (CBM); and, NM, for the present one. We proved in |28| that:

$$GM = GP.GS \qquad (1)$$

where

$$GM = \frac{NT}{NM}, \quad GP = \frac{NT}{NP} = \frac{N}{2} \qquad (2)$$

and

$$GS = \frac{NT}{NS} = \frac{n_p + n_{ci} + n_i}{n_p + n_{ci} + n_m}, \quad n_m << n_i \qquad (3)$$

Comparison With Other Methods. Considering GP Equation (2), it is obvious that WPM is a superior method when the number of repetitive sectors is numerous. On the other hand, if the basic sector presents a complicated geometry, NP is still large and a dynamic condensation technique has to be performed. In this case, the condensation technique is:

- Sensitive to the choice of the master DOF, for it is not obvious that the same ones are appropriate for any phase angle β
- Expensive, for it has to be performed again for each value of β

Considering GS equation (3), we see that CBM allows modeling of complicated basic repetitive sectors with few DOF (particularly when the basic sector is substructured in a way that δ_{ci} is minimized). Unfortunately, all the DOF being on the N left boundaries of the sectors are maintained and all the desired frequencies have to be calculated at one time. This method is then convenient for structures having a small number of repetitive basic sectors which have few subdivisions ($Ns = 1$ or 2).

Equation (1), shows that the union of WPM and CBM is interesting and efficient because the gain GM is the product of the gains of the above methods. Finally, the mixed method

provides a superior model of rotationally periodic structures whatever the number of substructures and their complexity.

Dynamic Analysis of the Impeller

The Structure. The present method is applied to an industrial structure. It is the first stage impeller of a centrifugal compressor developed by the Fives Cail-Babcock Company, Lille, France. The impeller has 24 blades ($N=24$). The basic repetitive sector is composed of a thick part (the hub) and thin parts (the blades and disk periphery); it is then straightfoward to split it into two substructures – the first one is the 15 deg circular sector lying between two blades, the second one SS2, is a single blade, Fig. 1.

Finite Element Modeling and Computation Procedure. Taking into account the structural complexity and the step capability of the program, we use the following step by step procedure.

First step, modeling of the substructure SS1. The right finite element mesh is checked by comparing the resonant frequencies of the hub clamped disk (without blade) computed with the present program, called DISCO and an axisymmetric program called AXYM [8].

Second step, modeling of the second substructure SS2. The thin blade is calculated clamped along the connection nodes with SS1. Two finite element frequencies are used – SAP IV and AUBE. The computed frequencies and nodal lines are compared to experimental results.

Third step, final calculation. The mass and stiffness matrices, and some dynamic characteristics of SS1 and SS2, checked and saved on data files in the previous steps, are used in DISCO for final dynamic analysis of the present impeller. Computation and experimental results are compared and discussed.

Experimental Technique. The impeller is tightened on a heavy casting block between two thick rings with a hexagonal nut. Electromagnet excitation is applied. The amplitude peaks of the response measured with a capacitive pick up and plotted versus excitation frequency give the natural frequencies. To obtain the nodal lines experimentally, the structure is excited with an electrodynamic shaker and the well-known classical sand technique is used. The results are photographed in order to be compared with the computed modes.

Step by Step Procedure for Computation of Frequencies and Mode Shapes

Step 1 – Single Disk Modeling. To insure the SS1 finite element modeling, frequencies and mode shapes of the single disk are computed by two methods, the axisymmetric one with AXYM and the present method with DISCO; comparison is made. The goal is to find the right and sufficient finite element mesh for the substructure SS1. The disk without blades is an axisymmetric structure. The main tests to determine the wave propagation mesh are performed with the cheaper AXYM program. The disk is first modeled with 3 DOF per node axisymmetric thick shell elements (triangular for the hub and isoparametric for the periphery). It is clamped along the hub-mesh a, boundary condition 1 – as shown in Fig. 3. The computed frequencies will be taken as reference values (case AXYM – a.1). Different meshes and boundary conditions were tried and some computed frequencies are reported in Table 1. In the case AXYM-b.2, isoparametric elements are replaced by thin shell elements. Continuity between 3 DOF per node thick shell elements and 6 DOF per node thin shell elements is ensured by massless special thin shell elements called "junction elements" whose thicknesses and Young Modulus values are derived from mechanical
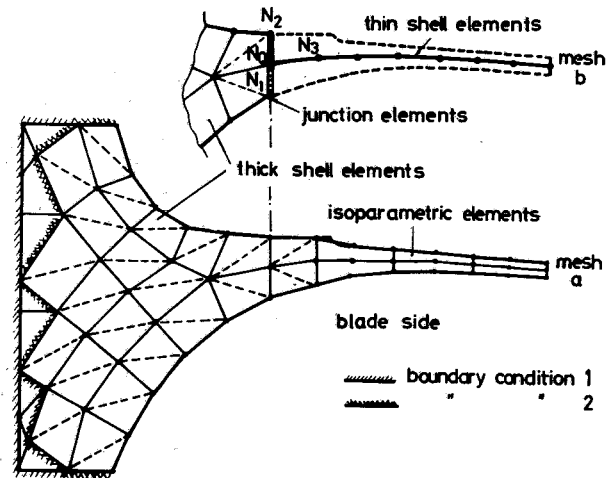
Fig. 3 The single disk finite element mesh, (axisymmetric view, blade below)
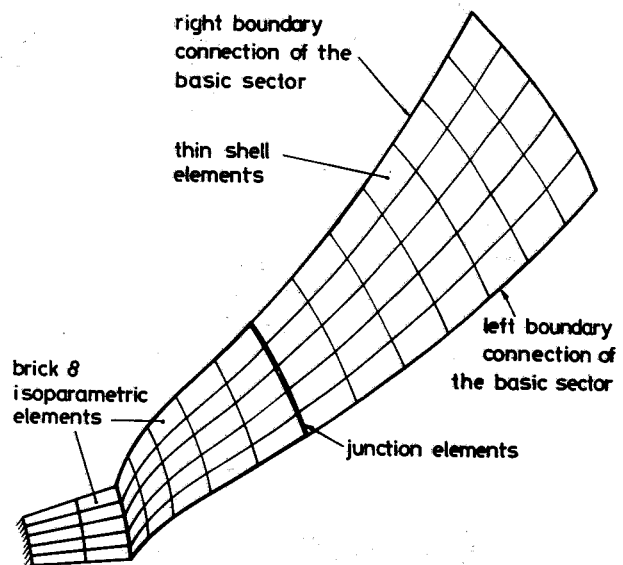
Fig. 4 Basic repetitive sector mesh (SS1, top view)

considerations [26]. For computation with the present method and program DISCO, the single disk basic sector is the 15 deg circular interblade sector of the impeller. A top view of the mesh is presented in Fig. 4 and the side view in Fig. 3 (same number of nodes as AXYM-b.2). The hub is modeled by 100 eight node isoparametric elements (brick 8) and the periphery with 35 four node thin shell elements. The 10 required junction elements are the previous thin shell elements adapted in the same way as for AXYM. The sector mass and stiffness matrices are computed with the SAP IV finite element program. Table 1 shows that mesh b is satisfactory to model the disk and that the boundary conditions 2 are valuable. The frequencies computed with DISCO, for $n_m = 4$ dynamic modes ϕ_n saved on SS1, are in very good agreement with the results of AXYM, see Fig. 5. The partial results of the basic sector used for the single disk computation (dynamic modes, ritz reduction) are saved on files for they are characteristics of the impeller basic sector SS1 substructure and will be used in step 3.

Step 2 – Blade Modeling. In this step we check the second substructure (SS2) of the impeller repetitive sector. Two finite element programs are used to compute the six lowest

Table 1 Single disk frequencies – check of SS1

DISK ND	f_0Hz AXYM-a1	f_1 AXYM-b1	$\Delta f/f_0$ %	f_2 AXYM-b2	$\Delta f/f_0$ %	f DISCO-b2	$\Delta f/f_0$ %
1	2426	2251	−7.2	2252	−7.2	2243	−7.5
	8272	8011	−3.2	8092	−2.2	8095	−2.1
2	2461	2328	−5.4	2330	−5.3	2322	−5.6
	8464	8492	0.3	8572	1.3	8539	0.9
5	3019	2948	−2.3	2948	−2.3	2994	−0.8
	10637	10410	−2.1	10411	−2.1	10481	−1.5
7	3928	3884	−1.1	3884	−1.1	3972	1.1
	12742	12279	−3.6	12279	−3.6	12442	−2.3
8	4557	4523	−0.7	4523	−0.7	4629	1.6
	13925	13419	−3.6	13419	−3.6	13629	−2.1
10	6141	6114	−0.4	6144	−0.4	6256	1.9
	16574	16079	−3.0	16079	−3.0	16392	−1.1
12	8124	8087	−0.5	8087	−0.5	8273	1.8
	19619	19183	−2.2	19183	−2.2	---	---

Table 2 Single clamped blade – check of SS2

BLADE f Hz	EXPERIM. f_E	SAP IV f_S	$\Delta f/f_E$ %	AUBE f_A	$\Delta f/f_E$ %
Mode 1	4876	4595	5.8	4836	0.8
2	9208	8600	6.0	9143	0.7
3	12467	11080	11.1	11519	7.6
4	13156	12030	8.6	12926	1.7
5	---	13660	---	13907	---
6	17189	16690	2.9	17188	0.0

Fig. 5 Single disk frequencies-check of SS1

Fig. 6 Basic sector finite element mesh for the impeller

frequencies and mode shapes of the blade clamped at the base. The blade is first modeled with 96 quadrilateral thin shell elements of the SAP IV program, secondly with 192 triangular thin shell elements of our AUBE program – previously developed [1, 2], for blade calculation. In the two cases, the number of 6 DOF nodes is equivalent; when boundary conditions are applied, the total number of effective DOF is 624. The computed results are compared to test data and presented in Table 2. All things equal, it is obvious that AUBE gives better results than SAP IV; thus the SS2

mass and stiffness matrices required by DISCO will be furnished by AUBE.

Step 3 – Frequencies and Mode Shapes of the Impeller. The basic repetitive sector required for the complete sector modeling is composed of the substructures SS1 and SS2 – checked in the two previous steps, Fig. 6. The junction between SS1 and SS2, imposed all along the right boundary, is of such a manner that all the connecting DOF of the blade (δ_{ci}) coincide with some propagation DOF of the right boundary DOF (δ_{cd}) of the disk. In that case, $n_{ci} = 0$, and the size of the matrices required for the eigenproblem solution is only increased by the few n_m modal coordinates corresponding to the modes ϕ_n of the clamped blade. Four dynamic modes ϕ_n are retained on SS1 ($n_m^1 = 4$) and six ϕ_n on SS2 ($n_m^2 = 6$). When

Table 3 Comparison with other methods – gains

IMPELLER N=24	Complete model	Sub-structure	Propagation	Present 2 SS
Nb. of nodes	6528	24×272	272	272
Nb. of DOF	29376	24×1362	1362	1362
Nb.eq.eigensol. for 52 freq.	29376	3552	2448	296
Nb.eigenvalues	≃100	≃100	8(13x)	8(13x)
Gains	1	8.3	12.0	99.2

Table 4 Impeller natural frequencies

IMPELLER freq. ND	Hz $\beta°$	MODES D1 TEST	MODES D1 COMPUT.	MODES D2 TEST	MODES D2 COMPUT.	MODES D3 COMPUTED	MODES D4 COMPUTED
0	0	3050	3886	4776	4965	6515	8924
1	15	3350	4027	4915	5373	7801	9291
2	30	3990	4069	5113	5575	8300	9669
3	45	4260	4103	5554	5741	8422	9880
4	60	4380	4145	5859	5888	8490	10008
5	75	4488	4197	5880	6031	8546	10100
6	90	4570	4255	6376	6175	8600	10177
7	105	4634	4316	6610	6321	8652	10251
8	120	4694	4374	6822	6465	8701	10333
9	135	4762	4423	7052	6600	8744	10423
10	150	4788	4461	7232	6713	8778	10520
11	165	4822	4485	7396	6789	8800	10602
12	180	4879	4493	7448	6815	8807	10635
BLADE CLAMPED		4876	AUBE 4836 SAP 4595	------		A.9143 S.8600	A.11519 S.11080

boundary conditions are applied, the problem is reduced to extract the 8 lowest eigenvalues of the 296 equation matrix, 13 times (N/2+1 values of β) to obtain the 52 desired frequencies. As a comparison, we note that modeling the complete impeller would have required the computation at one time of about 100 eigenvalues from a 29,376 equation system. The gain GM equation (1) obtained with the present method is then close to 100, when GP equation (2) is 12 and GS equation (3) is 8, see Table 3 for details.

Computations are performed on a CDC 6600 computer. The central core memory allowed to DISCO was limited to 170,000 Octals and imposed a block by block treatment of the matrices. Calculation of static modes ϕ_c and dynamic modes ϕ_n of the substructures is rather expensive, but done once and for all. Finally, on an average, computing a particular diameter (4 frequencies – 8 eigenvalues) needs about 600 s (C.P. time). This can be compared to the 500 s required by SAP IV to find two frequencies of the single disk basic sector clamped at the hub and free anywhere else. A partial conclusion can be made – three-dimensional finite element modeling must be reduced to a minimum as we did in step 1 when modeling the impeller rim with thin shell elements.

Results and Discussion

Frequencies. Table 4 and Fig. 7 present the computed and experimental frequencies versus phase angle β (or equivalently "nodal diameter," ND) which are arranged in families D1, D2, D3 and D4 to preserve analogy with the classical axisymmetric representation.

The highest relative error among the frequencies is less than 8 percent, except for the two lowest frequencies of D1. It should be observed that, as for axisymmetric models, the lowest 0 and 1 diameter frequencies are very sensitive to boundary conditions. Although satisfactory, the results would have been more accurate if a more refined finite element had been used (types and number of elements). Unfortunately, the mass and stiffness matrices of the disk (SS1, step 1) are calculated with the SAP IV program which has an interesting current element library but insufficient for
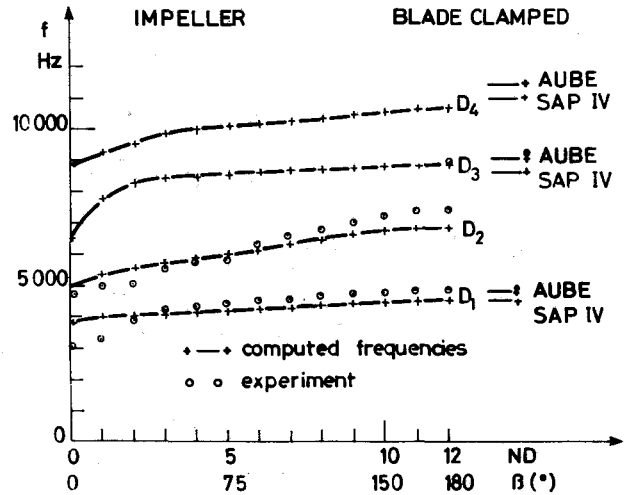
Fig. 7 Impeller natural frequencies versus phase angle

modeling such specific structures. In fact, concerning our problem, we note that:

(a) No element for transition between thick and thin regions of the structure exists in the SAP library.

(b) Mass matrices are lumped (no extradiagonal terms).

(c) Inertia terms are neglected in the thin shell mass matrix, (diagonal term is 0).

(d) The element stiffness in flexure is determined by the four nodes average thicknesses.

Point (a), has been partially resolved by using the technique suggested herein called "junction elements." They are ficticious massless and suitably stiff thin shell elements imposed on the brick 8 facets. Conformity is not strictly insured and accuracy is affected.

As to the other points, in step 2 (clamped blade computation), the thin shell elements of SAP and that of the program AUBE have been compared. With regard to the test results, the average error of SAP is about 7 percent and only 2

Fig. 8 Computed and experimental nodal lines of the 4 D1 and 4 D2 modes

Fig. 9 Some modes of the D1, D2, D3, D4 families for various β

values tend to the clamped blade frequencies computed with AUBE which are also close to the measured values.

Mode Shapes. The D1 and D2 nodal lines are compared in Fig. 8 for the $\beta = 60$ deg, 4 D1 and 4 D2 modes. The D3 and D4 families nodal lines were not experimentally determined, because of the high level required for the excitation force (at least 1g acceleration to allow sand motion) could have caused impeller failure. In this case, a more sophisticated method such as holography is required. Nevertheless we present in Fig. 9, the computed modes ND = 2, 8, 12, ($\beta = 30$, 120, 180 deg respectively) of the four D1, D2, D3, D4 families. Modes of the D1 and D2 families are all pseudo-axisymmetric; they are related to axisymmetric modes with n diameters and 0 circle. The D3 family consists of repetitive modes with twisted nodal lines which become regular when ND increases and looks like D1 and D2. The D4 family modes come from the axisymmetric modes with one circle. The circle exists in pure state for OD4; then when ND increases, it is driven outside the disk rim and shows the "scalloped" pattern, which finally vanishes for ND = 12. It is noted that each of the four families move to the pseudo axisymmetric 12 diameters, 0 circle.

About the Method. The rather high computation cost of the impeller did not allow us to try finer finite elements (mesh and modeling) nor to change the number of ϕ_n dynamic modes of the substructures SS1 and SS2. In this case, accuracy should have certainly been increased. However, the presented results, comparison with experiment, prove that the centrifugal impeller has been satisfactorily calculated with the present method and that its accuracy is closed linked to the finite element modeling of the components. In our opinion, it is possible to compute natural frequencies of any rotationally periodic structures within 5 percent accuracy at a reasonable cost.

Conclusions

In our opinion, this paper has contributed to a better and easier dynamic analysis of rotationally periodic structures, particularly for repetitively constructed components of turbomachines. Following a bibliography summarizing the state-of-the-art on the subject, and original method for the computation of frequencies and mode shapes of repetitive structures is described. Its application to a centrifugal compressor impeller is detailed along with experimental verification of the computed results. Performance of the method (precision, gain, CP. time, . . .) and its versatility compared to other methods have demonstrated its real efficiency.

References

1 Henry, R., "Calcul des coques minces en grandes deformations par éléments finis. Application aux aubes de compresseurs en rotation," These de Docteur-Ingénieur, Université Lyon I, Mar. 1973.

percent for AUBE. Errors induced by (a) (b) (c) (d) are found in SS1 (disk) modeling and consequently in the assembled model accuracy. As a matter of fact, this is partly proven when examining Fig. 7 and Table 4. If we remember that for bladed disk assemblies which can be calculated with axisymmetric assumptions [6, 7], the frequencies tend to those of the clamped blade when the number of diameters ND increases. We note that something equivalent arises here for D1, D3, D4. One can observe that for D1 the computed impeller frequencies (DISCO) tend to the clamped blade frequencies computed with SAP IV while the experimental D1

2 Henry, R., and Lalanne, M., "Vibration Analysis of Rotating Compressor Blades," ASME *Journal of Engineering for Industry*, Vol. 96, No. 3, Aug. 1974, pp. 1028–1035.

3 Henry, R., Lalanne, M., and Trompette, P., "Rotating Blade Analysis by the Finite Element Method," Symposium IUTAM, Dynamics of Rotors, Springer Verlag, Aug. 1974, pp. 299–318.

4 Tran, D. M., "Etude du comportement dynamique des rotors flexibles," Thèse de Docteur-Ingénieur, Université Lyon I, Dec. 1981.

5 Jager, B., "Die eigenfrequenzen einer scheibe mit verwundenen schaufeln," *Zeitschrift für flugwissenschaften*, Vol. 10, No. 12, Dec. 1962, pp. 439–446.

6 Kirkhope, J., and Wilson, G. J., "Analysis of Coupled Blade-Disc Vibration in Axial Flow Turbines and Fans," *41st Shock and Vibration Bulletin*, 1970, pp. 1–11.

7 Trompette, P., "Etude dynamique des structures, effet de rotation, amortissement," Thèse de Doctorat d'Etat, Université Lyon I, June 1976.

8 Ferraris, G., "Prévision du comportement dynamique des ensembles disque-aubes," Thèse de 3ème Cycle, Université Lyon I, Feb. 1982.

9 Dickens, J. M., "Numerical Methods for Dynamic Substructures Analysis," Ph. D. thesis, University of California, Berkeley, Dec. 1980.

10 Mak, S. W., Botman, M., "Substructures analysis of impeller vibration modes," ASME Paper No. 75-DET-112, Sept. 1975.

11 Hurty, W. C., "Dynamic Analysis of Large Structures by Modal Synthesis Techniques," *Computers and Structures*, Vol. 1, 1971, pp. 535–563.

12 Michimura, S., Nagamatsu, A., and Asazuma, K., "Vibration of Impellers," *Bulletin of the JSME*, Vol. 22, No. 171, Sept. 1979, pp. 1293–1298.

13 Craig, R. R., and Bampton, M. C. C., "Coupling of Substructures for Dynamic Analysis," *AIAA Journal*, Vol. 6, No. 7, July 1968.

14 Mac Neal, R. H., Harder, R. L., and Mason, J. B., "Nastran Cyclic Symmetry Capability," Nastran Users Experience, NASA, TMX 2893, Sept. 1973, pp. 395–421.

15 Kuo, P. S., and Collinge, K. S., "Structural Analysis of a Gas Turbine Impeller Using Finite Element and Holographic Techniques," *AGARD Conference Proceedings*, No. 248, Oct. 1978, pp. 1.1–1.15.

16 Kuo, P. S., "On the Formulation of Coupled/Uncoupled Dynamic Analysis of Blade-Disk Assemblies," ASME Paper No. 81-DET-126, 1981.

17 Thomas, D. L., "Dynamics of Rotationally Periodic Structures," *International Journal of Numerical Methods of Engineering*, Vol. 14, No. 1, Jan. 1979, pp. 81–102.

18 Guyan, R., "Reduction of Stiffness and Mass Matrices," *AIAA Journal*, No. 3, Mar. 1966.

19 Brillouin, L., *Wave Propagation in Periodic Structures*, Dover, 1946.

20 Sen Gupta, S., "Vibration of Periodic Structures," *Shock and Vibration Digest*, Vol. 12, No. 3, Mar. 1980, pp. 17–31.

21 Mead, D. J., "A General Theory of Harmonic Wave Propagation in Linear Periodic Systems With Multiple Coupling," *Journal of Sound and Vibration*, Vol. 27, No. 2, 1973, pp. 235–260.

22 Orris, R. M., and Petyt, M., "A Finite Element Study of Harmonic Wave Propagation in Periodic Structures," *Journal of Sound and Vibration*, Vol. 33, No. 2, 1974, pp. 223–236.

23 Thomas, D. L., "Standing Waves in Rotationally Periodic Structures," *Journal of Sound and Vibration*, Vol. 37, No. 2, 1974, pp. 288–290.

24 Salama, A. M., Petyt, M., and Mota Soares, C. A., "Dynamic Analysis of Bladed Disks by Wave Propagation and Matrix Difference Techniques," *Proceedings of the Symposium on Structural Dynamic Aspects of Bladed Disk Assemblies*, ASME Winter Annual Meeting, New York, Dec. 1976, pp. 45–56.

25 Wildheim, S. J., "Natural Frequencies of Rotating Bladed Discs Using Clamped Free Blade Modes," ASME Paper No. 81-DET-124, Sept. 1981.

26 Henry, R., "Contribution à l'étude dynamique des machines tournantes," Thèse de Doctorat d'Etat, Université Lyon I, Oct. 1981.

27 Henry, R., "Calcul des fréquences et modes des structures répétitives circulaires," *Journal de Mecanique Appliquée*, Vol. 4, No. 1, Jan. 1980, pp. 61–82.

28 Henry, R., and Der Hagopian, J., "Sous-structuration ou propagation d'ondes? Pourquoi pas l'une et l'autre? Application aux disque-aubes de turbomachines," Mécanique, Matériaux, Electricité, *Journal du GAMI*, No. 389-390-391, July 1982, pp. 226–233.

APPENDIX

Theoretical Background

The operations presented here are detailed in the Ph.D. thesis [26].

Wave Propagation. When a free wave propagates through the structure, the right and left hand boundary DOF and forces are related by

$$\delta_{cd} = e^{\mu} \delta_{cg}, \quad F_{cd} = -e^{\mu} F_{cg} \tag{A1}$$

where the propagation constant μ is pure imaginary for free, undamped vibrations.

$$\mu = j\beta \tag{A2}$$

To obtain all the possible modes of vibration of the repetitive structure (N sectors), the phase angle β takes the following values:

For N even, $N/2 + 1$ values: $\beta = 0, 2\pi/N, 4\pi/N, \ldots, 2\pi/N$ $(N/2 - 1), \pi$

For N odd, $(N+1)/2$ values: $\beta = 0, 2\pi/N, 4\pi/N, \ldots, 2\pi/N (N-1/2)$ \hfill (A3)

Since all the N sectors are identical, the potential energy U_T and the cinetic energy T_T of the complete structure is related to that of the basic sector I by:

$$U_T = \frac{N}{2} U_I; \quad T_T = \frac{N}{2} T_I \tag{A4}$$

Substructuring. The basic sector is divided into N_s substructures, (i.e., SS1 the disk sector, SS2 one blade). It follows that

$$U_I = \sum_{s=1}^{N_s} U_s; \quad T_I = \sum_{s=1}^{N_s} T_s \tag{A5}$$

U_s and T_s being, respectively, the potential and kinetic energy of the sth substructure which can be calculated from a finite element model.

The well-known Craig and Bampton substructure method is chosen [13]. The column matrix of DOF$_s$ of the sth substructure $\{\delta_s\}$ can be partitioned into n_c^s connecting DOF $\{\delta_c^s\}$ and n_i^s internal DOF $\{\delta_i^s\}$. The C.B.M. method uses two types of vectors for the Ritz vector group to reduce the substructure DOF. The first type of vectors is made of n_m^s vibration modes ϕ_n^s of the substructure with the boundary DOF fixed (called dynamic modes). The second type is made of n_c^s static displacement vectors ϕ_c^s for a unit displacement at each boundary DOF (called static modes).

The Ritz reduction can then be written:

$$\delta_i^s = \phi_c^s \delta_c^s + \phi_n^s p_n^s \tag{A6}$$

where p_n^s represent modal degrees of freedom.

Or on matrix form

$$\{\delta_s\} = \begin{Bmatrix} \delta_c^s \\ \delta_i^s \end{Bmatrix} = \begin{vmatrix} I & 0 \\ \phi_c^s & \phi_n^s \end{vmatrix} \begin{Bmatrix} \delta_c^s \\ p_n^s \end{Bmatrix} = |\Delta_s| \{\delta_\Delta^s\} \tag{A7}$$

The significant reduction in the number of DOF is obtained by only retaining a few dynamic modes of the substructure, say $n_m^s < < n_i^s$.

Finite element modeling yields

$$U_s + \frac{1}{2} \{\delta_s\}^t |K_s| \{\delta_s\}, T_s = \frac{1}{2} \{\dot{\delta}_s\}^t |M_s| \{\dot{\delta}_s\} \tag{A8}$$

where K_s, M_s are stiffness and mass matrices of the Sth substructure.

Applying the base transformation Δ_s (7), equation (8) becomes

$$U_s = \frac{1}{2} \{\delta_\Delta^s\}^t |K_\Delta^s| \{\delta_\Delta^s\}, T_s = \frac{1}{2} \{\dot{\delta}_\Delta^s\}^t |M_\Delta^s| \{\dot{\delta}_\Delta^s\} \tag{A9}$$

Some of the connection DOF $\{\delta_c^s\}$ can be part of the propagation displacements $\{\delta_{cd}^s\}^c$ or $\{\delta_{cg}^s\}$, the remaining being noted $\{\delta_{ci}^s\}$, see Fig. 2, then,

$$\{\delta_c^s\} = \{\delta_{cd}^s, \delta_{cg}^s, \delta_{ci}^s\}^t \tag{A10}$$

Final Assembly. Applying (4) and (5) it follows that

$$U_T = \frac{N}{2} \cdot \frac{1}{2} \{\delta_I\}^t |K_I| \{\delta_I\}; T_T = \frac{N}{2} \cdot \frac{1}{2} \{\dot{\delta}_I\}^t |M_I| \{\dot{\delta}_I\} \tag{A11}$$

where

$$\{\delta_I\} = \{\delta_{cg}, \delta_{cd}, \delta_{ci}, p_n\}^t \tag{A12}$$

are the degrees of freedom of the assembled repetitive sector.

Equations of Motion. The elimination of the right-hand

propagation DOF $\{\delta_{cd}\}$ is achieved by using equation (1) through Lagrange multipliers when applying Lagrange equations. In this case the resultant eigenvalue problem becomes

$$|K_T(\mu) - \omega^2 M_T(\mu)| \{\delta_\mu\} = 0 \qquad (A13)$$

where

$$\{\delta_\mu\} = \{\delta_{cg}, \delta_{ci}, p_n\}^t \qquad (A14)$$

since $K_T(\mu)$ and $M_T(\mu)$ are Hermitian matrices, equation (13) is replaced by the real symmetric eigenvalue problem.

$$|K(\beta) - \omega^2 M(\beta)| \{\delta_\beta\} = \{0\} \qquad (A15)$$

where

$$\{\delta_\beta\} = \{\delta_\mu^R, \delta_\mu^j\}^t$$
$$= \{\delta_{cg}^R, \delta_{ci}^R, p_n^R, \delta_{cg}^j, \delta_{ci}^j, p_n^j\}^t \qquad (A16)$$

It is a property of Hermitian matrices that the eigenvalues are double and real, and the associated eigenvectors are double and real, and the associated eigenvectors are in quadrature. All the eigenvectors of the complete structure can be obtained therefore from (15) and (3).

J. K. Lee

Associate Professor.

A. W. Leissa

Professor.

A. J. Wang

Graduate Associate.

Department of Engineering Mechanics,
The Ohio State University,
Columbus, Ohio 43210

Vibrations of Blades With Variable Thickness and Curvature by Shell Theory

A procedure for analyzing the vibrations of rotating turbomachinery blades has been previously developed. This procedure is based upon shallow shell theory, and utilizes the Ritz method to determine frequencies and mode shapes. However, it has been limited heretofore to blades of uniform thickness, uniform curvature, and/or twist and rectangular planform. The present work shows how the procedure may be generalized to eliminate the aforementioned restrictions. Nonrectangular planforms are dealt with by a suitable coordinate transformation. This, as well as variable thickness, curvature and twist, require using numerical integration. The procedure is demonstrated on four examples of cantilevered blades for which theoretical and experimental data have been previously published: (1) flat plate with spanwise taper, (2) flat plate with chordwise taper, (3) twisted plate with chordwise taper, and (4) cylindrical shell with chordwise taper.

Introduction

Recently a method of vibration analysis was developed for application to rotating turbomachinery blades [1–3]. The method treated the blade as a continuous shell, and the analysis was based upon shell equations. Shallow shell theory was used in order to avoid the complexities involved with a deep shell theory requiring nonorthogonal coordinates. The shallow shell theory was found to be sufficiently accurate to accommodate the chordwise curvature typically encountered in blades [4], although it was found to break down for large angles of pretwist [3]. The effect of adding spanwise curvature to the chordwise curvature was also studied [5]. The method was shown to be computationally very efficient and especially suitable for making parameter studies showing the effects of changing aspect ratio, thickness, curvature and pretwist angle upon free vibration frequencies and mode shapes. Rotational effects, including steady and displacement dependent centrifugal forces, were accounted for [1, 3].

However, the previously developed method is only capable of analyzing blades of uniform thickness, uniform curvature and/or twist, and rectangular planform. The purpose of the present work is to demonstrate how the method may be generalized to accommodate variable thickness, variable curvature and/or twist, and nonrectangular planforms, thereby providing more accurate representations of actual blade configurations.

As in the previous work, the Ritz method is used, with displacement components (u, v, w) expressed as algebraic polynomials. Nonrectangular planform is dealt with by a

suitable transformation which maps the shape into a rectangle. This, along with variable thickness and curvature, considerably complicates the two-dimensional integrals of strain energy and kinetic energy which must be evaluated, making intractable the exact integration procedures used previously. Instead, the integrations are performed numerically.

To demonstrate the efficacy of the method several types of problems are solved for which numerical results, both theoretical and experimental, are available in the previously published literature.

Analysis

The middle surface of a blade is shown in Fig. 1, along with coordinate systems. As is well known, a point (x, y, z) on the surface can be represented by two independent parameters as

$$x = f_1(\alpha, \beta), \quad y = f_2(\alpha, \beta), \quad z = f_3(\alpha, \beta) \tag{1}$$

and the position vector is expressed as

$$\mathbf{r} = x\hat{i} + y\hat{j} + z\hat{k} = \mathbf{r}(\alpha, \beta) \tag{2}$$

The set of functions (f_1, f_2, f_3) can be regarded as a mapping of a plane $\hat{s} = [-1, 1] \times [-1, 1]$ into a surface S as shown in the figure. The notion of geometric mapping such as this plays an important role during the numerical treatment to follow.

For simplicity, we assume that α- and β- curves intersect with right angles and their curvatures are related to the position vector by, respectively,

$$\frac{1}{R_\alpha} = -\frac{1}{A^2}\mathbf{r}_{,\alpha\alpha} \cdot \hat{i}_n, \quad \frac{1}{R_\beta} = -\frac{1}{B^2}\mathbf{r}_{,\beta\beta} \cdot \hat{i}_n \tag{3}$$

and the twist is
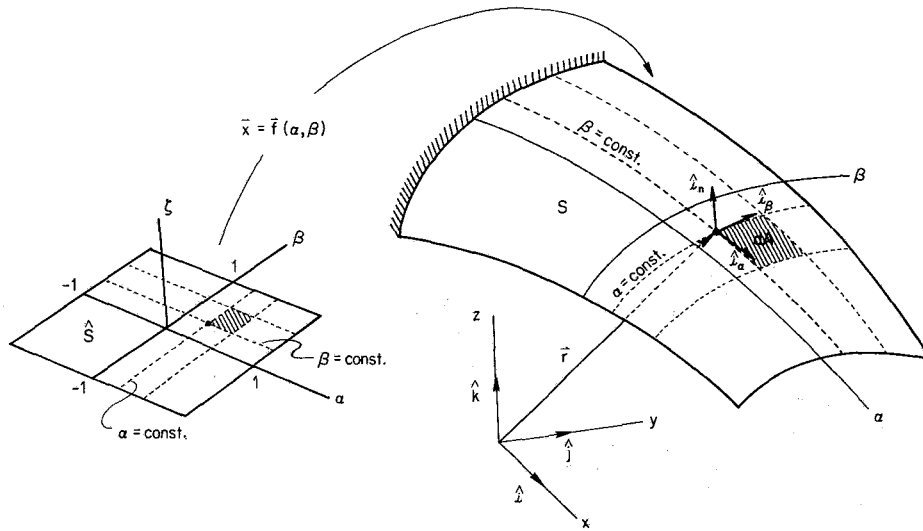
Fig. 1 Middle surface of a cantilevered shell and coordinate system

$$\frac{1}{R_{\alpha\beta}} = \frac{1}{AB} \mathbf{r}_{,\alpha\beta} \cdot \hat{i}_n \tag{4}$$

Here $\hat{i}_n$ is the unit outward normal, commas are used to denote partial derivatives, and

$$A = |\mathbf{r}_{,\alpha}| \quad , \quad B = |\mathbf{r}_{,\beta}| \tag{5}$$

Displacements of the thin shell are characterized by two tangential components u and v and the normal component w, i.e.,

$$\mathbf{u} = u\hat{i}_\alpha + v\hat{i}_\beta + w\hat{i}_n \tag{6}$$

According to the accurate thin shell theory of Goldenveizer [6] and Novozhilov [7], the membrane strains and curvature changes of the middle surface are related to the displacements by

$$\epsilon_\alpha = \frac{1}{A} u_{,\alpha} + \frac{v}{AB} A_{,\beta} + \frac{w}{R_\alpha} \tag{7a}$$

$$\epsilon_\beta = \frac{1}{B} v_{,\beta} + \frac{u}{AB} B_{,\alpha} + \frac{w}{R_\beta} \tag{7b}$$

$$\epsilon_{\alpha\beta} = \frac{B}{A} \left(\frac{v}{B}\right)_{,\alpha} + \frac{A}{B} \left(\frac{u}{A}\right)_{,\beta} - \frac{2w}{R_{\alpha\beta}} \tag{7c}$$

$$\kappa_\alpha = \frac{1}{A} \theta_{\alpha,\alpha} + \frac{\theta_\beta}{AB} A_{,\beta} \tag{8a}$$

$$\kappa_\beta = \frac{1}{B} \theta_{\beta,\beta} + \frac{\theta_\alpha}{AB} B_{,\alpha} \tag{8b}$$

$$\tau = \frac{1}{R_\alpha} \left(\frac{1}{B} u_{,\beta} - \frac{u}{AB} A_{,\beta}\right)$$

$$+ \frac{1}{R_\beta} \left(\frac{1}{A} v_{,\alpha} - \frac{v}{AB} B_{,\alpha}\right) \tag{8c}$$

$$- \frac{1}{AB} \left(w_{,\alpha\beta} - \frac{1}{A} A_{,\beta} w_{,\alpha} - \frac{1}{B} B_{,\alpha} w_{,\beta}\right)$$

in which rotations are defined by

$$\theta_\alpha = \frac{u}{R_\alpha} - \frac{1}{A} w_{,\alpha} \quad , \quad \theta_\beta = \frac{v}{R_\beta} - \frac{1}{B} w_{,\beta} \tag{9}$$

The strain energy for a homogeneous, isotropic, elastic shell having variable thickness and curvatures is given by (cf. [6] - [8])

$$V = V_m + V_b \tag{10}$$

in which V_m represents the membrane effects due to stretching of the middle surface,

$$V_m = \frac{E}{2(1-\nu^2)} \int \left[(\epsilon_\alpha + \epsilon_\beta)^2 \right.$$

$$\left. - 2(1-\nu) \left(\epsilon_\alpha \epsilon_\beta - \frac{\epsilon_{\alpha\beta}^2}{4}\right) \right] ABhd\alpha d\beta \tag{11}$$

and V_b the strain energy due to bending,

$$V_b = \frac{E}{24(1-\nu^2)} \int \left[(\kappa_\alpha + \kappa_\beta)^2 \right.$$

$$\left. - 2(1-\nu)(\kappa_\alpha \kappa_\beta - \tau^2) \right] ABh^3 d\alpha d\beta \tag{12}$$

where E is Young's modulus, ν is Poisson's ratio, and $h = h(\alpha,\beta)$ is the variable thickness.

For free vibrations of small amplitude, displacements can be expressed as

$$u(\alpha,\beta,t) = U(\alpha,\beta) \sin \omega t \tag{13}$$

and similarly for v and w. Then the maximum kinetic energy has the form

$$T_{max} = \frac{1}{2} \rho\omega^2 \int (U^2 + V^2 + W^2) ABhd\alpha d\beta \tag{14}$$

where ρ is the mass density per unit volume.

In this study, the displacement functions are taken to be simple polynomials given by

$$U(\alpha,\beta) = \sum_{i=1}^{I} \sum_{j=0}^{J} A_{ij} (\alpha+1)^i \beta^j \tag{15a}$$

$$V(\alpha,\beta) = \sum_{k=1}^{K} \sum_{l=0}^{L} B_{kl} (\alpha+1)^k \beta^l \tag{15b}$$

$$W(\alpha,\beta) = \sum_{m=2}^{M} \sum_{n=0}^{N} C_{mn} (\alpha+1)^m \beta^n \tag{15c}$$

The assumed displacement functions satisfy the clamped edge conditions exactly, that is,

$$U(-1,\beta) = V(-1,\beta) = W(-1,\beta) = \frac{\partial W}{\partial \alpha}(-1,\beta) = 0 \tag{16}$$

Simple polynomial displacement functions as in (15) are convenient to implement and computationally efficient, permitting relatively easy subsequent generalization and selection of differing order of approximations in each coordinate direction.

The Ritz method requires minimization of the functional $(T-V)_{max}$ in the usual manner [1-3], which yields a total of $I(J+1) + K(L+1) + (M-1)(N+1)$ simultaneous, linear, characteristic equations in an equal number of unknowns A_{ij}, B_{kl} and C_{mn}, viz.,

$$(\mathfrak{K} + \lambda^2 \mathfrak{M})\mathbf{a} = \mathbf{0} \qquad (17)$$

where $\mathfrak{K}$ and $\mathfrak{M}$ are stiffness and mass matrices resulting from (10) and (14), respectively, and λ is the frequency parameter. For a nontrivial solution, the determinant of the coefficient matrix is set equal to zero, which will result in a set of eigenvalues. Substituting each eigenvalue back into (17) yields the corresponding eigenvectors (amplitude ratio) in the usual manner. The mode shape corresponding to each frequency can then be determined by substituting the eigenvectors back into equations (15).

However, exact integration of (10) and (14) is seldom tractable except for special cases. Numerical integration must be employed. In selecting a numerical integration scheme, one can introduce a proper set of geometric mapping functions which will complement the scheme so as to minimize the necessary algebra and computations. One such natural choice would be the Gauss-Legendre quadrature rule (cf. [9] or [10]) along with the use of Lagrange interpolation functions for the geometry. Selected mapping functions for the geometric representation in this study are biquadratic Lagrange interpolation functions which will take the form

$$x = \sum_{p=1}^{9} x_p N_p(\alpha,\beta), y = \sum_{p=1}^{9} y_p N_p(\alpha,\beta), h = \sum_{p=1}^{9} h_p N_p(\alpha,\beta)$$
$$(18)$$

where x_p, y_p, and h_p are x- and y- coordinate values and thickness at point p, respectively, and $N_p(\alpha,\beta)$ are interpolation functions defined in the isoparametric coordinate system $[-1, 1] \times [-1, 1]$ (cf. Fig. 1 and reference [10] or [11] for the interpolation functions).

The third coordinate function is assumed to be quadratic in both x and y, i.e.,

$$z = \sum_{i=0}^{2} \sum_{j=0}^{2} Z_{ij} x^i y^j \qquad (19)$$

The coefficients Z_{ij} can be assigned directly for a simple geometry or they can be determined from the coordinate values at 9 points. In view of (18) and (19), we are assuming the shell middle surface to be quartic in (α,β) while (x,y) and h can vary quadratically in (α,β).

When (18) and (19) are introduced into (2), the geometric parameters can be computed by means of equations (3) - (5). Furthermore, when necessary substitutions are made in the strain energy and kinetic energy expressions, every integrand

can be expressed in terms of α and β explicitly, which vary from -1 to 1. Thus, it is ideal to employ the Gauss-Legendre quadrature rule to integrate (10) and (14) numerically. For example,

$$V_m = \int_{-1}^{1} \int_{-1}^{1} F(\alpha,\beta)\,d\alpha d\beta \simeq \sum_{p=1}^{P} \sum_{q=1}^{Q} F_{pq} W_p W_q \qquad (20)$$

where F_{pq} is the integrand F evaluated at Gauss point (α_p,β_q) and W_p is the weighting coefficient. For further detail on the quadrature rule, one may refer to [9] and [10]. In our study, only even numbers of quadrature points are used to avoid possible divisions by zero in the integrand.

Numerical techniques discussed here are commonly used in connection with the so-called isoparametric and Lagrangian type finite elements (cf. [11]). In this respect, the numerical procedure discussed here could be viewed as a finite element method using only one super element based on the accurate shell theory without having nodal variables. Advantages of the method entail less modeling effort and guaranteed monotonic convergence with an upper bound as long as enough quadrature points are used in the numerical integration. It is not as versatile as the finite element method in dealing with very complex geometry and different types of boundary conditions, however.

Convergence Studies

The polynomial displacement functions used in (15) form a complete set satisfying the fixed and conditions exactly, and therefore the method must yield solutions which converge to the exact solution as the number of terms used increases as long as sufficient accuracy is guaranteed during the numerical integration. Furthermore, the Ritz method yields monotonically convergent upper bound solutions.

Convergence studies are made in this section to determine the importance of the number of quadrature points used in the numerical integrations. Convergence studies to ascertain the number of terms needed in the displacement polynomials (15) have been made previously [2-3]. All components of displacement were given the same number of degrees of freedom in all cases.

Table 1 shows the effect of the number of quadrature points on the frequency parameters for a square flat plate having the constant thickness ratio $b/h = 20$. It also compares with the results obtained by using exact integration. From a previous study [2], it was found that two uncoupled solutions for symmetric and antisymmetric modes each having 6 terms in α and 3 terms in β are quite accurate when the energy terms are integrated exactly. A rapid convergence for the numerical integration technique is seen from the table for this sample problem. An interesting point to note here is monotonic convergence from below in the numerical integration as the number of Gauss points increases. This is because use of an insufficient number of quadrature points underestimates the system stiffness, resulting in less strain energy than when they are evaluated exactly. To be specific, consider a fixed order of

Table 1 Frequency parameter $(\omega a^2 \sqrt{\rho h/D})$ versus number of Gauss points (flat plate; $a/b = 1$, $b/h = 20$, 6×3 uncoupled solutions)

No. Gauss points in		Symmetric mode				Antisymmetric mode			
α	β	1	2	3	4	1	2	3	4
6	6	3.4734	21.312	27.461	54.996	8.5127	30.980	65.659	71.089
8	6	3.4739	21.313	27.461	55.000	8.5128	30.980	65.736	71.472
8	8	3.4739	21.313	27.461	55.000	8.5128	30.980	65.736	71.472
Exact Integration [2]		3.4739	21.313	27.461	55.000	8.5128	30.980	65.736	71.472

displacement approximation and stiffness matrices $\mathcal{K}_p$ and $\mathcal{K}_Q$ obtained by employing $P \times P$ and $Q \times Q$ quadrature rules, respectively, then for any mode $\mathbf{a}$, it can be shown numerically that

$$\mathbf{a}^T \mathcal{K}_p \mathbf{a} \leq \mathbf{a}^T \mathcal{K}_Q \mathbf{a} \quad \text{if and only if } P \leq Q \qquad (21)$$

The foregoing phenomenon is also observed in the finite element method (cf. [11~14]) and has been used to their benefit by many finite element analysts. It is known as the reduced integration technique.

The number of proper quadrature points in α (or β) direction can be estimated by

$$Q = L + 2$$

where L is the highest power of α (or β) in the normal displacement approximation.

Examples

The applicability of the method described in the previous sections will now be demonstrated on a number of example problems for cantilever blades of variable thickness. The examples chosen each have particular characteristics of turbomachinery blades, and each one has previous results in the published literature with which to compare.

For each of the problems described below, solutions were obtained using six terms of the polynomial functions (15) in each direction for the displacement components (u,v,w). The resulting problems have $6 \times 6 \times 3 = 108$ degrees of freedom. Because of symmetry, for the first two problems the transverse displacement (w) is uncoupled from the inplane (u,v) displacements. Then the bending-torsion modes (which are most important) are obtained by evaluating a determinant of 36th order. The higher frequency, inplane modes are then obtained from the remaining 72nd order determinant. The quadrature rule used for numerical integration in all the problems was 8×8, which was determined to be very accurate.

Flat Plate With Spanwise Taper. This problem is depicted in Fig. 2. It was examined by Dawe [15] for the case of a square planform $(a/b = 1)$, a taper ratio $h_{max}/h_{min} = 3.86$, for $h_{max}/a = 0.0576$, and $\nu = 0.3$. This problem has two symmetry axes. Therefore, modes may be separated into ones which are either symmetric or antisymmetric with respect to the symmetry axis, and bending and torsion are uncoupled. This reduces the problem solution by the present method for bending-torsion modes to one of finding the roots of two 18th order determinants. Numerical results for the nondimensional frequency parameter $\omega a^2 \sqrt{\rho h_{max}/D}$ are presented in Table 2, where $D_{max} = E h_{max}^3/12(1 - \nu^2)$.

Dawe [15] used a nonconforming finite element to analyze the bending-torsion modes for the same problem. He derived stiffness and inertia matrices for a typical rectangular plate element having linear thickness variation in one coordinate direction. Two mesh layouts having $3 \times 3 = 9$ and $5 \times 5 = 25$ square elements were used for the plate. Each free mesh point had three degrees of freedom (one displacement, two rotations) yielding 36 and 90 degrees of freedom (dof), respectively, for the two representations. Symmetry was not considered. Numerical results for the 5×5 mesh are given in Table 2, along with experimental results obtained for plates machined from steel [15].

Comparing the two sets of theoretical values in Table 2, one sees generally good agreement between the present method and the finite element solution. The greatest difference occurs for modes 6 and 7, which have rather close frequencies; the finite element solutions yield the modes in reverse order from the other two sets of data in Table 2. The two aforementioned finite element solutions showed that half of the first eight
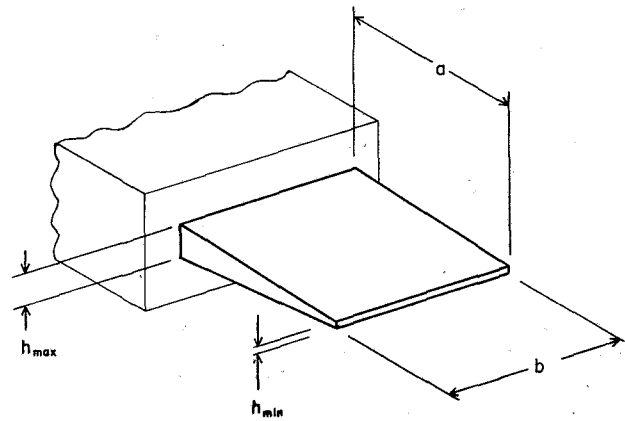
Fig. 2 Flat plate with spanwise taper
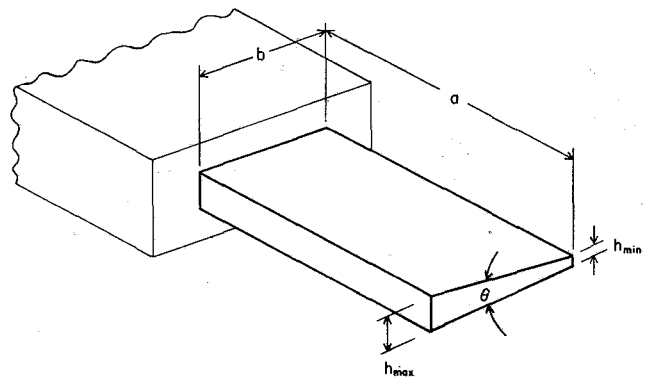
Fig. 3 Flat plate with chordwise taper

Table 2 Frequency parameters $\omega a^2 \sqrt{\rho h_{max}/D_{max}}$ for a flat plate with spanwise taper

Mode	Present (36dof)	FEM[15] (90dof)	Experiment [15]
1	4.137	4.083	4.069
2	6.992*	6.985*	7.127*
3	15.11	14.89	15.19
4	16.70	16.52	16.39
5	19.75*	19.35*	19.55*
6	31.34*	30.70	30.98*
7	32.09	30.51*	31.54
8	39.22	38.97	37.67
9	43.39*	42.30*	41.64*
10	51.09	51.65	51.30

* Antisymmetric modes

frequencies increase and the other half decrease as the mesh is refined, whereas the present method converges monotonically from above, guaranteeing upper bounds on the exact results.

The experimental results given in Table 2 agree well with both sets of theoretical results. One is surprised, however, to see some of the experimental frequencies greater than the theoretical ones, considering the difficulty in obtaining perfect clamping [16].

Flat Plate With Chordwise Taper. Another problem dealt with by Dawe [15] was a rectangular cantilever plate having a larger aspect ratio $(a/b = 2)$ and linear thickness variation in the chordwise direction (see Fig. 3). Here the taper ratio (h_{max}/h_{min}) was 3.26, h_{max}/a was 0.0352 and $\nu = 0.3$. For this problem the u and v displacements remain uncoupled from w,

Table 3 Frequency parameters $\omega a^2 \sqrt{\rho h_{avg}/D_{avg}}$ for a flat plate with chordwise taper

Mode	Present (36dof)	FEM[15] (90dof)	Exper. [15]	Const.h [2]
1	3.867	3.864	3.881	3.444
2	16.46	16.47	16.53	14.81*
3	23.65	23.78	23.72	21.45
4	48.23	48.19	48.85	48.21*
5	60.25	61.42	61.00	57.51
6	60.63	----	----	60.21
7	90.11	89.73	90.83	92.60*
8	95.19	94.05	95.76	93.26
9	109.4	106.9	105.4	123.9
10	125.1	121.7	124.6	130.6

* Antisymmetric modes

Table 4 Frequency parameters $\omega a^2 \sqrt{\rho h_{max}/D_{max}}$ for twisted plates of wedge-shaped cross-section

ϕ (degrees)	Method used	Mode					
		1	2	3	4	5	6
0	Present	2.438	11.41	15.01	29.00	34.91	47.40
	Exper.[18]	2.47	10.6	14.5	28.7	34.4	47.4
11.6	Present	2.419	11.91	15.03	30.29	35.82	48.76
	Exper.[18]	2.41	11.4	14.5	29.5	35.1	47.1
26	Present	2.432	12.84	15.79	33.42	39.14	52.58
	Exper.[18]	2.44	12.1	14.9	30.6	40.9	51.0
	FEM [19]	2.44	12.52	15.49	34.47	40.71	----
34.2	Present	2.866	12.50	17.37	34.17	42.65	53.94
	Exper.[18]	2.44	12.1	16.2	34.0	43.5	51.5

Fig. 4 Twisted plate with chordwise taper

Fig. 5 Cylindrical shell with chordwise taper

but the w displacements have no symmetry axis, giving coupling between bending and torsion.

The problem was solved by the present method using 36 terms for w as in the previous problem. Dawe's [15] finite element solution utilized the previously described finite element method with mesh layouts having 8 (4 spanwise × 2 chordwise) and 24 (6 spanwise × 4 chordwise) elements, again yielding 36 and 90 degrees of freedom, respectively, for the two solutions. Numerical data for the frequency parameter $\omega a^2 \sqrt{\rho h_{avg}/D_{avg}}$ resulting from both theoretical methods of solution are displayed in Table 3, along with experimental values [15]. In this case $D_{avg} = E h^3_{avg}/12(1 - \nu^2)$, where $h_{avg} = (h_{max} + h_{min})/2$.

The results from the present method are seen to agree well with those from finite element analysis and from experiment. The sixth mode, which is edgewise bending in the midplane of the plate (i.e., predominantly v-displacements) was not obtained in the study made by Dawe [15].

It is interesting to observe how closely the frequencies of the present tapered plate would be approximated by those of a plate having constant thickness equal to the average thickness of the tapered plate. It is for this reason that the frequency parameter used in Table 3 contains the average thickness. Accurate values of constant thickness plate vibration frequencies using the present method are available [2] and are shown in the last column of Table 3. It is seen that the constant thickness representation is a rather good one, except for the first three frequencies, which are each approximately 10 percent low. Of course, the constant thickness plate does not recognize the coupling between bending and torsion which is present in the tapered plate. For the previously considered plate having spanwise taper, the constant thickness model is much worse.

Twisted Plate With Chordwise Taper. A series of steel, cantilevered plates having a wedge-shaped cross-section and
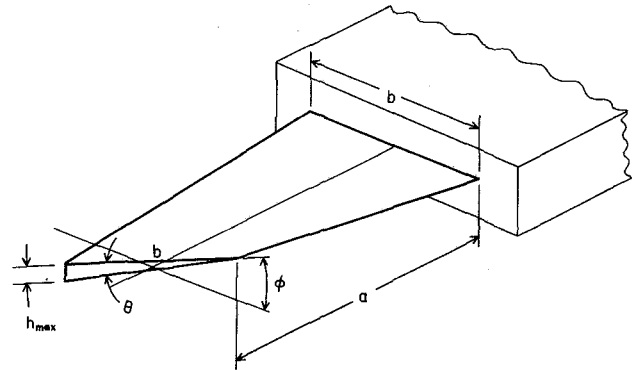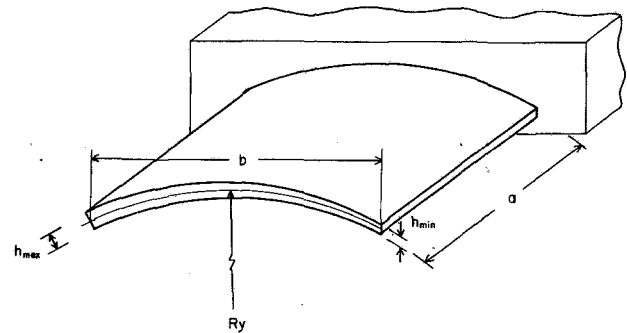
various angles of pretwist were investigated experimentally by Wilson and Plunkett [17, 18]. The plates were 5 in. long by 2.5 in. wide, with a maximum thickness of 0.162 in. and a wedge angle (θ) of 3.7 deg (see Fig. 4). Frequencies were measured for pretwist angles ϕ of 0, 11.6, 26, and 34.2 deg. Results expressed in terms of $\omega a^2 \sqrt{\rho h_{max}/D_{max}}$ are given in Table 4, for $\nu = 0.3$.

Results obtained by the present method are also shown in Table 4 for all values of ϕ. The same number of terms (36) were taken for the w-displacement as in the previous problems studied. But, because of the lack of any symmetry, here the tangential displacements (u and v) are coupled with w; thus, the complete solution had $3 \times 36 = 108$ degrees of freedom. The numerical results thus obtained agree well with the experimental data given in Table 4.

The problem was also solved by Bossak and Zienkiewicz [19] using a finite element method. Twelve (3 × 4 mesh), three-dimensional, isoparametric, brick-type elements were used in the analysis, for a total of 312 degrees of freedom. Numerical results were obtained only for $\phi = 26$ deg. They are shown in Table 4 and also agree well, in general, with those of the present method.

Cylindrical Shell With Chordwise Taper. Finally, let us consider a cambered blade (i.e., one having chordwise curvature) with variable thickness in the chordwise direction (see Fig. 5). Lindberg, Olson and Sarazin [20, 21] determined both theoretical and experimental results for the case of a circular cylindrical shell having square planform ($a = b = 12$ in.), linear chordwise taper ($h_{max} = 0.165$ in., $h_{min} = 0.048$ in.) and $R_y = 30$ in. Theoretical results were obtained by a finite element method with triangular shallow shell elements having linearly varying thickness. A 4 × 4 mesh layout was used, yielding 125 degrees of freedom.

The problem was solved by the present method, again using 36 terms for each displacement polynomial, giving a total of 108 dof. No symmetry exists in the problem. Walker [22] also

Table 5 Frequencies (Hz) of a cylindrical blade with chordwise taper

Mode	Present (108dof)	FEM[21] (125dof)	FEM[22] (205dof)	Experiment [20,21]
1	78.296	78.855	78.99	76.4
2	113.95	114.10	114.5	108
3	210.37	211.55	210.8	202
4	254.86	258.09	263.0	253
5	368.21	370.60	373.8	364
6	465.53	452.32	454.6	426
7	499.68	480.52	496.8	465
8	586.03	581.32	587.3	572
9	730.28	690.11	695.6	677
10	757.44	755.03	779.2	692

solved this problem using a finite element method with helicoidal shell elements, and a total of 205 dof.

Frequencies (in Hz) from the three analytical methods are listed in Table 5 and compared there with experiment. Calculations are based upon Poisson's ratio (ν) of 0.3, Young's modulus (E) of 30×10^7 lb/in.^{2}, specific weight (γ) of 0.284 lb/in.^{3} and a gravitational constant (g) of 386.4 in./s^2. All the theoretical results agree reasonably well with each other. Inasmuch as all three methods converge monotonically from above, giving upper bounds on the exact solution, the present method is seen to be the most accurate for the first five frequencies. Although experimental values differ somewhat more from the analytical results, they are lower, which may be the result of imperfect clamping. Thickness deviations of $\pm$ 10 percent in the experimental models [21] is another possible source of inaccuracy. The effects of transverse shear flexibility and rotating inertia, neglected in the thin shell theory, could cause additional errors for the higher modes.

Concluding Remarks

The method of analyzing the free vibrations of turbomachinery blades based upon thin shell theory and the Ritz method [1-3] has been extended further to accommodate blades of variable thickness, variable curvature and non-rectangular planform. The extended method has been demonstrated on several two-dimensional problems for blades having variable thickness. The results of applying the present method to the various problems show it to be quite accurate.

The present method is not intended to take the place of finite element methods, but rather to complement them. It is particularly well suited for making parametric studies to observe the effects of changing aspect ratio, thickness ratio, curvature ratio, taper ratio, etc. and thereby to acquire a better physical understanding of the vibrational characteristics of blades.

References

1 Leissa, A. W., Lee, J. K., and Wang, A. J., "Rotating Blade Vibration Analysis Using Shells," ASME JOURNAL OF ENGINEERING FOR POWER, Vol. 104, 1982, pp. 296-303.

2 Leissa, A. W., Lee, J. K., and Wang, A. J., "Vibrations of Cantilevered Shallow Cylindrical Shells Having Rectangular Planform," J. Sound Vib., Vol. 27, No. 2, 1981, pp. 311-328.

3 Leissa, A. W., Lee, J. K., and Wang, A. J., "Vibrations of Twisted Rotating Blades," ASME Paper No. 81-DET-127, J. Mech. Design (to appear).

4 Lee, J. K., Leissa, A. W., and Wang, A. J., "Vibration of Cantilevered Circular Cylindrical Shells: Shallow Versus Deep Shell Theory," Int. J. of Mech. Sci., (in press).

5 Leissa, A. W., Lee, J. K., and Wang, A. J., "Vibration of Cantilevered Doubly-Curved Shallow-Shells," Int. J. of Solids and Structures, (to appear).

6 Goldenveizer, A. L., Theory of Thin Shells, Pergamon Press, New York, 1961.

7 Novozhilov, V. V., The Theory of Thin Elastic Shells, P. Noordhoff Ltd., Groningen, The Netherlands, 1964.

8 Leissa, A. W., Vibration of Shells, NASA SP-228, U.S. Govt. Printing Office, Washington, D.C. 1973.

9 Stroud, A. H., and Secrest, D., Gaussian Quadrature Formulas, Prentice-Hall, 1966.

10 Hildebrand, F. B., Introduction to Numerical Analysis, McGraw-Hill, 1956.

11 Zienkiewicz, O. C., The Finite Element Method, 3rd Ed., McGraw-Hill, 1977.

12 Zienkiewicz, O. C., Taylor, R. L., and Too, J. M., "Reduced Integration Technique in General Analysis of Plates and Shells," Int. J. Num. Meth. in Eng., Vol. 3, 1971, pp. 295-290.

13 Hughes, T. J. R., Cohen, M., and Haroun, M., "Reduced and Selective Integration Techniques in the Finite Element Analysis of Plates," Nuc. Eng. Design, Vol. 46, 1978, pp. 203-222.

14 Reddy, J. N., and Chao, W. C., "A Comparison of Closed-Form and Finite Element Solutions of Thick Laminated Anistropic Rectangular Plates," Nuc. Eng. Design, Vol. 64, 1981, pp. 153-167.

15 Dawe, D. J., "Vibration of Rectangular Plates of Variable Thickness," J. of Mech. Eng. Sci., Vol. 8, 1966, pp. 42-51.

16 MacBain, J. C., and Genin, J., "Natural Frequencies of a Beam Considering Support Characteristics," J. Sound Vib., Vol. 27, No. 2, 1973, pp. 197-206.

17 Wilson, R. E., and Plunkett, R., Vibration of Cantilever Plate with Rectangular and Wedge-Shaped Cross-Section, Rept. DF53GL17, Gen. Elec. Co., Mar., 1953.

18 Plunkett, R., "Natural Frequencies of Uniform and Non-Uniform Rectangular Cantilever Plates," J. Mech. Eng. Sci., Vol. 5, No. 2, 1963, pp. 146-156.

19 Bossak, M. A. J., and Zienkiewicz, O. C., "Free Vibrations of Initially Stressed Solids, With Particular Reference to Centrifugal Force Effects in Rotating Machinery," J. of Strain Analysis, Vol. 8, No. 4, 1973, pp. 245-252.

20 Lindberg, G. M., Olson, M. D., and Sarazin, A. C., Finite Element Dynamic Analysis of Shallow Shell Structures, NRCC Aeronautics Report LR-500, 1970.

21 Olson, M. D., and Lindberg, G. M., "Dynamic Analysis of Shallow Shells with a Doubly Curved Triangular Element," J. Sound Vib., Vol. 19, No. 3, 1971, pp. 299-318.

22 Walker, K. P., "Vibrations of Cambered Helicoidal Fan Blades," J. Sound Vib., Vol. 59, No. 1, 1978, pp. 35-57.

R. E. Kielb

Aerospace Engineer,
Structures Branch,
National Aeronautics and
Space Administration,
Lewis Research Center,
Cleveland, Ohio 43135
Mem. ASME

K. R. V. Kaza

Aerospace Engineer,
National Aeronautics and
Space Administration,
Lewis Research Center,
Cleveland, Ohio 44135

Effects of Structural Coupling on Mistuned Cascade Flutter and Response

The effects of structural coupling on mistuned cascade flutter and response are analytically investigated using an extended typical section model. Previous work using two degree of freedom per blade typical section models has included only aerodynamic coupling. The present work extends this model to include both structural and aerodynamic coupling between the blades. The model assumes that the structurally coupled system natural modes have been determined and can be represented in the form of N bending and N torsional uncoupled modes for each blade, where N is the number of blades and, hence, is only valid for blade dominated motion. The aerodynamic loads are calculated by using two-dimensional unsteady cascade theories in the subsonic and supersonic flow regimes. The results show that the addition of structural coupling can affect both the aeroelastic stability and frequency. The stability is significantly affected only when the system is mistuned. The resonant frequencies can be significantly changed by structural coupling in both tuned and mistuned systems, however, the peak response is significantly affected only in the latter.

I Introduction

In references [1] and [2] the authors have investigated the effects of mistuning on cascade flutter and response by assuming that the individual blades in the cascade are coupled only aerodynamically. A typical section model, in which each blade has two degrees of freedom, one bending and one torsional, was used. In all bladed-disk assemblies the blades are structually coupled through the disk and often through a variety of other connecting parts such as shrouds, dampers, and lacing wires. In the case where there is only weak structural coupling between the blades (e.g., a relatively stiff disk and flexible blades), the effect of the structural coupling on individual blade frequencies is negligible and the method of analysis used in the previous publications is adequate. To handle cases where there is significant structural coupling, the typical section model must be refined. The purposes of this paper are to present such a refined model to account for structural coupling and to study its effects on cascade flutter and aeroelastic response of a mistuned bladed-disk. The work presented is limited to bladed-disks in which the motions are dominated by the blades and is based on a portion of the research described in [3].

The only known published work on mistuning including both aerodynamic and structural coupling is given in [4], in which each blade is allowed a single torsional degree of freedom and a subsonic aerodynamic theory is used to in-vestigate flutter. In the present paper the model is capable of considering coupled bending and torsional motion and both subsonic [5] and supersonic [6] two-dimensional unsteady cascade aerodynamic theories are used to investigate flutter and aeroelastic response. Since the effects of bending-torsion coupling were examined in [1] and [2], the parametric studies are limited to predominantly torsional motion with structural coupling. In addition to the references mentioned above, some other publications dealing with mistuning are (i) structural coupling without aerodynamics [7–10] and (ii) flutter and response using single degree of freedom blade models with aerodynamic coupling only [11–14]. Tuned systems with two degrees of freedom per blade have been considered in [15–20]. In [21] the authors have considered a more complex beam model which is capable of representing a twisted nonuniform blade.

II Theory

It is well known that the natural frequencies of annular plates depend upon the number of nodal diameters. In many publications (e.g., [7–10]) this behavior has also been shown to be true for bladed-disk assemblies. For tuned systems each single-blade mode, such as the first bending mode, becomes a family of modes, one for each nodal diameter pattern. In general, the frequencies for the first bending family of modes can vary considerably and depend monotonically on the number of nodal diameters. However, for torsional motion the frequencies are relatively insensitive to nodal diameter and do not increase monotonically. For a more detailed discussion of this behavior see [3].
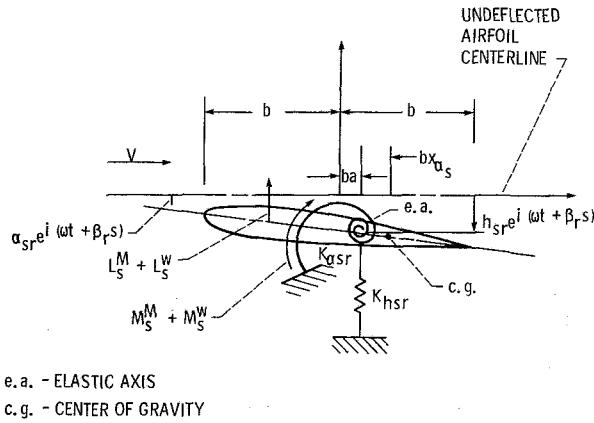
e.a. – ELASTIC AXIS
c.g. – CENTER OF GRAVITY

Fig. 1 Typical section model

In general, a complete bladed-disk model must include blade models, a disk model, and the appropriate continuity conditions. Simpler approaches can be used for the two limiting conditions of blade and disk dominated motion. For disk dominated motion, the blades can be considered to be lumped masses with no effect on the system stiffness. For blade dominated motion, the disk can be considered to be a spring support with no effect on the system mass. This latter approach is used herein and, hence, is only valid for blade dominated motion. The authors are developing a complete bladed-disk model which will be described in a future publication.

The approach used in formulating the mathematical model is to assume that the structurally coupled system modes (in a vacuum) have been determined and can be represented in the form of N bending and N torsional uncoupled modes for each blade. That is, each blade will appear to have two N natural frequencies: one bending and one torsion for each nodal diameter pattern. This description requires that the disk (and/or shroud ring) be a perfect body of revolution with all of the mistuning effects lumped in the individual blades. Since the number of nodal diameters, r, is directly related to the interblade phase angle by

$$\beta_r = 2\pi r / N \qquad (1)$$

each interblade phase angle mode is associated with a given nodal diameter. The parameter, β_r, is used in the "traveling wave approach" of describing blade motion. In this approach the motion of the airfoils in each mode of the tuned cascade is assumed to be simple harmonic with a constant phase angle between adjacent blades. This approach is entirely equivalent to the "standing wave approach" in which the motion is characterized by modes with nodal diameters fixed in the disk. For further discussion of the standing and traveling wave approaches see [20]. To include structural coupling, the equations of motion given in [2] have to be modified to reflect the fact that the blade frequencies in a vacuum depend on the number of nodal diameters. This is accomplished by assuming that only the stiffness terms are functions of the number of nodal diameters. Hence, the natural frequencies in a vacuum are given in additional subscript to reflect this dependency. Also, the force (or moment) associated with the stiffness in the equations of motion is assumed to be proportional to the displacement in the rth nodal diameter mode, and not to the physical blade deflection. As a result, the stiffness terms must be multiplied by the modal displacement and not the blade physical displacement. The term "modal displacement" is used since the physical displacements are expanded in terms of the nodal diameter modes. Also, the structural damping associated with the bending and torsional motions is also allowed to be a function of the number of nodal diameters.

As in [1] and [2], each blade is modeled as a two degree of freedom oscillator in which the plunging and pitching motions are inertially coupled (see Fig. 1). Including the nodal diameter dependence described above, the equations of motion of the sth blade are

$$\begin{bmatrix} m_s & S_{\alpha_s} \\ S_{\alpha_s} & I_{\alpha_s} \end{bmatrix} \begin{Bmatrix} \dfrac{d^2}{dt^2}\left(h_s e^{i\omega t}\right) \\ \dfrac{d^2}{dt^2}\left(\alpha_s e^{i\omega t}\right) \end{Bmatrix} +$$

───── **Nomenclature** ─────

$[A]$ = aerodynamic matrix due to motion
$\{AD\}$ = aerodynamic matrix due to wake induced flow
a = elastic axis position
b = semichord
c = chord
$[D], [D_s]$ = matrices defined in equation (6)
$[E]$ = transformation matrix
e = base for natural logarithm
$[G], [G_s]$ = matrices defined in equation (6)
$G_{\mathrm{Khsr}}, G_{\mathrm{K\alpha sr}}$ = defined in equation (6)
h_{ar} = bending deflection of blade in rth mode of tuned cascade
h_s = bending deflection of sth blade
I_{α_s} = mass moment of inertia of sth blade about elastic axis per unit span
i = square root of minus one, also a summation index
$K_{hsr}, K_{\alpha sr}$ = bending and torsional stiffness of sth blade in rth mode, respectively
k = reduced frequency based on semichord
L_s^m = lift due to motion of sth blade per unit span, positive up
L_s^w = lift due to wakes of sth blade per unit span, positive up

$1_{hhr}, 1_{h\alpha r}$ = nondimensional lift coefficients due to bending and torsional motions, respectively, in the rth mode
$1_{\alpha hr}, 1_{\alpha\alpha r}$ = nondimensional moment coefficients due to bending and torsional motion, respectively, in the rth mode
$1_{whr}, 1_{w\alpha r}$ = nondimensional lift and moment coefficients, respectively, due to wakes in the rth mode
M = Mach number
M_s^M = moment about the elastic axis due to motion of the sth blade per unit span, positive nose up
M_s^w = moment of sth blade per unit span about the elastic axis due to wake, positive nose up
m_s = mass per unit span of the sth blade
N = number of blades
$[P]$ = matrix defined in equation (10)
$[Q]$ = matrix defined in equation (7)
r = integer specifying the nodal diameter or interblade phase angle mode of the tuned rotor
$r_{\alpha s}$ = radius of gyration of sth blade, nondimensionalized with respect to b

$$+ \sum_{r=0}^{N-1} \begin{bmatrix} (1+2i\zeta_{hsr})\,m_s\omega_{hsr}^2 & 0 \\ 0 & (1+2i\zeta_{\alpha sr})\,I_{\alpha_s}\omega_{\alpha sr}^2 \end{bmatrix}$$

$$\cdot \begin{Bmatrix} h_{ar} \\ \alpha_{ar} \end{Bmatrix} e^{i(\omega t + \beta_r s)} = \begin{Bmatrix} -L_s^M - L_s^w \\ M_s^M + M_s^w \end{Bmatrix} \qquad (2)$$

These are identical to equation (4) of [2] with the following exceptions: the stiffness terms are now expanded to include the stiffness associated with each nodal diameter mode and the physical displacement terms are replaced with the modal displacements. Note that the real parts of the modal stiffnesses, K_{hsr} and $K_{\alpha sr}$, are expressed in the form of the mass times the square of the frequency. The aerodynamic forces are the same as those given in [2] and are also dependent on the nodal diameter. Nondimensionalizing equation (2) results in

$$\begin{bmatrix} \mu_s & \chi_{\alpha s}\mu_s \\ \chi_{\alpha s}\mu_s & r_{\alpha s}^2\mu_s \end{bmatrix} \begin{Bmatrix} -h_s/b \\ -\alpha_s \end{Bmatrix}$$

$$+ \sum_{r=0}^{N-1} \begin{bmatrix} (1+2i\zeta_{hsr})\,\mu_s\gamma_{hsr}^2\gamma & 0 \\ 0 & (1+2i\zeta_{hsr})\,\mu_s r_{\alpha s}^2\gamma_{\alpha sr}^2\gamma \end{bmatrix}$$

$$\cdot \begin{Bmatrix} h_{ar}/b \\ \alpha_{ar} \end{Bmatrix} e^{\frac{2\pi irs}{N}} = \sum_{r=0}^{N-1} \begin{bmatrix} 1_{hhr} & 1_{h\alpha r} \\ 1_{\alpha hr} & 1_{\alpha\alpha r} \end{bmatrix} \begin{Bmatrix} h_{ar}/b \\ \alpha_{ar} \end{Bmatrix}$$

$$\cdot e^{\frac{2\pi irs}{N}} + \sum_{r=0}^{N-1} \begin{Bmatrix} 1_{whr} \\ 1_{w\alpha r} \end{Bmatrix} e^{\frac{2\pi irs}{N}} \qquad (3)$$

where

$$\gamma_{hsr} = \omega_{hsr}/\omega_0$$
$$\gamma_{\alpha sr} = \omega_{\alpha sr}/\omega_0 \qquad (4)$$
$$\gamma = (\omega_0/\omega)^2$$

The other nondimensional variables are defined in the nomenclature and described in [1]. Writing these equations for all blades and arranging them in matrix form results in

$$[D]\{X\} + \gamma[Q]\{Y\} = [G][E][A]\{Y\} + [G][E]\{AD\} \qquad (5)$$

where

$$[D] = \begin{bmatrix} [D_0] & & & & \\ & [D_1] & & & \\ & & \cdot & & \\ & & & \cdot & \\ & & & & \cdot \\ & & & & & [D_{N-1}] \end{bmatrix}$$

$$[D_s] = \mu_s \begin{bmatrix} 1/G_{Khs0} & x_{\alpha s}/G_{Khs0} \\ x_{\alpha s}/G_{K\alpha s0} & r_{\alpha s}^2/G_{K\alpha s0} \end{bmatrix}$$

$$G_{Khsr} = \mu_s\gamma_{hsr}^2(1+2i\zeta_{hsr})$$
$$G_{K\alpha sr} = \mu_s r_{\alpha s}^2\gamma_{\alpha sr}^2(1+2i\zeta_{\alpha sr}) \qquad (6)$$

$$[G] = \begin{bmatrix} [G_0] & & & & \\ & [G_1] & & & \\ & & \cdot & & \\ & & & \cdot & \\ & & & & \cdot \\ & & & & & [G_{N-1}] \end{bmatrix}$$

$$[G_s] = \begin{bmatrix} 1/G_{Khs0} & 0 \\ 0 & 1/G_{K\alpha s0} \end{bmatrix}$$

and

_____ Nomenclature (cont.) _____

s = integer specifying blade number, also blade gap

S_{α_s} = static mass moment of the sth blade per unit span about elastic axis, positive when center of gravity is aft of the elastic axis

t = time

V = freestream velocity relative to the blade

$\{X\}$ = physical blade displacements

X, Z = rectangular coordinate axes

x_{α_s} = nondimensional static unbalance of sth blade

$\{Y\}$ = displacements in nodal diameter modes

α_s = amplitude of torsional motion of sth blade, positive clockwise

$\alpha_{s,id}$ = torsional amplitude of each blade of the tuned rotor

α_{ar} = amplitude of torsional deflection of a blade in the rth mode of a tuned cascade

β_r = interblade phase angle, $2\pi r/N$

γ = nondimensional eigenvalue, $(\omega_0/\omega)^2$

$\gamma_{hr}, \gamma_{\alpha r}$ = defined in equation (14)

$\gamma_{hsr}, \gamma_{\alpha sr}$ = defined in equation (4)

$\zeta_{hsr}, \zeta_{\alpha sr}$ = damping ratios of the sth blade in bending and torsion in rth mode, respectively

μ_s = mass ratio of the sth blade

$\bar{\mu}$ = real part of eigenvalue, defined in equation (12)

$\bar{\nu}$ = imaginary part of eigenvalue, defined in equation (12)

ξ = stagger angle

ω = frequency

ω_0 = reference frequency

$\omega_{hs} = \sqrt{K_{hs}/m_s}$

$\omega_{\alpha s} = \sqrt{K_{\alpha s}/I_{\alpha s}}$

ω_{hsr} = bending natural frequency, dependent on r

$\omega_{\alpha sr}$ = torsional natural frequency, dependent on r

ω_{hr} = tuned bending frequency, dependent on r

$\omega_{\alpha r}$ = tuned torsional frequency, dependent on r

$[\ \ ]^{-1}$ = inverse of a matrix

$$[Q] = \begin{bmatrix} 1 & 0 & \dfrac{(1+2i\zeta_{h01})\gamma_{h01}^2}{(1+2i\zeta_{h00})\gamma_{h00}^2}E(0,1) & 0 & \dfrac{(1+2i\zeta_{h02})\gamma_{h02}^2}{(1+2i\zeta_{h00})\gamma_{h00}^2}E(0,2) & \cdots \\ 0 & 1 & 0 & \dfrac{(1+2i\zeta_{\alpha01})\gamma_{\alpha01}^2}{(1+2i\zeta_{\alpha00})\gamma_{\alpha00}^2}E(0,1) & 0 & \cdots \\ 1 & 0 & \dfrac{(1+2i\zeta_{h11})\gamma_{h11}^2}{(1+2i\zeta_{h10})\gamma_{h10}^2}E(1,1) & 0 & \dfrac{(1+2i\zeta_{h12})\gamma_{h12}^2}{(1+2i\zeta_{h10})\gamma_{h10}^2}E(1,2) & \cdots \\ 0 & 1 & 0 & \dfrac{(1+2i\zeta_{\alpha11})\gamma_{\alpha11}^2}{(1+2i\zeta_{\alpha10})\gamma_{\alpha10}^2}E(1,1) & 0 & \cdots \\ \vdots & \vdots & \vdots & \vdots & \vdots & \end{bmatrix} \qquad (7)$$

The complex stiffness and mass matrices are represented by [G] and [D], respectively. The {X} and {Y} vectors represent the physical blade displacements and the modal displacements, respectively. The [E], [A], and {AD} matrices are defined in reference [2] and are not repeated here for brevity. Using the relationship

$$\{X\} = [E]\{Y\} \qquad (8)$$

to remove the physical blade displacements from the system of equations results in

$$[P]\{Y\} = \gamma[Q]\{Y\} - [G][E]\{AD\} \qquad (9)$$

where

$$[P] = [G][E][A] + [D][E] \qquad (10)$$

The aeroelastic stability of the system can be determined from the eigenvalues, γ's, of the generalized problem

$$[[P] - \gamma[Q]]\{Y\} = 0 \qquad (11)$$

The relation between the eigenvalue, γ, and the complex frequency is

$$\frac{i\omega}{\omega_0} = \frac{i}{\sqrt{\gamma}} = \bar{\mu} \pm i\bar{\nu} \qquad (12)$$

Therefore, $\bar{\mu}$ is a measure of the damping or stability of the mode and $\bar{\nu}$ is a measure of the frequency. For the discussion of results to follow, a mode is considered to be stabilized when $\bar{\mu}$ becomes more negative and destabilized when it becomes more positive. The aeroelastic response can be derived from equation (9) and is

$$\{Y\} = [\gamma[Q] - [P]]^{-1}[G][E][AD] \qquad (13)$$

II Results and Discussion

A computer program was written to calculate the stability and response of a mistuned bladed-disk including both aerodynamic and structural coupling of the blades using the formulation presented in the last section. In this program it is possible to consider arbitrary mistuning of the blade un-coupled bending and torsional frequencies and damping coefficients. The quantities γ_{hsr} and $\gamma_{\alpha sr}$, see equation (4), must be supplied as input to this formulation. The approach used herein is to calculate the frequencies of the tuned rotor for each nodal diameter up to $N/2$ ($N/2-1$ for an odd number of blades).

$$\gamma_{hr} = \omega_{hr}/\omega_0 = \gamma_{hN-r}$$

$$\gamma_{\alpha r} = \omega_{\alpha r}/\omega_0 = \gamma_{\alpha N-r} \qquad (14)$$

For example, for a 24 bladed rotor in vacuum the frequency of the $r = 5$ mode is the same as that of the $r = 19$ mode since the structural properties cannot distinguish between a forward and backward traveling wave of the same nodal diameter. There are a number of methods available to calculate the quantities γ_{hsr} and $\gamma_{\alpha sr}$; the most general being the finite element method. However, it is sufficient for the purposes of this paper to assume that the mistuned system frequencies are given by

$$\gamma_{hsr} = \gamma_{hr}(\omega_{hs}/\omega_0)$$

$$\gamma_{\alpha sr} = \gamma_{\alpha r}(\omega_{\alpha s}/\omega_0) \qquad (15)$$

in which ω_{hs} and $\omega_{\alpha s}$ are the blade alone frequencies. This has been shown in [22] to be a valid assumption for small deviations in ω_{hs} and $\omega_{\alpha s}$ when the bladed-disk motion is blade dominated.

In the following sections two different rotors are analyzed: (i) a twelve bladed rotor representative of a set of blades connected by midspan shrouds (considered in [4]) and (ii) a more realistic unshrouded bladed disk representative of an advanced fan stage. Both alternating and random torsional frequency mistuning are considered. Since the effects of bending-torsion coupling were examined in [1] and [2], the emphasis in this paper is on the torsional motion. As a result the predominantly bending modes are not shown in the results to follow.

(a) Flutter. To provide a check for a special case of the present formulation and computer code, an aeroelastic stability analysis is conducted for a tuned rotor with 12 blades which was considered in [4]. The blades have significant structural coupling due to the presence of midspan shrouds. In addition to providing a check, the results give an example of the effect of structural coupling due to midspan shrouds on the system eigenvalues. The formulaton in [4] includes only single degree-of-freedom torsional blade motion. As a result, the bending frequencies in the present formulation are set to 10 times the torsional frequencies. This minimizes the inertial coupling between the bending and torsional motions and provides a direct comparison with the results of [4]. The parameters of interest for this rotor are given in Table 1. The dependency of blade torsional frequencies on nodal diameter
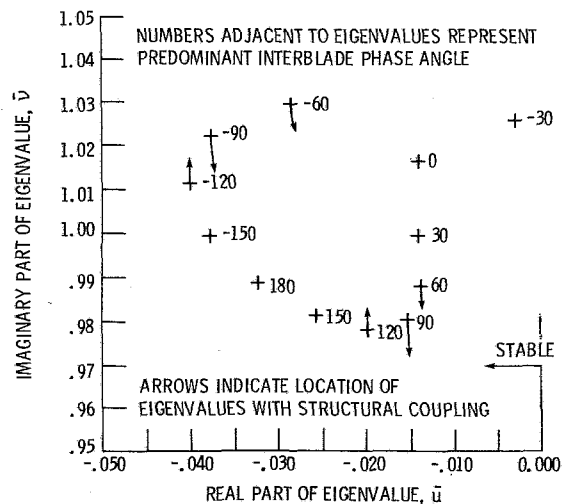

Fig. 2   Eigenvalues of rotor with 12 blades (tuned), M = 0.84

Table 1 Rotor parameters

Parameter	Symbol	Reference [4] rotor	Rotor I
Reduced frequency	k	0.75	0.441
Number of blades	N	12	32
Stagger angle	ξ	60°	62°
Elastic axis position	a	0.2	0
Gap-to-chord ratio	s/c	0.8	0.777
Mass ratio	μ_s	73.9	141
Radius of gyration	$r_{\alpha s}$	0.611	0.47
Elastic axis-C.G. offset	$x_{\alpha s}$	−0.2	0
Mach number	M	0.84	1.18
Bending to torsion frequency ratio tuned	$\omega_{hs}/\omega_{\alpha s}$	10	0.3

Table 2 Frequency distribution (in vacuum)

r	$\gamma_{\alpha r}$
0	1.0000
1 and 11	.99928
2 and 10	.99724
3 and 9	.98396
4 and 8	1.0027
5 and 7	1.0004
6	1.0000
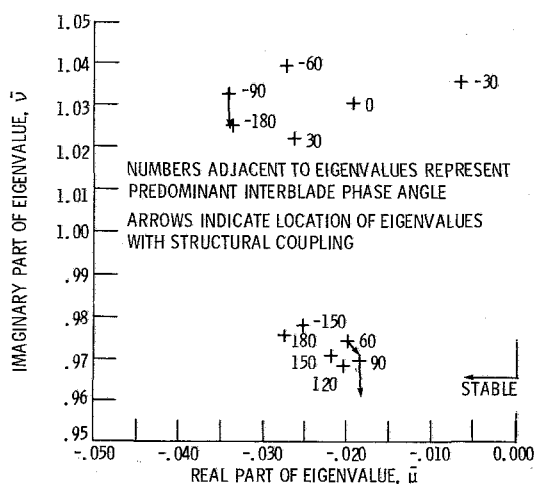
Fig. 3 Eigenvalues of rotor with 12 blades (5 percent alternating mistuning), M = 0.84

Fig. 4 Assumed frequency distribution of rotor I (in vacuum)
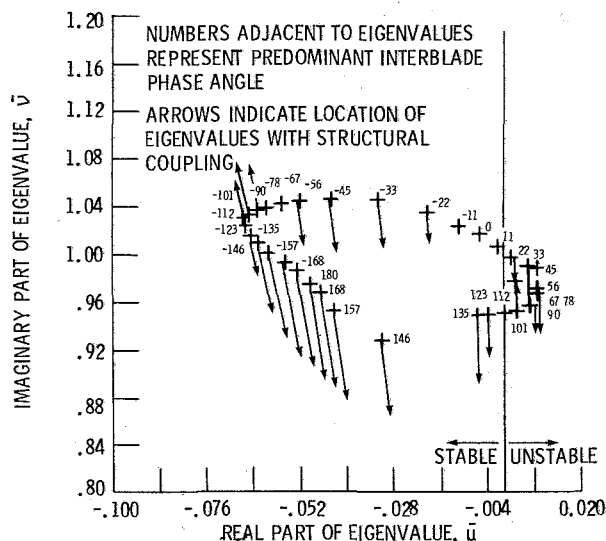
Fig. 5 Eigenvalues of rotor I (tuned), M = 1.18

as taken from [4] is given in Table 2 for the reader's convenience. Figure 2 presents the eigenvalues for two cases of the tuned system: (i) no structural coupling and where the uncoupled blade torsional frequencies are equal to ω_0 and (ii) a flexible shroud ring in which the frequency dependence is given in Table 2. In this figure the plus symbol represents the eigenvalue for the case in which there is no structural coupling. The number adjacent to the symbol gives the predominant interblade angle for that eigenvalue. The arrow represents the location to which the eigenvalue moves (the end of the arrowhead) when the effects of structural coupling are considered. Note that for some modes the movement is so small that the arrows are not drawn. Within plotting accuracy, the results obtained using the present formulation are identical to those of Fig. 6 in [4]. Note that there are different eigenvalue definitions between this paper and the reference. Since $\bar{\mu}$ only changes slightly, the addition of structural coupling has little effect on the stability of the individual modes. As expected, for certain modes the frequency is significantly affected. As was stated in [4], it is believed that this behavior is representative of shrouded blades when the shroud ring is relatively stiff compared to the blades.

To determine the effects of structural coupling on the

coupling between the interblade phase angle modes in the presence of mistuning, this rotor was analyzed with 5 percent alternating mistuning. With this type of mistuning the torsional frequency alternates from blade to blade as you proceed around the disk. All odd numbered blades would have the identical frequency and all even numbered blades have the same frequency. The percent mistuning being defined as the difference in these two frequencies divided by the average. The resulting eigenvalues both with and without structural coupling are given in Fig. 3. The structural coupling generally only affects the frequency of the modes. However, it is interesting to note that the predominantly 60 degree in-
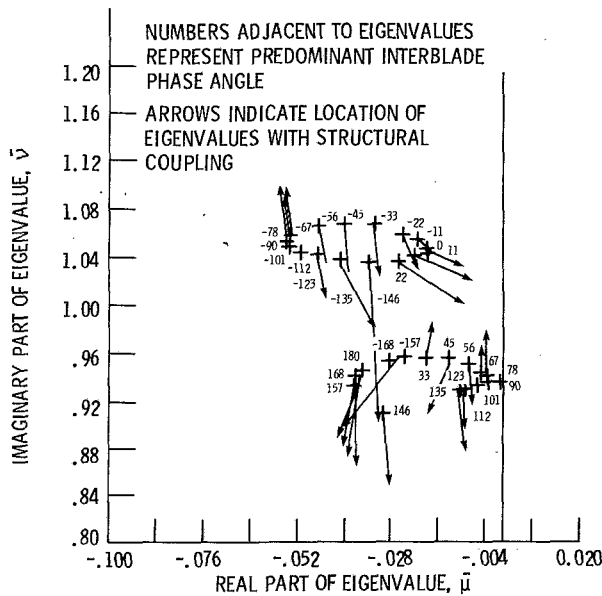
Fig. 6 Eigenvalues of rotor I (10 percent alternating mistuning), M = 1.18

Fig. 8 Eigenvalues of rotor I, no structural coupling (random mistuning), M = 1.18

Fig. 7 Random torsional frequency distribution
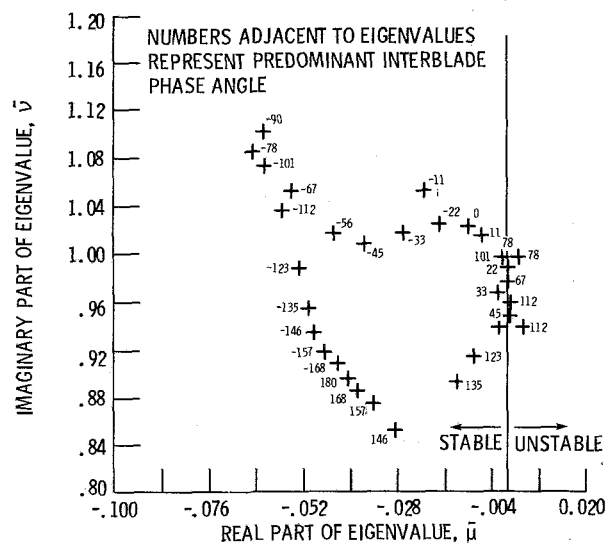
Fig. 9 Eigenvalues of rotor I, with structural coupling (random mistuning), M = 1.18
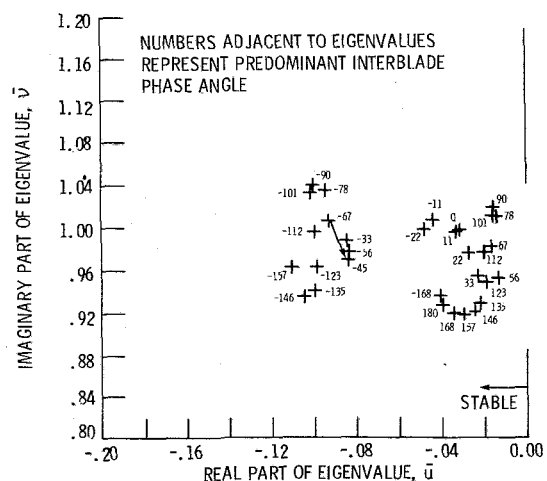
Fig. 10 Eigenvalues of rotor I, M = 0.8 (tuned)

terblade phase angle mode (2 nodal diameter) is somewhat destabilized.

To determine the effects of structural coupling on a more realistic rotor, an advanced fan stage called Rotor I is now analyzed. The parameters of this rotor are given in Table 1. The assumed dependency of the tuned torsional frequencies (in vacuum) versus the nodal diameter is shown in Fig. 4. This assumption is based on previous experience using finite element techniques to predict the natural frequencies of similar bladed-disks. Figure 5 shows the effect of the structural coupling on the tuned system. As in the previous case, the effect is to significantly change the frequency of certain modes with little effect on the stability. This behavior is to be expected since each of the nodal diameter modes is uncoupled from the others. Note that there are still a number of unstable modes.

Rotor I is now analyzed with the assumption of alternate mistuning. As seen in Fig. 6, all of the modes of Rotor I are stable in the presence of 10 percent alternating mistuning without structural coupling. However, certain modes are significantly destabilized by the inclusion of structural coupling. Although all of the modes are stable, this behavior

Fig. 11 Tuned 5E response of rotor I, M = 0.8
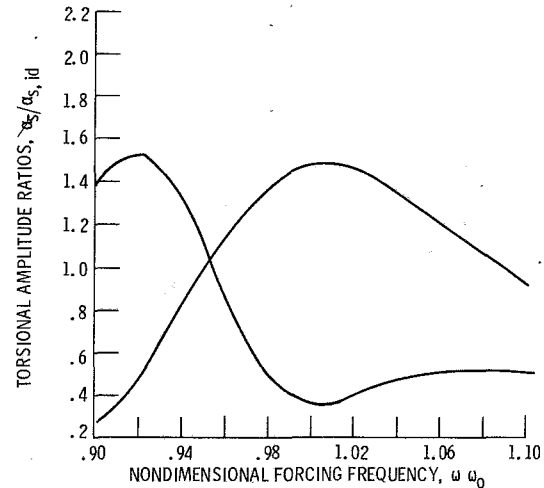
Fig. 13 5E response of rotor I with 10 percent alternating mistuning, M = 0.8
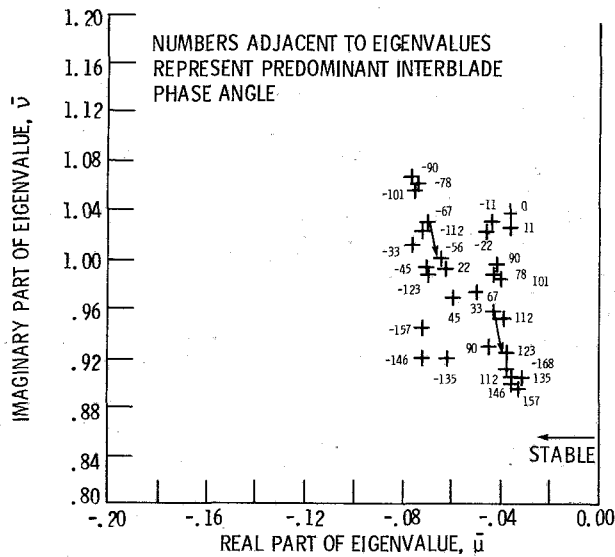
Fig. 12 Eigenvalues of rotor I, M = 0.8 (10 percent alternating mistuning)
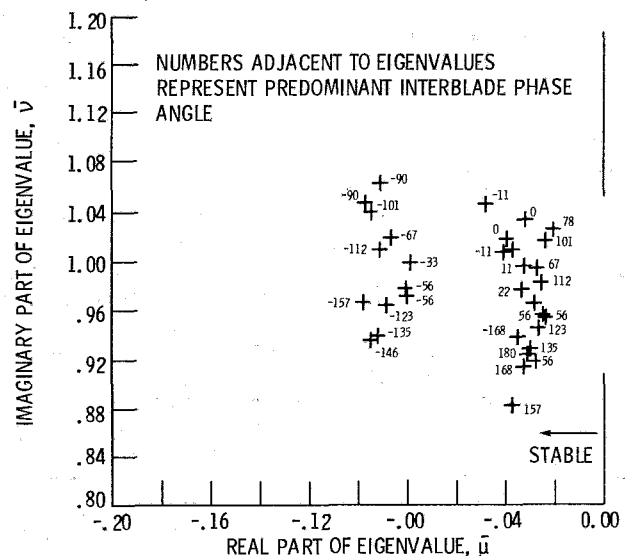
Fig. 14 Eigenvalues of rotor I, M = 0.8 (Random mistuning)

could result in a significant increase in aeroelastic response since the effective damping is decreased.

Random mistuning is now considered. Using the blade frequency distribution shown in Fig. 7 (mean of 1.001 and standard deviation of 0.034, a typical production distribution), the eigenvectors of Rotor I without structural coupling were calculated and are displayed in Fig. 8. The analysis was repeated including the effects of structural coupling and the corresponding results are shown in Fig. 9. Comparing Figs. 8 and 9, it is seen that both the frequency and stability of the modes is significantly affected. It is important to note tha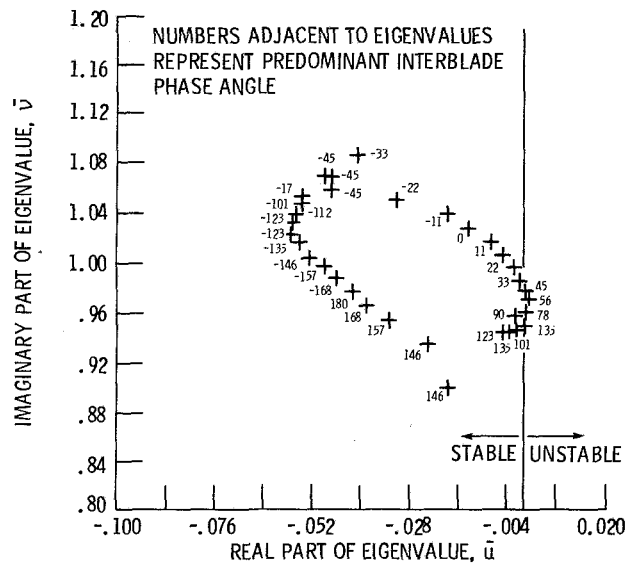t the predominantly 45 deg interblade phase angle mode is moved into the unstable region. Although not shown, the blade amplitude distributions for most of the modes are drastically different when comparing the results with and without structural coupling.

(b) Aeroelastic Response. In the present formulation it is possible to consider an excitation from symmetrically spaced obstructions located upstream from the blades. The number of obstructions is known as the engine order of the excitation and is usually represented by an integer followed by "E." For example, 5E would represent a perfectly sinusoidal excitation resulting from 5 upstream obstructions. For a more detailed

description of the formulation of the aeroelastic response problem see [1] and [2].

To illustrate the effect of structural coupling on response, Rotor I is again analyzed with the torsional frequency dependency shown in Fig. 4. The 5E resonance is investigated for the tuned, 10 percent alternating mistuned, and randomly mistuned conditions. The Mach number is 0.8 and the reduced frequency is 0.6. All other parameters are the same as those given in Table 1. These parameters were chosen so that all modes of the rotor are stable in the tuned condition.

The eigenvalues for the tuned condition including structural coupling are shown in Fig. 10. The movement of the eigenvalue of interest (-56 deg interblade phase angle or 5 nodal diameter backward traveling wave) is represented by the arrow in Fig. 10. That is, the tail of the vector represents the position of the eigenvalue without structural coupling. The resonance peaks both with and without structural coupling are shown in Fig. 11. As expected, the frequency at which the rotor has maximum amplitude is approximately 4 percent lower with structural coupling. In addition, the maximum amplitudes are approximately equal.

The eigenvalues for the system with 10 percent alternating mistuning are shown in Fig. 12. For this type of mistuning the 5E forcing function can excite only the -56 and 123 deg
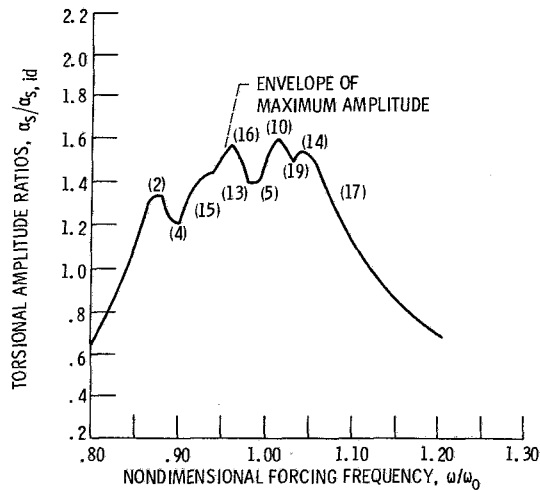
Fig. 15 5E response of rotor I with random mistuning, M = 0.8

interblade phase angle modes. The movement of these modes, depicted by the arrows in Fig. 12, represents primarily a change in frequency. As is the case for alternate mistuning, the single resonance peak is replaced by twin peaks which are shown in Fig. 13. Although not shown, the curves without structural coupling have the same general shapes and amplitudes with only shifts in frequency.

The final case to be investigated is that of random mistuning. The in vacuum frequency distribution of Fig. 7 is again used. The system eigenvalues are shown in Fig. 14. Comparing these eigenvalues with those without structural coupling (not shown), it is found that both the frequency and stability of certain modes was significantly affected. However, since the 5E forcing function excites all of the interblade phase angle modes in this case, it is difficult to predict whether the amplitude of response will be larger or smaller than those of the rotor with no structural coupling. The response curve with multiple resonance peaks is shown in Fig. 15. As expected, blade 2 has the maximum response at low forcing frequencies and blade 17 has the maximum response at high forcing frequencies. Comparing this curve with that for no structural coupling (not shown), it was found that the inclusion of structural coupling had not significantly changed the overall response amplitudes. However, the blade-to-blade amplitude distributions have changed somewhat. For example, blades 10 and 14 have the highest amplitudes when the forcing frequency is approximately in the range 1 to 1.05. When there was no structural coupling, blades 3 and 13 were found to have the maximum amplitude in this forcing frequency range.

III Conclusions

The analyses of the effects of mistuning on coupled bending torsion flutter and response which were developed in [1] and [2] have been extended to include the effects of structural coupling between the blades. The following conclusions are reached based on the parametric studies presented herein for bladed-disks in which the motion is dominated by the blades:

1 The addition of structural coupling can affect both the frequency and aeroelastic stability.

2 The stability is significantly affected only when the system is mistuned. The affect can be either beneficial or detrimental depending on the type of mistuning, the type of structural coupling, and the cascade parameters.

3 The resonant frequencies can be significantly affected by structural coupling in both tuned and mistuned systems, however, the peak response is significantly affected only for the latter.

References

1 Kaza, K. R. V., and Kielb, R. E., "Flutter and Response of a Mistuned Cascade in Incompressible Flow," *AIAA Journal*, Vol. 20, No. 8, Aug. 1982, pp. 1120–1127.

2 Kielb, R. E., and Kaza, K. R. V., "Aeroelastic Characteristics of Cascade of Mistuned Blades in Subsonic and Supersonic Flows," ASME Paper No. 81-DET-122, Sept. 1981.

3 Kielb, R. E., "Aeroelastic Characteristics of a Mistuned Bladed-Disk Assembly," Ph.D. dissertation, The Ohio State University, Columbus, Ohio, 1981.

4 Srinivasan, A. V., "Influence of Mistuning on Blade Torsional Flutter," R80-914545-16, United Technologies Research Center, East Hartford, Conn., Aug. 1980. (NASA CR-165137)

5 Smith, S. N., "Discrete Frequency Sound Generation in Axial Flow Turbomachines," A. R. C. R&M No. 3709, 1973.

6 Adamczyk, J. J., and Goldstein, M. E., "Unsteady Flow in a Supersonic Cascade with Subsonic Leading-Edge Locus," *AIAA Journal*, Vol. 16, No. 12, Dec. 1978, pp. 1248–1254.

7 Wagner, J. T., "Coupling of Turbomachine Blade Vibrations Through the Rotor," ASME JOURNAL OF ENGINEERING FOR POWER, Vol. 89, No. 4, Oct. 1967, pp. 502–512.

8 Dye, R. C. F., and Henry, T. A., "Vibration Amplitudes of Compressor Blades Resulting from Scatter in Blade Natural Frequencies," ASME JOURNAL OF ENGINEERING FOR POWER, Vol. 91, No. 3, July 1969, pp. 182–188.

9 Ewins, D. J., "Bladed Disk Vibration — A Review of Techniques and Characteristics," *Recent Advances in Structural Dynamics*, Vol. 1, edited by M. Petyt, University of Southampton, Southampton, England, 1980, pp. 187–210.

10 El-Bayoumy, L. E., and Srinivasan, A. V., "Influence of Mistuning on Rotor-Blade Vibrations," *AIAA Journal*, Vol. 13, No. 4, Apr. 1975, pp. 460–464.

11 Whitehead, D. S., "Effect of Mistuning on the Vibration of Turbomachine Blades Induced by Wakes," *Journal of Mechanical Engineering and Science*, Vol. 8, No. 1, Mar. 1966, pp. 15–21.

12 Whitehead, D. S., "Torsional Flutter of Unstalled Cascade Blades at Zero Deflections," ARC R and M-3429, 1964.

13 Hanamura, Y., and Tanaka, H., "A Modification of Flutter Characteristics by Changing Elastic Nature of Neighboring Blades in Cascades," Tokyo Joint Gas Turbine Congress, Gas Turbine Society of Japan, Tokyo, 1977, pp. 418–425.

14 Ford, R. A. J., and Foord, C. A., "An Analysis of Aeroengine Fan Flutter Using Twin Orthogonal Vibration Modes," ASME Paper 79-GT-126, Mar. 1979.

15 Hanamura, H., "Flutter of Cascading Blade Row," Institute of Space and Aeronautical Science, University of Tokyo, Vol. 36, No. 1, Report No. 459, 1971, pp. 1–36.

16 Shiori, J., "Nonstall Normal Mode Flutter in Annular Cascades, Part II-Experimental Study," *Transactions of Japan Society of Aeronautical Engineering*, Vol. 1, No. 1, 1958, pp. 26–45.

17 Carta, F. O., "Coupled Blade-Disk-Shroud Flutter Instabilities in Turbojet Engine Rotors," ASME JOURNAL OF ENGINEERING FOR POWER, Vol. 89, No. 3, July 1967, pp. 419–426.

18 Rao, B. M., and Kronenburger, L., Jr., "Aeroelastic Characteristics of a Cascade of Blades," AFOSR-TR-78-1027 Texas A&M Research Foundation, College Station, Texas, Feb. 1978.

19 Bendiksen, O., and Friedmann, P., "Coupled Bending-Torsion Flutter in Cascades," *AIAA Journal*, Vol. 18, No. 2, Feb. 1980, pp. 194–201.

20 Dugundji, J., "Flutter Analysis of a Tuned Rotor with Rigid and Flexible Disks," GT&PDL Report No. 146, M. I. T., Cambridge, Mass. July 1979.

21 Kaza, K. R. V., and Kielb, R. E., "Coupled Bending-Bending-Torsion Flutter of a Mistuned Cascade With Nonuniform Blades," AIAA Paper 82-0726, 1982.

22 Crawley, E. F., Massachusetts Institute of Technology, "Private Communication on Stiffness Matrix Perturbations."

Flutter of Mistuned Turbomachinery Rotors

O. O. Bendiksen

Assistant Professor,
Mechanical and Aerospace Engineering,
Princeton University,
Princeton, N.J. 08540

An investigation of the fundamental aspects of flutter in mistuned turbomachinery rotors is presented. Perturbation methods are used to obtain asymptotic solutions to arbitrary order in the mistuning parameter. These solutions require only the knowledge of the eigensolution of the tuned system, and thus provide efficient formulas for calculating the effect of mistuning without solving a new eigenvalue problem. Numerical results presented for design parameters representative of fan rotors indicate that a critical reduced frequency exists, below which mistuning alone cannot stabilize the rotor. The sensitivity of the stability boundaries to mistuning was found to depend fundamentally on relations between the left and right eigenvectors. For systems where the left and right eigenvectors form complex conjugate pairs, mistuning cannot destabilize the system unless the reduced frequency of the least stable mode is decreased by the perturbation. In general, only cascades and rotors with a single degree-of-freedom per blade belong to this class.

Introduction

The aeroelastic behavior of turbomachinery rotors is sensitive to relatively small variations in the natural frequencies or mode shapes between individual blades brought about by differences in their structural or inertial properties. Such differences, commonly referred to as "mistuning," are inherent in all real rotors due to material and manufacturing tolerances and, although small, can affect the amplitudes of individual blades by several hundred percent [1-3]. The high cycle fatigue life of high-amplitude blades can therefore be seriously reduced; hence, mistuning offers a plausible explanation for the existence of rogue blades [2]. Although the flutter boundaries exhibit similar sensitivity to mistuning, this phenomenon has received less attention, presumably because such effects are believed to be always stabilizing [4].

Results from recent research [5, 6] suggest the possibility of using mistuning as a passive flutter control. However, because mistuning generally introduces undesirable structural response characteristics of the blade-disk system, there is considerable danger in introducing intentional mistune into highly stressed airfoils that are otherwise susceptible to high cycle fatigue. This may limit the practical application of mistuning as a means for controlling flutter, unless reliable methods can be established for predicting the tradeoffs between flutter and forced response and the constraints involved.

This paper addresses the flutter aspect of this problem by attempting to identify the important characteristics of flutter of mistuned rotors from a theoretical standpoint. Although research to date has been very useful in calling attention to some key features of the aeroelastic behavior of mistuned rotors, calculations and numerical results presented tend to be rather specific, typically representing a single physical rotor. It is not possible to extrapolate or generalize such results without making additional calculations. The emphasis in this paper is therefore on identifying the basic characteristics of mistuned rotors in a manner which allows generalizations to be made regarding the aeroelastic behavior of certain classes of rotors of current interest.

In this approach the mistuned is considered a perturbed tuned rotor, where the perturbations are small, arbitrary changes in the inertial or structural operators, representing mistuning. The order of these perturbations is denoted by ϵ, and it is assumed that ϵ is small. Limit process expansions [7] of the aeroelastic eigenvalues and modes associated with the limit $\epsilon \rightarrow 0$, with certain other parameters fixed, can then be constructed to any order in the mistuning parameter ϵ. Such expansions provide insight into the order of the various effects, and are useful in visualizing how mistuning, which is only of order ϵ, can have a first-order effect on the flutter boundaries. These solutions require only the knowledge of the eigensolution of the tuned rotor and thus avoid the cost and numerical difficulties associated with solving the much larger aeroelastic eigenvalue problem for the mistuned rotor. Exact expressions are also obtained for the effect of alternating blade mistuning of arbitrary magnitude on the flutter boundaries, which provide an independent check on the accuracy of the asymptotic expansions as a function of ϵ.

Aeroelastic Equations

For the purpose of this paper, it will be assumed that the blade-disk system can be modeled using a finite number of degrees of freedom. The structural, inertial, and aerodynamic operators can then be represented by matrices of finite order.

This study is primarily concerned with the identification of general stability characteristics of mistuned rotors in terms of the mathematical properties of these operators. The actual construction of the corresponding matrices is therefore of secondary importance here, and any suitable procedure (e.g., Rayleigh-Ritz, Galerkin, or Finite Elements) may be used.

Tuned Rotor. Consider a rotor of N identical blades mounted identically at equidistant angular positions about an axially symmetric disk. Such a system, as well as its mistuned counterparts, is cyclic or periodic in the sense that the zeroth (reference) blade is adjacent to the $(N - 1)$th (last) blade. In a coordinate system rotating with the disk, any physical variable may therefore be considered periodic in the angular position variable, with a period of 2π. An important consequence of this is that certain rows (or columns) in the system matrices are cyclic permutations of each other.

The linearized equations of motion for the rotor system can be written in matrix form as

$$[M]\{\ddot{q}\} + [C]\{\dot{q}\} + [K]\{q\} = \{Q\} \qquad (1)$$

To keep the notation simple, it will be assumed that the equations have been suitably nondimensionalized. The generalized coordinate vector $\{q\}$ can, without loss of generality, be assumed partitioned as follows

$$\{q\}^T = \{\{q\}_0^T | \{q\}_1^T \} \ldots |\{q\}_{N-1}^T | \{q\}_d^T\} \qquad (2)$$

where $\{q\}_n$ and $\{q\}_d$ represent the degrees of freedom associated with the nth blade and the disk, respectively. The term "rotor" in this paper is limited to mean the bladed disk of a single stage, which is assumed to rotate with constant angular velocity about a fixed axis. The vectors $\{q\}_n$ are all of the same dimension, and describe the same physical degrees-of-freedom in the N local coordinate systems attached to the individual blades.

Equations (1) can be considered sufficiently general to include Coriolis forces as well, within the framework of linearized analysis. The generalized forces $\{Q\}$ represent both aerodynamic forces and external disturbances of nonaerodynamic origin. Because the equations are linear, the stability of equations (1) depends only on the aerodynamic forces $\{Q_A\}$ of $\{Q\}$, and these forces in turn depend both on the geometry and the motion of the bladed disk. If the blades

are modeled as typical sections, this dependence takes the form (inviscid flow)

$$\{Q_A\} = \{Q_A (k, M, \theta, \bar{s}, \sigma; \{\dot{q}\}, \{q\}, \{\ddot{q}\}, \ldots)\} \qquad (3)$$

If a distributed parameter model of the blades is used and the aerodynamic forces calculated by cascade theories applied in a strip theory fashion, k and M must be referred to some reference span location, and θ and $\bar{s}$ do not appear explicitly in equation (3).

In order to stay consistent with available unsteady cascade theories, the sytem will be assumed to execute simple harmonic motion, $\{q\} = \{q_0\} \exp (i\omega t)$. The aerodynamic forces can then conveniently be expressed in terms of nondimensional aerodynamic influence coefficients A_{ij} as follows

$$\{Q_A\} = \frac{\bar{\omega}^2}{\mu} [A]\{q\} \qquad (4)$$

If gyroscopic forces are present or damping forces are of the the viscous type, the aeroelastic eigenvalue problem takes the form

$$\left(-\bar{\omega}^2[M] + i\bar{\omega}[C] + [K] - \frac{\bar{\omega}^2}{\mu} [A]\right)\{q\} = 0 \qquad (5)$$

where, of course, $[A]$ still depends on ω through the reduced frequency k. If gyroscopic forces are neglected, it is convenient to model the structural damping differently, by multiplying the stiffness matrix by $(1 + ig)$. The aeroelastic eigenvalue problem can then be written in standard form as

$$[D]\{q\} = \lambda\{q\} \qquad (6)$$

where

$$\lambda = (1 + ig) / \bar{\omega}^2 \text{ and } [D] = [K]^{-1} \left([M] + \frac{1}{\mu} [A]\right) \qquad (7)$$

The cyclic structure of the matrices is best illustrated through examples. A simple model with a single elastic degree of freedom (bending or torsion) per blade is shown in Fig. 1(a). This model or its equivalent has been used by previous investigators [2, 8] in the study of forced response of mistuned rotors. Each blade is represented as a mass M_b on a cantilever spring K_b, and the effective mass and stiffness of the disk at the blade roots are represented by masses M_d and springs K_d and K_c. Corresponding to the generalized coordinates

$$\{q\}^T = \{q_0 q_1 \ldots q_{N-1} | q_N \ldots q_{2N-1}\} = \{q\}_b^T | \{q\}_d^T\} \qquad (8)$$

─────── **Nomenclature** ───────

a = location of elastic axis (Fig. 1(b))

$[A]$ = aerodynamic matrix

b, c = semichord and chord, respectively

g = structural damping

h = bending deflection (Fig. 1(b))

k = $\omega b / U$ = reduced frequency

$\bar{k}$ = $kM / (M^2 - 1)$

K_b, K_c, K_d = equivalent blade, coupling, and disk stiffness, respectively, in Fig. 1(a) model

K_h, K_α = blade bending and torsional stiffness, respectively, in Fig. 1(b) model

$[K]$ = stiffness matrix

L = lift, positive up, per unit span

m = mass per unit span of blade

M = free-stream Mach number; also aerodynamic moment per unit span about axis $x = ba$, positive clockwise (Fig. 1(b))

M_b, M_d = equivalent lumped mass of blade and disk, respectively, in Fig. 1(a) model

$[M]$ = mass matrix

N = number of blades in rotor

$\{q\}$ = generalized coordinate vector

r_α = radius of gyration, nondimensionalized with respect to semichord

s = blade spacing (Fig. 2)

$\bar{s}$ = s/b

$\bar{s}_2$ = $\bar{s} \cos \theta$

t = time

U = freestream velocity relative to blades

x_I = nondimensionalized CG-EA offset (Fig. 1(b))

α = torsional deflection, positive clockwise

ϵ = mistuning (perturbation) parameter

θ = stagger angle (Fig. 2)

λ = eigenvalue

μ = $m/\pi\rho_0 b^2$ = mass ratio of blade

ρ_0 = freestream air density

σ = interblade phase angle

ω = frequency in rad/s

ω_0 = reference frequency

$\bar{\omega}$ = ω/ω_0

$[\ ]^*$ = Hermitian conjugate

the mass and stiffness matrices are

$$[M] = \begin{bmatrix} [M]_b & \vdots & [0] \\ ------ & + & ----- \\ [0] & \vdots & [M]_d \end{bmatrix} ; [K] = \begin{bmatrix} [K]_b & \vdots & -[K]_b \\ ------ & + & ----- \\ -[K]_b & \vdots & [K]_D \end{bmatrix} \quad (9)$$

where
$$[M]_b = M_b[I]; \quad [M]_d = M_d[I]$$

$$[K]_b = K_b[I]; \quad [K]_D = (K_b + K_d)[I] + [K]_c$$

$$[K]_c = K_c \begin{bmatrix} 2 & -1 & 0 & 0 & \ldots & 0 & -1 \\ -1 & 2 & -1 & 0 & \ldots & 0 & 0 \\ . & & & & & & . \\ . & & & . & & & . \\ . & & & & . & & . \\ -1 & 0 & . & . & & -1 & 2 \end{bmatrix} \quad (10)$$

All the matrices in equation (10) are of order $N \times N$, and are, except for $[K]_c$ and $[K]_D$, simply scalar products of the identity matrix. All the submatrices are circulant [9]; each row is a circular shift right by one position of the previous row. This is a basic property of the tuned system, and holds for the most general case where the submatrices may be fully populated.

In many cases of practical interest the disk is much stiffer than the blades, and it is reasonable to eliminate the disk degrees-of-freedom through static condensation or any other suitable reduction procedure. The reduced $N \times N$ mass and stiffness matrices are then circulant, and share a complete set of N orthonormal eigenvectors

$$\{e\}_n^T = \frac{1}{\sqrt{N}} \{1 \quad e^{i\sigma_n} \quad e^{2i\sigma_n} \ldots e^{(N-1)i\sigma_n}\}$$

$$(n = 0, 1, \ldots, N-1) \quad (11)$$

where

$$\sigma_n = 2\pi n/N \text{ and } \{e\}_m^* \{e\}_n = \delta_{mn}$$

These are the system mode shapes for free vibration, in complex form. For this model with a single degree-of-freedom per blade, the $\{e\}_n$'s are also the eigenvectors of the aerodynamic matrix $[A]$ and thus also of $[D]$; hence, they are precisely the possible flutter modes of the system. To see this, consider the form of $[A]$ for this model. Now the A_{ij} coefficients are functions of the system mode shapes through the interblade phase, σ, so it is natural to expand $\{q\}$ in terms of the constant $- \sigma$ modes $\{e\}_n$

$$\{q\} = \sum_{n=0}^{N-1} \alpha_n \{e\}_n = [E]\{\alpha\} \quad (12)$$

where

$$[E] = [\{e\}_0 \{e\}_1 \ldots \{e\}_{N-1}]; \{\alpha\}^T = \{\alpha_0 \alpha_1 \ldots \alpha_{N-1}\} (13)$$

It follows from equations (11-12) that $[E]$ is a symmetric unitary matrix, and therefore

$$[E]^{-1} = [E]^* \quad (14)$$

$$\{\alpha\} = [E]^*\{q\} \quad (15)$$

The generalized force Q_n acting on the nth blade due to say, torsional oscillations of the blades, can now be written down as

$$Q_n = \frac{\bar{\omega}^2}{\mu} \sum_{m=0}^{N-1} \alpha_m A_{22}(\sigma_m) e^{in\sigma_m} = \frac{\bar{\omega}^2}{\mu} \{e\}_n^T [\tilde{A}]\{\alpha\} \quad (16)$$

where $[\tilde{A}]$ is diagonal with elements $A_{22}(\sigma_m)$, and Q_n has been nondimensionalized with respect to $\mu\pi\rho_0 b^4 \omega_0^2$ to make A_{22} consistent with equation (8) of [10]. Harmonic time dependence is implied in equations (12, 15-16), that is, $\{\alpha\} = \{\alpha_0\}$ exp $(i\omega t)$, etc. The generalized force (moment) vector becomes

$$\{Q_A\} = \frac{\bar{\omega}^2}{\mu} [E][\tilde{A}][E]^*\{q\} \quad (17)$$

Thus

$$[A] = [E][\tilde{A}][E]^{-1}; [\tilde{A}] = [E]^{-1}[A][E] \quad (18)$$

That is, $[A]$ is obtained from $[\tilde{A}]$ through a similarity transformation. They are therefore similar matrices and as such have identical eigenvalues, which in this case are simply the coefficient $A_{22}(\sigma_m)$; $m = 0, 1, \ldots, N-1$. Since $[\tilde{A}]$ is diagonal, it follows from equation (18) that the vectors $\{e\}_n$ are the eigenvectors of $[A]$, and thus of $[D]$, as asserted earlier. The corresponding eigenvalues of $[D]$ are

$$\lambda_n = \{e\}_n^* [D]\{e\}_n = \frac{1}{\bar{\omega}_{0n}^2} \left[1 + \frac{A_{22}(\sigma_n)}{\mu r_\alpha^2} \right] \quad (19)$$

where $\bar{\omega}_{on}$ is the corresponding natural frequency of the system in vacuum. In the absence of structural damping, flutter occurs when $Im(A_{22}) > 0$. Clearly, it is correctly predicted by performing a single-blade analysis and examining all permissible phase angles σ_n; $n = 0, 1, \ldots, N-1$, in accordance with the well-known results obtained by Lane [11].

This procedure is readily generalized to a model with p degrees-of-freedom per blade. Equations (17-18) still hold, but the columns of $[E]$ now consist of the orthonormal vectors $\{e_p\}_n$ obtained by repeating p times each element of $\{e\}_n$. Denoting the new version of $[E]$ by $[E_p]$, then $[E_p]$, has columns $\{e_p\}_n$, each repeated p times

$$[E_p] =$$

$$[\{e_p\}_0 \ldots \{e_p\}_0 | \{e_p\}_1 \ldots \{e_p\}_1 | \ldots | \{e_p\}_{N-1} \ldots \{e_p\}_{N-1}]$$

$$p \text{ times}$$

where $\quad (20)$

$$\{e_p\}_n^T = \frac{1}{\sqrt{pN}} \{1 \ldots 1 | e^{i\sigma_n} \ldots e^{i\sigma_n} | \ldots | e^{i(N-1)\sigma_n} \ldots \}$$

Note that $[E_p]$ is also unitary; thus equations (14, 15) continue to hold when $[E]$ is replaced by $[E_p]$. The "unassembled" aerodynamic matrix $[\tilde{A}]$ is a banded matrix with submatrices $[\hat{A}(\sigma_m)]$ of order $p \times p$ along its main diagonal, where $[\hat{A}(\sigma_m)]$ are the aerodynamic matrices of the reference blade in local blade coordinates for the permissible phase angles σ_m. For example, for the typical section model shown in Fig. 1(b), the elements of $[\hat{A}]$ are the A_{ij} coefficients defined in equations (7, 8) of [10].

Because $[A]$ and $[\tilde{A}]$ are similar, they have the same eigenvalues; these are precisely the eigenvalues of the submatrices $[\hat{A}(\sigma_m)]$. Unlike the SDOF case, however, stability is not governed by these eigenvalues, nor are the eigenvectors of $[A]$ the possible flutter mode shapes of the system. The flutter mode is still characterized by equal blade amplitudes and constant interblade phase, owing to cyclic relations between each pth row (and column) of $[D]$, but the amplitude and phase relations between the p individual blade modes can only be determined by solving the aeroelastic eigenvalue problem.

Mistuned Rotor. Mathematically, the difference between tuned and mistuned rotors can be defined in terms of the cyclic properties of the system matrices. For a tuned rotor with p degrees of freedom per blade, with $\{q\}$ partitioned as before, the $(n+p)$th row (or column) of any of these matrices is a cyclic permutation of the nth row (column), consisting of a circular shift right (down) by p positions, for all $1 \leq n \leq p(N-1)$. Formally, then, mistuning can be considered present whenever this cyclic structure is violated.

The governing aeroelastic equations and the procedure for synthesizing the matrices remain unchanged, but the submatrices representing mass and stiffness properties of the

individual blades are generally different. For the most general case of mistuning, all cyclic properties of $[D]$, which permit the aeroelastic analysis to be carried out for a single "equivalent" blade, are lost. The order of the eigenvalue problem which must be solved thus increases N-fold, where N is the number of blades in the rotor. Since N is typically in the range 20–100, this size increase represents a considerable increase in computational effort. For cases of practical interest the mistuning is small, and it is reasonable to use perturbation methods to evaluate the effect of mistuning on the flutter boundaries.

Perturbation Analysis

Basic Concepts. A mistuned rotor can be considered a "perturbed" tuned rotor, obtained by introducing small changes in the system mass or stiffness matrices. In the aeroelastic eigenvalue problem, equation (6), the perturbed matrix $[\tilde{D}]$ can then be written as

$$[\tilde{D}] = [D] + \epsilon[d] \qquad (21)$$

where ϵ is a small "mistuning parameter," and for scaling purposes it is assumed that $|d_{ij}| \leq 1$. The perturbed mass and stiffness matrices are written in similar form.

In the application of the method we are interested in determining the dependence of the eigensolutions of equation (6) on the parameter ϵ and the perturbation matrix $[d]$. In the limit $\epsilon \to 0$ these solutions are asymptotic to the exact and presumed known solution of the tuned system, corresponding to the limiting value $\epsilon = 0$. The solution of the perturbed system is sought in terms of asymptotic sequences involving the parameter ϵ. For further details on the underlying concepts of such limit process expansions, ordering, etc., see [7]. In calculating the terms of these sequences, it is important to understand which variables are kept fixed in the associated limit $\epsilon \to 0$.

A number of investigations of eigensolution sensitivity based on Taylor series expansions have been published recently (e.g., [12–15]), motivated to a large extent by problems in optimum design. This approach is natural in numerical optimization procedures, where Taylor series approximations play a central role and derivatives of dependent system variables with respect to design parameters can be calculated analytically. As a perturbation procedure, it is clearly needlessly restrictive, since it presupposes that the eigenvalues and eigenvectors are analytic functions of the perturbations Δx_i of the independent design variables x_i at $\Delta x_i = 0$. It is well known, for example, that for multiple eigenvalues this assumption is generally incorrect, even if the elements of $[D]$ are analytic functions of Δx_i as $\Delta x_i \to 0$ [16].

Multiple eigenvalues do, in fact, occur in the free vibration problem of axially symmetric structures, such as a tuned blade-disk system, but are "split" when aerodynamic forces or Coriolis forces are introduced. There are still good reasons for keeping the perturbation analysis within the framework of asymptotic expansions. As examples we mention the ability to consider singular perturbation problems, and the relative ease by which the transition from matrix to differential operators can be made.

Asymptotic Expansions. It will be assumed that the unperturbed (tuned) system has only simple eigenvalues. The procedure is readily extended to the degenerate case. Assume furthermore that the nth perturbed eigenvalue and corresponding eigenvector of equation (6) can be written as asymptotic sequences

$$\tilde{\lambda}_n = \lambda_n + \epsilon \nu_1 + \epsilon^2 \nu_2 + \ldots$$
$$\{\tilde{\phi}\}_n = \{\phi\}_n + \epsilon\{\psi\}_1 + \epsilon^2 \{\psi\}_2 + \ldots \qquad (22)$$

where ν_m, $\{\psi\}_m$ are independent of ϵ but functions of the

variables affecting the unperturbed aeroelastic eigenvalue problem, i.e. k, M, etc. The form of these expansions is readily established for the case where k, M, and μ are kept fixed as $\epsilon \to 0$; then equation (6) becomes an algebraic eigenvalue problem, for which the assumed form holds [17]. A different limit of practical interest has M, μ fixed but allows k to vary consistent with λ_n; this case is more complicated and will be considered later.

Substituting equations (21, 22) into equation (6) and collecting terms in powers of ϵ, the folowing equations are obtained in addition to the original equation (6)

$$0(\epsilon): \quad ([D] - \lambda_n[I])\{\psi\}_1 = \nu_1\{\phi\}_n - [d]\{\phi\}_n \qquad (23)$$

$$0(\epsilon^2): \quad ([D] - \lambda_n[I])\{\psi\}_2 = \nu_1\{\psi\}_1 + \nu_2\{\phi\}_n - [d]\{\psi\}_1 \qquad (24)$$

The $\{\psi\}_m$'s can be expanded in terms of the normalized eigenvectors $\{\phi\}_n$ of the tuned system

$$\{\psi\}_m = \sum_{n=1}^{M} c_{mn}\{\phi\}_n$$
$$c_{mn} = \{\phi^L\}_n^T \{\psi\}_m / \{\phi^L\}_n^T \{\phi\}_n \qquad (25)$$

where $\{\phi^L\}_n$ is the normalized left eigenvector of $[D]$ corresponding to λ_n. Also, $\{\overline{\phi^L}\}_n$ is the eigenvector corresponding to the eigenvalue $\overline{\lambda}_n$ of $[D]^*$, the Hermitian adjoint of $[D]$.

Since λ_n is an eigenvalue of the homogeneous part of equations (23, 24), the nonhomogeneous equations only have solutions if a solvability condition is satisfied. This condition requires $\{\phi^L\}_n$ to be orthogonal to the right-hand side of the equations, as is readily verified by premultiplying by $\{\phi^L\}_n^T$, using equation (25), and recognizing that the left and right eigenvectors form a biorthogonal set. For equation (23), the result is

$$(\lambda_m - \lambda_n)c_{1m}\{\phi^L\}_m^T\{\phi\}_m$$
$$= \nu_1\{\phi^L\}_m^T\{\phi\}_n - \{\phi^L\}_m^T[d]\{\phi\}_n \qquad (26)$$

Set $m = n$ to obtain (the solvability condition)

$$\nu_1 = r_{nn}/s_n \qquad (27)$$

where $r_{mn} = \{\phi^L\}_m^T[d]\{\phi\}_n$; $s_n = \{\phi^L\}_n^T\{\phi\}_n$

For $m \neq n$, we obtain

$$c_{1m} = r_{mn}/(\lambda_n - \lambda_m)s_m \qquad (28)$$

The magnitude of c_{1n} is arbitrary, since $c_{1n}\{\phi\}_n$ is a solution of the homogeneous part of equation (33). Now c_{1n} can be taken to be real, as it simply scales the component of the unperturbed eigenvector $\{\phi\}_n$ in the perturbed solution $\{\tilde{\phi}\}_n$. The value of c_{1n} can then be found by imposing the normalization condition $\{\tilde{\phi}\}_n^*\{\tilde{\phi}\}_n = 1$, to 0 (ϵ), from which one concludes that $c_{1n} = 0$. The first-order correction to $\{\phi\}_n$ then becomes

$$\{\psi\}_1 = \sum_{m=1}^{M}{}' \frac{r_{mn}}{(\lambda_n - \lambda_m)s_m}\{\phi\}_m \qquad (29)$$

where the prime on the summation sign indicates that the term $m = n$ is to be omitted.

The second-order correction terms are calculated by the same procedure, and one obtains

$$\nu_2 = \frac{1}{s_n}\sum_{m=1}^{M} c_{1m}r_{nm} = \frac{1}{s_n}\sum_{m=1}^{M}{}' \frac{r_{mn}r_{nm}}{(\lambda_n - \lambda_m)s_m} \qquad (30)$$

For $m \neq n$

$$c_{2m} = \frac{1}{(\lambda_n - \lambda_m)}\left[\frac{1}{s_m}\sum_{j=1}^{M} r_{mj}c_{1j} - \nu_1 c_{1m}\right] \qquad (31)$$

while for $m = n$

$$c_{2n} = -\frac{1}{2}\sum_{j=1}^{M} |c_{1j}|^2$$

Higher order terms in the asymptotic sequences are calculated in the same manner.

Mass or Stiffness Perturbations. In order to identify the effects of mass or stiffness perturbations individually, it is convenient to consider the aeroelastic eigenvalue problem in the general form

$$([B] - \lambda[K])\{q\} = 0$$

where $\qquad\qquad\qquad\qquad\qquad\qquad\qquad\qquad\qquad$ (32)

$$[B] = [M] + \frac{1}{\mu}[A]$$

For mass perturbations, let $[\tilde{M}] = [M] + \epsilon[m]$, then it is easy to verify that the perturbation equations are of the same basic form as equations (23, 24), with the substitutions $[D] \rightarrow [B]; [I] \rightarrow [K]$. Let

$$s_n^k = \{\phi^L\}_n^T[K]\{\phi\}_n \ ; \ t_{mn} = \{\phi^L\}_m^T[m]\{\phi\}_n \qquad (33)$$

then the substitutions $s_n \rightarrow s_n^k$; $r_{mn} \rightarrow t_{mn}$ in the formulas previously obtained yield the corresponding values for mass perturbations, i.e., $\nu_1 = t_{nn}/s_n^k$, etc.

For stiffness perturbations, $[\tilde{K}] = [K] + \epsilon[k]$, the equations obtained are slightly different than equations (23, 24)

$$O(\epsilon): \quad ([B] - \lambda_n[K])\{\psi\}_1 = \nu_1[K]\{\phi\}_n + \lambda_n[k]\{\phi\}_n \qquad (34)$$

$$O(\epsilon^2): \quad ([B] - \lambda_n[K])\{\psi\}_2 = \nu_1[K]\{\psi\}_1 + \lambda_n[k]\{\psi\}_1 \qquad (35)$$

$$+ \nu_1[k]\{\phi\}_n + \nu_2[K]\{\phi\}_n$$

The second equation now has an extra term on the right-hand side, but the solutions are obtained by following the same procedure as before. This yields

$$\nu_1 = -\frac{\kappa_{nn}}{s_n^k}\lambda_n; \quad \kappa_{mn} = \{\phi^L\}_m^T[k]\{\phi\}_n$$

$$\nu_2 = \frac{\lambda_n}{s_n^k}\left[\sum_{m=1}^{M}{}' \frac{\kappa_{mn}\kappa_{nm}\lambda_n}{(\lambda_n - \lambda_m)s_m^k} + \kappa_{nn}^2/s_n^k\right]$$

$$c_{1m} = -\lambda_n\kappa_{mn}/(\lambda_n - \lambda_m)s_m^k \quad (m \neq n) \qquad (36)$$

$$c_{1n} = 0$$

$$c_{2m} = \frac{-\nu_1}{\lambda_n - \lambda_m}\left[c_{1m} + \frac{\lambda_n}{s_m^k}\sum_{j=1}^{M}\kappa_{mj}c_{1j} + \kappa_{mn}/s_m^k\right] (m \neq n)$$

$$c_{2n} = \frac{-1}{2}\sum_{j=1}^{M}|c_{1j}|^2$$

Exact Solutions. For the general case of arbitrary mistuning distribution, the aeroelastic eigenvalue problem is of order $M = pN$, plus the number of disk degrees-of-freedom. If, however, some of the blades in the mistuned rotor are identical, the order can usually be reduced, often considerably.

This is the case for "periodic" mistuning distributions, where every qth blade is identical and N/q is an integer. The perturbed eigenvalue problem then decouples into N/q problems of order q which may be solved sequentially.

A simple but interesting example of mistuning of this form is obtained by taking $q = 2$ (N even); this is the so-called alternating blade mistuning studied in [5, 6]. For the single degree of freedom model in Fig. 1(a), with the disk degrees of freedom condensed out as outlined previously, the perturbation matrix $[d]$ has the property

$$[d]\{\phi\}_n = \gamma_n\{\phi\}_{n+s} \ ; \ s = \pm N/2 \qquad (37)$$

where γ_n is a constant. If the perturbation is brought about through *mass mistuning*, $[\tilde{M}] = [M] + \epsilon[m]$, then $[m]$ is diagonal (in this model), and we have that

$$m_{ij} = (-1)^{j+1}\delta_{ij} \ ; \ [m]\{\phi\}_n = \{\phi\}_{n+s} \ ; \ s = \pm N/2 \qquad (38)$$
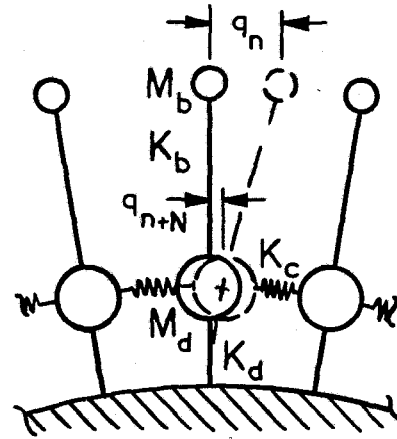

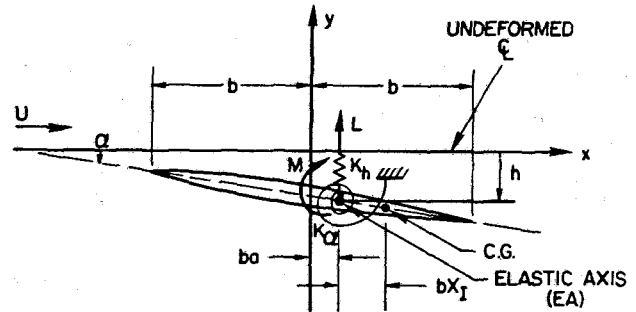
Fig. 1(a)   Structural model of bladed disk

Fig. 1(b)   Typical section model of blade

Assume the solution to the eigenvalue problem, equation (32), in the form

$$\{q\} = \sum_{n=1}^{N}\alpha_n\{\phi\}_n \qquad (39)$$

then $N/2$ decoupled eigenvalue problems are obtained

$$\begin{bmatrix} (\lambda_n - \tilde{\lambda}) & \bar{\epsilon} \\ \bar{\epsilon} & (\lambda_s - \tilde{\lambda}) \end{bmatrix}\begin{Bmatrix} \alpha_n \\ \alpha_s \end{Bmatrix} = 0 \qquad (40)$$
$$(n = 1, 2. . . .N/2)$$

with eigenvalues

$$\tilde{\lambda} = \frac{\lambda_n + \lambda_s}{2} \pm \sqrt{\left(\frac{\lambda_n - \lambda_s}{2}\right)^2 + \bar{\epsilon}^2} \qquad (41)$$

where

$$\bar{\epsilon}^2 = \frac{S_n S_s}{s_n^k s_s^k}\epsilon^2 = \frac{\epsilon^2}{s_n^k s_s^k} \qquad (42)$$

Note that in this model $[D]$ is a normal matrix; hence, $s_n = 1$ for all n.

For *stiffness mistuning* of a similar alternating (diagonal) form, $\epsilon[k]$; $k_{ij} = (-1)^{j+1}\delta_{ij}$, the eigenvalues are given by a slightly different expression

$$(1 - \bar{\epsilon}^2)\tilde{\lambda} = \frac{\lambda_n + \lambda_s}{2} \pm \sqrt{\left(\frac{\lambda_n - \lambda_s}{2}\right)^2 + \bar{\epsilon}^2\lambda_n\lambda_s} \qquad (43)$$

These formulas are exact for all physically realizable ϵ *if* k, M, μ remain fixed, i.e., $|\epsilon|$ need not be small. Indeed, they also apply to the case where M, μ are fixed and k is allowed to vary consistent with $\tilde{\lambda}$, provided λ_n and λ_s are recalculated as k changes. These quantities then become functions of ϵ, through a "frequency effect." In other words, equations (41) and (43)

can be used to locate the exact flutter boundary by efficient iterations involving only the two coupled modes n and s. Similar quadratic formulas can presumably be derived for the case of p degrees-of-freedom per blade.

Aeroelastic Stability

Flutter Boundaries. The flutter boundaries are defined by $Im\ \lambda = g\ Re\ \lambda$ where λ is related to the exponent p in the time dependence $\exp(pt)$ by

$$p/\omega_0 = \bar{p}_R \pm i\bar{\omega} = i\sqrt{(1 + ig)/\lambda} \qquad (44)$$

Flutter occurs when $\bar{p}_R > 0$ ($\bar{\omega} \neq 0$), and corresponds to $Im\lambda > 0$ in the absence of damping.

Although the aerodynamic operators used assume simple harmonic motion, typically $|\bar{p}_R| << |\bar{\omega}|$ for turbomachinery flutter, and $\bar{p}_R$ may therefore be interpreted as representing (approximately) the true damping in the system [18].

Sensitivity to Mistuning. The perturbed eigenvalues $\tilde{\lambda}_n$, given by equation (22), depend on certain products s_n, s_n^k, $t_{mn}, \ldots$ involving the right and left eigenvectors of the tuned system. These products are in general complex, thus the correction terms do affect the stability boundaries of the rotor. An important exception occurs for systems where the governing matrices $[D]$ or $[B]$ are normal. In this case the right and left eigenvectors are complex conjugates of each other, $\{\phi^L\}_n = \{\bar{\phi}\}_n$; $t_{mn}t_{nm} = |t_{nm}|^2$, etc., and the quantities s_n, $s_n^k, \ldots$ become Hermitian forms and therefore real. It then follows from equations (27, 33, 36) that ν_1 is real and hence, to $0(\epsilon)$, the stability boundaries are not affected by mistuning. This is because a real correction term ν_1 cannot change the sign of the imaginary part of any characteristic root $\tilde{\lambda}_n$; thus $\bar{p}_R$ cannot change sign as a result, although its magnitude may be affected. In the case of a diagonal mistuning matrix with zero trace, corresponding to a mistuning distribution with zero mean, the first-order term $\epsilon\nu_1$ vanishes identically.

The next term in the asymptotic sequence for $\tilde{\lambda}_n$ is not real, even for $[D]$ normal, because of the factor $(\lambda_n - \lambda_m)$ in the denominators of equations (30) and (36). This term does therefore affect the stability boundary, and although it is only a second-order term in the limit $\epsilon \rightarrow 0$, it can have a first-order effect on the stability boundary for $|\epsilon| > 0$, even if $|\epsilon| < < 1$. This will be illustrated shortly through numerical examples.

The reason for this sensitivity is generally not that the s_n, s_n^k's become arbitrarily small, as may happen in the general case [17], because the same behavior is observed for rotors where $[D]$ is normal, which have well behaved s_n, s_n^k's. Rather, the reason is that turbomachinery rotors tend to have a large number of blades; thus the sums in equations (30, 36) contain many terms. If the coupling between the blades is weak, such as in the case where no shrouds are present and the disk is relatively stiff, the unperturbed eigenvalues tend to be close together. The factor $(\lambda_n - \lambda_m)$ in the denominators of equations (30, 36) can therefore become sufficiently small such that the cumulative effect over M terms is to produce a correction term $\epsilon^2\nu_2$ with an imaginary part of $0(\epsilon)$, rather than $0(\epsilon^2)$. Since $Im\lambda_n$ is typically of $0(\epsilon)$, the result is an $0(1)$ effect on the flutter boundaries.

Essentially, mistuning alters the flutter boundaries by coupling otherwise orthogonal modes of the tuned system. For the case where $[D]$ is normal, it is readily shown that the second-order term $\epsilon^2\nu_2$ is always stabilizing for ϵ^2 sufficiently small, by the following argument: Let λ_n represent the least stable root, then $Im\lambda_n \geq Im\lambda_m$ for all m. Since each term in the sums in equations (30, 36) has a negative (or zero) imaginary part, $Im\nu^2 < 0$ and the term is therefore stabilizing. However, it is also clear that some of the other roots have destabilizing correction terms $\epsilon^2\nu_2$; thus for ϵ^2

sufficiently large one of these roots may become critical (but is shown later not to occur).

The role of the various parameters in determining flutter boundary sensitivity is now clear. To maximize this stabilizing effect on the critical mode, one should try to couple it as strongly as possible to the most stable mode. At the same time, coupling between modes of essentially the same level of damping is of little use, since $Im(\lambda_n - \lambda_m)$ will be small and the corresponding term will contribute little or nothing to the imaginary part of ν_2. Coupling between unstable modes is always detrimental, for as one mode is stabilized, another is further destabilized. In this case, mistuning cannot stabilize the system.

It should be emphasized that for the general case where $[D]$ is not normal, the quantities r_{mn}, t_{mn}, s_n, s_n^k are complex, and no *a priori* conclusions can be drawn regarding the stabilizing or destabilizing effect of mistuning. Also, it should be kept in mind that in the perturbation analysis, k, M, and μ are kept fixed as $\epsilon \rightarrow 0$. Thus for the practical case where k is allowed to vary consistent with $\tilde{\lambda}$, the effect of mistuning need not be stabilizing even for the case where $[D]$ is normal. In either case, the perturbation analysis can still be used to calcualte the perturbed stability boundary to any order in ϵ, as no assumption regarding $[D]$ being normal was used in deriving equations (22-36). Similarly, one can use the $p-k$ method [18] to iterate on p (or $\tilde{\lambda}$) and k until k is consistent with $\tilde{\lambda}$ in accordance with equation (44), i.e. $k/\omega_0 = \bar{\omega}b/U$.

Normal Versus Non-normal Systems. It is apparent that there is a fundamental difference between systems governed by normal as opposed to non-normal matrices. Normal matrices have the property that they commute with their Hermitian adjoints, (conjugate transpose), e.g., $[D][D]^* = [D]^*[D]$, and $[D]$ and $[D]^*$ then share a common set of complete orthonormal right eigenvectors. Hermitian matrices, corresponding to self-adjoint operators, are special cases of normal matrices.

It is a remarkable fact that the governing matrices in the aeroelastic eigenvalue problem for a certain class of tuned rotors are, indeed, normal. The rotor model in Fig. 1(a), with one elastic degree-of-freedom per blade and the disk degrees-of-freedom condensed out, belongs to this class. In this case, the mass stiffness and aerodynamic matrices are all circulant, and circulant matrices are normal [16]. Now sums and products of normal matrices are not necessarily normal, unless additional conditions are met. It turns out that for the rotor model in question, $[M]$, $[K]$, and $[A]$ all commute, since they have a complete set of orthonormal eigenvectors, $\{e\}_n$, equations (11), in common [16]. This is sufficient to guarantee that the system matrices $[D]$ and $[B]$ are also normal [19].

As soon as each blade is modeled using more than one degree-of-freedom, as for example in the typical section model in Fig. 1(b), the system matries cease to be normal. Such multi-degree-of-freedom systems may therefore respond differently, and not necessarily conservatively, to the introduction of mistuning. Published results [5, 6] for one rotor suggest that many of the features of the normal system are retained, but this could also be an indication that the essential aeroelastic behavior of this particular rotor can be modeled closely using a single degree-of-freedom per blade.

For systems where the matrices are normal, a useful stability theorem can be established. The imaginary part of the nth eigenvalue can be written as

$$Im\lambda_n = \frac{\{\phi\}_n^*[B]_2\{\phi\}_n}{\{\phi\}_n^*[K]\{\phi\}_n} \qquad (45)$$

where

$$[B]_2 = \frac{1}{2i}([B] - [B]^*)$$

Table 1   Verdon's cascades

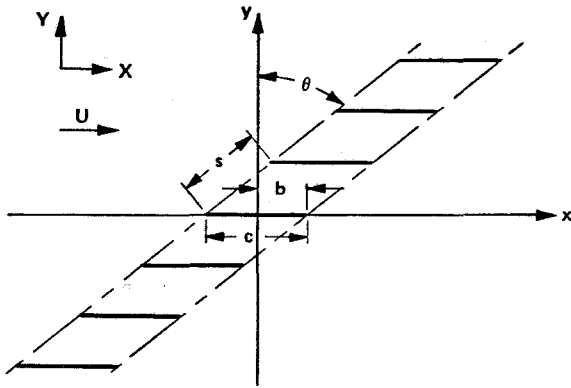| Parameter	Cascade A	Cascade B
Stagger angle, θ	59.5 deg	63.4 deg
Spacing, $\bar{s}_2 = (s/b)\cos\theta$	0.8	0.6
Mach number, M	1.345	1.281

Fig. 2   Cascade geometry

Fig. 4   Critical stiffness perturbation required for stabilization of rotor with Cascade B typical section (alternating blade stiffness mistuning, $a = 0$, $N = 20$ and 40)
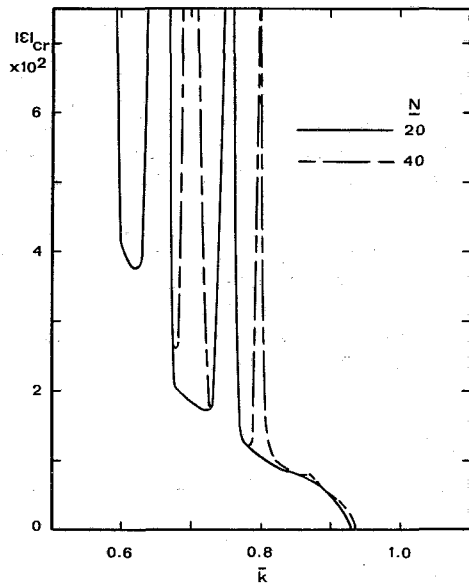

Fig. 3   Critical stiffness perturbation required for stabilization of rotor with Cascade A typical section (alternating blade stiffness mistuning, $a = 0$, $N = 20$ and 40)
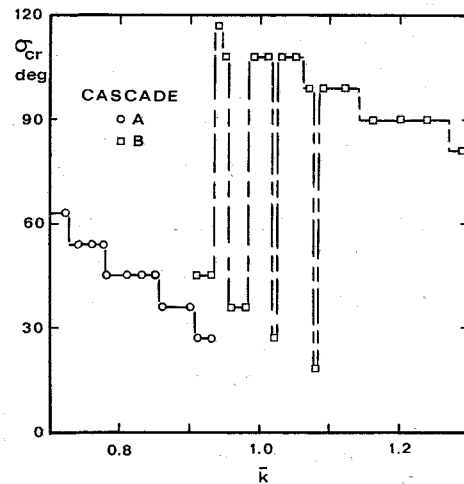
Fig. 5   Interblade phase of critical mode corresponding to Figs. 3 and 4, for $N = 40$

If $[B]$ and $[K]$ are normal, then $\{\phi\}_n$ is also an eigenvector of $[B]_2$, since in this case $[B]$ and $[B]_2$ have the same eigenvectors. Now $[K]$ is always symmetric by the Maxwell-Betti Reciprocity Theorem, and thus also both normal and Hermitian. In addition, $[B]_2$ is clearly also Hermitian; thus for the case of normal $[B]$, equation (45) is a Rayleigh Quotient in the usual sense. Consider first a mass perturbation $\epsilon[m]$, with k, M, μ, and $[K]$ fixed, then $[\bar{B}]_2 = [B]_2$, and it follows immediately from the extremum properties of the eigenvalues (or Rayleigh's Quotient) that

$$\min(Im\lambda_n) \leq Im\tilde{\lambda}_n \leq \max(Im\lambda_n) \tag{46}$$

If the unperturbed system is stable, $\max(Im\lambda_n) \leq 0$, and it follows from equation (46) that the perturbed system is also stable. Similarly, if every characteristic root of the unperturbed system is unstable, $\min(Im\lambda_n) > 0$, the the perturbed system is also unstable.
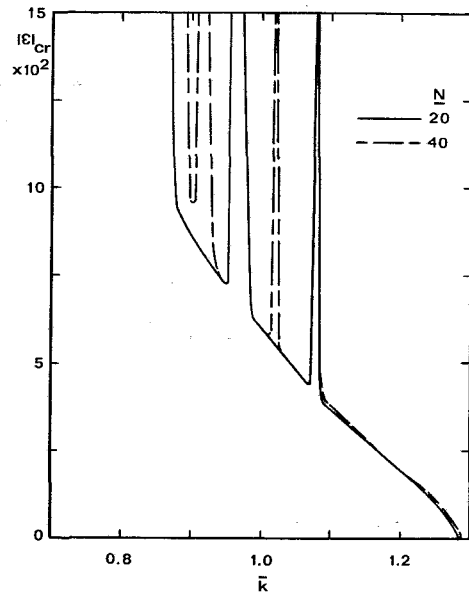
For stiffness perturbations equation (46) does not hold, but one can show that as long as $[\bar{K}]$ remains positive definite, the perturbed system is always stable if $\max(Im\lambda_n) \leq 0$, i.e., if the unperturbed system is stable. Similarly, $\min(Im\lambda_n) > 0$ guarantees that the perturbed system will also be unstable. Note carefully that these stability theorems do not apply to non-normal systems, or for systems where k, M, μ are not fixed as ϵ varies.

Numerical Results. Some illustrative results are shown in Figs. 3–7, for design parameters representative of fan rotors. The structural model of Fig. 1(a) is used, with one (elastic) torsional degree-of-freedom per blade and the disk degrees-of-freedom condensed out. Verdon's cascades A and B [20, 21], Table 1 and Fig. 2, were selected as representative of current technology supersonic rotor geometry, and the unsteady aerodynamic forces were calculated by the method used in [22]. Titanium blades were assumed, with $\mu = 200$ and $r_\alpha^2 = 1/3$.

Fig. 6 Comparison of exact and second-order perturbation solutions of flutter boundary (cascade A, alternating blade stiffness mistuning, $N = 100, a = 0$)
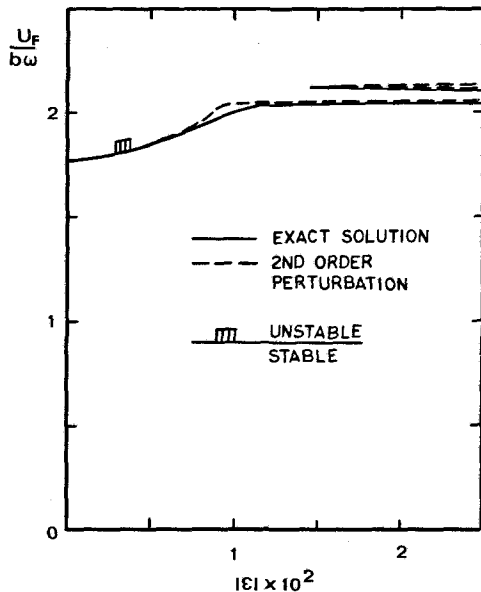

Fig. 7 Sensitivity of critical mistuning parameter to interblade phase of unstable mode, for alternating blade stiffness mistuning (cascade A, $a = 0$)

In Figs. 3–5, the effect of alternating blade stiffness mistuning, $\epsilon[k]$; $k_{ij} = (-1)^{j+1}\delta_{ij}$, is shown. The disk is considered infinitely stiff, and the diagonal stiffness matrix $[K]$ has been nondimensionalized such that $s_m^k = 1$ for all m, i.e., $\bar{\epsilon} = \epsilon$ represents the stiffness perturbation amplitude from a nominal tuned value of unity. The critical value $|\epsilon|_{cr}$ required to stabilize the rotors is plotted versus modified reduced frequency $\bar{k} = kM/(M^2 - 1)$. As $\bar{k}$ is reduced below the critical value for torsional flutter of the tuned rotor, $|\epsilon|_{cr}$ increases monotonically until a series of sharp peaks are encountered, defining narrow regions of $\bar{k}$ for which instability persists even in the limit $|\epsilon| \rightarrow 1$. The number of peaks increases with the number of blades N; it also depends on the aerodynamic configuration of the rotor. As $\bar{k}$ is reduced further the width of these narrow frequency regions of instability grows, until a critical value of $\bar{k}$ is reached below which the rotor is always unstable. Note that $\bar{k}_{cr}$ depends both on typical section geometry and number of blades in the rotor, in addition to the structural model and type of mistuning. For the rotors considered in Figs. 3 and 4, with $N=40$ blades and Cascade A and B typical sections, $\bar{k}_{cr} \cong 0.67$ and $\bar{k}_{cr} \cong 0.89$, respectively.

Two interesting features are apparent. First, both rotors are relatively sensitive to this type of mistuning, as stiffness perturbations of order 10^{-2} affect the flutter boundary to order one. The reason is that, for a range of $\bar{k}$, the least stable and most stable modes are approximately 180 deg apart in interblade phase, making alternating blade mistuning close to optimum. Second, because the stability boundaries are very steep in the vicinity of the critical reduced frequency, nothing is gained by increasing $|\epsilon|$ beyond about 5×10^{-2}.

In Fig. 6, a comparison is made between the perturbation solution and the exact solution, corresponding to Cascade A, plotted as nondimensional flutter speed $U_F/b\omega$ versus $|\epsilon|$. For this case, only even order terms in ϵ survive in the asymptotic sequence for $\bar{\lambda}$. The agreement with the exact solution is very good, indicating that the perturbation formulas provide a reliable estimate of the effect of mistuning on the flutter boundaries.

An important characteristic of mistuned rotors is the sensitivity of $|\epsilon|_{cr}$ to the interblade phase of the modes coupled. This is best illustrated for the case of alternate blade
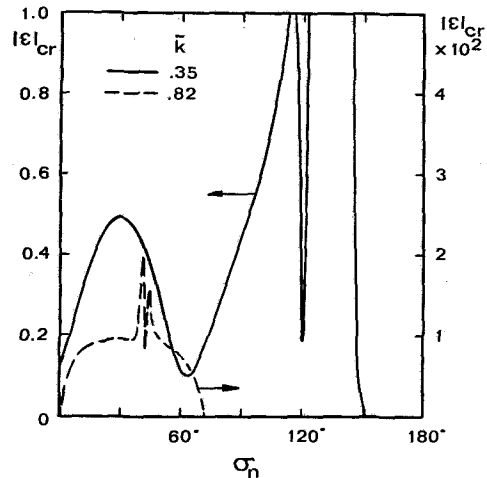
mistuning, since then there are only two modes involved. Figure 7 illustrates the sensitivity of $|\epsilon|_{cr}$ to σ_n ($\sigma_s = \sigma_n + 180$ deg), for Cascade A, both for $\bar{k} > \bar{k}_{cr}$ (which can be stabilized) and for $\bar{k} < \bar{k}_{cr}$ (which cannot be stabilized). Note that modes corresponding to σ_n in the vicinity of 0 deg, 60 deg, and between 150–180 deg can be stabilized down to values of $\bar{k}$ significantly below $\bar{k}_{cr}$. Modes corresponding to σ_n close to 30 or 120 deg are very difficult to stabilize, however. As indicated by the figure, for $\bar{k} = 0.35$, there is a region of values of interblade phase around 120 deg which cannot be stabilized.

If the number of blades is large and only a few are mistuned, the effect on the flutter boundaries is small. For example, if $N=50$ and only one blade is mistuned, then $\kappa_{nn} = \kappa_{mn} = 1/N = 2 \times 10^{-2}$, compared to $\kappa_{mn} \sim O(1)$ if every blade were mistuned. From equations (36) it follows that the correction terms ν_1 and ν_2 are small.

Conclusions

The major conclusions that can be drawn from this study can be summarized as follows:

1 The sensitivity of the flutter boundaries to mistuning depends on the mathematical nature of the system matrices, the closeness of the unperturbed eigenvalues, and the number of blades in the rotor.

2 If the system matrices are normal, mistuning cannot destabilize the rotor unless the reduced frequency of the least stable mode is decreased by the perturbation. In general, only cascades and rotors with a single degree-of-freedom per blade belong to this class.

3 A critical reduced frequency exists below which mistuning alone cannot stabilize the system. For supersonic fan rotors typical of current designs, narrow regions of instability also exist above this critical frequency, and mistuning beyond 3–5 percent appears ineffective as a passive flutter control.

4 Perturbation methods can be used effectively to provide quick and reliable estimates of the effect of mistuning on the aeroelastic stability boundaries of turbomachinery rotors.

References

1 Whitehead, D. S. "Effect of Mistuning on the Vibration of Turbomachine Blades Induced by Wakes," *Journal of Mechanical Engineering Science*, Vol. 8, No. 1, Mar. 1966, pp. 15–21.

2 Dye, R. C. F., and Henry, T. A., "Vibration Amplitudes of Compressor Blades Resulting from Scatter in Blade Natural Frequencies," ASME JOURNAL OF ENGINEERING FOR POWER, Vol. 91, July 1969, pp. 182–188.

3 El-Bayoumy, L. E., and Srinivasan, A. V., "Influence of Mistuning on Rotor-Blade Vibrations," *AIAA Journal*, Vol. 13, No. 4, Apr. 1975, pp. 460–464.

4 Whitehead, D. S., "Torsional Flutter of Unstalled Cascade Blades at Zero Deflection," Great Britain A.R.C. R&M 3429, 1964.

5 Kaza, K. R., and Kielb, R. E., "Flutter and Response of a Mistuned Cascade in Incompressible Flow," *AIAA Journal*, Vol. 20, No. 8, Aug. 1982, pp. 1120–1127.

6 Kaza, K. R. V., and Kielb, R. E., "Coupled Bending-Bending-Torsion Flutter of a Mistuned Cascade With Nonuniform Blades," AIAA Paper No. 82-0726, presented at the AIAA/ASME/ASCE/AHS 23rd Structures, Structural Dynamics, and Material Conference, New Orleans, May 10–12, 1982.

7 Cole, J. D., *Perturbation Methods in Applied Mathematics*, Blaisdell, Waltham, Mass., 1968.

8 Fabunmi, J. A., "Forced Vibrations of a Single Stage Axial Compressor Rotor," ASME Paper No. 79-GT-108, Mar. 1979.

9 Marcus, M., and Minc, H., *A Survey of Matrix Theory and Matrix Inequalities*, Allyn and Bacon, Boston, 1964.

10 Bendiksen, O., and Friedmann, P., "Coupled Bending-Torsion Flutter in Cascases," *AIAA Journal*, Vol. 18, No. 2, Feb. 1980, pp. 194–201.

11 Lane, F., "System Mode Shapes in the Flutter of Compressor Blade Rows," *Journal of the Aeronautical Sciences*, Vol. 13, Jan. 1956, pp. 54–66.

12 Fox, R. L., and Kapoor, M. P., "Rates of Change of Eigenvalues and Eigenvectors," *AIAA Journal*, Vol. 6, No. 12, Dec. 1968, pp. 2426–2429.

13 Rogers, L. C., "Derivatives of Eigenvalues and Eigenvectors," *AIAA Journal*, Vol. 8, No. 5, May 1970, pp. 943–944.

14 Plaut, R. H., and Huseyin, K., "Derivatives of Eigenvalues and Eigenvectors in Non-Self-Adjoint Systems," *AIAA Journal*, Vol. 11, No. 2, Feb. 1973, pp. 250–151.

15 Nelson, R. B., "Simplified Calculation of Eigenvector Derivative," *AIAA Journal*, Vol. 14, Sept. 1976, pp. 1201–1205.

16 Lancaster, P., *Theory of Matrices*, Academic Press, New York, 1969.

17 Wilkinson, J. H., *The Algebraic Eigenvalue Problem*, Clarendon Press, Oxford, 1965.

18 Hassig, H. J., "An Approximate True Damping Solution of the Flutter Equation by Determinant Iteration," *Journal of Aircraft*, Vol. 8, No. 11, Nov. 1971, pp. 885–889.

19 Fuglede, B., "A Commutivity Theorem for Normal Operators," *Proceedings of the National Academy of Sciences*, U.S.A., Vol. 36, 1950, pp. 35–40.

20 Verdon, J. B., and McCune, J. E., "Unsteady Supersonic Cascade in Subsonic Axial Flow," *AIAA Journal*, Vol. 13, No. 2, Feb. 1975, pp. 193–201.

21 Verdon, J. M., "Further Developments in the Aero-Dynamic Analysis of Unsteady Supersonic Cascades, Parts 1 and 2," ASME JOURNAL OF ENGINEERING FOR POWER, Vol. 99, Oct. 1977, pp. 509–525.

22 Bendiksen, O., and Friedmann, P., "Coupled Bending-Torsion Flutter in a Supersonic Cascade," *AIAA Journal*, Vol. 19, No. 6, June 1981, pp. 774–781.

Cascade Flutter Analysis of Cantilevered Blades

A. V. Srinivasan

Manager,
Applied Mechanics Research,
United Technologies Research Center,
East Hartford, Conn. 06108

J. A. Fabunmi

Assistant Professor of
Aerospace Engineering,
University of Maryland,
College Park, Md. 20742

An analysis has been developed to treat the aeroelastic behavior of a cascade of cantilevered blades. The unique features of the formulation include consideration of (a) coupling between bending and torsion in each of the blade modes, (b) coupling among blade modes, (c) spanwise variation of blade mode shapes, (d) mechanical damping in each mode, (e) aerodynamic coupling among all blades of the assembly, and (f) mistuning. The methodology leads to a complex eigenvalue problem of the form $[A (\lambda)] \{x\} = \lambda \{x\}$ the solution of which establishes the nature of stability and determines the flutter modes of vibration. A parametric study is made to examine the influence on flutter of (a) the strength of coupling between bending and torsion, (b) proximity of modal frequencies, (c) mass ratio, and (d) mistuning. Numerical results presented here are restricted to a twelve bladed system coupled aerodynamically. The flow conditions are assumed to be subsonic but the formulation of the problem and the organization of the computer program are such that other conditions can easily be considered in computation. The extension of the analysis to include mechanical coupling between the blades (through either shrouds or disk) is shown to be straightforward.

Introduction

An important factor that influences the development program of advanced gas turbines is the susceptibility of rotor blades to flutter instabilities. The structural integrity of a power plant depends, to a large extent, on the ability of the machine to withstand vibratory stresses due to either flutter or resonance. Rotor blade flutter is caused by an interaction between the vibratory motions of an assembly of blades and the aerodynamic forces resulting from these motions. Resonant vibration is caused when a vibratory pattern in the rotating system of blades matches both in time and space a distortion pattern in the stream. Considerable data obtained from tests conducted on an advanced engine over a wide range of realistic operating conditions [1] have revealed the complex nature of cascade flutter modes. The latter are characterized by the presence of several harmonics at the flutter frequency, underlining the influence of nonuniformities of blade properties around the rotor. The resulting system modes of the assembly depend on several important factors arising from the extent of aerodynamic and mechanical coupling present.

Modern fan and compressor blades resemble highly twisted and bent plate-type configurations, whose cross sections vary from root to tip. An assembly of such blades with or without part-span shrouds mounted on a support structure such as a hub or disk and subjected to a centrifugal and aerodynamic environment leads to an aeromechanical system of extreme complexity. The aerodynamic modeling of a vibrating cascade of blades under flow regimes typical of several operating

conditions over a speed range continues to be an important area of research. In addition, problem areas of equal complexity pertain to proper representation of the structural boundary conditions at the root and shroud interfaces.

An approach to the analytical modeling of an assembly of unstalled blades vibrating in a torsion mode was presented by Whitehead [2] and that approach has served well as a basis for a number of subsequent advances [3–7] which incorporate features that are considered to be important in practice. The advances in the past decade have thrown considerable light on the subject area so that the improved understanding is likely to influence future blade designs. Considerations in future design practice may include selective mistuning of blades, introduction of various damping mechanisms into blades to limit forced vibration response, elimination of part-span shrouds, etc. Additional analytical and experimental efforts are needed to continue to provide input into these design considerations so that the potentials of mistuning and damping mechanisms can be maximized. In particular, trends in regard to flutter susceptibility need to be established, based on which a designer can estimate the influence of (a) coupling between bending and torsion in a given blade mode, (b) coupling among blade modes, and (c) mass ratio and reduced frequency. These trends need to be determined analytically and confirmed experimentally in order to influence the structural design of blades.

With the exception of Carta's work per cycle approach [8] wherein the aerodynamic work was integrated over the blade span, most published work on cascade flutter analysis has considered the motions of an equivalent blade section only [2–7, and 9, 10, and 11]. In a typical fan, flap and torsional motions at a cross section occur together as a result of the
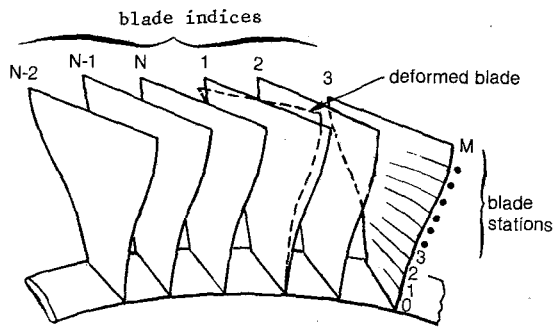
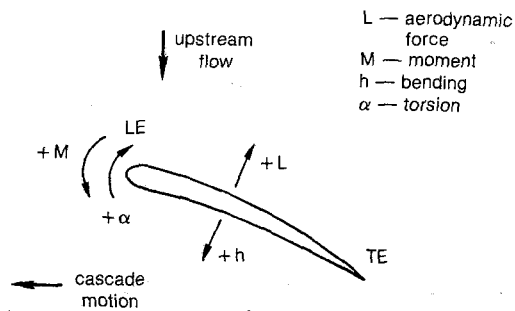**Fig. 1(a) Cascade of cantilevered blades**

Fig. 1(b) Coordinate system of blade cross section

overall motion of a nonuniform twisted platelike component. To designate a particular section of a blade (with whatever stiffness and mass properties assigned to it) as "equivalent" or "typical" must mean that such a section would exhibit, under given aerodynamic conditions, the same, yet to be determined flutter boundaries as the blade itself. The use of equivalent blade section analysis is principally to illustrate the characteristics of the unsteady two-dimensional aerodynamic coefficients under different conditions of flow and geometry. For the purposes of determining the flutter boundaries of a fan assembly, the analysis must be formulated in such a way that the spanwise variation of the blade elastic properties are included, along with the capability to consider different aerodynamic flow conditions at different blade sections. Most recently, Kaza and Kielb [12] have proposed an analysis which models each blade as a "straight, slender, twisted, nonuniform elastic beam with a symmetric cross section."

This paper presents a formulation of the cascade flutter problem in such a way that the modal characteristics of individual blades (frequencies, mode shapes, and damping) that may be available from a detailed finite element analysis or from direct experimental measurement can be used. The flow conditions may also vary along the span. The formulation includes considerations important in design so that parametric studies of real blade profiles can be made. Thus, coupling between the torsinal and bending degrees of freedom at each spanwise location of the blade, coupling among blade modes through either aerodynamic or mechanical means are inherent in the development. Individual blade modal characteristics

and unsteady aerodynamic coefficients for given operating conditions of the machine serve as input. The relative extent of displacement and rotation at each spanwise blade section present in the input modes is indicative of the strength of coupling between bending and torsion within the same blade mode. This is to be distinguished from the notion of bending-torsion coupling in an "equivalent section" in which a parameter that determines the strength of coupling is the proximity of arbitrarily assigned values of frequencies in the bending and torsional degrees of freedom.

Blade-to-blade differences in either frequency and/or damping are included in the analytical formulation. The systematic development leads to a complex eigenvalue problem the size of which, in general, depends upon the number of blades as well as the number of individual blade modes considered. The eigenvalue problem is solved for an assumed analysis frequency, a proper choice of which leads to an acceptable solution. A solution is acceptable if the computed eigenfrequency matches the assumed analysis frequency approximately. The nature of the eigenvalues establishes the extent of susceptibility to an aeroelastic instability. Flutter is predicted when the imaginary part of the square root of the eigenvalue is negative. The corresponding eigenvectors describe the nature of displacement around the rotor.

The analytical approach is shown in the following section. Numerical results are obtained for an assembly of 12 blades on a rigid disk coupled aerodynamically. A parametric study is made in which the strength of coupling (between bending and torsional degrees of freedom) in a given blade mode, mass ratio, reduced frequency, and mechanical damping are varied. Studies of flutter modes involving more than one blade mode were conducted to investigate the strength of coupling between the participating blade modes. Both selective and random mistuning are used with and without mechanical damping to establish trends of behavior in regard to flutter. The blade profile chosen represents an advanced research fan whose mode shapes are used in the baseline calculations as well as in forming new modes to vary bending-torsion coupling.

Analytical Development

A cascade of blades supported on a circular symmetric support and vibrating in a uniform flow field serves as the basic model. The coordinate system which has been used in deriving the governing equations of motion is shown in Fig. 1. It is assumed that the in vacuo frequencies, mode shapes, generalized masses and damping of the individual blades comprising the cascade are all known a priori for each mode.

For the kth blade

$$[m]^k\{\ddot{q}\}^k + [K+iD]^k\{q\}^k + \{A\}^k = \{0\} \qquad (1)$$

$[m]$ = blade mass matrix
$[k]$ = blade stiffness matrix
$[D]$ = blade hysteretic damping matrix
$\{A\}$ = vector of forces (aerodynamic and/or mechanical) on blade sections from root to tip
$\{q\}$ = vector of blade displacements/rotations at blade sections from root to tip

———— **Nomenclature** ————

A = vector of forces or moments acting on blade sections
C = matrix of unsteady aerodynamic coefficients
c = chord
h = blade translation
k = blade number
L = unsteady aerodynamic lift

l = length of blade segment
M = unsteady aerodynamic moment
m = mass or generalized mass
N = number of blades
p = spanwise blade mode number
q = vector of blade displacements/rotations
r = circumferential mode number

S = gap
X = matrix of eigenvectors
α = blade rotation
δ = modal damping
η = eigenvector
ω = circular frequency of vibration
λ = reduced frequency

$$\{q\} = \begin{Bmatrix} h_1 \\ \alpha_1 \\ h_2 \\ \alpha_2 \\ \cdot \\ \cdot \\ \cdot \\ \cdot \\ h_m \\ \alpha_m \end{Bmatrix} ; \quad \{A\} = \begin{Bmatrix} L_1 \\ M_1 \\ L_2 \\ M_2 \\ \cdot \\ \cdot \\ \cdot \\ \dot{L}_m \\ \dot{M}_m \end{Bmatrix} \quad (2)$$

where m represents the number of blade stations along its span.

Let $\{\phi\}$ represent the natural vibration modes of the blades obtained from solving equation (1) with $\{A\}$ set to $\{0\}$

$$\{\phi_i\} = C_i \begin{Bmatrix} h_{1i} \\ \alpha_{1i} \\ \cdot \\ \cdot \\ \cdot \\ \cdot \\ h_{mi} \\ \alpha_{mi} \end{Bmatrix} ; \quad \text{Where } C_i = \frac{1}{\sqrt{m_i}} \quad (3)$$

and m_i represents the generalized mass corresponding to the ith mode. $\{\phi_i\}$ for modes $p = 1, 2 \ldots P$ satisfy the orthogonality requirements, i.e.,

$$\begin{aligned} & [\Phi^k]^T[m]^K[\Phi^k] = [I] \\ \text{and} \quad & [\Phi^k]^T[K+iD]^K[\Phi^k] = [\omega_p^2(1 + i\delta_p/\pi)]^k \end{aligned} \quad (4)$$

where

$$[\Phi^k] \equiv [\{\phi_1\}\{\phi_2\} \cdots \{\phi_p\}]^k$$

If

$$\{q\}^k = [\Phi^k]\{\eta_p\}^k \quad (5)$$

then equation (1) may be shown to reduce to

$$\{\ddot{\eta}_p\}^k + \left[\omega_p^2\left(1 + \frac{i\delta_p}{\pi}\right)\right]\{\eta_p\}^k + [\Phi^k]^T\{A\}^k = \{0\} \quad (6)$$

The aeroelastic loads (lifts and moments) acting on the kth blade at the mth station can be represented as

$$\begin{aligned} L_m^k &= \sum_{n=1}^{N} (P_m^{kn} h_m^h + Q_m^{kn} \alpha_m^n) \\ M_m^k &= \sum_{n=1}^{N} (R_m^{kn} h_m^n + S_m^{kn} \alpha_m^n) \end{aligned} \quad (7)$$

where N is the number of blades and the expressions for P, Q, R, and S are derived in Appendix A. Equation (7) implies that an aerodynamic strip theory is assumed.

$$\{A\}^k = \sum_{n=1}^{N} [\psi]^{kn}\{q\}^n$$

Let $\quad (8)$

$$= \sum_{n=1}^{N} [\psi]^{kn}[\Phi^n]\{\eta\}^n$$

where

$$[\psi]^{kn} = \begin{bmatrix} \begin{pmatrix} P_1^{kn} & Q_1^{kn} \\ R_1^{kn} & S_1^{kn} \end{pmatrix} & & & \\ & \ddots & & \\ & & \ddots & \\ & & & \begin{pmatrix} P_m^{kn} & Q_m^{kn} \\ R_m^{kn} & S_m^{kn} \end{pmatrix} \\ & & & & \ddots \end{bmatrix} \quad (9)$$

It may be noted that equation (8) has the generality which permits the use of mode shapes that differ from blade to blade. The equation for the kth blade, i.e., equation (6) can be written as

$$\{\ddot{\eta}_p\}_{p \times 1} + \left[\omega_p^2 1 + \left(\frac{i\delta_p}{\pi}\right)\right]_{p \times p}\{\eta_p\}_{p \times 1}$$

$$+ \sum_{n=1}^{N} [\Phi^k]_{p \times 2M}^T [\psi]_{2M \times 2M}^{kn} [\Phi^n]\{\eta_p\} = \{0\} \quad (10)$$

Defining

$$[A]_{p \times p}^{kn} \equiv \frac{1}{\omega_0^2}[\Phi^n]^T[\psi]^{kn}[\Phi^n] \quad (11)$$

it can be shown that each element of $[A]^{kn}$ is given by

$$A_{ij}^{kn} = \sum_{m=1}^{M} C_i^k C_j^n \overbrace{h_{mi}\alpha_{mi}}^{k} \begin{bmatrix} \dfrac{P_m^{kn}}{\omega_0^2} & \dfrac{Q_m^{kn}}{\omega_0^2} \\[2ex] \dfrac{R_m^{kn}}{\omega_0^2} & \dfrac{S_m^{kn}}{\omega_0^2} \end{bmatrix} \begin{Bmatrix} h_{mj} \\ \alpha_{mj} \end{Bmatrix}^n \quad (12)$$

where, as before, $C_i = \sqrt{1/m_i}$ and $C_j = \sqrt{1/m_j}$ and m_i, m_j are the generalized masses of the indexed blade modes. The generality is retained in equation (12) so that the mode shapes of the kth and nth blades may be different. Equation (10) may be rewritten as

$$\{\ddot{\eta}_p\}^k + \left[\omega_p^2\left(1 + \frac{i\delta_p}{\pi}\right)\right]\{\eta_p\}^k + \omega_0^2 \sum_{n=1}^{N}[A]^{kn}\{\eta_p\}^n = \{0\} \quad (13)$$

If equation (13) is written for each of the N blades, then the resulting system of equations can be written in a compact form as

$$\frac{1}{\omega_0^2}\{\ddot{X}\} + ([\Omega] + [A])\{X\} = \{0\} \quad (14)$$

Matrix A can be considered a coupling matrix which, in

general, may include the influences of aerodynamic and/or mechanical coupling among all the blades of the cascade.

$$[\Omega] = \begin{bmatrix} \left[\dfrac{\omega_p{}^2}{\omega_0{}^2}\left(1+\dfrac{i\delta_p}{\pi}\right)\right]^{\#1} & & & \\ & \left[\dfrac{\omega_p{}^2}{\omega_0{}^2}\left(1+\dfrac{i\delta_p}{\pi}\right)\right]^{\#2} & & \\ & & \ddots & \\ & & & \left[\dfrac{\omega_p{}^2}{\omega_0{}^2}\left(1+\dfrac{i\delta_p}{\pi}\right)\right]^{\#N} \end{bmatrix} \tag{15}$$

$$[A] = \begin{bmatrix} [A]^{11} & [A]^{12} \dots [A]^{1N} \\ [A]^{21} & [A]^{22} \dots [A]^{2N} \\ \cdot & \\ \cdot & \\ \cdot & \ddots \\ [A]^{N1} & [A]^{NN} \end{bmatrix} \tag{16}$$

$$\{x\} = \left\{ \begin{matrix} \begin{Bmatrix} \eta_1 \\ \eta_2 \\ \cdot \\ \cdot \\ \cdot \\ \eta_p \end{Bmatrix}^{\#1} \\ \begin{Bmatrix} \eta_1 \\ \eta_2 \\ \cdot \\ \cdot \\ \eta_p \end{Bmatrix}^{\#2} \\ \cdot \\ \cdot \\ \begin{Bmatrix} \eta_1 \\ \eta_2 \\ \cdot \\ \cdot \\ \eta_p \end{Bmatrix}^{\#N} \end{matrix} \right\} \tag{17}$$

Solutions to equation (14) are sought in the form

$$\{X\} = \{\bar{X}\}e^{i\lambda_0} \tag{18}$$

then

$$\frac{\lambda_0^2}{\omega_0{}^2}\{\bar{X}\} = ([\Omega]+[A])\{\bar{X}\} \tag{19}$$

which is treated as an approximate eigenvalue problem. λ_0^2/ω_0^2 are the eigenvalues and $\{\bar{x}\}$ the desired eigenvector. Since $\lambda_0 = \lambda_0^R + i\lambda_0^I$, the flutter frequency

$$\omega = \lambda^R = \omega_0 \left(\sqrt{\frac{\lambda_0^2}{\omega_0{}^2}}\right)^R$$

It may be noted that the aerodynamic matrix, A, is computed using an analysis frequency, ω_0. An acceptable solution to the eigen problem requires that the difference between the flutter frequency and ω_0 be "small." In Appendix B, we derive an explicit expression for the eigenvalues for the special case of a rectilinear cascade, when only one mode per blade is being considered. This result sheds some light on the factors governing the relationship between the blade frequency and the analysis frequency which yields the correct eigenvalues.

Although the numerical results presented consider only aerodynamic coupling among cantilevered blades, it is possible to use the same formulation to include coupling through a support structure such as a hub or a disk. In order to include the flexibility of the support structure, the input blade modes should be free-free modes and suitable degrees of freedom (translations and rotations) should be specified at the blade attachment points. The coupling forces acting on each blade at the point of their attachment to a common flexible structure are treated in the same way as the aerodynamic coupling forces. In other words, dynamic influence coefficients at the analysis frequency, compatible with the definitions of the aerodynamic influence coefficients, are first obtained for the disk, hub, and/or shroud geometry. The [A] matrix is then assembled with the inclusion of the structural coupling coefficients.

Parametric Study

The principal issues that are addressed in the parametric study are limited to the following: given the aerodynamic design of the blades in a cascade and if it were possible to alter (by design) the modal characteristics of the blades, then: (a) what effect does increasing the coupling between torsion and bending have on the flutter boundary; (b) what frequency spacing between a torsional mode and a bending mode will result in a coupled flutter of these modes for various reduced frequencies, and what is the relative participation of these modes at flutter; (c) would mistuning the blades improve flutter behavior to the same degree as adding mechanical damping; and (d) how does random mistuning compare with selective mistuning?

In order to be able to answer these questions and to examine and establish possible trends, a series of numerical experiments were performed. As mentioned earlier, the basic "blade alone" mode shapes for an advanced research fan were used to form arbitrarily new mode shapes to vary the bending/torsion components in a given mode. Thus, varied amounts of bending from a predominantly bending mode were added to torsion motions of a predominantly torsion mode to form new mode shapes. If $\{\phi_F\}$ is the predominantly bending mode of the baseline blade, and $\{\phi_T\}$ is predominantly torsion, a parametric mode is then constructed as

$$\{\phi\} = C_F\{\phi_F\} + C_T\{\phi_T\}$$

where C_F and C_T are constants which are used to alter the mix of bending to torsion in each composite mode. Three such composite mode shapes were used and are tabulated in Table 1. The use of these modes in this analysis can be compared to that of considering different blade designs in a design analysis study. As the principal objective of this study was to determine the change in flutter characteristics, the blade alone natural frequencies were set arbitrarily low to result in flutter in all cases.

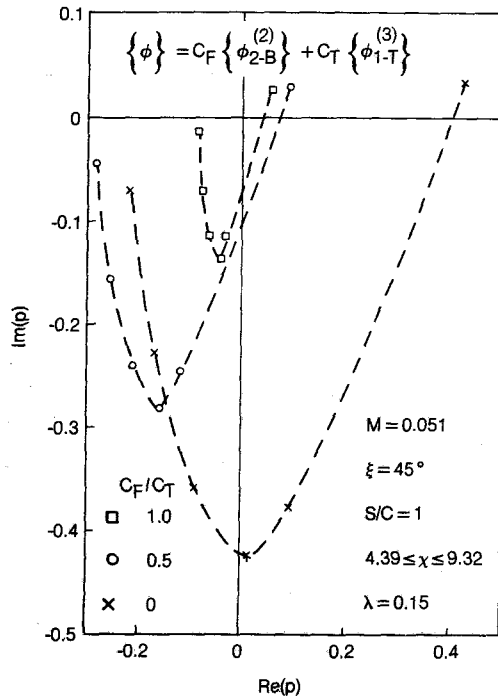In order to accentuate the effects of structural changes, the
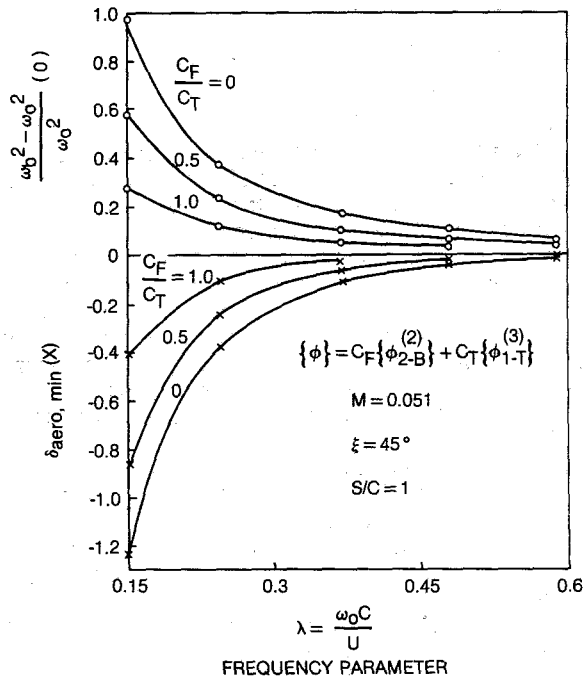
Fig. 2 Influence of coupling within the same mode

$$\{\phi\} = C_F \left\{\phi_{2\text{-}B}^{(2)}\right\} + C_T \left\{\phi_{1\text{-}T}^{(3)}\right\}$$

M = 0.051
$\xi = 45°$
S/C = 1
$4.39 \le \chi \le 9.32$
$\lambda = 0.15$

C_F/C_T	
□	1.0
○	0.5
×	0

Fig. 3 Influence of coupling within the same mode

$$\{\phi\} = C_F\left\{\phi_{2\text{-}B}^{(2)}\right\} + C_T\left\{\phi_{1\text{-}T}^{(3)}\right\}$$

M = 0.051
$\xi = 45°$
S/C = 1

$$\lambda = \frac{\omega_0 C}{U}$$

FREQUENCY PARAMETER

aerodynamics were kept nearly the same along the blade length. The aerodynamic input quantities are listed in Table 2 and were used to calcuate unsteady aerodynamic coefficients using a computer program based on the analysis of [13]. With the aerodynamic and structural inputs, the aeroelastic stability program was used to compute the levels of aerodynamic damping in each system mode. The calculations are made for an assumed analysis freuqency, ω_0, and repeated, if necessary, until the difference between the analysis frequency and flutter frequency is "small" for the least stable mode.

Figures 2 and 3 show the results of computation made to determine the influence on the parameters, of introducing

Table 1   Mode shapes used in the study to determine the strength of coupling in each mode

Mode 1; $C_F/C_T = 0$

Blade Station	Bending Deflection (in)	Torsion (rad)
1	0	0.328
2	0	0.444
3	0	0.584
4	0	0.627
5	0	0.693
6	0	0.742
7	0	0.793
8	0	0.889
9	0	0.937
10	0	1.000

Mode 2; $C_F/C_T = 0.5$

1	−0.082	0.329
2	−0.087	0.446
3	−0.070	0.586
4	−0.058	0.630
5	−0.034	0.696
6	0	0.745
7	0.076	0.796
8	0.203	0.892
9	0.358	0.940
10	0.502	1.003

Mode 3; $C_F/C_T = 1$

1	−0.165	0.330
2	−0.172	0.447
3	−0.137	0.589
4	−0.112	0.632
5	−0.064	0.698
6	0.020	0.748
7	0.153	0.799
8	0.407	0.895
9	0.714	0.944
10	1.002	1.007

more or less coupling between bending and torsion in a blade mode. Figure 2 is a plot of imaginary part of p ($p = \lambda_0^2 - \omega_0^2 / \omega_0^2$; the complex number λ_0 was defined in equation (18)) versus the real part of p. Three sets of calculations were made for a fixed frequency parameter $\lambda = 0.15$ (not to be confused with the λ_0 of equation (18)) and varying amounts of bending/ torsion, ($C_F/C_T = 0$, 0.5, and 1). Each calculated point in Fig. 2 represents the eigenvalue associated with a distinct circumferential distribution of amplitudes and phases around the periphery of the assembly, and the most negative value of IM (p) pertains to the most unstable mode for that value of C_F/C_T. One of the striking features of this analysis is that the stability characteristics show a definite improvement when some bending deformation accompanies torsion deformation. The implication is that blade designs that are prone to flutter in an essentially torsion mode could be improved by a design modification which leads to introduction of bending deformation into the vibratory mode.

Figure 3 is a study of the flutter characteristics for several values of the reduced frequency λ with C_F/C_T as parameter. At any given frequency parameter, λ, it is clear that a "pure" torsion mode tends to become stable with any addition of bending to that mode. As aerodynamic damping tends to increase as C_F/C_T increases, no instability is predicted for a "pure" bending mode, as expected. Further, the frequency of flutter ω_0 is close to the "blade alone" frequency for "large" values of the frequency parameter λ irrespective of the strength of coupling. The implication, for an essentially aerodynamically coupled system, is that for "small" Mach numbers, and "large" reduced frequencies the influence of aerodynamic coupling is negligible and therefore if flutter does take place, it will occur at a frequency close to the blade frequency. Figure 4 presents the results of a study of coupled

Table 2 Aerodynamic input parameters (table of station cascade properties)

Section Index	Stagger Angle (deg.)	S/c Ratio	Chord Length in.	Radius in.	Mach Number	Air Velocity (ft/sec)	Air Density Ratio	Section Length in.
1	45	1	3.145	5.407	.051	144	1	.1330
2	45	1	3.145	5.54	.051	144	1	.1335
3	45	1	3.145	5.674	.051	144	1	.1335
4	45	1	3.145	5.807	.051	144	1	.1335
5	45	1	3.145	5.941	.051	144	1	.1335
6	45	1	3.145	6.074	.051	144	1	.1335
7	45	1	3.145	6.208	.051	144	1	.1335
8	45	1	3.145	6.341	.051	144	1	.1335
9	45	1	3.145	6.475	.051	144	1	.1335
10	45	1	3.145	6.608	.051	144	1	.0669

Table 3 Mode (predominantly bending) used to couple aerodynamically with mode 1 shown in table 1

Blade Station	Bending Deflection (in)	Torsion (rad)
1	−0.165	0.002
2	−0.171	0.003
3	−0.133	0.004
4	−0.108	0.005
5	−0.060	0.005
6	0.023	0.006
7	0.155	0.006
8	0.407	0.006
9	0.713	0.007
10	1.000	0.007

Fig. 4 Coupled flutter involving two blade modes

Fig. 5 Mass ratio effects
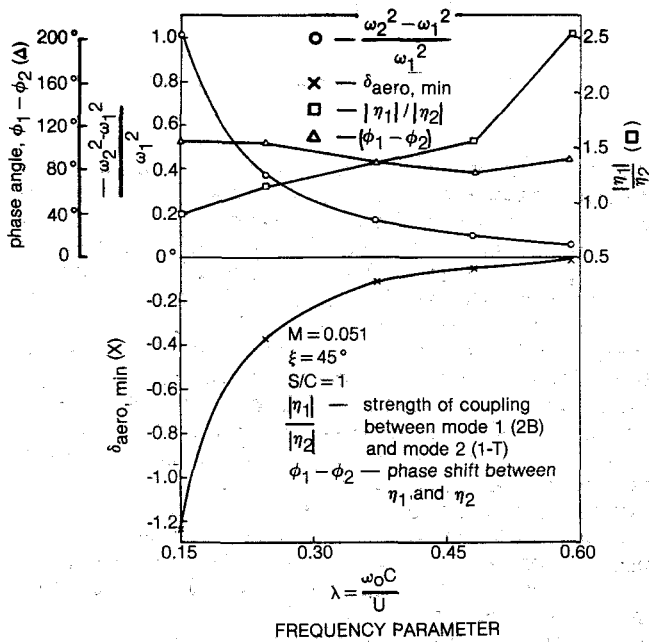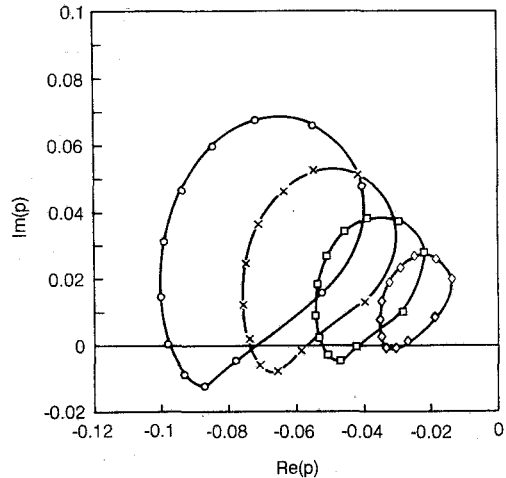
Fig. 6 Flutter eigenvalues for different mass ratios (two-dimensional analysis)

flutter, involving two neighboring blade modes. One of the modes (torsion) is mode 1 in Table 1. The other mode is listed in Table 3. The stability results were obtained by the solution of a (24×24) eigenvalue problem. These modes, by themselves, would indicate an unstable torsion mode and a stable bending mode for the specified aerodynamic conditions. However, when coupled flutter occurs, there is significant participation of both the bending and torsional modes in the resultant flutter mode. At any given value of the frequency parameter λ, the possibility of coupled flutter at ω_0 in a mixture of two modes, (i.e., the bending mode at ω_1 and the torsion mode at ω_2), is predicted when two conditions are satisfied. These conditions are (a) the analysis frequency $\omega_0 \sim \omega_1$ and (b) the flutter frequency of the torsional mode alone is
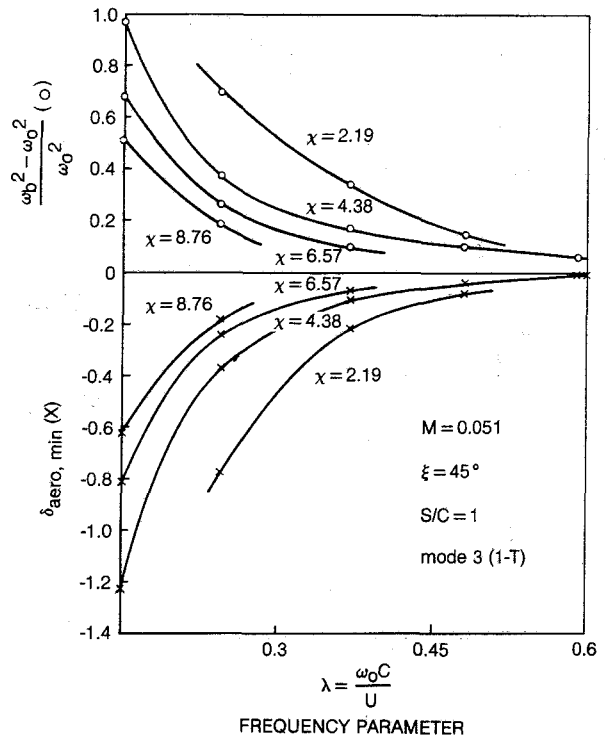
ω_1. This trend is plotted in Fig. 4 in terms of a dimensionless frequency spacing parameter $\omega_2^2 - \omega_1^2 / \omega_1^2$ against the frequency parameter $\lambda = \omega_0 C / U$. The logarithmic decrements calculated for these flutter modes were found to be almost the same as those calculated for the torsional mode alone (compare Fig. 3 for $C_F/C_T = 0$). The dependence of the ratios of the complex valued modal participation factor η_1 (bending mode) and η_2 (torsion mode) is plotted in terms of the ratios of the magnitudes $|\eta_1| / |\eta_2|$ and the phase differences, (the complex number $\eta = |\eta| e^{i\phi}$), $\phi_1 - \phi_2$. Thus, it
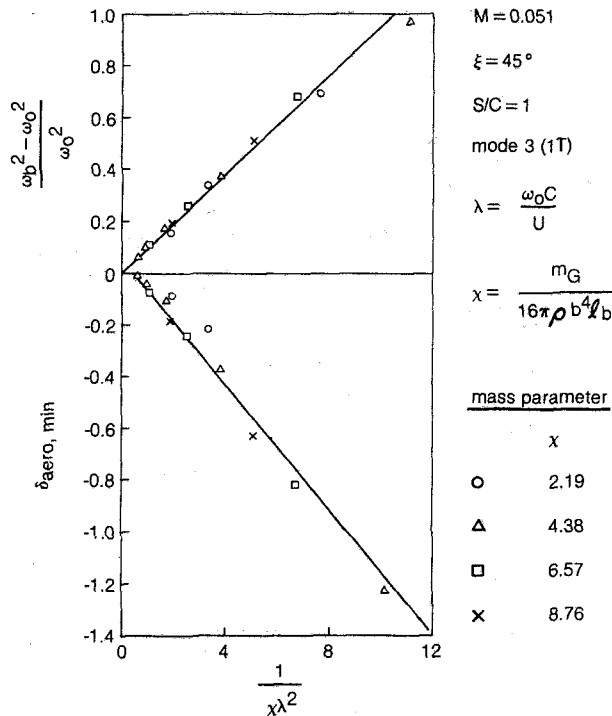
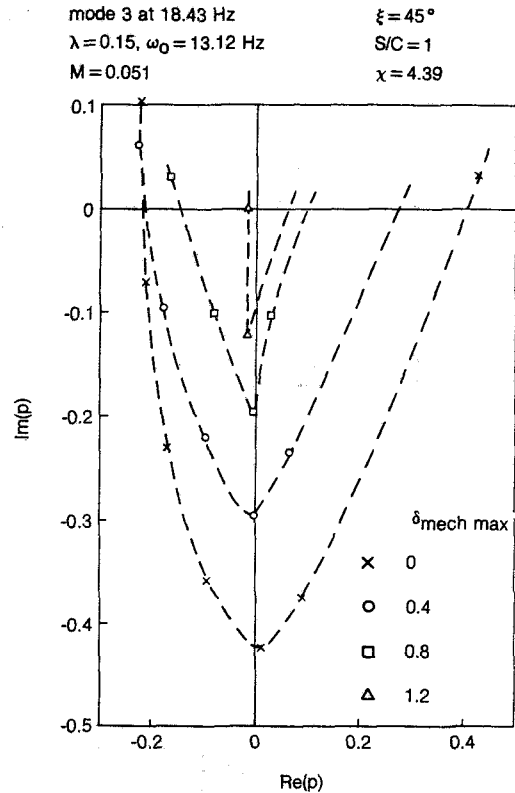Fig. 7 Stiffness ratio correlation of data of Fig. 5
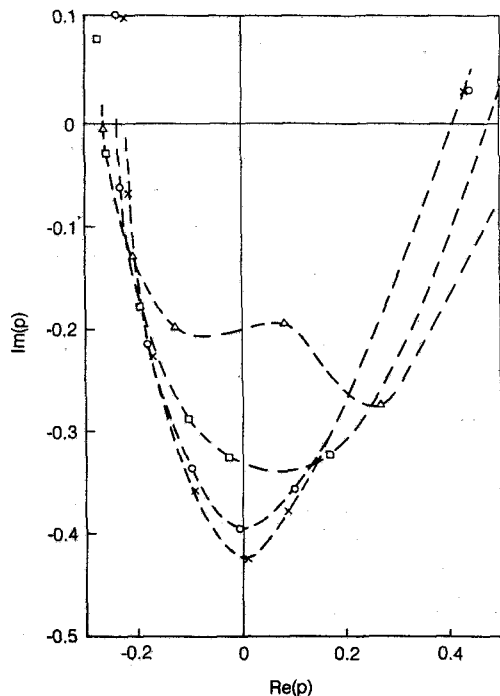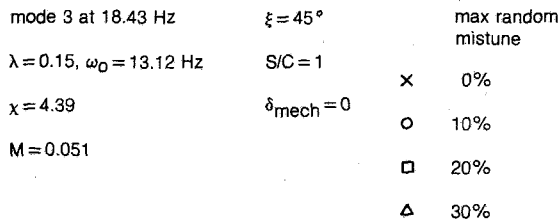

Fig. 9 Random damping effects (no mistune)

Fig. 8 Random mistuning effects (no damping)

is seen that with increasing frequency parameter λ, the relative participation of the bending mode in coupled flutter is increasing, along with the increasing tendency towards stability. It is interesting to note that the phase shift between the bending and torsional modes during coupled flutter remains approximately 90 deg. The corresponding motion of each blade in such a flutter mode is reminiscent of the classical flutter of a fixed airplane wing. This distinguishes the coupled flutter involving two blade modes from the flutter of a single blade mode which contains both bending and torsional degrees of freedom (the subject of an earlier discussion).

Figures 5 and 6 show the influence of mass ratio χ (defined in Appendix B) on the stability of the system vibrating in a torsion mode. Increase in mass ratio increases the tendency towards stability and results in a solution frequency close to blade frequency. A glance at equation (B-8) of Appendix B reveals the reason why all the points plotted in Fig. 5 collapse into an essentially straight line in Fig. 7 when $(1/\chi\lambda^2)$ is used as the abscissa. The physical meaning of $(1/\chi\lambda^2)$ emerges when we write

$$\frac{1}{\chi\lambda^2} = \frac{1}{\left(\dfrac{m_G}{16\pi\rho b^4 l_b} \cdot \dfrac{\omega_0^2 C^2}{U^2} \right)}$$

$$= \frac{8(\pi b^2 l_b)(\rho U^2/2)}{K_G} \qquad (20)$$

where $K_G = m_G\omega_0^2$ is a generalized stiffness of the blade mode based on the analysis frequency. $(1/\chi\lambda^2)$ can therefore be considered as a ratio of the dynamic "stiffness" of the air column around the blade to the generalized stiffness of the blade mode. Comparison of Figs. 5 and 7 leads one to state that this "stiffness ratio" overrides the "mass ratio" in in-
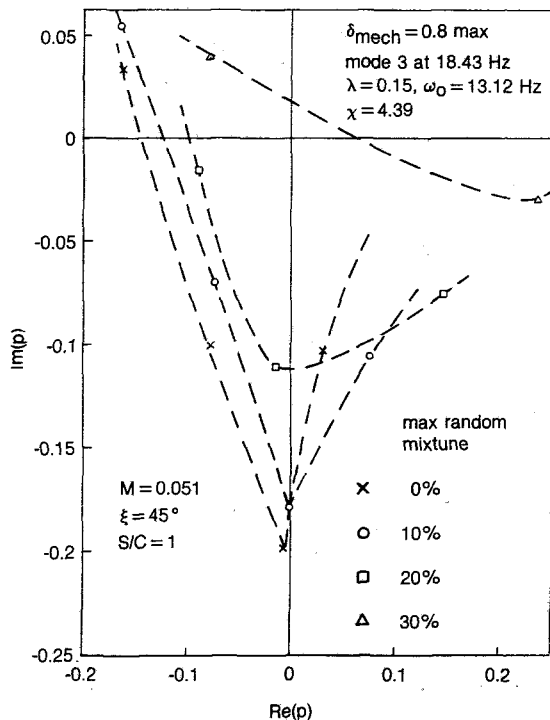
Fig. 10   Influence of combined random mistuning and damping

$\delta_{mech} = 0.8$ max
mode 3 at 18.43 Hz
$\lambda = 0.15$, $\omega_0 = 13.12$ Hz
$\chi = 4.39$

$M = 0.051$
$\xi = 45°$
$S/C = 1$

max random mixtune

×	0%
○	10%
□	20%
△	30%

Fig. 11   Selective mistuning of four blades

mode 3 at 18.43 Hz $\xi = 45°$
$\lambda = 0.15$, $\omega_0 = 13.12$ Hz $S/C = 1$
$\chi = 4.39$ $\delta_{mech} = 0$
$M = 0.051$

×	0% mixture
△	30% random ($\pm 15\%$ max)
○	30% higher freq. (1, 4, 7, 10)
□	15% higher freq. (1, 4, 7, 10)

fluencing the stability of the system. This observation is new and significant as it underscores the importance of considering actual blade mode shapes, frequencies, and generalized masses in cascade flutter analyses.

Figures 8 and 9 show the eigenvalue loops resulting from a random arrangement of blade frequencies and damping separately. The indications are clear that either method can be used in practice to improve stability conditions. A combination of these, i.e., both mistuning and damping arranged in a random manner increases, as expected, the stability even more as can be observed from Fig. 10.

A set of calculations were made for the same system to compare the improvement in stability between using random arrangement of blade frequencies and a selective arrangement of the frequencies. The latter was chosen to be a condition in which four blades in a system of 12 blades had frequencies 15 and 30 percent higher than the uniform frequencies of other blades. These blades were placed symmetrically around the rotor. The results are presented in Fig. 11. While the mistuned systems show a decided improvement over the corresponding tuned system, results indicate that the stability characteristics of the selectively mistuned system can be slightly better than the randomly mistuned system.

Conclusions

The formulation shown in detail in this paper presents a framework for flutter analysis of a cascade of cantilevered blades. Although the equations presented here do not include the considerations of forced vibration, the extension of the current procedures to solve for resonant amplitudes of the assembly at a given forcing frequency is straightforward. Similarly the matrix, which in the present analysis calculates the aerodynamic force on a given blade due to vibrations of all other blades, is conceptually the same for calculating the influences due to mechanical coupling and therefore can be replaced by coefficients appropriate to that coupling.

The limited parametric study presented here is meant mainly to establish trends and to generate information which may set directions for more detailed work. The next logical extension of this work is to examine if the results obtained under somewhat restrictive aerodynamic conditions continue to hold for a full fan under realistic operating conditions.

The results obtained for a single blade mode with several random distributions of frequencies and damping indicate the possibilities of improving the stability characteristics. The question of choice between mistuning or designing damping into the system can be addressed only upon additional analysis and some laboratory testing. The use of dampers in turbine blades has been in practice industry-wide but a combination of mistuning and damping, if proved to be substantially better by experimental data, would provide additional assurance in regard to rotor integrity.

The results in regard to the strength of coupling within a blade mode point to the benefit of coupling in regard to flutter. Clearly, the trend is an improvement in the levels of aerodynamic damping. Presence of bending deformation in a predominantly torsion mode improves stability. Studies of coupled flutter involving more than one blade mode, showed that although the overall frequency shift at flutter and the logarithmic decrement are governed by the unstable mode of the two modes (when it flutters by itself), the flutter frequency overlaps the natural frequency of an otherwise stable mode. The flutter mode shape will contain significant participation of both modes with a phase shift between the motions in these modes.

Flutter characteristics, such as the frequency shift at flutter and the aerodynamic logarithmic decrement, were found to relate more directly to the stiffness ratio $(1/\chi\lambda^2)$ than the mass ratio χ or the frequency parameter separately.

References

1 Kurkov, A. P., "Flutter Spectral Measurements Using Stationary Pressure Transducers," *Measurement Methods in Rotating Components of Turbomachinery*, ASME New York, 1980.

2 Whitehead, D. S., "Torsional Flutter of Unstalled Cascade Blades at Zero Deflection," R&M 3429, Cambridge University Engineering Laboratory, England, 1964.

3 Srinivasan, A. V., "Influence of Mistuning on Blade Torsional Flutter," NASA CR-165137, Aug. 1980.

4 Srinivasan, A. V., and Kurkov, A. P., "Effects of Mistuning on Blade Torsional Flutter," paper presented at the Fifth International Symposium on Airbreathing Engines, Bangalore, India, Feb. 16–21, 1981.

5 Kaza, K. V., and Kielb, R. E., "Effects of Blade Mistuning on Bending-Torsion Flutter and Response of a Cascade in Incompressible Flow," presented at the AIAA/ASME/ASCE/AHS 22nd Structures, Structural Dynamics and Materials Conference, Atlanta, Ga., Apr. 6–8, 1981. (Also DOE/NASA/1028-29, NASA TM-81674).

6 Kaza, K. V., and Kielb, R. E., "Effects of Mistuning on Bending-Torsion Flutter and Response of a Cascade in Incompressible Flow," paper presented at the AIAA Dynamics Specialists Conference, Atlanta, Ga., Apr. 9–10, 1981.

7 Kielb, R. E., and Kaza, K. V., "Aeroelastic Characteristics of a Cascade of Mistuned Blades in Subsonic and Supersonic Flows," paper presented at the Eight Biennial ASME Vibrations Conference, Hartfort, CT, Sept. 20–23, 1981.

8 Carta, F. O., "Coupled Blade-Disk-Shroud Flutter Instabilities in Turbojet Engine Rotors," ASME JOURNAL OF ENGINEERING FOR POWER, Vol. 89, July 1967.

9 Bendiksen, O., and Friedmann, P., "Coupled Bending-Torsion Flutter in Cascades," *AIAA Journal*, Vol. 18, No. 2, Feb. 1980, pp. 194–201.

10 BEndiksen, O., and Friedmann, P., "Coupled Bending-Torsion Flutter in a Supersonic Cascade," *AIAA Journal*, Vol. 19, No. 6, June 1981, pp. 774–781.

11 Bendiksen, O., and Friedmann, P., "The Effect of Bending-Torsion Coupling on Fan and Compressor Blade Flutter," ASME JOURNAL OF ENGINEERING FOR POWER, Vol. 104, July 1982, pp. 617–623.

12 Kaza, K. R. V., and Kielb, R. E., "Coupled Bending-Torsion Flutter of a Mistuned Cascade with Nonuniform Blades," AIAA Paper No. 82-0726, *Proceedings of the 23rd Structures, Structural Dynamics and Materials Conference*, pt. 2, New Orleans, May 1982, pp. 446–461.

13 Smith, S. N., "Discrete Frequency Sound Generation in Axial Flow Turbomachines," A.R.C. R&M No. 3709, 1973.

APPENDIX A

The forces and moments acting on the mth segment of the kth blade can be written generally as

$$
\left.
\begin{aligned}
L_M{}^k &= \sum_{n=1}^{N} \sum_{t=1}^{M} (P_{m,t}{}^{kn} h_t{}^n + Q_{m,t}{}^{kn} \alpha_t{}^n) \\
M_m{}^k &= \sum_{n=1}^{N} \sum_{t=1}^{M} (R_{m,t}{}^{kn} h_t{}^n + S_{m,t}{}^{kn} \alpha_t{}^n)
\end{aligned}
\right\}
\tag{A-1}
$$

where $h_t{}^n$, $\alpha_t{}^n$ represent the displacement/rotation of the tth segment of the nth blade. $P_{m,t}{}^{kn}$, $Q_{m,t}{}^{kn}$, $R_{m,t}{}^{kn}$ and $S_{m,t}{}^{kn}$ are influence coefficients specifying the forces and moments acting on the nth segment of the kth blade, due to unit displacements and rotations of the tth segment of the nth blade. N is the number of blades, and M is the number of segments per blade. These influence coefficients are the result of aerodynamic and/or structural dynamic coupling through the support structure and or shrouds. The theories presently available for determining the aerodynamic influence coefficients are based on two-dimensional strip theories. Within this limitation, the coupling forces due to aerodynamic coupling reduce to

$$
\sum_{t=1}^{M} P_{m,t}{}^{kn} h_t{}^n = P_{m,t}{}^{kn} h_t{}^n \delta_{m,t}
$$

$$
\equiv P_m{}^{kn} h_m{}^n
$$

where $\delta_{m,t}$ is the Kronecker delta, defined by

$$
\delta_{m,t} = \begin{matrix} 1, & m = t \\ 0, & m \neq t \end{matrix}
$$

Therefore, for analysis using two-dimensional aerodynamic theories

$$
\left.
\begin{aligned}
L_m{}^k &= \sum_{n=1}^{N} (P_m{}^{kn} h_m{}^n + Q_m{}^{kn} \alpha_m{}^n) \\
M_m{}^k &= \sum_{n=1}^{N} (R_m{}^{kn} h_m{}^n + S_m{}^{kn} \alpha_m{}^n)
\end{aligned}
\right\}
\tag{A2}
$$

By definition

$$
\sum_{n=1}^{N} P_m{}^{kn} \exp\left(i 2\pi r \frac{n}{N}\right)
$$

$$
= -2\pi i \omega_0{}^2 \rho_m \frac{b_m{}^2}{k_m} l_m (C_{Fq}{}^r)_m \exp\left(i 2\pi r \frac{k}{N}\right)
$$

$$
\sum_{n=1}^{N} Q_m{}^{kn} \exp\left(i 2\pi r \frac{n}{N}\right)
$$

$$
= -2\pi \omega_0{}^2 \rho_m \frac{b_m{}^3}{k_m{}^2} l_m (C_{F\alpha}{}^r)_m \exp\left(i 2\pi r \frac{k}{N}\right)
$$

$$
\sum_{n=1}^{N} R_m{}^{kn} \exp\left(i 2\pi r \frac{n}{N}\right)
$$

$$
= -4\pi i \omega_0{}^2 \rho_m \frac{b_m{}^3}{k_m} l_m (C_{Mq}{}^r)_m \exp\left(i 2\pi r \frac{k}{N}\right)
$$

$$
\sum_{n=1}^{N} S_m{}^{kn} \exp\left(i 2\pi r \frac{n}{N}\right)
$$

$$
= -4\pi \omega_0{}^2 \rho_m \frac{b_m{}^4}{k_m{}^2} l_m (C^r_{M\alpha})_m \exp\left(i 2\pi r \frac{k}{N}\right)
\tag{A3}
$$

where $(C_{Fq}{}^r)_m$, $(C_{F\alpha}{}^r)_m$, $(C_{Mq}{}^r)_m$, $(C_{M\alpha}{}^r)_m$ are the aerodynamic force and moment coefficients defined in [8], and are computed using cascade properties at the mth blade segments and interblade phase angle $\beta_r = 2\pi r/N$

$$
k_m = \frac{b_m \omega_0}{U_m}, \quad \rho_m = \text{density} \quad l_m = \text{segment length}
$$

at the mth blade segment.

By some manipulation of equation (A3), explicit expressions can be obtained for the aerodynamic influence coefficients as:

$$
P_m{}^{kn} = -\frac{2\pi}{N} i \, \omega_0{}^2 \rho_m \frac{b_m{}^2}{k_m} l_m \sum_{r=1}^{N} (C_{Fq}{}^r)_m e^{i \frac{2\pi}{N} r(k-n)}
$$

$$
Q_m{}^{kn} = -\frac{2\pi}{N} \omega_0{}^2 \rho_m \frac{b_m{}^3}{k_m{}^2} l_m \sum_{r=1}^{N} (C_{F\alpha}{}^r)_m e^{i \frac{2\pi}{N} r(k-n)}
$$

$$
R_m{}^{kn} = -\frac{4\pi}{N} i \omega_0{}^2 \rho_m \frac{b_m{}^3}{k_m} l_m \sum_{r=1}^{N} (C_{Mq}{}^r)_m e^{i \frac{2\pi}{N} r(k-n)}
$$

$$
S_m{}^{kn} = -\frac{4\pi}{N} \omega_0{}^2 \rho_m \frac{b_m{}^4}{k_m{}^2} l_m \sum_{r=1}^{N} (C_{M\alpha}{}^r)_m e^{i \frac{2\pi}{N} r(k-n)}
\tag{A4}
$$

APPENDIX B

When the cascade properties are uniform, i.e., stagger angle, solidity, Mach number, chord length, air velocity, and density are the same at each blade section, the following simplifications can be made in the flutter equations

$$A_{ij}^{kn} =$$

$$-\frac{1}{N\chi_{ij}\lambda^2}\left[\left(\sum_{m=1}^{M}\frac{h_{mi}}{b}\cdot\frac{h_{mj}}{b}\cdot\frac{1_m}{1_b}\right)\left(\frac{i\lambda}{4}\sum_{r=0}^{N-1}(C_{hh})^r e^{\frac{i2\pi}{N}r(k-n)}\right)\right.$$

$$+\left(\sum_{n=1}^{M}\frac{h_{mi}}{b}\cdot\alpha_{mj}\cdot\frac{1_m}{1_b}\right)\left(\frac{1}{2}\sum_{r=0}^{N-1}(C_{h\alpha})^r e^{\frac{i2\pi}{N}r(k-n)}\right)$$

$$+\left(\sum_{m=1}^{M}\alpha_{mi}\cdot\frac{h_{mj}}{b}\cdot\frac{1_m}{1_b}\right)\left(\frac{i\lambda}{2}\sum_{r=0}^{N-1}(C_{\alpha h})^r e^{\frac{i2\pi}{N}r(k-n)}\right)$$

$$+\left.\left(\sum_{m=1}^{M}\alpha_{mi}\cdot\alpha_{mj}\cdot\frac{1_m}{1_b}\right)\left(\sum_{r=0}^{N-1}(C_{\alpha\alpha})^r e^{\frac{i2\pi}{N}r(k-n)}\right)\right]$$

$$\tag{B1}$$

where $\lambda \equiv 2k$ is the frequency parameter

$$\chi_{ij} \equiv \frac{1}{16\pi C_i C_j \rho b^4 1_b} = \frac{\sqrt{m_i m_j}}{16\pi\rho b^4 1_b}$$

which is a generalized mass parameter for modes i and j of the blade, 1_b is the blade span; again, m_i and m_j are the generalized masses of the ith and jth blade modes, respectively. The subscript m has been dropped from the force and moment coefficients, since these coefficients are now the same for all the spanwise blade sections.

If only one blade mode is being considered in the analysis, equation (B1) can be simplified further. For this case, the aeroelastic $[A]$ matrix is now made up of $N \times N$ complex elements, each of which is made up of the expression in equation (B1) with the i and j subscripts dropped, i.e., if

$$S_{hh} \equiv \sum_{m=1}^{M}\frac{h_m^2}{b^2}\frac{1_m}{1_b}$$

$$S_{\alpha\alpha} \equiv \sum_{m=1}^{M}\alpha_m^2\frac{1_m}{1_b}$$

and $\chi = m_G/16\pi\rho b^4 1_b$, where m_G is the generalized mass of the blade mode then the complex element at the kth row of the nth column of the $[A]$ matrix now becomes

$$A^{kn} = -\frac{1}{N\chi\lambda^2}\left[\frac{i\lambda S_{hh}}{4}\sum_{r=0}^{N-1}(C_{hh})^r e^{\frac{i2\pi}{N}r(k-n)}\right.$$

$$+S_{h\alpha}\left(\frac{1}{2}\sum_{r=0}^{N-1}(C_{h\alpha})^r e^{\frac{i2\pi}{N}r(k-n)}\right)$$

$$+\frac{i\lambda}{2}\sum_{r=0}^{N-1}(C_{\alpha h})^r e^{\frac{i2\pi}{N}r(k-n)}$$

$$\left.+S_{\alpha\alpha}\sum_{r=0}^{N-1}(C_{\alpha\alpha})^r e^{\frac{i2\pi}{N}r(k-n)}\right]$$

$$\tag{B2}$$

The nth diagonal complex-valued element of the $[\Omega]$ matrix is

$$\Omega_n = \frac{\omega_n^2}{\omega_0^2}\left(1+i\frac{\delta_n}{\pi}\right)$$

$$\tag{B3}$$

where ω_n is the natural frequency of the nth blade for the mode in question, and δ_n is the mechanical logarithmic decrement of the same blade mode.

The eigenvectors of equation (19) can be represented as a linear combination of N orthonormal vectors of the form

$$\{\bar{X}\} = \sum_{R=0}^{N-1} y_R\left\{e^{\frac{i2\pi R}{N}j}\right\} \quad j=1,2,3\ldots N$$

$$\tag{B4}$$

It is sufficient to consider equation (B4) as merely an expansion of an N dimensional general vector into components of an N dimensional orthonormal vector space. It is clear that each of the orthonormal vectors represent a solution to the "tuned" flutter equations. If we denote the complex conjugate of y_R by y_R^* and that of $\{\bar{X}\}$ by $\{\bar{X}^*\}$, such that

$$\{\bar{X}^*\} = \sum_{R=0}^{N-1} y_R^*\left\{e^{-\frac{i2\pi R}{N}j}\right\}$$

$$\tag{B5}$$

Equation (19) can be manipulated to yield

$$\frac{\lambda_0^2}{\omega_0^2} = \frac{1}{N\sum_{R=0}^{N-1}|y_R|^2}\left\{\sum_{R,S,n}^{N-1}\left(y_R^* y_S \Omega_n e^{-\frac{i2\pi}{N}n(R-S)}\right)\right.$$

$$\left.+\sum_{R,S,k,n}^{N-1}\left(y_R^* y_S A_{kn} e^{-\frac{i2\pi}{N}(Rk-Sn)}\right)\right\}$$

$$\tag{B6}$$

where the notation

$$\sum_{R,S,n}^{N-1}(\quad) \equiv \sum_{R=0}^{N-1}\sum_{S=0}^{N-1}\sum_{k=0}^{N-1}\sum_{n=0}^{N-1}(\quad)\text{ etc.}$$

Upon substitution of equations (B2) and (B3) into (B6) and simplifying, we get

$$\frac{\lambda_0^2}{\omega_0^2} = \frac{1}{N\sum_{R=0}^{N-1}|y_R|^2}\left\{\sum_{R,S,n}^{N-1}\left[y_R^* y_S\left(\frac{\omega_n^2}{\omega_0^2}\left(1\right.\right.\right.\right.$$

$$\left.\left.\left.\left.+i\frac{\delta_n}{\pi}\right)\right)e^{-\frac{i2\pi}{N}(R-S)n}\right]\right\}$$

$$-\frac{1}{\chi\lambda^2\sum_{R=0}^{N-1}|y_R|^2}\left\{\sum_{r=0}^{N-1}|y_r|^2\left[\frac{i\lambda S_{hh}}{4}C_{hh}^r\right.\right.$$

$$\left.\left.+\frac{S_{h\alpha}}{2}(C_{h\alpha}^r + i\lambda C_{\alpha h}^r) + S_{\alpha\alpha}C_{\alpha\alpha}^r\right]\right\}$$

$$\tag{B7}$$

For a system of tuned blades, i.e., when all blade frequencies and damping are the same, equation (B7) reduces to

$$\left(\frac{\lambda_0^2}{\omega_0^2}\right)_{R,\text{tuned}} = \frac{\omega_b^2}{\omega_0^2}\left(1+\frac{i\delta}{\pi}\right)-\frac{1}{\chi\lambda^2}\left\{\frac{i\lambda S_{hh}}{4}C_{hh}^R+\right.$$

$$\left.+\frac{S_{h\alpha}}{2}(C_{h\alpha}^R + i\lambda C_{\alpha h}^R) + S_{\alpha\alpha}C_{\alpha\alpha}^R\right\}$$

$$\tag{B8}$$

for the Rth system mode, i.e., the tuned system mode for which the phase shift from one blade to the next is $2\pi R/N$.

Equation (B8), the main result of this appendix, is of interest in two regards. The first is that it provides a quick way of calculating the eigenvalues for any specified modeshape, cascade properties and interblade phase angle. Such quick calculations are useful in obtaining first approximations to the value of analysis frequency ω_0 which will yield a correct solution to the flutter eigenvalue problem. The second interesting aspect of this equation is that it crystallizes the role played by the parameter $(1/\chi\lambda^2)$ with regard to the frequency shift at flutter and the aerodynamic logarithmic decrement. Increasing values of $(1/\chi\lambda^2)$ leads to larger differences between the blade mode frequency and the flutter frequency and also to more negative values of the aerodynamic logarithmic decrement for the unstable system modes.

A. P. Kurkov

National Aeronautics and
Space Administration,
Lewis Research Center,
Cleveland, Ohio 44135

Measurements of Self-Excited Rotor-Blade Vibrations Using Optical Displacements

During the operation of a turbofan engine at part speed, near stall, and elevated inlet pressure and temperature, several vibratory instabilities were excited simultaneously on the first fan rotor. The torsional and bending contributions to the main flutter mode were resolved by using casing-mounted optical displacement sensors. Strain-gage spectra were used to identify other instabilities in the blade-deflection spectra. The characteristics of optical-displacement spectra and their role of monitoring rotor-blade vibrations are discussed.

Introduction

Turbomachinery vibrations can be classified either as forced vibrations, which occur in response to stationary upstream or downstream disturbances, or as self-excited vibrations for which no obvious source of excitation is present. Self-excited vibrations are usually associated with either the individual blade natural frequencies or a rotor-assembly natural frequency. In general, therefore, these vibrations occur at a nonintegral multiple of rotational frequency.

Flutter is the most frequent and best documented self-excited vibration. All blades in flutter vibrate at the same frequency and the phase angle between the two consecutive blades (i.e., interblade phase angle) is well defined. Thus, in a rotating frame of reference, flutter can be described by a traveling wave. However, the amplitudes and interblade phase angles do not necessarily have to be uniform around the rotor. In such a case several traveling waves are present simultaneously. This occurs, for example, when the single-blade natural frequencies are not all identical; that is, when rotor blades are mistuned [1].

Stationary optical sensors are well suited for displacement measurements during flutter or during any other self-excited vibration at a nonintegral multiple or rotational frequency. Optical sensors were discussed in [2] and the quantitative analysis methods in [3-5]. This paper presents results for a more complicated situation. Several vibratory modes were excited simultaneously, and flutter occurred in a second coupled mode which involves both bending and torsional blade displacements. (In [3-5] the vibratory mode was first torsion and no other excitations were present.) This paper is primarily intended to illustrate the capabilities and limitations of the optical displacement measurements and to illustrate the analysis procedure for this complex multiple-mode excitation.

However, certain results are also expected to be of more general interest.

The instabilities described in this paper (and in [3-5]) occurred in the first fan rotor during part-speed, near-stall operation at elevated inlet pressure and temperature. For the particular test point discussed herein, a tip-radial screen was installed in the inlet duct. The blade-tip relative Mach number was 0.954 and the reduced frequency (based on the blade chord) at the tip span was 1.39. The fan blades were equipped with shrouds at 54 percent of the span.

Personnel at Pratt & Whitney Aircraft, Government Products Division, and in particular Mr. A. W. Stoner is credited for obtaining the estimates for blade deflections, the streamline blade-element parameters, and the single blade holograms.

Experimental Measurements and Data Processing

Only a brief description of optical displacements measurements is given in this paper since a detailed description is reported in [2]. Figure 1 illustrates the position of optical ports in the engine casing relative to a rotor blade. As the blades passed optical ports, a light beam was reflected from the blade tips and conducted to a photomultiplier by a fiber-optics bundle. A voltage pulse was generated every time a blade passed an optical port. The position of this pulse relative to the once-per-revolution (1E) signal indicated the instantaneous position of a blade in flutter. The blade pulses and the reference 1E signal were recorded at 304.8 cm/s (120 in/s) on a wideband I FM tape recorder.

During the postrun analysis, the tape was played back at 1/64 of the recording speed, and the two channels of data (a once-per-blade pulse train generated by the optical sensor and the once-per-revolution reference signal) were digitized at the maximum possible rate (20,480 Hz/channel). The resulting resolution (about 8860 points/revolution) was sufficient to capture the blade motion corresponding to main flutter mode. However, to capture some of the smaller displacement associated with higher modes, it was desirable to attain a
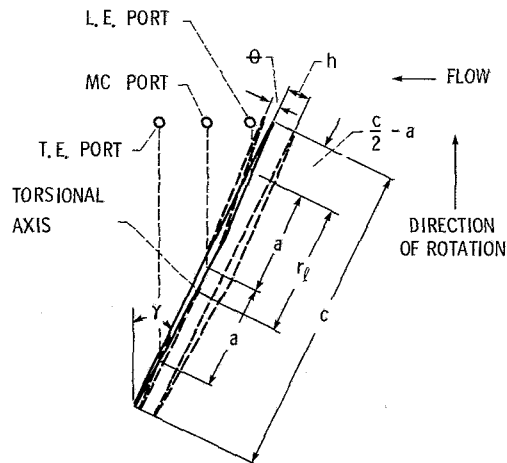
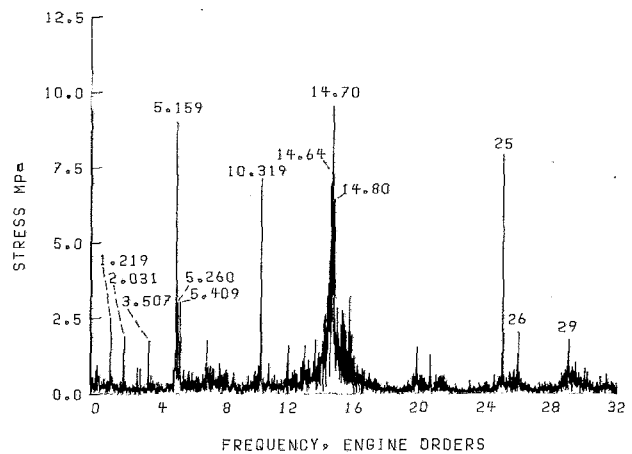**Fig. 1 Locations of measurement ports relative to a blade**

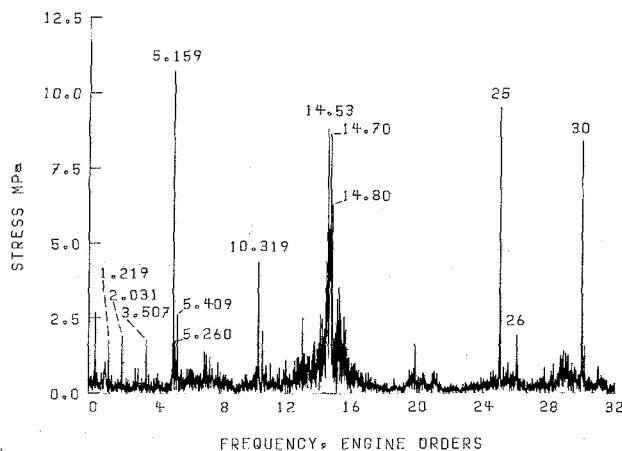**Fig. 3 Strain gage spectrum, blade 26**

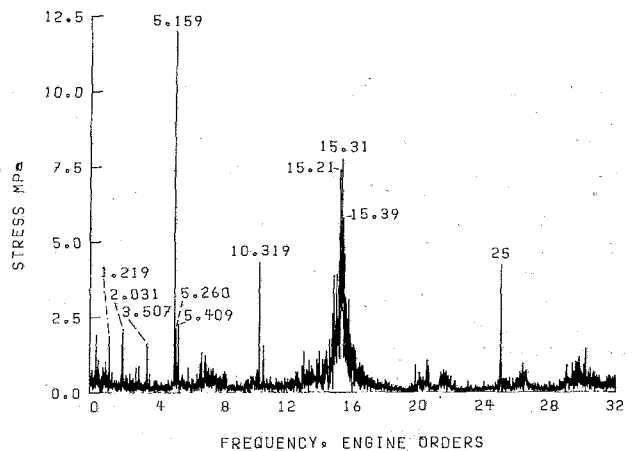**Fig. 2 Strain gage spectrum, blade 3**

Fig. 4 Strain gage spectrum, blade 17

higher resolution. This could only be achieved by reducing the signal frequency further during playback. Since no further reduction of the tape speed was possible, the data were recorded on another tape at four times the speed of the original tape. Thus four times higher resolution could be achieved during playback. However, experimentation showed that doubling the original resolution was sufficient. Therefore the number of points per revolution during the data analysis was 17,720.

One difficulty encountered during this procedure was the loss of precise synchronization between the displacement and the strain-gage tapes. It was intended to achieve this synchronization by using the time code signal recorded on all tapes. However, because the resulting frequency of the time code signal during playback was too low, it could not be read. Since the channel to channel synchronization depended on

using the time code signal, another time code had to be recorded on the second FM tape. (In this procedure [3–5] the data acquisition is initiated at the first 1E pulse after the preselected time instant is read from the tape.)

In this analysis the 1E reference pulse is used rather than the once per blade as in [3–5]. Therefore, when instantaneous blade positions were computed, a correction was applied to compensate for the slight variation in speed (and thus in the count per revolution) during the sampling interval. The compensation is accomplished by multiplying the instantaneous pulse positions by the ratio of the average count per revolution by the current count per revolution. This correction was not necessary when the once-per-blade reference was used [3–5] because of the closeness of the reference pulse to the blade pulse.

One problem encountered in triggering blade pulse signals,

_____ **Nomenclature** _____

A = amplitude
a = port separation along the chord, Fig. 1
c = blade chord
D = total tangential displacement
d = displacement component of D
h = bending displacement, Fig. 1
j = imaginary unit
k = revolution counter
l = blade counter
n = number of revolutions

Q = number of points per revolution
q = point-per-revolution counter
r = radial coordinate, Fig. 1
γ = stagger angle, Fig. 1
θ = angular displacement, Fig. 1
Φ = angular coordinate in rotating frame of reference
ϕ = phase angle
ω = circular frequency

Subscripts

f = flutter

h = bending
i = nodal diameter
l = leading edge port
m = midchord port
r = rotational
s = strain gage
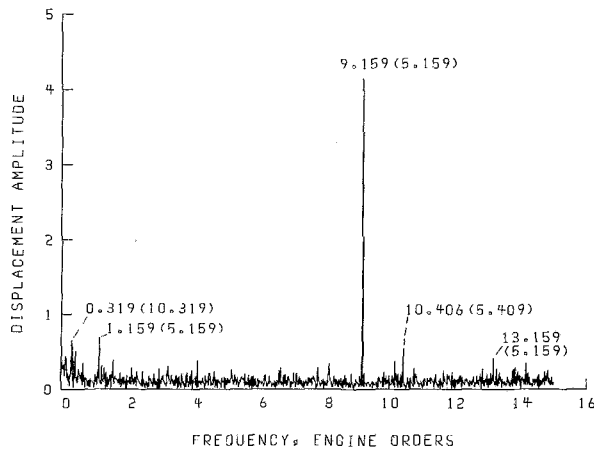t = trailing-edge port
u = unsteady component
θ = torsion

Fig. 5 Overall displacement spectrum, leading edge port. Frequencies in parenthesis correspond to associated peaks in the strain-gage spectra.

Fig. 6 Overall displacement spectrum, midchord port

Fig. 7 Overall displacement spectrum, trailing edge port

particularly for the leading and trailing edge ports, was the uneven pulse height. This problem was solved by assigning trigger levels based on blade pulse heights. The levels were derived from the averaged (each point q, $q = 1, ..., Q$, is averaged over n revolutions) pulse-train distribution, which was also used to derive a window for each blade. The search for a trigger was performed only in the immediate vicinity (i.e., window) of the particular blade pulse to avoid triggering on a spurious signal. In case a pulse was missing, its average trigger position (obtained from triggering the averaged distribution) was substituted.

As in [3–5], removing of the DC displacement component for each blade l to obtain the unsteady instantaneous tangential displacements is accomplished by using

$$D_u(l,k) = D(l,k) - (1/n) \sum_{k=1}^{n} D(l,k),$$

$$l=1,...,N \quad k=1,...,n \qquad (1)$$

The spectral analysis is performed for either a set of points $k = 1, ..., n$ for each blade l (i.e., individual blade spectra) or a set of points $l=1, ..., N$, $k=1$; $l=1, ..., N$, $k=2$; ... (i.e., overall spectrum). Because Singleton's [5] algorithm was used to obtain the spectra, neither set of points was restricted to a power of two points.

In a rotating frame of reference, flutter vibrations can be described [4, 5] by a summation of waves:

$$D = \sum_{i=1}^{N} A_i \cos(\omega_f t - \Phi i + \phi_i) \qquad (2)$$

where time t and angular coordinate Φ (positive in the direction of rotation) are independent variables. However, from the point of view of a stationary sensor, Φ is not arbitrary but equal to $-\omega_r t$. Thus the signal received by a stationary sensor becomes

$$D = \sum_{i=1}^{N} A_i \cos[(\omega_f + \omega_r i) t + \phi_i] \qquad (3)$$

and each constituent wave is shifted in frequency by $\omega_r i$.

Analysis of the Results

Strain-Gage and Overall-Displacement Spectra. The analysis of the blade deflection data for this engine is complicated by the fact that several nonintegral engine order modes with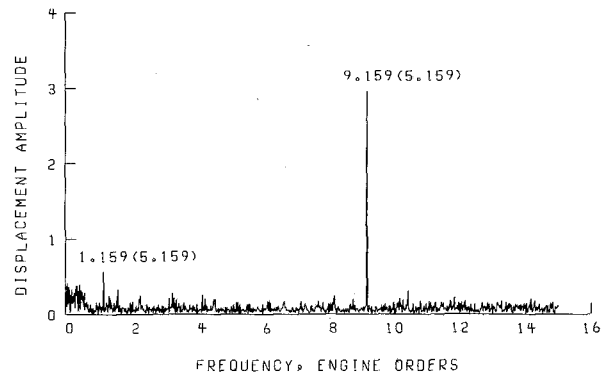 widely different frequencies were excited simultaneously. This is illustrated by the strain-gage spectra (Figs. 2–4). The strain gages were located close to the blade tip and about 31 percent of the chord from the leading edge. The highest stress levels for nonintegral engine order frequencies were observed at 5.159, 10.319 E, and around 14–16E. (The frequencies are presented in engine orders to clearly distinguish the integral and nonintegral engine-order responses and for convenience when correlating different peaks in the strain-gage and displacement spectra. One engine order corresponded to 147.7 Hz.)
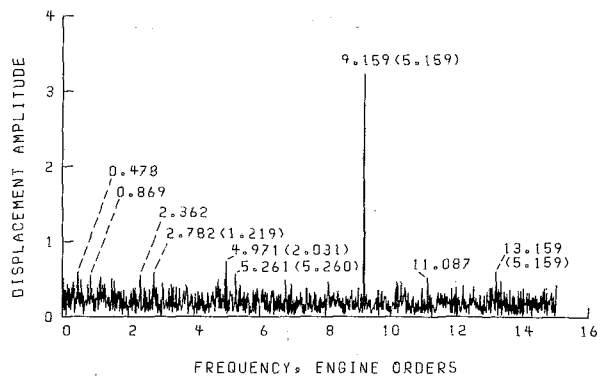
The 5.159 E frequency corresponds to the second coupled mode family. In this mode both bending and torsional deflections are significant. It can be seen that 10.319 E frequency is nearly twice 5.159 E. It appears, therefore, that 10.319 E response is the second harmonic of the coupled flutter mode. However, as will be seen, the lack of response in the displacement spectra at this frequency indicates that motion at this frequency corresponds to a higher mode. Based on a single-blade hologram, 10.319 E is very near the above-shroud bending mode frequency. The response at this frequency will, therefore, be considered as a separate mode. Note, however, that the factor of two difference with the 5.159 E frequency indicates a possible nonlinear coupling between these two responses. The frequencies in the 14–16E band are most closely associated with the above-shroud chordwise bending mode. (Most are 100 to 200 Hz lower than the frequency corresponding to this mode.)

In contrast to the strain-gage spectra, the overall tip-displacement spectra (Figs. 5–7) show that only one large peak is present at 9.159 E. This peak is associated with the 5.159 E major flutter mode in the strain-gage spectra and, therefore, the flutter mode can be described as a four-nodal-diameter forward traveling wave. (From equation (3), the frequency shift in a stationary frame is $\omega_r i$. Thus, $\omega_f/\omega_r + i = 9.159$, and for $\omega_f/\omega_r = 5.159$, $i = 4$.) The tangential displacements
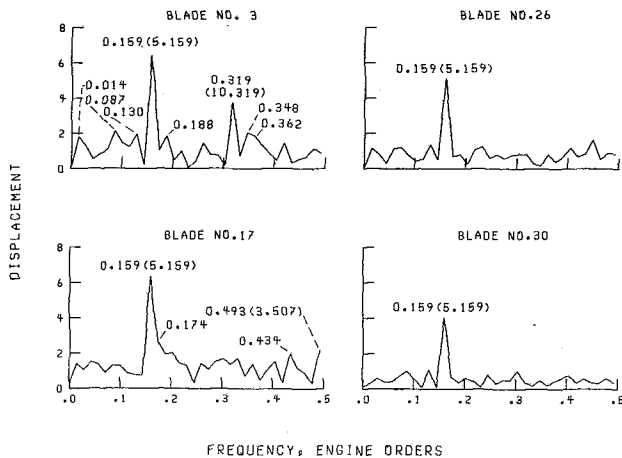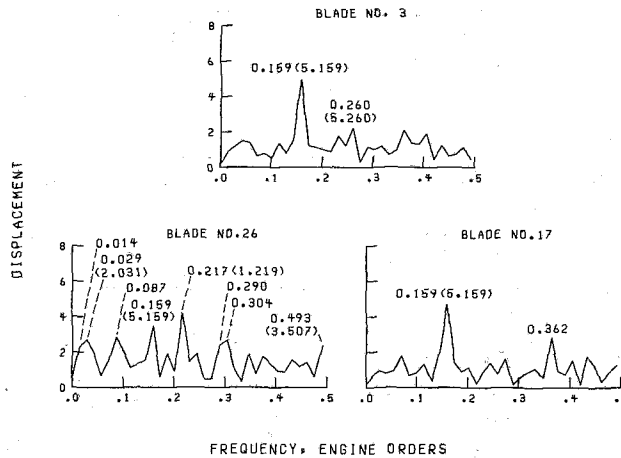
Fig. 8 Displacement spectrum, leading edge port
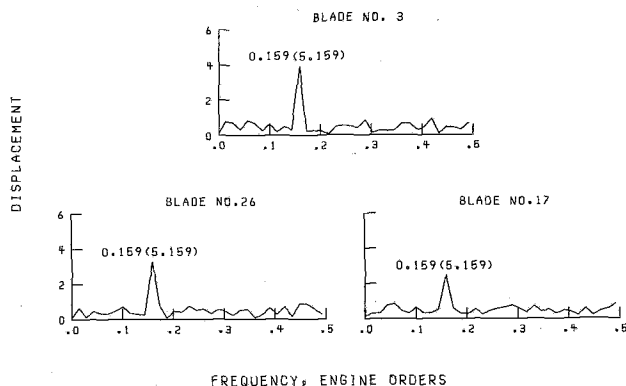

Fig. 9 Displacement spectrum, midchord port

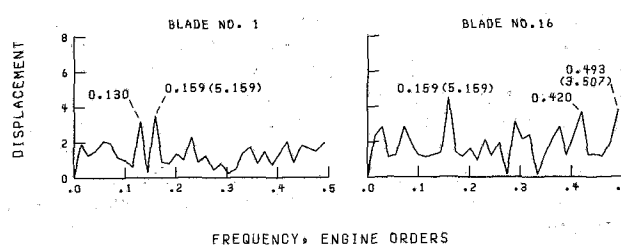Fig. 10 Displacement spectrum, trailing edge port

Fig. 11 Displacement spectrum, trailing edge port, blades 1 and 16

in Figs. 5–7 and subsequent figures are expressed in digitized units for convenience. For the main flutter mode, the displacements are also reported in a parametric form.

The correlation of the remaining peaks in the strain-gage and the blade-displacement spectra is based on several observations. First, considering the significant differences in frequencies for the modes in the 14-16E band (compare Figs. 2 and 3 with Fig. 4), one would suspect that this band is a single-blade response, most likely associated with the flow separation. Second, there was a lack of precise synchronization between the strain-gage and displacement-signal tapes. (As mentioned previously, this synchronization was lost at the expense of increased resolution of blade deflections.) Third, the frequencies for the major peaks in the 14-16E range in the strain-gage spectra shifted somewhat with time; however, no such shifts were observed for the other nonintegral order peaks.

It seemed best, therefore, to (1) exclude from consideration the response in the 14-16E range, (2) attempt to associate all other nonintegral order peaks in the strain-gage and the displacement spectra, and (3) attribute the remainder of the response in the displacement spectra to the 14-16E mode. For the relatively low deflections it is important not to overlook the lower modes corresponding to low stress levels (such as peaks at 1.219, 2.031, 3.507, 5.260, and 5.409 E in the strain-gage spectra) because, in general, for a given stress level, a lower mode generates higher deflections than does a higher mode. (Note that the first peak, at 0.406 E, in Figs. 2 and 4 is 60-Hz noise.) When associating different peaks in the two spectra it is also necessary to consider the complements of fractional parts of nonintegral order peaks. These appear in the overall-displacement spectra when a strain-gage

frequency, expressed in E's, plus or minus the corresponding nodal diameter is outside the range [0, $N/2$]. Thus frequencies associated with these peaks are folded frequencies.

For the major flutter mode (corresponding to the strain-gage frequency of 5.159 E), a slight mistuning was present as shown by the presence of peaks at 1.159 E (Figs. 5 and 6) and 13.159 E (Figs. 5 and 7). Aside from this family, the most noticeable peaks are at 10.406 and 0.319 E (Fig. 5) and at 0.478, 0.869, 2.362, 2.782, 4.971, 5.261, and 11.087 E (Fig. 7). These figures include frequencies corresponding to each peak and frequencies (in parentheses) of the associate peaks in the strain-gage spectra. (Note that peaks at 2.782 and 4.971 correspond to nodal diameters −5 and −7; hence, the fractional parts of these frequencies are complements of the fractional parts of the associated strain-gage frequencies.) The peaks at 0.478, 0.869, 2.362, and 11.087 E could not be associated with any peaks singled out in the strain-gage spectra, including the strong peaks in the 14-16E band.

Individual Blade Spectra. The leading-edge blade-deflection spectra for blades 3, 26, and 17, for which the strain-gage spectra are also available (Figs. 2–4), are presented in Fig. 8. In this figure the frequency is folded in the range 0–1/2 E. Aside from the response at 0.159 E, which is associated with the major flutter mode, the highest peak in Fig. 8, blade 3, is at 0.319 E. A peak at the same frequency was noted in the overall blade-displacement spectrum (Fig. 5) and it was associated with the 10.319 E mode in the strain-gage spectra. The peak at 0.493 E, blade 17, is attributed to 3.507 E mode in the strain-gage spectra. However, aside from these two peaks, significant amplitudes are present (Fig. 8) for blades 3, 26, and 17 at many frequencies as can be seen by comparing their spectra with the spectrum for a relatively quiet blade 30 or by comparing with the midchord port spectra (Fig. 9).

The peaks at 0.087, 0.130, and 0.362 E in Fig. 8, blade 3, can be associated with those at 11.087, 0.869, and 2.362 E in the overall spectrum (Fig. 7). The peaks at 0.014, 0.188, and

0.348 E in the spectrum for this blade and the peak at 0.434 E in the spectrum for blade 17 do not seem to be related to any peaks noted in Figs. 2-7. However, the peak at 0.174 E, blade 17, may be associated with the 15.21 response in the 14-16E band in Fig. 4.

The displacement spectra for the trailing-edge port for blades 3, 26, and 17 are given in Fig. 10. Most of the peaks noted in the strain-gage spectra do appear to be associated with the more visible peaks in these spectra. Moreover, most of the peaks singled out in the overall spectra also appear in Fig. 10. However, the peaks at 0.014, 0.290, and 0.304 E, blade 26, do not seem to be related to any in the strain-gage or the overall spectra. Possibly the last two peaks may be related to the 14.70 E peak in Fig. 3.

In Fig. 10, the peak at 0.217 E, blade 26, is higher than the one at the folded major flutter frequency 0.159 E. A similar situation exists, for example, for blade 1 (Fig. 11) where the peak at 0.130 E is almost as high as the one at 0.159 E. The responses at 0.130 and 0.217 E are associated with those at 0.869 and 2.782 E in the overall spectra. As already noted, the first one, 0.869 E, is not related to any of the responses singled out in the strain-gage spectra. Had blade 1 been strain gaged, it is possible that the source mode for this deflection could be found. However, even without resolving all the details, if the spectra in Fig. 10 or 11 were available during the run they would give a better warning as to the presence of secondary excitations (i.e., not at 0.159 E) than the overall displacement spectra. Another blade for which these secondary excitations were very pronounced was blade 16 (Fig. 11).

Discussion of Spectral Results. The most significant nonintegral response peaks outside the 14-16E range in the tip strain-gage spectra can be related to the distinct peaks in the individual blade spectra for either the leading- or the trailing-edge ports. The majority of these peaks can also be associated with the more visible one in the overall displacement spectra. Of the remaining peaks in the overall spectra, none could be related to the more significant peaks in the 14-16E band in the strain-gage spectra.

Possibly three of the distinct peaks in the individual blade-displacement spectra are related to the strain-gage response in the 14-16E band. However, one of the most striking characteristics of the individual blade spectra is the presence of significant displacement throughout the 0-1/2 E range. This characteristic was observed for most blades, especially the trailing edge. In the absence of any other broad band response, one is led to attribute this characteristic to the 14-16E response in the strain-gage spectra.

This observation has important implications for flutter monitoring, and it points out the need for online spectral analysis. Only with the spectral analysis is it possible to determine whether the blade displacement response corresponds to a single frequency, a multitude of frequencies, or a combination of both. In the region close to stall, the broad band of relatively low-level response in the individual blade-deflection spectra is likely to be associated with a single blade response at a high frequency and a significant stress level. To detect this condition it is important to establish the noise floor level during the operation away from instability.

In order to explain the lack of response in the displacement spectra for the 14-16E band and the 10.319E mode, it is desirable to obtain estimates for the deflections corresponding to these modes for the observed stress levels measured by the strain gages. These estimates were obtained by the engine manufacturer by using a finite element code (NASTRAN). The stress levels at the blade-tip strain gage were assumed to be 9.65 MPa (1.4 kpsi) for the chordwise bending mode and 6.89 MPa (1 kpsi) for the second bending mode (Figs. 2-4).
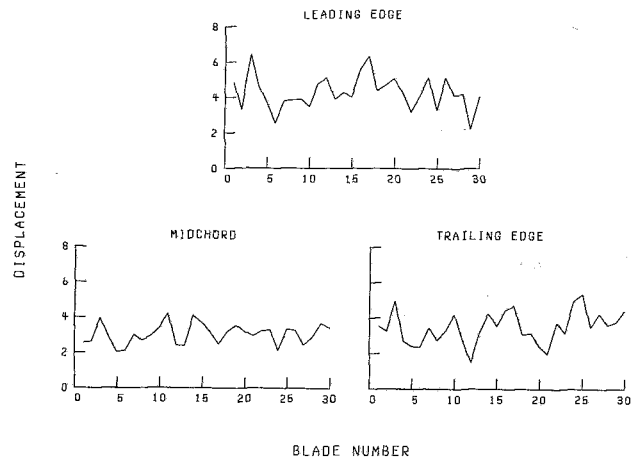

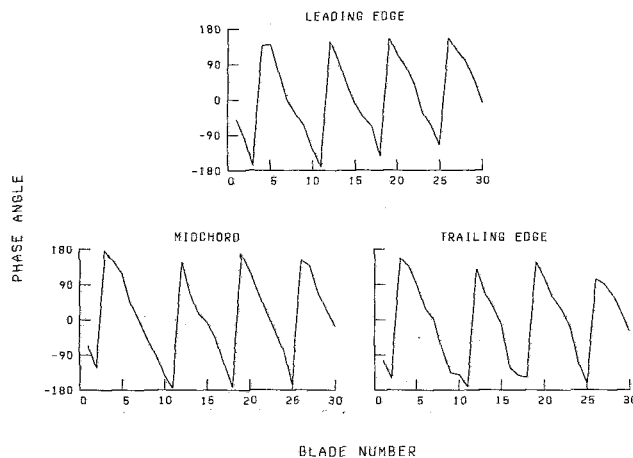Fig. 12 Displacement amplitudes for the main flutter mode

Fig. 13 Displacement phase angles for the main flutter mode

(The strain gage was aligned in the direction of the chord near the blade tip 31 percent of the chord from the leading edge.) The corresponding tangential deflections at the leading-edge optical port (located 16 percent of the chord from the leading edge) were 0.1 and 0.77 digital units. (The computed frequencies for these two modes were 2165 and 1332 Hz, respectively; the corresponding frequencies measured in the laboratory on a single blade were 2300 and 1550 Hz; and the associated frequencies measured during engine test were 2140-2270 and 1524 Hz.)

These results offer, therefore, a plausible explanation for the lack of response in the displacement spectra in the 2140-2270 Hz (i.e., 14-16E) range and also for the observed trace response at 0.319 E (which is associated with 10.319 E mode) in Fig. 5. The displacement for this mode is considerably higher for blade 3, Fig. 8. However, this can be attributed to the blade-to-blade amplitude variation. The displacements in Fig. 5 can be viewed as blade-ensemble averages. Hence, they are preferred over the particular values obtained from individual spectra.

Main Flutter Mode. The amplitudes for each blade for the main flutter mode (i.e., corresponding to the frequency of 0.159 E in the individual blade spectra) are presented in Fig. 12; the associated phase angles are shown in Fig. 13. On the whole, the amplitudes appear to be fairly uniform, and the phase angles clearly show the presence of a four-nodal-diameter forward traveling wave. Some of the departures from the constancy of amplitudes (Fig. 12) and slopes (Fig. 13) are undoubtedly caused by a slight mistuning (see Figs. 5-7); however, some of the variations may be caused by

inaccuracies associated with the occasional poor peak separation in the folded frequency range 0–1/2 E. This is particularly likely at the trailing edge.

As already indicated, flutter was associated with the second coupled mode. Thus, both bending and torsional deflections can be expected during flutter. In an attempt to separate these two contributions, the total deformations measured perpendicular to the chord are expressed as follows:

$$A_l e^{j\phi_l} = -r_l A_\theta e^{j\phi_\theta} + A_h e^{j\phi_h} \quad (4)$$

$$A_m e^{j\phi_m} = (a - r_l) A_\theta e^{j\phi_\theta} + A_h e^{j\phi_h} \quad (5)$$

$$A_t e^{j\phi_t} = (2a - r_l) A_\theta e^{j\phi_\theta} + A_h e^{j\theta_h} \quad (6)$$

The total deformations are actually measured in the tangential direction. The following relationships are used to obtain the deformations perpendicular to the chord:

$$\theta = (d_\theta \sin\gamma)/r_l$$
$$h = d_h \sin\gamma \quad (7)$$

The left sides of equations (4) to (6) can be considered known. They are obtained from the overall spectra by applying corrections to the phase angles to take into account the fact that optical displacements at the three ports are not measured simultaneously. After these corrections are applied, the phase angles are referenced to the time the once-per-revolution pulse is triggered to begin data acquisition. The variables A_θ, ϕ_θ, A_h, ϕ_h, and r_l are the unknowns. Note, however, that r_l appears only in the combination $r_l A_\theta e^{j\phi_\theta}$, which is not independent of $A_h e^{j\phi_h}$. Thus, although A_θ and ϕ_θ can be determined, additional input is required to determine A_h, ϕ_h, and r_l. Therefore, an assumption was made that the position of the torsional axis (specified by r_l) corresponds to the nodal line position in a single-blade hologram for the above-shroud first torsional mode. (The single-blade holograms were supplied by the engine manufacturer.)

Since there are now two complex unknowns ($A_\theta e^{j\phi_\theta}$ and $A_j e^{j\phi_h}$) and three complex equations, one equation is redundant. If the first two equations (corresponding to the leading edge and the midchord ports) are used, the following set of values are obtained: $r_l A_\theta = 4.15$, $\phi_\theta = 113$ deg, $A_h = 3.19$, and $\phi_h = -179$ deg. Because $r_l A_\theta$ and A_h displacements are small, it is convenient to express them in digitized units where one of these units corresponds to a displacement perpendicular to the blade chord of 0.0704 mm. If the first and the third equations (corresponding to the leading and trailing-edge ports) are used, $r_l A_\theta = 3.70$, $\phi_\theta = 100$ deg, $A_h = 2.20$, and $\phi_h = -175$ deg. These are fairly close to the previously obtained values except for A_h. Thus, blade deformation appears to be somewhat more complicated than assumed in the previous simple model. The main trend is that the bending amplitude is smaller at the trailing edge than at the leading edge. (Note that the same trend would follow had the second and the third equations been solved instead of the first and the third.)

If the average of the previous two sets of values is used, the phase difference $\phi_\theta - \phi_h = -76.5$ deg and the coupled flutter parameter [7] $cA_\theta/A_h = 3.52$. Note that the phase difference $\phi_\theta - \phi_h$ depends on the definitions of ϕ and h (Fig. 1).

To get some idea about the accuracy with which the complex torsional and bending displacement components could be determined, another segment of data was digitized at a slower speed ($Q = 8860$) and the described procedure was then repeated. The amplitudes $r_l A_\theta$ and A_h and the phase difference $\phi_\theta - \phi_h$ were again determined using two sets of equations. This allowed the comparison of four pairs of amplitudes and two pairs of phase angles. The maximum deviation for amplitudes was 8 percent and for the differential phase it was 2 deg.

Concluding Remarks

A complex stall-flutter mode can be reasonably resolved into its principal bending and torsional contributions using casing-mounted optical displacement sensors. For the chosen bending and torsional displacement definitions, bending leads torsional displacement by 76 deg and the coupled flutter parameter (cA_θ/A_h) is 3.52.

Detecting a nonintegral engine order excitation in the blade displacement spectra for higher modes was difficult. The difficulty was compounded by the presence of a wideband response near the chordwise bending mode. The lack of blade to blade coherence for this excitation indicates the lack of coupling between the blades (i.e., single-blade response). Such wideband high-frequency instability generates a response at virtually every frequency line in the folded individual blade spectra. Its recognition, therefore, requires that a noise-floor level be established during the operation away from instability.

The implementation of the online spectral analysis is essential when using optical sensors for vibration monitoring.

References

1 Whitehead, D. S., "Torsional Flutter of Unstalled Cascade Blades at Zero Deflection," Reports and Memoranda No. 3429, Aeronautical Research Council, Great Britain, 1966.

2 Nieberding, W. C., and Pollack, J. L., "Optical Detection of Blade Flutter," ASME Paper No. 77-GT-66, Mar. 1977.

3 Kurkov, A., and Dicus, J., "Synthesis of Blade Flutter Vibratory Patterns Using Stationary Transducers," ASME Paper No. 78-GT-160, Apr. 1978.

4 Kurkov, A. P., "Flutter Spectral Measurements Using Stationary Pressure Transducers," ASME JOURNAL OF ENGINEERING FOR POWER, Vol. 103, No. 2, Apr. 1981, pp. 461–467.

5 Kurkov, A. P., "Measurement of Aerodynamic Work During Fan Flutter," Fluid/Structure Interaction in Turbomachinery, The American Society of Mechanical Engineers, New York, 1981, pp. 9–18.

6 Singleton, R. C., "An Algorithm for Computing the Mixed Radix Fast Fourier Transform," IEEE Transactions on Audio and Electroacoustics, Vol. AU-17, No. 2, June 1969.

7 Halliwell, D. G., "Fan Supersonic Flutter: Prediction and Test Analysis," Aeronautical Research Council R. & M. No. 3789, 1977.

R. L. Jay

Detroit Diesel-Allison Division
of General Motors,
Indianapolis, Ind. 46206

J. C. MacBain

Aero Propulsion Laboratory,
AFWAL/POTA, WPAFB, Ohio 45433

D. W. Burns

Detroit Diesel Allison Division
of General Motors,
Indianapolis, Ind. 46206

Structural Response Due to Blade Vane Interaction

The structural response of a bladed turbine disk due to excitation from an upstream stator row was measured using strain gages. Rig testing performed in a realistic aerodynamic environment was preceded by a static vibratory search in which individual blade frequencies and system modes were identified by strain response and holography. In the rig testing special emphasis was placed on identifying the dynamic response resulting from the interaction between the vanes and blades. An analytical description of the forcing function which results from the difference between the number of blades and the number of vanes is presented and correlated with detailed blade responses both in terms of amplitude and interblade phasing. In particular, the combination of 26 inlet vanes and the 30 rotor blades yielded strong dynamic responses in two modes of the four diametral family. The experimental results augmented by the analytical formulation of excitation created by the difference in vane and blade numbers have conclusively identified a mechanism for large blade dynamic response which should be considered in the design phase of bladed disk systems.

Introduction

A complete and accurate definition of the resonant vibratory response of turbine engine bladed disks includes characterization of the structural dynamics and the forcing function. The dominant source of excitation can be attributed to the presence of circumferentially oriented flow distortions created by stator vanes, struts, bleed manifolds, rotating stall and inlet configurations. Fourier analysis of the distortions yields the significant integer components. These components have the potential to excite a bladed disk resonance at speeds corresponding to the intersection of the excitation frequency of the particular Fourier component, K, ($K \times$ rotational speed) with natural frequencies of the bladed disk system. In general, when a sinusoidal distortion field with K patterns acts on the tuned disk, response in the Kth diametral nodal pattern results. In addition, Ewins [1] suggests that other excitations can be obtained. He states a bladed disk with M number of blades can respond to a K component of excitation in harmonic or diametral patterns which are functions of the sums and differences in multiples of M and K.

To illustrate this (M-K) type excitation, an analytical model which assumed sinusoidal representations for the blades and vanes and used dual (orthogonal) [2, 3] mode definition of the diametral modes was made. The model yields the mechanism of the (M-K) type response for both tuned and mistuned systems. The validity of the model is verified from the experimental data.

The experimental effort supporting the analytical efforts consisted of the dynamic evaluation of an integrally bladed turbine disk. In this evaluation a survey of the in-vacuum frequencies and mode shapes of the disk was made. The strain-gaged turbine was tested in an aerodynamic rig in which the number of upstream vanes were chosen such that excitation of the four diametral nodal patterns resulting from the difference in the number of vanes — 26 — and blades — 30 — was possible. Strain gage data from these tests verified this excitation and resultant high amplitude response. Responses due to other excitations were evaluated and confirmed the phenomenological mechanism and provided further insight into the dynamics of tuned and mistuned bladed disks.

Blade Vane Interaction. Blade vibration due to an upstream vane row results when a uniform flow impinges on the set of K vanes, creating K distortions through which the set of M blades pass during rotation. The primary concern in this analysis is the fundamental harmonic resulting from these K distortions. In Fig. 1, the airfoils of a bladed disk, rotating in
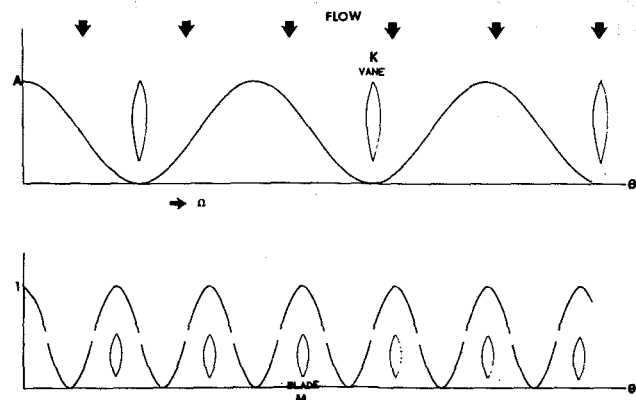
Fig. 1 Sign conventions for analysis
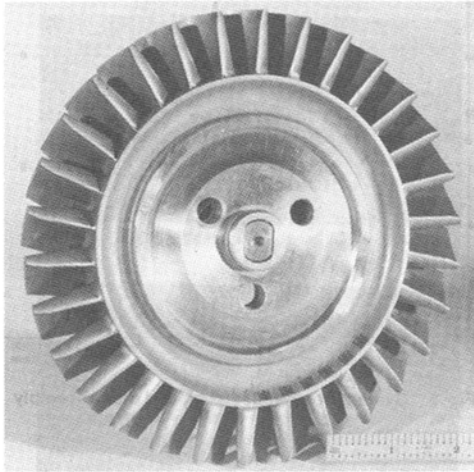
Fig. 2 Turbine stage used in experimental study

Fig. 3 Blade frequency variation around circumference
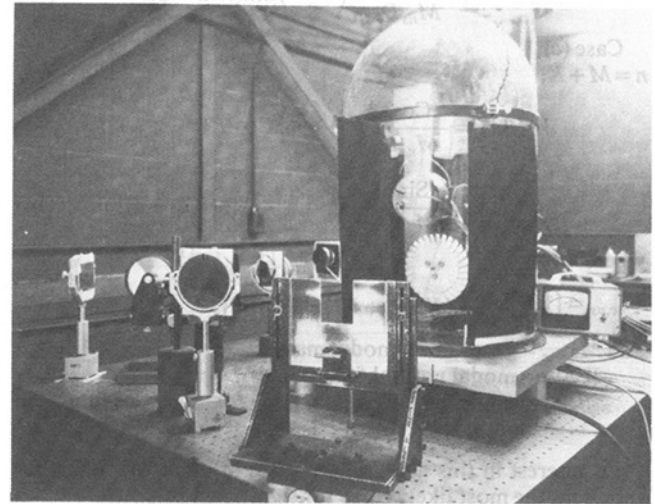
Fig. 4 Vacuum test set-up for turbine disk

the $+\theta$-direction at a speed of Ω, are assumed to present a sinusoidally varing obstruction to the incoming, distorted flow. Considering the bladed disk response with respect to the disk fixed coordinate system (θ), the sinusoidal excitation pattern created by the vane row can be regarded as moving in the $-\theta$-direction at a rotational speed Ω. This excitation pattern creates a force on the blades which can be expressed as

$$V(\theta,t) = \frac{A}{2} (1 + CosK(\theta + \Omega t)) \qquad (1)$$

where A is indicated in Fig. 1.

The presence of the blade cascade in the flow field can be represented by a Fourier Series in the circumferential direction. Considering the fundamental component of the series, the blades will be represented as,

$$B(\theta) = \frac{1}{2}(1 + CosM\theta) \qquad (2)$$

The force created on the blades then can be written

$$F(\theta,t) = V(\theta,t) \cdot B(\theta) \qquad (3)$$

With the forcing function defined, response of the bladed disk in the neighborhood of its dual nth mode [3] has been described by Tobias and Arnold [2] and Ewins [4]. For the details of their derivation, reference should be made to these papers. Following their approach, the effect of the forcing function on the Cos $n\theta$ and Sin $n\theta$ modes can be computed via generalized forces, N_{nc} and N_{ns}, as follows

$$N_{nc} = \int_0^{2\pi} F(\theta,t) \cdot Cosn\theta d\theta$$

$$N_{ns} = \int_0^{2\pi} F(\theta,t) \cdot Sinn\theta d\theta \qquad (4)$$

Substituting the expression for force into the integral for N_{nc} yields

$$N_{nc} = \frac{A}{4} \int_0^{2\pi} CosM\theta Cosn\theta d\theta + \frac{A}{4} CosK\Omega t \int_0^{2\pi} CosK\theta Cosn\theta d\theta$$

$$+ \frac{A}{8} CosK\Omega t \int_0^{2\pi} Cos(M-K)\theta Cosn\theta d\theta$$

$$+ \frac{A}{8} CosK\Omega t \int_0^{2\pi} Cos(M+K)\theta Cosn\theta d\theta \qquad (5)$$

The first term is independent of time and, thus, not considered for vibratory response. The remaining terms are zero unless $n = K$, $n = M - K$, or $n = M + K$, respectively. We then distinguish three cases.
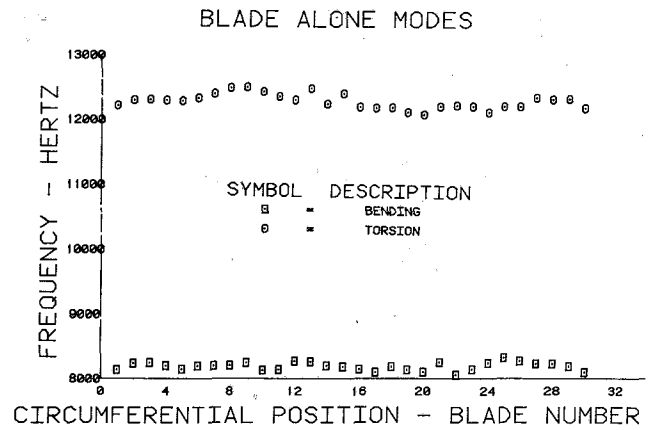
(a)
$n = k$

$$N_{nc} = \frac{A\pi}{4} CosK\Omega t \qquad (6)$$

(b)
$n = M - K$

$$N_{nc} = \frac{A\pi}{8} CosK\Omega t \qquad (7)$$

(c)
$n = M + K$

$$N_{nc} = \frac{A\pi}{8} CosK\Omega t \qquad (8)$$

Similarly for the Sine participation factor

$$n = K, N_{ns} = -\frac{A\pi}{4} SinK\Omega t \qquad (9)$$

$$n = M - K, N_{ns} = \frac{A\pi}{8} SinK\Omega t \qquad (10)$$

$$n = M + K, N_{ns} = -\frac{A\pi}{8} SinK\Omega t \qquad (11)$$

With nonzero participation factors, response of the bladed disk in diametral nodal lines described in cases (a), (b), and (c) are possible. These responses will occur at the intersection of the n diametral node family modes and the vane generated frequency $K\Omega$.

Disk Response. The response of the disk due to the forcing function of K order can be written for each of the cases discussed as

Case (a)
$n = K$,

$$W(\theta,t) = \frac{\text{Cos}n\theta}{M_{nc}D_{nc}}\left(\frac{A\pi}{4}\right)\text{Cos}(K\Omega t - \phi_{nc})$$

$$+ \frac{\text{Sin}n\theta}{M_{ns}D_{ns}}\left(-\frac{A\pi}{4}\right)\text{Sin}(K\Omega t - \phi_{ns}) \quad (12)$$

Case (b)
$n = M - K$

$$W(\theta,t) = \frac{\text{Cos}n\theta}{M_{nc}D_{nc}}\left(\frac{A\pi}{8}\right)\text{Cos}(K\Omega t - \phi_{nc})$$

$$+ \frac{\text{Sin}n\theta}{M_{ns}D_{ns}}\left(\frac{A\pi}{8}\right)\text{Sin}(K\Omega t - \phi_{ns}) \quad (13)$$

Case (c)
$n = M + K$,

$$W(\theta,t) = \frac{\text{Cos}n\theta}{M_{ns}D_{nc}}\left(\frac{A\pi}{8}\right)\text{Cos}(K\Omega t - \phi_{nc})$$

$$+ \frac{\text{Sin}n\theta}{M_{ns}D_{ns}}\left(-\frac{A\pi}{8}\right)\text{Sin}(K\Omega t - \phi_{ns}) \quad (14)$$

where

$$D_{nc,ns} = \{[W_{nc,ns}^2 - (K\Omega)]^2 + 4\beta_{nc,ns}^2 (K\Omega)^2\}^{1/2}$$

and $M_{nc,ns}$ = generalized modal masses
$W_{nc,ns}$ = modal natural frequencies
$\beta_{nc,ns}$ = modal damping factors for the Cos and Sin modes, respectively.

Of interest in this analysis are cases (a) and (b), since they represent the most likely cases for significant response.

Tuned Bladed Disk. Consider a perfectly tuned disk at resonance with equal modal damping, i.e.,

$$W_{nc} = W_{ns} = W_n$$

$$\phi_{nc} = \phi_{ns} = \phi_n = \pi/2$$

$$M_{nc}D_{nc} = M_{ns}D_{ns} = M_nD_n$$

for Case (a)
$n = K$

$$W(\theta,t) = \frac{\text{Cos}n\theta}{M_nD_n}\left(\frac{A\pi}{4}\right)\text{Sin}K\Omega t + \frac{\text{Sin}n\theta}{M_nD_n}\left(\frac{A\pi}{4}\right)\text{Cos}K\Omega t$$

$$= \frac{A\pi}{4M_nD_n} = (\text{Cos}n\theta\,\text{Sin}K\Omega t) + \text{Sin}n\theta\,\text{Cos}K\Omega t)$$

$$= \frac{A\pi}{4M_nD_n}\text{Sin}(K\Omega t + n\theta) \quad (15)$$

for Case (b)
$n = M - K$

$$W(\theta,t) = \frac{A\pi}{8M_nD_n}[\text{Cos}n\theta\,\text{Sin}K\Omega t - \text{Sin}n\theta\,\text{Cos}K\Omega t)$$

$$= \frac{A\pi}{8M_nD_n}\text{Sin}(K\Omega t - n\theta) \quad (16)$$

In case (a), equation (15), the diametral, pattern n is rotating opposite the direction of rotation. This is the normally assumed response of the disk. In case (b), equation (16), however, the direction of travel of the diametral pattern is dependent on the sign of quantity, M-K. If M is greater than
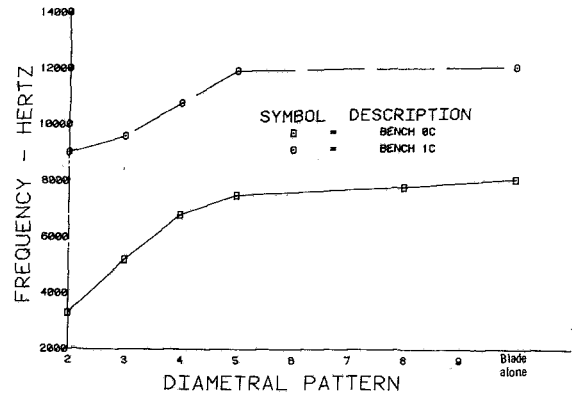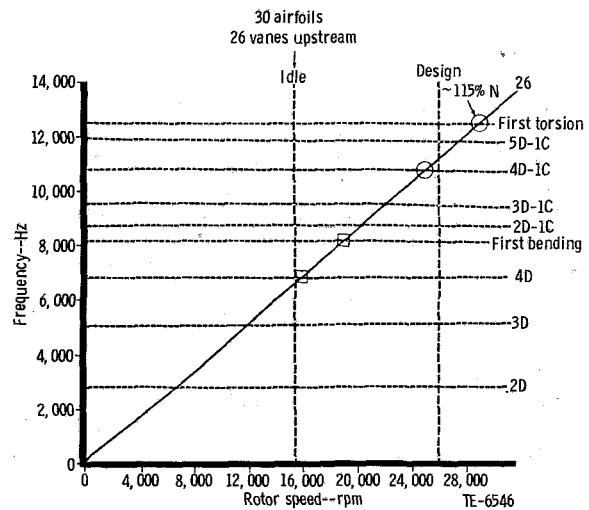

Fig. 5 System frequencies of bladed disk assembly

Fig. 6 Expected resonances for bladed disk assembly

K, the diametal pattern travels in the direction of rotation. With K greater than M, then the n diametral pattern travels opposite the direction of rotation. Thus, the number of vanes and blades determine the direction of travel of the n lobed pattern relative to the disk. In these traveling patterns, equal blade amplitudes would be expected with an interblade phase angle dependent on the number of blades M and the diametral pattern n.

Mistuned Bladed Disk. For this case, examine first the response when the excitation frequency, $K\Omega$, is equal to the resonant frequency of the Cosine component of the n diametral pattern. In this condition, the response of the Cosine component is the dominant of the pair of split modes. The response, at resonance, therefore, can be written for case (a), $n = K$

$$W(\theta,t) = \frac{\text{Cos}n\theta}{M_{nc}D_{nc}}\left(\frac{A\pi}{4}\right)\text{Sin}K\Omega t, \quad \phi_{nc} = \pi/2 \quad (17)$$

and for case (b), $n = M - K$

$$W(\theta,t) = \frac{\text{Cos}n\theta}{M_{nc}D_{nc}}\left(\frac{A\pi}{8}\right)\text{Sin}K\Omega t, \quad \phi_{nc} = \pi/2 \quad (18)$$

Examining equations (17) and (18), the forms indicate an n diametral pattern vibration which is fixed with respect to the disk. Similar development for the Sine component yields the same fixed vibration pattern. Therefore, with mistuned bladed disk systems having M blades under the excitation of K stator vanes, two vibration peaks created by the dual modes can occur. Furthermore, analysis has shown that these diametral modes will be fixed relative to the disk, and it can be
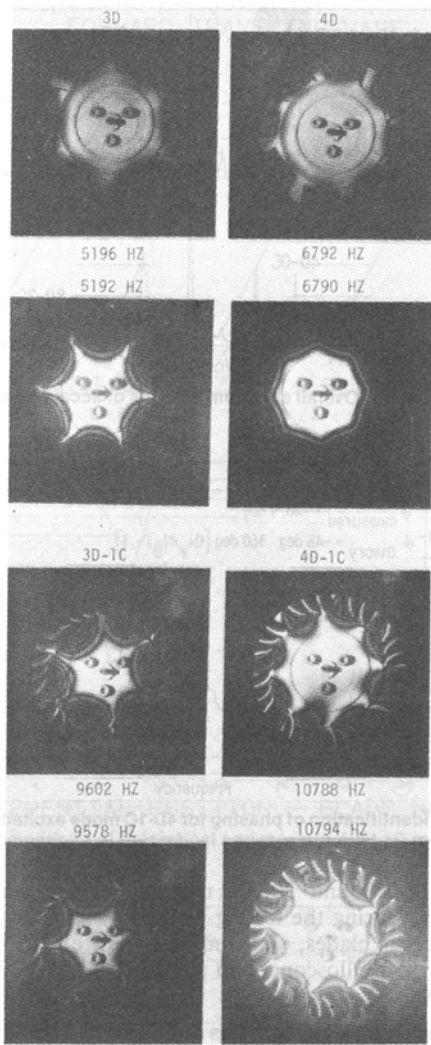
Fig. 7 Holograms for the three and four diametral patterns, split mode description

Fig. 8 Strain gage signatures for 3D-1C and 4D-1C split modes
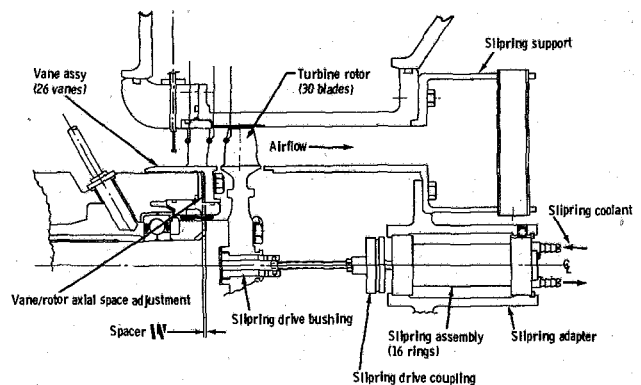
Fig. 9 Cross-sectional view of bladed disk test assembly

concluded that blading will have either 0 or 180 deg phasing and amplitudes with a sinusoidal variation around the circumference. It is important to note that equations (17) and (18) represent an idealized condition. Tobias and Arnold [2] show that the addition of damping can alter the mistuned response to include a travelling wave component.

The constants in equations (6–11) reflect the assumed sinusoidal variation for the blade representation. The main emphasis in this analytical discussion was to explain the $n = M\text{-}K$ type response, and the results of this excitation for both tuned and mistuned systems. The more usually experienced $n = K$ response was also shown for more clarity.

Description of Static Evaluation of Turbine Disk. The bladed disk assembly chosen for this investigation is shown in Fig. 2. The aerodynamic characteristics of this turbine stage are typical of advanced turbine designs. Thirty blades are machined integrally with the disk as shown. Definition of the "blade alone" first bending and first torsional modes was accomplished to indicate the degree of frequency mistuning in the blading. Two methods were used. In the first, each blade was individually excited while the others remained unconstrained. In the second method, all blades except the excited blade were damped and mistuned with the addition of Transeal, a puttylike material. Overall agreement between the two methods were excellent. The variation in frequencies around the circumference of the wheel is presented in Fig. 3
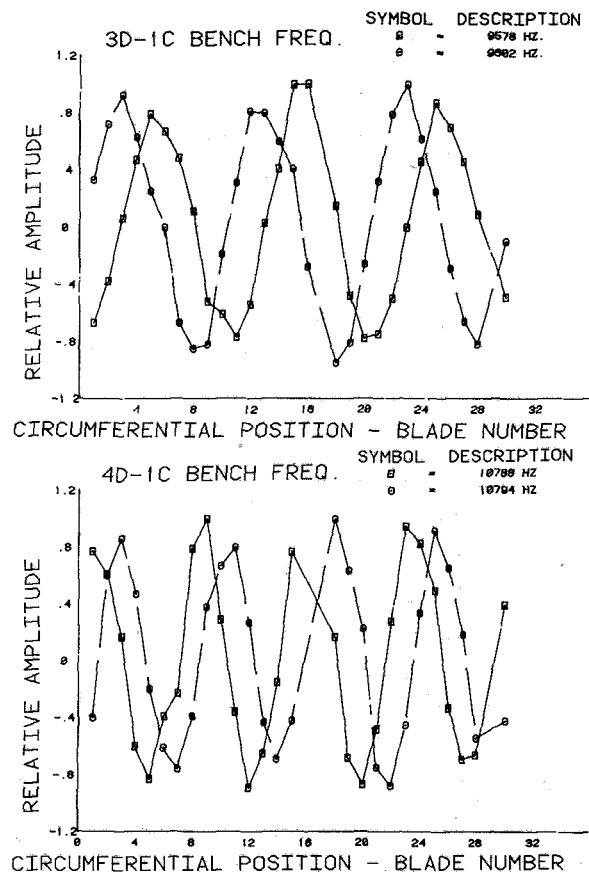
for the constrained blade configuration. The frequency range measured for first bending mode was from 8059 to 8323 Hertz and for the first torsional mode, 12074 to 12502 Hertz. The average first bending frequency was 8191.5 Hertz and the average first torsional frequency was 12279.7 Hertz. The frequency range compared to average frequencies were 3.22 and 3.48 percent for bending and torsion, respectively. Thus, mistuning in the two frequencies was very similar.

Holographic and strain gage data were obtained using the experimental set-up shown in Fig. 4. The disk was mounted on a stub shaft configured to represent the attachment provided in the rig test unit. The vacuum jar contained both the piezoelectric shaker and the bladed disk. The vacuum chamber pressure was adjusted to less than 5 mm Hg and excitation of the assembly accomplished. Modal identifications of the zero circumferential and one circumferential

Fig. 10 Waterfall chart for blade 12 dynamic response

Fig. 11 Overall spectrum analysis of acceleration

Fig. 12 Identification of phasing for 4D-1C mode excited by 26 EO

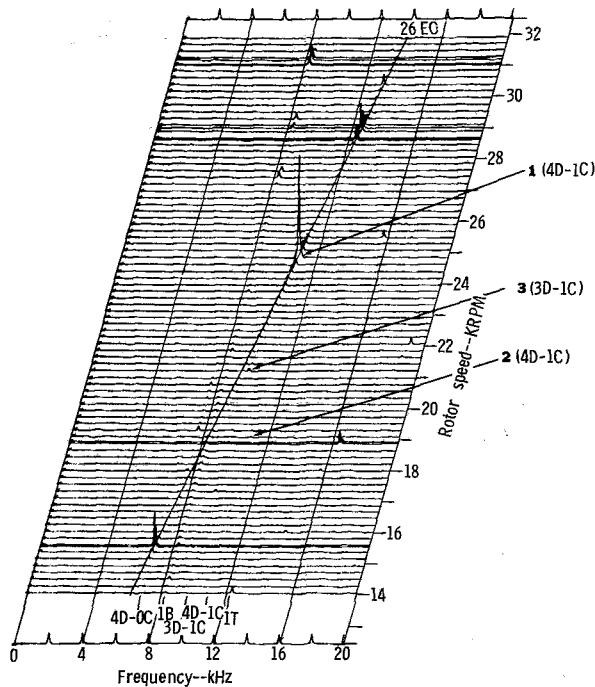families of diametral modes were made. The disk participation is clearly noted in Fig 5, which shows the dynamic characteristics of the in-vacuum bladed disk. The blade alone modes, which can be considerd as the combination of higher diametral modes, were identified as shown and are in agreement with the blade alone testing. In Fig. 6 the frequency-speed diagram, based on the bench tests, is presented. As noted previously, the expected engine order line of maximum response corresponded to the 26 upstream stators.

Particular emphasis will be focused on two sets of modes, the third and fourth diametral patterns, holograms of which are presented in Fig. 7. Orthogonal or dual modes were found for the modes as indicated. In the zero circumferential modes, the modal split for the third diametral pattern is only 4 Hertz or .07 percent of the mean frequency, while the fourth diametral pattern modal split was 2 or less Hertz (difficulty was experienced in obtaining meaningful holograms for both modes). In the one circumferential mode family, the orthogonality of the modes is clearly seen. Modal split factors are .25 percent for the third diametral modes and .056 percent for the fourth diametral modes. These results indicate a very closely tuned rotor, the largest mistuning being noted for the third diametral, one circumferential mode. Strain gages mounted on each airfoil during this testing confirmed the holographic studies. In Fig. 8 the variation in strain gage readings from the blades around the circumference of the disk demonstrate vividly the orthogonal nature of the third and fourth diametral, one circumferential modes. Thus, from the static testing on the bladed disk, identification of the blade alone and diametral modes was made. The mistuning of the stage was extremely low and identification of orthogonal or dual modes has been conclusively made.

Description of Rig Evaluation of Turbine Disk. A detailed view of the installed turbine stage is shown in Fig. 9. The vane assembly was made up of 26 blades and located immediately upstream of the test disk. Strain gage readout was accomplished via a 16-ring slip-ring attached to the turbine disk through a small diameter, flexibly coupled drive shaft.

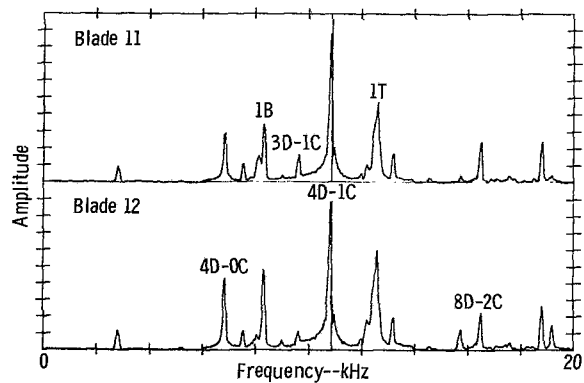The dynamic tests consisted of slow rotor acceleration
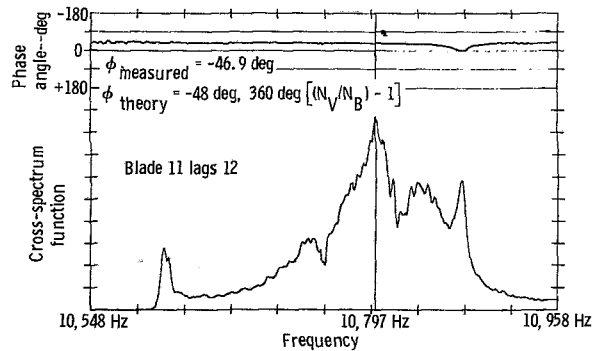
between 14,000 and 30,000 rpm at varying aerodynamic conditions. During the testing period, dynamic signals from eight adjacent blades, slot numbers 5–12 on the disk, were observed via oscilloscopes and recorded on magnetic tape for later analysis.

Description of Data Analysis and Results. The data analysis consisted of resonant definitions using the standard three axis "waterfall" chart shown in Fig. 10, which present dynamic stress amplitude and resonant intersections as a function of rotor speed . In Fig. 10, the dynamic behavior of blade #12 is indicated. The largest response, indicated by the number 1, occurs at a rotor speed of approximately 25,000 rpm, consistent with the excitation created by the 26 inlet vanes. Examination of this resonance by using the Campbell diagram (Fig. 6) would indicate a four diametral, one circumferential nodal pattern. Thus, the 26 vanes and 30 blades configuration yielded a four diametral pattern response. The highest stress measured on the blade hub exceeded 40,000 psi (275.79 MPa).

Two other resonances, smaller than the previously mentioned, are significant in this discussion. The small resonance denoted by 3 in Fig. 10 was identified as a third diametral, one circumferential nodal pattern excited by the 27th engine order. The resonance denoted by 2 in Fig. 10 corresponded to the four diametral, one circumferential nodal pattern excited by 34th engine order. The source of the 27 and 34 engine orders are most probably due to the interaction of the 26 vanes and upstream total pressure and temperature instrumentation. More detailed evaluations were performed using a dual channel FFT analyzer with the capability to perform cross-spectrum analyses at expanded frequency resolution about the resonant frequency. Figure 11 presents the amplitude content at various frequencies for strain gage signatures from blades 11 and 12 obtained during an acceleration. In this spectrum, modes of interest are identified. Discussion of the other responses presented in this spectrum is not necessary for this analysis.
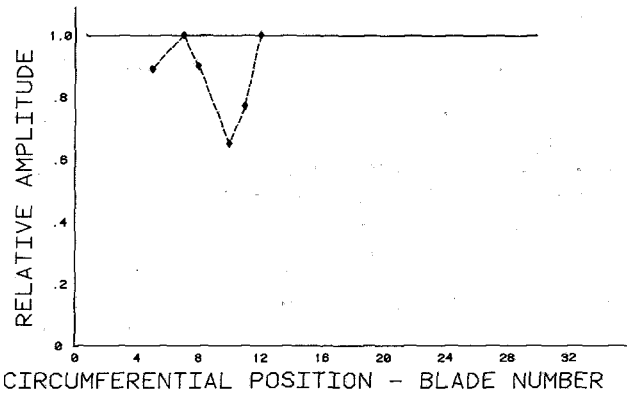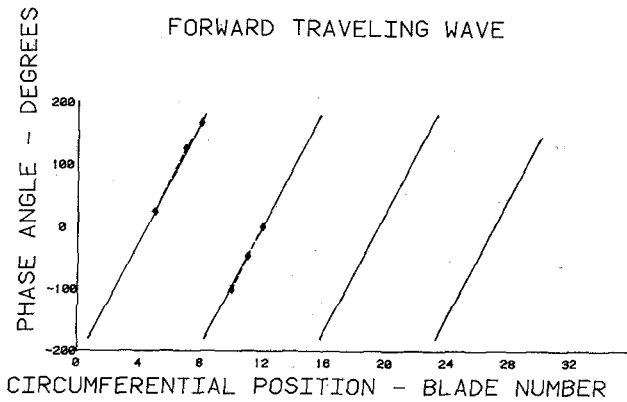
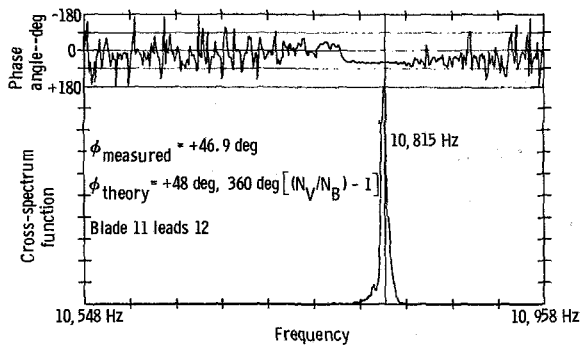Fig. 13 Comparison of theoretical and measured 4D-1C mode excited by 26 EO

Fig. 14 Phasing study for 4D-1C mode excited by 34 EO

Fig. 15 Phasing for 3D-1C/27 EO response showing dual mode behavior
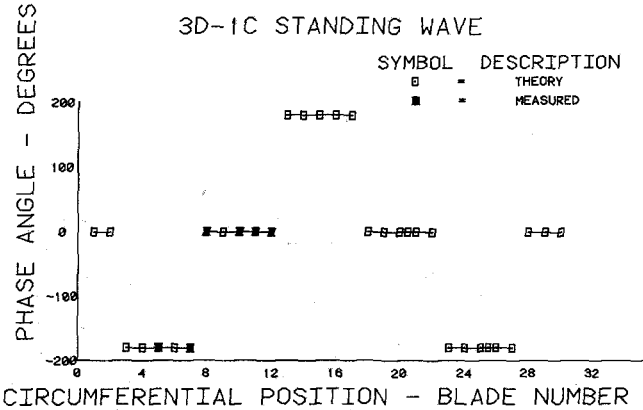
Fig. 16 Overlay of measured 3D-1C mode on theoretical standing wave

At each of the peaks noted, expanded frequency resolution was used to obtain the interblade phasing and amplitude. The center of the expanded frequency range was located on the peaks noted in Fig. 11. To properly obtain the phasing, the tape speed was slowed by a factor of 64, and the taped signals were analyzed at speeds in close proximity to the turbine speed at which response was noted. Figure 12 presents the cross-spectrum plot for the responses of blades 11 and 12 in the narrow speed range in the four diametral, one circumferential (4D-1C) nodal pattern. As noted in the figure, a phase angle of −46.9 deg between the response of blade 11 and 12 is measured in this region. The negative sign indicates that blade 12 leads blade 11 in the response. Similar analyses were performed using strain gage data from the other blades, two of which were inoperative. Figure 13 presents the results in terms of phasing of the various blades referenced to blade 12 and amplitude normalized to blade 12 stress. Plotted in the same figure is the theoretical phasing of a 4D-1C pattern traveling in the disk in the direction of rotation, a forward traveling wave. This vividly demonstrates the validity of the

analytical conclusion that the K vanes exciting M blades will excite a nodal pattern having $(M\text{-}K)$ nodal diameters. The direction of travel of the wave corresponds to the predicted direction and, furthermore, the condition of equal amplitude response of the blading is approximated by the data. The slight differences can be attributed most probably to small differences in gage locations.

In Fig. 14, the response of blades 11 and 12 have been phased in a small speed range about the 4D-1C/34th engine order resonance. Note that in this case the excitation order is 34, and the 30 blade configuration can theoretically respond in a four diametral pattern, but the four lobed wave should travel opposite the direction of rotation in the disk. The phase measured in Fig. 14 indicates that blade 11 leads blade 12. Agreement in amplitude and phasing for the other blades confirmed this. This provides the experimental evidence that the $(M\text{-}K)$ excitation, with K greater than M, results in a wave of nodal patterns $(K\text{-}M)$ traveling in the disk opposite to the direction of rotation.

3D-1C FREQUENCY - HZ

SYMBOL   DESCRIPTION
```
    B   -   9578 BCH
    ø   -   9602 BCH
    A   -   9612 ROT
    +   -   9638 ROT
```

Fig. 17 Overlay of bench and rotating strain gage signatures for 3D-1C modes

The traveling waves noted in the two previous examples indicate that the bladed disk was essentially tuned. The modal split factor for the 4D-1C mode was .056 percent, as previously discussed. Examination of the 4D-OC mode response, occurring at approximately 15,500 rpm (see Fig. 10), indicated tuned behavior in accordance with the 4D-1C/26 EO study discussed. The modal split factor for the 4D/OC mode was even smaller than the 4D-1C mode.

In the 3D-1C response, noted in Fig. 10 at approximately 21,200 rpm, phasing and amplitude studies were performed. Figure 15 presents the phasing study performed using the strain gage signals from blades 11 and 12. Two points of interest are of note in this figure. At a frequency of 9612 Hz the phasing between blades 11 and 12 goes to zero corresponding to the maximum coherence value. At 9638 Hz the phasing between these blades becomes 180 deg. A plot of all data from 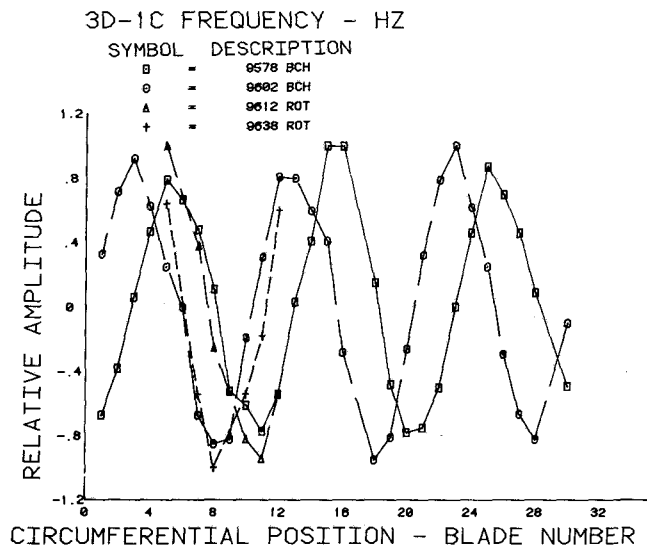the strain gages, both in terms of amplitude and phase, is presented for the 9612 Hertz resonance in Fig. 16. Phasing using blade 12 as a reference indicates that blades are either in-phase or 180 deg out of phase, a condition satisfied by only a standing wave. The agreement between the absolute magnitude of the response amplitude and the absolute value of a sine wave, as shown in the figure, indicates vibration in a fixed 3 diametral pattern.

This identification of a standing wave verifies the analytical results of the mistuned disk. The modal split factor for the 3D-1C mode was .25 percent, significantly higher than the .056 percent split in the 4D-1C dual modes.

As additional insight in mistuning, the strain gage results from the 3D-1C/27 EO resonance were overplotted on the 3D-1C bench test signatures for the dual modes. The results of that study are shown in Fig. 17 and are truly unique. The patterns as measured during bench testing and the patterns obtained during realistic aerodynamic testing are essentially the same, fixed at the same spatial locations on the disk, and exhibiting split factors of .24 and .27 percent, respectively. Therefore, conclusive proof of the existence of the standing 3D-1C mode in the disk has been made.

Conclusions

The major conclusions from the combined analytical/experimental investigation performed are as follows:

1 Significant response of a realistic bladed disk can result from an excitation created by the difference in the order of the forcing pattern, being the number of vanes or a Fourier component of an inlet distorted flow, and the number of blades on the disk.

2 The nodal diameter response pattern is determined by the order of the forcing pattern or, and equally valid, the difference in the order of the forcing pattern and the number of blades.

3 The tested bladed disk, having dual modes with split factors of .056 percent and less, acted as a tuned system, and the dynamic response consisted of a travelling wave in the disk.

4 The tested bladed disk, having dual modes with a split factor of .25 percent, acted as a mistuned system, and the dynamic response consisted of standing waves fixed in the disk frame of reference.

5 The dual modes of the 3D-1C diametral pattern as determined in the bench and rotating tests remained at the same spatial orientation with respect to the bladed disk and the separation frequency between the modes remained essentially constant.

6 The test and analytical results are in qualitative agreement. Thus validating the analytical model.

Based on these conclusions, the following recommendations are presented:

1 Using the analytical equations developed, the test experience should be modeled using proper mode splits and damping factors, so that further insight into effects of mistuning can be gained.

2 A bladed disk assembly should be tuned, then progressively mistuned relative to particular diametral patterns in order to examine the effects, in terms of response amplitude, of traveling waves versus standing waves in the disk frame of reference.

3 Extreme caution should be taken when instrumenting bladed disk assemblies for blade dynamic characterization. Using a minimal number of gages could lead to the unfortunate condition of locating a gage on a nonresponsive blade in a mistuned system.

4 Before operation of a bladed disk system, a careful search to determine the modal split factors should be made, both to identify the state of tuning and for aid in locating gages.

Acknowledgments

References

1 Ewins, D. J., "Bladed Disk Vibration—A Review of Techniques and Characteristics," *Recent Advances in Structural Dynamics; Proceedings of the International Conference*, Vol. 1, Southhampton, England, July 7-11, pp. 187-210.

2 Tobias, S. A., and Arnold, R. N., "The Influence of Dynamical Imperfection on the Vibration of Rotating Disks," *Proceedings of the Institution of Mechanical Engineers*, Vol. 171, 1957, pp. 669.

3 Stange, W. A., and MacBain, J. C., "An Investigation of Dual Mode Phenomena in a Mistuned Bladed Disk," ASME Paper 81-DET-133, Design Engineering Technical Conference, Sept. 20-27, 1981, Hartford, Conn.

4 Ewins, D. J., "The Effects of Detuning Upon the Forced Vibrations of Bladed Disks," *Journal of Sound and Vibration*, Vol. 9, No. 1, 1969, pp. 65-79.

Analysis of an Axial Compressor Blade Vibration Based on Wave Reflection Theory

J. A. Owczarek

Professor,
Department of Mechanical Engineering
and Mechanics,
Lehigh University, Bethlehem, Pa. 18015
Mem. ASME

The paper describes application of the theory of wave reflection in turbomachines to rotor blade vibrations measured in an axial compressor stage. The blade vibrations analyzed could not be explained using various flutter prediction techniques. The wave reflection theory, first advanced in 1966, is expanded, and more general equations for the rotor blade excitation frequencies are derived. The results of the analysis indicate that all examined rotor blade vibrations can be explained by forced excitations caused by reflecting waves (pressure pulses). Wave reflections between the rotor blades and both the upstream and downstream stator vanes had to be considered.

Introduction

The purpose of this study was to ascertain whether the wave reflection theory in a turbomachine stage based on the ray, or geometrical, acoustics, could offer a plausible interpretation of the unexplained axial compressor blade vibration data obtained during the 1977–1979 period by the Pratt & Whitney Aircraft Group of the United Technologies Inc. and made available to the writer by the NASA.

The blade flutter prediction methods frequently employed use an empirical parameter correlation or the aerodynamic damping correlation. In the empirical parameter correlation method, parameters thought to be influential in the blade instability are plotted and empirical stability limits generated. In the aerodynamic damping method, such as the method by F. O. Carta [1], the aerodynamic work done on all rotor blades over one cycle of harmonic oscillation at one of the rotor system natural frequencies is computed. Subsequently, this work is normalized by four times the rotor system kinetic energy to obtain the aerodynamic logarithmic decrement. If this logarithmic decrement is negative then the system is considered to be unstable when the (positive) structural modal damping is not sufficient to overcome it.

The Pratt & Whitney study, from which the data points analyzed in this paper were taken, concluded that neither the empirical parameter correlation method nor the aerodynamic damping correlation method predicted the first blade-disk mode to be the flutter mode. Neither the separated-flow unsteady aerodynamics models nor the unstalled flat-plate aerodynamics models proved to be successful. In addition, a general flutter theory was tried in which the effect of aerodynamic coupling of structural modes within a given nodal diameter is considered. The study recommended that

additional experimental and analytical effort be made to improve and extend the theory.

The wave reflection theory for high-frequency acoustic waves in the form of concentrated pressure pulses in turbomachine stages was advanced by the writer in 1966 [2]. It was at first hypothesized in order to explain peculiar shapes of efficiency curves of an air turbine and to explain turbine blade excitation frequencies measured by the NACA in 1952 on a J47 turbojet engine [3]. Subsequently, the reflecting concentrated waves, or pressure pulses, were observed and photographed by the writer on a water-table model of a turbine stage.

Since the wave theory was advanced, the ray acoustics method has been used with considerable success to explain the observed directivity of high-frequency sound produced in jet engines.

For the ray, or geometrical, reflection in a turbomachine stage to be valid, the sound wave, or the pressure pulse, in question must have its length very much shorter than the blade chord or spacing. The photographs of the pressure pulses obtained on the water-table model indicate that this condition is satisfied.

Wave Types of the Wave Reflection Theory

As was described in reference [2], the waves of the wave reflection theory can propagate in the space between rows of moving and stationary blades in the direction of rotation of the rotor or in the opposite direction. Thus we can differentiate between the forward-running waves and the backward-running waves. The waves can span one, two, or n upstream vane spacings. Thus we can talk about the "one reflection per n vane spacings, forward-running wave," or the $(1W \times nV)F$ wave. We can also talk about the "one reflection per n vane spacings, backward-running wave," or the $(1W \times nV)B$ wave. Waves reflecting more than once from a vane surface are also possible. In a turbomachine stage more
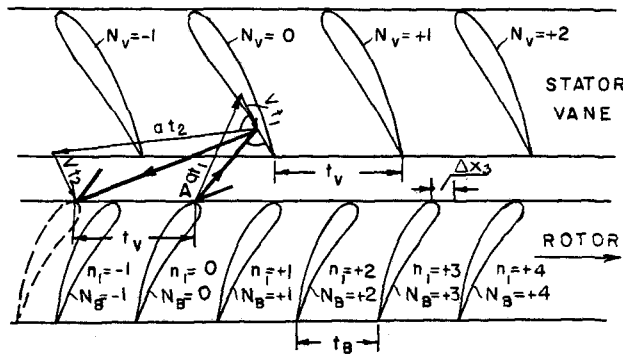
Fig. 1 Path of a wave of type $(1W \times 1V)B$, $n_1 = -3$ in a compressor stage
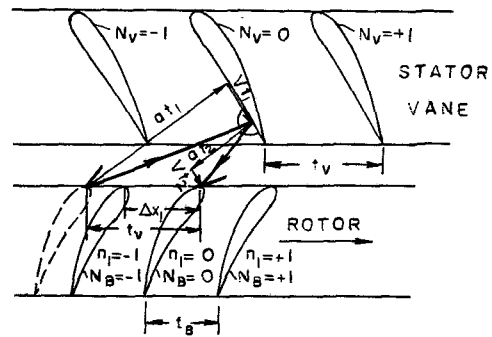

Fig. 2 Path of a wave of type $(1W \times 1V)F$, $n_1 = +1$ in a compressor stage

than one wave type, or pattern, may exist at the same time. Figures 1 and 2 show paths of waves $(1W \times 1V)B$ and $(1W \times 1V)F$ in an axial compressor stage, respectively.

In the case of reflection of the concentrated pressure waves in the space between the rotor blades and the downstream stator blades, the notation used will be $(1W \times nR)F$ and $(1W \times nR)B$ depending on whether the wave is travelling in space in the direction of rotation of the rotor blades, or in the opposite direction. Figure 3 shows a path of a wave $(1W \times 1R)B$.

Rotor Blade Excitation Frequencies of Waves of Type $(1W \times nV)F$ and $(1W \times nV)B$.

The time between successive reflections of a wave (pulse) from the blades, $t = t_1 + t_2$, in seconds is given by equation

$$t = (\pm nt_V - n_1 t_B)/W \quad (s) \tag{1}$$

where t_V denotes the upstream stator vane spacing, t_B represents the rotor blade spacing, W denotes the peripheral speed of the rotor blade at a given radius, and n_1 denotes the number of spacings between blades successively reflecting the same wave. (When $n_1 = 0$ the wave is always reflected by the
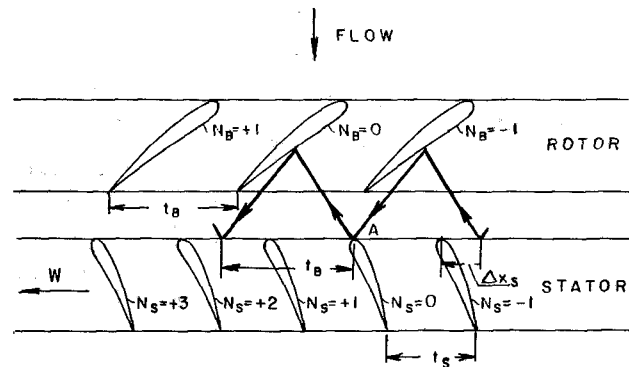

Fig. 3 Motion of the downstream stator relative to the rotor and path of a wave of type $(1W \times 1R)B$, $n_1 = 0$

same blade; when $n_1 = +1$, the blade to reflect the wave lies immediately in front (in direction of rotation) of the blade which was last to reflect it; when $n_1 = -1$, the blade to reflect the wave lies immediately behind the blade which was last to

Nomenclature

a	=	speed of sound	n	=	number of upstream blade spacings spanned by a wave	
C_S	=	axial distance between the rotor blades and the downstream stator vanes	n_B	=	number of rotor blades	
C_V	=	axial distance between the upstream stator vanes and the rotor blades	n_V	=	number of upstream stator vanes	
cpr	=	cycles per revolution	n_S	=	number of downstream stator vanes	
D	=	diameter	n_1	=	number of spacings between blades successively reflecting the same wave	
f_B	=	rotor blade excitation frequency	N	=	shaft rotational speed (rpm)	
f_N	=	blade natural frequency (characteristic flutter frequency)	N_B	=	rotor blade number	
k	=	an integer in equation (2)	N_S	=	downstream stator vane number	
k_1	=	an integer representing the number of times a wave travels around a rotor wheel before it returns to a given blade	N_V	=	upstream stator vane number	
M_V	=	flow Mach number between the upstream stator vanes and the rotor blades	t_1	=	time of propagation of a wave from a leading edge to a reflecting surface	
$M_{S,REL}$	=	Mach number of the flow relative to the rotor blades at exit	t_2	=	time of propagation of a wave from a reflecting surface to a leading edge	
			t	=	time between consecutive reflections of a wave from leading edges of a blade ($t = t_1 + t_2$)	

t_B = spacing (pitch) of rotor blades
t_S = spacing of downstream stator vanes
t_V = spacing of upstream stator vanes
T = expression given by equation (4)
T_S = expression given by equation (15)
V = flow speed
V_V = flow speed between the upstream stator vanes and the rotor blades
$V_{S,REL}$ = flow speed relative to the rotor blades at exit
W = peripheral speed of a blade at a given radius
Δx = expression given by equation (5)
Δx_S = expression given by equation (16)
ξ = number of reflections of a wave from the upstream vane surfaces before it returns to a given blade
σ = phase angle between blades

reflect it, and so on.) The upper $(+)$ sign is valid for the forward-running waves, and the lower $(-)$ sign to the backward-running waves.

The number of reflections of a wave from the upstream vane surfaces before it returns to a given blade and, hence, also the number of blades belonging to one "family" is given by

$$\xi = k \frac{n_B}{|n_1|} \qquad (2)$$

where k denotes the smallest integer which results in an integer for ξ, and $n_1 \neq 0$. (For $n_1 = 0$, $\xi = 1$.)

The equation for the rotor blade excitation frequencies is

$$f_B = \frac{60}{N\xi t} = \frac{n_V}{\xi \left(\pm n - n_1 \frac{n_V}{n_B} \right)} \qquad \text{(cpr)} \qquad (3)$$

or

$$f_B = \frac{1}{\xi t} \quad \text{(Hz)} \qquad (3A)$$

where $n_V/n_B = t_B/t_V$ denotes the ratio of the number of upstream vanes to the number of rotor blades. This equation gives the blade excitation frequency of a wave which returns to a blade after ξ reflections [2].

However, all blades of a family produce and reflect pressure pulses. For example, if the blade $N_B = 0$ in Fig. 1 reflects a pulse at point A at the moment shown, the blade $N_B = +3$ will reflect another pulse after it has travelled through a distance Δx_3 shown. This wave will reach blade $N_B = 0$ after an interval of time $T = t + \Delta x_3/W$. Similar situation will be true for other blades of the same family lying in front of the blade $N_B = 0$.

And so we can write the following general equation for the time interval T needed for a wave (pulse) generated by a blade N_B of one blade family to reach blade $N_B = 0$ which has just reflected a pulse

$$T = \frac{|N_B|}{|n_1|} t + \frac{\Delta x}{W} \qquad (4)$$

for all $n_1 \neq 0$. [For $n_1 = 0$ this equation does not apply and we have $f_B = n_V$ (cpr).] The distance

$$\Delta x = N_V t_V - N_B t_B \qquad (5)$$

can be positive (in direction of rotation) or negative (in direction opposite to rotation) for a given blade N_B. ($N_V = 0,1,2,...$ or $0,-1,-2,...$).

Since $W = \pi DN/60$, we have the following equation for the rotor blade excitation frequency

$$f_B = \frac{60/N}{T} = \frac{n_V}{\frac{|N_B|}{|n_1|} \left(\pm n - n_1 \frac{n_V}{n_B} \right) + \left(N_V - N_B \frac{n_V}{n_B} \right)} \quad \text{(cpr)} \quad (6)$$

Equation (6) is more general than equation (3) derived in reference [2] because it accounts for all waves generated by the blades of one family.

Only one value of N_B

$$N_B = -n_1 \qquad (7)$$

needs to be considered for the derivation of the equation for the blade excitation frequency because the pulses reflected by all blades of a family must reach blade $N_B = -n_1$ before reaching blade $N_B = 0$. As a result, we can consider only

$$T = t + \frac{\Delta x}{W} \qquad (4A)$$

and

$$\Delta x = N_V t_V + n_1 t_B \qquad (5A)$$

The values of N_V to be considered are such that $T > 0$, or, in view of equations (1), (4A), and (5A)

$$N_V > \mp n \qquad (8)$$

with sign $(-)$ corresponding to the $(1W \times nV)F$ waves, and sign $(+)$ corresponding to the $(1W \times nV)B$ waves. In addition, in order to insure that the pulses considered reach blade $N_B = 0$, we must have

$$\frac{N_V}{n} = \text{an integer}$$

As a result, the smallest value of N_V to be considered is

$$N_{V,\min} = -n + n = 0 \text{ for the } (1W \times nV)F \text{ waves,}$$

and

$$N_{V,\min} = +n + n = 2n \text{ for the } (1W \times nV)B \text{ waves.}$$

Hence, with $N_B = -n_1$, equation (6) simplifies to

$$f_B = \frac{n_V}{\pm n + N_V} = \frac{n_V}{ni} \quad \text{(cpr)} \qquad (6A)$$

with $i = 1,2,...$, for both types of waves.

Equation (6A) could have been expected since a pressure pulse may (although it does not have to) be reflected by a given blade every time the blade is in the same position relative to the wave-reflecting vane surfaces of a particular wave.

The rotor speed range in which waves of a given type should exist can be found by determining, for the given flow Mach number, the wave reflection path for the case when the wave reflects at a location furthest from the trailing edge on a given stator vane (just missing the trailing edge of the neighboring vane), and for the case when the wave reflects near the trailing edge of the given stator vane. From the velocity triangles of the reflection paths, the times t_1, t_2, and $t = t_1 + t_2$ can be determined since the flow speed is assumed to be known. Subsequently, the rotational speeds corresponding to the two cases can be calculated from an equation following from equation (1) into which the expression $W = \pi DN/60$ is introduced. The result is

$$N = \frac{60}{t} \frac{\left(\pm n - n_1 \frac{n_V}{n_B} \right)}{n_V} \quad \text{(rpm)} \qquad (9)$$

with the upper $(+)$ sign corresponding to the forward-running waves, and the lower $(-)$ sign to the backward-running waves.

Since, depending on their strength, the reflecting pressure pulses may represent weak shock waves, they can move with a speed relative to the fluid which is somewhat higher than the speed of sound. The speed of sound is normally used in construction of the velocity triangles, as shown in Figs. 1 and 2. As a result, the speed ranges may be somewhat higher than those normally calculated. In addition, the presence of wakes downstream of the stator vanes, of boundary layers on reflecting surfaces, and the fact that the flow variables (V and M) are not uniform along the paths of the waves should have some effect on the calculated speed ranges.

Rotor Blade Excitation Frequencies of Waves of Type $(1W \times nR)B$ and $(1W \times nR)F$

Figure 3 illustrates the relative motion of the downstream stator vanes with respect to the rotor blades of an axial compressor stage. For the waves $(1W \times nR)B$, which are *forward-running relative to the stator*, and hence *backward-running relative to the rotor*, the time between successive wave reflections by the stator vanes is given by:

$$t = t_1 + t_2 = (nt_B - n_1 t_S)/W \quad \text{(s)} \tag{10}$$

where n denotes the number of rotor blade spacings spanned by the wave, t_B denotes the rotor blade spacing, t_S denotes the downstream stator vane spacing, W represents the peripheral speed of the blade at a given radius, while n_1 denotes the number of spacings between the stator vanes successively reflecting the same wave. [When $n_1 = +1$, the vane to reflect the wave lies immediately in front (in direction of relative motion) of the vane which was last to reflect it.]

For the waves $(1W \times nR)F$, which are *backward-running relative to the stator*, and hence which are *propagating in the direction of the rotor rotation*, we have

$$t = t_1 + t_2 = (-nt_B - n_1 t_S)/W \quad \text{(s)} \tag{11}$$

The upstream rotor blade excitation frequency, f_B, caused by one reflecting wave is given by equation

$$f_B = \frac{60/N}{k_1 \dfrac{n_B}{n} t} \quad \text{(cpr)} \tag{12}$$

or

$$f_B = \frac{1}{k_1 \dfrac{n_B}{n} t} \quad \text{(Hz)} \tag{13}$$

where k_1 is the smallest integer which makes the term $k_1 n_B/n$ an integer. The term k_1 represents the number of times a wave travels around the rotor wheel before it returns to a given blade. In view of equations (11) and (10), equation (12) becomes

$$f_B = \frac{n}{k_1 \left(\mp n - n_1 \dfrac{n_B}{n_S} \right)} \quad \text{(cpr)} \tag{14}$$

where the upper $(-)$ corresponds to the $(1W \times nR)F$ waves, and the lower $(+)$ sign to the $(1W \times nR)B$ waves.

Since all vanes can be expected to produce and reflect pressure pulses, a given blade reflects these waves also. The time interval T_S needed for a wave (pulse) reflected by the vane N_S to reach the rotor blade $N_B = 0$ which has just reflected a pulse is the same as the time elapsed between reflection of pulses by the stator vane $N_S = 0$ (which reflected the pulse toward the blade $N_B = 0$) and stator vane N_S. Hence it is given by

$$T_S = \frac{|N_B|}{n} t + \frac{\Delta x_S}{W} \tag{15}$$

where N_B is the rotor blade number, and

$$\Delta x_S = N_B t_B - N_S t_S \tag{16}$$

Observe that, in Fig. 3, vane $N_S = -1$ generated or reflected a $(1W \times 1R)B$ wave time interval $\Delta x_S/W$ before vane $N_S = 0$ reflected a wave at point A. The time interval between consecutive reflections of these two pressure pulses is, in this case, $t - |\Delta x_S/W|$. This time interval, therefore, determines the frequency with which these pulses will strike blade $N_B = 0$.

For the rotor blade excitation frequency by the downstream stator vanes we obtain equation

$$f_B = \frac{60/N}{T_S} = \frac{n_S}{\dfrac{|N_B|}{n} \left(\mp n \dfrac{n_S}{n_B} - n_1 \right) + \left(N_B \dfrac{n_S}{n_B} - N_S \right)} \quad \text{(cpr)} \tag{17}$$

in view of equations (15), (16), (11), and (10).

Only two rotor blade numbers need be considered in rotor blade excitation frequency calculations: $N_B = +n$ for the $(1W \times nR)F$ waves, and $N_B = -n$ for the $(1W \times nR)B$ waves. This is so because all pressure pulses reaching blade $N_B = 0$ must reach these blades first. As a result, in view of equations (11) and (10),

$$T_S = -(n_1 + N_S) \frac{t_S}{W} \tag{18}$$

Since we must have $T_S > 0$, it follows that $N_S < -n_1$. Hence

$$N_S = -n_1 - i \tag{19}$$

where $i = 1, 2, 3, \ldots$, and the expression for T_S becomes

$$T_S = i \frac{t_S}{W} \tag{20}$$

Equation (17) simplifies now to

$$f_B = \frac{n_S}{-\dfrac{|N_B|}{n} n_1 - N_S} = \frac{n_S}{i} \quad \text{(cpr)} \tag{17A}$$

with $i = 1, 2, 3, \ldots$, for both types of waves, if we introduce equation (19) and $N_B = \pm n$.

The rotor speed range in which waves of a given type should exist can be determined as was described previously. First, the extreme paths and the reflection times $t = t_1 + t_2$ should be determined. Subsequently, the corresponding rotor speeds can be calculated from equation

$$N = \frac{60}{t} \frac{\left(\mp n - n_1 \dfrac{n_B}{n_S} \right)}{n_B} \quad \text{(rpm)} \tag{21}$$

with the upper $(-)$ sign corresponding to the $(1W \times nR)F$ waves, and the lower $(+)$ sign to the $(1W \times nR)B$ waves. This equation follows from equations (11) and (10).

Discussion of the Rotor Blade Excitation Phenomenon

The flow in the space between the rotor and the upstream and downstream stators is never truly steady. Slight transient circumferential variations of the Mach number can always be expected. As a result, the reflecting pressure pulses need not be produced or reflected every time a rotor blade passes a stator vane. For that reason, all values of i should be considered in the rotor blade excitation frequency equations (6A) and (17A). [Otherwise, we would have only $f_B = n_V$ and $f_{B_V} = n_S$ (cpr).] One of these excitation frequencies may correspond to one of the blade natural frequencies.

Once a rotor blade begins to vibrate at its natural frequency (or at the blade-disk mode frequency in case of relatively flexible disks) at a rotor speed such that the vibration frequency is equal, in number of cycles per revolution, to the number of stator vanes divided by an integer n_V/ni (or n_S/i), it will tend to lock in on the wave pattern that produces it. The possibility of reflection of pressure pulses which would result in a different excitation frequency will be diminished. This is so because the vibrating blades have zero phase angle and will be in identical position relative to the stator vanes only when reflecting pressure pulses every $n$ith (or ith) stator vane. The pressure pulses can be expected to be relatively weak until blades begin to vibrate. Subsequently, their strength will increase.

Let us consider the rotor blade excitation at a natural frequency $f_{N1} = 709$ Hz at a rotor speed $N = 10,871$ rpm which corresponds to the excitation frequency $f_B = 3.913 = n_V/i = 90/23$ (cpr). As will be shown in a section that follows, this blade excitation can be caused in the compressor stage analyzed in this paper (in which $n_V = 90$ and $n_B = 52$) by the waves $(1W \times 1V)B$ with $n_1 = -2$. From equations (6) and (6A) it follows that

$$ni = \frac{|N_B|}{|n_1|}\left(\pm n - n_1 \frac{n_V}{n_B}\right) + \left(N_V - N_B \frac{n_V}{n_B}\right) \quad (22)$$

where

$$N_V - N_B \frac{n_V}{n_B} = \frac{\Delta x}{t_V} \quad (23)$$

in view of equation (5). In this case we obtain equations

$$i = 23 = \frac{|N_B|}{2}(2.46154) + N_V - 1.73077 N_B$$

or

$$N_V = 23 + 0.5 N_B \quad (24)$$

since $N_B > 0$ for $n_1 < 0$, and

$$N_V = \frac{\Delta x}{t_V} + 1.73077 N_B \quad (23A)$$

From the last two equations it follows that

$$\frac{\Delta x}{t_V} = 23 - 1.2307 N_B \quad (25)$$

The smallest positive value of $\Delta x / t_V$ occurs for rotor blade $N_B = 18$ which is a distance $\Delta x = 0.846 \, t_V$ away from stator vane $N_V = 32$. (At this instant, rotor blade $N_B = 0$ reflects a pressure pulse toward stator vane $N_V = 0$.) Hence the pressure pulse generated (or reflected) by blade $N_B = 18$ when it reaches stator vane $N_V = 32$, (that is, when it is in the same position relative to stator vane $N_V = 32$ as blade $N_B = 0$ is relative to stator vane $N_V = 0$ at this instant), will reach rotor blade $N_B = 16$ at stator vane $N_V = 31$, rotor blade $N_B = 14$ at stator vane $N_V = 30$, ..., rotor blade $N_B = 4$ at stator vane $N_V = 25$, rotor blade $N_B = 2$ at stator vane $N_V = 24$, and, finally, will reach rotor blade $N_B = 0$ at stator vane $N_V = i = 23$. All these values of N_V follow from equation (24), while $N_B = -n_1 j$ with $j = 1, 2, ...\xi$. Thus, in this case, it is the reflection of a pressure pulse by rotor blade $N_B = 0$ at stator vane $N_V = 0$ and the generation (or reflection) of a pressure pulse by rotor blade $N_B = 18$ when it reaches stator vane $N_V = 32$ or by any of the other above-mentioned blades at corresponding vanes that are responsible for the rotor blade excitation at the frequency $f_B = 3.913$ cpr ($f_{N1} = 709$ Hz and $N = 10,871$ rpm) which, once started, sustains and reinforces itself.

It should be noted that the equations for the rotor blade excitation frequencies derived in this paper are valid for compressors and for turbines. In addition, the analysis has been limited to single reflections of waves from the upstream surfaces.

Reported Axial Compressor Blade Vibration

The five test points analyzed in this study were taken from a test program run on a turbojet engine by the Pratt & Whitney Aircraft Group in the late 1970's. Dynamic strain gages were used to sense airfoil motion. A 100-channel slipring allowed vibratory responses of the rotating stages to be transmitted to a data collection facility. All test points analyzed were for the same rotor and the flow conditions in the upper 20 percent of the rotor blade height. The blades in the stage analyzed vibrated predominantly in the first bending mode with some primary and secondary responses in the second mode. The test conditions for each test point are given below. The symbol RCVV refers to the setting of the adjustable guidevane located upstream of the moving blade row. The tests were run with decreasing rotor speeds and the speeds at which rotor blade vibration was first observed, N_{ONSET}, were recorded. The test speeds N_{TEST}, were close to N_{ONSET} but somewhat lower.

Test Point AD 06-21

RCVV $= -6.67$ deg, $N_{ONSET} = 12,540$ rpm, $N_{TEST} = 12,480$ rpm.

$M_V \quad = 0.35$ (at rotor blade inlet)
$M_{S,REL} = 0.44$ (at rotor blade exit)

Rotor blade vibration was observed at a frequency of $f_{N1} = 3.44$ cpr (716.2 Hz, first bending mode) with the stress level of 5.4 ksi, and $f_{N2} = 10.70$ cpr (2225 Hz, second bending mode) with the stress level of 2.0 ksi.

Test Point AD 08-19

RCVV $= +2.2$ deg, $N_{ONSET} = 12,030$ rpm, $N_{TEST} = 11,973$ rpm.

$M_V \quad = 0.355$ (at rotor blade inlet)
$M_{S,REL} = 0.43$ (at rotor blade exit)

Rotor blade vibration was observed at a frequency of $f_{N1} = 3.57$ cpr (711.7 Hz, first bending mode) with the stress level of 21.6 ksi.

Test Point AD 08-22A

RCVV $= +0.5$ deg, N_{ONSET} not reported, $N_{TEST} = 11,860$ rpm.

$M_V \quad = 0.355$ (at rotor blade inlet)
$M_{S,REL} = 0.43$ (at rotor blade exit)

Rotor blade vibration was observed at a frequency of $f_{N1} = 3.59$ cpr (710 Hz, first bending mode) with the stress level of 8.1 ksi, and $f_{N2} = 11.33$ cpr (2240 Hz, second bending mode) with the stress level of 1.8 ksi.

Test Point AG 10-23

RCVV $= +3.54$ deg, $N_{ONSET} = 11,650$ rpm, $N_{TEST} = 11,325$ rpm.

$M_V \quad = 0.43$ (at rotor blade inlet)
$M_{S,REL} = 0.53$ (at rotor blade exit)

Rotor blade vibration was observed at a frequency of $f_{N1} = 3.76$ cpr (709 Hz, first bending mode) and $f_{N2} = 12.16$ cpr (2295 Hz, second bending mode). The stress levels were not reported.

Test Point AG 10-35

RCVV $= -2.5$ deg, $N_{ONSET} = 10,800$ rpm, N_{TEST} not reported.

$M_V \quad = 0.39$ (at rotor blade inlet)
$M_{S,REL} = 0.52$ (at rotor blade exit)

Rotor blade vibration was observed at a frequency of $f_{N1} = 3.88$ cpr (700 Hz, first bending mode). The stress level was not reported.

The accuracy of the measured rotor blade vibration frequency was given as ± 1 percent. (A frequency of the first vibration mode in one test point was reported to be 739 ± 8 Hz.)

Rotor Blade Excitation Frequencies From the Wave Reflection Analysis

The rotor blade excitation frequencies and the speed ranges determined from the wave reflection analysis are given below. The axial spacing between the upstream guidevane and the rotor blades, C_V, was in the range 0.3 in. $< C_V < 0.5$ in. (0.3 in. $= 7.62$ mm; 0.5 in. $= 12.7$ mm). The axial spacing between the rotor blades and the downstream stator blades, C_S, was assumed to be in the same range. There were 90 adjustable upstream inlet guidevanes to the fourth stage, 52 rotor blades, and 64 downstream stator blades.

Results of Analysis for the Waves Reflecting Between the Rotor and the Upstream Stator

Waves of the types $(1W \times 1V)F$ and $(1W \times 2V)F$ have their predicted speed ranges falling outside the speed ranges of all five test points.

Waves of the type $(1W \times 1V)B$, $n_1 = -2$. These waves have proper speed ranges for all five test points:

For the *test point AD 06-21* the calculated speed range is:

13,380 rpm $> N >$ 9,155 rpm for $C_V = 0.5$ in.

while the reported $N_{\text{ONSET}} = 12,540$ rpm.

For the *test point AD 08-19* the calculated speed range is:

15,125 rpm $> N >$ 10,043 rpm for $C_V = 0.3$ in., and

11,543 rpm $> N >$ 7,725 rpm for $C_V = 0.5$ in.

while the reported $N_{\text{ONSET}} = 12,030$ rpm.

For the *test point AD 08-22A* the calculated speed range is:

12,460 rpm $> N >$ 9,048 rpm for $C_V = 0.4$ in., and

11,413 rpm $> N >$ 7,971 rpm for $C_V = 0.5$ in.

while $N_{\text{TEST}} = 11,860$ rpm.

For the *test point AG 10-23* the calculated speed range is:

12,641 rpm $> N >$ 9,241 rpm for $C_V = 0.3$ in.

while $N_{\text{ONSET}} = 11,650$ rpm.

For the *test point AG 10-35* the calculated speed range is:

14,827 rpm $> N >$ 9,789 rpm for $C_V = 0.3$ in., and

11,303 rpm $> N >$ 7,359 rpm for $C_V = 0.5$ in.

while the reported $N_{\text{ONSET}} = 10,800$ rpm.

With these waves are associated, among others, the following excitation frequencies of the rotor blades, (see Appendix A):

$f_B = 3.46$ cpr (or 720 Hz at $N = 12,480$ rpm),

$f_B = 3.60$ cpr (or 712 Hz at $N = 11,860$ rpm),

$f_B = 3.75$ cpr (or 709 Hz at $N = 11,325$ rpm),

$f_B = 3.91$ cpr (or 704 Hz at $N = 10,800$ rpm),

$f_B = 6.0$ cpr (or 2,265/2 Hz at $N = 11,325$ rpm), and

$f_B = 11.25$ cpr (or 2,224 Hz at $N = 11,860$ rpm).

These frequencies correspond closely, (to less than 1 percent), to the observed rotor blade vibration frequencies in the test points AD 06-21 ($f_{N1} = 3.44$ cpr or 716 Hz at 12,480 rpm), AD 08-22A ($f_{N1} = 3.59$ cpr or 710 Hz at 11,860 rpm, and $f_{N2} = 11.33$ cpr or 2,240 Hz at 11,860 rpm), and AG 10-35 ($f_{N1} = 3.88$ cpr or 700 Hz at 10,825 rpm). For the test point AG 10-23, $f_{N1} = 3.76$ cpr or 709 Hz and $f_{N2} = 12.16$ cpr or 2,295 Hz at 11,325 rpm.

Results of Analysis for the Waves Reflecting Between the Rotor and the Downstream Stator. The speed ranges of these waves are influenced only by the relative flow Mach number at the rotor blade exit and the edge-to-edge spacing, C_S. The wave-reflecting surface is the downstream-facing rotor blade surface which is not adjustable like the inlet guidevane upstream of the rotor blade row.

Waves of the type $(1W \times 1R)F$, $n_1 = -3$. These waves have speed range encompassing the test conditions only for the test points for which $M_{S,\text{REL}}$ was about 0.44 (test points AD 06-21, AD 08-19, and AD 08-22A). For these test conditions the calculated speed ranges are

13,180 rpm $> N >$ 10,715 rpm for $C_S = 0.2$ in., and

10,915 rpm $> N >$ 8,779 rpm for $C_S = 0.5$ in.

With these waves (and with all other waves of the $(1W \times nR)$ type) are associated, among others, the rotor blade excitation frequencies $f_B = 3.56$ cpr, and 10.67 cpr, (see Appendix A). They could explain the observed blade vibration frequencies of $f_{N1} = 3.57$ cpr of the test point AG 08-19 for which N_{ONSET}

= 12,030 rpm, $f_{N1} = 3.59$ cpr of the test point AD 08-22A for which $N_{\text{TEST}} = 11,860$ rpm, and $f_{N2} = 10.70$ cpr of the test point AD 06-21 for which $N_{\text{ONSET}} = 12,540$ rpm.

Waves of the Type $(1W \times 1R)F$, $n_1 = -4$. For the flow conditions of the test point AG 10-23, these waves should be expected in the approximate rotor speed range 12,926 rpm $> N >$ 10,874 rpm for $C_S = 0.4$ in. (10.2 mm). With these waves are associated, among others, the following rotor blade excitation frequencies:

$f_B = 3.76$ cpr (710 Hz at 11,325 rpm), and

$$f_B = 4.0 \text{ cpr} = \frac{1}{3}(12.0) \text{ cpr} (2263/3 \text{ Hz at } 11,314 \text{ rpm}).$$

Rotor blade vibration in the test AG 10-23 was observed at frequencies $f_{N1} = 3.76$ cpr (709 Hz) and 12.16 cpr (2296 Hz).

This wave type is outside the test speed range for the three tests in which the relative flow Mach number, $M_{S,\text{REL}}$, is about 0.4 (test points AD 06-21, AD 08-19, and AD 08-22A).

Waves of the Type $(1W \times 2R)F$, $n_1 = -6$. For the flow conditions of the test points AD 08-19 and AD 08-22A, these waves have the following calculated speed range:

12,327 rpm $> N >$ 11,758 rpm for $C_S = 0.4$ in.,

while for the test point AD 08-19 $N_{\text{ONSET}} = 12,030$ rpm and for the test point AD 08-22A $N_{\text{TEST}} = 11,860$ rpm. With these waves are associated, among others, the rotor blade excitation frequencies

$f_B = 3.56$ cpr (712 Hz at $N = 12,000$ rpm), and

$f_B = 10.67$ cpr (2217 Hz at $N = 12,480$ rpm).

The observed rotor blade excitation frequency for the test point AD 08-19 was $f_{N1} = 3.57$ cpr and for the test point AD 08-22A, $f_{N1} = 3.59$ cpr. During the test AD 06-21, which also falls within the speed range of these waves, one of the observed vibration frequencies was $f_{N2} = 10.70$ cpr.

Discussion of the Results

The results of the analysis presented indicate that all examined axial compressor rotor blade vibrations can be explained by forced excitation caused by reflecting waves (pressure pulses). The wave reflection between the rotor blades and both the upstream and downstream stator vanes must be considered.

It is of interest to note that the Pratt & Whitney study concluded that for the test point AD 08-19 the first flutter mode (at $f_{N1} = 3.57$ cpr) was a 2 nodal diameter forward-travelling wave. This agrees with the results of this analysis. The wave reflection theory predicts that this excitation can be caused by the waves $(1W \times 1R)F$, $n_1 = -3$ and $(1W \times 2R)F$, $n_1 = -6$. As far as the nodal diameter statement is concerned, as pointed out in the discussion of the phase angle between vibrating rotor blades in Appendix B, in the stage tested the rotor blades which are 180 deg apart are in the same position relative to the downstream (and upstream) stator vanes. As a result, all blades which are 180 deg apart should have the same phase angle, as was measured.

An understanding of the effect of the rotational speed on the rotor blade excitation at one of its natural frequencies can be obtained by drawing, on the blade natural frequency-rotational speed diagram, or the Campbell diagram, lines of constant blade excitation frequency f_B in cpr.

In view of equation (6A), the expression for the rotor blade excitation frequency f_B (Hz) caused by the waves reflecting between the rotor blades and the upstream stator vanes, that is, the $(1W \times nV)$ waves, can be written as
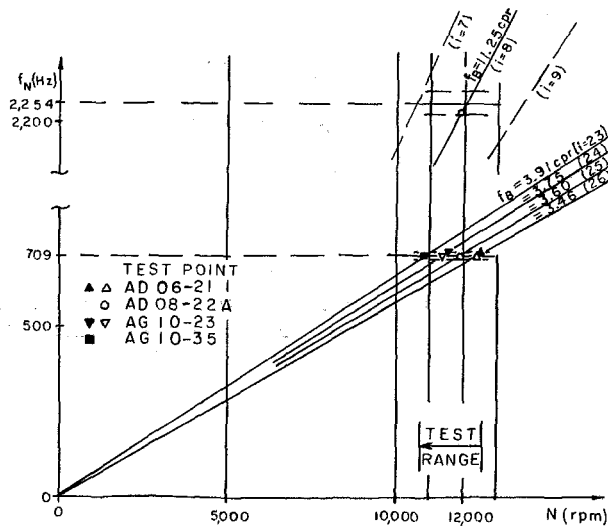
Fig. 4   Wave resonance diagram for the (1W × 1V) waves. (Full symbols denote onset of vibration; open symbols denote the test points.)

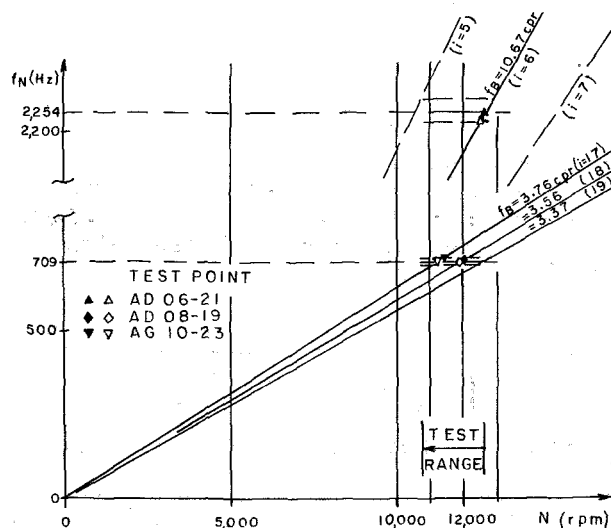**Fig. 5   Wave resonance diagram for the (1W × nR) waves. (Full symbols denote onset of vibration; open symbols denote the test points.)**

$$f_B(\text{Hz}) = f_B(\text{cpr})\frac{N}{60} = \frac{n_V}{ni}\frac{N}{60} \qquad (6B)$$

with $i = 1, 2, \ldots$.

For the compressor blade vibration analyzed in this paper $n_V = 90$, $n = 1$, while the operating speed varied from about 12,600 to 10,800 rpm. For the observed rotor blade vibration frequency $f_{N1} = 709 \pm 9$ Hz, the wave reflection theory predicts resonant forced vibration for four values of i, $i = 23$, 24, 25, and 26. The corresponding rotor blade excitation frequencies f_B are 3.91, 3.75, 3.60, and 3.46 cpr. All these excitation frequencies were observed in the tests analyzed.

For the observed rotor blade vibration frequency $f_{N2} = 2254 \pm 41$ Hz, the wave reflection theory predicts resonant forced vibration for $i = 8$ and 15. The corresponding values of f_B are 11.25 and 6 ($= 12/2$) cpr.

Figure 4 illustrates the results for the $(1W \times 1V)$ waves. The rotational speeds at which rotor blade vibrations at various frequencies f_B (cpr) were first observed as the speed was being decreased, N_{ONSET}, are indicated. They correspond very closely to the vibration onset speeds which can be predicted from the wave resonance diagram. The test conditions are also indicated.

The expression for the rotor blade excitation frequency caused by the waves reflecting between the rotor blades and the downstream stator blades, or the $(1W \times nR)$ waves, is

$$f_B(\text{Hz}) = f_B(\text{cpr})\frac{N}{60} = \frac{n_S}{i}\frac{N}{60} \qquad (17B)$$

with $i = 1, 2, \ldots$

For the stage analyzed $n_S = 64$. The wave reflection theory predicts resonant rotor blade vibration in the speed range of interest for $i = 17$, 18, and 19 for f_{N1}, and $i = 6$ for f_{N2}. These results are illustrated in Fig. 5. The blade excitation at the frequency of 3.37 cpr has not been reported. It is possible that it was masked by the reported vibration at 3.44 cpr which was explained by the $(1W \times 1V)B$ waves or was just outside the test speed range. The rotational speeds at which blade vibrations at various frequencies f_B (cpr) were first observed, N_{ONSET}, and the test conditions are indicated in Fig. 5. Again, there is a good agreement between the predictions of the theory and the speeds at which rotor blade vibrations were first observed.

Conclusions

The results of the analysis presented in this paper indicate that the wave reflection theory does offer a plausible explanation of the examined axial compressor blade vibration.

The forward-travelling waves, in this case the waves reflecting between the rotor and the downstream stator, can explain the observed rotor blade vibration at 3.57, 3.76, and 10.70 cpr, while the backward-travelling waves, in this case the waves reflecting between the rotor and the upstream stator, can explain the observed rotor blade vibration at 3.44, 3.59, 3.75, 3.88, 11.33, and 12.16 cpr.

The values of the highest engine speeds corresponding to particular blade excitation frequencies f_B (cpr) which can explain the rotor blade excitation, agree closely with the engine speeds at which blade vibrations were first observed to start (N_{ONSET}).

Acknowledgments

References

1 Carta, F. O., "Coupled Blade-Disk-Shroud Flutter Instabilities in Turbojet Engine Rotors," ASME JOURNAL OF ENGINEERING FOR POWER, Vol. 89, No. 3, July 1967, pp. 419–426.

2 Owczarek, J. A., "On a Wave Phenomenon in Turbines," ASME JOURNAL OF ENGINEERING FOR POWER, Vol. 88, No. 3, July 1966, pp. 262–276.

3 Morgan, W. C., and Morse, C. P., "Experimental Investigation of the Vibration Characteristics of Four Designs of Turbine Blades and of the Effect Produced by Varying the Axial Spacing Between Nozzle Blades and Turbine Blades," NACA RM E51J25, 1952.

APPENDIX A

Calculated Rotor Blade Excitation Frequencies

(A)   Blade excitation frequencies calculated for the waves reflecting between the rotor and the upstream stator.

From equation (6A)

$$f_B = \frac{n_V}{ni} \quad (\text{cpr})$$

with $i = 1$, 2, … and $n_V = 90$, we have for the waves

$(1W \times 1V)B$ (for which $n=1$), the following rotor blade excitation frequencies:

f_B = 90, 45, 30, 22.5, 18, 15, 12.86, 11.25, 10, 8.18, 7.5, 6.92, 6.43, 6.0, 5.63, 5.29, 5.0, 4.74, 4.5, 4.29, 4.09, 3.91, 3.75, 3.60, 3.46, 3.33, ...cpr.

(B) Blade excitation frequencies calculated for waves reflecting between the rotor and the downstream stator.
From equation (17A)

$$f_B = \frac{n_S}{i} \quad \text{(cpr)}$$

with $i = 1, 2, ...$ we obtain, for $n_S = 64$,

f_B = 64, 32, 21.33, 16, 12.8, 10.67, 9.14, 8.0, 7.11, 6.4, 5.82, 5.33, 4.92, 4.57, 4.27, 4.0, 3.76, 3.56, 3.37, ...cpr.

APPENDIX B

Phase Angle Between Vibrating Rotor Blades

For the wave of the type $(1W \times nR)$, the phase angle σ between the rotor blade $N_B = 0$ and a blade N_B of the same family $(N_B/n_1 = $ an integer) can be determined from equation

$$360j + \sigma_i = 360f_N \frac{\Delta x}{W}$$

$$= \frac{360f_N}{n_V} \frac{60}{N} \frac{\Delta x}{t_V} \qquad (1B)$$

for f_N in Hz and $j = 0, 1, 2..,$ or

$$360j + \sigma = \frac{360f_N}{n_V} \frac{\Delta x}{t_V} \qquad (2B)$$

for f_N in cpr, with

$$\frac{\Delta x}{t_V} = \frac{N_V t_V - N_B t_B}{t_V} = N_V - \frac{n_V}{n_B} N_B \qquad (3B)$$

in view of equation (5).

For example, for the wave $(1W \times 1V)B$, $n_1 = -2$ and the rotor blade excitation frequency $f_B = 3.60$ cpr, we may be interested in the phase angle between the blades $N_B = 0$ and $N_B = 6$. From equation (6)

$$f_B = 3.60 = \frac{90}{25} =$$

$$\frac{90}{\frac{6}{2}\left[-1-(-2)\frac{90}{52}\right]+N_V-\left(\frac{90}{52}\right)(6)} = \frac{90}{N_V-3}$$

from which $N_V = 28$ and

$$\frac{\Delta x}{t_V} = 28 - \left(\frac{90}{52}\right)(6) = 17.615$$

From equation (2B) for $f_N = f_B = 3.60$ cpr

$$360j + \sigma = (360)\left(\frac{3.60}{90}\right)(17.615) = 253.7 \text{ deg}$$

or

$$\sigma = 253.7 \text{ deg}$$

For the waves of the type $(1W \times nV)$, the phase angle σ between the rotor blade $N_B = 0$ and blade N_B of the same family $(N_B/n_1 = $ an integer) can be determined from equation

$$360j + \sigma = 360f_N \frac{\Delta x_S}{W}$$

$$= \frac{360f_N}{n_S} \frac{60}{N} \frac{\Delta x_S}{t_S} \qquad (4B)$$

for f_N in Hz and $j = 0, 1, 2..,$ or

$$360j + \sigma = \frac{360f_N}{n_S} \frac{\Delta x_S}{t_S} \qquad (5B)$$

for f_N in cpr, with

$$\frac{\Delta x_s}{t_S} = N_B \frac{n_S}{n_B} - N_S \qquad (6B)$$

in view of equation (16).

For example, for the wave $(1W \times 1R)F$, $n_1 = -3$ and the rotor blade excitation frequency $f_B = 3.7647$ cpr $(=64/17)$, we may be interested in the phase angle between the blades $N_B = 0$ and $N_B = 7$. From equation (17)

$$f_B = 3.7647 = \frac{64}{7\left[-\frac{64}{52}-(-3)\right]+(7)\left(\frac{64}{52}\right)-N_S} = \frac{64}{21-N_S}$$

from which $N_S = 4$. As a result, $\Delta x_S/t_S = 4.6154$ and $\sigma = 97.7$ deg.

Since, except for the blades located 180 deg apart and excited at 3.57 cpr, no information on the phase angles between blades was available for the compressor stage studied, no comparison with observations could be made.

Note that in the compressor stage studied the rotor blades which are 180 deg apart are in the same position relative to the upstream and downstream stator vanes $(90 \, t_V/2 = 52 \, t_B/2 = 64 \, t_S/2)$. Hence, all blades which are 180 deg apart should have the same phase angle when excited by the reflecting waves of the same type.

Effects of Static Friction on the Forced Response of Frictionally Damped Turbine Blades

A. Sinha
Graduate Student.

J. H. Griffin
Assistant Professor.

Department of Mechanical Engineering,
Carnegie-Mellon University,
Pittsburgh, Pa. 15213

The effect of static friction on the design of flexible blade-to-ground vibration dampers used in gas turbine engines is investigated. It is found that for γ (ratio of dynamic and static friction coefficients) less than 1, the steady-state response is essentially harmonic when the damper slip load, S, is small. However, as S increases beyond a certain value, the steady-state response ceases to be simply harmonic and, while still periodic, is a more complex waveform. The transition slip load is found to be lower for smaller γ. The maximum possible reduction in vibratory stresses increases as γ decreases. These analytical results are compared with those from the conventional numerical time integration method. In addition, an efficient time integration algorithm is described which can be used to predict the peak displacements of the transition solution without tracing the whole waveform, a useful procedure when no harmonic steady-state solution exists. The conditions under which blade response can be adequately modeled by simulating only dynamic friction are established.

1 Introduction

Friction interfaces dissipate energy and reduce vibratory stresses in gas turbine engines. Plunkett [1] reviews this topic and describes two types of mechanisms, micro-slip and macro-slip. Some recent publications [2–6] have concentrated on modeling macro-slip in an attempt to understand and predict the performance of turbine blade friction dampers. These devices are specifically designed to provide links between points experiencing relative motion caused by vibration. They transmit loads through friction contacts which dissipate energy when slip occurs and, consequently, reduce the amplitude of the vibration. In the previously cited papers that dealt with dampers, the magnitude of the friction force during slip was assumed to be independent of velocity. In [2], the damper's flexibility was modeled and it was found that if the damper's slip force was chosen to minimize a resonant response, then at resonance the friction interface would be stuck during a significant portion of each cycle (approximately 50 percent of the time). For conditions of stick-slip, motion variations in the coefficient of friction are known to occur [7]. The objective of the work reported in the present paper is to establish under what conditions variations in the coefficient of friction would significantly influence the dynamic response of a frictionally damped turbine blade.

The model used for this investigation, depicted in Fig. 1, represents a single mode of a blade with a massless, flexible, blade-to-ground friction damper. The nondimensionalized form of this model is shown in Fig. 2 and the nondimensional variables in this figure are described as follows

$$\epsilon = k_d/(k_d+k), \quad \zeta = C/[4m(k+k_d)]^{1/2}$$
$$x = x^*/x_0, \quad y=y^*/x_0$$
$$t = t^*/T, \quad \omega=\omega^*T$$
$$f_0 = Q/F_d=Q/(k_dx_0)$$

where

$$x_0 = F_d/k_d$$

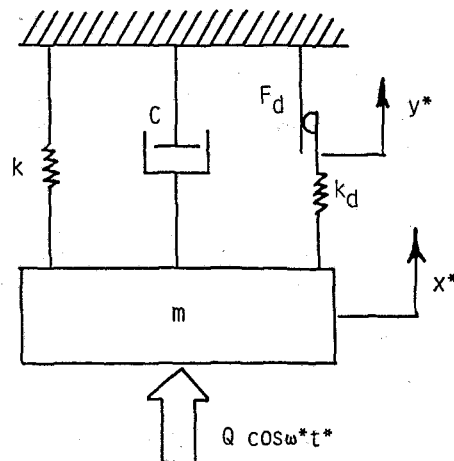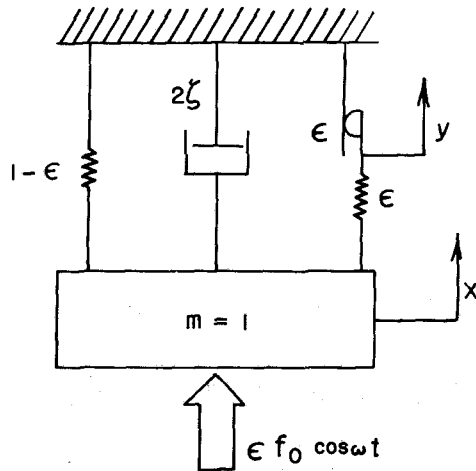Fig. 1 Equivalent single degree of freedom system

Fig. 2 Equivalent dimensionless single degree of freedom system

F_d = static friction force at the beginning of slip (1)

$T = [m/(k+k_d)]^{1/2}$

Except for a variable coefficient of friction, this model is the same as the one developed in [2] and [8]. The coefficient of viscous damping as a fraction of critical damping, ζ, is used to represent other sources of damping such as aerodynamic and material damping. From engine experience, ζ is relatively small and only values up to 2 percent are considered in the present study. The external excitation is characterized by f_0, the ratio of the amplitude of the external excitation to the static friction force. With this nondimensionalization, the slip load is equal to ϵ, and the damper link first slips when the magnitude of the mass's displacement is greater than one. Hence, the damper will be always stuck ($y=0$), if $1/f_0 \geq S_u$, where

$$S_u = \epsilon/[(1-\omega^2)^2 + (2\zeta\omega)^2]^{1/2} \qquad (2)$$

The response of this system provides a quantitative representation of the blade's resonant response if the blade's natural frequencies are adequately separated and if the damper is relatively flexible ($\epsilon \leq 0.4$), conditions which are met in many applications.

The model used for the variation of coefficient of friction is shown in Fig. 3. It assumes that there is a constant dynamic coefficient of friction at all sliding velocities and a higher static value that applies when the interface is locked [9]. It can be characterized by a single parameter, γ, the ratio of dynamic and static friction coefficients. Specifically, this research establishes the effect of γ on the selection of optimum damper contact pressure and its effect on the associated reduction in amplitude.

First, the solution technique used to find the steady-state response under harmonic excitation is discussed. Then the maximum amplitude, which occurs at a particular frequency for a given slip load, is determined as a function of slip load for a range of γ values. The optimum value of slip load corresponds to a minimum value of this resonant amplitude. The steady-state response is essentially harmonic when the damper slip load is small. However, when $\gamma < 1$ and the damper slip load is increased beyond a certain point, the steady-state response becomes a more complex wave form. An analytical expression for this transition slip load as a function of γ is determined. In order to visualize the nonharmonic response for the slip load beyond this transition value, a numerical integration method is used. Numerical integration also is used to verify the accuracy of the analytically obtained steady-state harmonic solutions for the range of slip load values where they exist.
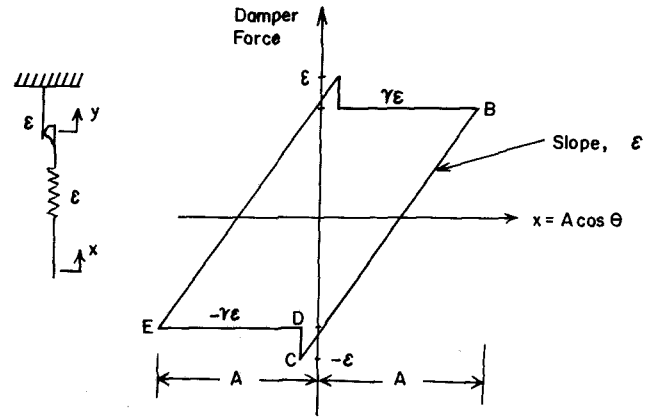
Fig. 3 Damper force versus displacement

An efficient numerical time integration procedure is developed on the basis of the method of slowly varying parameters [10] to predict the peak displacements ($x' = 0$) as a function of time without tracing the whole wave form. Amplitudes computed using this method are compared with those calculated using the traditional numerical integration procedure. This economical method is particularly useful when the steady-state response is not simply harmonic. Lastly, the stability of the solution in this region of slip load is discussed briefly.

2 Governing Equation of Motion

The equation of motion for the system depicted in Fig. 2 is

$$\frac{d^2x}{dt^2} + x + 2\zeta\frac{dx}{dt} = \epsilon y + \epsilon f_0 \cos\omega t \qquad (3)$$

The nonlinear aspect of the problem is embedded in the term $y(x)$ in Fig. 3. For quiescent initial conditions ($x(0) = x'(0) = 0$) the system is linear until slip occurs; i.e., the amplitude of response is greater than one. Once slip occurs the system is piecewise linear and the value of y can be found as a function of x as described in section 3.1.

3 Analytical Solution

3.1 Steady-State Response. The steady-state response of equation (3) has been obtained by using the procedure described by Caughey [10]. Assuming a small nonlinearity, an approximation to the solution of equation (3) is taken to be

$$x(t) = A(t)\cos(\omega t + \Phi(t)) \qquad (4)$$

where $A(t)$ and $\Phi(t)$ are slowly varying functions of time. Analogous to the method of variation of parameters, set

$$A'\cos\theta - A\Phi'\sin\theta = 0 \qquad (5)$$

where

$$\theta = \omega t + \Phi(t) \qquad (6)$$

Because of (5)

$$\frac{dx}{dt} = x' = -\omega A\sin\theta \qquad (7)$$

Equations (3), (4) and (7) imply

$-\omega A'\sin\theta + A(1-\omega^2)\cos\theta - \omega A\Phi'\cos\theta$

$\qquad -2\zeta\omega A\sin\theta = \epsilon y + \epsilon f_0\cos(\theta - \Phi) \qquad (8)$

From (5) and (8),

$-\omega A' + A(1-\omega^2)\sin\theta\cos\theta - 2\zeta\omega A\sin^2\theta$

$\qquad = \epsilon y\sin\theta + \epsilon f_0\cos(\theta - \Phi)\sin\theta \qquad (9)$

and

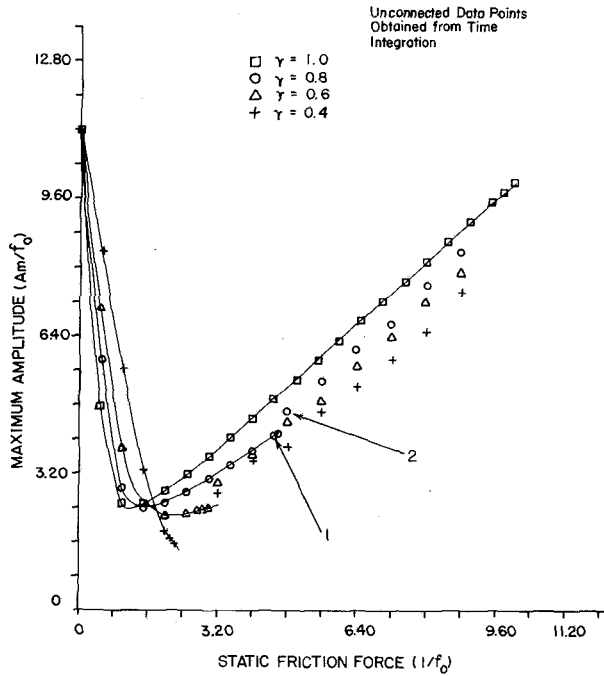**Fig. 4 Maximum response versus static friction force**

Fig. 5 Harmonic response corresponding to Point 1

Fig. 6 Nonharmonic response corresponding to Point 2

$$-\omega A\Phi' + A(1-\omega^2)\cos^2\theta - 2\zeta\omega A\sin\theta\cos\theta$$
$$= \epsilon y\cos\theta + \epsilon f_0\cos(\theta-\Phi)\cos\theta \tag{10}$$

Averaging equations (9) and (10) for one cycle of θ, the following two equations for A and Φ are obtained:

$$-2\omega A' - 2\zeta\omega A - \epsilon f_0\sin\Phi = \frac{\epsilon}{\pi}\int_0^{2\pi} y\sin\theta d\theta = R(A) \tag{11}$$

$$-2\omega A\Phi' + A(1-\omega^2) - \epsilon f_0\cos\Phi = \frac{\epsilon}{\pi}\int_0^{2\pi} y\cos\theta d\theta = T(A) \tag{12}$$

For a steady-state response the amplitude and phase of the long-time solution do not change, and $A' = \Phi' = 0$. Under this condition, the compressive force, F_c, in the damper spring will vary as a function of x as shown in Fig. 3. Since $F_c = \epsilon(x-y)$, y may be expressed from this figure as

On BC: $y = A - \gamma, \quad 0 \le \theta \le \theta_c$

On DE: $y = x + \gamma, \quad \theta_c \le \theta \le \pi$

and

$$y(\theta+\pi) = -y(\theta)$$

where

$$\theta_c = \cos^{-1}(1-(\gamma+1)/A) \tag{13}$$

is the value of θ corresponding to the point C in Fig. 3. Knowing y, the values of integrals $R(A)$ and $T(A)$ are calculated to be

$$R(A) = \frac{2\epsilon}{\pi}\left[(\gamma-1) - \frac{(\gamma^2-1)}{A} + \frac{1}{2}A\sin^2\theta_c\right] \tag{14}$$

$$T(A) = \frac{2\epsilon}{\pi}\left[\frac{A}{2}(\pi-\theta_c) - (\gamma-1)\sin\theta_c + \frac{A}{4}\sin2\theta_c\right] \tag{15}$$

Thus the resulting steady-state equations for A and Φ are

$$-2\zeta\omega A - \epsilon f_0\sin\Phi = R(A) \tag{16}$$

$$A(1-\omega^2) - \epsilon f_0\cos\Phi = T(A) \tag{17}$$

3.2 Resonant Amplitude as a Function of Slip Force. By
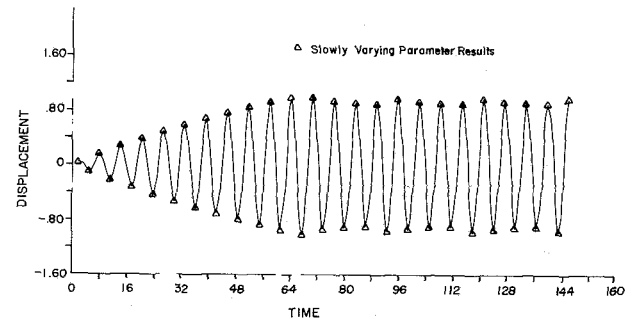
first eliminating Φ from equations (16) and (17) and then observing that, for a fixed value of f_0, the maximum value of the amplitude, A_m, will occur when the frequency is single valued, it can be shown that at this "resonance condition" A_m and ω_m satisfy the two simultaneous nonlinear equations

$$\frac{2\zeta}{\epsilon}A_m\omega_m + \frac{2}{\pi}\left(2\gamma - \frac{3\gamma^2+2\gamma-1}{2A_m}\right) = f_0 \tag{18}$$

$$A_m(1-\omega_m^2) = \frac{2\epsilon}{\pi}\left[\frac{A_m}{2}(\pi-\theta_c) - (\gamma-1)\sin\theta_c + \frac{A_m}{4}\sin2\theta_c\right] \tag{19}$$

These equations are solved for specified values of ϵ and ζ, and a typical result is depicted by the solid curves in Fig. 4. When the amplitude of the external excitation is constant then it can be seen from (1) that the maximum physical amplitude of the mass's displacement during an engine acceleration is proportional to A_m/f_0, while the slip load is proportional to S, where $S = 1/f_0$. Thus, plots of this type contain the essential information that is required for choosing the contact pressure so that the blade's resonant response will be minimized.

It can be seen that for $\gamma=1$, the steady-state solution, $x = A\cos\theta$, exists for all values of S. However, for $\gamma = 0.8, 0.6$, and 0.4 there is a range of slip load values for which there is no real solution for A_m, i.e., the steady-state solution is not harmonic in the region, $S_T < S < S_u$, where S_T is the "transition slip load," and S_u is given by equation (2) corresponding to the resonance condition for the stuck system, i.e., $\omega = 1$. S_T may be found from equations (13), (18) and (19) by considering the limiting case corresponding to $A_m = (1+\gamma)/2$. They yield

$$S_T = (2(1-\gamma)/\pi + \zeta(1+\gamma)/\epsilon)^{-1} \tag{20}$$

For systems with small amounts of proportional damping, $\zeta\pi/2\epsilon < 1$, S_T decreases as γ decreases. Physically, when $S = S_T$ the resonant amplitude, A_m, is just large enough for two-sided slip to occur during each cycle, i.e., the length of

Fig. 7 Maximum response versus dynamic friction force

Fig. 8 Nonharmonic response at a slip load $> S_T$

Fig. 9 Nonharmonic response at a slightly perturbed slip load

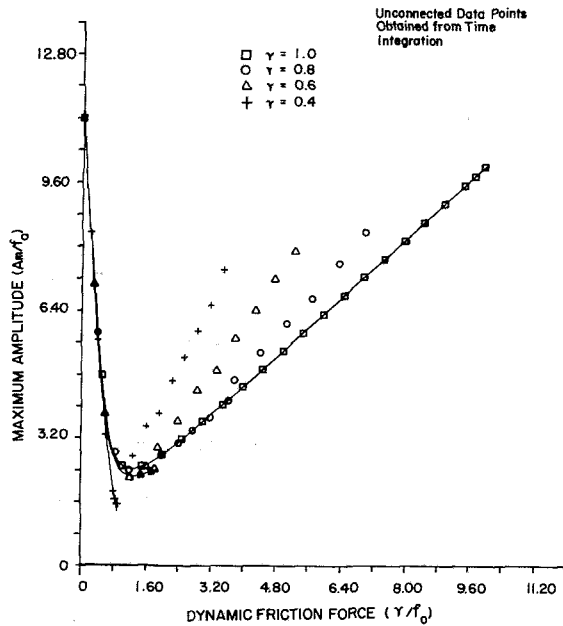the line segment DE is zero in Fig. 3. Thus, $S \leq S_T$ is a necessary condition for a constant amplitude steady-state response to exist. In addition, independent numerical integrations of the equation of motion when $S < S_T$ inevitably resulted in long time solutions which were essentially harmonic and agreed well with those estimated using the approximate procedure. For $S_T < S < S_u$, it is found that the steady-state response is not harmonic and slip does not occur at every peak ($x' = 0$). As an example of the effect of S_T on the response, the transient solutions were calculated for conditions corresponding to points 1 and 2 in Fig. 4 and are depicted by continuous curves in Fig. 5 and Fig. 6. Clearly, the transition from an essentially harmonic steady-state response to a more complex periodic motion coincides with that predicted by equation (20).

The plots of Fig. 4 correspond to a correlation of the resonant amplitudes with the static friction force in the damper slip joint. The data are plotted instead as a function of dynamic friction force, γS, in Fig. 7. From Fig. 7 it is apparent that for $S < S_T$ the response when correlated in this manner is almost independent of γ. In addition, the deviation that does occur when $\gamma \leq 0.4$ is upper bounded by the $\gamma = 1$ curve. This result is typical of that found over the entire range of ϵ and ζ values that were felt to potentially represent turbine blade damper configurations, i.e., $\zeta \leq 0.02$ and $\epsilon \leq 0.4$.

4 Time Integration Solution

4.1 Conventional Time Integration. In order to verify the analytical results for the steady-state response and also to visualize the response in the region of slip force and γ where the steady-state solution is not harmonic, the response was obtained using the Newmark method of time integration [11]. The numerically obtained steady-state solutions, e.g., the continuous curve in Fig. 5, compared well with those obtained analytically for $S < S_T$. The continuous curves in Figs. 6 and 8 show the results obtained in the region where the steady-state response is not harmonic. The wave form of the response points out that there is subharmonic oscillation superimposed on the harmonic oscillation. This type of response is described in [12] as frequency entrainment, i.e., the entrainment of subharmonic oscillation in the harmonic response at forced frequency.

For $S > S_T$, the transient behavior eventually dies out and
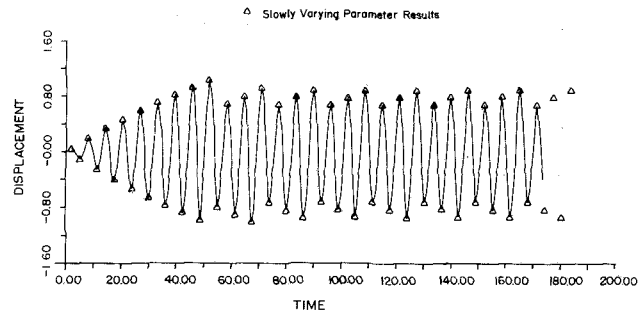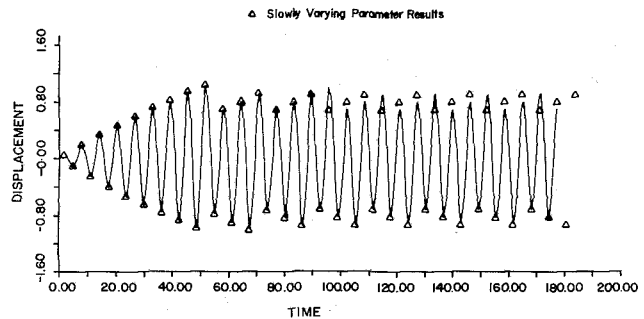
the solution settles down to a relatively complex, but periodic, wave form. The maximum peak amplitude that occurred in this "steady-state" response would induce the most high-cycle fatigue damage and, consequently, was selected as the measure of response in this regime. Some of the results are plotted as the discrete data points in Fig. 4. When $S > S_T$, slip occurs relatively infrequently and the value of the static friction force has a stronger influence on the maximum peak response. An important feature is that the $\gamma = 1$ response curve provides an upper bound on the amplitudes when the data are correlated with S rather than γS in this region.

4.2 Efficient Time Integration: Method of Slowly Varying Parameters. A time integration method was developed directly in terms of half-cycle amplitude and phase using the method of slowly varying parameters. This method directly predicts peak-to-peak displacements without tracing the entire wave form. This approach turns out to be useful when the steady-state solution is not harmonic and as a result there is no straightforward analytical method to find the response.

In the algorithm developed to exploit this approach, it was assumed that the phase and amplitude are constant over each half cycle. The equations (9) and (10) are averaged over a half cycle, e.g., $\theta = 0$ to π, rather than a full cycle as in section 3.1. The values of the half cycle integrals corresponding to $R(A)$ and $T(A)$ depend on whether slip has occurred in the current half cycle. The derivatives of the amplitude and phase are approximated by finite differences where the time step is half of the excitation period. The algorithm is described in [13].

Amplitudes calculated using this method are indicated by symbols (Δ) in Figs. 5, 6, and 8. In general, they compare well with those computed using the method described in section 4.1 except at those conditions where the solution is unstable. An example of instability in the response can be seen by comparing the solutions depicted in Figs. 8 and 9 (in both instances the position of the symbols (Δ) are essentially the same). In these two cases the value of the slip load was altered by less than 0.1 percent and yet the response was significantly different. This is because only a minor change in the am-

plitude of the response on a cycle where it is near slip can determine whether or not it slips, an event which then influences the subsequent wave form [13].

5 Conclusions

The following conclusions could be drawn concerning the influence of γ on the dynamic response of a single mode model of a frictionally damped blade for the range of ζ and ϵ considered representative of those potentially occurring in applications ($\zeta \le 0.02$ and $\epsilon \le 0.4$).

1 There is a transition slip load, S_T, given by equation (20), below which the long time response is essentially harmonic and above which it is a periodic but complex wave form.

2 For $S \le S_T$ the response can be calculated with reasonable accuracy by ignoring static friction (e.g., as in the analyses [2–6]) provided γ is approximately greater than 0.5. If γ is less than 0.5, then ignoring static friction can result in significant errors. However, the errors always result in a conservative estimate of how much the amplitude will be reduced. If required, a more accurate calculation of the steady-state response can be made using the procedure described in sections 3.1 and 3.2.

3 For $\gamma < 1$ and $S_T < S < S_u$, the long time dynamic response is periodic but complex. The maximum peak response of the system is less than that obtained from the $\gamma = 1$ curve for the same value of static friction force. Again, a constant slip force analysis upper bounds the response provided that the slip force is calculated using the static coefficient of friction and the dynamic value is ignored. If a more accurate assessment of the long time solution is required, either a traditional numerical solution of the transient response is needed or the efficient time integration procedure described in section 4.2 and documented in [13] may be used. These methods may not agree on a point-to-point basis in regions where the wave form of the response is inherently unstable.

References

1 Plunkett, R., "Friction Damping, Damping Application for Vibration Control," ASME, AMD, Vol. 38, 1980.

2 Griffin, J. H., "Friction Damping of Resonant Stresses in Gas Turbine Engine Airfoils," ASME JOURNAL OF ENGINEERING FOR POWER, Apr. 1980, Vol. 102, pp. 329–333.

3 Muszynska, A., and Jones, D. I. G., "A Parametric Study of Dynamic Response of a Discrete Model of a Turbomachinery Bladed Disk," ASME Paper No. 81-DET-137, presented at the Design Engineering Technical Conference, Sept. 20–23, 1981.

4 Muszynska, A., Jones, D. I. G., Lagnese,T., and Whitford, L., "On Nonlinear Response of Multiple Blade Systems," Shock and Vibration Bulletin, Vol. 51, pt. 3, May 1981, pp. 88–110.

5 Dowell, E. H., "The Behavior of a Linear Damped Modal System with a Nonlinear Spring-Mass-Dry Friction Damper Attached," accepted for publication in Journal of Sound and Vibration.

6 Srinivasan, A. V., Cutts, D. G., and Sridhar, S., "Turbojet Engine Blade Damping," NASA CR-165406, July 1981.

7 Brockley, C. A., Cameron, R., and Potter, A. F., "Friction-Induced Vibration," ASME Journal of Lubrication Technology, Apr. 1967, pp. 101–108.

8 Sinha, A., and Griffin, J. H., "Friction Damping of Flutter in Gas Turbine Engine Airfoils," AIAA Journal of Aircraft, Vol. 20, No. 4, Apr. 1983.

9 Rabinowicz, E., "The Nature of Static and Kinetic Coefficient of Friction," Journal of Applied Physics, Vol. 22, No. 11, Nov. 1951.

10 Caughey, T. K., "Sinusoidal Excitation of a System with Bilinear Hysteresis," ASME Journal of Applied Mechanics, Vol. 27, Dec. 1960, pp. 640–643.

11 Newmark, N. M., "A Method of Computation for Structural Dynamics," Journal of the Engineering Mechanics Division, Proceedings of the ASCE, Vol. 85, July 1959, pp. 67–94.

12 Hayashi, C., Nonlinear Oscillations in Physical Systems, McGraw-Hill, 1964.

13 Sinha, A., and Griffin, J. H., "A Comparison of Efficient and Conventional Time Integration Methods for Friction Damping," SM Report 82-14, Department of Mechanical Engineering, Carnegie-Mellon University, Pittsburgh, Pa.

Blade Vibration Measurements on Centrifugal Compressors by Means of Telemetry and Holographic Interferometry

U. Haupt
Research Assistant.

M. Rautenberg
Professor.

University of Hannover,
Hannover, West Germany

Blade vibration measurements have been carried out on a high-pressure, high mass-flow centrifugal compressor to determine the excitation mechanism. For the experimental investigation, semiconductor strain gages with a multichannel telemetry system were used. The measuring points on the blades have been chosen using the results of a stress calculation for the vibrating blade by means of the FE-method. A research program was started with blade vibration measurements in different operating ranges of the compressor and with two types of diffusers. Results are presented for the blade excitations obtained by throttling the compressor at various rotational speeds and for the cases of passing resonances by increasing the rotational speed at constant throttle valve position. Results were obtained for blade excitations caused by:

1) *the nonuniformity of the flow in the diffuser,*
2) *the stalled flow near the surge-line,*
3) *the blades of a vaned diffuser and*
4) *the surge.*

The investigations have been completed by optical measurements to find out the vibrational modes of the different blades in rotating operation. These tests were carried out by means of a holographic interferometric system using an optical derotator up to a rotational speed of n = 20,500 rpm.

Introduction

Today stress calculation is an important integral part in the design of modern high pressure high mass-flow centrifugal compressors. Blade vibration problems also have to be considered. Recently, they are becoming more significant because of the drive to reduce the blade thickness to obtain higher circumferential speed, although very little experience exists in this field. Some results and aspects from the investigations of blade vibration on axial compressors can be used. However, different conditions exist, for example, in the diffuser of a radial compressor with its nonuniformity of the flow due to the effect of the outlet tube.

Contrary to the axial compressor first results of blade vibration measurements on radial compressors indicated a considerable influence of the flow behavior downstream of the impeller outlet on the blade excitation. The necessity, to obtain fundamental and safe information about the intensity and the excitation mechanism of blade vibration in centrifugal compressors was the reason for establishing a wide research program in this subject in the Institute for Turbomachinery of Hannover.
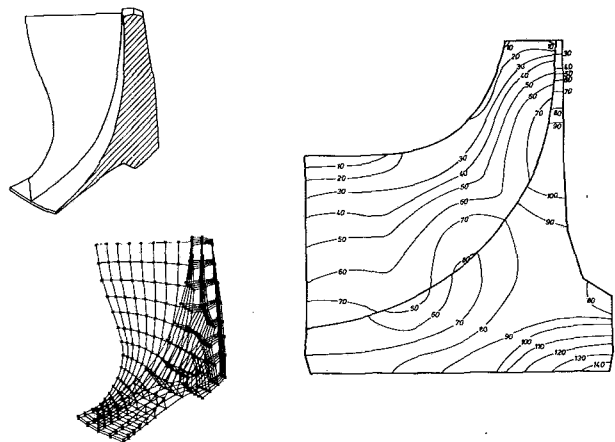

Fig. 1 Computed equivalent stress of the test impeller due to centrifugal force and temperature with cutout sector of the impeller for the computation and element distribution: $n = 20,000$ **rpm and** $\sigma_V =$ **equivalent stress in N/mm^2**

f_I = 764,5 Hz

f_{II} = 1687 Hz

f_{III} = 2301 Hz
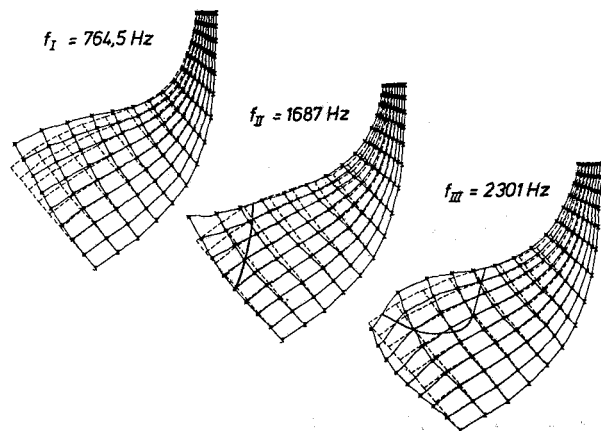
Fig. 2 Computed first three mode shapes of the radial blade of the test compressor. f = natural frequency

Fig. 3 Influence of the blade thickness on the first three blade frequencies
—— FE-Calculation, bending and membrane stress
— · — pure bending stress, constant blade thickness

Information about blade vibration behavior should be obtained by systematic measurements on the operating compressor. Special emphasis in this program was directed on the following excitation phenomena, derived from the experience in axial compressor blade vibration research and documented in detail in [1]:

* Blade vibration excitation by aerodynamic nonuniformity of the flow in the inlet or exit range of the compressor. Resonance occurs between the blade frequencies and the engine orders.
* Self-excited blade vibrations by operating the machine in the flutter regions of the compressor map
    * Blade excitation by the cells of rotating stall
    * Blade excitation by surge of the compressor

The test facilities for this investigation are described in [2]. The radial impeller of the compressor used for these measurements has a diameter of d_2 = 400 mm and 28 blades with every second blade cut back in the inlet. The impeller was suitable for the investigation because of the very thin blades. Semiconductor strain gages with their great sensitivity factor were chosen as the measurement technique to obtain information about the blade vibration stresses. For the signal transmission a multichannel telemetry system was selected.

Preparatory Theoretical and Experimental Activities

A considerable amount of theoretical and experimental preparatory work was necessary before the beginning of the measurements. At first the strain due to the centrifugal force had to be calculated by means of the finite element method. This was necessary because of the difficulty of measuring static stress with a superposed dynamic component with sufficient accuracy. With this calculation the measuring problem was reduced to the vibrational part of the stress. Figure 1 shows the segment of the impeller used for the computation, the element distribution and the results for a rotational speed of n = 20,000 rpm and for a measured temperature distribution. Maximum stress of the blade occurs in different hub sections with approximately $\sigma_V \approx$ 80 N/mm² while the stress in the impeller reaches a maximum near the shaft. Steady aerodynamic loads were also considered by means of experimental results. They turned out to be not very important compared with the stress due to centrifugal force.

Much work had to be carried out to choose the best measuring points on the blade where the strain gages had to be applied. For this purpose, a detailed knowledge, not only of the strain distribution during the vibrational motion, but also of the principal stress directions was essential. By means of a FE-program at first the natural frequencies and the mode-

shapes for the radial blade were computed. Figure 2 shows the result of this calculation for the important first three modes with nodal lines on the blade for the second and third mode. The information about the displacements of the nodal points was necessary to calculate the strain and the principle strain directions during a vibrational motion in the different modes. These computations were verified by an experimental investigation, in which one blade of the impeller at rest was equipped with 37 strain gage rosettes and excited to vibration. The results of this investigation as illustrated in [2] confirmed those obtained by the FE-calculation. According to this information strain gages were applied on all the blades with a wiring contact to a distribution pin plate in the spherical cap of the impeller, where the strain gages chosen for every measurement could be connected to the transmitter.
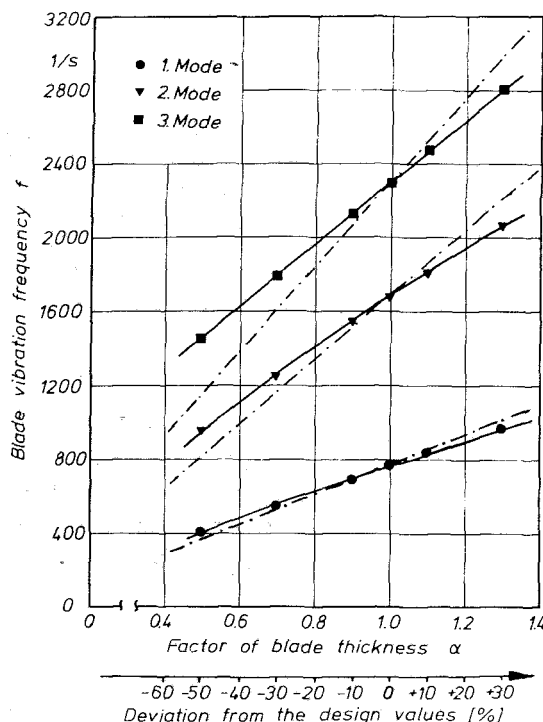
Considerable deviations of the sensitivity factors were obtained in preparatory tests with semiconductor strain gages. So they still had to be compared with foil strain gages—both applied to the blade very close to one another—in a calibration test before the investigation to insure sufficient accuracy.

The calculation of the blade frequencies was performed with the values of the blade thickness, which were chosen during the stress calculation of the impeller. This choice during the design procedure influences the occurrence of blade resonances. It is important to avoid resonances, particularly when the impeller blades are thin. Here a knowledge of how the increase or decrease of blade thickness influences a given blade frequency f is desired. For this purpose series of FE-calculations of blade frequencies have been executed for the test impeller by varying the blade thickness by means of a thickness factor α. This value is 1.0 for the design value and α = 0.9 for example means a 10 percent reduction of the thickness values of all the shell elements of the blade. As illustrated in Fig. 3 for the first three modes these results are compared with those obtained for the case of pure bending motion eliminating the membrane stress. The relationship

Fig. 4 Centrifugal compressor with installations for the telemetry transmission

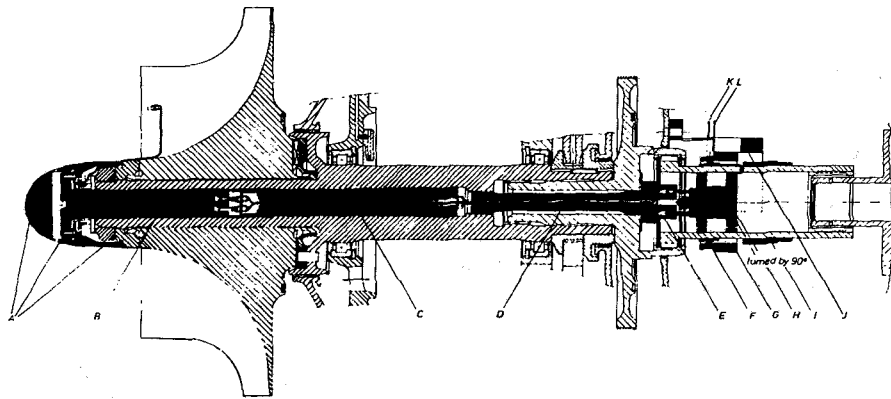|	
A modified hub section	G primary coil with coil carrier
B 8-channel telemetry transmitter	H voltage converter for the inductive power supply
C wiring-tube	I slotted tube for shaft speed measurement
D tension bolt with central bore	J adjustable coil mounting
E adapter and pin-connector	K stationary antenna
F secondary coil with rotating antenna	L inductive power supply
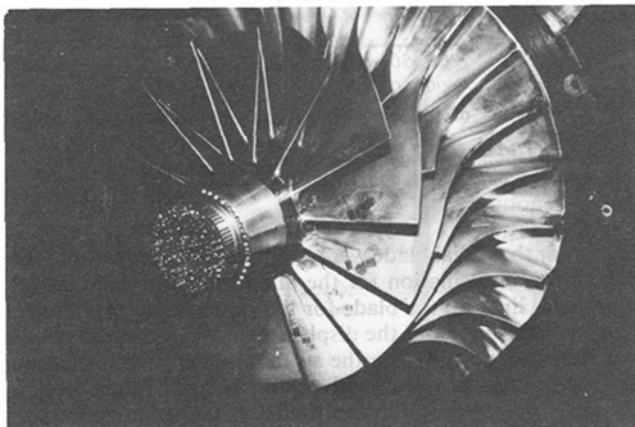
Fig. 5 Radial impeller with strain gages and mounted 8-channel telemetry transmitter

Fig. 6 Inductive power supply for the telemetry transmission

$$f \sim h$$

can be used for the constant blade thickness h. The diagram illustrates the magnitude of error using the simplification compared with the result of the more exact FE-computation. For the first mode there is a very small difference between the curves, because this vibration is quite similar to a bending motion. These differences, as it is shown in the graph, increase to higher modes, where the influence of the membrane stress becomes more significant.

Installation of a Multichannel Telemetry System

For the experimental investigation of blade vibration a transmission system was necessary to recover the stress signals from the rotating impeller. For this purpose an 8-channel telemetry system has been installed with an inductive power supply. Figure 4 shows the sectional view of the compressor with the new components of the telemetry system identified by the dark color. The transmitter with its plate at the top with the contacts to the strain gages is located in the bore of the impeller shaft as shown in Fig. 5. It is connected with the components of the inductive power supply mounted in the socket-tube, coupling the compressor and the gear-box. Figure 6 gives an illustration of the installation for the power supply with the view of the mounting shell for the primary coil. To facilitate frequent assembly and disassembly, all parts had to be constructed with pins and sockets. The

vibration signals leave the transmitter by the wiring for the power supply and they are transmitted at the coil system of the inductive supply. The FM-transmission system has proved operational up to highest rotational speed of more than $n = 22,000$ rpm.

Results of Blade Vibration Measurements

Blade Vibrations at Constant Rotational Speed and Various Throttle Valve Positions. The aim of the blade vibration measurements is to obtain information about the excitation mechanism and to evaluate the different excitation effects. For this purpose measurements were carried out with three versions of diffusers to find out to what extent the nonuniformity of the flow in the diffuser (due to the effect of the outlet-tube) causes blade vibration. For this reason extensive tests were executed on the compressor with a vaneless diffuser without and with a throttle ring unifying the velocity distribution downstream of the impeller. A vaned diffuser with 19 aerodynamic blades was mounted to investigate the influence of diffuser blades on the intensity of blade excitation. With these types of diffusers blade vibration was measured at numerous operating points of the compressor chart (at constant corrected rotational speed and various throttle valve positions). From the analog vibration signal an average value of the blade vibration stress ampltiude was determined using an RMS-Multimeter. In Figs. 7, 8, and 9 these values are plotted in the compressor chart as black bars with the length indicating the amount of stress amplitude ϵ in
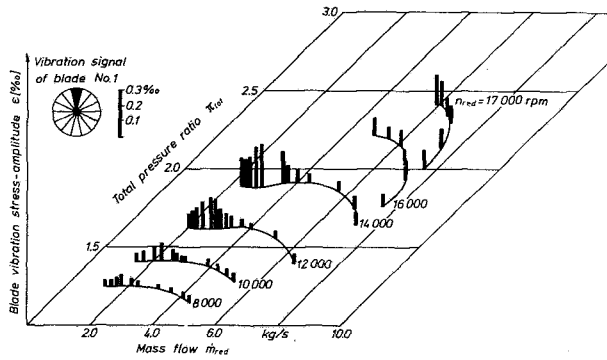
Fig. 7 Vaneless diffuser without throttle-ring
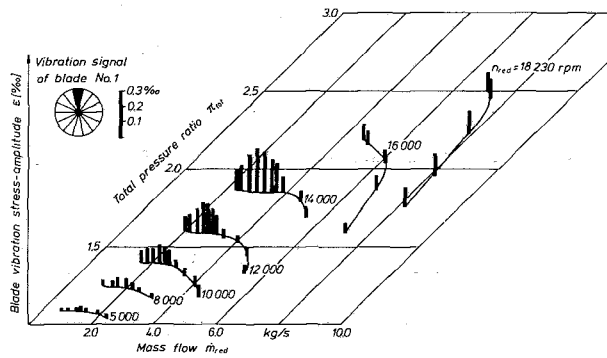
Fig. 8 Vaneless diffuser with throttle-ring
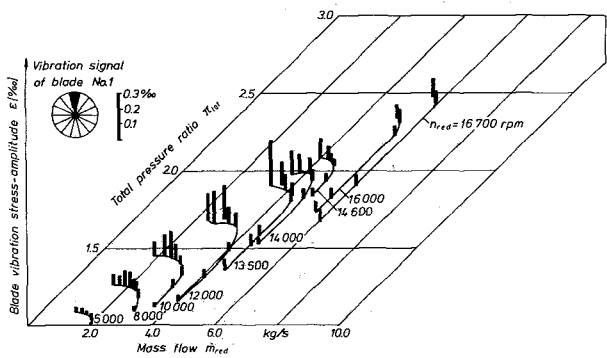
Fig. 9 Vaned diffuser 9 aerodynamic blades

Blade vibration at constant rotational speed and various throttle valve position

Impeller: 28 blades   Diffuser: vaneless   n = 14.000 rpm

Fig. 10 Blade vibration and pressure fluctuations at n = 14,000 rpm

Impeller: 28 blades   Diffuser: vaneless   n = 14 000 rpm
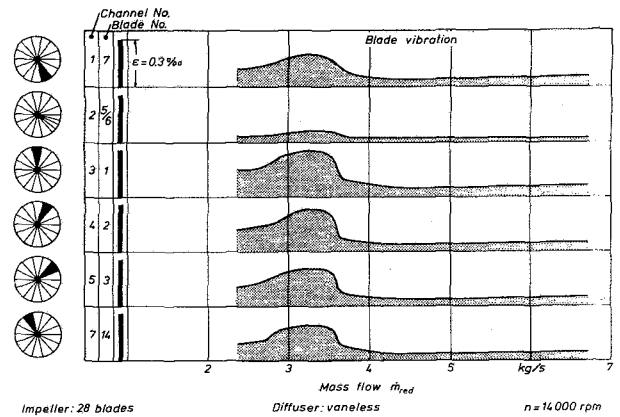
Fig. 11 Blade vibration of different blades at n = 14,000 rpm

Impeller: 28 blades   Diffuser: vaneless
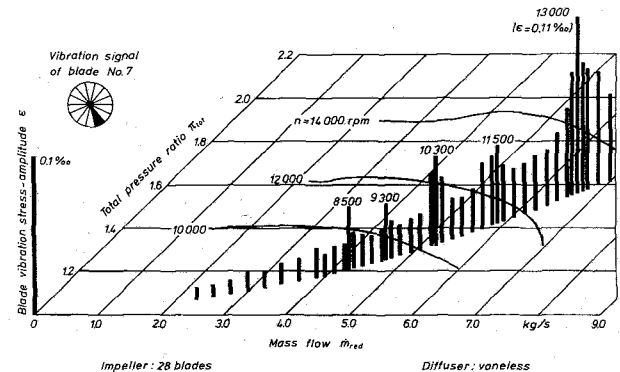
Fig. 12 Blade vibration at increasing rotational speed and constant throttle valve position up to n = 14,000 rpm

mm/m $= 1/1000 = 1000\ \mu$ strain. It should be mentioned that no measurements were carried out between $n = 17,500$ and 18,000 rpm because this is the range of the occurence of a resonance between the blade frequency at that speed and the third engine-order. Here small deviations for rotational speed as they were usual during the measurements cause considerable differences in blade excitation. Further, safety reasons made it necessary to restrict the operation of the compressor in the region of occurrence of rotating stall and surge to the range below $n = 14,000$ rpm.

The results of blade vibration measurements plotted in the compressor charts in Figs. 7, 8, and 9 show a considerable similarity for all three versions of diffusers. Away from resonance points towards high mass flow rates the intensity of blade vibration increases slightly at higher rotational speed due to the effect of increasing forces in the flow. Closing the throttle valve and driving the compressor from the choke-to the surge-line at constant rotational speed a strong increment of blade excitation can be observed up to a wide maximum.

In this range vibration signals show a very stochastic nature with certain indications of a stalled flow, while periodic vibration with one dominant frequency can be obtained when resonance occurs. The blade vibration stress amplitudes decreased again to a varying degree before the surge-point of the compressor.

An explanation of this blade vibration behavior observed for different rotational speed and for all types of diffusers can only be obtained from an investigation of the flow at the relevant measuring points. For this purpose four semiconductor pressure probes were installed and their signals were recorded with the blade vibration signals. Figure 10 shows the positions of these probes and the result in RMS-values at a corrected rotational speed of $n = 14,000$ rpm and in the whole range of mass flow. The curves signify the amount of
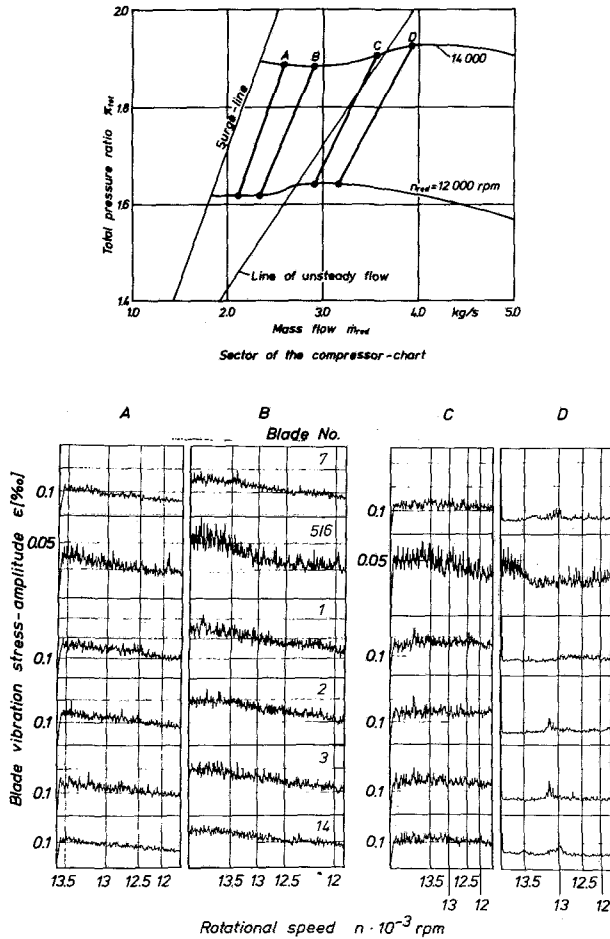
Fig. 13 Blade vibration in the zone of unsteady and stalled flow n = 12,000–14,000 rpm

Fig. 14 Blade vibration at increasing rotational speed and constant throttle valve position n = 16,000–19,000 rpm

pressure fluctuations. A comparison between the blade vibration signal in the upper part of the figure and the pressure fluctuation curves shows a similarity of the shapes. Closing the throttle valve an increase of pressure fluctuation amplitudes can be observed in those values of mass flow, where the blade signal has a considerable increase too. This is the zone, where rotating stall occurs as it was recognized in another parallel investigation [3]. This operating range of the compressor is characterized by a flow angle in the impeller inlet very close to stalled conditions. Stall occurred for small variations in this flow angle. Reducing the mass flow further means a more unfavorable velocity triangle in the inlet causing the stall to occur on all the blades. These operating conditions show very strong blade vibration signified by a wide maximum of the telemetry signal. In the zone of the compressor chart near the surge line a reverse flow in the inlet could be observed by the authors of [3]. Obviously, the decrease of blade vibration amplitudes when closing the throttle valve toward values of mass flow of approximately $\dot{m}_{red}$ = 2.5 kg/s can be explained by a damping effect by this reverse flow which has been measured near the shroud.

It was already mentioned that a comparison between the results of blade vibration in Figs. 7, 8, and 9 for different types of diffusers does not show great differences. The vibrational stress amplitudes up to n = 14,000 rpm are very similar for the compressor with the vaneless diffuser with and without throttle ring. The blade excitation is slightly stronger in the range of higher rotational speed, when the throttle ring is absent. If one considers the unifying effect of this ring for the flow downstream of the impeller, which was shown ex-
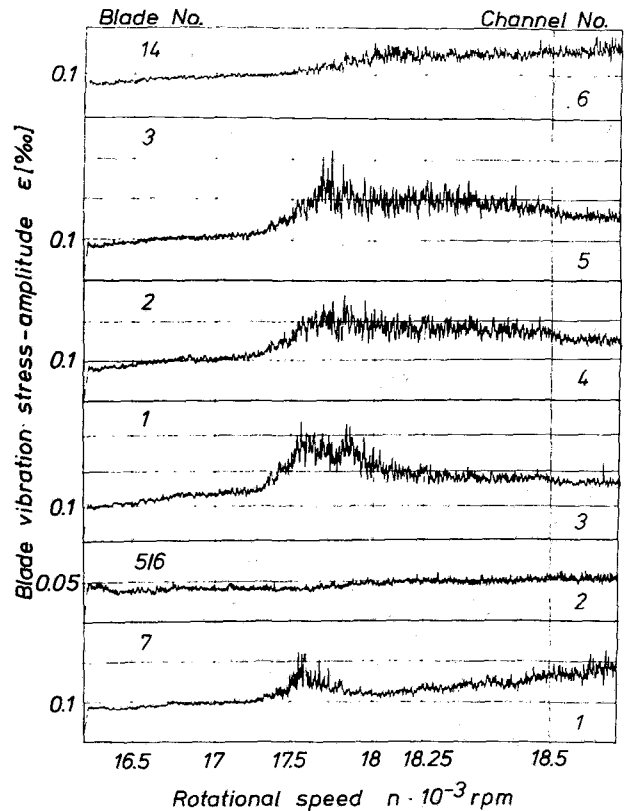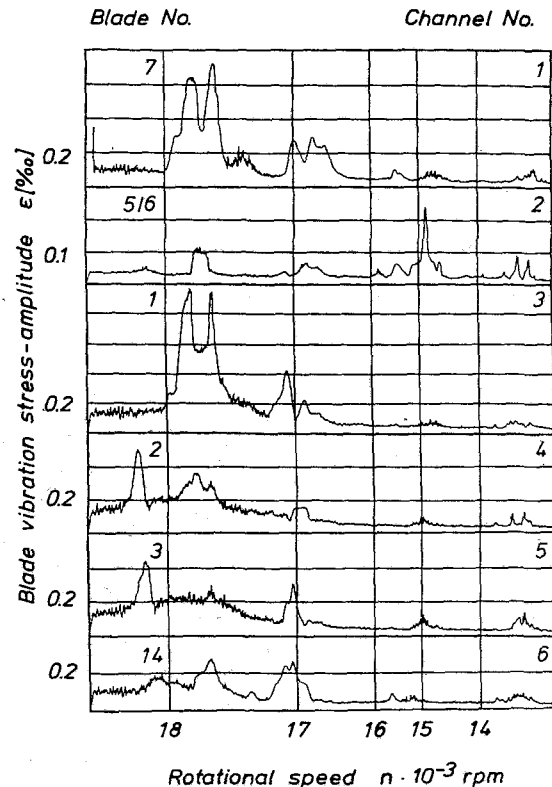
Fig 15 Blade vibration at decreasing rotational speed and constant throttle valve position on the compressor with the vaned diffuser (19 blades) n = 20,000–16,000 rpm

Fig. 16 Holographic interferogram of the radial impeller excited to vibration in a laboratory test at rest $f \approx 5500$ Hz

Fig. 17 Blade vibration during surge. Throttling from the choke to the surge-line at $n = 12,000$ rpm. Vaneless diffuser with the throttle ring.

Fig. 18 Holographic setup for the blade vibration measurements

H	hologram plate	ST	beam splitter
L	lens	F	photo-diode
O	object	FE	window
SP	mirror	R	inlet tube

Fig. 19 Principle of the control mechanism for the rotational speed of the derotator

operation compared with the compressor for the version with the vaneless diffuser due to the throttling effect of the diffuser blades. There is no significant difference in blade excitation comparing the results for constant rotational speed. Up to $n = 12,000$ rpm the decrease of the stress amplitude after the maximum toward the surge-line can be observed as in Figs. 7 and 8. For higher rotational speed this effect disappears and, reducing the mass flow, surge occurs in the increasing slope range of blade vibration curve. Obviously, in this operating zone there is no reverse flow due to the pressure conditions downstream of the impeller. It can be summarized that the type of diffuser is not significant for the excitation of blade vibration in the case of throttling the compressor at constant rotational speed. Blade excitation here is determined by the flow effects such as stall in the compressor inlet.

So far results of blade vibration have been presented for one blade only. The stress amplitudes of six vibrating blades are plotted in Fig. 11 for a rotational speed of $n = 14,000$ rpm and various mass flow rates. The characteristic shape of all the curves indicates a very similar behavior for the different blades. Even the signal of channel 2 from the splitter blade between blade-No. 5 and 6 shows a slight increase of stress amplitude. It can be seen by examining the slopes of the different curves that a similar stress intensity is excited due to the ocurrence of stall on all the blades in the uniform manner. This excitation is very different from a resonance vibration, where very different intensity of vibrational stress of every blade of the impeller can be observed, due to the interactions among the blades.

Blade Vibration With Increasing Rotational Speed at Constant Throttle Valve Position. Measurements with increasing rotational speed were carried out on the compressor with a vaneless diffuser without the throttle-ring up to $n = 14,000$ rpm. The result for one blade is shown in Fig. 12, with

perimentally, it is surprising that there is only a negligible difference in blade excitation. According to these results the nonuniform flow distribution in the diffuser can be considered as not significant for the blade vibration. The compressor with the vaned diffuser has a smaller range of
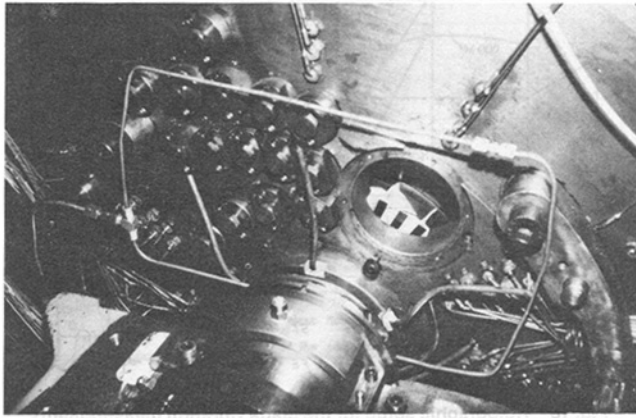
Fig. 20 View of the reverse of the compressor and of the markers for the derotator control unit
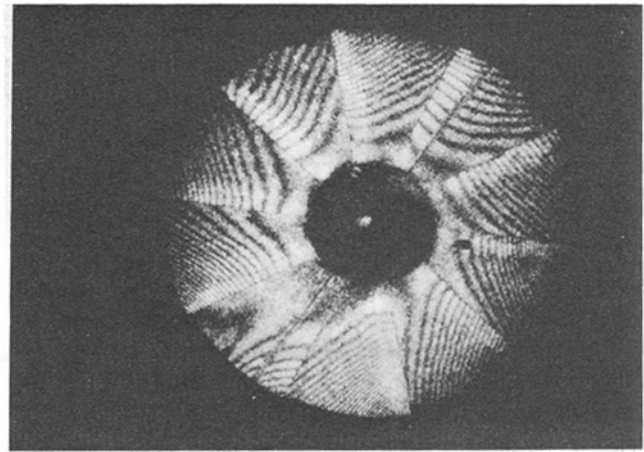
Fig. 22 Interferogram of the impeller at n = 7950 rpm
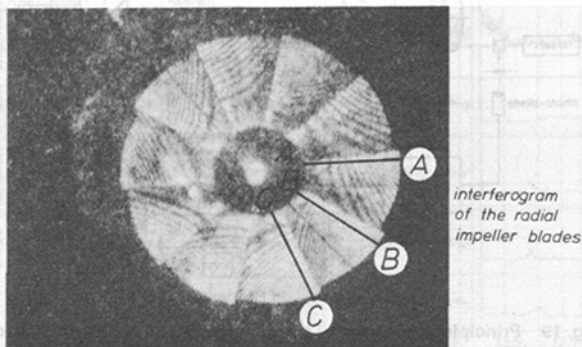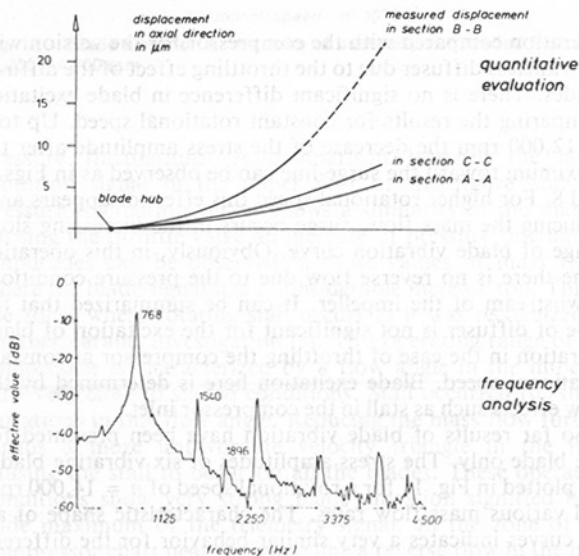
Fig. 21 Results of the optical blade vibration measurements, n = 3,007 rpm

the blade vibration stress amplitudes again as black bars. The resonance points turned out to be strong peaks with an intensity of excitation increasing with the rotational speed due to the stronger forces in the flow. The maxima all signify resonances between the first and the second blade frequency and the different engine-orders. Maximum stress in this range of the compressor chart occurs at an actual rotational speed of approximately n = 13,000 rpm with ϵ = 0.11 percent as a resonance between the first mode and the fourth engine-order.

A very interesting result could be obtained driving the compressor from n = 14,000 to 12,000 rpm in the zone of considerable vibration stress near the surge-line. These blade vibration signals are plotted in Fig. 13 and should be compared with the results in Fig. 12, where a resonance vibration occurs at approximately n = 13,000 rpm at high mass flow rate. This resonance vibration could not be observed in Fig. 13, where the blade forces due to stalled flow are so strong, that superposing periodic excitation effects do not show any influence. Only in the last diagram for a decrease of rotational speed near the range of stalled flow indic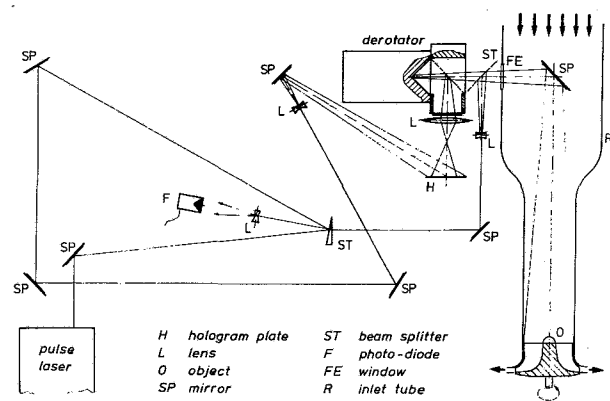ations of this resonance vibration can be observed. It should be mentioned that blade vibration stresses are much higher in the range of stalled flow than for the resonance at high mass flow rates. The results in Fig. 13 show RMS-values; however, especially in the zone of stalled flow peak stress were obtained which were more than twice the RMS-values.

Further tests were carried out increasing the rotational speed in the range of n = 16,000 rpm with the vaneless diffuser. Results have been plotted for 6 blades in Fig. 14. Considerable difference in blade vibratiory characteristics in this range of resonance (third engine-order) was obtained. Most signals are characterized by a wide maximum of vibratiory stress and do not show typical resonance behavior. An FFT-analysis resulted in peaks at different blade frequencies and confirmed this observation. Future analysis should reveal whether if stall occurs in the range of resonance due to the vibration of the blades.

Very different results were obtained in this range for the compressor with the vaned diffuser, shown in Fig. 15. In the zone of rotational speed between n = 17,000 and 18,000 rpm a typical resonance vibration occurs. Maximum vibrational stress of ϵ = 1 mm/m corresponds to $\sigma_V \approx 70$ N/mm^2 superposing the stresses due to the centrifugal force. Results of an FFT-analysis showed clear periodic blade signals with frequencies of f = 5650 and 5400 Hz excited by the 19 blades of the vaned diffuser. Because an excitation of a high blade frequency in such an extremely strong manner was considered unusal, a holographic interferogram was taken of the impeller excited in this frequency at rest. It is shown in Fig. 16 with the stripes very close to each other corresponding to large displacements during the vibrational motion. Strong vibrations were obtained in the zones between the blades at the impeller outlet and on the blades. The different mode shapes of the blades indicated that in this case not a specific blade frequency was excited, but an eigenfrequency of the whole impeller. The blades as subsystems in this case vibrate in different modes near this frequency and they receive their excitation energy from the blades in the outlet. To avoid this strong and dangerous vibration the impeller could be cut back to deminish the excitation.
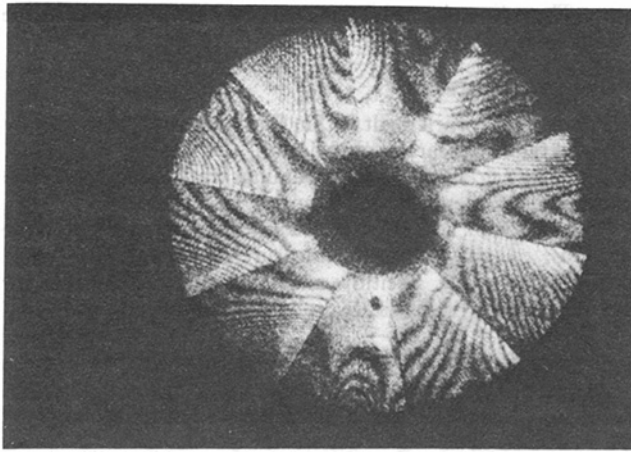
Fig. 23   Interferogram of the impeller at n = 10,940 rpm

Fig. 24   Interferogram of the impeller at n = 19,100 rpm

It should be mentioned, that the vibrational stress amplitudes of various blades differ very much. This effect cannot be explained only by manufacturing tolerances. A theoretical investigation with the FE-method indicated, that the blade-interactions, especially due to different phase-lags, might be a reason for this vibratory behavior, which is quite different from the blade excitation due to stalled flow as shown in Fig. 11. It confirms the necessity of measuring several blades by means of a multichannel transmission system.
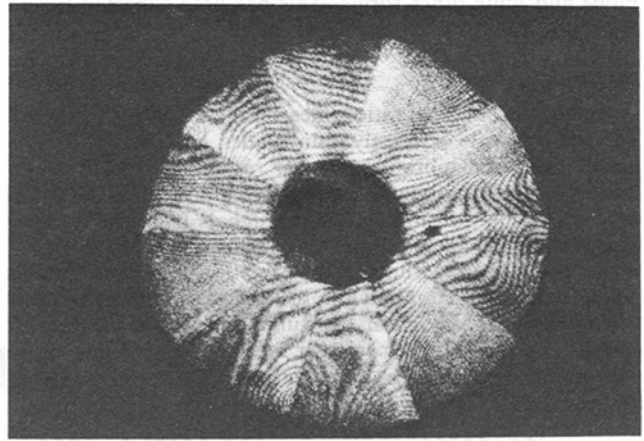
Blade Vibration During Surge of the Compressor

Extensive tests were carried out to measure the blade vibration during surge of the compressor. Results for 6 blades at a rotational speed of n = 12,000 rpm are shown in Fig. 17 with the vibrational stress amplitudes throttling from the choke - to the surge-line and vice versa. Strong vibration in the zone of stalled flow and the decrease of stresses due to the reverse flow before surge can be observed again in this graph, in agreement with results as presented in Fig 8. According to the results of Fig. 17 the very sharp peaks are significant for surge occurring with stress amplitudes which are less strong and dangerous as it was expected.

Blade Vibration Measurements at a Rotating Radial Compressor by Means of Holographic Interferometry

One fundamental disadvantage of strain gage measurements is the fact that information is obtained from one point only. It already has been mentioned that strong interactions between the blades occur that influence the mode shapes and probably the position of the stress maxima. So it might happen that a strain gage measuring point is not suitable for the stress maximum or the direction of the principal stress. The knowledge to what extent variations of the mode shapes occur due to centrifugal force and the interactions between the blades, could be obtained by a parallel investigation. It was carried out in cooperation with the Bremer Institut für angewandte Strahltechnik (BIAS). An optical method of investigation to measure vibrations in rotating systems had been developed, and its reliability could be proved in laboratory tests. This method, the holographic interferometry is implemented by use of a rotating prism and it is described in [4]. It was applied successfully under the rough conditions of one of the test compressor of the Institute for Turbomachinery, with an impeller with D_2 = 290 mm.

The principle of the holographic setup is illustrated in Fig. 18. The holographic interferometry is implemented with a rotating prism, a derotator, eliminating the rotational motion of the impeller. The optical components for this investigation had to be mounted in a vibration isolated manner because of

considerable motion of the operating compressor. First tests without inlet tube were carried out to prove the reliability of this method. To obtain realistic flow and excitation conditons a new inlet tube was manufactured. The laser beam now could enter into the inlet tube by a glass window and was turned into the axial direction to the impeller by a surface mirror, fixed in the inlet tube by three carrierblades. This setup, as it is outlined in Fig 18, proved operational up to highest rotational speeds.

One of the main problems to apply this method to the compressor was to ensure that the prism rotated exactly at one half of the rotational speed of the impeller. As shown in Fig. 19 this was achieved by scanning 200 markers from the reverse of the impeller disk using a glass fiber and by converting this signal for the control unit of the derotator. The photograph in Fig. 20 shows the markers of the impeller through a window from the reverse of the compressor.

During the measurements a vibration signal telemetered from one blade ensured driving the compressor in an operating range where blade vibration occurs. First results which include an interferogram, the analysis of the blade displacement, and the frequency analysis of the telemetry signal are shown in Fig. 21. At n = 3007 rpm all blades vibrate in the first mode excited by the teeth of the gear wheel. The same mode shapes are shown in the interferogram of the vibrating blades but with different displacements due to the coupling effects between the blades. This excitation turned out to be the strongest one for the compressor in the whole range of operation. Toward higher rotational speeds only very small increases in vibrational blade stress could be observed at resonance points. This is a consequence of the slightly greater blade thickness compared with the impeller with D_2 = 400 mm.

Another resonance vibration in the first mode was obtained at n = 7,940 rpm. As shown in the interferogram of the impeller in Fig. 22 vibrational shapes were very similar. Significant differences in the mode shapes due to interactions can be observed. The interferogram in Fig. 23 at a resonance vibration in the second mode was taken at n = 10,940 rpm. In this case not only various forms of this mode shapes with one nodal line can be observed, but also blades vibrating in the first and other mixed modes. In this case coupling effects in the vibrational motion are more significant.

Resonance vibrations only were obtained up to n = 16,000 rpm. In the range above this rotational speed the analysis of the telemetry signal showed a nearly constant blade vibration with a slightly increasing stress level. The interferogram in Fig. 24 was taken at n = 19,100 rpm and shows very different mode shapes, including variations of the first and second

mode and quite other forms. This has been expected for an excitation away from a resonance point.

Summary

Results of blade vibration measurements on a centrifugal compressor with extremely thin blades are presented. FE-calculations and vibration tests at rest were carried out to determine the locations of the measuring points for the strain gages. For the transmission of the signals from the rotating system a multichannel telemetry system has been installed.

Results of the experimental investigation show considerable vibrational stress amplitudes in the range of rotating stall and stalled flow, located near the surge-line in the compressor chart. For the compressor with the vaneless diffuser these vibrations are much stronger than for the cases of resonance. Using a vaned diffuser with 19 blades a strong resonance with maximum stress of $\sigma_V \approx 70$ N/mm^2 occurred at $n = 18,000$ rpm. An eigenfrequency of the whole impeller here is excited to vibration by the 19 blades of the diffuser. Measurements during surge of the compressor up to $n = 14,000$ rpm showed less significant vibrational stress amplitudes as expected.

Further an optical method of measuring the mode shapes of the vibrating blades of an operating compressor is presented. Results were obtained up to a rotational speed of $n = 20,500$ rpm. The adjustable mirror installation was mounted in the compressor inlet duct.

References

1 Haupt, U. and Rautenberg, M., "Zur Untersuchung von Schaufelschwingungen an Laufrädern hochbelasteter Radialverdichter mittels Datentelemetrie," MTZ 39, Vol. 4, 1978, pp. 177–183.

2 Haupt, U., and Rautenberg, M., "Investigation of Blade Vibration of Radial Impellers by Means of Telemetry and Holographic Interferometry," ASME Paper No. 82-GT-34.

3 Kämmer, N., and Rautenberg, M., "An Experimental Investigation of Rotating Stall Flow in a Centrifugal Compressor," ASME Paper No. 82-GT-82.

4 Beeck, M. A., and Kreitlow, H., "Conditions and Examinations of Vibration Analysis of Rotating Blades with the Help of the Holographic Interferometry," Proceedings of the Laser 77 Opto-Electronics Conference.

J. H. Lau[1]

Sandia National Laboratory
Albuquerque, N.M. 87185

S. S. Jung

Ebasco,
New York, N.Y.

T. T. Lau

Hewlett-Packard,
Palo Alto, Calif.

Creep of Thin-Walled Circular Cylinder Under Axial Force, Bending, and Twisting Moments

An exact analysis is presented for the creep deformation of a thin-walled circular cylinder subjected to the simultaneous actions of axial force, bending, and twisting moments. Dimensionless interaction curves and charts which relate the variables, axial force, location of neutral-axis, bending moment, maximum effective strain rate, twisting moment, and shear strain rate are also provided for engineering practice convenience. The constitutive relationship of the cylinder is described by Prandtl-Nadai creep law.

Introduction

Modern technological progress demands the use of materials in load-carrying members (e.g., circular cylinders) at increasingly higher stresses for long periods of time. Furtheremore, most of these cylinders, particularly in fields of gas turbine, jet propulsion, oil refinery, chemical process, and power systems, must be designed to carry their loads at high temperature in order to increase the system thermodynamic efficiency. Therefore, as recommended by ASME Boiler and Pressure Vessel Code [1], the effect of creep strains on stresses must be assessed.

Many different creep relations have been proposed in the literature (see [2] and [3] for listing). In general, different formulas are good for different materials. For metal components, however, most design charts and formulas have been derived from the Norton creep law [4] or the hyperbolic sine law proposed by Prandtl [5], and Nadai [6,7] (Fig. 1(a)). A detailed discussion of these two creep relations has been given by McVetty [8]. He favors the hyperbolic sine law not only because a sinh term is fundamental to rate processes, but also because the hyperbolic sine law fits the empirical data better than the power creep law. However, the hyperbolic sine law has not found as much use as the power creep law, on account of its greater mathematical complexity [9].

Some useful design charts and insight for thin-walled circular cylinders subjected to creep deformation have been given by Edstam and Hult [10], Spence and associates [11, 12, 13], and others [14–23]. Most of the results, however, were based on the power creep law or dealt with the case where the neutral axis due to deformations coincided with the centroidal axis of the cross section of the cylinder. In the present paper, the load-deformational behavior of bending and twisting of cylinders in the presence of axial force (Fig. 1(b)) is studied. In general, the neutral axis (Figs. 1(c)) and 1(d)) will move with the presence of axial force. Useful results are presented in the form of dimensionless curves and charts. The use of these charts is illustrated by example problems.

The cylinder material is assumed to have identical tensile and compressive stress-strain rate relations, and to obey Prandtl-Nadai creep law. Hencky's total-strain theory and incompressibility of the cylinder are assumed to be valid. The derivation is based on the Bernoulli-Euler theory which stated that plane sections before bending remain plane during bending. It is assumed also that the thickness of the cylinder is
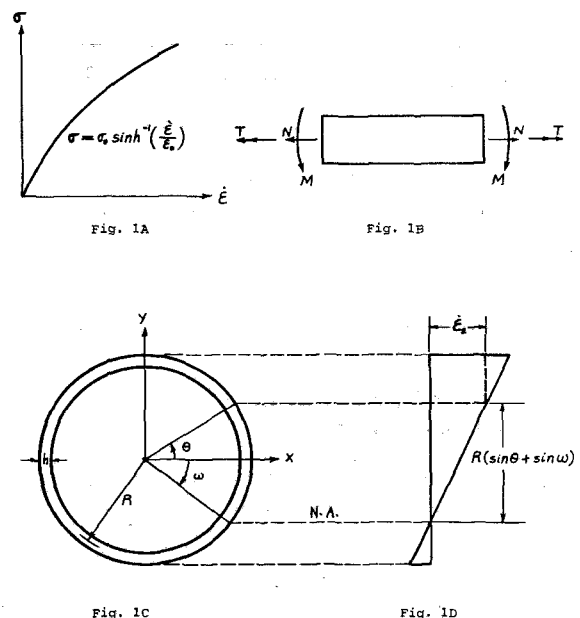

Fig. 1A   Fig. 1B

Fig. 1C   Fig. 1D

Fig. 1 Bending and twisting of thin-walled circular cylinder in the presence of axial force

so thin, compared with the inner radius, that all the nonzero stresses are uniformly distributed across the wall thickness. Due to the geometry of the cylinders and the loading conditions, the nonzero stress and strain rate components are

$$\sigma_z, \tau_{\theta z}, \dot{\epsilon}_r, \dot{\epsilon}_\theta, \dot{\epsilon}_z \text{ and } \dot{\gamma}_{z\theta}$$

while

$$\sigma_r = \sigma_\theta = \tau_{rz} = \tau_{r\theta} = \dot{\gamma}_{rz} = \dot{\gamma}_{r\theta} = 0$$

Analysis

Kinematics of Deformation. Since plane sections remain plane, the normal strain rate distribution is linear, Fig. 1(d),

$$\dot{\epsilon}_z = \frac{R(\sin\theta + \sin\omega)}{\dot{\rho}} \tag{1}$$

where $\dot{\rho}$ is the radius of curvature rate, and ω defines the location of the neutral axis. Defining the maximum normal strain rate as (when $\theta = \pi/2$)

$$\dot{\epsilon}_{zm} = \frac{R}{\dot{\rho}}(1 + \sin\omega) \tag{2}$$

Then equation (1) becomes

$$\dot{\epsilon}_z = \frac{\sin\theta + \sin\omega}{1 + \sin\omega} \dot{\epsilon}_{zm} \tag{3}$$

The shear strain rate for a thin-walled circular cylinder is given by

$$\dot{\gamma}_{z\theta} = R\dot{\zeta} = R\frac{d\dot{\phi}}{dz} \tag{4}$$

where $\dot{\zeta}$ is the twist rate per unit length and $\dot{\phi}$ is the total angle of twist rate.

Constitutive Relationships. The Prandtl-Nadai creep law is given by the average uniaxial stress-strain rate relation, Fig. 1(a),

$$\dot{\epsilon} = \epsilon_0 \sinh \frac{\sigma}{\sigma_0} \tag{5}$$

where ϵ_0 and σ_0 are material constants [6-8]. The multiaxial counterpart of equation (5) takes the form [2],

$$\dot{\epsilon}_e = \epsilon_0 \sinh \frac{\sigma_e}{\sigma_0} \tag{6}$$

where

$$\dot{\epsilon}_e = \frac{\sqrt{2}}{3}\sqrt{(\dot{\epsilon}_r - \dot{\epsilon}_\theta)^2 + (\dot{\epsilon}_\theta - \dot{\epsilon}_z)^2 + (\dot{\epsilon}_z - \dot{\epsilon}_r)^2 + \frac{3}{2}\dot{\gamma}_{\theta z}^2} \tag{7}$$

and

$$\sigma_e = \sqrt{\sigma_z^2 + 3\tau_{\theta z}^2} \tag{8}$$

are the effective strain rate and the effective stress, respectively.

Since

$$\sigma_r = \sigma_\theta = 0,$$

the strains in the radial and circumferential directions are equal, i.e.,

$$\dot{\epsilon}_r = \dot{\epsilon}_\theta \tag{9}$$

Also, because the cylinder material is assumed to be incompressible, i.e.,

$$\dot{\epsilon}_r + \dot{\epsilon}_\theta + \dot{\epsilon}_z = 0 \tag{10}$$

Then we have

$$\dot{\epsilon}_r = \dot{\epsilon}_\theta = -\frac{1}{2}\dot{\epsilon}_z \tag{11}$$

and equation (7) becomes

$$\dot{\epsilon}_e = \sqrt{\dot{\epsilon}_z^2 + \frac{1}{3}\dot{\gamma}_{z\theta}^2} \tag{12}$$

Substituting equations (8) and (12) into equations (6) leads to

$$\sqrt{\dot{\epsilon}_z^2 + \frac{1}{3}\dot{\gamma}_{z\theta}^2} = \epsilon_0 \sinh\left(\frac{\sqrt{\sigma_z^2 + 3\tau_{\theta z}^2}}{\sigma_0}\right) \tag{13}$$

For the problem under consideration, Hencky's theory [22] simplifies to

$$\sigma_z = 3\dot{\epsilon}_z \frac{\tau_{z\theta}}{\dot{\gamma}_{z\theta}} \tag{14}$$

By solving equations (13) and (14), we have

$$\sigma_z = \sigma_0\sqrt{1 - \beta^2}\frac{(\sin\theta + \sin\omega)\sinh^{-1}(\nabla)}{(1 + \sin\omega)\Delta} \tag{15}$$

$$\tau_{z\theta} = \sigma_0 \frac{\beta}{\sqrt{3}}\frac{\sinh^{-1}(\nabla)}{\Delta} \tag{16}$$

in which

$$K = \frac{\dot{\epsilon}_{em}}{\epsilon_0} > 0 \tag{17}$$

$$\beta = \frac{\dot{\gamma}_{z\theta}}{3\dot{\epsilon}_{em}} \qquad \epsilon[-1, 1] \tag{18}$$

$$\Delta = \sqrt{\beta^2 + (1 - \beta^2)\left(\frac{\sin\theta + \sin\omega}{1 + \sin\omega}\right)^2} \tag{19}$$

and

$$\nabla = K\Delta \tag{20}$$

have been introduced. In equations (17) and (18), $\dot{\epsilon}_{em}$ is the maximum effective strain rate which is defined as

$$\dot{\epsilon}_{em} = \sqrt{\dot{\epsilon}_{zm}^2 + 1/3\,\dot{\gamma}_{z\theta}^2} \tag{21}$$

Consequently, equations (3), (17), (18), and (21) yield

Nomenclature

h = wall thickness of cylinder
K = equation (17)
M = bending moment, equation (25)
m = dimensionless bending moment, equation (28)
N = axial force, equation (24)
n = dimensionless axial force, equation (27)
R = middle radius of thin-walled cylinder
T = twisting moment, equation (26)
t = dimensionless twisting moment, equation (29)
$\sigma_z, \tau_{\theta z}$ = nonzero stress components
$\dot{\epsilon}_r, \dot{\epsilon}_\theta, \dot{\epsilon}_z, \dot{\gamma}_{z\theta}$ = nonzero strain rate components

σ_0, ϵ_0 = material constants
$\sigma, \dot{\epsilon}$ = average uniaxial stress and strain rate
$\sigma_e, \dot{\epsilon}_e$ = effective stress and strain rate
$\dot{\epsilon}_{em}$ = maximum effective strain rate
$\dot{\epsilon}_{zm}$ = maximum normal strain rate
β = equation (18)
$\dot{\rho}$ = radius of curvature rate
$\dot{\zeta}$ = twist rate per unit length
$\dot{\phi}$ = total angle of twist rate
ω = location of the neutral axis
Δ = equation (19)
∇ = equation (20)
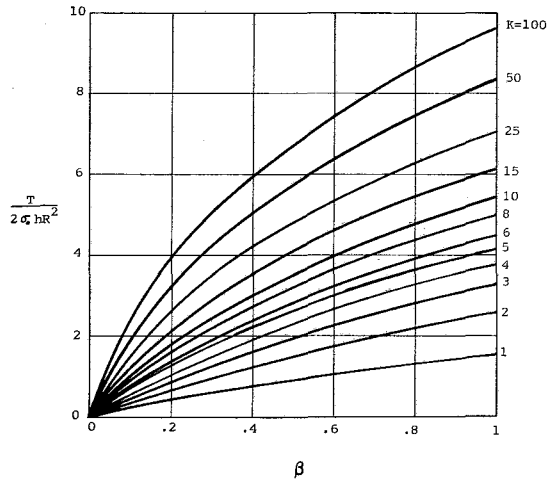
Fig. 2 Twisting moment for various values of K and β
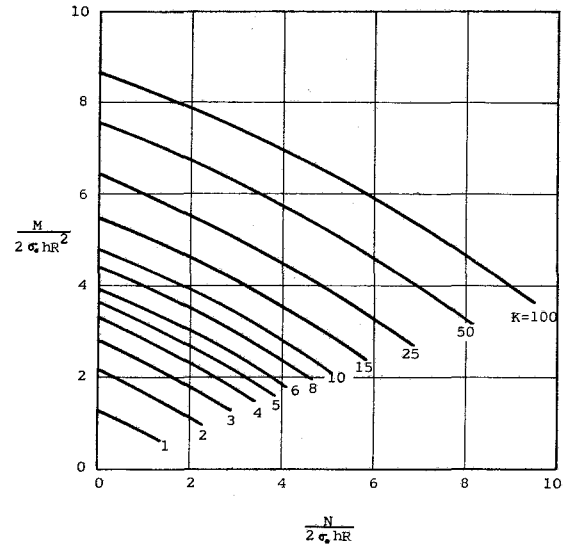
Fig. 5 Dimensionless moment-axial force interaction curves for $\beta = 0.4$
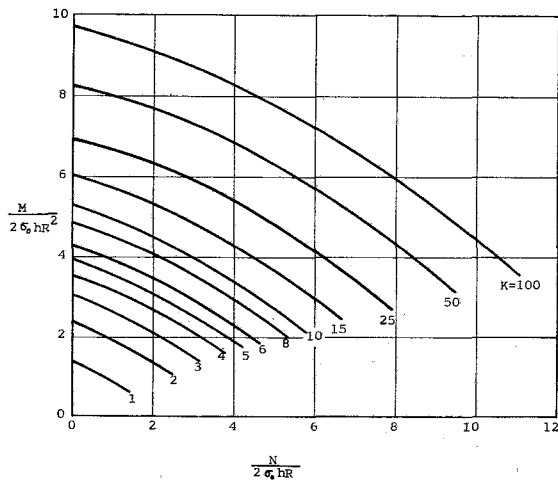
Fig. 3 Dimensionless moment-axial force interaction curves for $\beta = 0.2$

Fig. 6 Neutral-axial locations for $\beta = 0.4$

Equilibrium Equations. The equilibrium equations are

$$N = 2hR \int_{-\frac{\pi}{2}}^{\frac{\pi}{2}} \sigma_z d\theta \qquad (24)$$

$$M = 2hR^2 \int_{-\frac{\pi}{2}}^{\frac{\pi}{2}} (\sin\theta + \sin\omega)\,\sigma_z d\theta - NR\sin\omega \qquad (25)$$

$$T = 2hR^2 \int_{-\frac{\pi}{2}}^{\frac{\pi}{2}} \tau_{\theta z}\, d\theta \qquad (26)$$

Substituting equation (15) and (16) into equations (24) to (26), we have

$$n = \sqrt{1-\beta^2} \int_{-\frac{\pi}{2}}^{\frac{\pi}{2}} \frac{(\sin\theta + \sin\omega)\,\sinh^{-1}(\nabla)}{(1+\sin\omega)\,\Delta} d\theta \qquad (27)$$

$$m = \sqrt{1-\beta^2} \int_{-\frac{\pi}{2}}^{\frac{\pi}{2}} \frac{\sin\theta(\sin\theta + \sin\omega)\sinh^{-1}(\nabla)}{(1+\sin\omega)\,\Delta} d\theta \qquad (28)$$
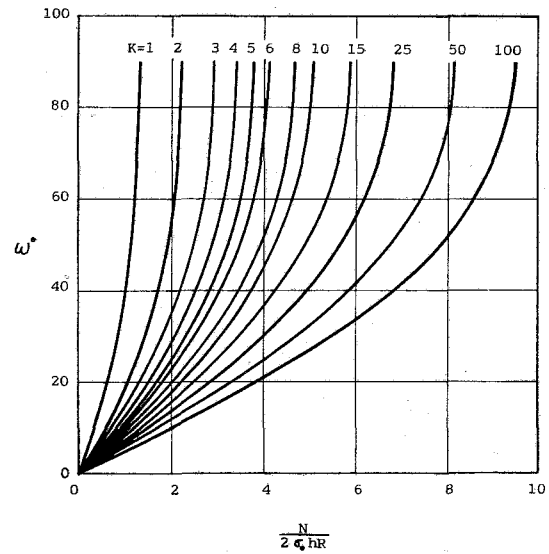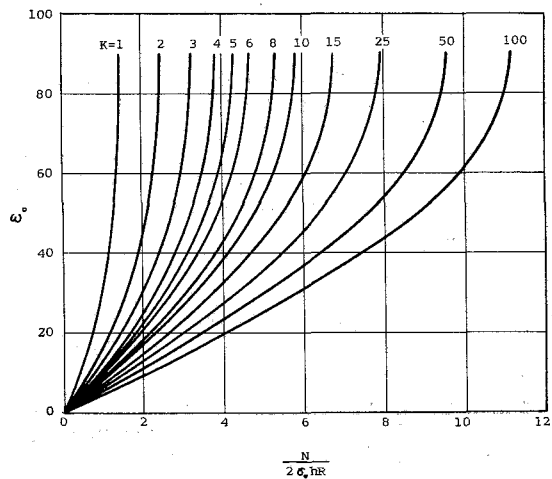
Fig. 4 Neutral-axial locations for $\beta = 0.2$

$$\dot{\epsilon}_z = \frac{\sin\theta + \sin\omega}{1 + \sin\omega} K\epsilon_0 \sqrt{1-\beta^2} \qquad (22)$$

$$\dot{\gamma}_{z\theta} = \sqrt{3}\,\beta K\epsilon_0 \qquad (23)$$
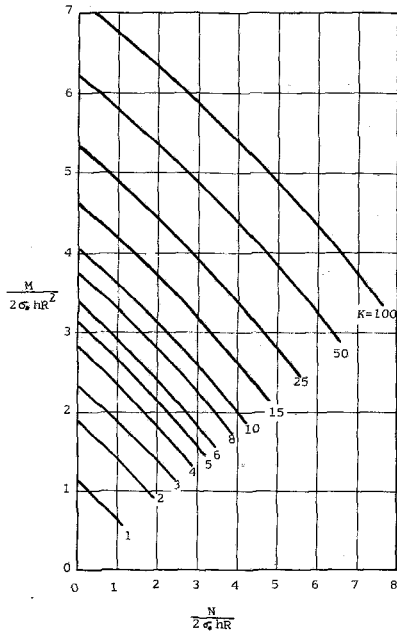
Fig. 7 Dimensionless moment-axial force interaction curves for $\beta = 0.6$

Fig. 8 Neutral-axial locations for $\beta = 0.6$

Fig. 9 Dimensionless moment-axial force interaction curves for $\beta = 0.8$

Fig. 10 Neutral-axial locations for $\beta = 0.8$

$$t = \frac{\beta}{\sqrt{3}} \int_{-\frac{\pi}{2}}^{\frac{\pi}{2}} \frac{\sinh^{-1}(\nabla)}{\Delta} d\theta \tag{29}$$

where

$$n = \frac{N}{2hR\sigma_0} \tag{30}$$

$$m = \frac{M}{2hR^2\sigma_0} \tag{31}$$

$$t = \frac{T}{2hR^2\sigma_0} \tag{32}$$

The above equations reduce to those in [24], if $\beta = t = 0$, and the material constants σ_0 and ϵ_0 are generated from the average isochronous stress-strain diagram [25] and the strain rate component is changed to strain component. Simpson's 1/3 rule [26] with 180 equal intervals is employed to evaluate the integrals in equations (27) to (29). Numerical results show that for large values of β and small values of K, t is constant

for all the values of ω. Even for small values of β and large values of K, t is almost constant for all the values of ω. This result permits us to present Fig. 2 (twisting moment for various values of K and β) with less than 5 percent errors, while Figs. 3-5, and 6-8, and 9 and 10 show the interaction relations between the variables m, n, and ω for $\beta = 0.2$, 0.4, 0.6, and 0.8, respectively.

Examples

Consider a circular cylinder with a thickness of 0.8 in. and a radius of 12 in. The material properties for the cylinder are σ_0 = 21,000 psi and ϵ_0 = 0.001.

Problem 1. Given twisting moment (T = 2016 ft-kip) and axial force (N = 1360 kip), determine the magnitude of the bending moment, so that the maximum effective strain rate is 0.05.

Solution. From equation (17), we have K = 50. From equations (30) and (32), we have n = 3.373 and t = 5, respectively. From Fig. 2 with K = 50 and t = 5, we have β = 0.4. From Fig. 5 with K = 50 and n = 3.373, we have m = 6.12, i.e., M = 2468 ft-kip.

Problem 2. Given N = 1283 kip, M = 997 ft-kip, and T = 1613 ft-kip, determine the stress and strain rate distributions.

Solution. Equations (30)–(32) give $n = 3.18$, $m = 2.47$, and $t = 4$. From Figs. 3, 5, 7, and 9 with $n = 3.18$ and $m = 2.47$, we have four sets of values of (β, K): (0.2, 5.2); (0.4, 6.3); (0.6, 10); and (0.8, 30). The right set of (β, K) can be found from Fig. 2 with $t = 4$. It is seen that the correct set is $\beta = 0.6$ and $K = 10$. From Fig. 8 with $n = 3.18$ and $K = 10$, we have $\omega = 40$ deg. The stress distributions are given by equations (15) and (16) as

$$\sigma_z = \frac{10227(0.643 + \sin\theta)\,\sinh^{-1}(10\,\Delta)}{\Delta}\,\text{psi}$$

$$\tau_{\theta z} = \frac{7275\,\sinh^{-1}(10\,\Delta)}{\Delta}\,\text{psi}$$

where

$$\Delta = \sqrt{0.36 + 0.64\left(\frac{\sin\theta + 0.643}{1.643}\right)^2}$$

The strain rate distributions are given by equations (22) and (23) as $\dot{\epsilon}_z = 0.00313 + 0.00487 \sin\theta$, and $\dot{\gamma}_z = 0.0104$.

Conclusions

An exact analysis has been presented for the bending and twisting of thin-walled circular cylinders with Prandtl-Nadai creep law in the presence of axial force. Useful curves and charts which relate the variables, axial force, location of neutral-axis, bending moment, maximum effective strain rate, twisting moment, and shear strain rate have also been provided for a wide range of conditions. The use of these charts has been illustrated by examples for determining the stress and strain rate distributions and resultant forces.

It is noted that the results presented here can also be applied to nonstationary creep, provided that the material constants σ_0 and ϵ_0 are generated from the average isochronous stress-strain diagram [25] and the strain rate component is changed to strain component.

References

1 ASME Boiler and Pressure Vessel Code, Section III, Division 1, "Class One Components in Elevated Temperature Service," 1977.

2 Boresi, A. P., and Sidebottom, O. M., TAM Report No. 347, Department of Theoretical and Applied Mechanics, University of Illinois, Urbana, Ill., 1971.

3 Lin, T. H., *Theory of Inelastic Structure*, John Wiley and Sons, New York, 1968.

4 Norton, F. H., *The Creep of Steel at High Temperature*, McGraw-Hill Book Company, New York, 1922.

5 Prandtl, L., "Ein Gedankenmodell sur kinetischen Theorie der festen Korper," *ZAMM*, Vol. 8, 1928, pp. 85–106.

6 Nadai, A., "The Influence of Time Upon Creep, The Hyperbolic Sine Law," *S. Timoshenko Anniversary Volume*, The Macmillian Co., New York, 1938, p. 155.

7 Nadai, A., *Theory of Flow and Fraction of Solids*, 2nd ed., McGraw-Hill Book Company, New York, 1950.

8 McVetty, P. G., "Creep of Metals at Elevated Temperature—The Hyperbolic-Sine Relation between Stress and Creep Rate," ASME *Transactions*, Vol. 65, 1943, p. 761.

9 Hult, J., *Creep in Engineering Structure*, Blaisdell Publishing Company, London, 1966.

10 Edstam, U., and Hult, J., *Recent Progress in Applied Mechanics*, edited by Broberg, Wiley, 1967.

11 Spence, J. R., *Nuclear Engineering and Design*, Vol. 24, 1974, pp. 411–420.

12 MacDonald, D. Q., and Spence, J., *Nuclear Engineering and Design*, Vol. 26, 1974, pp. 305–308.

13 Boyle, J., and Spence, J., *ROZPRAWY INZ YNIERSKIE*, Vol. 22, 1974, pp. 411–420.

14 Bernasconi, G., and Piatti, G., *Creep of Engineering Materials and Structures*, Applied Science Publishers, London, 1978.

15 Penny, R. K., and Marriott, D. L., *Design for Creep*, McGraw-Hill Book Company, U.K., 1971.

16 Lau, J. H., "Bending of Circular Cylinder with Creep," *Journal of Engineering Mechanics*, ASCE, 1981, pp. 265–270.

17 Lau, J. H., "Bending of Circular Thin-Walled Cylinder with Creep," *Journal of Engineering Mechanics*, ASCE, pp. 704–710.

18 Lau, J. H., "Torsion of Hollow Circular Cylinder with Creep," *Journal of Engineering Mechanics*, ASCE, 1982, pp. 185–190.

19 Lau, J. H., and Lau, T. T., "Creep of Pipe under Axial Force and Twisting Moment," *Journal of Engineering Mechanics*, ASCE, 1982, pp. 174–179.

20 Lau, J. H., "Bending and Twisting of Pipe with Creep," *Journal of Nuclear Engineering and Design*, 1981, p. 367–374.

21 Lau, J. H., and Listvinsky, G. K., "Bending and Twisting of Internally Pressurized Thin-Walled Cylinder with Creep," ASME *Journal of Applied Mechanics*, Vol. 48, 1981, pp. 439–441.

22 Rabotnov, Y. N., *Creep Problem in Structural Members*, North-Holland Publishing Company, 1969.

23 Kachanov, L. M., *Creep Theory*, Fizmatigiz, Moscow, 1960.

24 Lau, J. H., and Lau, T. T., "Creep of Pipes under Axial Force and Bending Moment," *Journal of Engineering Mechanics*, ASCE, 1982, pp. 190–195.

25 Smith, J. O., and Sidebottom, O. M., *Inelastic Behavior of Load-Carrying Members*, John Wiley and Sons, New York, 1965.

26 McCalla, T. R., *Introduction to Numerical Methods and FORTRAN Programming*, John Wiley and Sons, New York, 1967.

Improved Stress Simulation With Simple Finite Element Meshes

J. W. Harvey[1]

Polygonal finite elements displaying linear displacement on specified edges and quadratic displacement elsewhere are formed. Models composed of these elements identified with simple quadrilateral meshes produce marked improvement in stress simulation with the same global degrees of freedom used in conventional models. The polygonal elements are constructed of quadratic triangular subelements with appropriate sides constrained to displace linearly. Compatible mesh refinement capability is shown.

Introduction

Stress simulation of complex machine components using finite element models is markedly enhanced by automated mesh generation techniques [1]. Two-dimensional shapes are often subdivided into regions which are further subdivided into quadrilateral grids. Typically, all grid points on common boundaries are identical in adjacent regions to permit compatible finite element modeling.

The simplest, and most popular, technique to identify finite elements with such a mesh is to form quadrilateral [2] elements with corner nodes corresponding to mesh points. These elements display linear displacement behavior on their edges and consequently result in compatible models. (In some situations improved stress predictions result from selectively integrated [3] elements which do not offer detailed interlement compatibility.)

Higher-order elements [4], which are well known to provide more accurate simulations for a given mesh, introduce complexities into the modeling process. Compatible meshes of conventional higher order finite elements require mating element edges to be of the same order with connections at all nodal points along the interface.

The scheme presented in this paper identifies higher-order polygonal elements with an established quadrilateral mesh. Linear displacements are prescribed on each edge which is shared with another finite element. Compatibility is completely established by nodel connectivity. The polygonal elements are constructed from quadratic triangle [5] subelements having corner and midside nodes. Midside degrees of freedom are eliminated, where appropriate, to

specify linear displacement variation alog designated edges. All nodal freedoms internal to a polygon and not belonging to the original mesh are eliminated by static condensation resulting in a discrete model of higher order described with precisely the global degrees of freedom used in conventional modeling techniques. Quite evidently, the scheme can be viewed as a form of substructuring where each polygonal element is in fact a substructure with certain boundary constraints. Modeling potential is further enhanced by the development of element configurations permitting the compatible attachment of dissimilar quadrilateral meshes.

Basic theory is presented in the first section, followed by illustrative examples. Results are then summarized and conclusions drawn. Small deformations of linearly elastic materials are assumed. Plane stress problems are treated explicitly while the extension to axisymmetric models is implied. Symbols are defined at first appearance.

Basic Development

Basic Element Stiffness Matrix. The basis for this work is the quadratic triangular finite element shown in Fig. 1. The
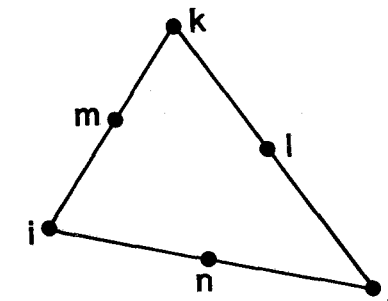
(a) BASIC
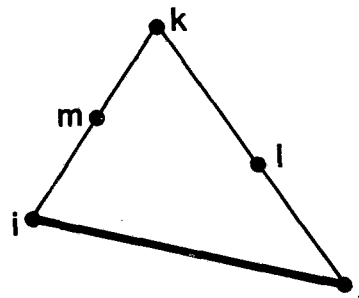
(b) MODIFIED ij LINEAR

Fig. 1   Triangular finite element

displacement components are interpolated with quadratic polynomials in the Cartesian coordinates (X, Y):

$$\left\{ \begin{array}{c} u \\ v \end{array} \right\} = \left[\begin{array}{cc} \lfloor Q \rfloor & \lfloor 0 \rfloor \\ \lfloor 0 \rfloor & \lfloor Q \rfloor \end{array} \right] \left\{ a \right\} \qquad (1)$$

where

$u(v)$ = component of displacement in the $X(Y)$-direction at coordinate location (X, Y);

$\lfloor Q \rfloor$ = quadratic interpolation polynomial;

$$\lfloor Q \rfloor = \lfloor 1, X, Y, X^2, XY, Y^2 \rfloor \qquad (2)$$

and

$\{a\}$ = vector of generalized displacements.

The development of the element stiffness matrix follows from well known procedures and will not be repeated here. The resulting matrix notation is adopted:

$[K]$ = element stiffness matrix

$\{\rho\}$ = local displacement vector

$$\{\rho\}^T = [U_i \; V_i \; U_j \; V_j \; U_k \; V_k \; U_l \; U_l \; U_m \; V_m \; U_n \; V_n] \qquad (3)$$

Modified Element Stiffness Matrix. Some of the triangular subelements are required to exhibit linear rather than quadratic displacement interpolation on one edge. This is achieved by constraining the midside node to displace an amount equal to the average of the corresponding corner values [6]. For side ij specified as linear, the constraint conditions are

$$\left[\begin{array}{cccccccccccc} -\frac{1}{2} & 0 & -\frac{1}{2} & 0 & 0 & 0 & 0 & 0 & 0 & 0 & 1 & 0 \\ & & & & & & & & & & & \\ 0 & -\frac{1}{2} & 0 & -\frac{1}{2} & 0 & 0 & 0 & 0 & 0 & 0 & 0 & 1 \end{array} \right] \left\{ \rho \right\}$$

$$= \left\{ 0 \right\} \qquad (4)$$

The modified 10×10 stiffness matrix in the remaining independent coordinates is given by the congruent transformation

$$[k_{10}] = [A]^T [k] [A] \qquad (5)$$

where

$$[A] = \left[\begin{array}{c} [1] \\ [B] \end{array} \right] \qquad (6)$$

$[1]$ = the identity matrix of order 10

$$[B] = \left[\begin{array}{cccccccccc} \frac{1}{2} & 0 & \frac{1}{2} & 0 & 0 & 0 & 0 & 0 & 0 & 0 \\ & & & & & & & & & \\ 0 & \frac{1}{2} & 0 & \frac{1}{2} & 0 & 0 & 0 & 0 & 0 & 0 \end{array} \right] \qquad (7)$$

Polygonal Elements. Basic and modified elements can be assembled to form polygons of virtually any shape, with
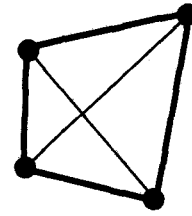
(a) QUADRILATERAL
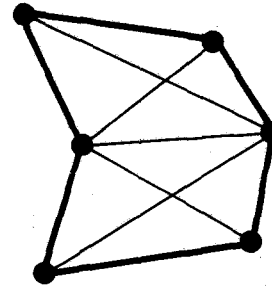
(b) HEXAGON
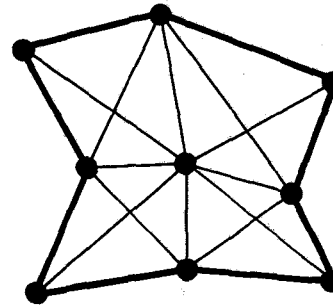
(c) OCTAGON

Fig. 2 Higher-order polygonal elements

linear displacement specified on designated edges. A few shapes particularly relevant to regular trapezoidal meshes are shown in Fig. 2.

The best performance is obtained with the octagonal elements, as less co. ·traint is imposed on a model comprised of the. elements than that of any combination of quadrilaterals and hexagons. The hexagons and quadrilaterals are intended only for meshes which cannot be completely described with octagons. The quadrilateral element, with all edges specified linear, offers little improvement over the conventional isoparametric formulation. However, in situations where one or more edges need not be so constrained (part boundaries) significant improvement is achieved. Also, the hexagon is always better than adjacent quadrilaterals.

Clearly, polygonal elements having other external and/or internal configurations are possible. Subelements, other than the quadratic triangle, are also available and are quite possibly better.

Dissimilar Meshes. The previous basic ideas are directly applicable to the formation of compatible interfaces of regions with different meshes.

Transition elements for mesh grading are shown in Fig. 3. As in the basic models best accuracy is achieved with the type "c" elements while type "a" performs least satisfactorily.

TYPE a

TYPE b

TYPE c

Fig. 3 Transition elements

Numerical Example

Triangular Plate With Uniform Load. The triangular plate of constant thickness loaded as shown in Fig. 4 is studied. This problem has characteristics which facilitate comparison of clasical stress predictions with conventional and suggested finite element simulations. The classical solution, given by Timoshenko and Goodier [7] predicts constant stresses along radial lines emanating from the wedge tip. The exactness of the solution relies on reactive stresses along the "fixed" edge being distributed in the same manner as the corresponding interior stresses. Kinematic constraint, implied by the term "fixed," is not established. This constant stress feature permits the direct assessment of mesh refinement in a single model, as each successive section (as shown in Fig. 4) represents a more refined approximation of the same problem. An additional feature of this problem is that all three Cartesian stress components are of the same order of magnitude (identical along the inclined edge). This tends to preclude misleading conclusions which might be drawn from special problems where particular stress components can be safely simulated with lower precision than others.

A conventional finite element model is identified with the mesh shown in Fig. 4. Four node isoparametric quadrilaterals are employed as the basic elements while a few constant stress triangles are used to complete the fixed edge. In order to avoid the perturbations caused by kinematic constraint, the model is supported only statically and loaded on the vertical face with forces representing the classical stress distribution. The same mesh is used to develop the higher-order polygonal model of Fig. 4. Octagonal elements are used wherever possible; note a few quadrilaterals and triangles are used at the fixed edge to complete the model. Bold lines connencting mesh points indicate element edges constrained to displace linearly. The previous scheme of load application is used for the fixed edge while forces kinematically consistent with the uniform load undergoing quadratic displacemnt are applied along the horizontal edge.

The quality of the simulations are compared on the basis of the error in the prediction of the maximum effective stress (based on the strain energy of distortion yield theory) on successive cross sections. Figure 4 shows the marked improvement in stress simulation provided by the polygonal elements. The alternating nature of the polygon curve apparently reflects the local influence of the constrained element
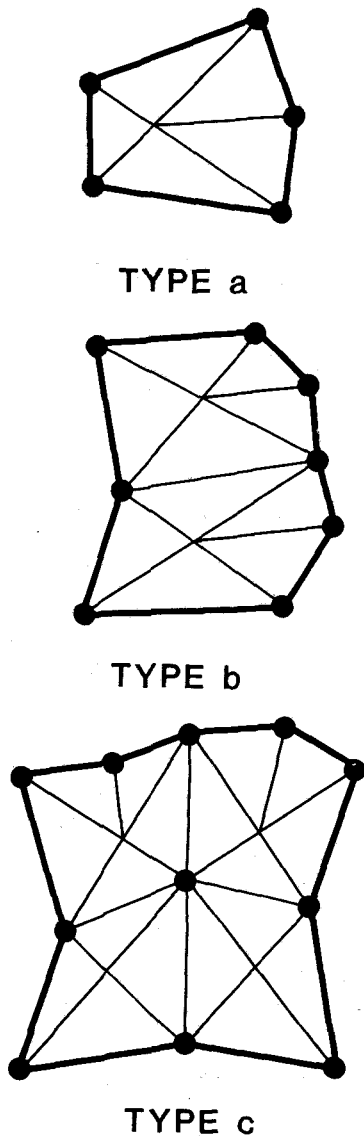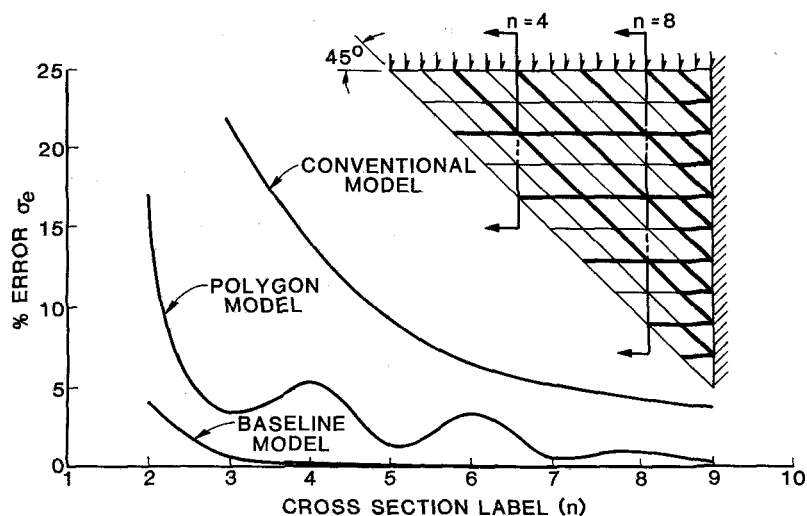
Fig. 4 Quality of approximation (percent error predicted effective stress)

edges. The lower curve represents the simulation achieved with the higher-order elements with no edge constraints imposed. Compatibility is established by nodal connection of all appropriate midsides. This requires retention of midside nodes at polygon interfaces in the global model. The results are included to gauge the upper limit on the accuracy achievable with polygonal elements formed from quadratic triangles.

Conclusions

This paper demonstrates marked improvement in stress predictions is achievable using higher-order polygonal finite elements which are adaptable to conventional mesh generators. Polygonal elements of virtually arbitrary shape are readily formed from quadratic triangular subelements having vertex and midside nodes. Designated edges of polygonal elements are constrained to deform linearly to provide compatible interfaces. The resultant model retains the same global freedoms as conventional models, permitting ready interfacing with existing input/output software, such as temperature tables, isarithm plotters, etc. A concomitant capability for mesh grading flexibility is provided.

References

1 Tree, D. J., and Alderson, R. G., "User's Manual Programs MESHD and ISOPDQ," Turbine Engine Components Stress Simulation Program, AFAPL Contract No. F33615-74-C-2012, Feb. 1977.

2 Ergatoudis, J. G., Irons, B. M., and Zienkiewicz, O. C., "Curved Isoparametric Quadilateral Elements for Finite Element Analysis," International Journal of Solids Structure, Vol. 4, 1968, pp. 31–42.

3 Doherty, W. P., Wilson, E. L., and Taylor, R. L., "Stress Analysis of Axisymmetric Solids Using Higher Order Quadrilateral Finite Elements," Structural Engineering Laboratory Report No. SESM 69-3, University of California at Berkeley, 1969.

4 Zienkiewicz, O. C., The Finite Element Method, McGraw-Hill, New York, 1977.

5 Fraeijs, De Veubeke, "Displacement and Equilibrium Models in the Finite Element Method," Stress Analysis, edited by O. C. Zienkiewicz, and G. S. Holister, Wiley, New York, 1965.

6 Greene, B. E., "Application of Generalized Constraints in the Stiffness Method of Structural Analysis," AIAA Journal, Vol. 4, No. 9, Sept. 1966, pp. 1531–1537.

7 Timoshenko, S. P., and Goodier, J. N., Theory of Elasticity, McGraw-Hill, New York, 1951.

The Rolls-Royce Annular Vaporizer Combustor

A. Sotheran

Chief Combustion Engineer,
Rolls-Royce Limited,
Bristol, England

The term "vaporizer" continues to be used to describe the well-known Rolls-Royce fuel injector, although its most important action is probably that it fires the fuel upstream towards the combustor head. This and the annular configuration are the distinguishing combustor features which have been retained through a long series of engines which include the Royal Aircraft Establishment/Metropolitan Vickers F-series engines and the Sapphire/J65 which used the first annular vaporizer. It is represented today in the engines of Concorde, Tornado, and Harrier/AV-8. With the wealth of experience obtained from these many applications, the operating characteristics of the combustor are very firmly established and new combustors can be designed with confidence that project requirements will be met with minimum development. For the future, the system is well set to accommodate anticipated operating environments and duties and is competitive enough to have been specified for the Rolls-Royce RB211-CE[3] advanced technology engine.

Introduction

Over the years the vaporizer combustor has several times seemed likely to be displaced by alternative systems and has often been claimed to have reached the limit of its useful potential. Each time the system has proved well able to meet the prevailing new challenge, whether of duty or application, or at least to be very amenable to whatever development or change was necessary to satisfy the new requirement. Its ability, with very little modification, to meet pending emissions legislation, to accept gaseous or heavy liquid fuels, to provide civil standards of mechanical reliability during sustained supersonic flight, and to withstand the highly cyclic conditions of a VTOL fighter are only the most recent examples of the flexibility and extreme applicability of this kind of combustor. This is further illustrated in Fig. 1, which gives the complete list of Rolls-Royce vaporizer combustors and shows the wide range of scale and duty for which they have been used.

With the wealth of experience obtained in such a wide range of engine types, sizes, and applications, the operating characteristics of the annular vaporizer combustor are established to a uniquely firm extent, so that new designs can be specified with confidence that project requirements will be met with minimum development.

With this background, it is clear that the vaporizer is very proficient as a fuel injector, but it also offers the very significant incidental advantage that its operation is unaffected by fairly substantial relative movements between the vaporizer and the injector which supplies its fuel. This insensitivity and the similar insensitivity of the dump diffuser to combustor head movements are utilized in the rear mounting and single-piece construction of the modern annular vaporizer. Apart from exploiting the side benefits of vaporizer fuel injection, these combustor features offer considerable aerodynamic and structural advantages in their own right and have been adopted elsewhere for these reasons alone. However, it is only in their original combination with the vaporizer fuel injector that they permit the simplest possible single-skin combustor from which all sliding joints and even the head cowl is eliminated.

The annular vaporizer combustor is not, therefore, simply a combustor which uses the vaporizer fuel injection system but is rather a comprehensive and integrated design concept which

OLYMPUS 593	CONCORDE CIVIL TURBOJET	40 000 lb	
PEGASUS	HARRIER/AV-8B VTOL TURBOFAN	23 000 lb	
VIPER	HS125, MACCHI, ORAO ETC CIVIL/MILITARY JET	4 000 lb	
RJ500-01	CIVIL TURBOFAN	20 000 lb	
RB199	TORNADO SUPERSONIC, MILITARY TURBOFAN	17 000 lb	
M45	VFW614 CIVIL TURBOFAN	7 500 lb	
RB401	CIVIL TURBOFAN	5 500 lb	
GEM	LYNX TURBOSHAFT	900 lb	

Fig. 1 Vaporizer combustion – current applications
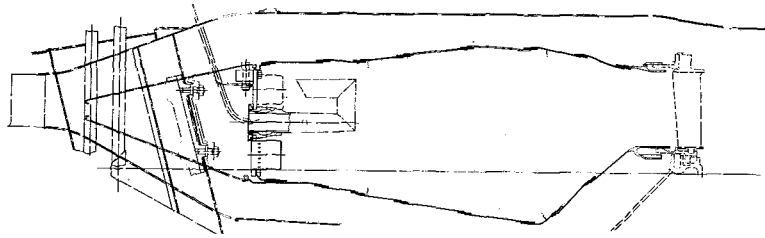
Fig. 2   Sapphire 7 combustion chamber
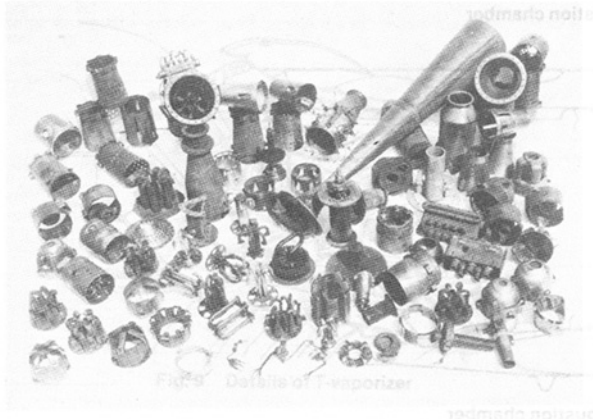
Fig. 3   Early vaporizer designs

affects all parts and aspects of the combustion system and in which the individual features are chosen and arranged to complement and exploit each other to maximum advantage. The following sections give a more or less chronological account of how the concept evolved and then indicate its future potential.

The Annular Configuration

The annular vaporizer first entered service in the Armstrong Siddeley turbojet engines, the Viper and the Sapphire. The second of these had been acquired from Metropolitan Vickers and was the last of the F-series of engines which were jointly designed and manufactured by Metropolitan Vickers and the Royal Aircraft Establishment. The first of these engines to run, in December 1940, was the F2 and this, like the rest of the series, differed from the contemporary Whittle engines in its all axial flow configuration and annular combustor. Another combustion feature of later significance was the use of upstream fuel injection, that is from fuel injectors which protruded radially into the downstream end of the primary zone and fired forward towards the baseplate. Remarkably, for most early testing and after comparative trials, what was described as a "solid jet" fuel injection system was used rather than "controlled atomization," although, in his later account of the development program, Constant [1] concedes the latter to be "definitely preferable" without explaining his reasons. However, when Armstrong Siddeley acquired the engine the solid injection system was replaced not by fuel atomizers but by another upstream firing system, the "vaporizer." At the time the supposed prevaporizing effect of the injector was held to be its chief characteristic feature and, of course, gave it its name but, today, the upstream firing action is given at least as much importance.

Vaporizer Fuel Injection

In 1940, Whittle [2] took delivery of a Shell designed combustion chamber which used a downstream firing fuel atomizer [3], and this proved to be such an improvement over his previous combustors that the "combustion problem" ceased to be the "obstacle to development" of his engines which it had previously represented. Whittle's own attempts to develop liquid fuel injection had met with very little success and his main effort seems to have been to develop a primus-type fuel vaporizer system. Although better, this also had many problems, including blockage and burning of the vaporizers themselves [2], and this initial poor experience of vaporizer fuel injection apparently discouraged its use throughout most of the growing U.K. industry and, in particular, in the Royal Aircraft Establishment/Metropolitan Vickers engines [1].

However, the first Armstrong Siddeley Motors gas turbine engines, the ASX turbojet and the Python turboprop both used an early type of vaporizer fuel injector quite satisfactorily in their can-type combustion chambers. Despite this success, and to the obvious displeasure of the combustion team under S. Allen [4], it was decided to fit the axial flow Mamba engine with a can-type combustion system employing pressure fuel atomizers. This decision was quickly part-reversed when the fuel atomizers were replaced by a system of "walking stick" or "candy cane" vaporizers in time for the engine's first type test. In later developments of the engine, the can combustors were replaced by an annular arrangement.

The Sapphire and Viper Engines (1952)

After the Sapphire engine was acquired by Armstrong Siddeley Motors, it was immediately reequipped with a locally designed combustion chamber (Fig. 2). This annular design had been developed in 1947 as a research project and again employed the walking stick vaporizer. This differed from the Whittle vaporizer in that a proportion of compressor air was admitted into its inlet at the same time as the fuel, a feature which is retained in the modern vaporizer and continues to ensure its integrity and effectiveness. As already noted, the injector was originally intended to prevaporize the fuel and, in common with the Whittle vaporizers, it protrudes into the combustor primary zone and exhausts its fuel air mixture forwards toward the baseplate. The comparatively large volumetric output of the vaporizer drives the primary zone flow recirculation [5] and, indeed, this is the only mechanism provided to promote this necessary aerodynamic feature.

The success of the walking stick vaporizer was not, of course, achieved without considerable development effort. Figure 3 shows a number of alternative designs which were evaluated before the eventual design was adopted. During early trials of the walking stick there were a number of failures due to burning at the base of the vaporizer stem. A wrapping of asbestos string around the stem of the vaporizer was found not to worsen its performance and this was interpreted as showing that the main fuel vaporization occurred in the downstream bends and hence that air cooling of the stem of the vaporizer would not impair its effectiveness. This feature no doubt satisfied its short term purpose very well, but it was automatically and, it transpires, unnecessarily retained
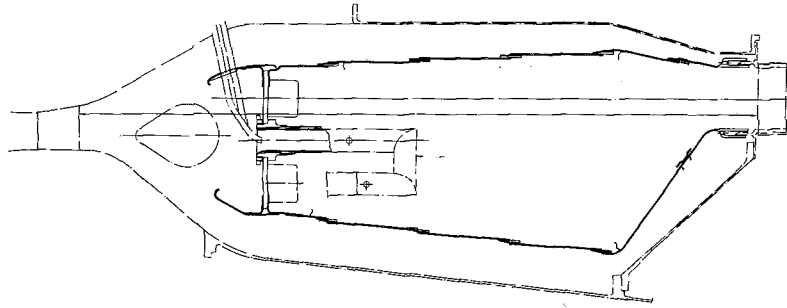
Fig. 4   Viper 8 combustion chamber
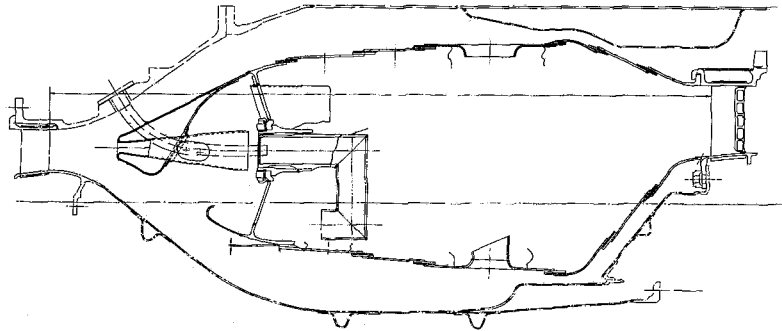
Fig. 5   Pegasus 5 combustion chamber
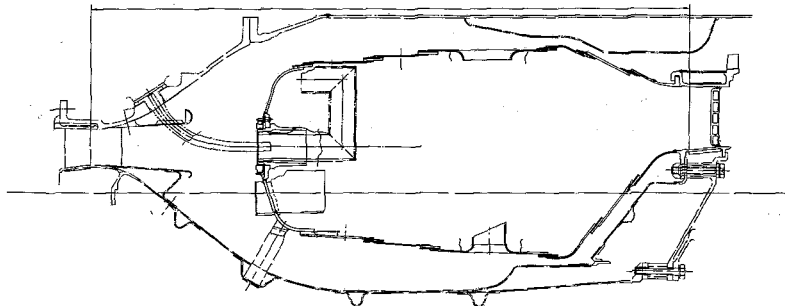
Fig. 6   Pegasus 6 combustion chamber
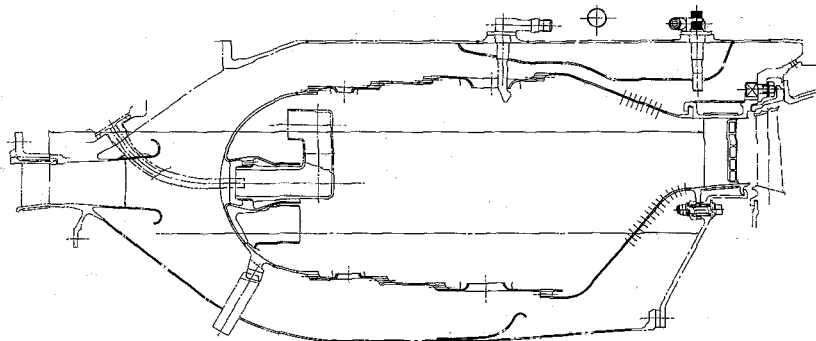
Fig. 7   Pegasus 103 combustion chamber

in successive combustor designs until eventually it proved to be extremely troublesome. The early walking stick vaporizers were nut-held to a thick, flat, combustor baseplate which also featured "secondary" air inlets into the primary zone. These were not simple apertures but short tubes with slotted end caps which were intended to generate additional turbulence within the primary zone.

Vaporizer combustors do not light satisfactorily on the vaporizer fuel itself and, like some nonvaporizing engines, use one or two small pressure atomizing starter fuel jets to start the engine and light the main fuel. Starter fuel jets are ob-viously inconvenient and an extra expense but they are very effective so that the use of the vaporizer combustor in no way restricts the circumstances in which the engine can be suc-cessfully lit and accelerated.

The general geometry of the Viper and Sapphire com-bustors later became standard for annular types. A cowl was bolted to the head of the combustor to form the inner walls of a split "faired" diffuser and to provide a plenum feed to the vaporizers and other baseplate features (Fig. 2). The com-bustor was pin-mounted to the casing at the head end to help maintain the diffuser geometry during thermal expansions.
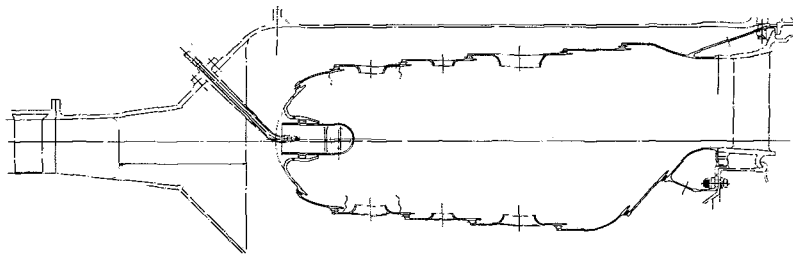
Fig. 8 Olympus 593 combustion chamber
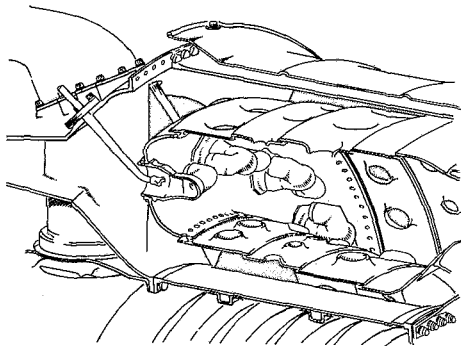
Fig. 9 Details of T-vaporizer
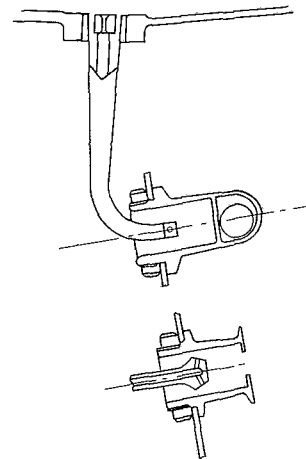
Axial expansions were accommodated by birdsmouth seals at the turbine end of the combustor.

Several attempts were made to improve the faired diffuser geometry. In one (Fig. 4), a central island, ahead of a twin intake to the cowl, was intended to divide the flow as required between the inner and outer liners. However, compressor exit flow profiles induced recirculations around the island and the arrangement was quickly replaced by a one-side cowl intake (Fig. 5).

The Pegasus Engines

The early Pegasus engines were designed by Bristol Aero-Engines Limited before its merger with Armstrong Siddeley and they used the "cannular" combustor arrangement which Bristol had helped to pioneer. Two special features of the Bristol combustion system at this time were its rudimentary dump diffuser and the integration of the turbine nozzle guide vanes (NGV) into the combustor outlet duct.

On the formation of Bristol Siddeley Engines Limited it was decided to refit the Pegasus 5 with an annular vaporizer combustor but to retain the integral nozzle guide vane arrangement of the earlier Pegasus. A faired diffuser (Fig. 5) was employed, as in previous vaporizer systems, but a further innovation was to weld the head cowl to the combustor and to mount the single unit of cowl, combustor, and NGV section from the rear end. Relative expansion of the inner and outer liners were accommodated by a radial sliding joint between the outer liner and the NGV section and by a break in the inner liner near the baseplate. These arrangements allowed both radial and axial relative movement between the vaporizers and the fuel injectors, which proved to be of no consequence, and between the head cowl and the diffuser inner and outer walls. It is not clear to what extent this last geometric uncertainty spoiled the diffuser flows, but all aspects of combustor performance were adversely affected by poor diffuser and head aerodynamics and were only partly alleviated when pitot intakes to the vaporizers were introduced (Fig. 5).

A much more complete and satisfactory remedy to this problem was incorporated into the Pegasus 6 combustor which introduced the dump diffuser in its modern form (Fig.

Fig. 10 Fuel feed arm geometry

6). The virtues of the dump diffuser, apart from its simplicity and competitive performance, are as follows:

1 It achieves high diffusion rates and combines high diffuser area ratio with short length.

2 Like the vaporizer fuel injection system, it is insensitive to relative movements of the combustor head and hence allows the rear mounted, single piece combustor configuration.

3 It eliminates the need for a head cowl, at least for diffusion purposes.

4 Removal of the head cowl exposes the combustor baseplate to the compressor efflux gases and eliminates the need to provide any other cooling means.

The latest Pegasus combustor, the Pegasus 103, is now a fairly old design (Fig. 7). It introduced the welded-in vaporizer and machined cooling ring which had been under development with Lucas Aerospace Limited for the cannular Olympus combustion system. More importantly, the break between the combustor head and the inner liner was eliminated without any adverse consequence.

The Olympus 593 Combustor

In the mid-sixties, the Pegasus vaporizer and the Olympus cannular sprayer combustors were both undergoing flight trials for the Harrier and Concorde, respectively. The sea level environment of the two combustors and their duties were very similar but their smoke characteristics transpired to be very different. The Pegasus exhaust has always been very clean whilst the Olympus exhaust was typical for a sprayer combustor of its generation. As a result of this difference it was decided to refit the Olympus with an annular vaporizer combustor as a joint enterprise with the French partner SNECMA.

The design which emerged (Fig. 8) followed previous Bristol Siddeley practice fairly closely but the main SNECMA contribution, the T-vaporizer, has proved to be most valuable. The T-vaporizer (Fig. 9) doubles the fuel input points into the combustor for a set number of fuel injectors,
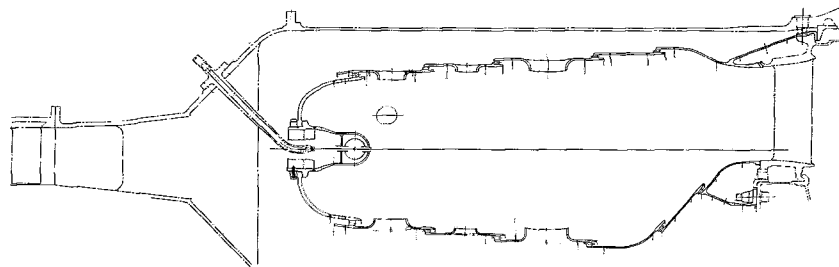
Fig. 11 Olympus 593 combustion chamber

ORIGINAL STANDARD WITH AIR COOLED STEM

UNCOOLED VAPORISER
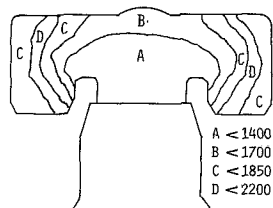
A <1400 (750)
B <1700 (930)
C <1850 (1000)
D <2200 (1200)

• TEMPERATURES AT TAKE-OFF

• DELETION OF STEM COOLING REDUCES ALL
  TEMPERATURES BELOW 1550°F (840°C)

FUEL

CIRCUMFERENTIAL CRACKS

WELD

HOT SPOT
1500 (815) 950 (500)
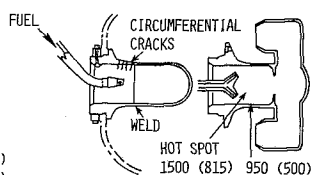
• TEMPERATURES IN °F (°C)

Fig. 12 Olympus 593 vaporizer failure modes

METAL TEMPS (°C)

FUEL INJECTOR

2 WAY
4 WAY
4 WAY 45°
4 WAY 45°
RETRACTED 5"

THERMOCOUPLES

15
14+
13+
11+

T/C No
11 13 14 15

NB COLD FUEL
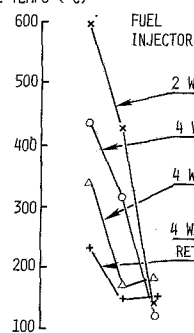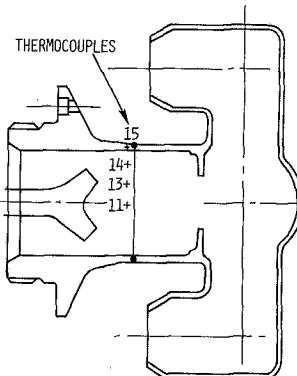
Fig. 13 Vaporizer temperatures

at the cost only of a slightly more complicated fuel injector. The simplicity of the fuel injector is, of course, one of the very major advantages of the vaporizer system. In the Pegasus, the injector is nothing but a 5-mm bore tube fed by flow metering orifices at the feed manifolds (Fig. 10). The Pegasus has two feed manifolds, for low and high flows, respectively, and this is the only measure taken to ensure a circumferentially uniform feed to the individual vaporizers. On the Olympus the fuel is divided equally between manifolds feeding the vaporizers at the top and bottom of the engine, respectively. The individual fuel injectors are fed via metering orifices and these in turn divide the fuel equally between the two outlets of the T-vaporizer (Fig. 10). There are no small holes or fine passages within the injector, which is single walled with plain drillings. Even at the high compressor exit temperature reached during sustained supersonic cruise there is no history of fuel gumming or injector blockage.

Further innovations of the Olympus 593 and contemporary combustors are the elimination of the "secondary" air inlet tube features in the combustor head, the skirted cooling ring, an additional pair of cooling rings in the combustor head, and the separation of the combustor from the NGV section. The secondary air inlet tubes are deleted because they are thought to introduce undue mechanical and aerodynamic complexity into the semitoroidal head of the modern combustor. The cooling ring skirts are introduced to discourage entrainment of the hot combustor gases into the cooling air jets and to protect the jets until they coalesce into a continuous wall film. The additional cooling ring in the combustor head was originally thought necessary to maintain acceptable head temperatures during supersonic flight but is now known to be unnecessary. The combustor is still rear mounted but from attenuating drums attached to the rear of both liners. The inner drum is bolted to the combustion chamber inner casing. The outer drum is wedged between the NGV sections and the engine casing and is held firm by the rearward pressure loads on the NGVs.

A number of mechanical problems have been encountered in the Olympus combustor, mainly associated with its very large size. In the early standards, mechanical vibration caused some distress to the liners and particularly at the plungings in
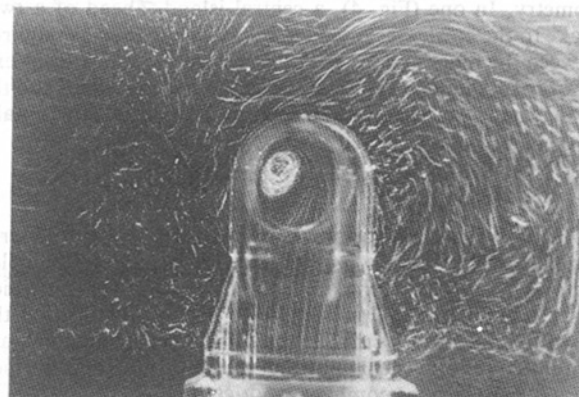
Fig. 14 Internal vaporizer flow

the baseplate to which the vaporizers were welded. In the latest standard, the walls are thickened two gauges and the baseplate has been flattened to accept a nut-held vaporizer. The opportunity was also taken to eliminate the unnecessary cooling ring (Fig. 11). Since these modifications, there have been no further problems due to combustor vibrations on Olympus 593, and there is no history of similar problems on the other (smaller) combustors. Nevertheless, the possibility remains that, because the single-piece construction and rear mounting arrangement lacks damping, it gives an especially "lively" combustor, and this is the subject of a number of current research programs in which design rules are being developed to avoid any recurrence of the Olympus experience.

The Olympus 593 vaporizer is also outsized compared with other examples, and, again partly for this reason, it has incurred durability problems which have not been experienced on any other vaporizer. During supersonic cruise the vaporizer air inlet temperature is very high at 840K (1050°F) and this clearly adds to the problem. Figure 12 shows the very high temperatures reached on the vaporizer cross arms. From
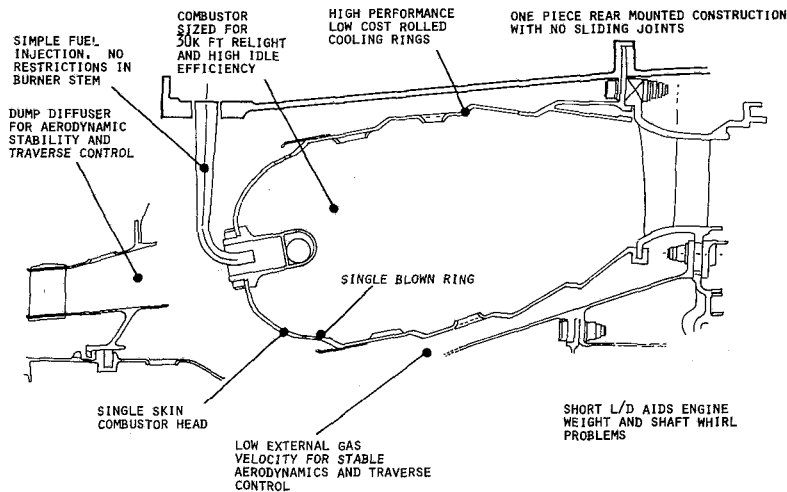
Fig. 15   RJ500 combustor
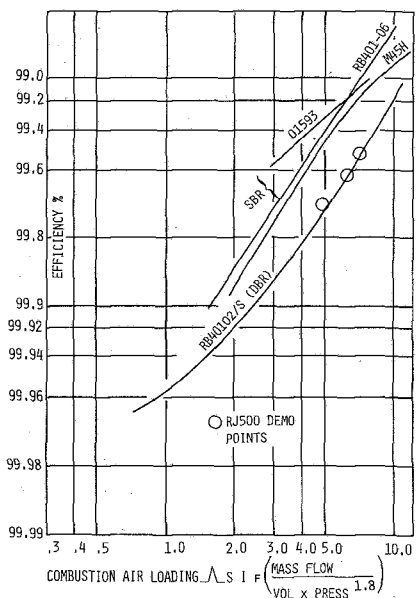
Fig. 16   Combustion efficiency versus air loading

Fig. 17   Idle efficiency versus air/fuel ratio
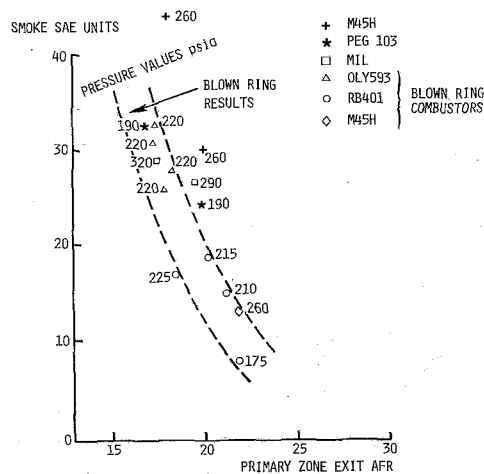
Fig. 18   Smoke versus PZ exit AFR

the shape and location of the contours it can be seen that the high temperatures are due to an invigoration of the burning adjacent to the cross arms caused in turn by the injection of the fresh vaporizer stem cooling air into the over-rich local environment. Deletion of the stem cooling air has completely eliminated this problem but has left a residual temperature differential problem in the stem itself. A single stem failure has occurred at the midstem weld which is to be eliminated as soon as possible. This in itself should give a satisfactory vaporizer life, but a four-way fuel injector will also eliminate the temperature differentials (Fig. 13).

A vaporizer design rule which has emerged from the Olympus experience is to ensure that no fresh air jets are directed at the vaporizers, and this adds to the several rules which have evolved during previous vaporizer development and which have helped to avoid vaporizer durability problems in all recent engines other than the Olympus. In-service vaporizers now operate dependably at compressor exit temperatures in excess of 860K (1100°F) and pressures above 450 psia and have demonstrated high cyclic lives under extreme operating conditions. While, to achieve this dependability, it is important to minimize heat input to the vaporizer from the hot gases, it is also necessary to ensure

adequate cooling flows over all the internal surfaces of the vaporizer walls. This is achieved partly by generating strongly swirling flows inside the vaporizer as photographed (Fig. 14) in the water analogy rig at Cranfield Institute of Technology (6). The swirling flows help to ensure that all the internal walls of the vaporizer are washed with fuel. For the future, more easily cooled vaporizer shapes and new vaporizer materials are being researched in preparation for the even more arduous environments and duties of projected civil and military engines.

EMISSION SPEC	PROPOSED 1986 STANDARDS (L50)	SINGLE ENGINE COMPLIANCE VALUES	DESIGN VALUES	EPA STANDARDS
CO	118	80.3	36.9	20.9
HC	19.6	8.8	4.6	2.3
NOx	92.3	69.9	52.7	29
SMOKE	23.3	14.5	7.13	19

EPA LIMITS EXCEPT NOx CAN BE ACHIEVED WITH MINOR
COMBUSTOR HEAD MODIFICATIONS (DOUBLE BLOWN RING)

Fig. 19   RJ500 emissions

ENGINE	OVERALL (%)	RADIAL (%)
MILITARY EXPERIENCE	24 – 29	8 – 9
RB401-06	22 – 28	8 – 10
M45H	30	7.5
RJ500 DEMONSTRATOR (RIG)	25	7

Fig. 20   Z-ring vaporizer combustor pattern factors

Fig. 21   Annular vaporizer concept

The RB401 and RJ500 Combustors

The RB401 combustor is canted 11 deg outward between the compressor and the turbine and introduces the "blown ring," a low pollutant emissions head feature, and the "Z" wall cooling ring. These, with the flat baseplate and the uncooled, nut-held vaporizer constitute the modern combustor as typified by the RJ500 combustor (Fig. 15), and demonstrator versions of it are now undergoing rig and engine trials.

The "blown ring" is no more than a row of small, closely pitched holes on the shoulder of the combustor. The entering air jets remove any fuel migrating along the inner wall of the combustor before it can be entrained into the liner cooling films. The effect on idling efficiency and emissions is dramatic. A vaporizer combustor designed for a modern engine cycle and sized to light at 30,000 ft will idle at about 95 percent without blown rings. A single blown ring (SBR) raises the efficiency to 99.5 percent, while a double blown ring (DBR) halves the emissions again to give an efficiency of 99.75 percent (Fig. 16). These efficiency levels have been measured in numerous combustion chamber rigs and, as Fig. 16 shows, the single blown ring performance has been confirmed on four separate engines. To date the double blown ring levels have been validated on only one. Within wide limits, these efficiencies are independent of the primary zone stoichiometry (Fig. 17), which is fortunate since smoke emissions depend heavily on the stoichiometry but are, once again, significantly reduced by the introduction of blown rings (Fig. 18). Figure 18 shows the smoke characteristic of virtually all annular vaporizer combustors, engine-measured at take-off, so that the scatter of results is surprisingly small and reduces even further for the most recent combustors. The figure also demonstrates that engine pressure ratio has no influence on takeoff smoke levels.

There is inferential evidence that a blown ring, lean primary zone eliminates erosive carbon emissions as well as smoke. On the Olympus 593, which is not a particularly clean engine by modern standards, turbine blades reach 2500 hrs and above without significant loss of material. On other engines with rich primary zone combustors, turbines have been damaged by carbon impact and the glowing carbon particles have been easily detectable by a pyrometer at turbine inlet. Sufficient weakening of the combustor primary zone has eliminated both turbine damage and the pyrometer signals.
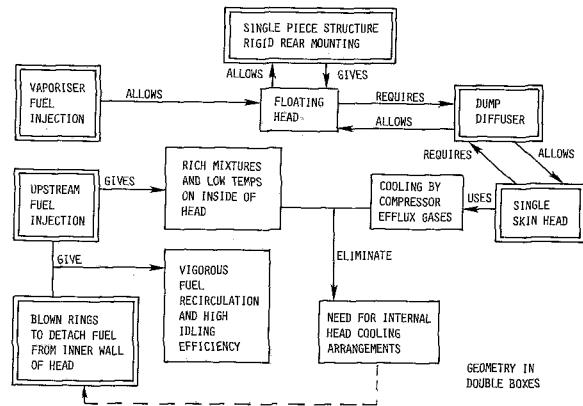
In the Z-cooling ring the conventional single row of large cooling holes is replaced by at least two rows of much smaller holes. The air jets from the small holes quickly coalesce into a continuous film without the initial protection of a cooling skirt and the cooling effectiveness is significantly better than the conventional ring and, indeed, approaches that of the clean slot. The Z-ring section is, of course, extremely simple to manufacture and when roll-formed virtually no material is swarfed off so that material costs are minimised. Accurate multihole drilling and inspection have not proved easy to perfect but laser drilling techniques are showing much promise and will also allow hole shapes to be further optimised.

The RJ500 demonstrator combustors are undergoing rig and engine trials. Figure 16 shows the rig measured idle emissions to be exactly on the design values. These were to meet the original, very stringent idle emissions proposal of the U.S. Environmental Protection Agency so that a double blown ring primary zone was specified for the demonstrator combustor. To meet the pending regulations of the International Civil Aviation Organization only a single blown ring will be required. There are no specific features in the annular vaporizer design to reduce emissions of the nitrogen oxides, although the effectiveness of the blown ring in limiting the idle emissions allows the smallest possible combustor volume to be specified and the resulting low residence time helps to control the NO_x emissions, at least to below the levels allowed by the International Civil Aviation Organization regulations (Fig. 19).

The outlet pattern factor of the RJ500 demonstrator is similar to that of the RB401 and other modern combustors (Fig. 20). Under takeoff conditions wall temperatures average 800°C with only very local hot spots above 840°C.

Design Concept

The RJ500 demonstrator combustor brings the account up to date and allows the modern design concept of the annular vaporizer to be described in detail. An attempt to summarize the concept is shown in Fig. 21, from which it will be seen that the insensitivity of the dump diffuser and vaporizer fuel injector to combustor head movements permits the use of the single-piece rear-mounted construction. Dump diffusion also allows the head cowl to be discarded and exposes the baseplate to the compressor efflux which, with upstream fuel injection and rich burning mixtures on the inside of the

baseplate, provides all the cooling which is necessary. Upstream fuel injection ensures an adequate degree of recirculation for all the fuel injected and, in this circumstance, it transpires that the only significant cause of poor idling efficiency is the entrainment of fuel into the liner cooling films. Since there are no cooling films on the baseplate itself this is easily prevented by the provision of blown rings ahead of the first liner cooling rings.

Presumably the fuel which is likely to become entrained into the cooling films is still in liquid form so that any vaporization which occurs within the vaporizer would tend to minimize this effect. However, the extent of the vaporization, either at idle or full power, and its importance to the burning processes are still not well understood and an extensive research program is now under way to resolve these issues.

Concluding Remarks

Perhaps the greatest advantage of the annular vaporizer is that it has evolved over very many engine types designed for very many applications, as Fig. 1 shows. As a result, the validity of the design parameters now in use has been confirmed to a uniquely great extent, and the performance characteristics of new combustors can be predicted with considerable confidence.

For the immediate future, the effectiveness of the blown ring, which allows a small combustor to be specified without risking unacceptable pollutants emission rates, and of the Z-ring both help to minimize cooling flow requirements and permit the very lean primary zone which is necessary for low smoke and carbon emission rates. However, as compressor exit and turbine entry temperatures rise this situation becomes increasingly difficult to maintain and new materials and cooling techniques will become urgently necessary.

An important requirement of future gas turbine combustors will be to burn wide ranges of fuel satisfactorily. For heavy fuels the simplicity of the vaporizer's fuel injector offers very positive advantages since there are no fine holes or passages which can become blocked by fuel gums and lacquers. The vaporizer system requires a finely atomizing starter jet for light-up even on kerosine so that heavier fuels introduce no extra complication here. Lastly, the burning characteristics on heavy fuels are broadly similar to those on kerosine except for the expected increases in flame radiation and wall temperatures. In fact, most vaporizer engines have undergone trials on diesel fuels, and no unacceptable consequences have been recorded. Nevertheless, for an engine intended to operate habitually on low-grade fuels, the modern very lean primary zone would obviously be even more necessary to control the carbon and smoke emissions and avoid turbine erosion problems.

Operation on gaseous fuels also appears to be quite satisfactory and has so far involved no undue difficulties or problems. Indeed, the vaporizer combustor, of the Sapphire/J65 engine, enjoys the distinction of being the only combustor so far to have flown on hydrogen [7] and the only modification needed to convert the combustor to dual-fuel operation was to add the hydrogen supply pipe to the vaporizer. Very low calorific value fuels, which need to be injected at very high volumetric flow rates, apparently reduce the air flow rate through the vaporizer and may displace it altogether, but again, no ill-effects have been recorded.

References

1 Constant, H., "The Early History of the Axial Type of Gas Turbine Engine," *I. Mech. E. Proceedings*, Vol. 153, 1945, pp. 411–426.

2 Whittle, F., "The Early History of the Whittle Jet Propulsion Gas Turbine," *I. Mech. E. Proceedings*, Vol. 152, 1945, pp. 419–435.

3 Allen, S., Internal Report, Armstrong Siddeley Motors Limited, 1948.

4 Stokes, M. A., "Annular Combustion for Gas Turbine Engines," *The Aeroplane*, Jan. 14th, 1955, pp. 48–52.

5 Parnell, E. C., and Williams, M. R., "A Survey of Annular Vaporising Combustion Chambers," *Combustion and Heat Transfer in Combustion Systems*, edited by E. R. Norster, First edition, Pergamon, Oxford, 1971.

6 Jasuja, A. K., "Vaporizer Research Studies," *Internal Report*, Cranfield Inst. of Technology, 1982.

7 Conrad, E. W., "Turbine Engine Altitude Chamber and Flight Testing with Liquid Hydrogen," NASA TM79196.

Comparison-Effects of Broadened Property Jet Fuels on Older and Modern J79 Combustors

D. W. Bahr

General Electric Company,
Aircraft Engine Business Group,
Cincinnati, Ohio 45215
Mem. ASME

The results of parallel investigations to determine the impacts of jet fuel property variations on the performance, life, and pollutant emission characteristics of two different J79 engine combustor designs are compared. One of the designs embodies older technology features. The other design was developed more recently and embodies several advanced technology features to provide lower smoke levels and longer liner life capabilities. Both combustors were evaluated with the same set of thirteen fuels. The fuels were selected to provide fuel property ranges which span those of current jet fuels and of possible future broadened-specification jet fuels. The modern technology combustor was found to be considerably more tolerant of fuel property variations than the older technology design. The relative insensitivity of the modern technology design is primarily attributed to its lean-burning features, which result in low smoke and low flame radiation levels even with low hydrogen content fuels.

Introduction

Because of the dwindling world supply of high-quality petroleum crude oil and the increasing world-wide demand for middle-distillate petroleum fuels, jet fuel specifications may have to be significantly modified during the next decade [1, 2, 3]. Specifically, broadening of several of the limits defined in existing jet fuel specifications may be necessary to assure adequate and economically acceptable supplies of petroleum-derived jet fuels. Fuel specification broadening may also be needed to permit the use, in the longer-term future, of jet fuels derived from oil shale or coal.

Such fuel specification broadening could necessitate the accommodation of lower quality fuels, compared to presently available jet fuels, in aircraft turbine engines. In particular, accommodation of fuels with increased aromatic contents and, as a result, decreased hydrogen contents could be required. Also, accommodation of fuels with decreased fluidity, volatility, and thermal stability characteristics could be needed as a consequence of such specification broadening.

These possible needs have prompted various investigations by both government and industry organizations during the past few years to assess the impacts of such fuel property changes on the performance and operation of engine fuel systems, combustors, and turbines. The findings of some of these studies are summarized in [3, 4, 5]. Many of these investigations are still underway and other new studies of this kind are being initiated.

Several such investigations have been conducted by the General Electric Aircraft Engine Business Group. The initial results of these investigations are summarized in [6]. The more recent efforts included two parallel investigations to determine the impacts of jet fuel property variations on the performance, pollutant emission, and life characteristics of two different J79 engine combustor designs. The detailed results of these latter two investigations, which were conducted under the sponsorship of the U.S. Air Force Aero Propulsion Laboratory, are presented in [7] and [8].

Both of these combustor designs are used in operational J79 engines. However, the technology vintage of the two designs is significantly different and, thus, they have much different configurational features. Versions of one of these combustor designs have been in production for many years. This design embodies generally older technology features, especially with regard to smoke abatement and liner cooling features. The other design was developed more recently and embodies several advanced technology features. This design was evolved to provide a configuration with much lower smoke emission levels and improved liner cyclic life capabilities.

In the investigations described in [7] and [8], the performance and operational characteristics of these two J79 combustors were experimentally determined in the same test rig, over the same ranges of engine operating conditions. In these tests, both combustors were operated with the same set of thirteen jet fuel blends. The thirteen test fuels were selected to provide ranges of fuel properties which span those of current and possible future JP-4/JP-5/JP-8/JET A fuels. With these selected test fuels, systematic variations in hydrogen content, aromatic content and type, and volatility/fluidity characteristics were obtained.

The important findings of these J79 combustor investigations are summarized in this paper. Because of the

parallel nature of these investigations, direct comparisons can be made of the two sets of results.. Such comparisons provide a direct assessment of the broadened property fuel accommodation capabilities of an older technology combustor design relative to those of a modern technology design.

Test Combustors

Two different J79 engine combustor configurations were used in these investigations. Both of these configurations are currently used in operational J79 engines.

The J79 engine is a turbojet engine with variable afterburner thrust. This engine was originally qualified in 1956. Various models have been used in several military aircraft. Nonafterburning versions of this engine were also used in commercial aircraft applications. The engine compressor pressure ratio is approximately 13.4:1. The engine combustion system is a cannular design with ten individual combustor cans located in an annular passage between inner and outer casings.

In the engine assembly, two of the combustors are provided with spark igniters for starting and relight. Adjacent combustors are joined near the forward ends by cross-ignition tubes to allow propagation of the flame from the combustors with spark igniters to the other combustors. The combustors are each positioned and held in place by mounting bolts at their forward end. Axial stack-up and thermal growth are accommodated by a sliding seal between the combustors and the transition duct.

J79-17A Engine Combustor. The older technology combustor design is currently used in the J79-17A engine model. A pictorial drawing of this combustor is presented in Fig. 1. The combustor is comprised of three main parts riveted together to form an assembly — a snout/outer liner, a dome/inner liner, and a rear liner. The primary material of each of these parts is Hastelloy X.

Cooling air for the inner surfaces of the sheet metal dome, inner liner, and rear liner is admitted through punched louvers. Combustion and dilution air is admitted through a series of dilution holes in the inner and rear liners. These holes are arranged to provide airflow patterns for flame stabilization in the primary combustion zone and turbine inlet temperature profile control at the aft end. Fuel is delivered by a dual-orifice, pressure-atomizing nozzle with a flow-dividing valve external to the mounting flange.

J79-17C Engine Combustor. The modern technology combustor design is currently used in the J79-17C engine model. Pictorial and schematic drawings of this combustor are presented in Figs. 2 and 3, respectively. Like the J79-17A combustor, the J79-17C combustor is comprised of three main parts — a cowl/outer liner, a dome/inner liner, and rear liner — riveted together to form an assembly. The primary material of each of these parts is Hastelloy X.

The cowl/outer liner, dome/inner liner, and fuel nozzle of the J79-17C combustor are significantly different than those of the J79-17A combustor. In particular, the J79-17C dome/inner liner subassembly is shorter and consists of a machined ring shell, with continuous film cooling air slots in both its conical and cylindrical sections. Impingement cooling is used in the conical section, in addition to film cooling. Combustion air is introduced into the forward end of the
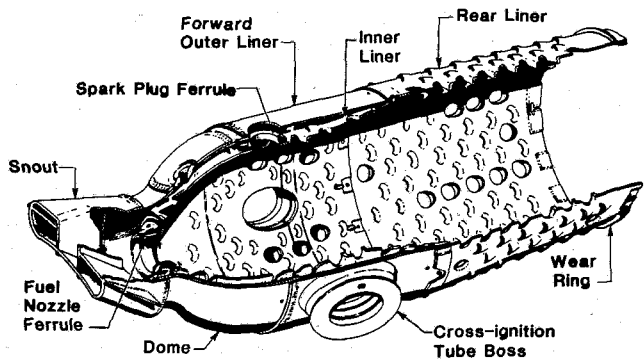
Fig. 1 Pictorial view of J79-17A combustor
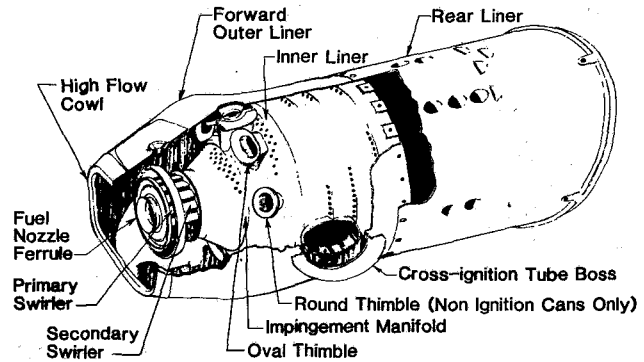
Fig. 2 Pictorial view of J79-17C combustor
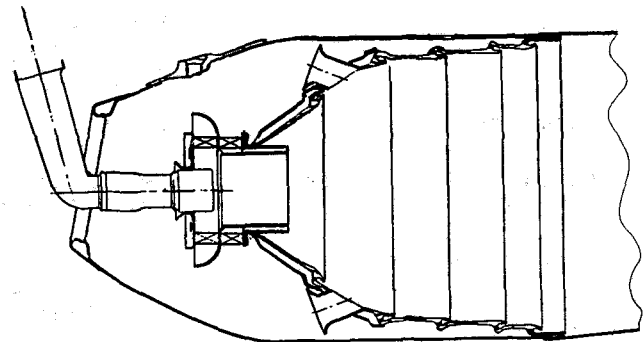
Fig. 3 J79-17C combustor flowpath schematic

dome through a swirl cup, comprised of two corotating swirlers, and bellmouthed thimble holes. In nonignition combustors, six of these holes are used; ignition combustors have four holes.

To provide the required high dome airflows, the outer liner is equipped with a high-flow cowl. The rear liner is essentially the same as that of the J79-17A combustor and consists of a sheet metal shell with punched cooling louvers and dilution holes.

Fuel is delivered by a hybrid nozzle with a centrally located pressure-atomizing primary circuit surrounded by an airblast-atomizing secondary circuit, which operates with low fuel pressures. The airblast-atomizing secondary circuit is one of

_____ Nomenclature _____

M_0 = flight Mach number
T_F = fuel temperature at combustor inlet, K
T_3 = combustor inlet air temperature, K
W_c = combustor airflow rate, kg/s
W_F = combustor fuel flow rate, g/s

the important design features included to obtain uniform fuel-air mixtures in the primary combustion zone.

Comparison – J79-17A/J79-17C Combustors. As is described above, many of the design features of the J79-17C combustor are significantly different than those of the J79-17A combustor. The J79-17A embodies generally older technology and has relatively high smoke levels and relatively short cyclic life capabilities. The life-limiting element of this combustor is its inner liner, because of its relatively simple construction and cooling features. The J79-17C combustor was developed more recently to meet low smoke level and long cyclic life requirements. To meet these requirements, this combustor embodies several advanced technology design features.

A key difference in the combustors is their airflow distributions. In the J79-17C combustor, much greater air-flow qualities are introduced into the forward end of the dome to reduce dome fuel-air ratios and, thereby, reduce smoke levels. The airflow distributions of the two combustors are compared in Table 1. Another advanced technology feature of the J79-17C combustor is its airblast-type fuel injection, which is an additional smoke abatement feature. To meet the long cyclic life requirement, advanced technology cooling and structural features are used in the inner liner. A comparison of the key design features and associated performance capabilities of the two combustors is presented in Table 2.

Test Fuels

Both combustors were evaluated with the same set of thirteen test fuels. The fuels consisted of three base fuels – JP-4, JP-8, and Number 2 diesel – and five blends of the JP-4 fuel plus five blends of the JP-8 fuel. The blends were formulated by adding aromatic and/or paraffinic constituents to the base fuels. The key properties of these test fuels are shown in Table 3.

The fuel property variations encompassed by these fuels were intended to systematically span the likely ranges of fuel properties of possible future jet fuels. With these test fuels, variations were obtained in hydrogen content, aromatic content and type (monocyclic or bicyclic), boiling temperature range, and viscosity. The fuels with hydrogen contents of

Table 1 Comparison of combustor airflow distributions (% total combustor flow)

Airflow element	J79-17A combustor	J79-17C combustor
Dome swirl cup	0.0	6.2
Dome dilution holes	0.0	19.7
Inner liner dilution holes	12.5	0.0
Dome/inner liner cooling	18.7	30.4
Rear liner dilution holes	48.1	29.7
Rear liner cooling	20.7	14.0
Total	100.0	100.0

Table 2 Key design features/performance characteristics of test combustors

Design Feature	J79-17A combustor	J79-17C combustor
• Dome air quantity/insertion	low airflow via downstream-located inner liner dilution holes – high (rich) dome fuel-air ratios at high power	high airflow via dome swirl cup plus forward-located dome dilution holes – near stoichiometric fuel-air ratios at high power
• Fuel insertion	dual-orifice, pressure-atomizing nozzle	hybrid nozzle – pressure-atomizing primary and airblast-atomizing secondary
• Dome/inner liner construction/cooling	sheet metal liner with cooling via punched louvers	machined-ring liner with cooling via film cooling slots plus impingement cooling (of conical section)
Performance characteristic		
• Smoke emission level	high – smoke number of 65 at takeoff power with JP-5/JP-8	low – smoke number of 20 at takeoff power with JP-5/JP-8
• Starting/altitude relight	superior	acceptable
• Liner cyclic life	short – less than 500 cycles to first repair	long – greater than 1200 cycles to first repair

Table 3 Key properties of test fuels

Fuel number	Fuel description	Hydrogen content, weight %	Aromatic content, volume %	Naphthalenes content, volume %	Kinematic viscosity at 294.3 K, mm²/s
1	JP-4	14.5	10.0	0.5	0.96
2	JP-4/2040[a] blend	12.0	41.7	24.5	1.21
3	JP-4/2040 blend	13.0	27.7	13.7	1.07
4	JP-4/XB[b] blend	12.0	53.5	0.4	0.90
5	JP-4/XB blend	13.0	35.3	0.4	0.91
6	JP-4/XB/GMSO[c] blend	14.0	15.4	0.5	1.11
7	JP-8	13.9	13.2	1.9	2.23
8	JP-8/GMSO blend	13.9	12.8	1.8	2.45
9	JP-8/2040 blend	11.9	38.9	22.0	2.13
10	JP-8/XB blend	13.0	31.3	1.6	1.69
11	JP-8/XB blend	12.0	52.2	0.8	1.24
12	JP-8/2040 blend	13.0	26.0	11.9	2.17
13	No. 2 diesel	13.1	21.6	7.5	3.27

[a]2040 solvent, a naphthalene concentrate (dicyclic aromatics)
[b]Xylene bottoms, monocyclic aromatics blend
[c]Gulf mineral seal oil, a predominately paraffinic white oil

about 13.0 percent, including the Number 2 diesel fuel, were intended to be representative of petroleum-derived or oil shale-derived products. The fuels with hydrogen contents of about 12.0 percent were primarily intended to be representative of coal-derived fuels. At each of these nominal hydrogen content values, an aromatic content range of about 10 percent was encompassed by the selected blends, as is shown in Table 3.

Test Methodology

The experimental investigations consisted of single combustor tests. Both combustors were tested in the same test rig, over the same ranges of engine operating conditions. The test rig duplicates the combustor flow path of the engine. In each test series, evaluations were conducted at both high-pressure and ground starting/altitude relight operating conditions, which exactly duplicate the actual engine operating conditions. The test conditions and measured combustion parameters are summarized in Tables 4 and 5, respectively.

In the high-pressure tests, both combustors were instrumented with the same inlet air temperature/pressure probes and exit gas temperature/pressure/sampling probes. Flame radiation levels were determined with a total-radiation pyrometer, which was positioned in one of the cross-ignition tubes. Emission levels were determined with standard smoke and gaseous emission analyzers. Inner liner metal temperatures were measured with an array of 24 thermocouples, which were positioned at various radial and circumferential locations. For the starting/relight tests, the combustors were instrumented with thermocouples to detect lightoff and blowout.

Test/Analysis Results

Experimental evaluations of both combustors were conducted with all 13 test fuels. In addition, a repeat test of each combustor with the baseline JP-4 fuel was conducted. Collectively, the results of these 28 individual tests provide a detailed comparative assessment of the effects of fuel property variations on the performance and operating characteristics of the two test combustors.

In any combustor, decreases in fuel hydrogen content — and the associated increases in fuel aromatic content — can generally be expected to have adverse impacts on several combustor performance characteristics. Also, decreases in fuel volatility/fluidity can generally be expected to adversely affect starting, altitude relight, and other low power performance characteristics. These general trends, which are discussed in more detail in [6], are summarized in Table 6. The results obtained in the two J79 combustor investigations are very consistent with these general trends.

As expected, the exit temperature distribution characteristics of the two J79 combustors were found to be insensitive to fuel property variations. Except for a small effect at the idle operating condition in the case of the J79-17C combustor, their CO/HC emission levels — and, thus, their combustion efficiency characteristics — were also found to be insensitive. Large decreases in fuel volatility/fluidity were found to result in small increases in the CO levels of the J79-17C combustor at the idle operating condition. Its HC level at this operating condition was essentially the same with all test fuels. With respect to NO_x emissions, similar and relatively minor increases were observed with both combustors as fuel hydrogen content was decreased. The magnitudes of these small increases were found to be directly related to the impacts of fuel hydrogen content on the calculated stoichiometric flame temperatures of the various test fuel-air mixtures.

The test fuel property variations were, however, found to

Table 4 Combustor test conditions

Elevated pressure tests	Low-pressure tests
• Ground idle	• Ground starting - standard day
• Takeoff	• Ground starting - cold day
• Subsonic cruise	• Altitude windmilling
• Supersonic dash	

Table 5 Measured combustor performance/operational parameters — at each test condition

Elevated pressure tests	Low-pressure tests
• Combustor pressure drop	• Lightoff fuel-air ratio
• Combustion efficiency	• Lean blowout fuel-air ratio
• Exit temperature pattern/ profile factors	• Pressure blowout limit (at altitude relight conditions)
• Combustor metal temperatures	
• Combustion flame radiation	
• Carbon deposition/emission tendency	
• Smoke emission level	
• Carbon monoxide (CO) emission level	
• Unburned hydrocarbon (HC) emission level	
• Nitrogen oxides (NO_x) emission level	

Table 6 Typical impact of fuel property variations on current technology combustors

• Due to decreased hydrogen content (increased aromatic content)
  - Increased smoke levels resulting in increased exhaust visibility
  - Increased flame radiation resulting in increased combustor/turbine metal temperatures
  - Increased carbon formation/deposition resulting in increased combustor hot streaking/pattern factors and increased turbine erosion
  - Increased NO_x levels

• Due to decreased fuel volatility/fluidity
  - Decreased engine starting/relight capabilities
  - Increased CO/HC levels

significantly influence several other important performance and operating characteristics of the two combustors at some test conditions. In most instances, the magnitudes of these fuel property effects on the two combustors were considerably different. The following is a summary comparison of these significant fuel property impacts.

Smoke Levels. Consistent with results obtained in previously conducted tests, the highest smoke levels of both combustors were measured at the takeoff operating condition. The measured smoke level-fuel hydrogen content relationships at the takeoff operating condition are compared in Fig. 4. As is shown, decreases in fuel hydrogen content resulted in large smoke number increases in both combustors. The J19-17A combustor was found to be slightly more sensitive than the J79-17C combustor. As a result, its already high smoke levels with JP-4 fuels were significantly increased with lower hydrogen content fuels. Although generally higher with low hydrogen content fuels, the smoke levels of the J79-17C combustor were relatively low with all but one of the test fuels. As such, only minor smoke visibility problems, if any, would be expected in the J79-17C engine with low hydrogen content fuels.

Flame Radiation Levels. The observed effects of fuel hydrogen content on flame radiation levels at the takeoff operating condition are compared in Fig. 5. In the case of the J79-17A combustor, considerable data scatter was obtained due to soot deposition on the viewing window, which was located in the cross-ignition tube. However, consistent with
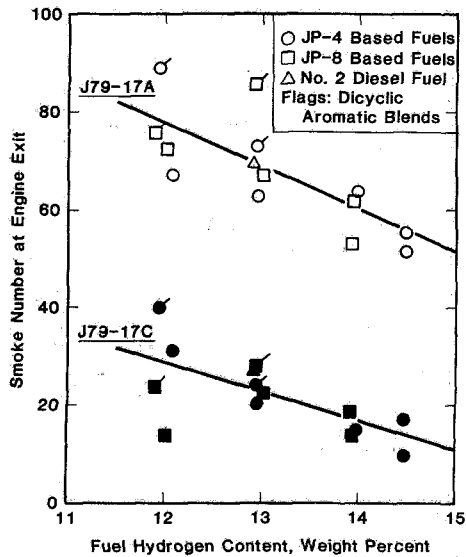
Fig. 4 Comparison of smoke emission levels at nonaugmented takeoff condition
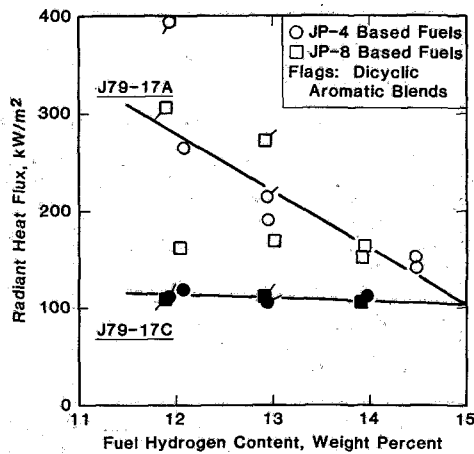
Fig. 5 Comparison of flame radiation levels at nonaugmented takeoff condition
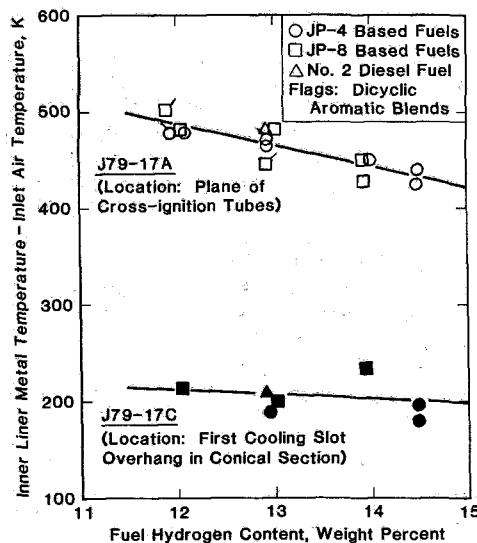
Fig. 6 Comparison of metal temperature at life limited locations within inner liner and at nonaugmented takeoff condition
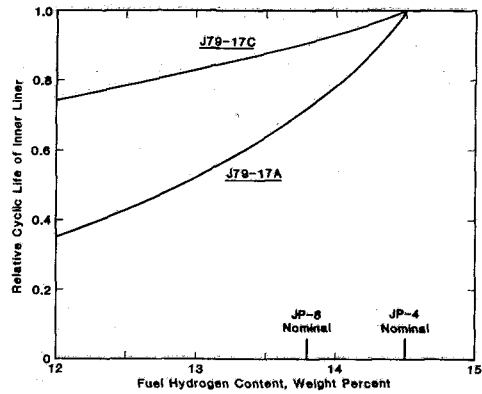
Fig. 7 Comparison of predicted effects of fuel hydrogen content on inner liner cyclic life characteristics

the smoke characteristics of the two combustors, the radiation levels of the J79-17A combustor with all fuels were found to be significantly higher than those of the J79-17C combustor and to be strongly affected by fuel hydrogen content. Only a minor sensitivity was observed in the J79-17C combustor, indicating that its radiation characteristics are essentially non-luminous even with the low hydrogen content fuels.

Inner Liner Metal Temperatures. Some of the observed effects of fuel hydrogen content on inner liner metal temperatures, at the takeoff operating condition, are compared in Fig. 6. In both cases, these data are the peak temperatures measured at the axial station where the low cycle fatigue life of the inner liner is limiting. In the case of the J79-17A combustor, this location is in the plane of the cross-ignition tubes. In the J79-17C combustor, it is the first film cooling slot overhang in the conical section of the dome/inner liner subassembly. Consistent with the smoke and flame radiation results, decreases in fuel hydrogen content were found to result in somewhat larger metal temperature increases in the J79-17A combustor than in the J79-17C combustor. As is also shown in Fig. 6, the measured metal temperatures of the J79-17A combustor with any fuel were substantially higher. The generally lower metal temperatures of the J79-17C combustor inner liner are due to its advanced cooling and construction features. Similar data trends, with regard to fuel hydrogen content effects and to the generally lower metal temperatures of the J79-17C combustor, were observed at all other inner liner temperature measurement stations.

Inner Liner Life Characteristics. The cyclic life capabilities of the two inner liners were calculated with the use of the inner liner metal temperature data, especially the data shown in Fig. 6, and the stress/cyclic life analysis methods described in [7] and [8]. These results, expressed in terms of cyclic life relative to the cyclic life obtainable with typical JP-4 fuels, are compared in Fig. 7. As is shown, the predicted effects of fuel hydrogen content decreases are much larger in the J79-17A combustor than in the J79-17C combustor. These findings are quite consistent with the flame radiation results and the associated inner liner metal temperature results. These life estimates indicate that a 50 percent reduction in the inner liner life of the J79-17A combustor can be expected with a fuel hydrogen content reduction from that typical of JP-4 (14.5 percent) to a value of about 13.0 percent.

Carbon Deposition/Emission Tendencies. In both test series, efforts were made to quantify carbon deposition/emission tendencies. Carbon formation/deposition tendencies were qualitatively assessed by visual observations of the dome/inner liner parts. The emission rates of this deposited carbon were also measured. However, the same

Table 7 Summary of key findings

Combustor performance/ operating parameter	Predominate fuel property effect (both combustors)	Magnitude of effect	
		J79-17A combustor	J79-17C combustor
• Exit temperature distribution	none	none	none
• smoke emission level		large	moderate - but no significant visibility increase
• flame radiation level	increase with decreased fuel hydrogen content	large	small
• carbon deposition/emission tendency		moderate	small
• NO$_x$ emission level		small	small
• Inner liner cyclic life	decrease with decreased fuel hydrogen content	large	moderate
• Ground starting capability	decrease with decreased fuel volatility/fluidity	moderate	moderate
• Altitude relight capability		none measurable	small-at most flight conditons
• CO/HC emission levels	increase with decreased fuel volatility/fluidity	none	small
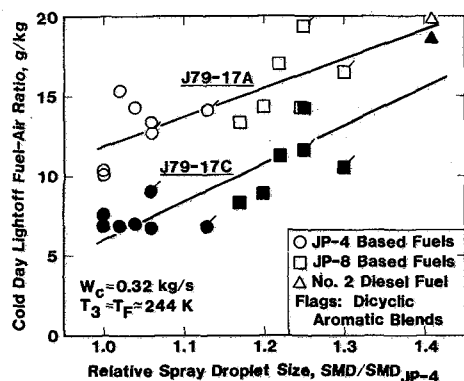
Fig. 8 Comparison of cold day ground start characteristics

Fig. 9 Altitude relight limits of J79-17C combustor

techniques for measuring these rates were not used in the two investigations. Direct comparisons of these quantitative results are, therefore, not possible. In general, the observed carboning tendencies and emission rates were much greater in the J79-17A combustor than in the J79-17C combustor. No significant deposition in the J79-17C combustor was observed with any of the test fuels and its carbon emission rates were very low.

Ground Start Characteristics. Some typical results on the effects of fuel volatility/fluidity variations on the cold day ground start characteristics of the two combustors are compared in Fig. 8. In this comparison, volatility/fluidity variability is expressed in terms of a relative Sauter Mean Diameter (SMD) parameter. This parameter consists of a test fuel-to-reference fuel SMD ratio at a constant fuel flow rate. In the case of the Fig. 8 ratios, the applicable fuel flow rate is that required for lightoff with the JP-4 test fuel. As is discussed in [7] and [8], the SMD is an indicator of fuel atomization quality and is calculated with the use of the relevant fuel physical properties — viscosity, surface tension, and density. Because the fuel flow rates at lightoff conditions are very low, only the fuel nozzle primary circuit of each test combustor was operative in these starting tests. The Fig. 8 SMD ratios for both combustors were therefore calculated with a spray droplet size equation for pressure-atomizing nozzles. As is shown in Fig. 8, both combustors were found to be similarly affected by increases in SMD ratio and thus by decreases in fuel volatility/fluidity. With most of the test fuels, the observed lightoff characteristics of J79-17C combustor were appreciably better than those of the J79-17A combustor. This difference is primarily due to the better fuel atomization quality provided by the J79-17C fuel nozzle at low fuel flow rates, due to the smaller flow number of its primary circuit.
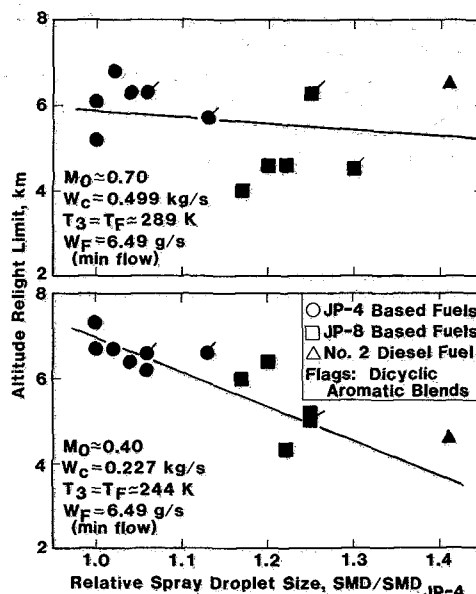
Altitude Relight Characteristics. Because of its low dome airflows and associated rich dome fuel-air ratios, the J79-17A has superior altitude relight capabilities. No effects of fuel property variations on these capabilities were observed because, with all of the test fuels, these capabilities were beyond the low pressure limits of the test facility. In the case of the J79-17C combustor, small-to-moderate effects of fuel volatility/fluidity variations were observed at some flight altitude-Mach number combinations. Some typical results are presented in Fig. 9.

Concluding Remarks

A summary of the key test findings is presented in Table 7. Because of the back-to-back nature of the two series of combustor tests, direct comparisons of the results can be made — thereby, providing specific comparative assessments of the broadened property fuel accommodation capabilities of an older technology combustor design relative to those of a modern technology design.

As is shown in Table 7, the modern technology configuration is significantly more tolerant of fuel property variations than the older technology configuration — especially at high power operating conditions. The relative insensitivity of its smoke levels, flame radiation levels, and carbon deposition/emission tendencies to decreases in fuel

hydrogen content are attributed to its lean-burning primary zone at the high power operating conditions. The relatively small adverse impact of reduced fuel hydrogen content on inner liner life is also attributed to this lean-burning feature — as well as to the advanced cooling and structural design features embodied in the inner liner of the J79-17C combustor.

With regard to ground starting capabilities, both combustors exhibited similar sensitivities to decreases in fuel volatility/fluidity. In both combustors, these effects were found to be relatively small, except with Number 2 diesel fuel in the case of the J79-17C combustor. This generally small sensitivity of the J79-17C combustor, in spite of its lean-burning design feature, is attributed to the excellent atomization quality provided at low fuel flows by its advanced fuel nozzle configuration. As expected, the altitude relight capabilities of the rich-burning J79-17A combustor are not appreciably affected by decreases in fuel volatility/fluidity. However, even with the lean-burning J79-17C combustor, these effects were found to be relatively small.

Based on these comparative assessments, it is concluded that combustors with modern technology features — especially advanced smoke abatement features and advanced liner cooling/construction features — can generally be ex-

pected to be more tolerant of fuel property variations than older technology combustors. Accordingly, current and future engines, equipped with such modern technology combustors, can generally be expected to have appreciably better capabilities for accommodating lower quality jet fuels than engines with older technology combustors.

References

1 Longwell, J. P., "Jet Aircraft Hydrocarbon Fuels Technology," NASA CP-2033, Jan. 1978.

2 Churchill, A. V., Delany, C. L. and Lander, H. R., "Future Aviation Turbine Fuels," AIAA Paper 78-268, Jan. 1978.

3 Rudey, R. A., and Grobman, J. S., "Characteristics and Combustion of Future Hydrocarbon Fuels, NASA TM-78865, Oct. 1978.

4 "Aircraft Research and Technnology for Future Fuels-Symposium Preprint," NASA Lewis Research Center, Apr. 1980.

5 Jackson, T. A., "The Evaluation of Fuel Property Effects on Air Force Gas Turbine Engines—Progam Genesis," ASME Paper 81-GT-1, Mar. 1981.

6 Bahr, D. W., "Impacts of Broadened-Specification Fuels on Aircraft Turbine Engine Combustors," ASME Paper 81-GT-2, Mar. 1981.

7 Gleason, C. C., Oller, T. L., Shayeson, M. W., and Bahr, D. W., "Evaluation of Fuel Character Effects on J79 Engine Combustion System," AFAPL-TR-79-2015, Apr. 1979.

8 Gleason, C. C., Oller, T. L., Shayeson, M. W., and Kenworthy, M. J., "Evaluation of Fuel Character Effects on J79 Smokeless Combustor," AFAPL-TR-80-2092, Nov. 1980.

R. M. Himes
Research Assistant.

R. L. Hack
Research Assistant.

G. S. Samuelsen
Professor.
Mem. ASME

UCI Combustion Laboratory,
Mechanical Engineering,
University of California,
Irvine, Calif. 92717

Chemical and Physical Properties of Soot as a Function of Fuel Molecular Structure in a Swirl-Stabilized Combustor

Soot samples were extracted from a swirl-stabilized, liquid-fuel fired laboratory combustor to (i) assess the validity of the ASTM smoke point test in predicting the sooting characteristics of fuels in complex combustion systems and (ii) assess the effect of fuel molecular structure and smoke suppressant additives on the physical and chemical properties of soot. Fuels utilized were shale JP-8, iso-octane, and blends of iso-octane with either decalin, toluene, tetralin, or 1-methylnaphthalene such that smoke points similar to JP-8 were achieved. Each fuel was separately blended with 0.05 percent (by weight) ferrocene smoke suppressant. The results indicate that the ASTM test can be misleading, increased fuel molecular complexity increases soot content of higher molecular weight polycyclic aromatics, and ferrocene additive reduces small particle number density but not necessarily the soot mass loading.

Introduction

With the continued consumption of petroleum resources outpacing discovery, the use of fuels derived from shale and coal is evolving as a practical alternative for jet fuels. Liquid synfuels, however, are typically less volatile and have a lower hydrogen content than petroleum fuels due to their higher aromaticity. The net result is an increased propensity of liquid synfuels to form soot with an attendant increase in flame radiation, deposit of carbonaceous material, and emission of particulate. The widespread use of these synfuels in aircraft propulsion and power generation systems will depend on overcoming the propensity of these fuels to form soot. Approaches under consideration to reduce this soot production include the future development of fuel-flexible gas turbines through combustor modification and the use of smoke suppressant fuel additives for the current generation of gas turbines.

Two questions arise in the resolution of problems associated with the use of liquid synfuels in complex (i.e., recirculating and turbulent) flows typical of gas turbine combustors. First, what are the mechanisms responsible for soot formation and burnout in complex flows? Such information could provide direction for the use of additives in suppressing the soot production in existing engines and identify paths for combustor modification in next generation gas turbines. Second, what methods are appropriate for testing the sooting propensity of fuels in complex flows? In

particular, is the ASTM-D1322 smoke point [1] method a suitable or meaningful test of sooting propensity of jet fuels?

The current interest in the mechanisms of soot formation and burnout is directed to both simple and complex flows, and the results from recent studies are beginning to identify the correspondence between sooting, and fuel properties and flame conditions. For example, in simple diffusion flames, the flame temperature is asserted to be the dominant parameter affecting sooting propensity with fuel molecular structure playing a role only as it affects the flame temperature [2]. In complex flows, the evidence is not yet sufficient to assess the causal/effect relationships. On one hand, soot production has been found to correlate with fuel hydrogen content in a practical combustor [3]. However, an influence of fuel molecular structure has been reported with fuels containing high concentrations of polycyclic aromatics [4]. And the role of aerodynamics in complex flows as it relates to both soot production and perturbation of diagnostics employed for soot measurements is just now being addressed [5].

The soot measurements employed in the conduct of these studies include the gross weight emission and flame radiation. Additional measurements will be both desirable and necessary if the mechanisms governing the formation and burnout of soot in complex flows are to be resolved. In particular, measurements of both the physical properties of soot (e.g., size and morphology) and the chemical properties of soot (e.g., polynuclear aromatic content) are required to assess (i) the chemical mechanisms active in the production of soot, (ii) the radiative properties of the soot, and (iii) the environmental impact associated with the emission of the soot.

Journal of Engineering for Gas Turbines and Power   JANUARY 1984, Vol. 106 / **103**

Copyright © 1984 by ASME

Downloaded 01 Jun 2010 to 171.66.16.70. Redistribution subject to ASME license or copyright; see http://www.asme.org/terms/Terms_Use.cfm

Fig. 1 ASTM smoke point tests

Table 1 Fuel summary

Fuel		Smoke point[a] mm	H wt. %
Iso-octane		43.0	15.79
Shale JP-8		23.0	13.89[b]
Blend 1	86% decalin		
	14% iso-octane	24.3	13.35
Blend 2	21% toluene		
	79% iso-octane	24.0	14.02
Blend 3	8% tetralin		
	92% iso-octane	25.3	15.06
Blend 4	5% 1-methylnaphthalene		
	95% iso-octane	22.2	15.16

[a] Distance above base of burner at which sooting first occurs
[b] Wright Patterson AFB

Fig. 2 Combustor configuration

One element of the present study is directed to the acquisition of these data.

The second element of the present study addresses the ASTM-D1322 method historically used to establish the sooting propensity of aviation fuels. Because of the substantial differences in aerodynamics between the ASTM method (which employs a laminar diffusion flame) and a gas turbine (which features a complex flow), the reliability of the method for predicting the relative smoking intensity of different fuels in gas turbine combustors has, for some time, been open to question (e.g., [6]). The advent of syncrudes and their attendant propensity to form soot is renewing interest in this question. Although smoke point has been found to correlate with flame radiation in a practical combustor operated with different fuels [7], gravimetric data must also be obtained for a variety of fuel types, combustor configurations, and combustor operating conditions before the adequacy of the ASTM smoke point method can be fully assessed.

Objectives

The objectives of this study were to assess:

• The effect of fuel molecular structure and the smoke suppressant fuel additive ferrocene on the chemical and physical properties of soot in complex flows
• The validity of the ASTM method in predicting the smoke point of turbine fuels in complex flows

Approach

The present study employed six liquid fuels of varying molecular structure operating in a swirl-stabilized, spray-atomized combustor. Iso-octane served as the baseline fuel as it represents a major component of JP-8 and serves as the reference fuel in the ASTM smoke point test. The five remaining fuels consisted of shale-derived JP-8 and mixtures of iso-octane with either decalin (decahydronaphthalene), toluene, tetralin (1, 2, 3, 4 tetrahydronapthalene), or 1-

methylnaphthalene. The amount of hydrocarbon blended with the iso-octane was selected to yield the same ASTM smoke point as that attained with the shale derived JP-8. The choice of the pure hydrocarbon liquids represented both a broad variation in fuel molecular structure and classes of compounds found in petroleum and synthetic fuels.

The amount of each compound blended with iso-octane was determined by first preparing a curve of smoke point versus volume percent iso-octane (Fig. 1). Table 1 summarizes the composition and the actual smoke point found for each blend. The smoke points, while not exact, are well within the achievable accuracy of the smoke point test (± 1mm) shown by the error bands in Fig. 1.

Each fuel was injected as a liquid spray into a complex-flow laboratory combustor. Soot samples were obtained using an extractive probe and subsequently analyzed to determine weight concentration, chemical composition, and morphology. In a second series of tests, a soot suppressant additive (ferrocene) was mixed with each fuel to assess the effect on sooting propensity as a function of fuel molecular structure. A single ferrocene additive concentration of 0.05 percent by weight was selected based on data in Naval Air Propulsion Test Center reports [8] and work conducted by Moses and Naegeli [9].

Facility

The combustor (Fig. 2) was comprised of a quartz tube with an i.d. of 80 mm (3.15 in.). Fuel was injected at the face of a centerbody with a flush-mounted, twin-fluid atomizer (Spraying Systems J-Series, 2050 Fuel Cap, 67147 Air Cap). To create a toroidal recirculation zone, and thereby centralize and remove the region of soot formation from the effect of solid boundaries, swirl vanes with a turning angle of 60 deg (swirl number of 1.4 as calculated in [10]) were located 41.3 mm (1.6 in.) upstream of the centerbody face. The length of the quartz tube was arbitrarily selected at 1.22 m (48.0 in.).

The combustor was operated in the present study at a reference velocity of 15 m/s, an overall equivalence ratio of 0.2, and at atmospheric pressure. The rationale for this rests with the interest in (i) establishing a record of soot production performance at a base condition of atmospheric pressure, and

Fig. 3 Extractive probe

Table 2 Gravimetric results

Fuel	Smoke point mm	Weight concentration[a] mg/m^3
Iso-octane	43	1.06
86% decalin 14% iso-octane	24.3	5.37'
21% toluene 79% iso-octane	24.0	6.74
8% tetralin 92% iso-octane	25.3	4.10'
5% 1-methyl-napthalene 95% iso-octane	22.2	5.12
Shale JP-8	23.0	23.52

[a] Average of two determinations except where noted with (')
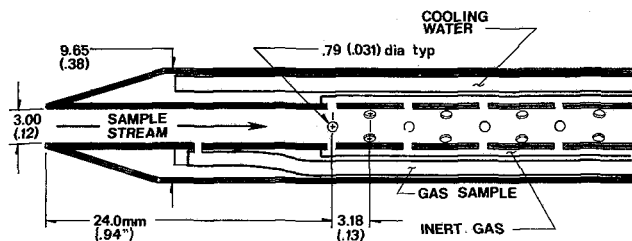
(ii) comparing sooting propensity between the ASTM-D1322 smoke point test and a complex flow at a common pressure, the magnitude of which is fixed by the ASTM method.

The sample probe used in this study (Fig. 3) was of stainless steel construction with an overall o.d. of 9.5 mm (3/8 in.) and a 3.0 mm (1/8 in.) i.d. sampling tube. The overall length of the probe was 616 mm (24 1/4 in.), including a large radius bend of 508 mm (20 in.) to clear the combustor exhaust stream. The probe was water cooled to approximately 40°C and was fitted with a gas sampling port for gas analysis and a set of inert gas injection ports. The purpose of the inert gas was to dilute the mixture and thereby quench reactions, lower the dew point of the sample, and prevent deposition of particles along the tube wall. The multiple injection ports served to diffuse the inert gas injection and thereby eliminate any undesirable jetting.

The sample system consisted of a heated sample line leading from the probe to an oven. The oven, heated to 50°C, housed a four-way flow switching valve which permitted sequential filtration between three sample filters and a bypass filter. Two of the filters consisted of 47-mm single stage, Gelman microquartz fiber filters (DOP efficiency of 99.9 percent). These filters were used to collect sample for the weight concentration, chemical, and elemental analysis segments. Downstream of one of the microquartz filters and located outside of the oven was an aluminum chamber containing 20 grams of XAD-2 resin to absorb any vapor phase polycylic aromatic hydrocarbons (PAH). The third filter used two-stage filtration consisting of 47-mm Nuclepore membrane filters with 5.0-μm and 0.2-μm pore size. Nuclepore filters were selected for their adaptability to scanning electron microscopy.

The sampling location selected for the collection of soot was at an axial location x/d = 18 (81.3 cm, 32.0 in.) downstream of the centerbody face and a radial position adjacent to the duct wall 31.8 m (1.25 in.) from the centerline. The axial location was removed sufficiently from the primary zone to avoid any effect of probe perturbation. The radial location was selected to minimize sampling time by locating the probe at the point of peak soot loading, a condition set up by the swirl-induced transport of soot toward the duct wall.

Analysis

Prior to use, the microquartz filters were dried for 1 hr at 400°C to remove any residual organics and absorbed water. They were subsequently stored in a desiccator until required. A electromicrobalance (Cahn Model 26) was used to weigh the filters before and after the sample collection period, with the filters being desiccated for another 24 hrs prior to reweighing to remove any water absorbed during the collection period. The weight concentration was calculated using the following equation:

$$C = \frac{\text{weight gain}}{\text{net sample volume (STP)}}$$

Approximately 2 mg of sample was collected on the

microquartz fiber filter used for PNA analysis. The filter and XAD-2 resin were separately soxhlet-extracted for 20 hrs with 200 ml of methylene chloride. All of the solvents used were distilled in glass purity. The extract was then evaporated to dryness under reduced pressure in a rotary evaporator with the residue resuspended in 10 ml cyclohexane. A dimethylsulfoxide (DMSO) separation scheme [11] was then employed to isolate the PNA component. PNA identification was accomplished with the use of a HP 5830A gas chromatograph and a HP 5992A gas chromatograph/mass spectrometer in conjunction with a J & W 30 M SE-54 capillary column. The column was used in a splitless mode, with an inlet purge of 50:1 and with a helium carrier flow rate of 1 ml/min.

A C-H-N analyser (Perkin Elmer Model 240B) was used to determine the carbon weight percent of the soot particles before and after the PNA extraction step. For those fuels to which ferrocene was added, an absorption spectrophotometer (Perkin Elmer Model 403) was used to determine the amount of iron incorporated into the soot. As this step was performed after the soxhlet extraction, both the organic extraction and insoluable fraction remaining on the filter were analyzed for iron content. Physical characterization of the particles was conducted utilizing a Hitachi 5-500 scanning electron microscope (SEM).

Results

Physical Properties.

Gravimetric Results. The sooting propensity of the fuels under complex flow conditions are presented in Table 2. The soot weight concentrations of iso-octane and the pure fuel blends were consistent with the sooting propensity indicated by the ASTM method, whereas the soot weight concentration of the chemically complex shale JP-8 was significantly higher (>400 percent) than the soot weight concentrations produced by the fuel blends prepared with a similar smoke point.

The ASTM smoke point tests results obtained with the fuels after the addition of ferrocene are presented in Table 3. The additive resulted in an increase in the smoke point in all cases. However, the effectiveness varied with fuel type.

Under complex flow conditions, the weight concentration results obtained with the ferrocene additive (Table 3) divide into two distinct groups – a general *increase* in the particulate weight concentration (pure iso-octane and the fuel blends), and a substantial *reduction* in particulate weight concentration (shale JP-8). In an effort to explain the weight increase on all but the shale JP-8 samples, the amount of iron present in the collected samples was required.

Table 3 Gravimetric results with ferrocene additive

Fuel	With ferrocene additive			Change in	
	Smoke point mm	Uncorrected weight concentration mg/m^3	Corrected weight concentration^a mg/m^3	Smoke point mm	Weight concentration^b %
Iso-octane	>50	1.98	1.48	+ >7	0
86% decalin 14% iso-octane	28.3	5.65	5.54	+4.0	0
21% toluene 79% iso-octane	26.3	7.80	7.45	+2.3	0
8% tetralin 92% iso-octane	30.0	6.82	6.00	+5.3	+50%
5% 1-methyl- napthalene 95% iso-octane	35	8.40	8.12	+12.8	+50%
Shale JP-8	24.7	9.75	9.22	+1.7	−60%

^{a} Subtracting weight contribution of iron using data of Table 4
^{b} Within accuracy

Table 4 Iron content of samples

Fuel	Soluble fraction (soxhlet extracted) μg	Insoluble fraction μg	Iron corrected to iron oxide mg	Total particulate weight collected mg	Corrected particulate weight^a mg
Iso-octane	<1	166	0.214	1.02	.81
86% decalin 14% iso-octane	<1	191	0.246	2.49	2.34
21% toluene 79% iso-octane	<1	225	0.289	4.47	4.18
8% tetralin 92% iso-octane	<1	223	0.287	3.32	3.03
5% 1-methylnaphthalene 95% iso-octane	<1	402	0.517	5.00	4.48
Shale JP-8	<1	132	0.170	2.66	2.49

^{a} Total particulate weight collected less iron corrected to iron oxide

The fraction of particulate present after the soxhlet extraction was first examined to assess the extent to which iron was organically complexed. The results are presented in Table 4. In all cases, organically complexed iron accounted for less than 1 μg (< 1 percent by weight of the total measured). To assess the amount of iron contained in the nonorganic fraction, the collected sample that remained after the soxhlet extraction was washed in concentrated nitric acid to remove the nonorganic fraction and the weight of iron was determined from atomic absorption spectrophotometry, corrected to iron oxide, and subsequently subtracted from the gross sample weight to yield the true weight of soot collected. The net result, shown in Table 3, was that no significant difference in soot weight concentration was found between the ferrocene and nonferrocene runs with the pure iso-octane, and the decalin and toluene blends. In direct contrast, the soot weight concentration of the tetralin and 1-methylnaphthalene blends increased 50 percent in the presence of ferrocene, and the soot weight concentration of the chemically complex JP-8 decreased 60 percent.

Ferrocene is thought to first be occluded in the soot particle and act in the later regions of the flame by both lowering the ignition temperature of the soot and acting as an oxidizing agent via the mechanism [12]

$$M_x O_y + C(s) \rightarrow CO + M_x O_{y-1}$$
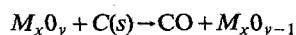
The effect of ferrocene is likely a function of temperature, residence time, and chemical structure of the soot matrix.

Recognizing that, in the present study, the temperature field and residence times remain relatively uniform between the different runs (as a result of the consistency in aerodynamics and narrow range of fuel heating values), the gravimetric results suggests that the effect of the ferrocene additive is strongly tied to the chemical structure of the soot matrix which, in turn, is tied to the fuel molecular structure.

Morphology (SEM Analysis). Typical results of the scanning electron microscope (SEM) analysis of the Nuclepore filter samples are shown in Fig. 4. Only the second stage (0.2-μm) filters are shown, as the first stage (5.0-μm) filters experienced no deposition.

All the soot collected was 0.5-1.0 μm agglomerates with either lacy chain or semispherical structure comprised of smaller, individual 0.05-0.1 μm spherules. This is consistent with the structure and size observed in full-scale combustor studies [13, 14], as well as in small-scale lab combustors [6].

The effect of the ferrocene additive becomes apparent upon close examination of Fig. 4. Note the reduction of the number density of the small particulate ($d < 0.1$ μm) in the presence of the additive. A decrease in the number of smaller particles is expected as these would be the first to burnout if, in fact, ferrocene acts to reduce the ignition temperature for oxidation. Such a decrease is also consistent with ferrocene additive studies in full-scale jet engines in which reductions in the number density of small particles have been observed [8].

The SEM results are consistent with and help to interpret
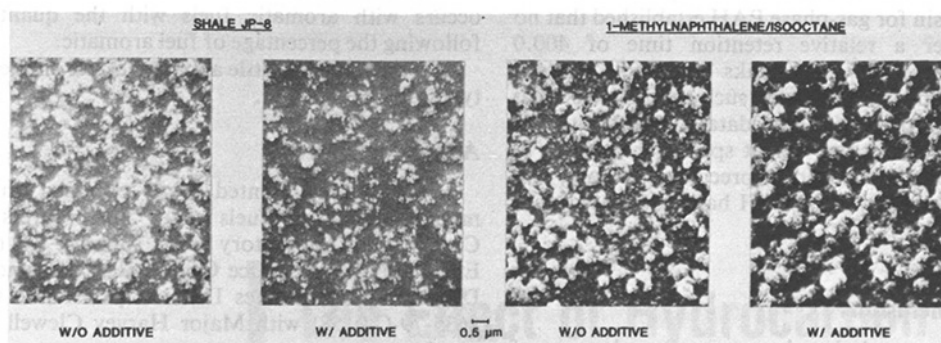
Fig. 4 Particulate morphology

Table 5 Soot PAH content

Compound name	Retention indices[a]	Isooctane w/o add.	Isooctane w/f add.	86% decalin 14% isooctane w/o add.	86% decalin 14% isooctane w/f add.	21% toluene 79% isooctane w/o add.	21% toluene 79% isooctane w/f add.	8% tetralin 92% isooctane w/o add.	8% tetralin 92% isooctane w/f add.	5% 1-methyl % isooctane w/o add.	5% 1-methyl % isooctane w/f add.	JP-8 w/o add.	JP-8 w/f add.
Naphthalene	200.00		(3.8)[g]			(0.8)	(0.8)						
	$206.67 \pm .14^{b}$	(4.2)		(0.7)		(0.3)				(0.4)			
	$252.73 \pm .25^{c}$					(0.2)	(1.1)						
	$285.98 \pm .29^{c}$		(50.2)		(8.8)		(11.6)		(0.7)				
	$290.98 \pm .01^{c}$		(3.7)				(0.6)						
	$298.75 \pm .24^{c}$				(4.4)								(3.3)
Phenanthrene	300.00		(63.0)			(7.1)				(1.0)			
	303.32 ± 0^{c}												(0.5)
	$318.15 \pm .09^{c}$				(6.4)		(10.6)						
	$343.79 \pm .0^{c}$						(0.8)						
	$348.77 \pm .11^{c}$		(6.0)		(1.0)		(0.6)						
	$396.90 \pm .20^{d}$					(1.4)	(1.4)	(1.4)	(1.3)	(1.7)	(1.4)	(0.9)	(1.8)
Chrysene	400.00		(39.0)		(3.9)	(4.4)	(2.2)	(1.0)		(0.6)			(4.0)
	$407.40 \pm .04^{d}$											(0.2)	
	445.99 ± 0^{d}					(0.6)							
	$451.47 \pm .19^{e}$							(0.7)					
	$452.99 \pm .21^{e}$	(4.0)				(3.8)	(0.9)	(5.1)	(1.4)	(2.0)	(1.7)	(0.8)	
	483.56 ± 0^{e}				(1.6)								
	$491.69 \pm .13^{e}$					(1.4)		(1.6)		(0.6)			
Benzo[ghi] Perylene	500.00	(5.5)	(20.3)		(2.6)	(4.7)	(2.0)	(4.3)	(2.8)	(2.2)	(1.5)	(0.4)	(2.7)
	$503.18 \pm .15^{e}$					(0.7)		(1.9)		(0.6)			

[a] Retention indices are the relative positions of the compounds retention times to the PAH Standards. The PAH standards are assigned values corresponding to the number of aromatic rings in the standard.
[b] Reported as naphthalene equivalent
[c] Reported as phenanthrene equivalent
[d] Reported as chrysene equivalent
[e] Reported as benzo[ghi]perylene equivalent
[f] DMSO separation procedure not carried out on these runs (no interfering aliphatic peaks).
[g] Number in parenthesis = μ g PNA/mg Soot/M^3 recovered; blank indicates no evidence of species

the gravimetric data of Table 3. The weight concentration will primarily depend on agglomerate size and number density with little effect exerted by the number density of the small particulate. As a result, the effect of ferrocene on weight concentration (Table 3) should be reflected by the effect of ferrocene on the agglomerate. This is, in fact, the case. The ferrocene had little impact on the size and number density for iso-octane and the decalin and toluene blends. The soot agglomerates of the JP-8, however, were substantially reduced in size (Fig. 4), which corresponds with the reduced weight concentration found with the presence of the ferrocene. The agglomerate size as well as the number density were substantially increased in the case of the double-ring fuel blends, tetralin, and 1-methynapthalene, which again parallels the gravimetric data.

Chemical Properties. Gas chromatographic analysis of the methylene chloride extracts identified the presence of a variety of polycyclic aromatic hydrocarbons (PAH) in the extracted soot samples. In order that the peaks from different chromatograms could be interrelated with this and future studies, relative retention indices scheme developed for PAH was used [15]. A tabulation of the compounds found with the various fuels is presented in Table 5. The presence of aromatic groups in the fuel is shown to carry over to the chemical structure of the soot matrix. For example, the toluene blend (21 percent by volume) contained the largest amount of aromatics which is reflected in the amount of PAH found with the soot. A trend toward higher molecular weight PAH is also evident with an increase in the complexity of the fuel molecular structure (reading table from top left to bottom right).

Integration of the chromatographic peaks and calibration with known amounts of four PAH allowed a quantitative determination of the PAH present. It is noteworthy that small quantities of high molecular weight PAH are present with even iso-octane and decalin, although there are far fewer species present at a significant level ($> 1~\mu$g). The presence of the ferrocene additive had little effect on the quantities and types of PAH present.

Analysis of the resin for gas-phase PAH established that no peaks evolved after a relative retention time of 400.0 (chrysene). The majority of peaks evolved between naphthalene and phenanthrene in such abundance that resolution was compromised. These data suggest that (i) a large number of low molecular weight species are present in the vapor phase, possibly as residual precursors to soot, and (ii) all the high molecular weight PAH have condensed onto the soot particulate.

Summary and Conclusions

The present study was designed to assess the adequacy of the ASTM smoke point method in characterizing the sooting propensity of fuels in complex flows, and to initiate an impact assessment of fuel molecular structure on the physical and chemical properties of soot. The conclusions derived from the results are as follows:

1 The ASTM smoke point method can be misleading in the prediction of the smoking tendency associated with fuels burned in complex flows. Mixtures of pure aromatic hydrocarbons in iso-octane, blended to produce the same ASTM smoke point as shale JP-8, produced similar soot loadings in a complex flow. The chemically complex JP-8, however, produced soot concentration a factor of four higher in the same flow. The inconsistency between the ASTM test and the complex flow results is attributed to the dependency of sooting on flame temperature and residence time on the one hand, and the role of aerodynamics dictating the turbulent diffusion of oxygen, the temperature field, and distribution of residence times in a complex flow field.

2 The ASTM smoke point failed also to predict the effect of a ferrocene additive in the complex flow. The smoke point increased for all fuels and blends tested indicating a reduction in soot propensity. In the complex flow, the ferrocene additive was found to be effective in reducing only the soot concentration of shale JP-8. In the remaining cases, ferrocene had either no effect or a significant adverse effect. The chemical structure of the soot matrix appears to govern the effectiveness of the iron additive in oxidizing the soot.

3 The soot morphology exhibited the classical size (0.5–1.0 μm) and structure (agglomerates of 0.05–0.1 μm). In the presence of ferrocene, the number density of the smaller particles was reduced. The effect of ferrocene on the agglomerates, however, depended on fuel type. For the chemically complex JP-8, the size of agglomerates was reduced. For two double-ring aromatic blends, both the agglomerate size and number density were increased with an associated impact on weight concentration.

4 A greater proliferation of PAH species in the soot occurs with aromatic fuels with the quantities of PAH following the percentage of fuel aromatic.

5 Ferrocene has little apparent effect on the quantities and types of PAH present.

Acknowledgment

References

1 "Standard Method of Test for Smoke Point of Aviation Turbine Fuels," ASTM Designation: D 1322-75, *1975 Annual Book of ASTM Standards*, pt. 17, Philadelphia, American Society for Testing and Materials, 1975.

2 Glassman, I., and Yaccarino, P., "The Temperature Effect in Sooting Diffusion Flames," *Eighteenth Symposium (International) on Combustion*, The Combustion Institute, 1981, p. 579.

3 Jackson, T. A., and Blazowski, W. S., "Fuel Hydrogen Content as an Indicator of Radiative Heat Transfer in an Aircraft Gas Turbine Combustor," *Gas Turbine Combustion and Fuels Technology*, ASME, New York, Nov. 1977, p. 59.

4 Dodge, L. G., Naegeli, D. W., and Moses, C. A., "Fuel Property Effects on Flame Radiation in Aircraft Turbine Combustors," WSS/CI Paper 80-9.

5 Hack, R. L., Samuelsen, G. S., Poon, C. C., and Bachalo, W. D., "An Exploratory Study of Soot Sample Integrity and Probe Perturbation in a Swirl-Stabilized Combustor," ASME JOURNAL OF ENGINEERING FOR POWER, Vol. 103, No. 10, Oct. 1981, p. 759.

6 Schirmer, R. M., "Effect of Fuel Composition on Particulate Emissions from Gas Turbine Engines, *Emissions from Continuous Combustion Systems*, Plenum Publishing Co, New York, 1972, p. 189.

7 Naegeli, D. W., and Moses, C. A., "Effect of Fuel Molecular Structure on Soot Formation in Gas Turbine Engines," ASME Paper 80-GT-62, presented at ASME Gas Turbine Conference, New Orleans, Mar. 1980.

8 Klarman, A. F., "Evaluation of the Extended Use of Ferrocene for Test Cell Smoke Abatement; Engine and Environmental Test Results," Report No. NAPTC-PE-110, Oct. 1977.

9 Personal communication, May 1981.

10 Beer, J. M., and Chigier, N. A., *Combustion Aerodynamics*, Applied Science Publishers, London, 1972.

11 Natusch, D. F. S., and Tomikins, B. A., "Isolation of Polycyclic Organic Compounds by Solvent Extraction with DMSO," *Analytical Chemistry*, Vol. 50, 1978, p. 1429.

12 Howard, J. B., and Kausch, W. J., Jr., "Soot Control by Fuel Additives," *Progress in Energy and Combustion Science*, Vol. 6, 1980, p. 203.

13 Sawyer, R. F., "Experimental Studies of Chemical Processes in A Model Gas Turbine Combustor," *Emissions From Continuous Combustion Systems*, Plenum Publishing Co., New York, 1972, p. 243.

14 Fenton, D. L., Luebeck, E. H., and Norstrom, E., "Physical Characterization of Particulate Material from a Turbine Engine," ASME Paper 79-GT-179, Presented at the ASME Gas Turbine Conference, San Diego, Mar. 1979.

15 Lee, M. L., Vassilaros, D. L., White, C. M., and Novotny, M., "Retention Indices for Programmed-Temperature Capillary Column Gas Chromatography of Polycyclic Aromatic Hydrocarbons," *Analytical Chemistry*, Vol. 51, 1979, p. 768.

The Effect of Hydrocarbon Structure Upon Fuel Sooting Tendency in a Turbulent Spray Diffusion Flame

T. T. Bowden

J. H. Pearson

Shell Research Limited,
Thornton Research Center,
Chester, England

The sooting tendencies of various hydrocarbon structures have been studied in a model gas turbine combustor at a pressure of 0.35 MPa and a preheated air temperature of 530 K. The results of this study have indicated that the sooting tendencies of fuels containing only single ring aromatics, fused bicyclic saturates, and unsaturated nonaromatics will be related to the overall hydrogen content of the fuel. However, experimental fuel blends with high concentrations (> 20 percent wt) of naphthalenes or tetralins exhibit sooting properties that are dependent upon the presence of such components. It is suggested that a kinetic scheme utilizing aromatic rings as nuclei upon which reactive fragments may stabilize can explain the present results.

Introduction

In recent years the continued growth in the market for aviation fuels coupled with the uncertainty over conventional crude supplies has led to greater interest in the possible use of aviation kerosines derived wholly or partially from unconventional sources. These sources could include oil sands, oil shales, coal, and the products of petroleum residue conversion. It is probable, therefore, that some future aviation fuels may have compositions different from those of present day fuels, consequently it is of importance to determine the effect these different compositions will have upon fuel performance.

The inclusion of fuels derived from nontraditional sources in kerosine streams could increase fuel aromatic content and decrease the fuel hydrogen content. Such changes are expected to promote the formation of soot in the combustion system, leading to increased soot emission and, more importantly, increased radiative heat transfer from the flame to the engine flame tube. The impact of the latter is emphasized by recent studies [1] which indicate that moderate increases in flame-tube temperature may decrease the lifetime of critical engine components. It is, therefore, essential to be able to relate the composition of fuels to their soot-forming properties.

Previous investigations [2,3] concerning the influence of hydrocarbon type upon sooting tendency have indicated the incipient sooting limit (i.e. the air/fuel ratio at which a fuel just begins to produce soot) increases in the following manner.

paraffins $\simeq$ naphthenes < olefins
      < dicycloparaffins < mono-aromatics
                  < naphthalenes

Although these earlier studies have in general concentrated upon laminar diffusion flames or premixed flames and hence cannot be related directly to the conditions prevailing within gas-turbine combustors it is reasonable to assume that the trends observed will give some indication of actual fuel performance.

The above observation that different hydrocarbon classes begin to soot at differing values of air/fuel ratio (AFR) is particularly pertinent to aviation gas turbine performance where engines operate over wide ranges of AFR, from fuel rich at takeoff to fuel-lean during cruise. It is therefore quite possible that not only will the inclusion of unconventional components, beyond the present specification limits, increase soot emissions but they may also produce high concentrations of soot under certain operating conditions which have not previously been conducive to soot formation, e.g., fuel-lean conditions.

Little work has been reported concerning the sooting tendencies of hydrocarbons in the turbulent spray diffusion flames which are usually present in gas turbine combustors. Therefore the influence of air/fuel ratio upon the sooting tendencies of various hydrocarbons has been studied in the Thornton Research Centre high-pressure aviation combustion rig.

The compounds chosen for study were 1-methyl naphthalene, tetralin, dicyclopentadiene, toluene, and decalin. All these hydrocarbons, except for dicyclopentadiene, are likely to be present in greater concentrations in future aviation turbine fuels.

Previous workers [3,4] have suggested that aromatic

compounds soot more easily than nonbenzenoid materials because their six-membered ring structure remains intact during the combustion process, undergoing dehydrogenation and polymerization to form soot. Dicyclopentadiene was chosen because, although it is both cyclic and unsaturated, it does not contain a benzene ring and hence could provide a test of the above hypothesis.

Experimental

The TRC high-pressure aviation combustion rig has been developed specifically in order to study the influence of fuel properties upon combustion performance and consists of three major parts:

The Model Combustor. The combustor is a tubular multi-hole design (i.d. 40 mm, length 150 mm), fabricated from Nimonic 75 alloy. The air inlet hole pattern was determined empirically and provides for complete combustion within the first half of the combustion tube. Flame stabilization is achieved by a swirler installed at the inlet to the combustor, and fuel injection is by either pressure jet or air assist atomizers. The combustion tube is housed in a 50-mm i.d. tubular casing provided with calcium fluoride optical windows which align with three of the air-inlet holes corresponding to the primary, secondary, and dilution zones of the combustor. A diagram of the flame tube is given in Fig. 1.

Preheated Air Supply. Combustion air is preheated by means of an oil-fired heat exchanger capable of heating a maximum of 2.5 kg s^{-1} air to 900 K. Air is supplied by two sources, compressors up to 1.2 MPa and a blowdown facility for higher pressures. The latter system comprises 20 m^3 of air storage at 10 MPa which allows a running time of approximately 60 min at the maximum design pressure of 3 MPa. Air mass flows are determined via turbine meters and digital flow computers. Combustion chamber pressures and air temperatures are controlled automatically via control valves and proportional temperature controllers. A diagram of the rig is shown in Fig. 2.

Instrumentation. The parameters monitored are flame-tube temperatures, flame radiation, and exhaust-soot concentrations. The first of these is determined by a Vanzetti-type 3015 thermal monitor. Thermal radiation emitted from the surface of the flame tube is monitored by six water-cooled fiber optic probes which transmit to pyro-electric detectors; the response of the detectors is then converted into a temperature and displayed. Flame radiation is determined using Moll-type pyrometers which view the flame through the optical ports referred to in section 2.1. Exhaust soot concentration is determined utilizing a Richard Oliver Engine
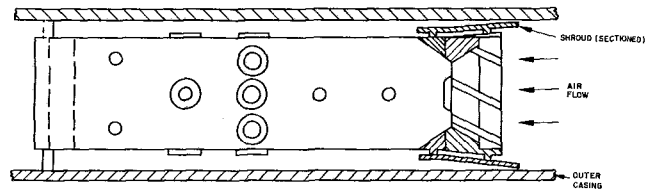
Fig. 1 Small scale flame-tube

1. STORAGE VESSELS
2. HAMWORTHY COMPRESSOR
3. AIR DRYING SYSTEM
4. 1.38 MPa COMPRESSOR
5. 0.4 MPa COMPRESSOR
6. HIGH PRESSURE AIR- REDUCING VALVE
7. SHUT—OFF VALVES (REMOTE CONTROLLED)
8. OVERPRESSURE RELIEF VALVES
9. SHUT—OFF VALVES (MANUAL)
10. AIR FLOW METER
11. AIR HEATER EXHAUST
12. AIR HEATER
13. EXPANSION BEND
14. AIR FLOW CONTROL VALVE
15. EXPANSION BELLOWS
16. SYSTEM PRESSURIZED LAMP
17. 50mm COMBUSTOR
18. 75mm COMBUSTOR

Fig. 2 Schematic arrangement of the small-scale, high-pressure, aviation combustion rig

Smoke Measuring Instrument, model 1023. An air-cooled rake extracts exhaust gases for transmission to the smoke monitor and exhaust gas analysis equipment. This latter equipment measures CO, CO_2, NO_x, and unburnt hydrocarbons.

Originally it was intended to burn the components undiluted. However, as 1-methyl naphthalene did not burn efficiently, in order to include this compound and still be able to draw comparisons between the hydrocarbon types it was necessary to blend each one with Shellsol T (a solvent containing 99 percent C isoparaffins) to a concentration of 1 part test component to 2 parts Shellsol T by weight. Combustion tests using Shellsol T alone produced little or no soot over a wide range of mixture strengths and therefore it was assumed that, although some synergism is likely, any changes in soot formation observed during the experiments were due mainly to the influence of the test hydrocarbon.

In order to determine whether the hydrogen contents of

Table 1 Details of fuels used in experimental program

Fuel component	% by weight in fuel	Hydrogen content % wt	Aromatic content % v	Smoke point (mm)	Naphthalene content % v
1-methyl naphthalene	33	12.65	27.8	13	39.4
1-methyl naphthalene	21	13.69	16.8	18	23.7
Tetralin	33	13.21	29.52	15	—
Tetralin	27	13.70	23.21	17	—
Toluene	33	13.2	36.1	19	—
Toluene	26	13.685	26.15	23	—
Decalin	33	14.75	0.62	34	—
Decalin	78	13.68	0.61	26	—
Dicyclopentadiene	33	13.2*	—	—	—
Dicyclopentadiene	27	13.7*	—	—	—
Jet A1	—	13.77	18.8	27	2.64

*Calculated
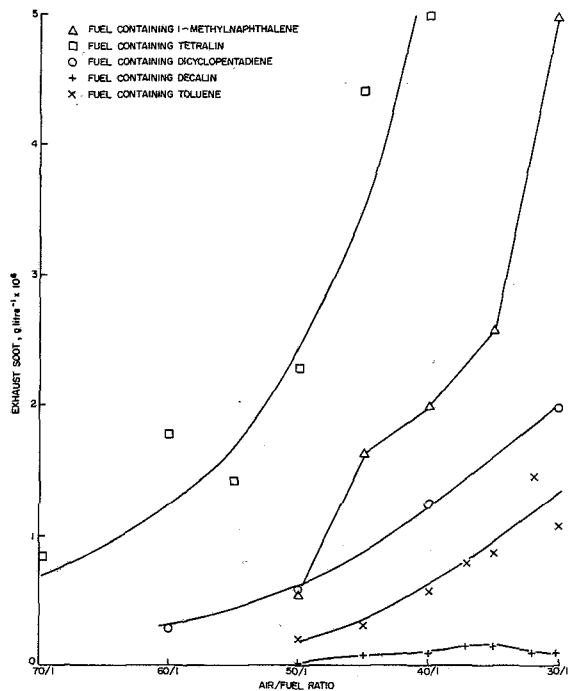
Fig. 3 Exhaust soot concentration versus air/fuel ratio for test hydrocarbons blended with Shellsol T to a ratio of 1 part test hydrocarbon to 2 parts Shellsol T by weight

Fig. 4 Flame radiation versus air/fuel ratio for test hydrocarbons blended with Shellsol T to a ratio of 1 part test hydrocarbon to 2 parts Shellsol T by weight

experimental fuels containing the test hydrocarbons would correlate with their combustion performance, a further set of blends were produced in which Shellsol T and the pure hydrocarbons were blended to the same hydrogen content. The hydrogen content chosen was that corresponding to a standard Jet A1 (13.8 percent wt). These fuels plus the Jet A1 were tested under the same conditions used for the first set of fuels. Details of fuel blends used are given in Table 1.

The blends were burnt in the aviation combustion rig at a pressure of 0.35 MPa and a preheat temperature of 530K. Exhaust soot was collected on glass-fiber filter papers by drawing a portion of the exhaust gas through a trap at a constant rate of 25 litres min^{-1}. Samples of soot were collected for a fixed period of 5 min. The air/fuel ratio in the rig was altered in the range 70/1 to 30/1 and soot was collected at various selected conditions; flame-tube wall temperatures and flame radiation were also measured. The reflectivity of the filter papers was measured and the weight of soot collected was derived from the expression [5]

$$Ms = -\frac{A}{Sp} \ln \frac{Rs}{Rw} \qquad (1)$$

where Ms = mass of soot, (mg)
A = stained area of filter paper, (m^2)
Rs = reflectivity of soot stain
Rw = reflectivity of unstained filter paper
Sp = attenuation coefficient (m^2 mg^{-1})

The parameter Sp has been determined previously at TRC to be 1.5×10^{-2} m^2 mg^{-1}.

Accuracy of Data.   In order to determine the accuracy of the data repeat runs were performed using Jet A1. These experiments indicated that the precision of the data was, to within a 95 percent confidence limit, ± 20 K for flame tube temperature and ± 30 kW m^{-2} for flame radiation. Exhaust soot concentration gave its poorest precision at low soot loadings, due to the difficulty of accurately measuring reflectivities. Precisions of ± 10 percent were determined for soot loadings less than 0.2×10^{-6} g.L^{-1}, at higher loadings the precision was ± 5 percent. The errors were made up of
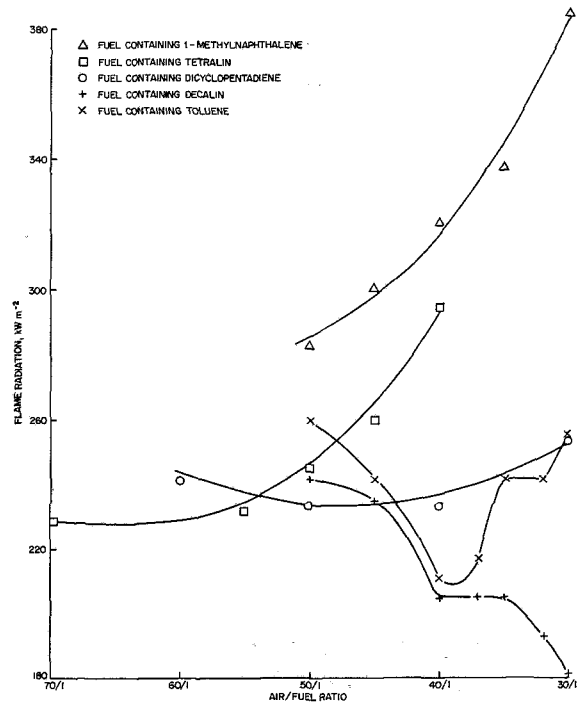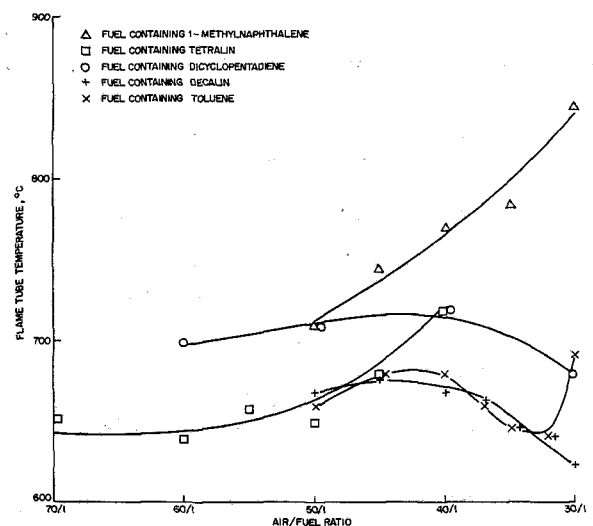
Fig. 5 Flame tube temperature versus air/fuel ratio for test hydrocarbons blended with Shellsol T to a ratio of 1 part test hydrocarbon to 2 parts Shellsol T by weight

within run errors and run to run errors; of the two, the run to run errors accounted for the major source of lack of precision, generally of the order of 80 percent of the total error.

Results

Figures 3-5 show the variation of soot concentration, flame radiation and flame-tube temperatures with air/fuel ratio for the test fuels in which the pure hydrocarbons were blended to the same concentration by weight. Figures 6-8 give the results for the same combustion parameters obtained from the fuels blended to similar hydrogen contents.

Examination of the results for the fuels in which the hydrocarbons were blended to the same concentration in-
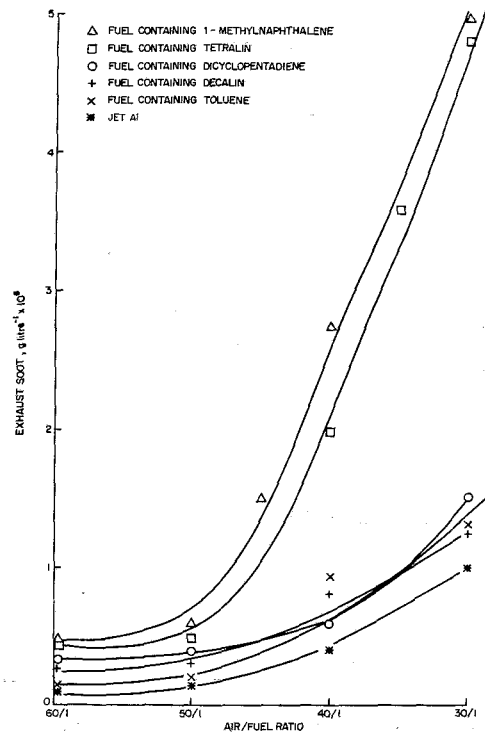
Fig. 6 Exhaust soot concentration versus air/fuel ratio for test hydrocarbons blended to a hydrogen content of ~13.8% wt

Fig. 7 Flame radiation versus air/fuel ratio for test hydrocarbons blended to a hydrogen content of ~13.8% wt

Fig. 8 Flame tube temperature versus air/fuel ratio for test hydrocarbons blended to a hydrogen content of ~13.8% wt

dicate that the sooting tendency of the test hydrocarbons rank as follows:

decalin < < toluene < dicyclopentadiene
< 1-methyl naphthalene < tetralin

The foregoing results show a number of interesting features:

1 Tetralin, although both less aromatic and more hydrogen rich than 1-methyl naphthalene, produces more soot than 1-methyl naphthalene.

2 Dicyclopentadiene, although nonaromatic in nature, produces similar amounts of soot to toluene.

3 Although both dicyclopentadiene and tetralin have the same carbon/hydrogen ratio and the same molecular weight their sooting tendencies differ widely.

4 In general, apart from tetralin, the sooting tendency of the fuels rank in a similar order as do the C/H ratios of the fuels.

5 Broadly, the above comments also apply to the observed variation in flame-tube temperature and flame radiation. However, there are two noticeable differences:

(a) The blends containing 1-methyl naphthalene give higher values of flame radiation and flame-tube temperature than the blends containing tetralin.

(b) Decalin, and to a lesser extent toluene, exhibit decreases in flame radiation when, from the soot measurements, increases may have been expected.

These differences are possibly explicable in terms of variations in flame temperature. If the flame temperature of the 1-methyl naphthalene blend is higher than that of the tetralin blend, then this could lead to higher values of flame radiation and increased soot consumption for the blends containing 1-methyl naphthalene compared with those containing tetralin. Measurements of the exhaust temperatures of these blends did indicate that the experimental
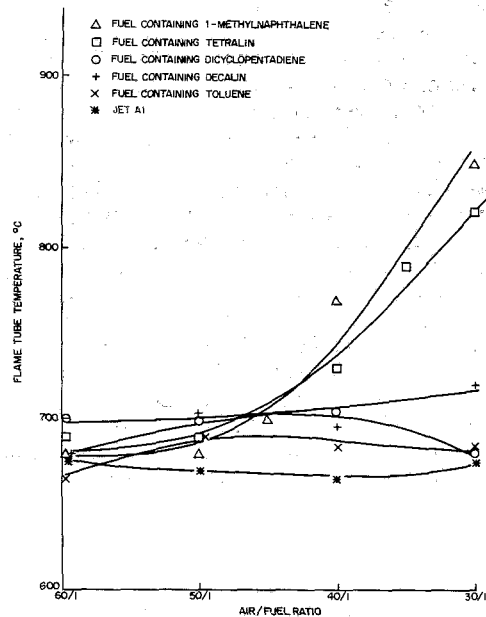
fuel containing naphthalene was burning hotter, at a given AFR, than the blend containing tetralin.

The second effect mentioned above is probably due to decreases in flame temperature caused by richer mixtures, a variation masked by the higher soot concentrations produced by the other fuels.

The results obtained for those fuels blended to a constant hydrogen content exhibit many of the above trends; however, in addition:

6 Those fuels containing decalin, toluene, and dicyclopentadiene show almost identical sooting tendencies and very similar flame-tube temperatures and flame

radiation. The results can be seen to be reasonably equivalent to those observed with the Jet A1 fuel.

7 Both tetralin and 1-methyl naphthalene give more soot, higher flame-tube temperature and greater flame radiation than any of the other fuels. At an air/fuel ratio of 45/1, which corresponds to a stoichiometric primary zone, tetralin and 1-methyl naphthalene produce almost twice as much soot as any of the other blends.

Discussion of Results

The experimental results indicate that the hydrocarbons studied fall into two groups with regards to their soot-forming properties: Group 1, which comprises toluene, decalin, and dicyclopentadiene, and Group 2, which comprises tetralin and 1-methyl naphthalene. The hydrocarbons in Group 1 produce less soot for a given air/fuel ratio and given concentration than those in Group 2 and, when blended to a similar hydrogen content, appear to behave like a normal aviation kerosine. Group 2 hydrocarbons behave quite differently from the Group 1 fuels, with their sooting tendency being a more sensitive function of mixture strength. It would also appear that the sooting tendency of the Group 1 hydrocarbons is more closely related to the fuel hydrogen content than is that of the Group 2 hydrocarbons.

The present results bear some similarity to previous studies utilizing a well-stirred reactor [6] in which it was observed that pure hydrocarbons could be grouped into three classes regarding their sooting tendencies. The first group contained paraffins and cycloparaffins which produced no soot over a wide range of equivalence ratios;[1] the second group contained aromatics which produced soot in the range of equivalence ratios of 1.4-1.6; and the third group contained 1-methyl naphthalene which produced large quantities of soot at an equivalence ratio of 1.3. In contrast with the present work, tetralin was considered to be equivalent in its behavior to simple aromatics such as toluene, and the combustion of decalin gave no soot at all. However, studies of the sooting tendencies of both premixed [3] and diffusion flames [7] have shown that tetralin produces soot at lower values of equivalence ratios than do single ring aromatics, whilst shock-tube studies [8] have demonstrated that decalin can produce more soot than aromatics. It is probable that these apparent variations are caused by the differing experimental environments utilized, and hence highlight the advantages of the use of combustion rigs in studies of the behavior of fuel components in gas-turbines.

As naphthalene and tetralin, which are condensed hydrocarbons, gave the most soot of all the hydrocarbons tested it would appear that the present results are consistent with mechanisms of soot formation which postulate the presence of high molecular weight polycyclic aromatics as soot precursors. Early workers proposing polycyclic aromatics as intermediates in the formation of soot tended to assume that direct condensation of aromatic rings was the most important pathway to soot formation [4]. The results of shock-tube studies of soot formation performed at TRC [8] have often been cited as evidence for the above belief. This work showed that at relatively low carbon concentrations – approximately 2×10^{23} carbon atoms m^{-3} – there appeared to be two routes to soot formation. The first, a fast efficient route, apparently involved the condensation of aromatic rings; the second, much slower route, formed soot via reaction between products of the fragmentation of the original hydrocarbons. It was observed that at temperatures

in excess of 1800 K the second of the two reaction pathways dominated and soot formation dropped rapidly. It should be noted, however, that the first of the two routes does not exclude condensation reactions between aromatic nuclei and products of fragmentation processes.

Higher carbon atom concentrations – approximately 10^{24} carbon atoms m^{-3} – were found to dramatically increase the rate at which both fragmented aromatic molecules and small unsaturated molecules, e.g., acetylene, formed soot so that at these concentrations soot formation via both pathways occurred at comparable rates. A similar reaction scheme to the first route described above has recently been proposed to explain mass spectroscopic studies of a benzene flat flame [9]. In both schemes the role of the aromatic ring is to act as a relatively stable nucleus upon which reactive fragments may condense and be stabilized by resonance effects. The above schemes would therefore explain the present results inasmuch as naphthalene and tetralin, which can readily dehydrogenate to form naphthalene, would act as relatively more efficient nuclei for condensations owing to their greater molecular complexity and larger resonance stabilization energies. This conclusion has been supported by thermodynamic calculations which show that condensation reactions involving naphthalene will be more efficient than those involving benzene [10].

Additionally, the work described earlier [8] provides an explanation for the behavior of the experimental fuels containing decalin and dicyclopentadiene. It was suggested that certain hydrocarbons, including decalin and dicyclopentadiene, could act as "pseudo" aromatic at combustion temperatures by rapidly dehydrogenating and/or rearranging to form aromatic species. Such behavior highlights a major inadequacy of the aromatic content specification requirement as a measure of combustion quality, for it takes no account of the presence of hydrocarbons like decalin. A strength of hydrogen content is that it at least provides some measure of the presence of those hydrocarbons which can efficiently form soot and yet are not inherently aromatic.

If the foregoing mechanisms apply, some inferences as to the regions in which soot is formed in gasturbines may be drawn. As some sensitivity to molecular structure is observed it is probable that significant quantities of soot are being formed by the pyrolysis of fuel in regions of both relatively low hydrocarbon concentration and high temperatures. Such regions would correspond to the recirculation zone in which some unburnt fuel will be mixed with hot products of combustion. Evidence for this suggestion can be found from studies of the effect of metal-containing additives upon soot formation in gas turbine engines [11]. In this work it was found that metal-containing additives such as barium and calcium compounds dramatically reduced the amount of soot formed. As there is strong evidence [12] that such metal-containing additives act by catalysing, at high temperature, the formation of hydroxyl radicals from water vapor then the above work would tend to support a hypothesis that the main region of soot formation in gas-turbines is the recirculation zone. It is therefore possible that engines designed such that combustion occurs before significant recirculation could greatly reduce soot formation.

Conclusions

1 The amount of exhaust soot produced by the combustion of fuels containing only single ring aromatics, fused bicyclic saturates, and unsaturated nonaromatics is related to the overall C/H ratio of the fuel.

2 The sooting tendency of experimental fuels containing significant concentrations of fused aromatics or tetralins (> 20 percent wt) is more dependent upon the presence of such components than on the fuel C/H ratio.

---

[1] Equivalence ratio

$$= \frac{\text{Stoichiometric air/fuel ratio}}{\text{Actual air/fuel ratio}}$$

3 The difference in sooting tendency exhibited by different hydrocarbons may be explained by a reaction mechanism which utilizes aromatic rings as nuclei upon which reactive fragments may be stabilized.

Acknowledgments

References

1 Gleason, C. C., and Bahr, D. W., "Fuel Property Effects on Life Characteristics of Aircraft Turbine Engine Combustors," *J. Energy*, Vol. 4, No. 5, 1980, pp. 216–222.

2 Clarke, A. E., Hunter, T. G., and Garner, F. H., "The Tendency to Smoke of Organic Substances on Burning. Part I," *J. Inst. Petrol.*, Vol. 32, 1946, pp. 627–642.

3 Street, J. C., and Thomas, A., "Carbon Formation in Pre-Mixed Flames," *Fuel*, Vol. 34, 1955, pp. 4–36.

4 Gordon, A. S., Smith, S. R., and McNesby, J. R., "Study of the Chemistry of Diffusion Flames," 7th Sym. (Int.) Comb., 1959.

5 Wood, A. D., "Correlation Between Smoke Measurements and the Optical Properties of Jet Engine Smoke," Paper presented at the National Aerospace Engineering and Manufacturing Meeting, Culver City, Los Angeles, Nov. 17-20, 1975.

6 Blazowski, W. S., "Dependence of Soot Production on Fuel Blend Characteristics and Combustion Conditions," ASME Paper 79-GT-155.

7 Coward, H. F., and Woodhead, D. W., "The Luminosities of the Flames of Some Individual Chemical Compounds, Alone and Mixed," 3rd Symposium on Combustion, Flame and Explosion Phenomena, 1949.

8 Graham, S. C., Homer, J. B., and Rosenfeld, J. L. J., "The Formation and Coagulation of Soot Aerosols Generated by the Pyrolysis of Aromatic Hydrocarbons," *Proc. R. Soc.*, A.344, 1975.

9 Bittner, J. P., and Howard, J. B., "Composition Profiles and Reaction Mechanisms in a Near Sooting Premixed Benzene/Oxygen/Argon Flame," 18th Sym. (Int.) Comb., 1981.

10 Stein, S. E., "On the High Temperature Equilibria of Polycyclic Aromatic Hydrocarbons," *J. Phys. Chem.*, Vol. 82, 1978, pp. 566–571.

11 Friswell, N. J., "Emissions from Gas-Turbine-Type Combustors," *Emissions from Continuous Combustion Systems* (editors W. Cornelius and W. G. Agnew), Plenum Press, New York, 1972.

12 Cotton, D. H., Friswell, N. J., and Jenkins, D. R., "The Suppression of Soot Emission From Flames by Metal Additives," *Comb. Flame*, Vol. 17, 1971, pp. 87–98.

A. K. Moza

Exxon Research and Engineering Company,
Baytown, Texas 77520
Mem. ASME

T. B. Molitaris

Calgon Corporation,
Pittsburgh, Pa. 15230
Assoc. Mem. ASME

The Preparation and Combustion of Coal-Oil Mixtures

This paper describes a series of tests that involved incorporating a coal cleaning step, namely oil agglomeration as part of a procedure to prepare COM (coal-oil mixture). The combustion characteristics of the COM were improved by introducing 7-8 percent water. A large fraction of the ash particles from this COM were found to melt during combustion. Most of these molten particles contained vanadium, which was concentrated on their surfaces.

Introduction

Although the idea of COM (coal-oil mixture) combustion dates as far back as 1879 [1], it is only in the last few decades that it has been seriously considered for use in existing utility and industrial furnaces and for blast furnace injection. The recent motivation for COM use is the economic incentive to convert existing oil and gas fired steam generators to burning 40–50 percent coal with minimal new equipment and downtime. Such use is based on the fact that handling, storage, and combustion characteristics of COM are similar to number 6 fuel oil.

COM is generally prepared by grinding coal to 80 percent less than 75 μm and mixing it with preheated no. 6 fuel oil to give a COM containing 30–50 percent coal [2, 3, 4, 5]. Since COM is viscous and thixotropic, it must be heated to make it pumpable. The hot COM is pumped and atomized for combustion in boilers by conventional equipment. One area of concern with COM's has been its instability; the coal particles start settling during storage. The settled coal particles form a thick packed bed which is difficult to redisperse. Various chemical additives have been proposed and used [6, 7, 8] to impart stability to COM.

The present study had been divided into two parts: preparation of COM and combustion of COM. The preparation involved incorporating oil agglomeration (a coal cleaning step) as part of the preparation step [9, 10, 11, 12]. Oil agglomeration involved grinding the coal to about 75 μm, followed by mixing with oil to form an oil wetable, coal-rich phase which could be physically separated from a water wetable, ash-rich phase in order to reduce ash in the coal. Since preparation of COM involved most of these operations anyway, it was felt logical to use the oil agglomeration step as part of COM preparation. .

The combustion studies of COM were carried out in a down-fired, plug flow type of combustor and were designed to determine whether the preparation procedure effected the combustion characteristics of the slurry. The incorporation of water in such slurries has been suggested to improve their combustion characteristics.

Preparation of Coal-Oil Mixtures

Preparation of COM involved a cleaning step, oil agglomeration. The basis of oil agglomeration lies in the surface chemistry of the coal and mineral matter. High and medium rank coals generally have a nonpolar surface as opposed to the polar surface that is exhibited by the mineral matter. It is this difference that is exploited in oil agglomeration. In a coal-water-oil system, oil which is nonpolar, selectively wets the nonpolar coal surface, leaving the polar mineral matter untouched. Stirring of such a suspension leads to collision of oil-coated coal particles and results in their agglomeration. The initial addition of the oil to a coal-water mixture leads to the formation of oil lenses between the coal particles. Further addition results in the drawing of the particles closer by capillary forces and, when sufficient oil is added, compact agglomerates with considerable strength are obtained. At the same time, most of the ash particles remain dispersed in the water phase and may be separated with the water. This type of coal cleaning has been known since World War I when the Trent process was developed by the U.S. Bureau of Mines. In the past, it has generally been found to be too expensive due to degradation of the value of the oil when mixed with coal. If COM is justified economically, this constraint no longer exists.

Experimental

The coal used in the preparation of our COM was from the Orient No. 3 mine in the Illinois No. 6 seam. Coarse coal was mixed with water and No. 2 oil (diesel oil) to give a slurry composed of: 50 percent coal, 49.8 percent water, and 0.2 percent No. 2 oil by weight. The slurry was ground in a rod mill, until 85 percent by weight smaller than 75 μ m. It was then diluted with water followed by the addition of fuel oil to give a slurry containing 10 percent coal, 1 percent oil and 89 percent water by weight. This slurry was agitated vigorously for 120 s to permit agglomeration of oil coated coal particles.

It was then allowed to stand for 5 min during which time the agglomerates floated up. These were skimmed off and dried for about 2 hrs at 365 K. The partially dried coal contained about 9 percent oil and 5 percent water. The material that sank was discarded as it contained the mineral matter with very little coal or oil.

Table 1 Size analysis of ground coal (wet sieving using micromesh sieves)

Size (μm)	Cumulative weight% below
125	100.0
106	92.5
75	85.3
53	66.6
38	54.1
30	35.0
20	20.6
10	11.4

Table 2 Ultimate/proximate analysis of coal (all values except moisture on dry basis)

	Raw coal	Clean coal
Moisture	2.04	1.78
VM (dry basis	35.45	42.52
% Ash	14.83	8.26
F.C. (dry basis)	49.75	49.22
C	60.9	70.50
N	1.17	1.32
H	3.80	5.09
S	4.37	3.56
0 (by difference)	14.96	11.27

Table 3 Ash analysis

	Raw coal	Clean coal
SiO_2	44.9	42.6
Al_2O_3	17.3	17.0
TiO_2	0.79	1.79
Fe_2O_3	21.0	26.7
MgO	1.09	1.27
CaO	4.8	3.15
Na_2O	0.59	0.53
K_2O	1.86	2.05
SO_3	6.0	3.8
Rest	1.67	1.11

Table 4 Combustion test conditions

Feed rates:

Pulverized coal	:	8 K gm/hr (17.7 lb/hr)
30% coal-oil mixture	:	6 K gm/hr (13.3 lb/hr)
Heat release rate	:	212,000 KJ/hr (210,000 BTU/hr)
Excess air	:	15%
Feed temperatures	:	Pulverized coal : 300 K 30% COM : 343 K
Sauter mean diameter	:	Pulverized coal : 53 μm 30% COM : 131 μm

Atomizing conditions:

Atomizer type	:	Twin fluid nozzle
Spray pattern	:	Narrow angle, full cone
Spray angle	:	27 deg
Spraying distance	:	0.35 m
Atomizing pressure	:	11 K Pa ($\sim$50 psi)

Combustion efficiency:

Pulverized coal	:	94%
30% COM	:	87%

To prepare COM, the clean coal was added to No. 6 oil preheated to a temperature of 340 K. (The oil used was a Venezulean fuel oil containing 250 ppm vanadium.) During addition of coal, the oil was constantly stirred. The COM mixture so obtained showed excellent stability. Samples allowed to settle for one month could be reconstituted by slow agitation (50–100 rpm) in 5–10 min.

Results and Discussions

The proximate and ultimate analysis of the raw coal prior to agglomeration is shown in Table 2. Also included in the table is the analysis of oil-free dry coal after agglomeration, referred to as clean coal. The analysis indicates that the oil
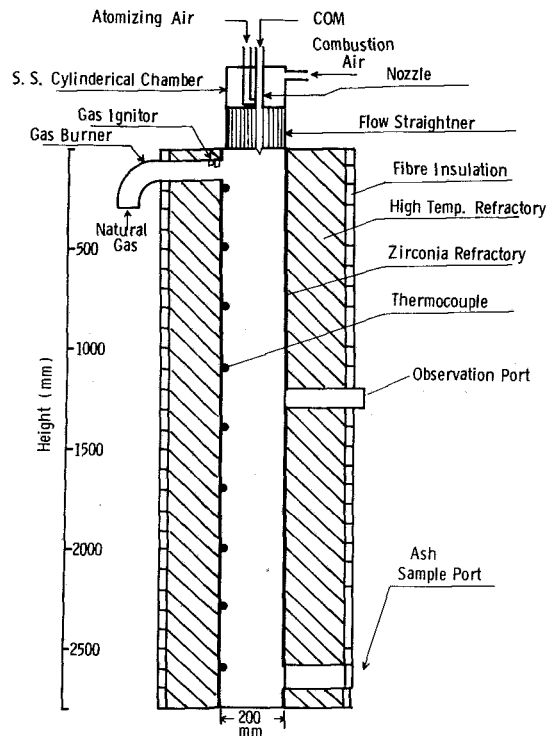
Fig. 1 Sketch of the vertical section through the combustor

agglomeration led to a 45 percent reduction in ash and 20 percent reduction in sulfur content of the coal. The latter corresponded to about 20 percent reduction in the pyritic sulfur and 10 percent in organic sulfur.[1] The ash composition of the raw coal and clean coal are shown in Table 3. The two analyses are fairly similar, indicating that oil agglomeration is nonselective in removing mineral matter. There does seem to be a concentration of iron in the clean coal which is attributed to the fact that pyrite, due to its nonpolar characteristics [12], tends to behave like coal during agglomeration. The same seems to be true of titanium dioxide, too.

A mass balance showed recovery of 80 percent of the feed in the agglomerate product including 90 percent of the carbonaceous matter. About 90 percent of the oil used during agglomeration reported to coal and about 5 percent to the water. The rest was lost to the rejects. The water was reused for successive experiments.

Combustion of Coal-Oil Mixtures

The combustion operations involved pumping the COM, atomizing it, stabilizing the flame, and collecting the ash particles. The ash particles from the combustor were subjected to computerized scanning electron microscope image analysis [13, 14]. By this method, it was possible to perform a rapid size, shape, and chemical analysis on a particle by particle basis for several thousand particles. This permitted characterization of the ash particles in terms of their size, shape, and elemental compositions. The shape of the particle was used to determine whether that particle had melted, since upon melting particles tend to achieve a round shape.

Experimental

The down-fired combustor used for the combustion studies is shown in Fig. 1. A similar type of combustor had been used

---

[1] The reduction in organic sulfur is attributed to the rejection of high sulfur containing macerals (Fusinites) during oil agglomeration.
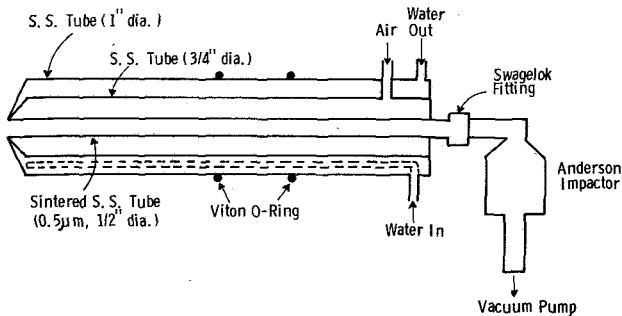
Fig. 2 Probe for collecting overall ash samples

Fig. 3 Probe for collecting the sticking type of ash particles

previously by Howard [15] to study combustion of pulverized coal. In the present work it was used to study the combustion of pulverized coal, No. 6 fuel oil, and COM.

The top portion of the combustor was fitted with a stainless steel cylindrical chamber, having ports to introduce the nozzle and tubes carrying atomizing air, and combustion air. An alumina honey comb disk in the chamber acted as the flow straightener. Along its height, the combustor was fitted with 10 Pt/Pt-Rh thermocouplers, one ash sampling port, four gas sampling ports, and a natural gas burner at the top to preheat the furnace before actual firing with COM. The feed system for COM or No. 6 oil consisted of a tank fitted with an agitator, a variable speed Moyno pump, and heat traced 13-mm stainless steel feed tubes. The furnace was also fitted with a forced draft fan and an induced draft fan. The atomizing air was supplied by a compressor. The feed system for pulverized coal consisted of a variable speed screw feeder that fed coal into an air venturi, from which it was conveyed by air into a pyramid-shaped mixing chamber. The latter also received combustion air, which was mixed thoroughly with the pulverized coal. The pyramid-shaped mixing chamber fitted on the top of the combustor replaced the S.S. cylindrical chamber shown in Fig. 1.

Two types of probes shown in Figs. 2 and 3 were used to collect ash from the combustor. The probe shown in Fig. 2 was used to collect an overall sample of the ash particles. The one shown in Fig. 3 was used to collect only those ash particles what would stick to a replaceable metal substrate indicated as ash collector coupon in the figure. The temperature of this coupon could be varied by changing its thickness and the water flow rate.

The sintered steel tube in the probe shown in Fig. 2 allowed air to seep through its pores and thus prevented ash deposition in the probe. The Anderson impactor was used to collect the ash particles. The collection efficiency of the probe was determined to be in excess of 95 percent for particles of sizes greater than 5 microns and about 80 percent for sizes between 1 and 5 microns. There was no loss of ash particles to the collection surfaces in the Anderson impactor as is the case with common filters.

The procedure for start-up of the combustor consisted of preheating the furnace with gas alone until an average temperature of 1100–1200 K (1500–1700°F) was obtained in the furnace. At that stage, the test fuel was introduced gradually with a corresponding reduction in gas supply rate. The procedure was continued till a stable flame was obtained without the gas.

Results and Discussion

Before conducting experiments with the COM, the combustor was characterized in terms of combustion efficiency with pulverized coal. The combustion efficiency was expressed as a function of unburned carbon in the overall ash samples collected from the combustor. Figure 4 shows a plot

—▲— Percent Unburned Carbon

—✕— Approx. Residence Time, Sec.
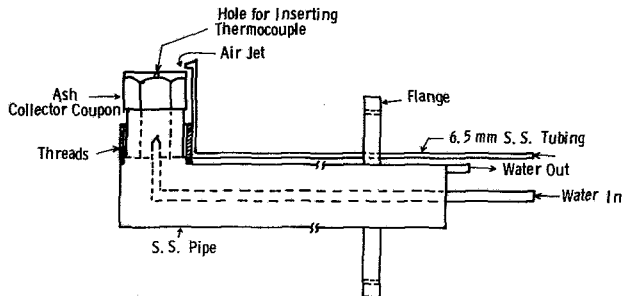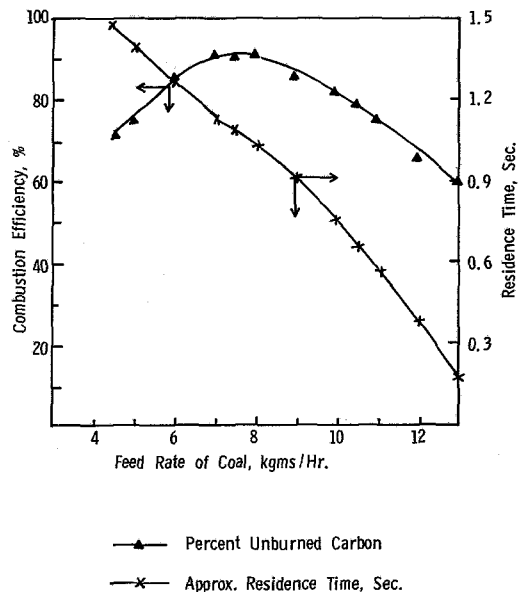
Fig. 4 Combustion efficiency and gas residence time as a function of feed rate in the combustion

Table 5 Test conditions during the combustion studies COM containing water

Composition of the mixture		
Coal	:	30%
Oil	:	62.1%
Water	:	7.8%
Surfactant	:	0.1%
Feed rate	:	6.3 K gm/hr
Feed temp	:	343 °K
Excess air	:	15%
Sauter mean diameter	:	139 μm
Atomizing conditions	:	Same as in Table 4
Combustion efficiency	:	94%

of this efficiency and percent unburnt carbon as a function of coal feed rate at 15 percent excess air. By invoking the assumption of a one-dimensional nature of the furnace and knowing the temperature and composition profile of the gas in the furnaces, the residence time of the gas was computed numerically in a step by step marching down procedure. The particle residence time should be very similar to gas residence time, since the slip velocity between pulverized coal particles and gas is expected to be small. The terminal velocity for a 100-μm coal particle in air at combustion temperature is estimated to be 0.2 m/s compared to 1–3 m/s for gas. Hence, the relative motions due to the settling of particles should not cause much divergence of particles and gas flow patterns, since the flow velocity is much higher than the terminal velocity.
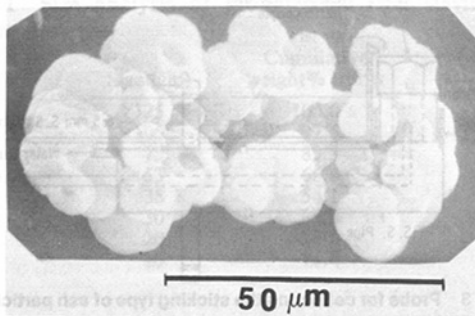
Fig. 5 Micrograph of the partially burnt agglomerate of coal particles from COM

Table 6 Analysis of ash particles

(a) Particle type	Raw coal	Clean coal	Coal + oil	Coal + oil + 8% water
Si	15.6	12.7	1.8	5.6
Si-Al	10.5	11.4	2.9	4.8
Si-Al-Ca/K	14.4	11.4	4.8	5.3
Fe-S	15.8	16.6	1.4	3.8
Fe-S-Si-Al/Ca	21.6	25.7	2.4	11.6
Fe-S-K-Al/Ca	18.6	22.3	1.9	9.7
Va-Fe-S	–	–	12.8	7.5
Va-Fe-Al-Si/Ca	–	–	32.6	26.6
Va-Fe-K/Al-Si/Ca/S	–	–	34.6	22.5
Rest	3.5	4.8 –	4.8	2.6
(b) average size (μm)	9.30	6.9	18.2	7.9
(c) volume % of molten ash particles	24	31	69.6	57.6

Volume percent of particles

Table 7 Analysis of ash particles from COM containing water

Particle type	Ash sticking to S.S coupon	Total ash from the fuel
Va containing particles	87.3	56.6
Si-Al-Ca	4.2	5.3
Si-Al-Ca/K/S	4.9	3.8
Others	3.60	34.3
Average size (μm)	9.8	7.9
Volume % of spherical particles	96	57.6

Volume % of particles

Fig. 6 Micrograph of a thin layer of COM containing water

Fig. 7 Micrograph of a thin layer of COM containing water and surfactants

The plot in Figure 4 shows that a maximum combustion efficiency of 94 percent was obtained at a coal feed rate of 7-8 kgm/hr. Higher feed rates resulted in higher carbon loss because of lower residence time. A lower feed rate gave lower combustion temperatures due to excessive heat loss as compared to heat generation and resulted in unstable flame conditions. To obtain maximum combustion efficiency all of the tests with pulverized coal were carried out at a feed rate of 8 Kgms/hr. The tests with COM were conducted with heat release rates equivalent to 8 kgms/hr giving a residence time of about 1 s.

The combustion tests were carried with raw coal, cleaned coal, and COM prepared with cleaned coal. The test conditions are outlined in Table 4. The combustion efficiency obtained with COM was found to be lower than with pulverized coal. Observation of the ash particles from COM under the scanning electron microscope indicated extensive agglomeration. A picture of a typical agglomerate is shown in Fig. 5. Apparently, when the COM was atomized into droplets, each contained a number of coal particles. A rough calculation showed that on an average a 30 percent COM droplet of 131-μm dia contained about 5 coal particles of 53 percent μm size. During combustion, the oil from the droplet
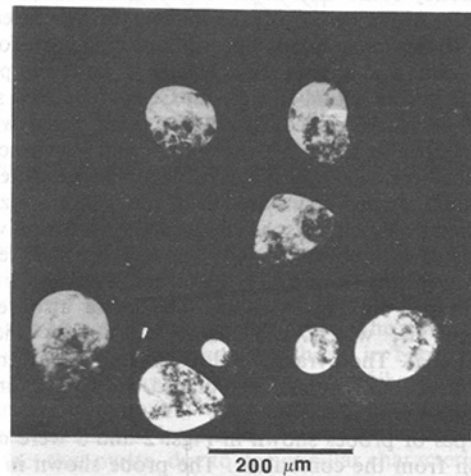
evaporated, leaving behind the agglomerate of coal particles and nonvolatile components of oil such as ash and high boiling point hydrocarbons.

It has been suggested [16] that one way to prevent this agglomeration would be to introduce water into the COM. The presence of water in liquid fuels has been shown [17] to cause microexplosions in fuel droplets. In the case of COM, Law et al. [16] observed that the presence of 5 percent water caused catastropic explosions of the droplets. A COM with 5-10 percent water was prepared by mixing partially dried coal slurry from the oil agglomeration test with No. 6 oil.

Combustion tests with this slurry did not indicate any improvement in combustion efficiency. Further, there were still a lot of agglomerates present in the ash particles indicating the absence of microexplosions. Had the expected microexplosions occurred, the coal particles should have been dispersed in the combustion zone of the furnace giving rise to fine ash particles.

A possible reason for this behavior was found by observing a thin layer of this COM sandwiched between two glass slides under an optical microscope. A photograph is shown in Fig. 6. The micrograph shows large water droplets with sizes ranging from 50 to 500 μm. It seems likely that during atomization such a slurry would give rise to separate discrete droplets of water rather than droplets of water in a droplet of COM. During combustion, the water droplets then evaporate
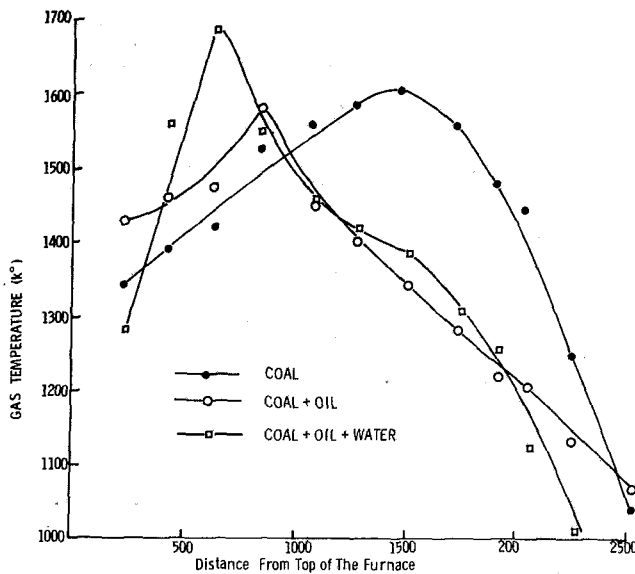
Fig. 8 Gas temperature profiles with coal, COM and COM containing water
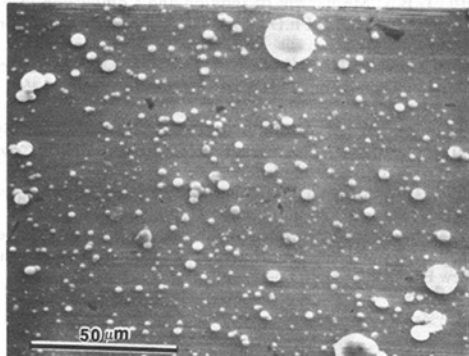
Fig. 9 Micrograph of ash particles sticking to a S.S. coupon from COM containing water and surfactants

separately without giving the microexplosion effect. For microexplosions to occur, water must be present inside the COM droplet, or on an average, the size of the water droplet has to be less than the mean diameter of COM droplet.

In addition, the water should be firmly attached to the coal surface; otherwise, due to intense recirculation within the droplet, it might be brought to the COM droplet surface, where it would evaporate in preference to oil due to its lower boiling point. Such a situation would not lead to microexplosions, because no pressure would be built within the droplet. (The intense recirculation within the droplet is caused by the high shear rate between the droplet and the surrounding medium during atomization and combustion.) Hence, it was felt that microemulsification of water alone would not be sufficient to cause microexplosions but that such water had to be firmly attached to the coal particle surface.

A COM with the proper characteristics was made by adding suitable surfactants to COM so that a stable coal-water-oil interface was formed. A nonionic water soluble surfactant was mixed with the coal slurry (22 percent water) after the oil agglomeration step to stabilize the coal-water interface. To stabilize the water-oil interface another nonionic oil soluble surfactant was added to the No. 6 oil prior to its addition to the coal-water mixture.

This procedure for COM preparation also eliminated the drying step after oil agglomeration and the water

emulsification step generally necessary in the preparation of water-oil suspensions. A photograph of a thin layer of the coal particles surrounded by water in such a COM diluted with oil shown in Fig. 7. The dark areas refer to oil and white areas refer to water phase with coal particles in it. This COM had to be diluted with oil to get a good picture that illustrated the form in which water was physically present.

Table 5 lists the test conditions employed for the combustion studies of the COM containing water and surfactants. The chief point to note is that combustion efficiency had gone up to 94 percent from the 87 percent observed for coal-oil mixture without water. The gas temperature profiles in the furnace for this pulverized coal and COM without water. The temperatures indicated in Fig. 8 are the thermocouple temperatures corrected for convection and radiation [18]. The results indicate that COM with water burns much more rapidly than either coal or COM. The peak temperature was highest with COM containing water despite the cooling effect of the water due to of the rapid rate of heat release.

The results of a particle by particle analysis of the ash using the computerized scanning electron microscope technique are given in Table 6. It should be noted that the COM's with or without water were both prepared from the clean coal, which in turn was prepared by oil agglomeration. The main difference between the ash particles from various fuels is in the average ash particle size and volume percent of the molten particles. The average ash particle size from the COM drops from 18.2 μm to 7.9 μm when 8 percent water with the surfactants was introduced. This reduction is believed to result from better dispersion of the burning particles due to the occurrence of the microexplosions during combustions. The volume percent of molten ash particles from COM with or without water is almost twice as great as that from pulverized coal. The molten particles are characterized as those particles which were spherical in shape [19].

The composition of these spherical particles indicated that most of them contained vanadium. A composition profile analysis by the computerized scanning electron microscope indicated that most of the vanadium in such particles was on the surface. This suggests the formation of a low melting phase on the surface of the ash particles. Molten particles are undesirable because such particles tend to stick to heat transfer surfaces in a boiler, leading to fouling and slagging. To collect sticking ash particles from COM containing water with surfactants, the probe shown in Fig. 3 was used. The water cooled probe was inserted in the furnace for about 5 min. Air was blown gently over the S.S. ash collector once a minute to dislodge any particles that were not adhering to the surface. The coupon was removed from the probe and viewed under the scanning electron microscope. A photomicrograph of the coupon with particles is shown in Fig. 9.

The computerized scanning electron mircoscope image analysis data from these particles and shown in Table 7. For comparison purposes, the data on total ash (last column from Table 6) are also included in this table. Most of these particles sticking to the coupon contain vanadium with a smaller percentage of pyrite and calcium aluminum silicate. To prevent sticking and possible slagging and fouling from COM, such particles need to be modified. Such a modification could be brought about by incorporating suitable additives in the oil phase that would influence the liquidus temperature of the vanadium containing particles.

Conclusions

1 It has been shown that by incorporating an oil agglomeration step in the preparation of COM, it is possible to reduce ash by about 50 percent and pyrites by about 30 percent in a high sulfur coal.

2 The coal agglomerates from the oil-agglomeration step

need not be dried since water in the agglomerates has the beneficial effect of causing microexplosions during combustion.

3 The microexplosions improve combustion efficiency and reduce the average ash particle size.

4 For microexplosions to occur, the water in COM should be firmly attached to the coal surface. This can be accomplished by using suitable nonionic surfactants.

5 A large fraction of the ash particles from the combustion of COM, with or without water, melted.

6 The composition of molten particles indicated that they were predominantly vanadium containing particles.

7 The composition of the particles sticking to a S.S. coupon further confirmed that particles likely to cause slagging and fouling problems contained vanadium.

8 Vanadium was found to be concentrated on the surface of molten ash particles. This suggests the possibility of a low melting phase on the surface.

9 To combat slagging and fouling from COM, it may be possible to incorporate suitable additives in the COM.

Acknowledgments

References

1 Smith, H. R., and Hunsell, H. M., "Liquid Fuel," U.S. Patent 291,181, Feb. 24, 1879.

2 Manning, A. B., and Taylor, R. A. A., "Colloidal Fuel," *J. Inst. Fuel* Vol. 9, 1936, p. 303.

3 Jonnard, A., "Colloidal Fuel Development for Industrial Use," Bulletin No. 48, Kansas State College, Expt. Station, Manhattan, Kansas, 1946.

4 Sharpe, S. C. H., "Colloidal Fuel," *The BCURA Monthly Bulletin*, Vol. 19, No. 3, 1955, pp. 97–106.

5 Demeter, J. J., McCann, C. R., Bellas, G. T., Ekmann, J. M., and Bienstock, B., "Combustion of Coal-Oil Slurry in a 100 H.P. Fire Tube Boiler," *ASME Publications* 77-WA/FU-5.

6 Metzge, W. W., "Slurry Fuels and Use of Additives," *Proceedings of International Symposium on Coal-Oil Mixture Combustion*, Fla., May 1978, pp. 341–343.

7 Sawyer, E. W., "The Use of Attapulgite Clay-Surfactant Gels to Stabilize Coal-Oil Mixtures," ibid, pp. 317–321.

8 Kugel, R. W., "The Determination of Coal-Oil Mixture Stability," ibid, pp. 300–316.

9 Caper, C. E., Smith, A. E., and Puddington, I. E., "Pilot Plant Testing of Spherical Agglomeration Process in Coal Preparation Proceedings," 16th Biennial Conference, *Institute of Briquetting and Agglomeration*, 1979.

10 Moza, A. K., Kini, K. A., and Sarkar, G. G., "Basic Studies in the Mechanism of Oil Agglomerations," *Proceedings 7th International Coal Preparation Conference, Sydney Australia*, Paper No. 113, 1977, pp. 8–18.

11 Nicol, S. K., and Brown, A., "An Experimental Appraisal of the Beneficiation of Fine Coal by Selective Agglomeration," *Proceedings, Australian Institute of Mining and Metallurgy*, No. 262, 1977, pp. 49–55.

12 Mezey, E. J., M. N. S., and Folsom, D., *Fuel Contaminants*, Vol. 4, Application of Oil Agglomeration to Coal Wastes," U.S. Environmental Protection Agency, Report No. EPA-600/7-79-025b, Jan. 1979.

13 Leibdzik, J., Burke, K. J., and Troutman, S., "New Methods for Quantitative Characterization of Multiphase Particulate Materials Including Thickness Measurement," SEM/1973, IIT Research Institute, Chicago, Ill. pp. 121–128.

14 Moza, A. K., "A Study of Coal Ash With Respect to Slag Deposits," Ph.D. thesis, The Pennsylvania State University, University Park, 1980.

15 Howard, J. B., "Mechanism of Ignition and Combustion in Flames of Pulverized Bituminous Coal," Ph.D thesis, The Pennsylvania State University, University Park, 1965.

16 Law, C. K., Law, K. H., and Lee, C. H., "Combustion Characteristics of Droplets of Coal/Oil and Coal/Oil/Water Mixtures," *Energy*, Vol. 4, 1979, pp. 329–339.

17 Dryer, F. L., "Water Addition to Practical Combustion Systems— Concepts and Applications," *Proceedings of 16th Symposium on Combustion*, Cambridge, Massachusetts, 1976, pp. 279–295.

18 Chedaille, J., and Brand, Y., "Gas Temperatures," *Measurements in Flames*, Vol. 1, Edward Arnold, London, 1972, pp. 9–14.

19 Moza, A. K., Paper presented at the conference on "Experimental Research into Fouling and Slagging Due to Impurities in Combustion Gases," Henniker, New Hampshire, July 12–17, 1981.

Statistical Characteristics of Velocity, Concentration, Mass Transport, and Momentum Transport for Coaxial Jet Mixing in a Confined Duct

B. V. Johnson

Supervisor,
Heat Transfer Technology,
United Technologies Research Center,
East Hartford, Conn. 06108

J. C. Bennett

Associate Professor,
Mechanical Engineering Department,
University of Connecticut,
Storrs, Conn. 06268

An experimental study of mixing downstream of coaxial jets discharging into an expanded circular duct was conducted to obtain data for the evaluation and improvement of turbulent transport models currently used for combustor flow modeling. A combination of turbulent momentum transport rate and two velocity component data were obtained from simultaneous measurements with a two-color LV system. A combination of turbulent mass transport rate, concentration and velocity data were obtained from simultaneous measurements with laser velocimeter (LV) and laser induced fluorescence (LIF) systems. These measurements were used to obtain mean, second central moment, skewness and kurtosis values for three velocity components and the concentration. These measurements showed the existence of countergradient turbulent axial mass transport where the annular jet fluid was accelerating the inner jet fluid. Results from the study are related to the assumptions employed in the current mass and momentum turbulent transport models.

Introduction

Computational procedures to predict combustion processes are being developed and refined by a number of researchers (e.g., see [1] and surveys in [2, 3]. These computational procedures predict the velocity, species, concentration, temperature, and reaction rate distribution within the combustors which are used to determine combustor linear heat loads, engine performance (combustion efficiency), pollution emissions (reactant products), and pattern factor (temperature distribution at turbine inlet). Because combustors of practical interest have turbulent flow, the calculation procedures usually include mathematical models for the turbulent transport of mass (or species), momentum, and heat. However the prediction of combustion processes with improper models result in inadequate predictions of combustion efficiency, liner heat load, emissions, and exit temperature pattern factor.

The data used to formulate and validate the turbulent transport models have been obtained primarily from velocity and momentum transport measurements because only a limited amount of concentration and mass transport data are available. The mass (species) transport data presently available for recirculating flows like those occurring in

combustors are not sufficient to determine where inadequacies exist in the present models or to formulate improvements for the models. One reason for this situation is that the methods used prior to the mid-1970s for simultaneously obtaining turbulent mass (species) and momentum transport data often have been indirect, requiring compromising assumptions or requiring probes unsuitable for recirculating flows.

To overcome these limitations, new optical techniques have been developed to simultaneously measure a scalar quantity and velocity and, therefore, to obtain mass transport data. These techniques include fluorescence of a trace material in water or gases to measure concentration, Mie scattering of a trace material to measure concentration, fluorescence of gas molecules to measure species and temperature, and Rayleigh scattering from gas molecules to measure temperature (e.g., surveys in [4, 5]. All these techniques use lasers as a light source and have been used recently (since 1979) with laser velocimetry to obtain combined scalar/velocity measurements. The fluorescence of dye in water was selected as an appropriate technique for this mass and momentum turbulent transport study with constant density fluids.

A preliminary effort at UTRC to obtain quantitative concentration measurements with fluorescent dye in 1975 was described by Owen (paper 28 of [5]). The current effort makes use of improved optics, data handling capabilities, and operative procedures. Initial results from the current effort

were presented in [6]. These measurements were limited in scope as only mean and fluctuating axial and radial velocities and radial mass transport measurements were obtained. The experimental capabilities for the present study were expanded to include measurement of the mass transport in the z-r and z-θ planes. Data acquisition and storage techniques were used in the present study which allowed the calculation of the higher moments from the velocity, concentration, and turbulent transport rate probability density functions (pdf's).

The current application of the combined LV/LIF measurement techniques along with the available data handling procedures provides an opportunity to obtain data which can be used to evaluate a number of computational methods and turbulent transport models. Results from the present study can be used to evaluate (i) the two-equation turbulence model, (ii) the Reynolds stress transport model, and (iii) the probability density function formulation for predicting turbulent transport and concentration fluctuations.

The present study was initiated with a flow visualization phase to qualitatively determine the effects of velocity ratio, U_i/U_a, and the Reynolds number on the flow characteristics within the duct ([7]). Results from the study were also used to determine the streamwise locations for obtaining detailed velocity, concentration, and mass transport rate measurements. A sketch of the shear regions, which existed for the flow condition measured, is shown in Fig. 1. Although the flow condition reported in [6] was the same as that for the present study, the additional measurements of the present study produced several interesting and important results. The axial mass transport results showed countergradient mass transport rates larger than the radial mass transport rates in a large central region of the flow. The skewness and kurtosis of the transport rate probability density functions were found to vary from region to region. The present paper is focused on the turbulent transport characteristics not reported in [6].

Description of Experiment

Measurement Techniques. The experimental method employed a laser velocimeter (LV) to obtain velocity data, a laser induced fluorescence (LIF) technique to obtain con-
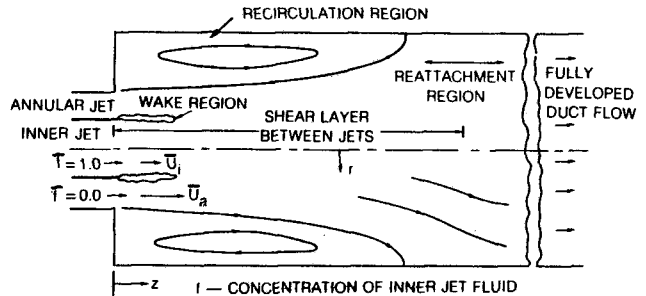
Fig. 1 Shear regions of coaxial jets in an enlarged duct
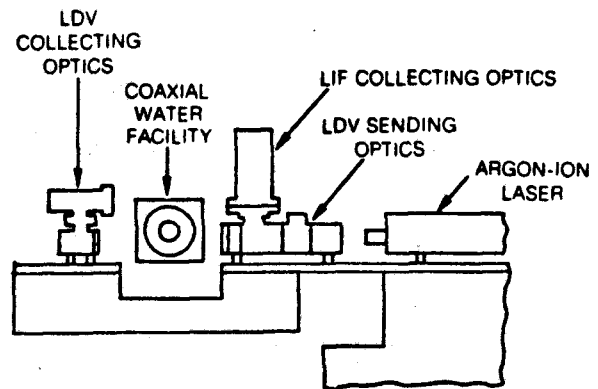
Fig. 2 Sketch of optics arrangment

centration data, and a microcomputer to control the data acquisition and to store and reduce the data. Commercially manufactured equipment was used for the optics and most of the electronic components. For the LV/LIF measurements, the equipment was arranged as shown in Fig. 2. The light source used was the 0.488-μm line with a 1-mm-dia. beam from a Spectra-Physics argon ion laser. The laser was operated in the constant light amplitude mode with a power of 0.4 W. Fluctuations in the light intensity were estimated to be

──────── Nomenclature[1] ────────

$\bar{u}$ = local instantaneous axial velocity component

$B(\bar{u})$ = probability density function (p.d.f.) of $\bar{u}$ with properties $B(\bar{u}) \geq 0$ and

$$\int_{-\infty}^{\infty} B(\bar{u})\, d\bar{u} = 1.0$$

U = mean value of axial velocity component defined:

$$U = \int_{-\infty}^{+\infty} \bar{u}\, B(\bar{u})\, d\bar{u}$$

u = local instantaneous axial velocity fluctuation from the mean, defined: $u = \bar{u} - U$

σ_u or u' = second central moment of velocity, u, defined: $\sigma_u^2 =$

$$u'^2 = \int_{-\infty}^{+\infty} u^2\, B(\bar{u})\, d\bar{u}$$

Will also be denoted as rms fluctuation.

u^n = nth central moment of velocity defined:

$$\overline{u^n} = \int_{-\infty}^{-\infty} u^n\, B(\bar{u})\, d\bar{u}$$

S_u = skewness of velocity component, u, p.d.f. defined: $S_u = \overline{u^3}/\sigma_u^3$

K_u = kurtosis (or flatness factor) of velocity component, u, p.d.f. defined: $K_u = \overline{u^4}/\sigma_u^4$

uv = local instantaneous momentum turbulent transport rate: $(\bar{u}-U)\,(\bar{v}-V)$

$B(uv)$ = probability density function (p.d.f.) of uv with properties $B(uv) > 0$ and

$$\int_{-\infty}^{+\infty} B(uv)\, d(uv)$$

$\overline{uv}$ = mean value of turbulent momentum transport rate defined: $uv =$

$$\int_{-\infty}^{\infty} (\bar{u}-U)\,(\bar{v}-V)\, B(uv)\, d(uv)$$

$(uv)'$ = local instantaneous fluctuation of momentum transport rate from mean, defined: $(uv)' = uv - \overline{uv}$

σ_{uv} = second central moment of momentum transport rate:

$$\sigma_{uv} = \int_{-\infty}^{\infty} (uv)'^2\, B(uv)\, d(uv)$$

$(uv)^n$ = nth central moment of momentum transport rate:

$$(uv)^n = \int_{-\infty}^{\infty} (uv)'^n\, B(uv)\, d(uv)$$

S_{uv} = skewness of momentum transport rate: $S_{uv} = (\overline{uv})^3/\sigma_{uv}^3$

K_{uv} = kurtosis of momentum transport rate: $K_{uv} = (\overline{uv})^4/\sigma_{uv}^4$

────────

[1] Terms for the velocity components, concentration and transport rates are defined using the notation of [8]. These mentioned in this section are definitions for the axial velocity and the momentum transport in the r-z plane.
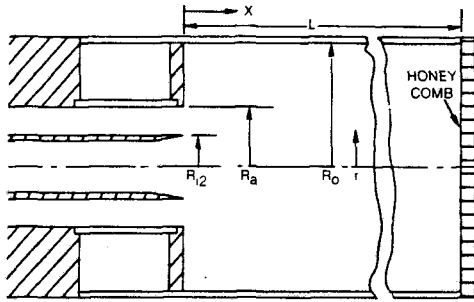
Fig. 3 Sketch of inlet and test section; $L = 1016$ mm, $R_{i1} = 12.5$ mm, $R_{i2} = 15.3$ mm, $R_a = 29.5$ mm, $R_o = 61.0$ mm

Fig. 4 Probability density functions for axial velocity and concentration at $r/R_o = 0.2$; $\Delta u = 0.1$ m/s, $\bar{u} = 1.20$ m/s, $u' = 0.22$ m/s, $S_u = -0.15$, $K_u = 216$; $\Delta f = 0.02$, $f = 0.28$, $f' = 0.18$, $S_f = 0.91$, $K_f = 4.0$

less than 1 percent. The LV optics were arranged to use the dual-beam laser-Doppler velocimeter system. The sending optics consisted of a beam splitter, Bragg cell, 2.7X beam expander, and a 378-mm focal length lens. The collection optics were arranged for forward scattering. The input to the photomultiplier was optically filtered to receive only 0.488-μm light. The photomultiplier signal was mixed to achieve a 1.0-MHz signal for zero velocity. These optical components were manufactured by TSI. The mixed signal was processed with a SCIMETRICS signal processor and the acceptable signals were fed through an electronic interface to a Digital Equipment Corporation (DEC) PDP 11/10 computer. The DISA 55 × 00 laser velocimeter system and the 0.5145- and 0.488-μm lines of the laser were used in the direct backscatter mode for the simultaneous two velocity measurements.

The circular duct test section was enclosed in a rectangular, glass-walled optical box filled with water to reduce beam direction distortion as the laser beams passed from air through the glass wall of the duct and into the test section water. A ray tracing program was used to determine that the radial displacement of the probe volume was less than 0.03 mm and the offset of the measurement direction from radial was less than 0.05 deg for $r/R_o < 0.9$. The LV probe volume was calculated to have dimensions of 0.12-mm dia and 2.3-mm length and 24 fringes.

The LIF measurement technique used fluorescein dye as a trace element in the inner jet of the coaxial flow streams. This dye absorbs light at 0.488 μm and emits light with highest intensities at wavelengths between 0.5 and 0.6 μm [13]. Direct back-scattering, light-collection optics were used for the LIF system. The light was focused through a Kodak No. 15 Wratten filter onto a photomultiplier tube. The photomultiplier tube current was converted to voltage, was filtered with a 2 KHz low pass filter and was fed into a 12 bit analog-to-digital converter in the computer. The LIF data were digitized 25 microseconds after the LV data sample was obtained. The time between the LV and LIF data acquisition was less than 0.25 and 0.02 times the minimum transit time across the probe volume diameter and length, respectively. Therefore, no correction to the LV or LIF data was necessary for this short time period.

One thousand pairs of data samples were obtained at each data acquisition point. The LV data acquisition rate was slowed, by controlling the signal processor A + start signal to less than 10 per s, to prevent the data from being acquired too fast and probably biasing the measurements with short-term statistics [15]. The data were stored on flexible disks and are available for future additional data processing.

**Flow Conditions.** The geometry for the experiment is shown in Fig. 3. This configuration with coaxial jets discharging into an enlarged circular duct is similar to the configuration used in previous momentum transport experiments (e.g., [14]). The configuration had ratios of annular
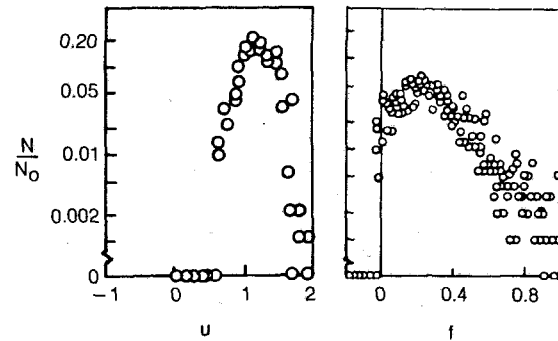
jet diameter to inner jet diameter (R_a/R_i) and outer wall diameter to inner jet diameter (R_o/R_i) of approximately 2 and 4. The inner jet, annular jet, and total flows through the system were held constant at 23.5, 200.0, and 223.5 L/min, respectively.

The water temperature varied from 50 to 70°C causing the duct Reynolds numbers, $U_o D_o/\nu$ to vary from 30,000 to 40,000. (These Reynolds numbers are an order of magnitude above the transitional range.) In reducing the data, the turbulent transport characteristics were assumed to be independent of the Reynolds number. All the turbulent mass transport data and most of the velocity data were obtained over a one-month period when the water temperature varied less than 3°C from the average value and the Reynolds number varied less than ± 5 percent. For a typical 2-hr test period, the water temperature varied less than 1°C.

Discussion of Results

The objective of this study was the acquisition, reduction, and analysis of velocity, concentration, mass transport rate, and momentum transport rate measurements at seven axial locations within the duct test section. Single-component velocity data and inner-jet fluid concentration data were obtained simultaneously to determine the local mass (or scalar) transport rate. Two velocity components were obtained simultaneously to determine the local momentum transport rates. The data sets for each measurement location were analyzed and reduced to obtain the mean and three central moments from each probability density function (p.d.f.).

The focus of this paper is on the new information obtained with the additional data, compared to that presented in [6]. Data obtained at one of seven axial stations will be used to illustrate the principal new results. This axial location, 103 mm (4.0 in.) from the inlet plane, contains (i) a shear region between the inner stream and annular stream fluid, (ii) a shear region between the annular stream and the recirculation cell, and (iii) the approximate axial midplane of the recirculation cell, as shown in Fig. 1. The complete data set for this study is available in a limited distribution report [7].

Probability Density Functions. Velocity and concentration probability density functions (p.d.f.'s) were plotted for data sets obtained at $r/R_o = 0.2$ (Fig. 4). This radial location was chosen for detailed analysis of the flow characteristics because both the momentum and mass transport rates are relatively high. These data were obtained as part of the momentum and mass transfer data acquisition. Consequently, the axial velocity and concentration p.d.f.'s are comprised of data from two and three different runs, respectively. These data were obtained at approximately the same radial location along the horizontal and vertical axes. The mean ($\bar{U}$), rms variation

from the mean (u'), skewness (S_u) and the kurtosis or flatness factors (K_u) values tabulated are averages from the 2 or 3 runs.

The axial velocity p.d.f. is skewed slightly to the lower velocities ($S_u = -0.15$) and has a relatively flat peak ($K_u = 2.16$) compared to a normal Gaussian p.d.f. ($S_u = 0.0$ and $K_u = 3.0$). As will be shown, these characteristics vary across the shear layer, depending on the local velocity profile shape.

The inner-jet fluid concentration p.d.f. shows the range of the concentration fluctuations which occurred at $r/R_o = 0.2$. The peak in the p.d.f. appears near 0.2, however, the profile shows a skewness toward the higher concentrations. As a result, the mean concentration is 0.28. Note the concentration fluctuation rms value is high, 0.18, for the mean value of 0.28. Other concentration p.d.f.'s at locations near the inlet and with average concentrations near 0.5 showed peaks at the concentration values near 0.0 and 1.0 indicating eddies of unmixed fluid were passing through the probe volume.

The concentration p.d.f.'s show some probabilities greater than 1.0 and less than 0.0, the limits for the inner jet concentration. The concentration measurements less than 0.0 were attributed to photomultipler dark current. The concentration measurements greater than 1.0 were attributed to nonuniformity of the dye/inner-jet water mixture and shifts in the inlet dye concentration as well as zero shift and dark current. The concentration p.d.f.'s have some variations due to differences in acquisition location. These data were obtained at three different azimuthal locations and at slightly different radii; $\Delta r/R_o \approx 0.02$. With only 1000 samples in the p.d.f., there were also some variations in the individual p.d.f. values. However, for the same flow conditions and measurement location, the mean values were repeatable ± 1 percent of the inner-jet concentration level.

The probability density function for the momentum transport in the r-z plane, uv, (Fig. 5), shows a peak about the zero uv transport rate. All of the momentum transport rates for $0.0 < r/R_o < 0.7$ had the highest probabilities in the two bins adjacent to $uv = 0$. For $r/R_o = 0.2$ (shown), the r-z momentum transport rate, uv, is negative, i.e., inward. This shape of the momentum transport rate also occurs in turbulent boundary layers [9].

The radial mass transport rate (vf) p.d.f. shows similar characteristics to the uv p.d.f. Note the average radial mass transport rate is positive (radially outward), however, the peak probability occurs for a small negative value of vf. The skewnesses for the absolute values of both the radial mass transport rate and the momentum transport rate are approximately the same, although the sign of each skewness is opposite the other.

Although mean and fluctuating velocity and concentration distributions and transport rate distributions are required to evaluate the accuracy of predictions with a given turbulent transport model, they do not provide the insight required to determine where the deficiencies in a turbulent transport model are located. Examination of the probability density functions for each data set can show if the experimental conditions are compatible with the assumptions in current or proposed models.

Axial Velocity. The first four moments of the axial velocity p.d.f.'s at $z = 102$ mm are presented in Fig. 6. This axial location is downstream of the wake region (Fig. 1) at the approximate center of the recirculation cell. These data include measurements along four radii from three different sets of measurements: uv along $\theta = 0$ and 180 deg, uw along $\theta = 90$ and 270 deg, and uc along $\theta = 90$ and 270 deg. The variations of the data from a single profile is attributed to slight asymmetries in the flow.

The mean axial velocity shows annular stream shear regions where the annular stream is accelerating the inner stream
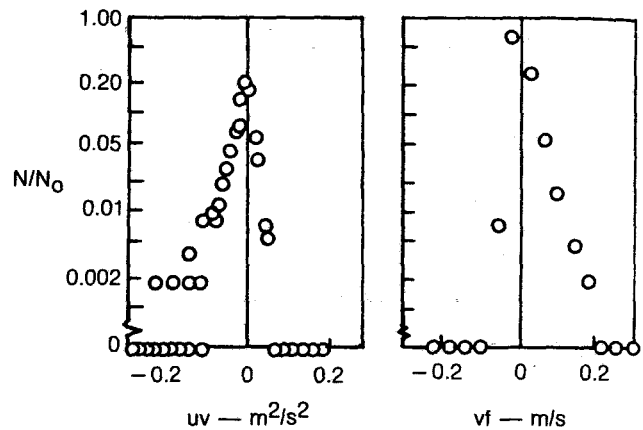
Fig. 5 Probability density functions for r-z momentum and radial mass transport ratio at $r/R_o = 0.2$; $\Delta uv = 0.01$ m^2/s^2, $\overline{uv} = 0.0142$ m^2/s^2, $\sigma_{uv} = 0.030$ m^2/s^2, $S_{uv} = -2.14$, $K_{uv} = 11.9$; $\sigma_{vf} = 0.04$ m/s, $\overline{vf} = 0.0165$ m/s, $\sigma_{vf} = 0.028$ m/s, $S_{vf} = 2.23$, $K_{vf} = 10.4$

RADIUS RATIO — r/R_0
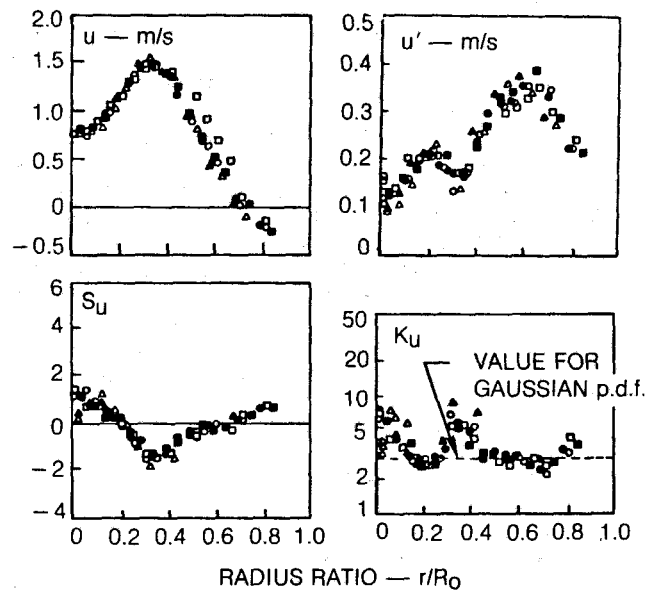
Fig. 6 Moments of axial velocity profile; $\theta = 0$ deg — o △, 180 — ● ▲, 90 — ■, 270 — □

fluid, $0 < r/R < 0.3$ and where the annular stream is interacting with the fluid in the recirculation zone, $0.5 < r/R_o < 0.8$. Note the peak velocities measured in the recirculation zone are approximately 15 percent of the peak annular velocity. The fluctuating axial velocity, u', shows peaks at the radial locations where the shear rates are the greatest. The peak values of u' were approximately 50 percent greater than the values of v' and w' at the peak axial shear locations and approximately equal to values of v' and w' at the zero shear locations. This result is compatible with results from previous shear layer experiments [9–11].

The skewness profiles show that the velocity p.d.f.'s had positive skewness in the center region ($r/R_o < 0.20$). This indicated that the longer tails of the p.d.f.'s are in the positive velocity direction; a few eddies of fluid with higher axial velocities penetrated into the inner jet region to accelerate the flow. The skewness factors for $0.2 < r/R_o < 0.55$ are negative which indicates the longer tails of the p.d.f.'s were in the lower velocity direction. Note the skewness is near zero in the peak shear regions at $r/R_o < 0.2$ and 0.55. The kurtosis tended to be greater than 3.0, the value for a Gaussian distribution, when the skewness factor deviated from zero.

The kurtosis, K_u, for $r/R_o < 0.2$ and 0.66 was less than 3.0 which indicates a tendency toward a flat top on the p.d.f.

The variation of the skewness and kurtosis from the value for a Gaussian p.d.f. appeared to be correlated to the local curvature of the axial velocity profile. The relationship is that $S_u < 0$ if $\partial^2 U/\partial r^2 < 0$ and $S_u > 0$ if $\partial^2 U/\partial r^2 > 0$. The kurtosis is also related to the curvature of the axial velocity profile. When the absolute value of curvature is high, the kurtosis is also higher than occurs for a Gaussian p.d.f. When the velocity profile curvature passes through zero, the kurtosis is approximately equal to 3, the value for a Gaussian p.d.f. The magnitude of the deviations from the values for a Gaussian p.d.f. also appears to be proportional to the magnitude of $\partial^2 U/\partial r^2$. The aforementioned relationships may not be universal but existed for the flow at the axial locations analyzed.

Concentration. The moments of the inner jet concentration are presented in Fig. 7. The mean value of $r/R_o = 0$ is approximately 0.90. The concentration p.d.f. at this radius showed the most probable concentration was the inlet concentration. The concentration rapidly decreased with increasing r/R_o to a value of zero at $r/R_o \approx 0.4$. At values $r/R_o > 0.6$, the concentration increased due to the recirculation cell. Note that high concentration fluctuations, f', occur at $r/R_o = 0.2$ where the mean and fluctuating concentrations are approximately equal. This can occur if the inner jet fluid passing through the probe volume has concentrations near 1.0 or 0.0. These data were obtained along radii at four azimuthal locations as part of the uf, vf, and wf mass turbulent transport data acquisition.

The values of S_f for $r/R_o < 0.15$ were negative, indicating the tails of the concentration p.d.f.'s were toward low values of f. At $r/R_o = 0.4$, the skewness factor reached a value of 4 to 6. These values were higher than the skewness factors obtained for the velocity p.d.f.'s.

The flatness factor or kurtosis profile has an interesting variation. Near $r/R_o = 0$, where the mass transport rates are near zero, the K_f is above 10. In the high radial mass transport region, $0.1 < r/R_o < 0.2$, the K_f is less than 3. The shape of the concentration p.d.f.'s with $K_f < 3$ either flat topped or double-peaked. As the mean concentration approaches zero at $r/R_o = 0.35$, K_f increases indicating few occurrences of large variations from the mean concentration. Although the concentrations are low in the recirculation cell, $r/R_o < 0.6$, and therefore the relative accuracy of the measurements are low, the measurements show that S_f and K_f are close to the values for a Gaussian concentration distribution, 0 and 3, respectively.

R-Z Momentum Transport. The moments of the r-z momentum transport are presented in Fig. 8. Because most of the momentum transport in this plane is due to the radial variation of the axial velocity, the discussion of the turbulent momentum transport rate distribution will be related to the axial velocity profile and the shear regions presented in Fig. 6. The negative momentum transport rate for $r < 0.3$, due to the radially-inward transport, decreased with increasing z from $z = 102$ mm and was essentially zero at 254 mm. Radial outward momentum transport for $r > 0.35$ occurred in the free shear layer between the annular stream and the recirculating fluid at all axial locations. At the upstream end of the recirculation zone, $z = 13$ mm and 51 mm, the radial transport in the backward flowing region of the recirculation cell had approximately zero transport. At locations further downstream ($z > 100$ mm), the low or zero transport rate locations were estimated to lie closer to the wall.

The second central moment (or rms fluctuation from the mean) of the turbulent transport in the r-z plane, σ_{uv}, has been previously used to analyze and evaluate the turbulent trans-
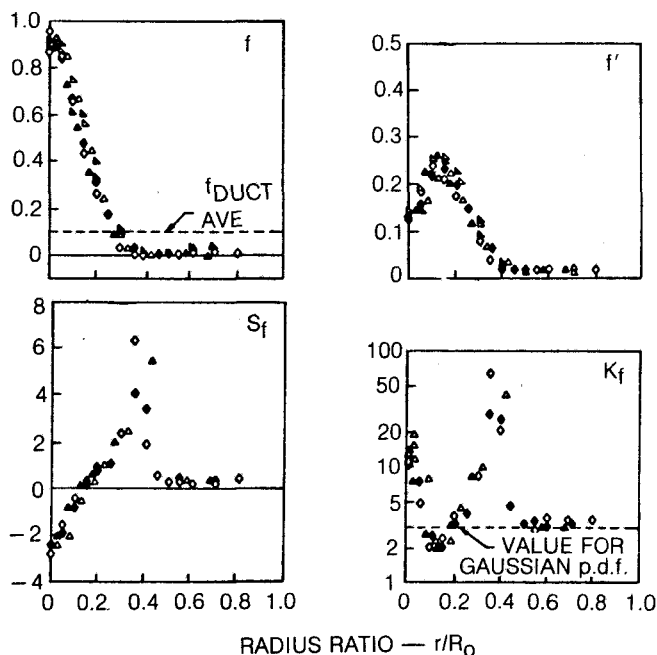
Fig. 7 Moments of concentration profiles; $\theta = 0$ deg $- \triangle \triangle$, 180 $- \blacktriangle \blacktriangle$ 90 $- \blacklozenge$, 270 $- \lozenge$
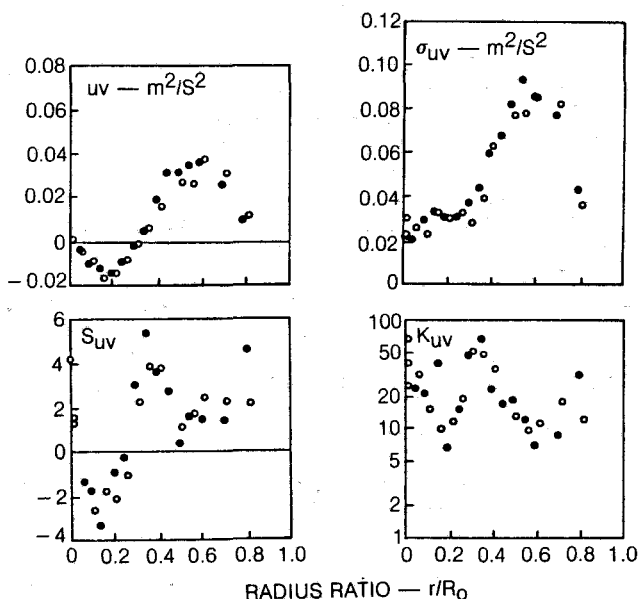
Fig. 8 Moments of turbulent momentum transport profiles; $\theta = 0$ deg $- \circ$, 180 $- \bullet$

port processes in the boundary layers, e.g., [10]. A comparison of σ_{uv} with $\overline{uv}$ shows that σ_{uv} was always at least a factor of 1.5 greater than $\overline{uv}$. Ratios of $\sigma_{uv}/\overline{uv}$ approximately equal to 3 were previously reported for boundary layers [10].

The skewness factor should have approached zero at $r/R_o = 0$ due to the zero shear stress at that location and symmetry of the flow. S_{uv} is generally positive where $\overline{uv}$ is positive and negative where $\overline{uv}$ is negative; however, the peak values of S_{uv} occur when the shear is near zero, $r/R_o = 0.35$ and 0.8. The kurtosis, K_{uv}, also varied across the shear layer. The values for $r/R_o \approx 0.0$, where the shear is zero, ranged from 30 to 70. The values of K_{uv} at $r/R_o \approx 0.2$ and 0.6, which were the locations with the peak negative and positive shears, decreased to values of approximately 10. Near the zero shear

RADIUS RATIO — r/R_O
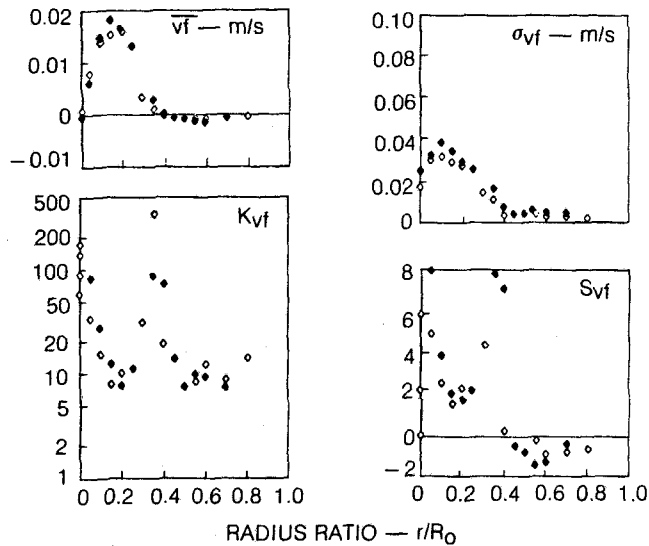
Fig. 9 Moments of turbulent radial mass transport profiles; $\theta = 0$ deg — $\diamond$, 180 — $\bullet$

RADIUS RATIO, r/R_O

Fig. 10 Axial mass transport rate profiles; $\theta = 0$ deg — $\triangle$, 180 — $\blacktriangle$

Fig. 11 Regions of countergradient axial mass transport and axial velocity accelerations; $\overline{uf} < 0$ is countergradient region

location, $r/R_o \approx 0.35$, the flatness factor K_{uv} increased to 50. These flatness factor results are similar to the results obtained in a turbulent boundary layer by Gupta and Kaplan [10].

Radial Mass Transport. The measured radial mass transport rate profiles are presented in Fig. 9. The radial mass transport rate is associated with the radial gradient of the mean concentration profiles. Discussions of the mass transport rate will be related to these profiles, the shear regions, and the flow visualization results. The peak outward mass transport occurred at $r/R_o = 0.15$ which is also the radial location of the peak concentration gradient. The transport at $r = 0$ approaches 0, as expected, for axisymmetrical profiles. The negative (inward) mass transport for $r/R_o > 0.4$ is due to the turbulent transport of inner jet fluid from the recirculation cell. The peak value of σ_{vf} is approximately twice the peak value of vf. The skewness, S_{vf}, has characteristics similar to those for S_{uv}, i.e., positive values for when vf is positive, negative values when vf is negative, and large values of S_{vf} when vf is near zero at $r/R_o = 0$ and 0.4. The shape of the K_{vf} profile is also similar to that of the K_{uv} profiles. K_{vf} is near 10 in the transport regions and increases by a factor of 10 when the transport is near zero, $r/R_o = 0$ and 0.35. The values of K_{vf} at these two radii are a factor of 3 to 5 greater than the peak values of K_{uv} in the low shear regions.

Axial Mass Transport. Turbulent scalar (mass) transport is generally associated with the scalar (concentration) gradients and a transport diffusion coefficient, $\dot{m}_i = -\epsilon_m (\partial f/\partial x_i)$. However, for some classes of flows with turbulent transport, notably atmospheric transport of heat, the scalar transport can be opposite the direction of the scalar gradient. This class of scalar transport is denoted "countergradient" transport and requires a "Reynolds stress" formulation to calculate the scale (mass) transport rate (e.g., [12]). Some of the axial mass transport rate measurements obtained in this study fall into the "countergradient diffusion transport" category. Discussion of these flows will relate the measured axial mass transport to the velocity shear field which produces the mass transport mechanism.

The axial mass transport rate, $\overline{uf}$, profiles are presented in Fig. 10. The most important feature on these figures is the negative mass turbulent transport which occurred in the central region of the test session at $z = 51, 102, 152$, and 203 mm from the inlet plane. Note the axial mass transport rate decreased from near zero at $z = 13$ mm to a maximum
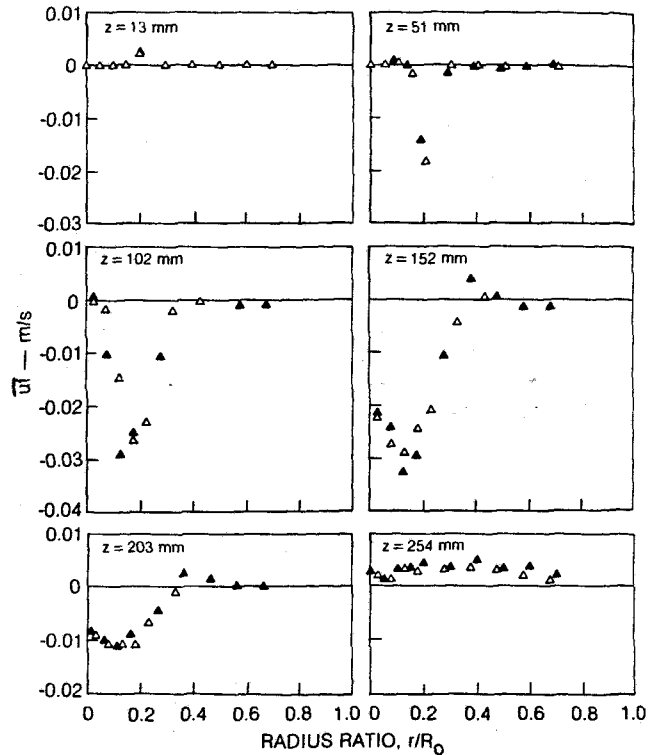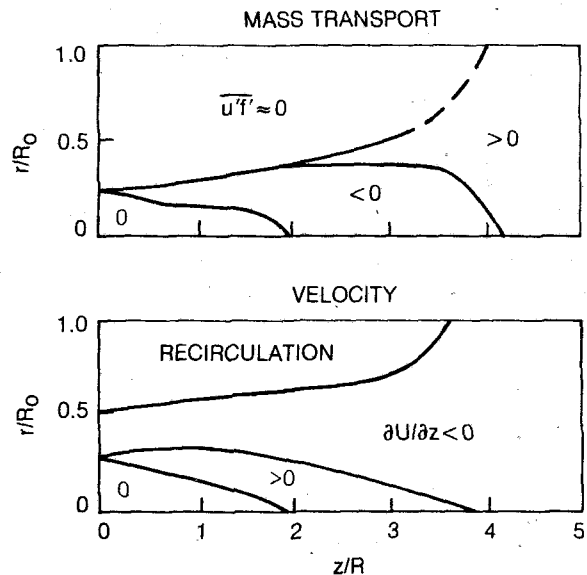
negative level at $z = 152$ mm from the inlet plane. Through the region of the test section, the inner stream mass concentration decreased with increasing axial location. Note that the peak absolute values of the axial transport rates were higher than the values for the radial transport (Fig. 9) even though the peak radial concentration gradients were more than ten times the axial concentration gradients.

The countergradient transport process can be explained by considering the shape of the axial velocity profiles in the countergradient transport region (Fig. 6) and the eddy structure associated with the momentum transport. In the region where the inner jet was being accelerated by the an-

nular jet, the large eddies in that velocity shear layer near the centerline were "rolling" with the negative fluctuating axial velocities near the inner jet fluid. The results was that the preferred rotational orientation of these eddies retarded the flow in the streamwise direction and resulted in $uf < 0$ and, hence, countergradient mass transport. The regions with countergradient, $uf < 0$, and gradient, $uf > 0$, axial mass turbulent transport, and positive and negative axial velocity accelerations are shown in Fig. 11. The region with the countergradient mass turbulent transport was larger than the region where the flow from the inner jet was accelerated by the flow from the annular jet. The larger size of the countergradient region may be due to the response time or distance required to change the character of the turbulent structure.

The countergradient axial mass turbulent transport may be an appreciable portion of the mean convective mass transport. For example, at $z = 103$ mm and $r/R_o = 0.2$, the values of uf and $\bar{u}\bar{f}$ are -0.025 and 0.336, respectively; thus, $uf/\bar{u}\bar{f} = -0.074$. In the high countergradient axial mass transport region, the ratio of $uf/\bar{u}\bar{f}$ ranged from -0.05 to -0.10. Thus, it is apparent that the local turbulent transport coefficients are not isotropic. Further analysis of the experimental results and comparisons with predictions will be required to determine the extent of deficiencies in the turbulent transport models, the impact of these deficiencies on the numerical predictions, and the effects of improved turbulent transport modeling on the predictions.

Concluding Remarks

The velocity, concentration, and transport rate distributions measured downstream of coaxial jets discharging into an expanded circular duct showed region-to-region variations in the transport processes. Typical results were presented to describe the mixing characteristics. The accurate prediction of the phenomena measured is a difficult task which will probably require improvements in both the currently used transport models and mathematical methods. Following are the principal results from this study:

1 The turbulent momentum transport rate measurements in the r-z plane documented the local momentum fluxes due to turbulent mixing.

2 Countergradient turbulent axial mass transport was measured in the shear region between jets. The peak axial mass transport rates were greater than the peak radial mass transport rates, even though the axial concentration gradients were less than 1/10 the radial gradients.

3 The countergradient turbulent axial mass transport was related to the general direction of the eddies between the inner and annular jets. The countergradient axial mass transport occured when the annular jet was accelerating the inner jet fluid.

4 The skewness and kurtosis of the momentum transport p.d.f.'s in the peak shear region were approximately the same as previously measured in turbulent boundary layers. However, the kurtosis in the low shear region was greater than

previously measured in the wake region of turbulent boundary layers.

5 The skewness of the axial velocity p.d.f.'s was related to the curvature of the axial velocity profiles. $S_u > 0$ was obtained for $\partial U^2/\partial r < 0$; $S_u < 0$ was obtained for $\partial^2 U/\partial r^2 < 0$. The skewness was also proportional to the magnitude of $\partial^2 U/\partial r^2$.

6 The peak values of kurtosis for the mass transport p.d.f.'s were greater than the peak values for the momentum transport p.d.f.'s.

7 The kurtoses for all the transport p.d.f.'s were an order of magnitude greater in the low transport rate regions, including the recirculation region, than in the high transport rate regions.

Acknowledgment

References

1 Gerstein, M., ed., *Fundaments of Gas Turbine Combustion.* NASA Conference Publication 2087, 1979.

2 Hudson, D. W., "Combustion Modeling Needs for the 80s," AIAA Preprint 80-1288.

3 Mellor, A. M., "Turbulent Combustion Interaction Models for Practical High Intensity Combustors," *Seventeenth Symposium on Combustion,* Combustion Institute, 1979, p. 377.

4 Demetriades, A., "Probes for Multivariant Flow Characteristics," *Proceedings of the Dynamic Flow Conference,* 1978.

5 Anon., "Application of Nonintrusive Instrumentation in Fluid Flow Research," AGARD Conference Proceedings, No. 193, May, 1976.

6 Johnson, B. V., and J. C. Bennett, "Velocity and Concentration Characteristics and Their Cross Correlations for Coaxial Jets in a Confined Sudden Expansion," Symposium on the Fluid Mechanics of Combustion Systems, 1981 ASME Fluids Engineering Division Meeting, Boulder, Colo., June 22-24, 1981.

7 Johnson, B. V., and J. C. Bennett, "Mass and Momentum Turbulent Transport Experiments with Confined Coaxial Jets," NASA Contractor Report NASA CR-165574, UTRC Report R81-915540-9, Nov. 1981.

8 Tennekes, H., and J. L. Lumley, *A First Course in Turbulence,* ch. 6. MIT Press, 1972.

9 Lu, S. S., and W. W. Willmarth, "Measurements of the Structure of the Reynolds Stress in a Turbulent Boundary Layer," *Journal of Fluids Mechanics,* Vol. 60, pt. 3, 1973, pp. 481-511.

10 Willmarth, W. W., "Structure of Turbulence in Boundary Layers," *Advances in Applied Mechanics,* Vol. 15, Academic Press, N.Y., 1975.

11 Hinze, J. O., *Turbulence,* ch. 7, McGraw-Hill, N.Y., 1959.

12 Lumley, J. L., "Computational Modeling of Turbulent Flows," *Advances in Applied Mechanics,* Vol. 18, Academic Press, 1978.

13 *Data for Dye Lasers,* Kodak Publication No. JJ-169, Mar. 1972.

14 Habib, M. A., and J. H. Whitelaw, "Velocity Characteristics of Confined Coaxial Jets With and Without Swirl," ASME *Journal of Fluids Engineering,* Vol. 102, pp. 47-53.

15 McLaughlin, D. K., and W. G. Tiederman, "Biasing Correcting for Individual Realization of Laser Anemometer Measurements in Turbulent Flows," *Physics of Fluids,* Vol. 16, 1973, pp. 2082-2088.

Turbulent Flow Between Coaxial Cylinders With the Inner Cylinder Rotating

J. W. Polkowski

Brown, Boveri & Company,
Gas Turbines Division,
Baden, Switzerland

Turbulent flow in an annular gap between coaxial cylinders with the inner cylinder rotating is studied. It is shown that the circumferential and axial flows are independent of each other after the moment of momentum of the axial through flow acquires its final value along certain initial distance of the duct. This implies the applicability of Dorfman's solution of the momentum equation (developed for a purely circumferential motion) to the system with axial through flow; the moment coefficient is a function of circumferential flow only, being insensitive to the possible existence of Taylor vortices. Using a mixing length profile identical to that used by Dorfman, an analytic solution of the energy equation, which includes dissipation function, is found for a simplified model of Couette flow with crossflow and with constant heat flux at the boundaries. The correlation between the two flow models is assessed. The influence of the thickness of the laminar sublayer and of the mixing length profile on the solution of the momentum and energy equations is quantified.

Introduction

Flow between concentric cylinders (one of them rotating) occurs in various rotating machinery. One of many examples is the cooling system of gas turbine rotor, where some portion of the cooling air can be supplied to the rotor area through an annular duct, formed by two coaxial cylinders, with the inner cylinder rotating. Flow in such a system is usually characterized by very high Reynolds number ($Re_r \sim 10^6$). Most papers dealing with this type of flow analyze the problem in the range of low or moderate Re, in an effort to explain the nature of Taylor vortices and to quantify their complex effects. There are very few data, both experimental and theoretical, from the range of high Re.

The only papers dealing with high rotational Re and axial throughflow, are those of Yamada [1, 2]. When the axial Reynolds number (Re_z) and Taylor number are used as criteria, characterizing the flow, then, according to Kaye and Elgar [3] four regions can be distinguished. Their experiments were extended to higher Reynolds and Taylor numbers by Kosterin, Koshmanow, and Finatyew, and are quoted in [4], see Fig. 1.

In the first part of the paper Dorfman's solution of the momentum equation and its applicability for the process with axial throughflow is discussed. In the second part, the solution of the energy equation for constant heat flux at the boundaries is presented for Couette flow with crossflow. Such a flow, being interesting itself, constitutes an approximation of the flow between cylinders, provided that the flow conditions of the latter correspond to the region 3 (including the upper part of the region 4) as defined by Kaye and Elgar [3].

Discussion of Dorfman's Solution

Provided that V_r, V_z, $\partial/\partial z$, $\partial/\partial\Theta$, and ∇p are negligible, the momentum equations are reduced to

$$\frac{V_\Theta^2}{r} = \frac{1}{\rho}\frac{\partial p}{\partial r} \tag{1}$$

$$\frac{2}{r}\tau_{r\Theta} + \frac{\partial \tau_{r\Theta}}{\partial r} = 0 \tag{2}$$
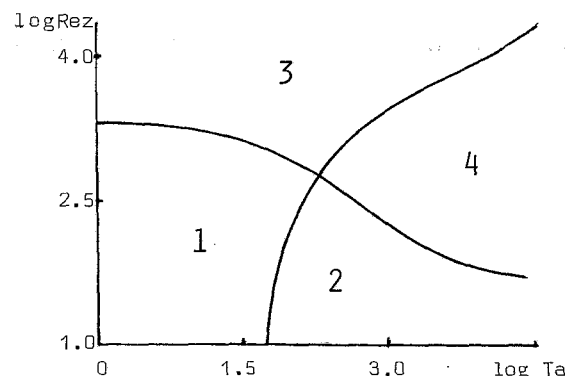
Fig. 1   Distribution of the state of flow: 1—laminar, 2—laminar with Taylor vortices, 3—turbulent, 4—turbulent with vorticity

where

$$\tau_{r\Theta} = -\rho \epsilon r \frac{\partial}{\partial r}\left(\frac{V_\Theta}{r}\right) \qquad (3)$$

Equation (2) implies

$$\tau_{r\Theta} r^2 = \text{const.} \qquad (4)$$

It was assumed that the mixing length $l = \epsilon/\nu*$ satisfies the relation

$$l = k \frac{(r_2 - r)(r - r_1)}{r_2 - r_1}, k = 0.4 \qquad (5)$$

From (3), (4), and (5) the following equation was obtained

$$\frac{k}{v*_1 r_1} \frac{\partial}{\partial r}\left(\frac{V_\Theta}{r}\right) = \frac{-(r_2 - r_1)}{r^2(r_2 - r)(r - r_1)} \qquad (6)$$

Linear velocity profiles in the laminar sublayers were assumed and the maximum dimensionless friction length $y^+ = y_{int}\nu*/\nu$ (dimensionless thickness of the laminar sublayer), denoted by α in [5], was assumed to be the same for both cylinders.

Integration of (6) gives $V = V(r)$ with two constants, ν_{*1} and C, that can be determined from the conditions at the two interfaces between laminar sublayers and turbulent layers (equations (7.79) and (7.80) in [5]). The final solution is given by equations (7.81) and (7.82). They can easily be rewritten to the following, for the present analysis more convenient form

$$2k(C_M)^{-0.5} = k\alpha\left(1 + \left(\frac{r_1}{r_2}\right)^2\right) - \left(1 - \frac{r_1}{r_2}\right)^2$$
$$+ ln\left(\left(1 + \frac{\text{Rer}(C_M)^{0.5}}{2\alpha}\right) \times \left(1 - \frac{r_1}{r_2}\right)\right)$$
$$+ \left(\frac{r_1}{r_2}\right)^2 ln\left(\left(\frac{r_2}{r_1} - 1\right)\left(\frac{\text{Rer}(C_M)^{0.5}}{2\alpha} - 1\right)\right) \qquad (7)$$

$$\frac{r_1}{r} k \frac{V}{V_1} 2C_M^{-0.5} = k(2C_M^{-0.5} - \alpha) + 1 - \frac{r_1}{r_2}$$
$$- \left(1 - \frac{r_1}{r_2}\right)\frac{r_1}{r} - ln\frac{r - r_1}{r} - ln\left(1 + \frac{\text{Rer}}{2\alpha}C_M^{0.5}\right)$$
$$- \left(\frac{r_1}{r_2}\right)^2 ln\left(\frac{r}{r_2 - r}\frac{r_2 - r_1}{r_1}\right) \qquad (8)$$

For the assumed values of k and α, and the known Rer, equation (7) determines C_M. Then by inserting C_M into (8),

stationary wall (cyl.)

$\leftarrow V_1$

moving wall (rotating cyl.)
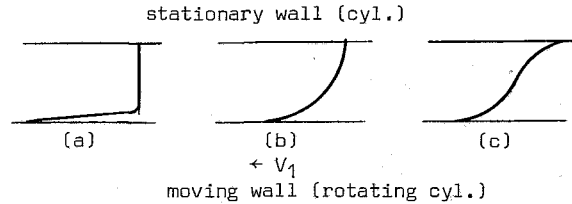
Fig. 2 The process of formation of the boundary layer
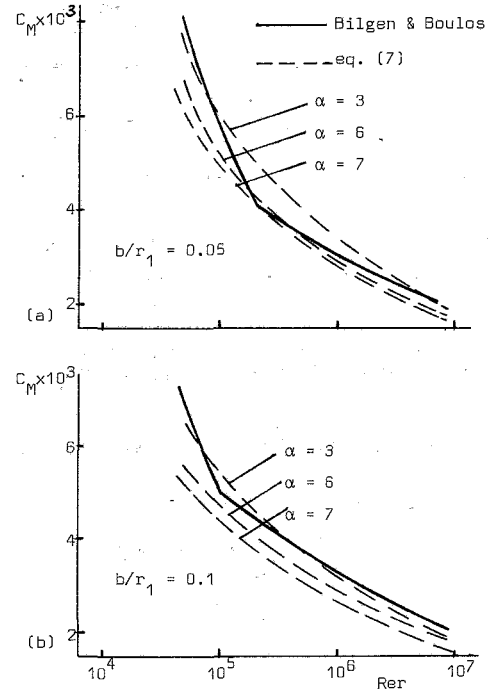
Fig. 3 Comparison of moment coefficient (C_M), computed from Bilgen and Boulos [7] empirical formula with Dorfman's [5] solution, equation (7)

the velocity profile can be found. Having given C_M from experimental results, α can be determined from (7). Dorfman found $\alpha = 7.5$ to give the best correlation between his solution and experimental data of Wattensdorf and Taylor.

If $r_1 \rightarrow \infty$ and $r_2 \rightarrow \infty$, whereas $r_2 - r_1 = b$, we have a flow between two parallel walls (Couette flow). It follows from (4)

Nomenclature

$b = r_2 - r_1$, width of the gap between cylinders; distance between the moving and the stationary plate, m
$C_M = M/(0.5\pi\rho\omega^2 r_1^4 l)$, moment coefficient
$C_f = \tau/(0.5\rho V_1^2) = 0.5C_M$, friction coefficient
$C_p =$ specific heat at const. pressure, J/(kgK)
$l =$ length of the cylinder in z direction, or "mixing length," m
$M =$ moment, Nm
$\dot{m} =$ mass flow rate, kg/s
$p =$ pressure, N/m^2
$r_1, r_2 =$ radius of inner and outer cylinder, respectively, m
$\text{Rer} = V_1 r_1/\nu =$ (tip) Reynolds number
$\text{Reb} = V_1 b/\nu =$ (Couette) Reynolds number
$\text{Rez} = V_z b/\nu =$ (axial) Reynolds number
$T =$ temperature, K
$\Theta, r, z =$ circumferential, radial, and axial

directions in cylindrical coordinate system
$x, y, z =$ corresponding directions in Cartesian coordinate system
$\Phi =$ dissipation function, W/m^3
$\lambda =$ thermal conductivity, W/(mK)
$\mu =$ dynamic viscosity, kg/(sm)
$\nu =$ kinematic viscosity, m^2/s
$\rho =$ density, kg/m^3
$\tau =$ shear stress, N/m^2
$\omega =$ angular velocity, rad/s

Subscripts

$ax =$ axial
$in =$ inlet
$out =$ outlet
$l =$ laminar
$T =$ turbulent

$C_f \times 10^3$

α = 6

α = 7

α = 11.5

10^4 10^5 10^6 Reb

10^5 10^6 10^7 Rer(b/r₁=0.1)

2×10^5 2×10^6 2×10^7 Rer(b/r₁=0.05)

——— $C_f = C_f(\alpha, \text{Reb})$, eq. (9)

– – – – $C_f = C_f(\alpha, \text{Rer})$, $b/r_1 = 0.1$

–·–·– $C_f = C_f(\alpha, \text{Rer})$, $b/r_1 = 0.05$ eq. (7)

Fig. 4 Comparison of friction coefficient (C_f), computed from Dorfman's general solution with the solution for Couette flow

that $\nu* = $ constant, while Rer and C_M are to be replaced by Reb and C_f.

From equation (7) and (8) we obtain

$$\frac{1}{(C_f)^{0.5}} = \sqrt{2}\left(\alpha - \frac{\ln\alpha}{k} - \frac{\ln 2}{2k} + \frac{1}{k}\ln(\text{Reb}C_f^{0.5})\right) \qquad (9)$$

$$\frac{V}{V_1} = 1 - \alpha\left(\frac{C_f}{2}\right)^{0.5} - \frac{1}{k}\left(\frac{C_f}{2}\right)^{0.5}\ln\left(\frac{\text{Reb}}{\alpha}\left(\frac{C_f}{2}\right)^{0.5}\frac{y/b}{1-y/b}\right) \qquad (10)$$

Sometimes the friction coefficient is defined as $C_f' = \tau/(\rho V_1^2)$, so $C_f' = 0.5\,C_f$ (e.g., Yamada in [2]), and then, for $k = 0.4$ and $\alpha = 9.363$, equation (9) takes on the form

$$\frac{1}{(C_f')^{0.5}} = 7.54 + 11.51\log(\text{Reb}(C_f')^{0.5}) \qquad (11)$$

which is identical to Yamada's equation (3) in [2]. Gazley [6] used the definition $C_f'' = \tau/(0.5\rho(V_1/2)^2)$, so $C_f'' = 4C_f$ and equation (9) for $k = 0.4$ and $\alpha = 11.6$ takes on the form

$$\frac{1}{(C_f'')^{0.5}} = 2.032 + 1.768\ln(\text{Reb}(C_f'')^{0.5}) \qquad (12)$$

which is identical to his formula (7) in [6]. Both, Yamada and Gazley, derived their formulae from the known relation $\bar{U}/v* = 5.5 + 2.5\,\ln\,(v*/\nu y)$. Substituting $\bar{U} = 0.5V_1$, and $y = 0.5b$ into this formula, one obtains the expression identical to (9) with $k = 0.4$ and $\alpha = 9.358$. It is an interesting conclusion, that Dorfman's general solution can be reduced for the specific conditions to the known formulae obtained in a different way. Figures 3(a) and 3(b) present $C_M = C_M(\text{Rer})$ for three different values of α computed from equation (7) for $k = 0.4$ as compared with the empirical formulae of Bilgen and Boulos in [7].

The relations $C_f = 0.5\,C_M$ and Reb $= $ Rer (b/r_1) make it possible to compare (for the same geometry) C_f computed from (9) (Couette flow) with the original solution for cylinders (7). The results are presented in Fig. 4.

It is clearly evident from Figs. 3 and 4 that:

• C_M increases with the decrease of α
• Approximation of the flow between coaxial cylinders by the Couette flow results in significant underestimation of the friction coefficient; the greater is b/r_1, the greater the difference between C_f (Couette) and C_f (cylinder) becomes. This explains, for example, why Gazley's formula (7) in [6] gives

persistently lower values of C_f than any experimental results, including his own (he assumed $\alpha = 11.5$).

Process With Axial Throughflow

Equation (4) is valid either in the absence of the axial flow ($V_z = 0$), or if the moment of momentum of the throughflow remains constant ($d\mu/dz = 0$). All measurements (e.g., Yamada in [1] and [2]) are based on the presumption, that after passing certain initial section of the duct, which is thought to "absorb" all inlet effects, the moment of momentum of the throughflow remains constant. Consequently, the torque of the inner cylinder in the central test section is measured from the reaction of the outer cylinder and this implies the validity of equation (4).

The moment of momentum of the axial flow is

$$\mu = \int rV_\Theta d\dot{m} \qquad (13)$$

where $d\dot{m} = 2\pi\rho V_z rdr$, so we have

$$\mu = 2\pi\rho\int_{r_1}^{r_2} V_\Theta V_z r^2 dr \qquad (14)$$

introducing mean values of velocities, $\bar{V}_z$ and $\bar{V}_\Theta$ we have

$$\Delta\mu = 2/3\pi\rho\bar{V}_z(r_2^3 - r_1^3)\Delta\bar{V}_\Theta \qquad (15)$$

Between any two cross sections, say $z = 0$ and $z = 1$, the following relation holds

$$\Delta\mu = 2\pi r_1^2\int_0^l(\tau_{r\Theta})_{r1}dz - 2\pi r_2^2\int_0^l(\tau_{r\Theta})_{r2}dz \qquad (16)$$

There is an absence in the literature of any indication how to determine the initial section of the duct.

The sample calculation presented below shows the moment, exerted by the rotating cylinder, necessary for $\dot{m}$ to attain the final value of μ, as compared with the moment for established conditions ($\mu(z) = $ constant).

It is usually assumed that for the established conditions $\bar{V}_\Theta \simeq 0.5\,V_1$. Dorfman's solution for any α implies $\bar{V}_\Theta \simeq 0.48\,V_1$. In the present calculation $V_\Theta = 0.48\,V_1$ is assumed. The flow conditions are as follows:

$\rho = 4.34$; $r_1 = 0.252$; $r_2 = 0.272$; Rer $= 5.268\times10^6$,

$\omega = 663.7$; $\dot{m} = 2$; $V_{\Theta in} = 0$.

From the previous analysis for $\dot{m} = 0$, the moment per/m of the rotating cylinder can be written as

$$M/l = C_M 0.5\pi\rho\omega^2 r_1^4 = 27.65, \quad (\tau_{r\Theta})_{r_1} = 69.29$$

while the moment of momentum, acquired by the throughflow, found from equation (15)

$$\mu = 2/3\pi\rho(r_2^3 - r_1^3)\bar{V}_z\bar{V}_\Theta = 42.1$$

The calculation clearly indicates the significant influence of the mass flow rate and inlet conditions on the total torque of the rotating cylinder, including the inlet section.

If $\mu = $ constant after passing the initial section, and compressibility can be neglected, it can be shown that the circumferential and axial flows are independent of each other.

We have under these conditions

$$\frac{\partial}{\partial\Theta} = 0, \quad V_r = 0, \quad \frac{\partial V_\Theta}{\partial z} = 0 \qquad (17)$$

and Navier Stokes equations, expressed in terms of stress tensor components, are reduced to the following form

$$\rho\frac{V_\Theta^2}{r} = \frac{\partial p}{\partial r} \qquad (18)$$

$$\frac{2}{r}\tau_{r\Theta} + \frac{\partial\tau_{r\Theta}}{\partial r} = 0 \qquad (19)$$

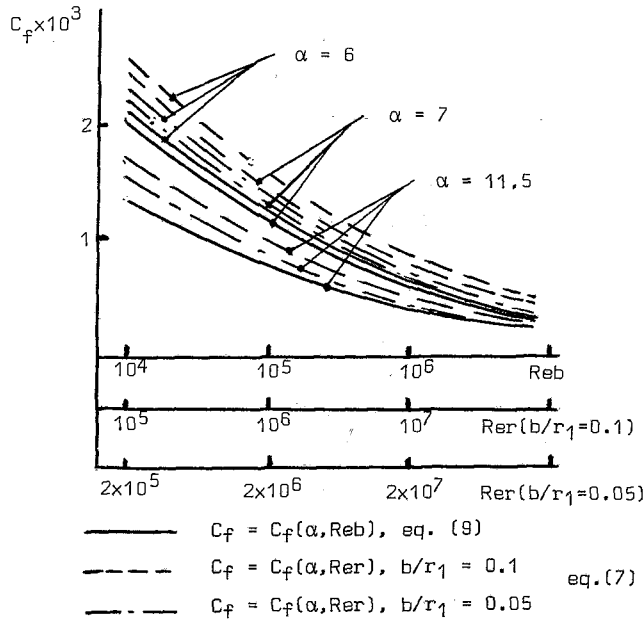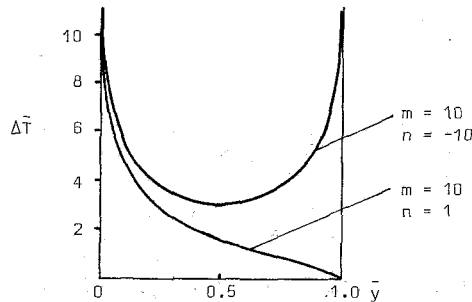**Fig. 5 Temperature profiles for two different boundary conditions (from Table 1)**

$$\rho V z \frac{\partial V z}{\partial z} = \frac{\partial \tau_{rz}}{\partial r} + \frac{\partial \tau_{zz}}{\partial z} + \frac{\tau_{rz}}{r} \qquad (20)$$

Equation (19) is equivalent to (4), and it is a function of V_Θ alone, while (20) is a function of V_z alone. This leads to the following conclusion: if $\mu(z)$ = constant, the torque depends only on V_Θ, while the pressure drop along the duct depends only on the axial flow. It is obviously not valid along the inlet section of the duct or in the presence of vortices. Experiments show, however, that unlike pressure coefficient, the moment coefficient is insensitive to the existence of vortices.

Pressure Drop Along the Duct. Yamada's experimental results in [1], so far the most extensive on the subject, verify the postulate that as long as the flow is purely turbulent without vortices (zone 3 as defined in [3]), pressure coefficient, λ, remains constant for a given Rez within the wide range of Reb, being equal to λ for Reb=0. If, however, flow is within the zone 3, but close to the boundary between the zone 3 and 4, λ is greater than that for a pure axial flow.
This implies two things:

• There is some transition area between the zones 3 and 4, rather than a line; in [3] the authors admitted themselves that "it is felt that this boundary line was not as clearly measurable or discernable as the three other boundaries."
• Pressure drop depends strongly on the existence of vortices. Yamada's empirical formula (13) in [1] gives values of λ relatively close to the experimental results in the flow regime with vortices.

Moment Coefficient in the Presence of Axial Flow. One of the conclusions drawn here is that after the final value of the moment of momentum of the throughflow (μ) is attained (being constant along the remaining section of the duct); the moment coefficient (C_M) does not depend on Rez. Yamada's results in [2] verify the conclusion. For example, Fig. 6 in [2] shows that in the range of Rez from 10^3 up to 6×10^3 and 8×10^3 for Reb = 1.5×10^4 and 2×10^4, respectively, C_f remains constant and almost identical to the empirical formula in [7], which, in turn, is in a fairly good agreement with Dorfman's solution, though it depends on the selected value of α (see Fig. 3). For Rez > 10^4, there is a sharp increase of C_f and it becomes a strong function of Rez.

It is postulated that C_f increases, starting from certain critical value of Rez (for Reb = constant), because the inlet section is not long enough and that an increase of μ takes place within the test section. Consequently the relation πr^2 = constant is not satisfied.

In order to estimate the initial distance of the annular duct (l_{cr}), which is necessary for μ to acquire its final value (provided $\mu_{in} = 0$), the existing empirical relation for a growth of turbulent boundary layer along a flat plate will be applied. The formula, based on 1/7 power law, reads

$$\delta = 0.379 x \left(\frac{\nu}{U_\infty x} \right)^{0.2} \qquad (21)$$

where x is a distance along the plate from the leading edge. Setting $V_1 = u_\infty$ the distance x, corresponding to $\delta = b$ can be found from equation (21). This distance is interpreted as a path, covered by any point on the surface of the inner, rotating cylinder, in time $t' = x/V_1$. Time, t', is multiplied by 2, because first the boundary layer (of the circumferential flow) is growing from the surface of the inner (rotating) cylinder to the outer cylinder, and then it propagates back in opposite direction until the final V_Θ profile is formed. The process of formation of the boundary layer is illustrated in Fig. 2.

(a) Situation at the inlet: $t = 0$, $l = 0$, $d\mu/dl > 0$, $\pi r^2 \neq$ const., $V_\Theta = 0$ except the area next to the wall.
(b) Some distance from the inlet: boundary layer touches the opposite wall and the effect of the upper plate starts propagating down, $d\mu/dl > 0$, $\pi r^2 \neq$ constant.
(c) Final, stable situation: $t = 2t'$, $l = l_{cr}$, $\mu(z) =$ constant, $\pi r^2 =$ constant.

If time, necessary for axial throughflow to pass the initial distance, l_{cr}, is denoted by t_z, then we have:

• if $t_z > 2t'$, the final V_Θ profile is formed within l_{cr} and μ = constant in the remaining part of the duct, including test section. Hence, $C_M = C_M$(Reb), and it does not depend on Rez.
• if $t_z < 2t'$, the formation of the final V_Θ profile, as well as the increase of μ, takes place beyond l_{cr} and $C_M = C_M$(Reb, Rez).

For ν and V_1 as parameters, l_{cr} depends on the absolute value of b and V_z. The sample calculation was performed for data of some of Yamada's experiments.

The inlet (upstream) section of his test rig was $l_{in} = 0.09$. Temperature of water assumed to be either 10° ($\nu = 1.3 \times 10^{-6}$) or 20° ($\nu = 1.01 \times 10^{-6}$). It was assumed as an approximation that $t_z = l_{cr}/\bar{V}_z$. The results showed that $t_z > 2t'$ for Rez < 10^4 (C_f = constant, as it is evident in Fig. 6 in [2]), whereas for Rez = 10^4, both t_z and $2t'$ are of the same order, being equal to ~ 0.01s. C_f increases sharply for Rez > 10^4, and $2t'$ becomes greater than t_z. In the range of Rez in Yamada's experiments, μ is sometimes a few times greater than moment within the test section, corresponding to $\mu =$ constant.

Using equation (21), the dimensionless critical distance of the duct can be expressed as a function of Rez and Reb. For $\delta = b$ and $U_\infty = V_1$, equation (21) can be rewritten in the form

$$x = \frac{b^{5/4} V_1^{1/4}}{(0.379)^{5/4} \nu^{1/4}} \qquad (22)$$

From the relation

$$2t' = t_z \qquad (23)$$

where $2t' = 2x/V_1$ and $t_z = l_{cr}/\bar{V}_z$, using equation (22) we obtain

$$\frac{l_{cr}}{b} = \frac{2}{(0.379)^{1.25}} \text{Rez Reb}^{-0.75} = 6.725 \text{ Rez Reb}^{-0.75} \qquad (24)$$

For a given test rig, l_{in} and b are given, so the maximum value of Rez, corresponding to C_f = constant (in the test section) takes on the form

$$\text{Rez}' = \frac{1}{6.726} \frac{l_{cr}}{b} \text{Reb}^{0.75} \qquad (25)$$

The sample calculation showed a fairly good agreement between Yamada's results (for a turbulent flow) and equation (25). Rez' from equation (25) corresponds to the beginning of

a sharp increase of C_f, although in some of his experiments a slight increase of C_f was observed from Rez < Rez'.

The foregoing analysis can be summarized as follows. If the entire length of the duct is l, then along $(l-l_{cr})$, μ = constant and moment coefficient (C_M) is a function of the circumferential flow only. The initial section l_{cr} can be determined from equation (25). If the initial section l_{cr} is a part of the system, the total moment, exerted by the rotating cylinder can be determined from the relation

$$M = C_M 0.5\pi\rho\omega^2 r_1^4 l + \Delta\mu$$

where C_M is that found for a purely circumferential flow, and $\Delta\mu$ is defined by equation (15).

Unlike pressure drop, moment coefficient is insensitive to the existence of vortices. It is evident from Yamada's experiments that even in the zone 4, C_f is equal to that for a purely circumferential flow, if $l_{in} \geq l_{cr}$.

Heat Transfer and Temperature Field

The equation of energy can be written as

$$\frac{dH}{dt} = \frac{1}{\rho}\,\Phi + \mathbf{V}\cdot\mathbf{f} + \frac{1}{\rho}\,\nabla\cdot(\lambda\nabla T) \qquad (26)$$

where specific total enthalpy $H = u + p/\rho + V^2/2$. Multiplying scalarly each term of the equation of motion

$$\frac{d\mathbf{V}}{dt} = -\frac{1}{\rho}\,\nabla p + \mathbf{f} \qquad \text{by } \mathbf{V} \text{ we obtain}$$

$$\frac{1}{\rho}\frac{dp}{dt} = \frac{1}{\rho}\,\mathbf{V}\cdot\nabla p = \mathbf{V}\cdot\mathbf{f} - \frac{d}{dt}\left(\frac{V^2}{2}\right) \qquad (27)$$

If p = constant along V and C_p = constant, we have from (26) and (27)

$$C_p\frac{dT}{dt} = \frac{1}{\rho}\,\Phi + \frac{1}{\rho}\,\nabla\cdot(\lambda\nabla T) \qquad (28a)$$

Bearing in mind that

$$\frac{dT}{dt} = \mathbf{V}\cdot\nabla T = V_r\frac{\partial T}{\partial r} + V_\Theta\frac{\partial T}{r\partial\Theta} + V_z\frac{\partial T}{\partial z} = V_z\frac{\partial T}{\partial z}$$

Equation (28a) takes on the form

$$C_p V_z\frac{\partial T}{\partial z} = \frac{1}{\rho}\,\Phi + \frac{1}{\rho}\,\nabla\cdot(\lambda\nabla T) \qquad (28b)$$

The problem will be solved for a Couette type flow with crossflow (with the throughflow in the direction normal to the path of the moving plate). In view of the foregoing analysis such a solution can be considered only as an approximation of the flow between cylinders, only in the absence of Taylor vortices (regime 3) and not in the inlet section, as defined above. The relations, corresponding to (4) and (5), can now be written as

$$\tau = \text{constant} \qquad (29)$$

$$l = k\frac{(b-y)y}{b} = kb(1-\bar{y})\bar{y} \qquad (30)$$

From (30) we have

$$\epsilon = k(\tau/\rho)^{0.5}b(1-\bar{y})\bar{y} \qquad (31)$$

Dissipation function takes on the form[1]

$$\Phi_T = \frac{\tau^2}{\rho\epsilon} = \tau^{1.5}\rho^{-0.5}(kb(\bar{y}-\bar{y}^2))^{-1} \qquad (32)$$

$$\Phi_l = \frac{\tau^2}{\mu} \qquad (33)$$

and thermal conductivity

$$\lambda_T = (\rho\epsilon C_p)/Pr_T = (C_p/Pr_T)kb(\tau\rho)^{0.5}(\bar{y}-\bar{y}^2) \qquad (34)$$

$$\lambda_l = \mu C_p/Pr_l = \text{const.} \qquad (35)$$

According to the standard approach it is assumed that the net heat flux is negligible in the x and z directions; hence, $\nabla\cdot(\lambda\nabla T) = \partial/\partial y(\lambda\partial T/\partial y)$. From (28) we now obtain

$$\rho C_p V_z\frac{\partial T}{\partial z} = \Phi + \frac{\partial\lambda}{\partial y}\frac{\partial T}{\partial y} + \lambda\frac{\partial^2 T}{\partial y^2} \qquad (36)$$

Assuming that V_z profile satisfies 1/7 power law (being linear in laminar sublayer) we get

$$V_z = V_{z\max}\left(\frac{y}{\delta}\right)^{1/7}, \text{ where } \delta = 0.5b, \text{ hence}$$

$$V_z = V_{z\max}(2)^{1/7}(\bar{y})^{1/7} = a(\bar{y})^{1/7}, \qquad (37)$$

$$\text{valid for } \delta_l \leq \bar{y} \leq 0.5$$

$$\text{and } V_z = a(1-\bar{y})^{1/7}\text{valid for } 0.5 \leq \bar{y} \leq (1-\delta_l).$$

Parabolic equation (36) can easily be solved using finite difference method. The importance of the phenomena, occurring in laminar sublayers, would make it necessary to have a step in y-direction of the order of (and less than) the thickness of the laminar sublayer, leading to the enormous time of computation, whatever method is chosen. If, however, $\partial T/\partial y$ = constant at $y = 0$ and $y = b$, i.e., $\bar{y} = 0$ and 1; (constant heat flux at the boundaries), then $\partial T/\partial z$ = constant, except some initial distance, and (36) becomes an ordinary equation, which can be solved analytically.[2]

Energy (mechanical) transferred to the flow from unit of an area of the moving plate is equal to $A\tau V_1$ $(A = 1m^2)$. For the flow conditions under consideration, this energy is entirely converted into heat, and dissipation function is a measure of heat generated. It is easy to check that $A\tau V_1$ is equal to $\int\Phi dv$, where v is a parallelopiped of the size $1\times1\times b$. It is convenient to take τV_1 as a unit of heat flux at the boundaries, and to denote heat transferred to the system at $\bar{y} = 0$ by $q_{in} = mTV_1$, and $q_{out} = nTV_1$ at $\bar{y} = 1$. Hence, the energy transferred to the system $q' = (m+1)\tau V_1$. Dissipation function is symmetrical with respect to $\bar{y} = 0.5$; consequently, temperature profile is also symmetrical for $m = -n$; while $\partial T/\partial z = 0$ for $n = m+1$.

Mass flow rate can be expressed as

$$\dot{m} = 2s\rho b\int_0^{0.5} V_z d\bar{y} = 2s\rho ba\int_0^{0.5}\bar{y}^{1/7}d\bar{y} \qquad (38a)$$

where s is the extension in x-direction. From (38a) we get

$$\dot{m}/s = \dot{m}' = 0.7925082\rho ab \qquad (38b)$$

It follows that $\partial T/\partial z$ can be written as

$$\frac{\partial T}{\partial z} = \frac{(m-n+1)\tau V_1}{\dot{m}'C_p}$$

or

$$\frac{\partial T}{\partial z} = \frac{e\tau V_1}{h\rho aC_p} \qquad (39)$$

where $e = m - n + 1$ and $h = 0.7925082$.

Velocity in z-direction in the laminar sublayer takes on the form

$$V_z = a(\delta)^{-6/7}\bar{y}, \quad 0 \leq \bar{y} \leq \delta \qquad (40)$$

found from the condition at the interface, where $V_z = a\delta^{1/7}$. Inserting (32) or (33), (34) or (35), (37) or (40), and (39) into (36) and using definition of friction coefficient, C_f, we obtain for turbulent zone

$$\frac{\partial^2 T}{\partial \bar{y}^2} + \frac{1-2\bar{y}}{\bar{y}-\bar{y}^2}\frac{\partial T}{\partial \bar{y}} = \frac{E}{(1-\bar{y})(\bar{y})^{6/7}} - \frac{F}{(\bar{y}-\bar{y}^2)^2} \quad (41)$$

where

$$E = \frac{Pre}{kh}\frac{V_1^2}{Cp}(C_f/2)^{0.5}, \quad F = \frac{Pr}{2k^2}\frac{V_1^2}{Cp}C_f$$

for laminar sublayer

$$\frac{\partial^2 T}{\partial \bar{y}^2} = Pr\left(\frac{V_1^2}{2C_p}\right)\left(\frac{e}{h}Reb\ C_f(\delta)^{-6/7}\bar{y} - 0.5Reb^2C_f^2\right) \quad (42)$$

where

$$\delta = \alpha/(Reb(C_f/2)^{0.5})$$

The first integration gives the following results

Laminar 1, $0 \le \bar{y} \le \delta$

$$\frac{\partial T}{\partial \bar{y}} = Pr\left(\frac{V_1^2}{2C_p}\right)\left(0.5RebC_f\frac{e}{h}(\delta)^{-6/7}\bar{y}^2\right.$$
$$\left. - 0.5Reb^2C_f^2\bar{y} - RebC_fm\right) \quad (43)$$

Laminar 2, $1 - \delta \le \bar{y} \le 1$

$$\frac{\partial T}{\partial \bar{y}} = Pr\left(\frac{V_1^2}{2C_p}\right)\left(-0.5RebC_f\frac{e}{h}(\delta)^{-6/7}(1-\bar{y})^2\right.$$
$$\left. + 0.5Reb^2C_f^2(1-\bar{y}) - RebC_fn\right) \quad (44)$$

Constants of integration have been found from the boundary conditions at $\bar{y} = 0$ and $\bar{y} = 1$.

Turb. 1, $\delta \le \bar{y} \le 0.5$

$$\frac{\partial T}{\partial \bar{y}} = Pr\left(\frac{V_1^2}{2C_p}\right)\left(\frac{7}{4}\frac{e}{kh}(C_f/2)^{0.5}\frac{\bar{y}^{1/7}}{1-\bar{y}}\right.$$
$$\left. - \frac{C_f}{k^2}\frac{ln\left(\frac{\bar{y}}{1-\bar{y}}\right)}{(\bar{y}-\bar{y}^2)} + \frac{C_T'}{\bar{y}-\bar{y}^2}\right) \quad (45a)$$

Turb. 2, $0.5 \le \bar{y} \le (1-\delta)$

$$\frac{\partial T}{\partial \bar{y}} = Pr\left(\frac{V_1^2}{2Cp}\right)\left(-\frac{7}{4}\frac{e}{kh}(C_f/2)^{0.5}\frac{(1-\bar{y})^{1/7}}{\bar{y}}\right.$$
$$\left. - \frac{C_f}{k^2}\frac{ln\left(\frac{\bar{y}}{1-\bar{y}}\right)}{\bar{y}-\bar{y}^2} + \frac{C_T''}{\bar{y}-\bar{y}^2}\right) \quad (46a)$$

Here the constants have been determined from the condition of equality of the heat flux at the interfaces between laminar sublayers and turbulent zone, they are as follows:

$$C_T' = -\frac{3}{4}\frac{e}{kh}\left(\frac{\alpha}{Reb}\right)^{8/7}\left(\frac{C_f}{2}\right)^{-1/14} - 2\frac{\alpha}{k}\left(\frac{C_f}{2}\right)$$
$$- 2\frac{m}{k}\left(\frac{C_f}{2}\right)^{0.5} - \frac{2}{k^2}\left(\frac{C_f}{2}\right)ln\left(\frac{Reb(C_f/2)^{0.5}}{\alpha} - 1\right) \quad (45b)$$

$$C_T'' = \frac{3}{4}\frac{e}{kh}\left(\frac{\alpha}{Reb}\right)^{8/7}\left(\frac{C_f}{2}\right)^{-1/14} + 2\frac{\alpha}{k}\left(\frac{C_f}{2}\right)$$
$$- 2\frac{n}{k}\left(\frac{C_f}{2}\right)^{0.5} + \frac{2}{k^2}\left(\frac{C_f}{2}\right)ln\left(\frac{Reb(C_f/2)^{0.5}}{\alpha} - 1\right) \quad (46b)$$

At $\bar{y} = 0.5$, (45) and (46) give the same results. Setting $\Delta\bar{T} = \Delta T/(Pr(V_1^2/(2C_p)))$, we finally obtain

Table 1 Dimensionless temperature differences $(\Delta\bar{T})$/for six different boundary conditions and for $\alpha=3$, $k=0.4$

Reb	10^4				10^6
$\Delta\bar{y}$	lam. 1	lam. 2	0-0.5	0-1.0	0-1.0
$m=0$ $n=0$	−0.0101	+0.0101	−0.1469	0	0
$m=0$ $n=1$	−0.0103	−0.1923	−0.2492	−0.999	
$m=10$ $n=1$	−2.0342	−0.1943	−9.2108	−10.983	−11.005
$m=10$ $n=-10$	−2.0320	+2.0320	−8.0854	0	0
$m=10$ $n=11$	−2.0361	−2.2181		−20.968	−21.009
$m=20$ $n=21$	−4.0619	−4.2440		−40.937	

Table 2 Effect of α and k on dimensionless temperature differences $(\Delta\bar{T})$ for Reb $= 10^6$

	$\Delta\bar{y}$	lam. 1	lam. 2	0-1.0	k
	α				
$m=10$ $n=1$	3	− .67996	− .06674	−10.9950	0.2
	11.3	−2.52987	− .23583	−11.0098	
	3	−1.20359	− .11641	−11.0050	0.4
	11.5	−3.90640	− .34969	−10.9988	
$m=10$ $n=11$	3	− .67998	− .74555	−20.9906	0.2
	11.5	−2.53010	−2.74990	−21.0189	
	3	−1.20360	−1.31640	−21.0090	0.4
	11.5	−3.90660	−4.21869	−20.9977	

Table 3 Effect of α and k on friction coefficient $(C_f \times 10^3)$

k \ α	3	6	11.5	
0.2	0.433	0.433	0.395	
0.3	0.818	0.780	0.625	Reb $= 10^5$
0.4	1.270	1.138	0.837	
0.2	0.256	0.261	0.239	
0.3	0.502	0.482	0.403	Reb $= 10^6$
0.4	0.799	0.730	0.566	

Lam 1

$$\Delta\bar{T}_{0,\delta} = \frac{1}{3}\frac{e}{h}\frac{\alpha^{15/7}}{Reb^{8/7}(C_f/2)^{1/14}} - \alpha^2(C_f/2) - 2\alpha m(C_f/2)^{0.5} \quad (47)$$

Lam 2

$$\Delta\bar{T}_{(1-\delta),1} = -\frac{1}{3}\frac{e}{h}\frac{\alpha^{15/7}}{Reb^{8/7}(C_f/2)^{1/14}} + \alpha^2(C_f/2)$$
$$- 2\alpha n(C_f/2)^{0.5} \quad (48)$$

Turb. 1

$$\Delta\bar{T} = \frac{7}{4}\frac{e}{kh}\left(\frac{C_f}{2}\right)^{0.5}\int_{\bar{y}_1}^{\bar{y}_2}\frac{\bar{y}^{1/7}}{1-\bar{y}}d\bar{y}$$
$$- \frac{C_f}{k^2}\int_{\bar{y}_1}^{\bar{y}_2}\frac{ln\left(\frac{\bar{y}}{1-\bar{y}}\right)}{\bar{y}-\bar{y}^2}d\bar{y} + C_T'ln\left(\frac{\bar{y}_2(1-\bar{y}_1)}{\bar{y}_1(1-\bar{y}_2)}\right) \quad (49)$$

Turb. 2

$$\Delta\bar{T} = -\frac{7}{4}\frac{e}{kh}\left(\frac{C_f}{2}\right)^{0.5}\int_{\bar{y}_1}^{\bar{y}_2}\frac{(1-\bar{y})^{1/7}}{\bar{y}}d\bar{y}$$

$$- \frac{C_f}{k^2} \int_{\bar{y}_1}^{\bar{y}_2} \frac{ln\left(\frac{\bar{y}}{1-\bar{y}}\right)}{\bar{y}-\bar{y}^2} d\bar{y} + C_T''ln\left(\frac{\bar{y}_2(1-\bar{y}_1)}{\bar{y}_1(1-\bar{y}_2)}\right) \quad (50)$$

The first terms on the right-hand side of equations (45b) and (46b) as well as (47) and (48) are negligible; they do not exceed 1.5 percent of the value of the sum of the remaining terms for Reb = 10^4 and become even smaller for higher Reb.

Table 1 presents some results of the computation of temperature profiles for dimensionless friction length $\alpha = 3$, mixing length profile corresponding to $k = 0.4$ and for Couette Reynolds number Reb equal to 10^4 and 10^6.

Figure 5 shows two temperature profiles selected from Table 1.

Table 2 presents $\Delta \bar{T}$ for two different boundary conditions as a function of α and k.

The results show, that $\Delta \bar{T}$ within laminar sublayers can be quite significant. It increases with the increase of the assumed thickness of the layer, to some extent also with the increase of k, and amounts sometimes to more than 30 percent of the total $\Delta \bar{T} = \bar{T}_{y=1} - \bar{T}_{\bar{y}=0}$. $\Delta \bar{T}_{0,1}$ satisfies the following relationship

$$-\Delta \bar{T}_{0,1} \approx m+n \quad (51)$$

which does not depend on Reb, α, or k.

Having m and/or n equal to 0 corresponds to the adiabatic wall conditions. $n = m+1$ describes the situation in which heat transferred out of the system equals the sum of heat, transferred to the system and heat, generated within the system. Hence $\partial T/\partial z = 0$ and T = constant at the boundaries. The shape of the $T(y)$ profile does not depend on mass flow ($\dot{m}$), but it is slightly affected by the profile of V_z; the first terms on the right-hand side in equations (47–50) are very small as compared with other terms.

$\partial T/\partial z$ depends on $\dot{m}$ and on the net energy transfer to the system. Hence, it depends on friction coefficient (C_f), which in turn depends on k and α. C_f, as a function of α and k, computed from (9) is presented in Table 3. Using equation (51), the Nusselt number can be found as a function of Reb, C_f, m, and n in the following way:

heat flux at $\bar{y}=0$: $|q| = m\tau V_1 = 0.5mC_f\rho V_1 V_1^2$

heat flux at $\bar{y}=1$: $|q| = n\tau V_1 = 0.5nC_f\rho V_1 V_1^2$

Defining the Nusselt number as

$$Nu = \frac{|q|b}{\lambda|\Delta T_{0,1}|} \quad (52)$$

we obtain

$$Nu = RebC_f\frac{m}{m+n} \text{ at } \bar{y}=0 \quad (53a)$$

$$Nu = RebC_f\frac{n}{m+n} \text{ at } \bar{y}=1 \quad (53b)$$

Another form of Nusselt number can be obtained, replacing $\Delta T_{0,1}$ by $T-T_{ad}$ in its definition, hence

$$Nu = \frac{|q|b}{\lambda|(T-T_{ad})|} \quad (54)$$

where T_{ad} is temperature at the thermally insulated wall. Temperature at y_0 can be written as

$$T = Az(m-n+1) + T' + B(m+n) \quad (55)$$

where $A = \tau V_1/(\dot{m}'C_p)$, $B = Pr\ V_1^2/(2C_p)$ and T' is certain initial temperature. For $m = 0$, equation (55) gives T_{ad} at y_0, hence

$$T - T_{ad} = (Az+B)m \quad (56)$$

Equation (56) is valid for n = const., i.e., for any $T(z)$ at y_0 there is a const. heat flux at y_1.

Substituting (56) into (54) we obtain

$$Nu = PrC_fReb\Big/\left(\frac{1}{\dot{m}'}C_f\rho V_1 z + Pr\right) \quad (57)$$

Equation (57) is valid for either y_0 or y_1, provided a constant heat flux at the opposite boundary.

Assuming $T(z)$ = const., corresponding to $n = m+1$, we have

$$T - T_{ad} = 2mB \quad (58)$$

at y_0. From (54) and (58) we obtain

$$Nu = 0.5C_fReb \quad (59)$$

This result is identical with Reynolds analogy solution in a classic problem of a boundary layer along a flat plate with Prandtl number equal to 1.

Conclusions

1 Prandtl mixing length model of turbulence has been applied to solve the momentum and energy equations. The mixing length distribution is determined by equation (5).

2 The solution obtained is basically valid for a flow without Taylor vortices (zone 3 as defined by Kaye and Elgar [3], see Fig. 1).

3 The axial and circumferential flows are independent of each other in the flow in an annular gap between cylinders, if moment of momentum of the throughflow remains constant ($d\mu/dz=0$). It follows, that the moment coefficient (C_M) can be determined from the circumferential flow alone, while pressure coefficient depends only on the axial throughflow.

4 The dimensionless initial (critical) distance of the duct (l_{cr}/b) has been defined, along which moment of momentum of the throughflow (μ) increases from zero up to its final value. In the range of validity of 1/7 power law $l_{cr}/b = 6.726$ Rez Reb$^{-0.75}$. This formula can easily be generalized for 1/n power law, resulting in the expression of the type $l_{cr}/b = A$Rez Reb^{-m}.

5 The moment coefficient is insensitive to vortices. Yamada's experiments show that even in the flow with vorticity (regime 4, see Fig. 1), C_f is equal to that for a purely circumferential flow, if $l_{in}>l_{cr}$. Pressure coefficient depends strongly on the existence of vortices; even if the flow is within regime 3 (purely turbulent without vortices), but close to the boundary line between regime 3 and 4, pressure coefficient becomes greater than that for an axial flow. It has been found that in some of Yamada's experiments the initial section of the duct was not long enough (was less than l_{cr}), and this explains the curious shape of the curves, C_f, as function of Rez for a given Reb.

6 Approximation of the flow between coaxial cylinders by the Couette flow results in underestimation of the friction coefficient (see Fig. 4). This explains, as well as the selected value of $\alpha = 11, 5$, why Gazley formula (7) in [6] gives persistently lower values of C_f than any experimental results, including his own. On the other hand, all restrictions arising from the existence of Taylor vortices are not present in Couette type flow and the effects of compressibility are negligible.

7 Equation of energy, including dissipation function, has been solved for Couette flow with crossflow for constant heat flux at the boundaries. The solution shows, that the temperature profile ($T(y)$) depends on the boundary conditions, thickness of the laminar sublayer, and, to a lesser extent, on the mixing length profile (see Table 2). Temperature difference within laminar sublayers can be quite significant, and sometimes amounts to about 30 percent of the temperature difference between the plates.

Temperature difference between the plates ($\Delta T_{0,1}$) depends only on the boundary conditions (equation (51)); Tables 1 and 2 show that $\Delta T_{0,1}$ does not depend on α, mixing length profile (k) or Reynolds number (Reb). If heat transferred out of the system at one boundary is equal to the sum of heat transferred to the system at another boundary and heat generated within the system ($n = m + l$), resulting in $T(z) = $ const., then Nusselt number is identical with the Reynolds analogy solution of the boundary layer along a flat plate (equation (59)).

References

1 Yamada, Y., "Resistance of a Flow Through an Annulus With an Inner Rotating Cylinder," *Bulletin of J.S.M.E.*, Vol. 5, No. 18, 1962, pp. 302–310.

2 Yamada, Y., "Torque Resistance of a Flow Between Rotating Coaxial Cylinders Having Axial Flow," *Bulletin of J.S.M.E.*, Vol. 5, No. 20, 1962, pp. 634–642.

3 Kaye, J., and Elgar, E. C., "Modes of Adiabatic and Diabatic Fluid Flow in an Annulus With an Inner Rotating Cylinder," ASME *Transactions*, Vol. 80, 1958, pp. 753–765.

4 Berannek, K., and Streda, J., "On the Flow of Viscous Liquids Through Annular Clearances With the Rotating Inner Cylinder," *Acta Technica CSAV*, No. 6, 1979, pp. 665–676.

5 Dorfman, L. A., *Hydrodynamic Resistance and Heat Loss of Rotating Solids*, Oliver and Boyd, Edinburgh, 1963, pp. 144–189.

6 Gazley, C., "Heat Transfer Characteristics of the Rotating and Axial Flow Between Concentric Cylinders," ASME *Transactions*, Vol. 80, 1958, pp. 79–89.

7 Bilgen, E., and Boulos, R., "Functional Dependence of Torque Coefficient of Coaxial Cylinders on Gap Width and Reynolds Numbers," ASME *Transactions*, Mar. 1973, pp. 122–126.

N. Kobayashi

M. Matsumato

M. Shizuya

Mechanical Engineering Research
Laboratory,
Hitachi Ltd.,
Hitachi-shi,
Ibaraki, Japan

An Experimental Investigation of a Gas Turbine Disk Cooling System

Introduction

To achieve the improvement of thermal efficiency in a combined cycle system, "The Research and Development of Advanced Gas Turbines," [1] was conducted by the Agency of Industrial Science and Technology of Japan. The authors' company contracted to design and manufacture the low-pressure turbine rotor, four-stage disk rotor, and casing of an advanced gas turbine that had been conceptually designed by the Engineering Research Association for Advanced Gas Turbines.

The improvement of thermal efficiency has been mainly achieved by increasing the turbine inlet temperature and pressure ratio. The hot parts of the gas turbine, particularly blades, rotor, and casing have to be cooled extensively. But excessive use of cooling air has a negative effect on the thermal efficiency.

In recent years, the search for improved performance has led to great interest in the research of disk cooling and sealing air systems of gas turbines. Knowledge of the minimum cooling and sealing air flow rate, while maintaining a relatively low disk temperature, is very important for designing a turbine cooling system. There are several papers available on studies concerned with the cooling of rotating disks. Phadke and Owen [2] studied several different rotor-stator seals with radial clearance between cylindrical shrouds on both the rotor and stator. The minimum dimensionless mass flow rate to prevent ingress was shown by experiment. Abe et al. [3] used a model disk similar to an engine disk and conducted detailed studies of ingress with an external axial air flow over the disk periphery. Their results showed that the rotating disk speed had no effect on ingress of the external axial air flow in the range of rotational Reynolds number, $Re_\omega = 3 \times 10^5 \sim 1 \times 10^6$. Kessler et al. [4] investigated the disk cooling performance of a prototype gas turbine. The comparison of the calculated disk temperatures with the measurement showed that the ingress of main hot gas flow along the disk surface was one of the main problems in the design of a disk cooling system. However, insufficient experimental data are available for practical use to predict the

minimum cooling air flow rate and determine cooling air temperatures in the case of hot gas inflow [5].

Because of the importance of the problem of ingress and insufficient available data, it is the object of the present experimental investigation to determine more accurately the variation of the minimum cooling air flow rate required to prevent ingress with various rotational speeds. This paper is concerned with the cooling of a model disk similar to an engine disk. The experimental results of the disk temperatures are compared with the results of three-dimensional finite difference computation.

Experimental Apparatus

Figure 1 shows the testing apparatus of a four-stage disk cooling system. Figure 2 provides the details of wheel space between stator and first stage disk, the position of the thermocouples and pressure taps, and the configuration of radial seal fins. In the apparatus, the radial clearance ratio s_c/r_f and axial gap ratio S/r_0 were 0.0049 and 0.028, respectively (where $s_c = 1.3$ mm, $r_f = 275$ mm, $S = 8.0$ mm, $r_0 = 285$ mm).

The cooling air flow 1 was supplied to the plenum between the casing and entered the cooling air holes of the stub-shaft. It then passed through the center bore of the disk rotor and was distributed to a radial cooling passage at each stage. The cooling air flow 2 was supplied to the plenum between the casing and high-pressure side disk rotor to cool the first stage
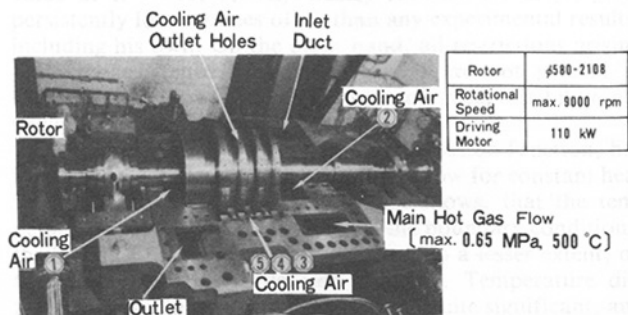
Fig. 1 Testing apparatus of four-stage disk cooling system
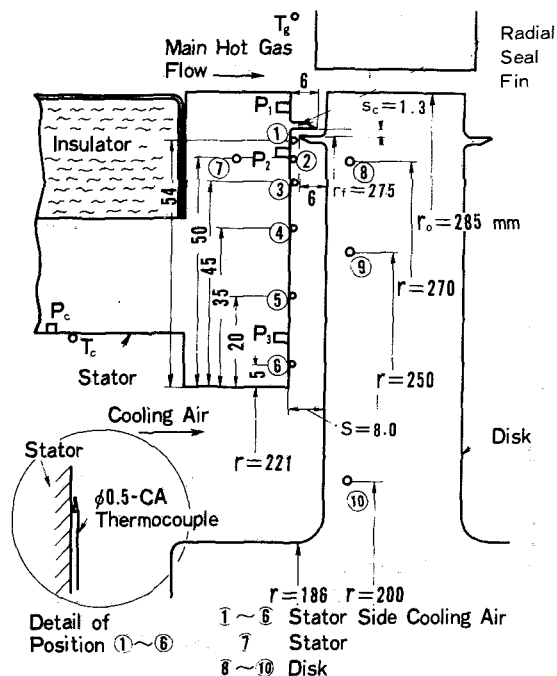
Fig. 2 Position of temperature and pressure measurement

Fig. 3 Heat transfer coefficients used in the disk temperature calculation
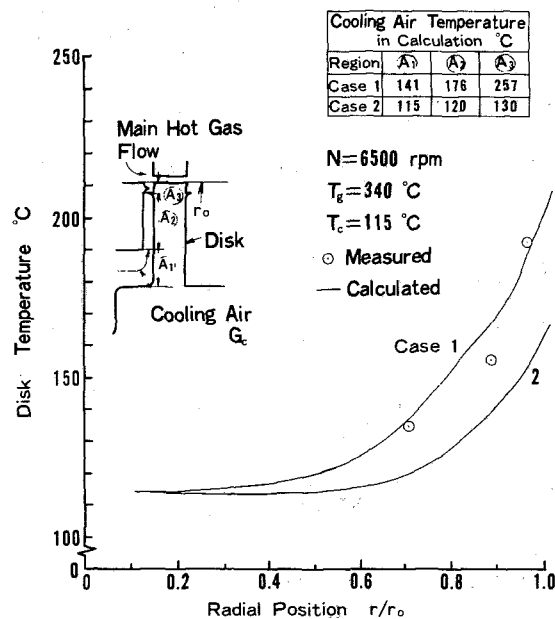
Fig. 4 The effect of cooling air temperature on the disk temperature

disk and to prevent the entrance of hot gas. During the experiment, the flow rate of cooling air 2 was kept constant by the control valve. This cooling air flow was used to obtain data on the relationship between the cooling air flow rate and the ingress of the main flow for rotational speed. Cooling air flows 3, 4, and 5 passed through the nozzle diaphragm and was supplied to the labyrinth seal between the two disks thus preventing the ingress of hot gas.

The main hot gas flow (max. 0.65MPa, 500°C), supplied by a centrifugal compressor and combustor, was introduced over the disk periphery, and the flow rate was measured by the orifice. The main hot gas temperature and pressure were controlled by the fuel flow rate and the main air flow rate, respectively.

The rotating disk assembly could be driven at speeds up to 6500 rpm (Re$_\omega$ = 6 × 10^6) by a 110-kW variable speed electric-motor. The rotational speed was measured by a magnetic transducer in conjunction with an electronic counter.

The temperature of the disk rotor and the pressure inside the disk rotor were measured with thermocouples (ϕ1.0 CA) and static pressure taps (ϕ1.0 SUS tube). The disk rotor was equipped with 17 thermocouples and 23 pressure taps. The signals were transmitted through a Scanivalve (temperature/pressure 36 channels) at the end of the rotor to the

Nomenclature

b = height of hot gas channel
c_f = friction coefficient
C_1 = constant
G = mass flow rate
G_A = blade cooling air flow rate
N = rotational speed of disk
Nu = Nusselt number, = $\alpha r/\lambda$
P = pressure
P_{ij}^* = pressure coefficient, = $(P_i - P_j)/P_i$
ΔP_{ij} = pressure difference, = $P_i - P_j$
Pr = Prandtl number
Q_c = volume flow rate
Re$_\omega$ = rotational Reynolds number, = $\omega r_0^2/\nu$
Re$_m$ = Reynolds number of cooling air flow, = $G_c/(2\pi S \mu)$
r = radial distance from disk center line

r_f = radius at radial seal fins
r_0 = radius of disk periphery
S = axial gap between disk and stator in the wheel space
s_c = radial clearance between stator fin and rotor fin
T = temperature
α = heat transfer coefficient
λ = thermal conductivity
μ = viscosity
ν = kinematic viscosity
ρ = density
ω = angular velocity of disk

Subscripts

c = disk cooling air flow
g = main hot gas flow
min = minimum value

Fig. 5 Calculated results of the disk temperature distribution
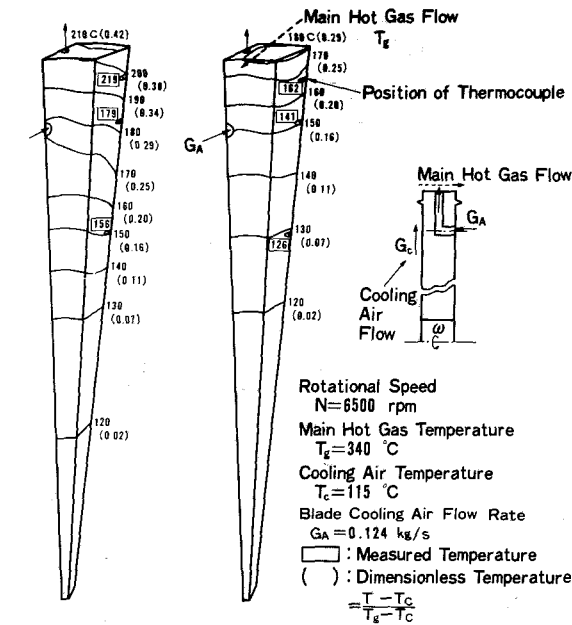
(a) Cooling Air Flow Rate G_c = 0.065 kg/s   (b) Cooling Air Flow Rate G_c = 0.204 kg/s

Rotational Speed
N=6500 rpm
Main Hot Gas Temperature
T_g=340 °C
Cooling Air Temperature
T_c=115 °C
Blade Cooling Air Flow Rate
G_A =0.124 kg/s
▢ : Measured Temperature
( ) : Dimensionless Temperature
$= \dfrac{T - T_c}{T_g - T_c}$

Fig. 6 Records of cooling air temperature at position 1 in Fig. 2

Fig. 7 The effect of cooling air flow rate on the stator side cooling air temperature at position 1 ~ 6 in Fig. 2 (N = 1000 rpm)
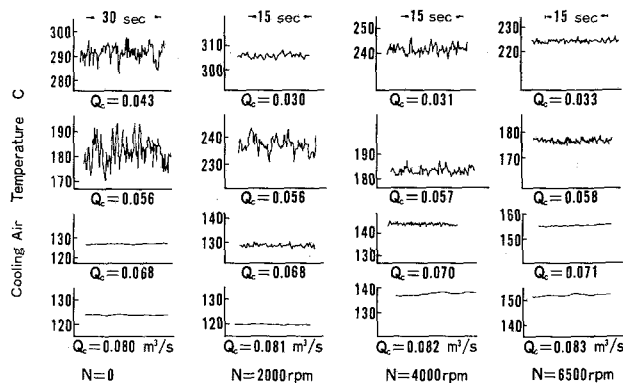
recorder. The hot gas temperature and pressure were measured at each stage with 45 thermocouples (ϕ1.6 CA) and pressure taps (ϕ1.6 SUS tube) in total. The temperature and pressure of the cooling air flow 2 were measured with thermocouples at the position 1 ~ 7 and four pressure taps in Fig. 2. The leakage of each cooling air flow was checked experimentally, and the calibration data of the mass flow rate was obtained. The pressure measurements were made with either a manometer bank (resolution 1 mm Aq) or a digital manometer. The temperatures were recorded by a multi-pen-recorder or a digital voltmeter.

Experimental and Computational Results of the Disk Temperature

A sensitivity analysis of disk cooling [4] clearly showed that a change in cooling air temperature caused the largest change in disk temperature. Therefore, the data of such temperatures are very important for increasing the accuracy of disk temperature analysis.

In order to fully analyze the temperature field in the disk, the three-dimensional temperature distribution was calcu-

lated. In the calculation, heat transfer coefficients of the disk surface and cooling air temperature used as follows were:

1 The calculated heat transfer coefficients using the equations below are described in Fig. 3.

Region A and C (side surface with the cooling air flow [6])

$$\text{Nu} = 0.0346 \, \text{Re}_\omega^{0.8} Kv (r_0/r_c)^{-0.3} (S/r_0)^{0.06} \text{Pr}^{0.6}$$

$$Kv = (\text{Re}_\omega(\text{Re}_m) \, (r_c/r_0)$$

Region B (side surface without the cooling air flow)

$$\text{Nu} = 0.023 \, \text{Re}_\omega^{0.8} \text{Pr}^{0.6}$$

Region D (periphery surface with the hot gas flow [7])

$$\text{Nu} = C_1 (c_f/2)(\rho_g \omega r_0 b/\mu_g) \text{Pr}^{\frac{1}{3}}$$

2 The two cases of cooling air temperatures were considered variable along the disk radius as described in the table in Fig. 4:

Case 1   Temperatures based on the measurement with hot gas ingress

Case 2   Assumed temperatures considering temperature rise due to heat transfer and friction (without hot gas inflow)

3 The measured temperature at position, T_g, in Fig. 2 was used as the main hot gas temperature.

Figure 4 shows the experimental and calculated results of the disk temperature. The variation of the cooling air temperature was caused by heat transfer from the disk, by friction, and by the inflow of hot gas. A cooling air temperature rise of 15°C at 6500 rpm could be explained by heat transfer and friction, but a temperature rise of the cooling air of over 15°C which appeared in the experiment couldn't be explained by heat transfer and friction alone. Only an inflow of hot gas could cause such a large temperature rise. Figure 5 shows the measured and calculated temperatures of the first stage disk for the different cooling air flow rate. It was clear
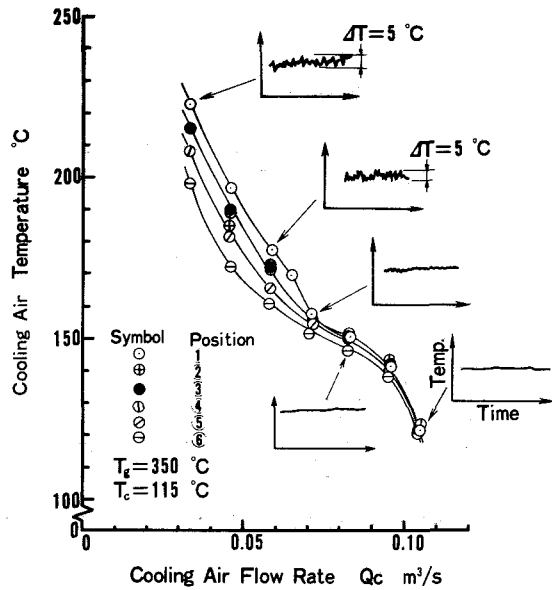
Fig. 8 The effect of cooling air flow rate on the stator side cooling air temperature at position 1 ~ 6 in Fig. 2 (N = 6500 rpm)

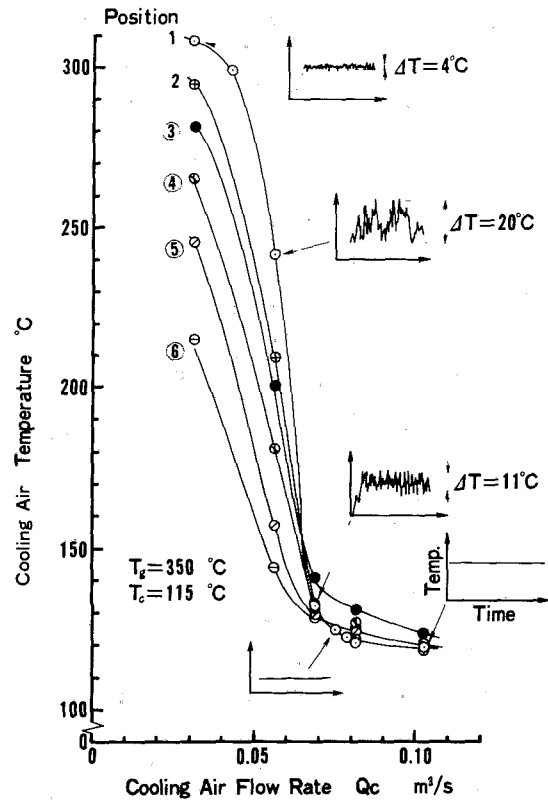Fig. 9 The effect of cooling air flow rate on the stator side cooling air temperature at position 1 in Fig. 2

Fig. 10 The effect of cooling air flow rate on the disk temperature at position 8 ~ 10 in Fig. 2 for rotational speed

that the disk temperature significantly varied with the cooling air flow rate. But sufficient experimental data were not available to predict the minimum cooling air flow rate required to prevent the ingress of hot gas and to determine cooling air temperature in the case of hot gas inflow. In the next section, the problem of hot gas ingress is experimentally investigated.

Determination of Ingress

In order to determine the onset of hot gas ingress, the rotational speed was kept constant and the cooling air flow rate was varied. The exact point at which the ingress occurred was determined by the onset of the fluctuation of the cooling air temperatures at the position 1 ~ 6 in Fig. 2, because the ingress of hot gas takes place due to the mixing of the cold plume (cooling air) and the hot plume (hot gas), and the mixing process is an unsteady phenomenon in nature. Thus, the temperature fluctuation criterion is thought to be a direct and better indication of the hot gas ingress than other criteria such as pressure difference at the seal fins.

Figure 6 shows the records of cooling air temperature at the position 1 in Fig. 2 with the change of cooling air flow rate for various rotational speeds. To correlate the cooling air flow rate with other parameters, volumetric cooling air flow rate at the inner entrance of wheel space, Q_c, was used in this experiment, and cooling flow static pressure, P_c, and temperature, T_c, were about 0.34 MPa and 115°C, respectively, throughout the experiment. For irrotational experiment, a fluctuation of temperature was not observed at the cooling air flow rate Q_c = 0.068 m³/s, but at lower flow rates fluctuation was clearly observed. From these results, the minimum cooling air flow rate to prevent the ingress of hot gas was estimated to be between 0.056 m³/s and 0.068 m³/s. In the same way, for rotational experiment, the minimum cooling air flow rate, Q_{min}, was determined by the onset of temperature fluctuation. It could be seen that the amplitude of fluctuation became smaller with increasing rotational speed at a constant cooling air flow rate.

Figures 7 and 8 show the effect of the cooling air flow rate on the cooling air temperature at the position 1 ~ 6 in Fig. 2 for rotational speeds of 1000 rpm and 6500 rpm. The cooling air temperature increased with a decreasing cooling air flow rate, and the temperature abruptly rose when the cooling air
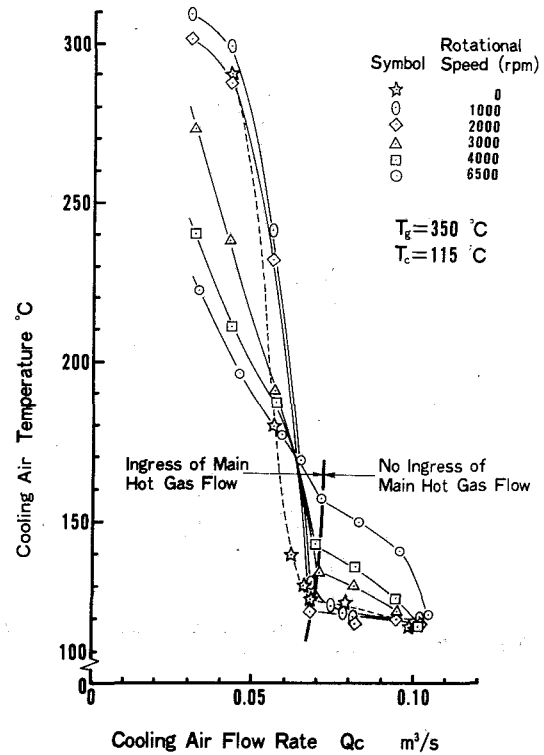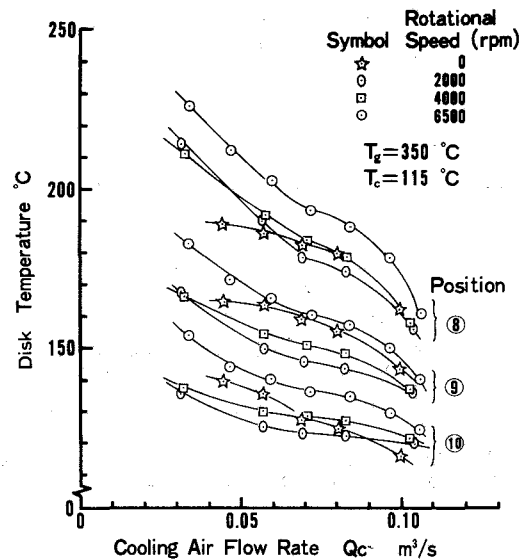
flow rate was about Q_c = 0.07 m³/s for both rotational speeds. The temperature distribution of cooling air after hot gas ingress for the two above mentioned rotational speeds were significantly different. Such a difference in the distribution of cooling air indicated that the flow pattern and the amount of hot gas inflow varied with the rotational speed.

The effect of rotational speed on Q_{min} is shown in Fig. 9. The variation of the minimum cooling air flow rate Q_{min} is shown by the solid line. The influence of rotational speed on Q_{min} was found to be negligible.

The change of disk temperature with the cooling air flow rate is shown in Fig. 10. After the ingress of hot gas, the disk

$\times 10^{-3}$

30

Rotational
Symbol Speed (rpm)
☆ 0
◇ 1000
0 2000
△ 3000
□ 4000
○ 6500

$P_g = 0.34 \sim 0.35$ MPa
$Q_g = 1.38 \sim 1.67$ m³/s

20

$P_{21}^* = \dfrac{P_2 - P_1}{P_1}$

10

Ingress of Main   No Ingress of
Hot Gas Flow   Hot Gas Flow

0

0.05   0.10

Cooling Air Flow Rate Qc m³/s

Fig. 11 The effect of cooling air flow rate on the pressure difference at the radial seal fins for rotational speed

$\times 10^{-3}$

12

10   6500 rpm

$P_g = 0.34 \sim 0.35$ MPa
$Q_g = 1.38 \sim 1.67$ m³/s

8

6

$P_{21}^* = \dfrac{P_2 - P_1}{P_c}$

4   4000 rpm

2   3000 rpm
    0
2000 rpm

0
1000 rpm   0.05   0.10

Cooling Air Flow Rate Qc m³/s

−2

Fig. 12 The effect of cooling air flow rate on the radial static pressure difference inside the wheel space for rotational speed

$\times 10^{-2}$

10

Present Results

(Temperature fluctuation criterion)

8

6

Q_{min} m³/s

($\Delta P_{21} = 0$ in Fig.11)

4

2

Phadke & Owen's
Experimental Result

0
0   2   4   6   8   10 $\times 10^6$

Re_ω

Fig. 13 The minimum cooling air flow rate to prevent the ingress

amount of Q_{min} became smaller than the result obtained by the temperature fluctuation in Fig. 9, and the variation of Q_{min} with rotational speed was clearly manifested.

Figure 12 shows the variation of radial pressure differences inside the wheel space according to the cooling air flow rate. For rotational speeds of 2000, 3000, 4000 rpm, the minimum pressure differences appeared at the cooling air flow rate Q_c = 0.081, 0.081, 0.094 m³/s, respectively. At a low cooling air flow rate (under Q_c = 0.05 m³/s), the pressure difference increased with rotational speed. This phenomenon was called the "pressure inversion" by Phadke and Owen [2]. For a cooling air flow rate over Q_c = 0.07 m³/s, at the rotational speeds under 3000 rpm, the pressure difference ΔP_{23} decreased with increasing rotational speed, but over 3000 rpm, the "pressure inversion" could be seen. The variation of this pressure difference, ΔP_{23}, has probably some relation with the sealing characteristics, but up to the writing of this paper the relationshp is not clear.

Figure 13 shows the variation of the minimum cooling air flow rate, Q_{min}, required to prevent the ingress of hot gas with rotational Reynolds number Re_ω, and, comparison is made between the value of Q_{min} based on temperature fluctuation criterion and that based on pressure difference criterion. The present results of Q_{min} by pressure difference criterion showed similar tendency to those of Phadke and Owen, who gave experimental results of the Q_{min} versus Re_ω relationship without external axial flow. It could be seen that the value of Q_{min} based on temperature measurements was nearly constant with Re_ω. This result showed that there was almost no effect of disk rotational speed on the minimum cooling air flow rate with external axial hot gas flow, in contrast with the linear Re_ω dependency of Q_{min} based on pressure difference criterion. It should be pointed out that the determination of the ingress of hot gas based on pressure difference criterion underestimated the minimum cooling air flow rate required to prevent the ingress of hot gas.

Conclusion

A comparison of the measurements with the computed results reconfirmed that the determination of cooling air temperature was one of the most important data for predicting the disk temperature.

The minimum cooling air flow rate, Q_{min}, necessary to prevent ingress of external hot gas was determined by the fluctuation of cooling air temperature inside the wheel space with the external axial hot gas flow for values of the rotational Reynolds number $0 < Re_\omega < 6.5 \times 10^6$. From the

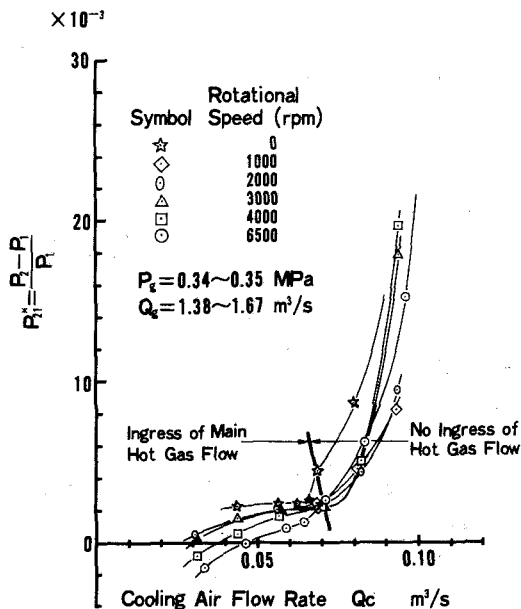temperature increased rapidly with decreasing Q_c in comparison with the condition of no hot gas ingress.

As a criterion for determining the ingress of hot gas, the radial pressure distribution was used in [2]. It was determined that hot gas ingress occurred when the pressure difference between the wheel space and the hot gas flow became negative. Figure 11 shows the effect of the cooling air flow rate on the pressure difference, ΔP_{21}, between the wheel space pressure, P_2, and the pressure, P_1, outside the radial seal fins, for rotational speed. The pressure difference coefficient P_{21}^*, decreased rapidly with decreasing, Q_c, until Q_c = 0.07 m³/s, whereafter the pressure difference coefficient decreased moderately. According to the measurement of cooling air temperature fluctuation, hot gas ingress occurred before the pressure coefficient, P_{21}^*, became negative. If $P_{21}^* = 0$, that is, $\Delta P_{21} = 0$, was used as the criterion to determine Q_{min}, the

experimental results, the effect of rotational speed on the minimum cooling air flow rate was found to be negligible, and it became clear that the determination of the ingress of hot gas by pressure difference criterion underestimated the minimum cooling air flow rate.

Acknowledgments

References

1 Hori, A., and Takeya, K., "Outline of Plan for Advanced-Research Gas Turbine," ASME Paper No. 81-GT-28.

2 Phadke, U. P., and Owen, J. M., "An Investigation of Ingress for an Air-Cooled Shrouded Rotating Disk System With Radial-Clearance Seals," ASME Paper No. 82-GT-145.

3 Abe, T., Kikuchi, H., and Takeuchi, H., "An Investigation of Turbine Disk Cooling," CIMAC Conference, Vienna, May 1979.

4 Kessler, W., et al., "Experimental and Analytical Investigation of Turbine Disk Cooling," Joint Fluids Engineering Gas Turbine Conference, Mar. 1980, p. 327.

5 Sokolov, V. S., "Determining the Temperature of the Cooling Air Around the Side Surface of a Rotor Disk with Radial Cooling," Teploenegetika, Vol. 21, 1974, p. 94.

6 Kapinos, V. M., "Heat Transfer From a Disk Rotating in a Housing with a Radial Flow of Coolant," Journal of Engineering Physics, Vol. 8, 1965, p. 35.

7 Heat Tansfer and Fluid Flow Data Books, General Electric Co., section 511.3.

E. W. Adams
Research Assistant.

J. P. Johnston
Professor.

Heat Transfer and Turbulence
Mechanics Group,
Thermosciences Division of
Mechanical Engineering,
Stanford University,
Stanford, Calif. 94305

A Mixing-Length Model for the Prediction of Convex Curvature Effects on Turbulent Boundary Layers

A mixing-length model is developed for the prediction of turbulent boundary layers with convex streamwise curvature. For large layer thickness ratio, $\delta/R > 0.05$, the model scales mixing length on the wall radius of curvature, R. For small δ/R, ordinary flat wall modeling is used for the mixing-length profile with curvature corrections, following the recommendations of Eide and Johnston [7]. Effects of streamwise change of curvature are considered; a strong lag from equilibrium is required when R increases downstream. Fifteen separate data sets were compared, including both hydrodynamic and heat transfer results. In this paper, six of these computations are presented and compared to experiment.

Introduction

The improvement of the performance and energy efficiency of today's gas turbine engines requires accurate prediction of turbine-blade convective heat transfer. Calculation schemes for turbulent boundary layers have long been used in this application. Research at Stanford and elsewhere has investigated effects of pressure gradient, blowing, suction, roughness, and free-stream turbulence on boundary layers. These effects have been incorporated in the turbulence models of a number of standard computer codes. The effect of streamwise curvature on the hydrodynamic and thermal properties of turbulent boundary layers has also been studied; a few of these studies are [2–4, 6, 8–15]. This paper presents a simple turbulence model to predict the effects of streamwise convex curvature on boundary layers.

In laminar boundary layers, the effects of streamwise curvature are second order in terms of δ/R, the strength of curvature parameter [1]. For turbulent boundary layers, significant (10 percent) effects on skin friction and heat transfer are seen even when δ/R is as small as 0.01 [2], and the effect of curvature is even greater as δ/R grows [3, 4]. Bradshaw [2] has shown that, for small curvature, the mean flow boundary layer equations are unchanged; that is, the direct effects of curvature on the various terms in dynamic equations are of second order. However, curvature affects the boundary layer to first order by changing the turbulent shear stress $(-\rho \overline{u'v'})$ in a significant way.

An improved mixing length model is presented for the computation of turbulent boundary layers with convex

(stabilizing) longitudinal curvature. The goal of the present work is to generate a simple, easily implemented model of the turbulent shear stress which includes all the known effects of convex curvature. Specifically, the paper will motivate our choice for modeling curved boundary layers, describe the proposed convex curvature model, discuss the method for evaluation of the model constants, explain the computer implementation of the model, and, finally, discuss the positive and negative features of some predicted results.

The model successfully predicted Stanton number or wall skin friction for 12 different experiments over a wide range of the strength of curvature parameter (δ/R). Prediction of results for three other experiments was judged less satisfactory, for various reasons.

Model Assumptions and Descriptions

Figure 1 shows the shear-stress profiles obtained by Gillis et al. [3] for a boundary layer in large convex curvature ($\delta/R \simeq 0.1$). The effects of curvature appear rather suddenly in the outer layers of an established boundary layer. For strong curvature, nominally when $\delta/R > 0.05$, a number of investigators, including Gillis et al. [3] and, earlier, So and Mellor [11], have shown that turbulent shear stress is rapidly destroyed (not just dissipated) by negative turbulence stress production. This is the effect referred to as curvature stabilization. Stabilization also causes the turbulence kinetic energy to drop in the curved region (Fig. 2). The reduction is especially strong in the outer part of the layer. Hunt and Joubert [13] distinguish between two cases—small curvature which is "shear dominated" and large curvature which is "inertia dominated." Muck's measurements [12] indicate that a boundary layer with small curvature is structurally like a noncurved boundary layer, while other data [3, 10, 11] suggest that layers subjected to large convex curvature are

---

structurally different from noncurved boundary layers, especially far from the wall.

For large convex curvature, the data suggest a layered model (see [3], for example). The wall layer (viscous, buffer, and turbulent parts below $y^+ \simeq 150$) is structurally the same as a flat-wall flow. In the outer, turbulent part of the wall layer, stabilizing curvature reduces $-\rho \overline{u'v'}$, but the ratio of production to dissipation is nearly equal to its noncurved value. In the layer farthest from the wall, stabilization effects are largest, and turbulence is rapidly damped by negative production. The shear stress tends toward laminar levels. In between this outer, strongly stabilized region and the turbulent portion of the wall layer is a zone of flow structure with characteristics not seen in flat-wall flows. This region is turbulent, and, as we shall attempt to show, has eddy length scales which are proportional to wall radius of curvature rather than to the total boundary layer thickness, as is the case for flat-wall flow.

Contrary to the rapid onset and development of the stabilization effect, Gillis et al. [3] and Simon et al. [4] have shown that the effects of curvature, once developed, last for long distances downstream of the end of curvature in a flat-wall recovery region. A distance about equal to 50 or 100 boundary layer thicknesses is required to recover equilibrium, flat-wall conditions. In other words, recovery is very slow upon elimination of the stabilizing effects of strong convex curvature.

For simplicity, we chose to model the effect of curvature using a mixing length model. The model was designed to predict the (i) rapid reduction in "outer-layer" shear stress of a convexly curved boundary layer, and (ii) the slow recovery to a normal turbulent boundary layer in regions where wall curvature, $k = (1/R)$, is decreasing in the flow direction.

While mixing length turbulence models cannot be claimed to be universal in nature, they have been successful in boundary layer applications. Mixing length models are the simplest (and cheapest) of the turbulence models available for boundary layer computation by differential methods. In addition, mixing length turbulence models are easily altered, and the changes explicitly affect the shear-stress distribution without interaction with other constitutive equations.

The computational method used was STAN5, a differential boundary layer method based on the Patankar-Spalding algorithm [5]. The model developed here is easily adapted to any particular boundary layer method that uses a mixing length model. STAN5 is based upon the thin, time-averaged, two-dimensional, steady-flow boundary layer equations. There is no curvature term explicitly appearing in the equations.
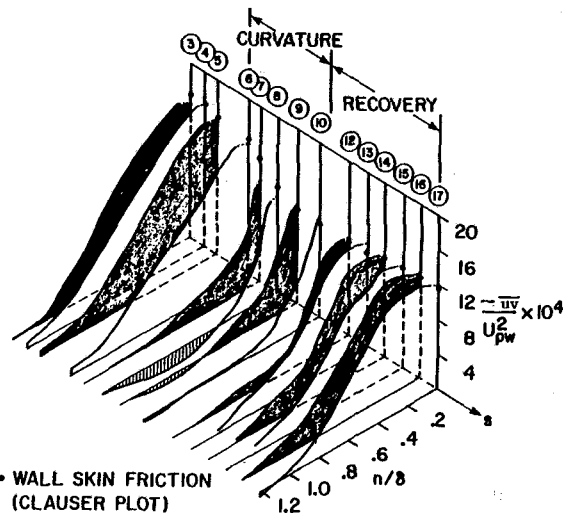
Fig. 1 Isometric plot of shear-stress profiles versus distance in flow direction for the second experiment of Gillis
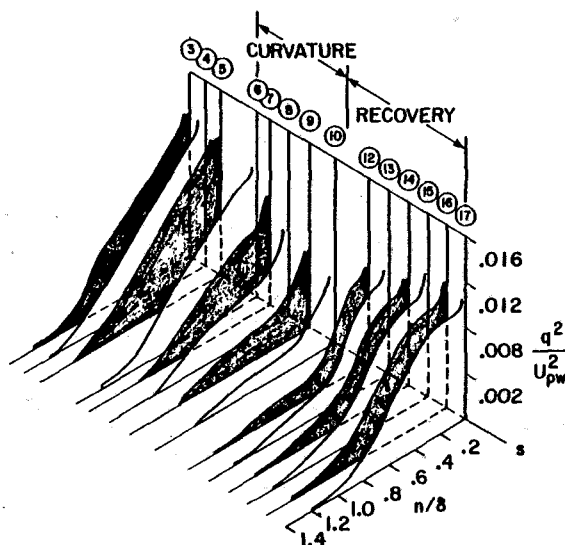
Fig. 2 Isometric plot of TKE profiles versus distance in flow direction for the second experiment of Gillis

$$U\frac{\partial U}{\partial x} + V\frac{\partial U}{\partial y} = -\frac{1}{\rho}\frac{\partial P}{\partial x} + \frac{\partial}{\partial y}\left(\frac{\tau}{\rho}\right) \qquad (1)$$

─────── Nomenclature ───────

A^+ = constant in the Van Driest damping function
C = outer region lag constant, see equation (13)
C_f = skin friction coefficient, $2\tau_w/\rho U_{pw}^2$
l = mixing length
P = static pressure
R = wall radius of curvature
Re_{Δ_2} = enthalpy thickness Reynolds number, $U_{pw}\Delta_2/\nu$
Ri = Richardson number, see equation (11)
St = Stanton number, $h/\rho U_{pw}C_p$

U = mean velocity parallel to the wall
u_τ = wall shear velocity, $U_{pw}\sqrt{C_f/2}$
U_{pw} = potential velocity at the wall (obtained by extrapolation through the boundary layer)
$-\rho\overline{u'v'}$ = turbulent "shear stress"
V = mean velocity normal to the wall
x = distance along and tangent to the wall
y = distance normal to the wall

y^+ = inner layer distance, yu_τ/ν
β = log region curvature correction constant, see equation (12)
δ = boundary layer thickness
Δ_2 = enthalpy thickness
κ = Von Kármán constant (value of 0.41 assigned here)
ρ = density
τ = total shear stress
τ_w = wall shear stress
ν = kinematic viscosity
ν_T = turbulent eddy viscosity

The total shear stress, τ, is the sum of a laminar and a turbulent portion.

$$\frac{\tau}{\rho} = \nu \frac{\partial U}{\partial y} - \overline{u'v'} \qquad (2)$$

An effective "eddy" viscosity is introduced to represent the turbulent part of the shear stress. Unlike the laminar viscosity, which is constant (for isothermal flows), the turbulent eddy viscosity varies across and along the boundary layer. The eddy viscosity, ν_T, is defined using

$$\frac{\tau}{\rho} = (\nu + \nu_T) \frac{\partial U}{\partial y} \qquad (3)$$

To describe the eddy viscosity, a mixing length, l, is introduced.

$$\nu_T = l^2 \left| \frac{\partial U}{\partial y} \right| \qquad (4)$$

For flat-wall boundary layers, many methods, including STAN5, employ a multilayer model for the mixing length. In the wall-layer region, the formulation is based on the law of the wall modified by the Van Driest damping function. Denoting flat-wall mixing length by the subscript o, the relationship used is

$$l_o = \kappa y (1 - \exp(-y^+/A^+)) \qquad (5)$$

where

$$y^+ = y \frac{u_\tau}{\nu}$$

κ is the von Kármán constant, chosen here to be 0.41, a typical value. A^+ is a sublayer constant which has been shown to be a strong function of pressure gradient and wall transpiration flow (blowing and suction) [5]. We considered including effects of curvature in A^+, but the data [3] indicate that if A^+ is affected by curvature, the effect is probably very weak. In addition, A^+ affects the wall-layer region most strongly, while curvature affects the outer layer most. Consequently, no effect of curvature is added to the A^+ function used in STAN5.

In the outer part of a flat-wall boundary layer, the mixing length scales on the boundary layer thickness. The formulation used is

$$l_o = .086 \, \delta \qquad (6)$$

In any boundary layer, the mixing length can be computed from measured profiles of velocity and shear stress.

$$l^2 = \frac{-\overline{u'v'}}{\partial U/\partial y} \qquad (7)$$

Since this calculation requires differentiation of velocity profile data, the uncertainties in the mixing length, l, when evaluated from experimental data, are generally large, as illustrated by the fluctuations on the points taken from [3] and shown in Fig. 3. Despite this, the effect of curvature on the mixing length is properly represented in Fig. 3. There is a drastic drop in the outer-layer mixing length upon entering the curved region, indicative of the powerful effects of stabilization on the outer layers.

For thick boundary layers, $\delta/R > .05$, Gillis [3] found that the outermost portion of the boundary layer lacked any significant turbulent shear stress shortly after the start of the curved region. Both Stanford experiments [3] and [4] indicated clearly that the conditions in the outer portion of the turbulent boundary layer in the curved region became independent of initial conditions for initial values of $\delta > 0.05$ R. In such a circumstance the mixing length (and the shear stress) should not be expected to scale on the velocity boundary layer thickness. Dimensional arguments suggest that the large eddy lengths in the layers outside the wall layers,
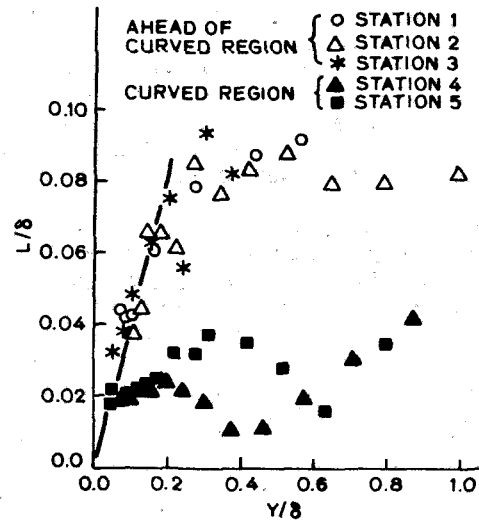
Fig. 3 Mixing length profiles, Gillis experiment #1, strong curvature $\delta/R \approx 0.1$
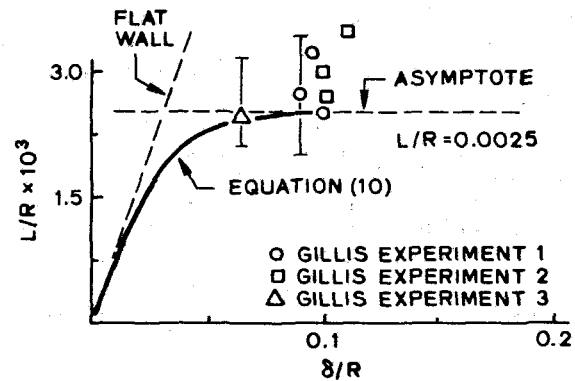
Fig. 4 Asymptotic outer-region mixing length in the curved region versus strength of curvature for the Gillis experiments

but inside the region of total collapse of turbulence, must scale on the length most typical of the stabilizing centrifugal force, U^2/R, namely, the wall radius of curvature, R. Equation (6) is thus replaced in the curved region by a model scaling the mixing length on R.

Figure 4 shows the outer-layer mixing length normalized on R as a function of "strength of curvature" (δ/R). This plot uses the Gillis data [3] for three separate experiments which covered a small (2:1) range of δ/R. The data were generated by averaging experimentally obtained mixing length data between $y/\delta = 0.2$ and $y/\delta = 0.5$. This is approximately the area between the turbulent part of the wall layer and the region of total collapse of turbulence. For large curvature, the mixing length normalized on R appears to be constant. More data at higher δ/R values are needed to confirm this trend. Nevertheless, the curvature model chosen for large δ/R is that l is proportional to R, i.e.,

$$l/R = .0025 \qquad (8)$$

The constant was evaluated from the data in Fig.4, and on our judgment concerning the quality of the various results computed later.

The asymptotic limit for very small curvature and also for flat walls should be the flat-wall mixing length. Normalized on R, equation (6) becomes

$$\frac{l}{R} = .086 \frac{\delta}{R} \qquad (9)$$

This line is also reproduced on Fig. 4. A simple function which includes equations (8) and (9) as asymptotic limits is

$$\frac{l}{R} = .0025 \tanh\left(34.5 \frac{\delta}{R}\right) \qquad (10)$$

Equation (10) is also plotted on Fig. 4. Equation (10) replaces equation (6) for computation of curved flows.

Curvature also has an effect on the shear stress (hence on mixing length) nearer the wall, in the log region. In this area, our model follows the ideas of Bradshaw [6] who proposed that the dissipation length scale is related to the Richardson number. The Richardson number is a nondimensional, local, boundary layer curvature stability parameter defined as the ratio of Coriolis force to viscous force. The particular Richardson number formulation used in our method is discussed in [15] and given here as

$$\mathrm{Ri} = S(1 + S) \qquad (11)$$

where

$$S = \frac{2U/R}{\dfrac{\partial U}{\partial y} - \dfrac{U}{R}}$$

The Bradshaw correction is usually given as a multiplicative factor. We used a formulation which will not predict negative mixing lengths for large convex curvature.

$$\frac{l}{l_o} = \frac{1}{1 + \beta \mathrm{Ri}} \qquad (12)$$

l_o is the flat-wall mixing length, and β is a constant whose value is generally set between 1 and 10 [7]. Mixing length profiles for typical conditions using both inner and outer layer models proposed here are plotted in Fig. 5 for various values of the strength of curvature parameter. Figure 5 indicates that the modeled effects for large convex curvature are different than for small curvature. When $\delta/R > .05$, the outer layer model dominates over the Richardson number wall layer correction. When $\delta/R < 0.01$, the outer layer model is seen to be of no importance.

Figure 5 illustrates the effects caused by a change in outer region scaling. The outer layer is seen to move much closer to the wall as curvature strength increases. On flat walls, the outer region model begins at $y/\delta \approx 0.2$, while for $\delta/R = 0.1$, the beginning of the outer layer has moved inward to $y/\delta \approx 0.1$. Other simple curvature models [7, 15] use a multiplicative correction factor for the shear stress (the Bradshaw correction or equivalent) across the entire boundary layer. Our model represents a change in viewpoint from a view that curvature merely alters the value of shear stress to a view that the structure of the shear stress is different in different layers, and an appropriate turbulence model for the layers away from the wall must be represented by a different kind of scaling.

In a recovery region, $dR/dx > 0$, the boundary layer must return to a normal flat-plate structure. Whenever the wall radius curvature changes from a small value to a larger one, i.e., when $dR/dx > 0$, a lag model is employed to smoothly change the outer-layer mixing length from the old value to a value closer to its new equilibrium value. The lag model formulation is

$$\frac{d(l/\delta)}{d(x/\delta)} = C\left[\left(\frac{l}{\delta}\right)_{eq} - \left(\frac{l}{\delta}\right)\right] \qquad (13)$$

$(l/\delta)_{eq}$ defines the local equilibrium outer-layer mixing length, which in our case is given by equation (10).

The lag constant, C, can be chosen using equation (13) together with recovery region data for the mixing length. Using the idea that recovery will occur in 50 to 100 boundary layer thicknesses, the value of C in equation (13) should be in the range 0.05–0.1. The data of Gillis [3] confirm this range of
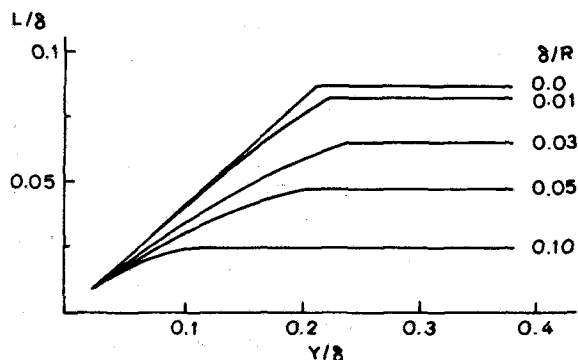
Fig. 5 Typical model mixing length profiles for inner and outer layers combined
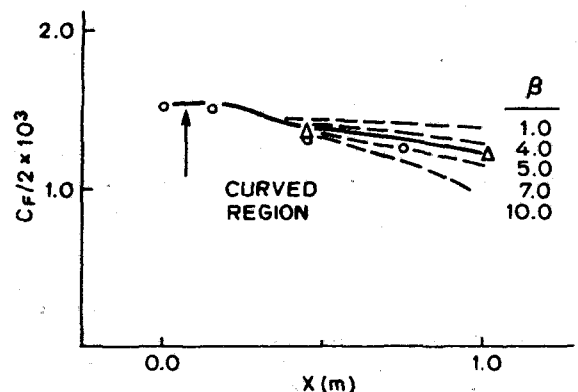
Fig. 6 Selection of the log-layer curvature correction constant β, using skin friction data for the Hoffman and Bradshaw experiment, $\delta/R \approx 0.01$

values. This lag equation is empirically based, and predictions in the recovery region indicate that this formulation may not be universal. However, better models for this hard-to-predict effect are yet to be discovered.

If the wall curvature changes from a larger radius of curvature to a smaller one (e.g., the condition encountered upon entering a region of curvature), the effects of curvature are assumed to develop instantly, and the outer-region mixing length is computed using its equilibrium value defined by equation (10). No lag model is used when $dR/dx < 0$.

In summary, in the innermost, turbulent region of the outer portion of the boundary layer, the mixing length was found to scale on the radius of curvature, not the boundary layer thickness. In the wall layer region, the presence of the wall still dominates the scale length, but scales are reduced by curvature. Any reasonable turbulence model may be used to predict l_o, the flat-wall mixing length in the wall layer region. This flexibility allows pressure gradient effects and blowing/suction effects to be modeled separately from the curvature effects on mixing length.

Evaluation of Model Constants

The model described has three constants that need to be evaluated from data: (i) the asymptotic value of the mixing length, normalized on R, for large curvature, (ii) the constant β for the log region correction factor, and (iii) the recovery region lag constant, C.

Skin friction was the dependent variable which was matched to experiments to obtain the curvature model constants. "Best fit" was defined by simple inspection.

We chose to optimize β using the Hoffmann-Bradshaw convex curvature experiment [9]. This experiment has small strength of curvature ($\delta/R \approx .01$), and the outer region model

is not important (see Fig. 5). Figure 6 shows that $\beta = 5$ does a good job of predicting the value and slope of this set of skin-friction data.

The asymptotic value of the mixing length, scaled on R, was found by matching the second experiment of Gillis [3]. $l/R = .0025$ produces the best fit to the skin-friction data. This value also produces agreement, to the experimental uncertainty, with the mixing length data (see Fig. 4). The computations are quite sensitive to the l/R value chosen. Variation of l/R up to 0.003 or down to 0.002 produced noticeably poorer predictions.

The recovery region lag constant, C, was checked against wall stress data from the second experiment of Gillis. Figure 7 summarizes the results of several computer runs. $C = 0.06$ provides the best fit.

Implementation of the Model

In the computer program (STAN5), a subroutine is used to calculate the shear stress profiles from local derivatives of computed mean velocity profiles and the assumed mixing length distribution. Upon entering the routine, the equilibrium outer layer mixing length $(l/\delta)_{eq}$ is computed (equation (10)) and compared with the outer layer mixing length (l/δ) at the previous step. If the mixing length is constant or falling with streamwise distance (corresponding to $dR/dx \leq 0$), the equilibrium outer layer mixing length is used. If the mixing length (l/δ) is increasing with streamwise distance ($dR/dx > 0$), equation (13) is integrated to compute the outer layer mixing length. Each point's mixing length is also computed, using equations (5) and (12). Close to the wall, in regions where the mixing length based on this inner layer formulation is less than the outer-layer mixing length, the inner-layer mixing length is used.

Results

A summary of all experiments we have computed to date is shown below. When evaluating results, it should be remembered that typical experimental uncertainties in C_f and St are ± 5 percent. The second experiment of Gillis and the Hoffmann and Bradshaw experiment are postdictive rather than predictive, since these experiments were used to evaluate the model constants. δ/R values are the nominal values at the start of curvature effects. Selected results for six of the fifteen cases are shown in the indicated figures.

Successful predictions:

1 Hoffmann-Bradshaw, $\delta/R = 0.01$ (Fig. 6)
2 Gillis experiment 2, $\delta/R = 0.1$ (Fig. 7)
3 Simon run 070280, $\delta/R = 0.1$ (Figs. 8 and 9)
4 Simon run 022680, $\delta/R = 0.05$ (Fig. 13—St No)
5 Simon run 060480, $\delta/R = 0.02$
6 Simon run 112779, $\delta/R = 0.05$, higher Re number
7 Simon run 113079, unheated starting length, $\delta/R = 0.05$
8 Simon run 030280, unheated starting length, $\delta/R = 0.05$
9 Smits, Young, and Bradshaw (Figs. 11 and 12)
10 So and Mellor—adverse pressure gradient, $\delta/R = 0.1$ (Fig. 12)
11 So and Mellor—zero pressure gradient, $\delta/R = 0.1$
12 Nagano and Gibson—heat transfer $\delta/R = 0.01$

Less successful predictions:

13 Simon run 022680 (same as Gillis experiment 3), C_f predictions in the recovery region too high (Fig. 13 - C_f)
14 Simon run 051080, strong favorable pressure gradient. Prediction too high in the curved region due to an incorrect pressure gradient model
15 Simon run 011380, in the recovery region, prediction of Stanton number too high
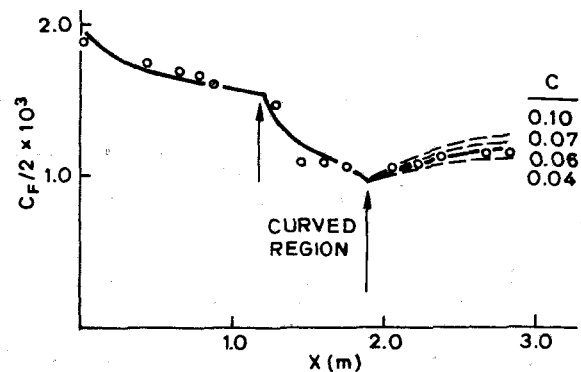
Fig. 7 Selection of the recovery region lag parameter C using skin-friction data from the second Gillis experiment, $\delta/R \simeq 0.1$
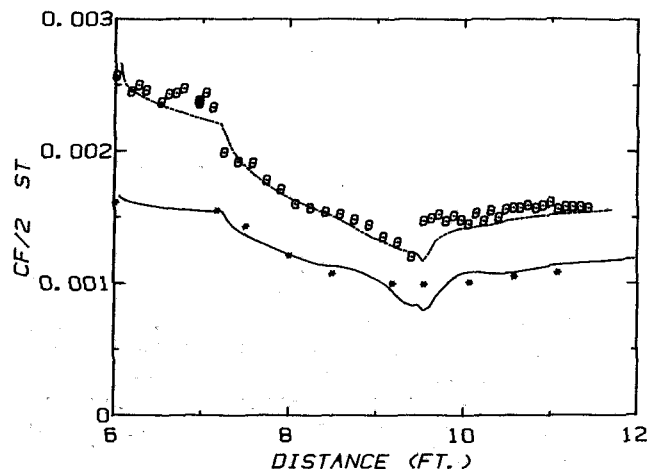
Fig. 8 Prediction of skin friction and heat transfer coefficient for Simon run 070280, $\delta/R \simeq 0.1$
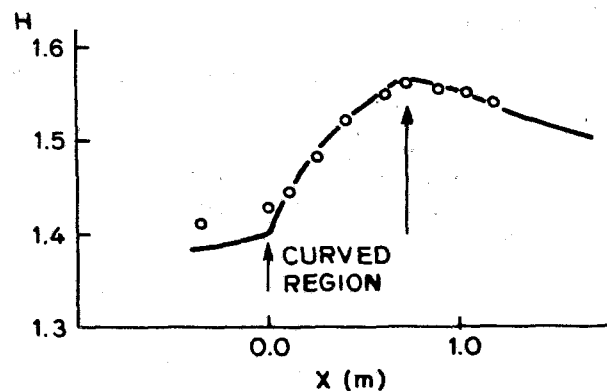
Fig. 9 Shape-factor prediction for Simon run 070280, $\delta/R \simeq 0.1$

Figure 6 compares the predicted and measured values of skin friction for the Hoffmann and Bradshaw [4] convex curvature experiment, a flow with a slight favorable pressure gradient. This case was used to set $\beta = 5$.

Figure 7 compares the measured and calculated skin-friction values for the second Gillis experiment. In this experiment, the opposite or concave wall was adjusted to maintain the pressure gradient along the test surface very close to zero. Simon used the same experimental apparatus and also controlled wall static pressure. Because the initial computed profile had a somewhat different value of H from that found by the experimenter, the agreement between computation and experiment for shape factor (not shown
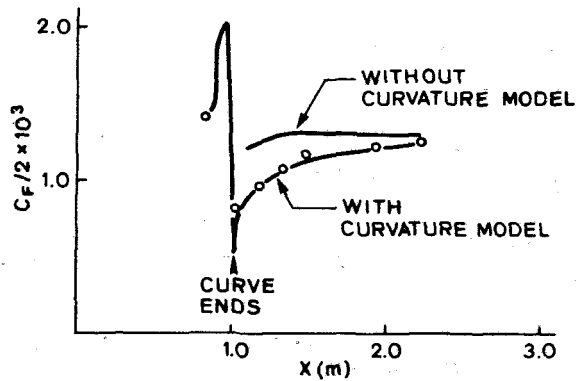
Fig. 10 Prediction of skin-friction coefficient for the Smits, Young, and Bradshaw experiment, $\delta/R \simeq 0.15$
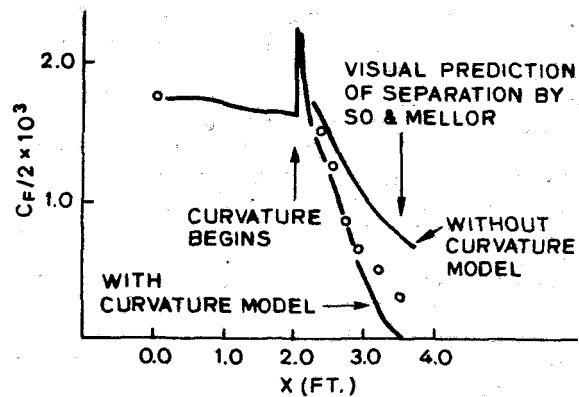
Fig. 12 Prediction of skin-friction coefficient of So and Mellor adverse pressure-gradient experiment, $\delta/R \simeq 0.1$
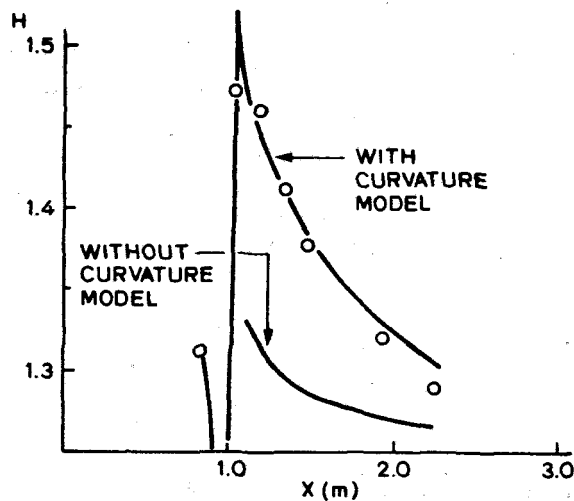
Fig. 11 Shape-factor prediction for the experiment of Smits, Young, and Bradshaw, $\delta/R \simeq 0.15$
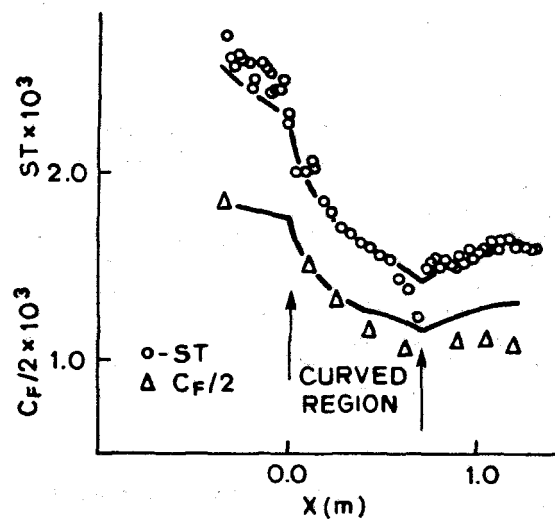
Fig. 13 Prediction of skin friction and heat transfer coefficient for Simon run 022680, $\delta/R \simeq 0.05$

here) was not quite as good. However, the trends were predicted nicely.

Figures 8 and 9 display the results for the baseline heat transfer experiment by Simon et al. [4]. The nominal "strength of curvature" (δ/R) was 0.1. Stanton number, skin friction, and shape factor were all computed quite successfully.

Figures 10 and 11 compare the prediction with the experiment of Smits, Young, and Bradshaw [10]. This experiment contained a short 30 deg turn, of strong curvature $(\delta/R = 0.15)$, followed by a flat-wall recovery region. In addition, the experiment had strong pressure gradients at entry to and exit from the curved region. The effect of the curvature model on the prediction of skin friction and shape factor is quite dramatic. The 30–50 percent reduction in skin friction in the recovery region is well predicted.

The comparison of computation with experiment for the So and Mellor [11] adverse pressure gradient experiment appears in Fig. 12. The pressure gradient on the test wall was altered by adjusting the location of the opposite wall. The experimenters could not completely eliminate a sudden acceleration at the start of the convex curve. This acceleration caused the sudden change in skin friction which the model predicts at the start of curvature. So and Mellor located detachment by visual means at $x = 2.5$ ft. around the curve. The computer predicted detachment within two boundary thicknesses of this station (see Fig. 12). So and Mellor characterized the flow near detachment as very three-dimensional. The last data points before separation most

probably reflect this effect (C_f too high), and thus agreement with the data may be better than it appears.

Comparing results (in Fig. 12) for calculations with and without the curvature model, it is apparent that the separation point is strongly affected by the convex curvature. The prediction using a flat-walled turbulence model results in a large error in the predicted separation point. Accurate prediction of the strong adverse pressure gradient combined with curvature gives confidence that the curvature turbulence model can predict combined inner layer/outer layer effects on turbulent mixing. These combined effect flow situations have historically been difficult to predict by mixing length method.

The cases—13, 14, and 15—where the predictive method was less successful require discussion. Figure 13 presents the prediction of Simon experiment 022680. The Stanton number prediction was a success, while the skin-friction coefficient prediction in the recovery region is higher than the experimentally measured values. Since heat transfer is correctly predicted, but not skin friction, these results are puzzling. The strength of curvature $(\delta/R = 0.05)$ and free-stream velocity had values which were close to the third Gillis experiment [3]; the computation of this flow produced almost identical results. Gillis noted that the secondary flows are worse in this experiment than in his second one $(\delta/R = 0.1)$. This may help explain the discrepancy, but we are not satisfied with this explanation, nor has it been tested quantitatively.

The Stanton values computed for Simon run 051080 fall above the experimental points in the curved region. This experiment had large free-stream acceleration effects combined with the curvature effects. A computation made without curvature effects added to the turbulence model failed to predict the expected effects of strong acceleration on Stanton number. The problem appears to lie in the code implementation of the pressure gradient model for strong, favorable pressure gradient and not with the curvature modifications.

The prediction of Simon run 011380 lay somewhat above the experimental Stanton number data. Trials showed that the computation was very sensitive to the prescribed velocity boundary conditions. The mismatch between data and prediction first appears upstream of the curved region, and its magnitude remains constant throughout the remaining downstream regions. For this reason, we believe the curvature model is not causing the disagreement between the prediction and the experiment. There may be some difficulty with matching initial conditions in this case.

Conclusion

In the outer portion of a strong, convex curved boundary layer, between the turbulent wall layers and the region of total turbulence suppression, the mixing length was found to scale on the radius of curvature, not on the boundary layer thickness. In the inner regions, the presence of the wall still dominates the scale length, but scales are reduced by curvature. This paper presents a useful calculation method for boundary layer flows with convex curvature. Within some limitations, the model performs well. While the less successful cases are not fully explained, the number of successes gives confidence in the method.

Acknowledgments

This work was supported by NASA-Lewis Research Center

References

1 Van Dyke, M., "Higher-Order Boundary-Layer Theory," *Annual Review of Fluid Mechanics*, Vol. 1, 1969.

2 Bradshaw, P., "Effects of Streamline Curvature on Turbulent Flow," AGARDograph No. 169, 1973.

3 Gillis, J. C., Johnston, J. P., Kays, W. M., and Moffat, R. J., "Turbulent Boundary Layer on a Convex, Curved Surface," Report HMT-31, Thermosciences Division, Mechanical Engineering Department, Stanford University, 1980.

4 Simon, T. W., Moffat, R. J., and Kays, W. M., "Turbulent Boundary Layer Heat Transfer Experiments: Convex Curvature Effects, Including Introduction and Recovery," Report HMT-32, Thermosciences Division, Mechanical Engineering Department, Stanford University, Nov. 1980.

5 Crawford, M. E., and Kays, W. M., "STAN5—A Program for Numerical Computation of Two-Dimensional Internal and External Boundary Layer Flows," NASA CR-2742, Dec. 1976.

6 Bradshaw, P., "The Analogy between Streamwise Curvature and Buoyancy in Turbulent Shear Flow," *Journal of Fluid Mechanics*, Vol. 36, Part 1, 1969.

7 Eide, S. A., and Johnston, J. P., "Turbulent Boundary Layers on Centrifugal Compressor Blades: Prediction of the Effects of Surface Curvature and Rotation," *Journal Fluids Engineering*, Vol. 98, 1976, pp. 374–381.

8 So, R. M. C., "On the Curvature/Buoyancy Analogy for Turbulent Shear Flows," *ZAMP*, Vol. 31, Fasc. 5 (1980), pp. 628–633.

9 Hoffman, P. H., and Bradshaw, P., "Turbulent Boundary Layers on Surface of Mild Longitudinal Curvature," Imperial College IC Aero Rept. 78-04, Dec. 1978.

10 Smits, A. J., Young, S. T. B., and Bradshaw, P., "The Effects of Short Region of High Surface Curvature on Turbulent Boundary Layers," *Journal of Fluid Mechanics*, Vol. 94, Part 2, Dec. 1978.

11 So, R. M. C., and Mellor, G. L., "Experiment on Convex Curvature Effects in Turbulent Boundary Layers," *Journal of Fluid Mechanics*, Vol. 60, Part 1, 1973.

12 Muck, K., "Turbulent Boundary Layers on Mildly Curved Surfaces," PhD thesis, Imperial College, London, Jan. 1982.

13 Hunt, I. A., and Joubert, P. N., "Effect of Small Streamline Curvature on Turbulent Duct Flow," *Journal of Fluid Mechanics*, Vol. 91, p. 633.

14 So, R. M. C., and Mellor, G. L., "An Experimental Investigation of Turbulent Boundary Layers along Curved Surfaces," NASA Contractors Report No. 1940, (1972).

15 Ro, S. M. C., and Mellor, G. L., "Turbulent Boundary Layers with Large Streamline Curvature Effects," *ZAMP*, Vol. 29, Fasc. 1 (1978), pp. 54–74.

Measurements of Heat Transfer Distribution Over the Surfaces of Highly Loaded Turbine Nozzle Guide Vanes

D. A. Nealy

M. S. Mihelc

L. D. Hylton

Detroit Diesel Allison,
Division of General Motors Corporation,
Indianapolis, Ind. 46206

H. J. Gladden

NASA,
Lewis Research Center,
Cleveland, Ohio 44135

The results of an experimental study of aerodynamic (surface velocity) and heat transfer distributions over the surfaces of two different, highly loaded, low-solidity contemporary turbine vane designs are presented. The aerodynamic configurations of the two vanes were carefully selected to emphasize fundamental differences in the character of the suction surface pressure distributions and the consequent effect on surface heat transfer distributions. The experimental measurements were made in moderate-temperature, three-vane cascades under steady-state conditions. The principal independent parameters (Mach number, Reynolds number, turbulence intensity, and wall-to-gas temperature ratio) were varied over ranges consistent with actual engine operation, and the test matrix was structured to provide an assessment of the independent influence of each parameter. These measurements are intended to serve as verification data for a parallel analytical code development effort. The results of this parallel effort are briefly reviewed, and the principal conclusions to date are summarized.

Introduction

Overview of the Problem. The thermal design of contemporary air-cooled, high-pressure (HP) turbine nozzle guide vanes clearly represents one of the more difficult engineering tasks in the design of any modern aircraft gas turbine. Uncertainty in the prediction of local gas-to-wall heat transfer rates on turbine airfoils remains a principal obstacle to timely and cost-effective development of high-temperature turbine components. In general, internal coolant heat transfer correlations developed from simple bench/rig tests have proved highly reliable, and calculation of heat flow within the airfoil structure via finite element techniques is well in hand. The external (gas-to-wall) heat transfer coefficient, however, still eludes satisfactory prediction because of a highly complex and interactive external flow field environment. In addition to the vagaries of gas temperature distribution, the airfoil row is characterized by a flow field reflecting surface Mach number variations from the low subsonic levels (≤ 0.15) to the transonic range (≥ 1.0). The flow field is strongly influenced by viscous effects in the near-wall region where, in turn, heat flow is alternately governed by molecular diffusion, laminar convective transport, turbulent shear transport, or combinations thereof. Although the character of the boundary layer over the greater radial extent of most airfoils is nominally two-dimensional, local boundary layer behavior (and, hence, surface heat transfer rate) is strongly influenced

by the several complex and interactive mechanisms summarized in Table 1.

Presently, a variety of predictive techniques is brought to bear on this complex problem with varying degrees of success. The simpler, well established correlative and integral techniques have met with some success [1–4]. However, only recently have the more powerful numerical solutions of the complete time-averaged boundary layer equations shown real promise [5–11]. Reinforced by carefully derived empirical turbulence modeling, the numerical techniques have yielded reasonable predictions of the effects of strong acceleration/deceleration and distributed injection in cases in which the external flow field and state of the boundary layer are well defined. However, direct comparisons of predicted and measured metal temperature distributions on airfoils continue to show considerable disagreement in many instances. For non-film-cooled airfoils, deviation of actual heat transfer predictions from true or indicated levels can most probably be attributed to one or more of the following analytical deficiencies:

•Lack of precision in the prediction of the inviscid flow field around the airfoil, particularly in the forward, highly accelerated stagnation region

•Uncertainties regarding the surface location at which transition is initiated as well as the surface extent of the transition zone

•Uncertainties regarding the influence of free-stream turbulence on local heat transfer rates in the laminar region as well as on initiation and extent of the transition region

Table 1 Basic mechanisms influencing gas-to-blade heat transfer

Mechanism	Nature/Manifestation
Transitional behavior	Transition from laminar/molecular diffusion transfer to turbulent shear transfer. Direct effect on heat transfer.
Free-stream turbulence	Temporal small-scale combustor or blade-passing induced stream velocity fluctuations. Influences production and diffusion of boundary layer turbulence and boundary layer stability (transition behavior).
Airfoil surface curvature	Influences boundary layer turbulence and dissipation. Affects boundary layer stability. May produce Goertler vortices (periodic large-scale disturbances along concave surface) with consequent strong effect on heat transfer.
Airfoil surface roughness	Directly influences boundary layer turbulence production and stability.
Strong mainstream velocity acceleration/deceleration	Direct influence on boundary layer thickness, profile shape, and stability. Controls turbulence production (decel) and dissipation (accel).
Distributed surface injection	Strong influence on turbulence production in injection region. Directly affects near-wall temperature profile and downstream boundary layer profiles and thickness.
Flow separation and reattachment	Affects local character and thickness distribution of boundary layer. Produces sharp local heat transfer rate increases.
Shock/boundary layer interaction	Causes boundary layer separation and consequent effects.

Fig. 1 Aerothermodynamic cascade facility

Table 2 Aerothemodynamic cascade facility specifications

Operational specifications

Air supply	4.309 kg/s at 723.9 kPa or 2.263 kg/s at 1689.2 kPa
Inlet pressure	413.4 kPa to 1689.2 kPa
Stagnation temperature	477 K to 2033 K
Primary fuel	Natural gas
Duct Wall temperature	1227 K at gas temperature of 2033, K, 533 K at gas temperature of 1089 K

Instrumentation specifications

Pressure scanner	Scanivalve system with 288 ports
Pressure transducers	Druck with ranges from 0–68.9 kPa to 0–3447.4 kPa
Accuracy	±0/0.6 percent BSL
Thermocouple channels	300 CR-A1 + 40 Pt/Pt-10 percent Rh ±0.3°C with calibration
Accuracy	tion
Traversing gear	United Sensor traversing probe mountes with computer interfaces Precision two-axis digital traversing mount with discrete stepping capability to 0.0025 cm
Anemometers	Single- and dual-sensor hot wire hot film anemometry Laser Doppler anemometer (LDA)
Survey probes	Traversing Cr-A1 thermocouple Traversing five-port cone and prism probes.

•Limited understanding of role of airfoil surface curvature on turbulence production/dissipation and boundary layer stability.

Even if consideration is restricted to the nominally two-dimensional midspan region, the complex and unforgiving environment described previously suggests the need for an improved, rational design approach based on numerical predictive tools with sufficiently enlightened turbulence modeling to accommodate the several interactive influences described previously. A corollary requirement is posed by the clear need to confirm, through realistic experiments, that the physical details of the inviscid/visocus flow field are in fact correctly modeled.

Relevant Background Studies. While a number of experimental turbine vane heat transfer studies have been reported over the past 25 years [12–20], the applicability of these data to contemporary low-solidity, highly loaded vane rows is limited by conservatism in profile shape and/or M_N range [12–15] or by incompleteness in availabilty or range of

Nomenclature

arc = total airfoil surface distance from geometric stagnation point to trailing edge

H = local surface heat transfer coefficient

LER = leading edge radius

M_N = Mach number (at cascade exit unless otherwise noted)

P_S = local airfoil surface static pressure

P_T = cascade inlet total pressure

Re, Re$_2$ = cascade Reynolds number (based on cascade exit Mach number and airfoil true chord)

S = airfoil surface distance measured from geometric stagnation point

TER = trailing edge radius

T_G = average gas stream inlet total temperature

T_u = free-stream turbulence intensity at cascade inlet

T_w = average vane surface temperature
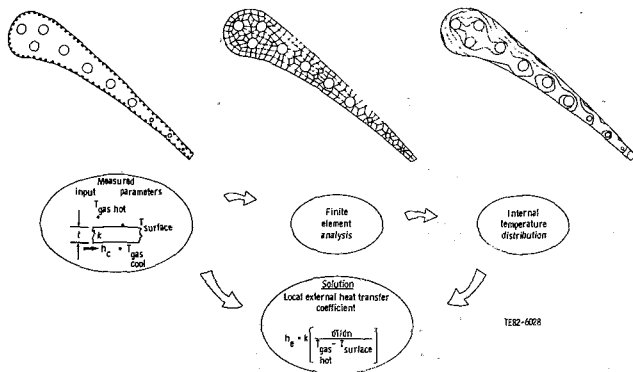
Fig. 2 Heat transfer data reduction technique

data [16–20]. In general—[20] being the exception—the studies cited above were not conducted under conditions that ensured coincident similarity of the principal independent aerothermo parameters (Mach no., Reynolds no., T_w/T_g, and turbulence intensity) to those existing in current-generation core engines.

A more recent program [21] was initiated at DDA in 1980 in an attempt to rectify several of the analytical and experimental deficiencies cited previously. This program—currently restricted to non-film-cooled airfoils—is keyed to the following objectives: (i) to assess the deficiencies of current (practical) analytical prediction tools, (ii) to recommend and incorporate empirically indicated changes to those tools, and (iii) to verify that the changes achieve the desired result. The initial assessment phase of the program focused on the comparative evaluation of selected analytical prediction tools [3, 8] against certain existing data sets [15, 16, 20]. This program phase will not be reported in detail herein but is fully documented in a forthcoming report [22]. The principal conclusion reached in the assessment study (similar in scope and observations to that reported by Daniels & Browne [23]) was that the numerical boundary layer code [8] with zero-order (mixing length hypothesis) turbulence modeling offered the greatest potential for *near-term* improvement of predictive capability relative to the combined effects of pressure gradient, free-stream turbulence, and curvature on transitional behavior and heat transfer distribution. It is, of course, recognized that this approach requires a high degree of empiricism, particularly with respect to prediction of transitional behavior and free-stream turbulence effects on heat transfer to a nominally laminar zone. Attempts to reduce the heavy dependence on empiricism via higher order turbulence modeling (including the Jones-Launder K-ϵ model [24]) were not successful in the initial assessment study, but the potential of higher order turbulence modeling is recognized and was recommended as a longer term development effort.

Scope of Present Paper. The work reported herein focuses on the experimental phase of the current NASA/DDA program [21] with emphasis of both the aerodynamic (surface velocity) and heat transfer distributions over the surfaces of two different highly loaded, low-solidity contemporary turbine nozzle guide vanes designs. The aerodynamic configurations of the two vanes were carefully selected to emphasize fundamental differences in the character of the suction surface pressure distributions and the consequent effect on surface heat transfer distribution. The experimental measurements were conducted in moderate-temperature, three-vane cascades under steady-state conditions. The principal independent parameters (M_N, Re, T_u, and T_w/T_g) were varied over ranges consistent with actual engine operation, and the test matrix was structured to provide an assessment of the independent influence of each parameter on airfoil surface heat transfer.

In the following sections, the experimental cascade apparatus is reviewed in some detail and the experimental results for surface velocity and heat tranfer distributions are presented and discussed. Finally, the basic elements of the parallel analytical code development effort are briefly reviewed, and the principal conclusions to date are summarized.

Description of Experimental Apparatus

The experimental data presented in this paper were acquired in the Detroit Diesel Allison (DDA) Aerothermodynamic Cascade Facility (ACF), a linear, two-dimensional, steady-state cascade facility specifically designed to obtain turbine vane heat transfer and aerodynamic data under simulated engine conditions. Operationally, the facility consists of an inlet air control valve, a water-cooled, natural-gas-fired burner, a convergent section, an instrumented free-stream section, a test section with instrumentation, a quench zone with back pressure regulation, and an exhaust system. The facility is shown schematically in Fig. 1 and operating specifications are given in Table 2.

Facility instrumentation includes the capability of measuring up to 288 pressures and 300 temperatures during a test. Facility operation and data acquisition are handled by a dedicated computer-controlled data acquisition system. A multitask, facility oriented software system containing general subprograms is used to do all routine control and measurement tasks.

The wide operating range of the ACF permits geometric scale-up of test hardware for ease in instrumentation while maintaining Mach and Reynolds number and temperature ratio similarity with engine hardware. In addition, the close coupling of the burner to the test section generates combustor-induced, free-stream turbulence intensities. The control system for the facility makes it possible to independently vary the key similarity parameters namely, Mach number, Reynolds number, wall-to-gas temperature ratio, and turbulence intensity. This capability allows the generation of a data matrix that separates the effects of each of these parameters.

The method used to obtain heat transfer measurements is based on the work of Turner [15], who employed a two-dimensional plane of the test vane as a fluxmeter. The technique can be implemented by installing thermocouples in grooves on the interior and exterior surfaces of the test piece, which is then exposed to the test environment until thermal equilibrium is obtained. The steady-state surface temperature data then become the boundary conditions for a finite element solution of the internal temperature field of the test piece. The surface normal temperature gradient is derived from this solution, and the local heat transfer coefficient distribution can be directly evaluated. The method has several advantages. First, test hardware cost is reduced because the method requires only thermocouple instrumentation. Second, the approach provides good spatial resolution, limited only by the grid size selected for thermocouple locations. Finally, testing is conducted with the correct heat flux sense—i.e., hot gas with cold wall—and with similitude to engine temperature ratios (T_w/T_g).

For the current study the technique was modified slightly. Rather than using internal thermocouples to supply temperatures as the internal boundary condition, a series of ten radial cooling holes was provided in the vane, and the average heat transfer coefficients and coolant temperatures for each hole were used as the internal boundary conditions. The heat transfer coefficient for each cooling hole was calculated from

Table 3 Mark II vane coordinates

Position number	X dimension (cm)	Y dimension (cm)	Position number	X dimension (cm)	Y dimension (cm)
1	0.0	10.8943	31	6.8544	0.0
2	1.0310	12.1521	32	6.4912	−0.0686
3	1.4006	12.1844	33	6.3409	0.3119
4	1.9025	12.1067	34	6.1874	0.6927
5	2.3584	11.8803	35	6.0315	1.0729
6	2.7259	11.5263	36	5.8727	1.4521
7	2.9812	11.0833	37	5.7112	1.8306
8	3.1923	10.6175	38	5.5466	2.2080
9	3.3978	10.1491	39	5.3792	2.5844
10	3.5994	9.6794	40	5.2090	2.9594
11	3.7976	9.2083	41	5.0358	3.3345
12	3.9919	8.7356	42	4.8593	3.7076
13	4.1824	8.2616	43	4.6797	4.0792
14	4.3688	7.7866	44	4.4961	4.4498
15	4.5517	7.3101	45	4.3104	4.8186
16	4.7308	6.8326	46	4.1201	5.1859
17	4.9063	6.3538	47	3.9258	5.5588
18	5.0777	8.4140	48	3.7274	5.9144
19	5.2456	7.9329	49	3.5240	6.2748
20	5.4099	4.9113	50	3.3157	6.6327
21	5.5702	4.4282	51	3.1016	6.9873
22	5.4099	3.9444	52	2.8809	7.3378
23	5.4099	3.4597	53	2.6528	7.6838
24	5.4099	2.9741	54	2.4158	8.0239
25	5.4099	2.4877	55	2.1687	8.3451
26	5.4099	2.0005	56	1.9088	8.6792
27	5.4099	1.5128	57	1.6337	8.9891
28	5.4099	1.0244	58	1.3396	9.2809
29	5.4099	0.5354	59	1.0208	9.5456
30	5.4099	0.0467	60	0.6744	9.7666

LER = 1.280 cm
TER = 0.0000 cm (blunt)
Throat dimension = 3.983 cm
Vane setting angle = 63.69 deg
Vane spacing = 12.974 cm

Mark II thermocouple locations

Mark II static pressure tap locations

C3X thermocouple locations

C3X static pressure tap locations
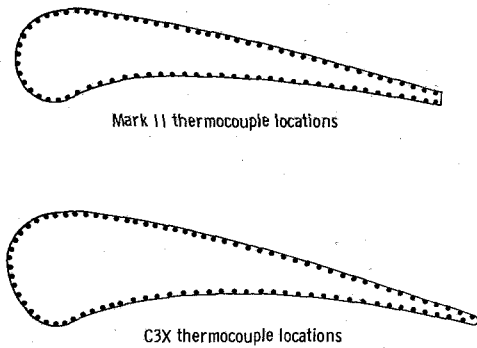
Fig. 3 Surface profiles and thermocouple locations for Mark II and C3X cascade vanes
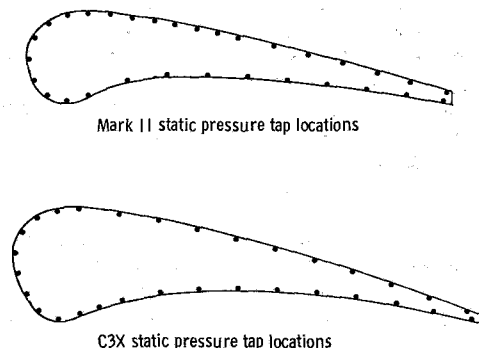
Fig. 4 Surface profiles and static pressure tap locations for Mark II and C3X cascade vanes

the hole diameter, measured flow rate, and coolant temperature, with a correction applied for thermal entry length. The modified technique is illustrated in Fig. 2.

This modification, coupled with the use of a larger-scale, three-vane cascade (rather than a five-vane cascade), reduced the uncertainty associated with making ΔT measurements across relatively thin vane walls. As a result the average uncertainty in the vane surface heat transfer coefficients obtained with this method has been reduced to 12 percent when calculated by the method of Kline and McClintock [25]. This compares with an average uncertainty of 15 percent using the internal thermocouple technique.

The studies reported in this paper were performed on two different highly loaded, low-solidity turbine nozzle guide vanes. The two vane designs, identified as Mark II and C3X, were specifically selected to provide an insight into the effect

of suction surface pressure distribution on surface heat transfer. The significantly different suction surface geometries of the two airfoils are illustrated by the vane cross sections shown in Figs. 3 and 4. Coordinates for the two profiles are given in Tables 3 and 4, respectively.

As indicated previously, a three-vane cascade design was employed to increase the scale of the test vanes, thus allowing higher instrumentation density. The three-vane cascade, however, required flow splitters (adjacent to the outer vanes) and a tailboard to ensure periodicity and the proper surface pressure distribution on the center, instrumented vane. The cascade endwalls were instrumented with static pressure taps at both the inlet and exit of the vane row to provide the information required to establish periodicity and to set cascade expansion ratio.

A photo of the C3X cascade is shown in Fig. 5. The outer

Table 4 C3X vane coordinates

Position number	X dimension (cm)	Y dimension (cm)	Position number	X dimension (cm)	Y dimension (cm)
1	0.1097	11.6548	40	7.4849	-0.0617
2	0.3894	12.1890	41	7.3188	0.3559
3	0.7658	12.6764	42	7.1483	0.7737
4	1.2723	13.0233	43	6.9736	1.1895
5	1.8743	13.1376	44	6.7950	1.6035
6	2.4707	12.9939	45	6.6116	2.0155
7	2.9835	12.6538	46	6.4237	2.4254
8	3.3985	12.1976	47	6.2309	2.8329
9	3.7376	11.6817	48	6.0328	3.2380
10	4.0272	11.1364	49	5.8296	3.6406
11	4.2885	10.5766	50	5.6203	4.0401
12	4.5326	10.0094	51	5.4051	4.4364
13	4.7648	9.4369	52	5.1834	4.8290
14	4.9870	8.8605	53	4.9548	5.2177
15	5.2019	8.2814	54	4.7191	5.6020
16	5.4110	7.7003	55	4.4760	5.9817
17	5.6157	7.1176	56	4.2248	6.3563
18	5.8171	6.5336	57	3.9654	6.7249
19	6.0160	5.9487	58	3.6975	7.0874
20	6.2126	6.3632	59	3.4204	7.4430
21	6.4074	4.7767	60	3.1339	7.7909
22	6.5997	4.1897	61	2.8374	8.1308
23	6.7894	3.6015	62	2.5314	8.4615
24	6.9756	3.0122	63	2.2149	8.7826
25	7.1575	2.4221	64	1.8885	9.0935
26	7.3335	1.8301	65	1.5519	9.3932
27	7.5024	1.2357	66	1.2052	9.6815
28	7.6624	0.6391	67	0.8494	9.9578
29	7.8115	0.0411	68	0.4999	10.2116
30	7.8161	-0.0053	69	0.3848	10.3035
31	7.8082	-0.0516	70	0.2822	10.4094
32	7.7879	-0.0935	71	0.1938	10.5273
33	7.7572	-0.1288	72	0.1212	10.6556
34	7.7180	-0.1542	73	0.0650	10.7920
35	7.6736	-0.1681	74	0.0264	10.9342
30	7.6269	-0.1699	75	0.0063	11.0802
37	7.5816	-0.1587	76	0.0046	11.2278
38	7.5408	-0.1356	77	0.0216	11.3741
39	7.5077	-0.1026	78	0.0569	11.5171

LER = 1.168 cm
TER = 0.173 cm
Throat dimension = 3.292 cm
Vane setting angle = 59.89 deg
Vane spacing = 11.173 cm

two slave vanes are cooled by an array of radial cooling holes identical to those in the center, instrumented vane. However, they are supplied from a common plenum, whereas each hole in the center vane is supplied from a separate metered line to calculate the internal heat transfer coefficient in each of the holes. The two slave vanes were instrumented with surface thermocouples so that the coolant could be adjusted to eliminate radiation heat transfer to the center vane. The cascade endwalls were also cooled for this purpose.

The center vane contained instrumentation for determining both the surface static pressure distribution and the surface heat transfer coefficient distribution around the airfoil. Measurement planes were near midspan. The surface thermocouple leads are visible as lines on the surface of the center vane in Fig. 5. In this installation, 0.051-cm-dia CA thermocouples were placed in 0.058-cm-deep grooves and cemented over. The cement was then blended by hand to provide a smooth surface. The spatial density of the surface thermocouples for the two cascades is shown in Fig. 3. The closely spaced arrays of thermocouples provide excellent sensitivity to changes in the external heat transfer and ensure resolution of the rapid changes associated with boundary layer transition or separation. Figure 4 illustrates the location of static pressure taps on the airfoil surface for the two cascades. The patterns are not as dense as the thermocouples but provide adequate measurement density in the leading edge regions and along the suction surface up to the expected transition point. In addition to the instrumentation illustrated
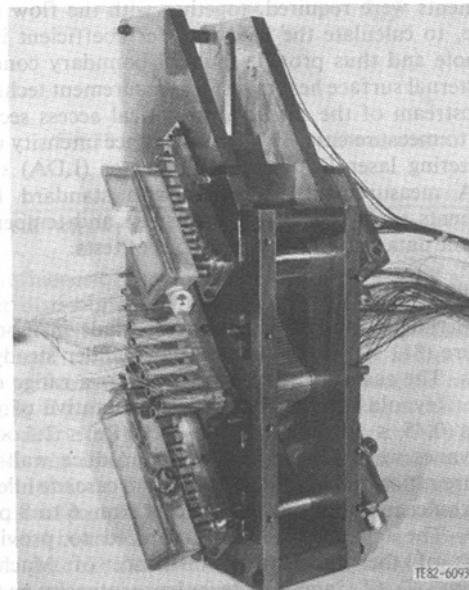

Fig. 5 C3X cascade assembly

in Figs. 3 and 4, the center vane was also instrumented with static pressure taps and thermocouples at the inlet and exit of each coolant tube. The instrumentation at the coolant tube
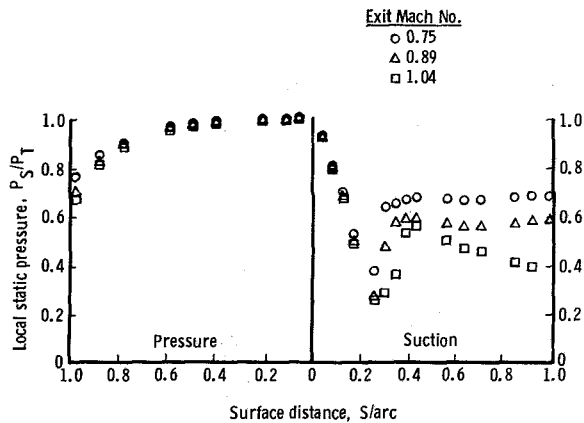
Fig. 6 Effect of exit Mach number on Mark II vane surface static pressure distribution

Fig. 8 Effect of exit Mach number on Mark II vane heat transfer distribution
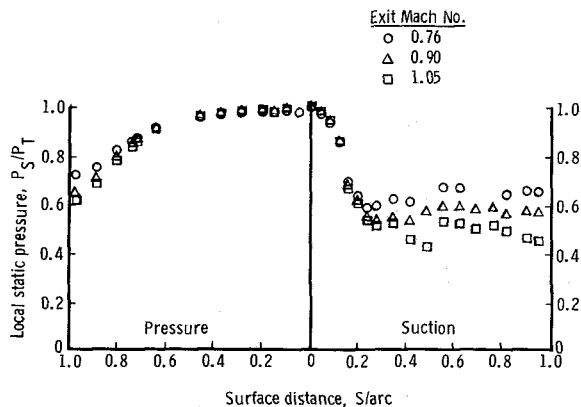

Fig. 7 Effect of exit Mach number on C3X vane surface static pressure distribution

exit can be seen in Fig. 5. The coolant temperature measurements were required, together with the flow rate to each tube, to calculate the heat transfer coefficient in each cooling hole and thus provide internal boundary conditions for the external surface heat transfer measurement technique.

Just upstream of the cascade, an optical access section is provided to measure cascade inlet turbulence intensity using a back-scattering laser Doppler anemomenter (LDA) system. The LDA measurements, together with standard facility measurements such as inlet total pressure and temperature, complete the data required for this series of tests.

Experimental Results

The experimental measurements were made in moderate-temperature (811 K), three-vane cascades under steady-state conditions. The cascades were operated over a range of exit Mach no./Reynolds no. conditions representative of engine conditions ($0.45 \leq M_N \leq 1.05$; 0.5×10^6 Re $\leq 2.5 \times 10^6$). The test vanes were actively cooled to produce wall-to-gas temperature ratios in the 0.7–0.8 range, and cascade inlet free-stream turbulence intensities were varied from 6 to 8 percent (nominal). The test matrix was structured to provide an assessment of the independent influence of Mach no., Reynolds no., T_w/T_g, and inlet turbulence intensity on airfoil surface heat transfer. The exit Reynolds numbers are based on airfoil true chord (13.61 cm for the Mark II airfoil and 14.50 cm for the C3X airfoil) while the indicated exit Mach numbers are based on measured inlet total pressure and average measured exit plane static pressure (13 endwall static pressure
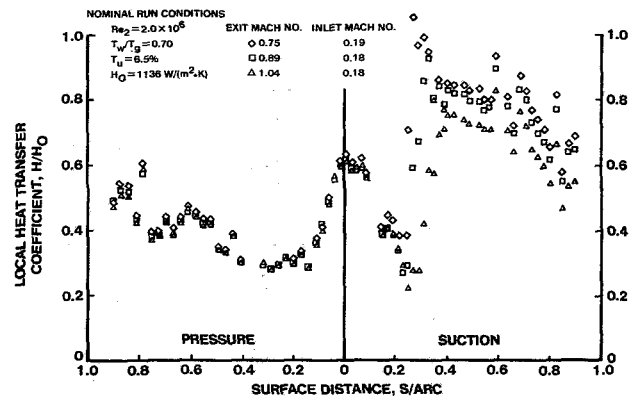
taps at cascade exit plane). All tests were conducted at a nominal gas stream total temperature of 811 K.

The cascade Reynolds number range was achieved by varying cascade mass flow rate from 1.134 kg/s to 4.536 kg/s. At a given Reynolds number condition, exit Mach number levels could be independently established by adjusting cascade exit pressure with a controllable exhaust valve. T_w/T_g levels were varied by controlling coolant flow rate. The cascade combustor-induced inlet turbulence intensity level was found to be approximately 6.5 percent based on preliminary LDA measurements. This level was augmented for selected test points by installing circular rods upstream of the cascade. The augmented turbulence intensity levels were approximately 8.3 percent based on subsequent LDA measurements.

Static pressure measurements were made at 30 locations around the perimeter of each airfoil at approximately mid-span position. The measured surface static pressure distributions corresponding to a range of cascade expansion ratios are shown in Figs. 6 and 7 for the Mark II and C3X airfoils, respectively. The marked difference in the suction surface Mach number distribution over the two airfoils is evident in these measurements. A very strong adverse pressure gradient is apparent at about 20 percent suction surface arc length on the Mark II airfoil. On the other hand, the C3X suction surface static pressure distribution exhibits only moderate downstream diffusion.

The measured surface heat transfer distributions over the two airfoils also exhibit correspondingly different characteristics. In the case of the Mark II airfoil, the independent influence of exit Mach number (surface Mach number distribution) on heat transfer distribution is shown in Fig. 8. In general the suction surface heat transfer distributions tentatively indicate laminar boundary layer separation, free transition, and turbulent reattachment starting at about 20 percent of suction surface arc length. The location of incipient separation as well as the character and level of the downstream (reattached) heat transfer distributions exhibit a distinct Mach number distribution dependence. This observation is consistent with predictions made via the STAN5 [8] code, which indicates boundary layer separation at the experimentally observed locations regardless of the nature of the turbulence or transition model employed. Comparison of Figs. 6 and 8 shows a clear correlation between the location of separation (as indicated by the heat transfer data) and the strong adverse spike in the pressure distribution. On the other hand, no independent effect of Mach number level on heat transfer level is apparent in the regions in which the boundary layer remains attached (and largely laminar), an observation which is fully consistent with theoretical expectations.

The influence of exit Mach number level on heat transfer distribution over the C3X airfoil surface is shown in Fig. 9.
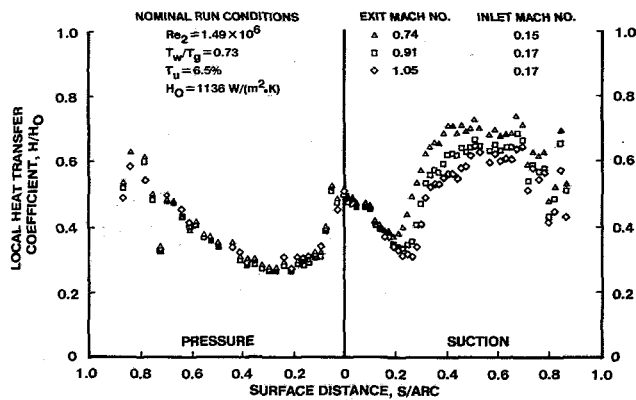
Fig. 9 Effect of exit Mach number on C3X vane heat transfer distribution
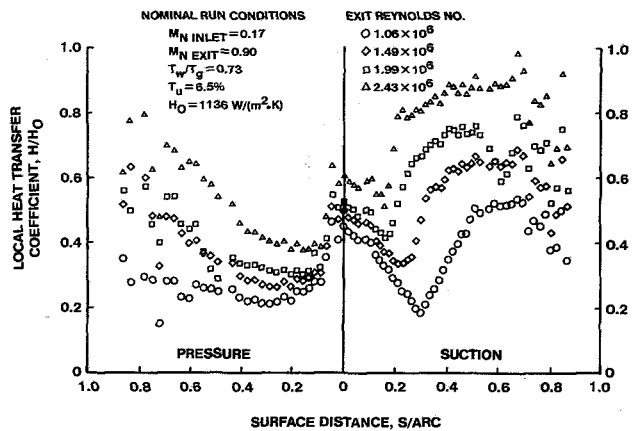
Fig. 11 Effect of Reynolds number on C3X vane heat transfer distribution
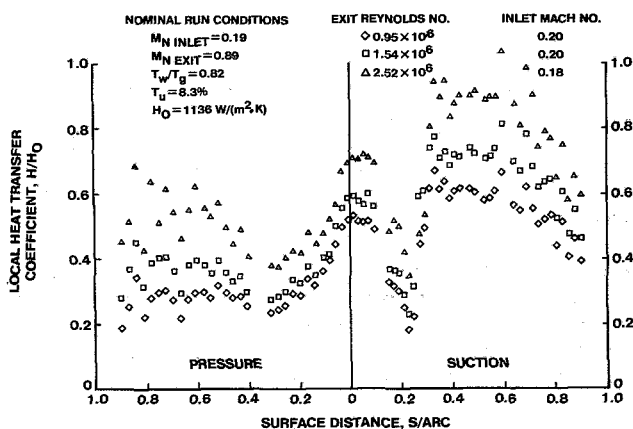
Fig. 10 Effect of Reynolds number on Mark II vane heat transfer distribution

LEGEND
K
A   478
B   505
C   533
D   561
E   589
F   616
G   644
MAX 663
MIN 457

Fig. 12 Typical test airfoil isotherm pattern

The C3X airfoil clearly exhibits a more classical transitional behavior on the suction surface. Pressure surface heat transfer level and distribution appear to be relatively insensitive to Mach number level, but downstream suction surface heat transfer trends reflect the differences in pressure gradient history along that surface (exit Reynolds number is constant).

The influence of Reynolds number level on airfoil heat transfer distribution is shown in Figs. 10 and 11 for the Mark II and C3X airfoils, respectively. In the case of the Mark II airfoil, the Reynolds number effect (at a given exit M_N level) appears to be largely reflected as a shift in general heat transfer level rather than in heat transfer distribution (see Fig. 10). This sharp jump in suction surface heat transfer level occurs at essentially a fixed surface location, implying a strong dependence on M_n distribution (also fixed) rather than Reynolds number level. This observation gives some support to the contention that the abrupt change in suction surface heat transfer is caused by separation/reattachment phenomena rather than simple transitional behavior. The pressure surface, on the other hand, exhibits an increased tendency toward transitional behavior as the Reynolds number is elevated. The downstream suction surface heat transfer levels vary approximately with Reynolds number to the 0.8 power, as might be expected from first order considerations. The trend here is consistent with that for fully developed turbulent flow over a flat plate, which is not surprising in view of the nature of the downstream suction

surface curvature and static pressure distributions (see Figs. 4 and 6).

The influence of Reynolds number level on C3X airfoil heat transfer distribution is reflected in the transitional behavior along the suction surface as well as in the general level of surface heat transfer (see Fig. 11). The onset and extent of the suction surface transitional zone exhibit a marked response to increasing Reynolds number level. Airfoil heat transfer levels also appear to increase systematically with increasing Reynolds number in a manner similar to that observed for the Mark II airfoil. The heat transfer distributions over the pressure surface of the C3X airfoil exhibit a tendency toward transitional behavior at the higher Reynolds numbers, a trend which is quite similar to that observed on the Mark II airfoil.

At this point, some comment may be in order regarding the relatively large scatter in the heat transfer data at downstream surface locations. This behavior is largely a consequence of the airfoil heat flow patterns in the trailing edge region illustrated by the typical isotherm plot shown in Fig. 12. In this region, the heat flow pattern is dominantly axial (due to
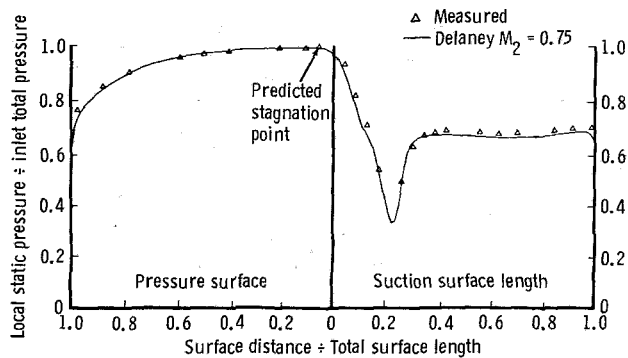
Fig. 13 Comparison of predicted and measured surface static pressure distributions for Mark II airfoil
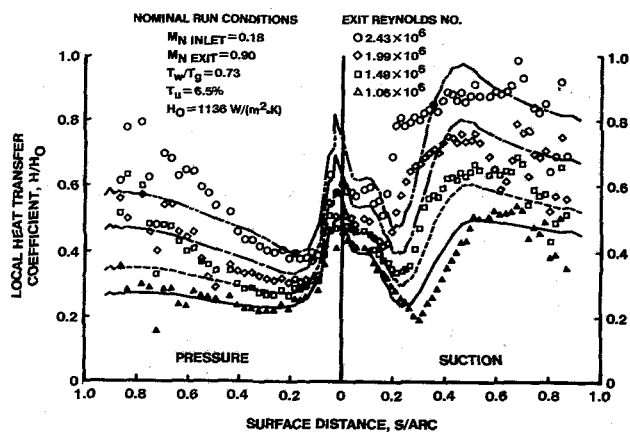
Fig. 15 Predicted versus measured heat transfer distributions for C3X airfoil
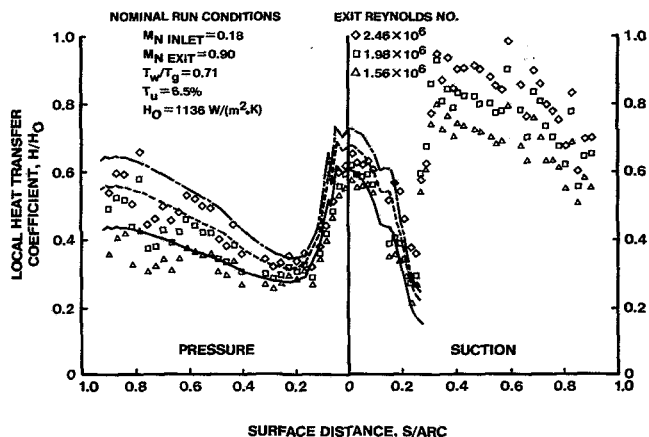
Fig. 14 Predicted versus measured heat transfer distribution for Mark II airfoil

unfavorable internal/external surface area ratios), giving rise to relatively small surface-normal metal temperature gradients $(\delta T_M/\delta n)$, which in turn are highly sensitive to small variances in the (measured) surface temperature boundary condition. This can be contrasted to the heat flow patterns in the forward regions, where metal temperature gradients are largely normal to the surface and yield well-behaved surface-normal flux data. While the downstream scatter is troublesome and clearly exceeds the average uncertainty level of 12 percent, the data in the regions of key interest (leading edge, pretransition, and transitional zone) are well behaved and yield distribution trends that can be reasonably well extrapolated through the regions of high scatter. To the extent this experimental technique is employed in the future, data scatter could be reduced to more manageable levels by increasing hardware scale size. In this manner internal cooling surface area to external surface area ratios could be favorably enhanced, resulting in more dominantly surface-normal temperature gradients.

Over the range of turbulence intensity levels achieved in the test program, small but systematic changes in heat transfer level were observed on both airfoils. The mean level of free-stream turbulence (6–8 percent) was also reflected in a general elevation of laminar region heat transfer over that which would be expected for the zero turbulence situation (≈ 50 percent). While the general level of free-stream turbulence in the cascade would also be expected to influence transitional

behavior and/or the tendency toward boundary layer separation, the relatively small changes in turbulence intensities achieved during operation (6.5–8.3 percent) were masked by the more significant changes in Mach number and Reynolds number level. Thus, changes in the character of airfoil heat transfer distribution were observed to be almost entirely attributable to changes in either M_N distribution or Reynolds number level.

Similarly, the range of T_w/T_g level in the experiment produced small but systematic shifts in heat transfer level and distribution. The observed trends here are consistent with previous observations [26] relative to fluid property effects inasmuch as reduced T_w/T_g levels were reflected in reduced laminar stagnation region heat transfer levels and in increased turbulent region heat transfer levels.

In closing this section some comments regarding the parallel, analytical code development and validation activity are in order. The cascade test results reported herein have been compared with predictions made by a recently developed time-dependent, transonic inviscid cascade code [27] coupled to a special version of the STAN5 [8] boundary layer code featuring zero order turbulence modeling. The boundary layer calculation is started at the aerodynamic stagnation point using initial profiles generated by a laminar stagnation point similarity solution, which in turn reflects the stagnation point free-stream velocity gradient, $(dV_\infty/dx)_{x=0}$, predicted by the inviscid code [27].

Space limitations preclude a detailed discussion of the analytical effort, but some key observations may be worth noting:

• The inviscid code [27] shows excellent agreement with the measured static pressure distributions for both airfoils, including the strong adverse pressure spike on the Mark II airfoil. (Typical comparative results for the Mark II airfoil are shown in Fig. 13.)

• The predicted aerodynamic stagnation point for both airfoils is indicated to be displaced toward the pressure surface by as much as 5 percent of pressure surface arc length from the geometric stagnation point.

• The stagnation point free-stream velocity gradient, $(dV_\infty/dx)_{x=0}$, is predicted to be significantly less than that which would be expected based on the conventional simulation of that region as a cylinder in cross flow.

• Heat transfer distributions for both the C3X and Mark II airfoils are qualitatively well predicted by the modified STAN5 boundary layer code (see Figs. 14 and 15).

• The predicted trends of heat transfer with Reynolds number level for the Mark II airfoil are in reasonable

quantitative agreement with the data as shown in Fig. 14. Heat transfer predictions downstream of the suction surface separation point were precluded, however, due to limitations in the present code framework.

●Predicted C3X airfiil heat transfer trends show reasonable quantitative agreement with data at the lower Reyolds numbers but progressively deviate from the measurements at the higher Reynolds numbers (see Fig. 15). In general, the suction surface transitional trends are correctly predicted, but the degree to which transition initiation is advanced (with increasing Reynolds number) is underestimated. Also, downstream pressure surface heat transfer levels are progressively underestimated at the higher Reynolds numbers.

●The small but systematic shifts in heat transfer attributable to changes in free-stream turbulence and/or T_w/T_g level were correctly predicted in terms of trend and level for both airfoils.

The reader is referred to [22] for a more detailed discussion of the analytical modeling effort and the comparative studies summarized above.

Summary and Conclusions

Results of an experimental investigation of heat transfer to two different highly loaded, low-solidity turbine nozzle guide vanes have been presented. The aerodynamic designs of the two vanes were selected to emphasize fundamental differences in the character of the suction surface pressure distribution and the consequent effect on surface heat transfer distribution.

The experimental measurements were made in moderate-temperature (811 K), three-vane cascades under steady-state conditions. The cascades were operated over a range of exit Mach number/Reynolds number conditions representative of engine conditions ($0.45 \leq M_N \leq 1.05; 0.5 \times 10^6 \leq Re \leq 2.5 \times 10^6$). The test vanes were actively cooled to produce wall-to-gas temperature ratios in the 0.7–0.8 range and cascade inlet free-stream turbulence intensities were varied from 6 to 8 percent (nominal). The test matrix was structured to provide an assessment of the independent influence of Mach number, Reynolds number, T_w/T_g, and inlet turbulence intensity on airfoil surface heat transfer.

The principal observations regarding the cascade test program described herein can be summarized as follows:

1 The measured static pressure distributions over the two airfoils tested confirmed the fundamentally different aerodynamic character of the two designs.

2 The suction surface heat transfer distributions on the Mark II airfoil exhibited a sharp separation/free transition/turbulent reattachment spike that was coincident with the strong adverse pressure spike on that surface. The behavior of the heat transfer distribution in the vicinity of the adverse pressure spike appear largely dependent on the details of the Mach number distribution in the region.

3 The character of the suction surface heat transfer distribution on the C3X airfoil (moderate downstream diffusion) was clearly transitional in nature, showing a strong Reynolds number level dependency.

4 The independent effect of exit Mach number level on heat transfer to the pressure surfaces of both airfoils was negligible over the Mach number range tested. The heat transfer distributions over the downstream suction surfaces of both airfoils exhibited some response to pressure gradient history, the effect being more pronounced in the case of the Mark II airfoil.

5 The character of the pressure surface heat transfer distributions was essentially the same for both airfoils. In both instances, pressure surface heat transfer distributions

were largely dependent on Reynolds number, exhibiting a moderate transitional trend at the higher Reynolds numbers.

6 The independent effect of both T_w/T_g and free-stream turbulence intensity was observed to be small but systematic over the relatively narrow test ranges of these parameters.

7 Based on limited comparisons to date, boundary layer codes of the STAN5 genre show tentative promise relative to predicting the observed heat transfer trends.

In conclusion, the experimental program appears to have provided results that are both operationally realistic and computationally interesting. The limited results reported herein were selected to specifically highlight the fundamentally different nature of the suction surface heat transfer distributions on two different airfoil profiles. The markedly different observed distributional characteristics (Mach number dominated separation/reattachment versus Reynolds number dominated transitional behavior) represent data sets that hopefully will be of value in validating contemporary inviscid flow field and boundary layer computational techniques.

References

1 Brown, A., and Martin, B. W., "Heat Transfer to Turbine Blades with Special Reference to the Effects of Mainstream Turbulence," ASME Paper No. 79-GT-26, Mar. 1979.

2 McNally, W. D., "FORTRAN Program for Calculating Compressible Laminar and Turbulent Boundary Layers in Arbitrary Pressure Gradients," NASA TN D-5681, 1970.

3 Nealy, D. A., "Some Effects of Variable Surface Temperature on Heat Transfer to a Partially Porous Flat Plate," ASME JOURNAL OF ENGINEERING FOR POWER, Oct. 1973, pp. 317–325.

4 Gauntner, D. J., and Sucec, J., "Method for Calculating Convective Heat Transfer Coefficients Over Turbine Vane Surfaces," NASA TP-1134, 1978.

5 McDonald H., and Fish, R. W., "Practical Calculations of Transitional Boundary Layers," *International Journal of Heat & Mass Transfer*, Vol. 16, No. 9, 1972.

6 Herring, H. J., and Mellor, G. L., "A Computer Program to Calculate Incompressible Laminar & Turbulent Boundary Layer Development," NASA CR 1564, Mar. 1970.

7 Cebeci, T., Smith, A. M. O., and Wang, L. C., "Finite Difference Method for Calculating Compressible Laminar and Turbulent Boundary Layers," Douglas Aircraft Co. Report DAC 67131, 1969.

8 Crawford, M. E., and Kays, W. M., "STAN 5—A Program for Numerical Computation of Two-Dimensional Internal and External Boundary Layer Flows," NASA CR-2742, 1976.

9 Crawford, M. E., Kays, W. M., and Moffatt, R. J., "Full Coverage Film Cooling on Flat, Isothermal Surfaces: A Summary Report on Data and Predictions," NASA Report CR-3219, 1980.

10 Kwon, O. K., and Pletcher, R. H., "Prediction of Incompressible Separated Boundary Layers Including Viscous-Inviscid Interactions," ASME *Journal of Fluids Engineering*, Vol. 101, 1979, pp. 466–472.

11 Forest, A. E., "Engineering Predictions of Transitional Boundary Layers," AGARD-CP-224, 1977.

12 Wilson, D. G., and Pope, J. A., "Convective Heat Transfer to Gas Turbine Blade Surfaces," *Proceedings of the Institution of Mechanical Engineers*, Vol. 168, 1954, pp. 861–876.

13 Hodge, R. I., "A Turbine Nozzle Cascade for Cooling Studies," ARC CP 492 493, 1960, pp. 1–39.

14 Dunham, J., and Edwards, J. P., "Heat Transfer Calculations for Turbine Blade Design," AGARD CP 73, No. 2, 1971.

15 Turner, A. B., "Local Heat Transfer Measurements on a Gas Turbine Blade," *Journal of Mechanical Engineering Sciences*, Vol. 13, 1971, pp. 1–12.

16 Lander, R. D., "Effect of Free-Stream Turbulence on the Heat Transfer to Turbine Airfoils," AFAPL-TR-69-70, Air Force Systems Command, September 1969.

17 Brown, A., and Burton, R. C., "The Effects of Free-Stream Turbulence Intensity and Velocity Distribution on Heat Transfer to Curved Surfaces," ASME JOURNAL OF ENGINEERING FOR POWER, Vol. 100, 1978, pp. 159–168.

18 Martin, H. W., Brown, and Garrett, S. E., "Heat Transfer to a PVD Rotor Blade at High Subsonic Throat Mach Numbers," *Proceedings of the Institute of Mechanical Engineers*, Vol. 192, 1978, pp. 225–235.

19 Kohler, H., Henneke, D. K., Pfaff, K., and Eggebrecht, R., "Hot Cascade Test Results of Cooled Turbine Blades and Their Application to Actual Engine Conditions," AGARD CP 229, 1977, pp. 6-1-6-12.

20 York, R. E., Hylton, L. D., Fox, R. G., Jr., and Simonich, J. C., "An Experimental Investigation of the Heat Transfer to a Turbine Vane at Simulated Engine Conditions," ASME Paper 79-GT-23, 1979.

21 "Development of Analytical Techniques for Improved Prediction of Local Gas to Blade Heat Transfer Coefficients," NASA Contract NAS 3-322761, 1980.

22 Hylton, L. D., Mihelc, M. S., Turner, E. R., Nealy, D. A., and York, R. E., "Analytical and Experimental Evaluation of the Heat Transfer Distribution over the Surfaces of Turbine Vanes," NASA CR-168015, Nov. 1982.

23 Daniels, L. D., and Browne, W. B., "Calculation of Heat Tranfer Rates to Gas Turbine Blades," *International Journal of Heat and Mass Transfer*, Vol. 24, No. 5, 1981, pp. 871–879.

24 Jones, W. P., and Launder, B. E., "Prediction of Low-Reynolds-Number Phenomena with a Two-Equation Model of Turbulence," *International Journal of Heat and Mass Transfer*, Vol. 16, 1973, pp. 1119–1130.

25 Kline, S. J., and McClintock, F. A., "Describing Uncertainties in Single-Sample Experiments," *Mechanical Engineering*, Vol. 75, Jan. 1953, p. 3.

26 Kays, W. M., *Convective Heat and Mass Transfer*, McGraw-Hill, 1966, ch. 12, pp. 256–269.

27 Delaney, R. A., "Time-Marching Analysis of Steady Transonic Flow in Turbomachinery Cascades Using the Hopscotch Method," ASME Paper No. 82-GT-152, 1982.

R. E. York
Chief,
Aerothermodynamics Research.

L. D. Hylton
Supervisor,
Experimental Heat Transfer.

M. S. Mihelc
Experimental Engineer.

Detroit Diesel Allison Division,
General Motors Corporation
Indianapolis, Ind. 46206

An Experimental Investigation of Endwall Heat Transfer and Aerodynamics in a Linear Vane Cascade

The purpose of this experimental investigation was to produce a data base of end-wall heat transfer data under conditions that simulate those in the passage of the first-stage stator in advanced turbine engines. The data base is intended to be sufficiently complete to provide verification data for refined computational models, and to provide a basis for advanced core engine endwall cooling designs. A linear, two-dimensional cascade was used to generate the data base. The test plan provided data to examine the effects of exit Mach number, exit Reynolds number, inlet boundary layer thickness, gas-to-wall temperature ratio, inlet pressure gradients, and inlet temperature gradients. The data generated consist of inlet, intrapassage, and exit aerodynamic data plus intrapassage endwall heat flux, adiabatic wall temperature measurements, and inlet turbulence data.

Introduction

Motivation and Objective. Advancing performance requirements for engines have resulted in dramatic increases in turbine durability problems. For many years much of the engineering attention has been directed toward developing improved cooling design methods for turbine blades and vanes, because they are most directly exposed to the hot gas path. Now, however, conditions are such that the endwall structures also require sophisticated cooling schemes. The magnitude of the endwall cooling problem has increased not only in response to increased operating pressure and temperature levels but also because the endwall represents a larger fraction of the surface to be cooled in a modern low aspect ratio, low solidity design.

Unfortunately, analysis of the endwall region is a more complex problem than design of the airfoils because the flow is strongly three dimensional. In fact, in the low aspect ratio vane rows of modern gasifier turbines, the entire passage contains strong secondary flow features. The essential characteristics of the three-dimensional, viscous vane row flow field are qualitatively well understood. They include:

• The existence of pressure and temperature gradients in the inlet flow that induce large-scale secondary flows as the flow is turned
• Roll-up of the inlet boundary layer at the leading edge of each airfoil into a discrete horseshoe vortex that is convected into the passage

• Three-dimensional boundary layers on the endwall with large crossflow components induced by the strong cross-passage pressure gradients
• Interaction of the horseshoe vortex and the cross-passage flow to form a streamwise vortex in the suction surface-endwall corner

Engine experience at Detroit Diesel Allison (DDA) has indicated that the endwall thermal field is responsive to these secondary flow phenomena. Engine thermal paint results, field corrosion/deposition patterns, and some durability problems correlate well with the spatial features exhibited in laboratory studies of endwall flows.

Design methods routinely in use in the industry are not capable of analyzing the full three-dimensional, viscous flow through a vane or blade row. Typically, simple two-dimensional boundary layer analyses or correlations are applied along the meridional streamline nearest the endwall as predicted by stacked two-dimensional, inviscid, blade-to-blade analysis. Such methods are thought to predict the average endwall heat transfer rates and are used to roughly set endwall coolant requirements. However, these estimates are adjusted by development experience to account for hot spots. Such procedures are costly because they result in conservative estimates of coolant requirements to cover large analysis uncertainties and because of the expensive development iterations required to attain acceptable durability.

The advanced finite difference computational methods under development for three-dimensional viscous flows have the potential for accounting for the strong coupling between such three-dimensional viscous flows and endwall heat transfer. Such methods are items of research themselves at

present and require advancements to reduce their cost and extend their applicability.

Before they can be used by the cooling systems design engineer, however, any of these new methods must be verified against data representative of the gas turbine environment. Classical large-scale, low-speed studies do not meet this need because such experiments do not reproduce all the parameters which regulate boundary layer behavior as they occur in the engine. The experimental investigation reported here had as its objective the development of a data base of endwall heat transfer data under conditions that simulate those in the passage of the first-stage vane of an advanced turbine. The data base is intended to be sufficiently detailed in content and broad in the range of variables considered that it will serve as verification data for the refined computational models as they become available.

Related Work. Most prior work has focused attention on the fluid mechanic aspects of flow through vane and blade rows. Sjolander [1] and Waterman and Tall [2] reported studies in large-scale, full-annular vane rows. The latter were the first to include analytical comparisons. Marchal and Sieverding [3] followed with an extremely detailed description of the development of secondary flows by using hot wires to map out the intrapassage details. They also examined the effects of varying inlet boundary layer thickness. Langston et al. [4] reported the first of their detailed studies with a high turning blade cascade and showed significant stalling of flow in the endwall-suction surface corner. Liu et al. [5] reported the first attempt to apply the understanding gained in the fundamental experiments of their earlier work [2] to design a vane row using secondary flow concepts. Bailey [6] used a combination of hot wire and laser anemometry to acquire both mean and fluctuating-velocity data in the low-speed rig first used by Blair [7]. Gaugler and Russell [8] used helium filled bubbles and movies in a large-scale cascade to record vortex motions within the flow field to complement endwall flow traces. Langston [9] at the same time reported more detailed analysis of the crossflows from his blade cascade and proposed a general profile model. Sieverding and Wilputte [10] extended their low-speed ($M_2 = 0.1$) tests [3] to intermediate exit Mach numbers ($0.6 < M_2 < 0.8$) and showed that compressibility does not significantly alter the secondary flow field either qualitatively or quantitatively. Carrick [11] and Bindon [12] made a further departure by introducing skewed inlet boundary layers, and although the crossflow velocity magnitudes increased, the gross features of the flow were similar to those with collateral inlet boundary layers.

All of these studies showed consistency in the qualitative features of the flow mentioned earlier. They clearly showed that large-scale discrete secondary flow structures exist within turbine passages that have a pronounced effect on the spanwise distribution of aerodynamic behavior. A logical conclusion from such evidence would be to expect significant local heat transfer consequences as well.

Much less work has been done on the heat transfer aspects of the problem. Blair [7] used a large-scale, turning channel rig to obtain measurements of endwall heat flux and showed
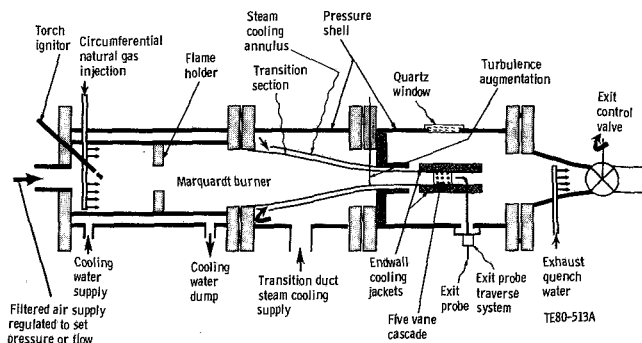
Fig. 1 Aerothermodynamic cascade facility
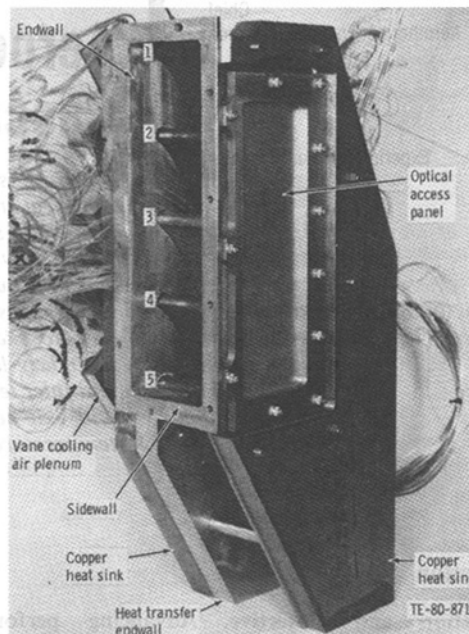
Fig. 2 Endwall heat transfer cascade assembly

4:1 differences could exist in local rates. Dunn and Stoddard [13] utilized transient techniques to obtain local heat transfer rates to both the hub and tip endwalls of a full annular vane row and reported similar streamwise gradients in heat transfer. More recently Dunn and Hause [14] reported results from a full stage that showed the stator endwall heat transfer to be independent of the downstream rotating blade row. Georgiou et al. [15] also used transient techniques in a linear cascade. They reported little response to inlet boundary layer thickness changes or low (Tu < 0.05) free-stream turbulence levels. Finally, Graziani et al. [16] applied a refined heater strip method to study heat transfer to both the airfoil and the passage endwall in a blade cascade like Langston's [4, 9]. Their data included the effect of inlet boundary layer thickness also and showed greater impact on the airfoil heat

---

Nomenclature

M = Mach number
q = heat flux per unit area
St = local Stanton number, $q/(\rho V c_p)_\infty (T_{aw} - T_w)$
St* = nondimensional heat flux, $q/[(\rho V c_p)_1 (T_{t1} - T_w)]$
T = temperature
Tu = turbulence level
V, V^* = velocity, critical velocity

Greek

β = air angle measured from tangential
ρ = density
ω = total pressure loss coefficient

Subscripts

aw = adiabatic wall

g = gas
t = total
w = wall
1 = cascade inlet state
2 = cascade exit state
3 = cascade exit mixed-out state
∞ = local free-stream static state

AXIAL CHORD = 2.067 INCHES (5.250 CM)
TRUE CHORD = 3.670 INCHES (9.322 CM)
SETTING ANGLE = -57.95°
AIR EXIT ANGLE = 71.3°
SPAN = 3.000 INCHES (7.620 CM)
THROAT HEIGHT = 0.8356 INCHES (2.1224 CM)
SPACING = 2.660 INCHES (6.7564 CM)

Fig. 3 Linear cascade vane profile

Fig. 4 Thermocouple instrumented vane

Fig. 5 Endwall static pressure tap locations

transfer field than on the endwall in agreement with [15]. All of these heat transfer studies have thus been in general agreement. They have shown similar levels and patterns of heat transfer to the endwalls, and like the aerodynamic studies, no major changes due to thickened inlet boundary layers.

None of these studies has yet shown the correlation between the relatively well-established fluid mechanics of the endwall flow and the heat transfer field. Also, the range of operating conditions has been quite limited in each study so that the response of endwall heat transfer to Reynolds number, expansion ratio, blade design, etc. cannot yet be evaluated. The present study seeks to resolve some of these questions while providing a data base for future analytical verifications.

The program described herein was a multiyear effort funded by AFAPL and NASA-LeRC. The purpose of this paper is to place the results of this program in the open literature. Due to the length and complexity of the programmed effort, only a summary can be presented here. Complete details are available in the final report [17].

Experimental Approach

Similarity Requirements. It is widely understood that there exists a set of similarity requirements that must be met in order to directly apply experimental results to engine design
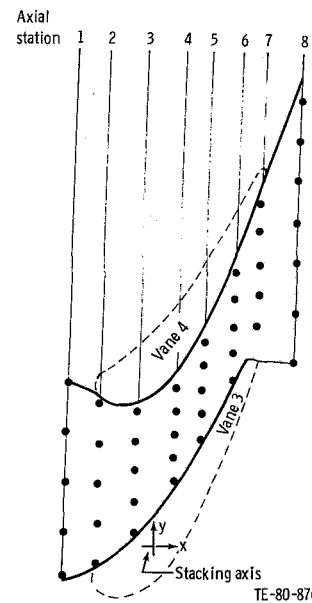
[18]. These include scaled geometry, Reynolds number, Mach number, wall-to-gas temperature ratios, etc. In addition to satisfying these classical similarity constraints, it was necessary to control, or intentionally vary, additional phenomenological factors such as inlet momentum and thermal boundary layer scales, inlet turbulence intensity, and inlet vorticity due to large-scale pressure or temperature gradients.

Facility Description. Most of the experimental program was conducted in the DDA Aerothermodynamic Cascade Facility (ACF). The ACF was specifically designed to acquire both aerodynamic and heat tr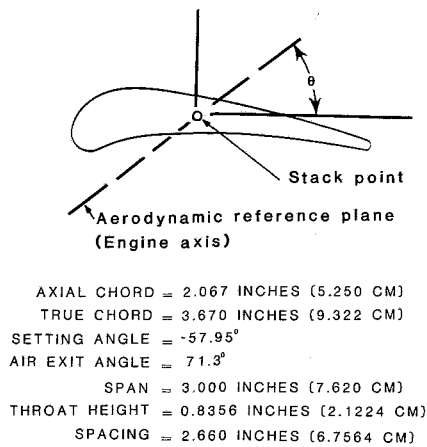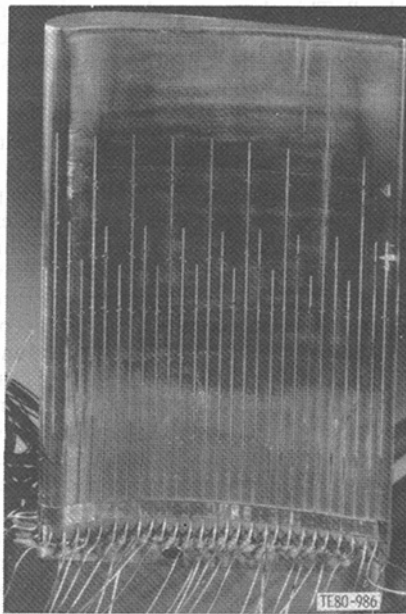ansfer information with engine similitude and has been used previously to study vane, rather than endwall, heat transfer [19]. The facility, shown schematically in Fig. 1, consists of a gas-fired burner, a convergent transition nozzle, an instrumented inlet section, an instrumented cascade, and an exhaust section. The ACF has a wide operating range and can achieve transonic exit Mach numbers, Reynolds numbers up to 2×10^6 per foot, and temperature levels to 1500°F (800°C) as currently equipped. The test section incorporates both aerodynamic and heat transfer data acquisition in a single test, thereby ensuring correlation of data and reducing costs.

Inlet Section. The inlet section contains fixed core total pressure and temperature rakes, boundary layer velocity and temperature rakes, wall static pressure taps and a traversing dual element total pressure and temperature probe. The inlet instrumentation was placed in the constant-area inlet section from about one to three axial chords upstream of the vane row so as not to disturb, or be disturbed by the vanes.

The inlet section also contained provisions for inserting boundary layer trips at the start of the constant area section 13 in. (33 cm) upstream of the vane leading edge plane. These tube locations were also used to produce distorted inlet and temperature profiles during one phase of the tests.

Cascade Section. The principal test article was a five-vane linear cascade, shown in Fig. 2. The vane profiles are representative of the first stage of a typical advanced core turbine as shown in Fig. 3. Specific geometric details are given in [17]. The outer two vanes carried no instrumentation. Vanes 2 and 4 carried static pressure taps on the pressure and suction surface, respectively, at 50, 20, and 5 percent of span. The center vane of Fig. 2 had thermocouples installed in
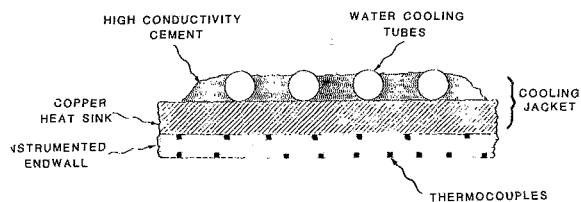
Fig. 6 Heat transfer endwall cross section
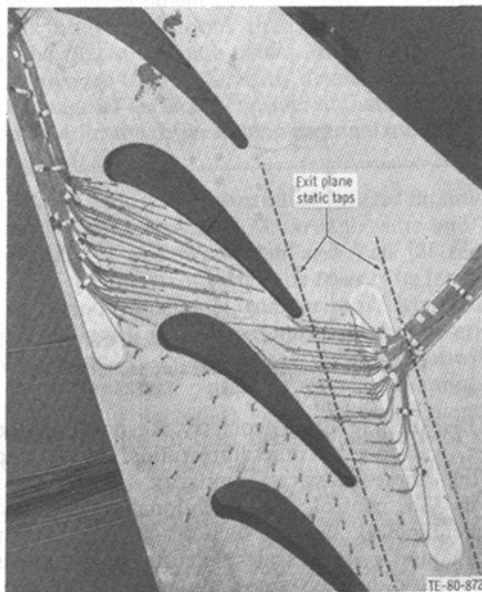
Fig. 7 Heat transfer endwall during instrumentation

Fig. 8 Finite element model and thermocouple locations

grooves at these same spanwise locations. The central passage between vanes 3 and 4 contained 42 endwall surface static pressure taps, distributed as shown in Fig. 5.

The key to conducting heat transfer investigations with full similarity in wall-to-gas and coolant-to-gas temperature ratios is the availability of a heat flux measurement method capable of operating at elevated temperatures. The method proposed by Turner [20] has been successfully applied to the study of vane heat transfer [19, 21] and has also been used at DDA to study various internal heat transfer problems. In this method, the test piece itself becomes the fluxmeter. Basically, the method consists of installing thermocouples on the hot and cold surfaces of the test piece, which is then placed in the test environment and run until thermal equilibrium is obtained. The temperature data then become the boundary conditions for a finite element solution of the internal temperature field of the test piece. The surface normal temperature gradient is derived from this solution, and the local heat transfer coefficient distribution can be directly evaluated.

Turner's method was applied to the endwall as follows. Of the two endwalls of the cascade shown in Fig. 2, the left one was designated as the "heat transfer endwall." It was a sandwich of an inner 1.00-in. (2.54-cm) thick nickel plate backed by a 1.00-in. (2.54-cm) thick copper plate and a coolant manifold, as shown in a cross section in Fig. 6. The combination of material thickness and thermal conductivity of the nickel plate provided temperature differences through the wall that were large enough (50–100°F) (30–55K) to minimize thermometry errors. In addition, the relatively thick wall resulted in negligible errors being introduced by the surface grooves required to install the thermocouples. The function of the copper plate was to smooth out the temperature distribution of the coolant manifold so that fewer backside thermocouples were needed.

Figure 7 shows the installation of 53 0.020-in. (0.51-mm)
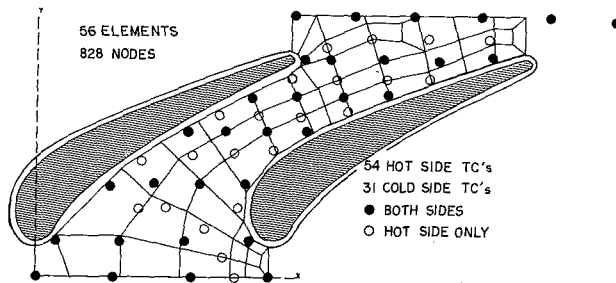
dia sheathed thermocouples on the hot side of the heat transfer endwall. This photo was taken at an intermediate step in the instrumentation just before the thermocouples and grooves were covered with cement to provide a smooth endwall surface. A similar, but less dense, pattern of 31 thermocouples was installed on the cooled backside of the heat transfer endwall. The passage instrumented with the thermocouples for the heat transfer measurements is between vanes 2 and 3 in Fig. 2. Figure 7 also shows the passage and exit plane static pressure tap locations noted earlier. The tubes shown extending through the wall were brazed in place and then machined smooth with the surface. Also shown in Fig. 7 are the electrochemically machined contours through which the vanes were ultimately inserted. The vane openings included an extra 0.040-in. (1.02-mm) clearance. During assembly, the vanes were positioned within this gap to closely controlled throat measurements and were held in place at a few points by small shims. The balance of the gap around the vane contour was filled with a low thermal conductivity ceramic cement in order to thermally isolate the vane from the end-wall.

Figure 8 shows the finite element model used to solve for the local surface heat flux and the relative location of hot and cold side thermocouples. Each element contains twelve nodes. Grid refinements and cross-checks against a finite difference solution were used to verify the grid selection and solution procedure. As can be seen in Fig. 8, there were fewer thermocouple measurements than nodes, so a special version of the finite element method was formulated. A finite element method involves the conversion of the differential equation and its boundary conditions into an error expression which is minimized with respect to all unknown nodal temperatures. The resulting minimum error is shared by the differential equation and the boundary conditions with the result that neither is perfectly satisfied. In the current application the boundary condition errors to be minimized were taken as the temperatures at the thermocouple locations, rather than at the surface nodes.

The uncertainty associated with the data acquired by this technique is primarily dependent on the accuracy with which the surface temperatures can be measured, in comparison with the temperature difference through the structure. The cumulative errors attributable to reference junction drift, thermocouple wire calibration, voltage measurement, and calibration table interpolation amount to less than 1.0°F (0.6K). Uncertainties in the corrections to account for installation in cement-filled grooves and variations in the details of physical installation are more significant, about 2°F (1K). Turner [22] presents an analysis of the error induced by the presence of the thermocouple and groove. It is important in the design of a grooved thermocouple installation to be conscious of the potential thermometry errors, and to structure the design to minimize the size of temperature
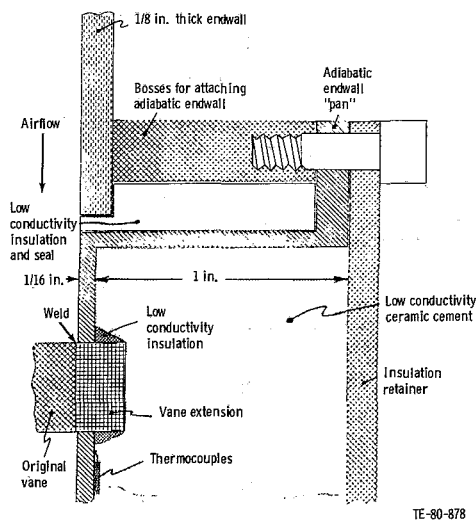
Fig. 9 Adiabatic endwall cross section

Fig. 11 Adiabatic endwall thermocouple locations

Fig. 12 Inlet profiles

Fig. 10 Adiabatic endwall pan

correction that must be made. Careful design can result in a nearly negligible correction. By material selection and strong cooling, a large ΔT can be established so that the relative uncertainty in ΔT and, ultimately, heat flux, can be made acceptably small. Additional errors in translating ΔT data to heat flux values can be minimized. Thermal conductivities are well established if materials are bought by specification. The finite element accuracy can be verified by successive grid refinement and comparison with exact solutions. The method inherently includes conduction corrections. The method also measures the total heat flux due to both convection and radiation. The radiation contribution is kept small by keeping the cascade wall temperatures near that of the vanes so that little potential exists for radiation exchange. With the equipment designed and assembled as described above, the cumulative uncertainty in heat flux values due to these factors is estimated at ±10–15 percent by the method of Kline and McClintock [23].

Figure 2 also shows an optical access panel, containing a steel blank, on the endwall opposite the endwall instrumented for heat transfer and surface statics. This opening provided optical access for laser anemometry measurements as detailed in [17]. In addition, the opening was subsequently utilized to obtain endwall adiabatic wall temperatures to accompany the

heat flux data. A special pan was fabricated to fit in this space as shown in Figs. 9 and 10.

While the entire adiabatic passage was heavily instrumented, the 90 thermocouples were concentrated in the vane leading edge suction surface region and near the vane suction surface downstream of the throat, in an attempt to better define the temperature patterns in areas most affected by the secondary flow structure. The locations of the thermocouples are illustrated in Fig. 11.

Cascade Exit Surveys. Detailed surveys of the three-dimensional flow exiting the cascade were obtained using miniature aerodynamic probes. The probe used to acquire data for this program was a five-port, conical-tipped probe. These probes are calibrated in a small instrumentation tunnel up to a Mach number of 1.6. They provide five output parameters: Mach number, total pressure, static pressure, and pitch and yaw flow angle components (spanwise and circumferential). When aligned closely with the streamwise flow, the 0.125-in. (3.18-mm) dia cone probe provides very low blockage and does not appreciably disturb the flow field. Special methods have been developed to correct the probe readings when the probe is in a shear flow region, such as in the vane wake. Data repeatability indicates the probe accuracies to be about ±0.25 percent for total pressure, ±1.0 percent for static pressure, and ±1 percent for Mach number, except when the flow is very near sonic. The angular sensitivity is better than ±0.25 deg, but the physical setup of the probe in the traverse unit increases the angular uncertainty to ±1.0 deg in the absolute reference. Mass flow balance checks

Fig. 13 Vane surface static pressure data

LEGEND

SYMBOL	% SPAN
△	5
○	20
□	50
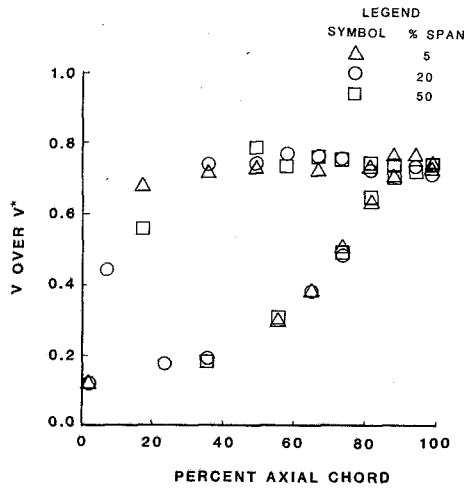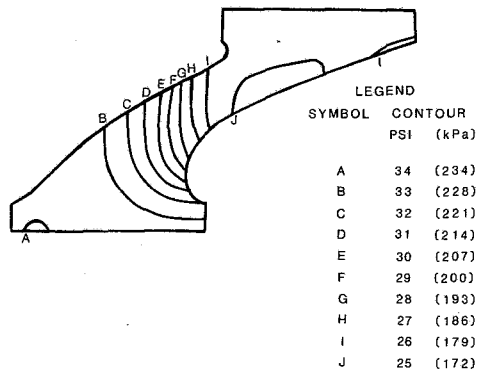
Fig. 14 Endwall static pressure contours

LEGEND

SYMBOL	CONTOUR	
	PSI	(kPa)
A	34	(234)
B	33	(228)
C	32	(221)
D	31	(214)
E	30	(207)
F	29	(200)
G	28	(193)
H	27	(186)
I	26	(179)
J	25	(172)

Fig. 15 Endwall adiabatic temperature contours (Taw)

LEGEND

SYMBOL	CONTOUR	
	°F	(K)
A	716	(653)
B	708	(649)
C	700	(644)
D	692	(640)
E	684	(636)
F	676	(631)

Fig. 16 Endwall temperature contours (Tw)

LEGEND

SYMBOL	CONTOUR	
	°F	(K)
A	542	(557)
B	534	(552)
C	526	(548)
D	518	(543)
E	510	(539)
F	502	(534)
G	494	(530)

Fig. 17 Endwall nondimensional heat flux (St*)

LEGEND

SYMBOL	CONTOUR
A	.003
B	.004
C	.005
D	.006
E	.007
F	.008

Fig. 18 Endwall local stanton number contours (St)

LEGEND

SYMBOL	CONTOUR
A	.0015
B	.0020
C	.0025
D	.0030
E	.0040
F	.0060
G	.0080
H	.0100
I	.0150
J	.0200

between a uniform inlet and the integrated exit survey usually check within ±2–5 percent, and a part of this difference can be attributed to the change in endwall boundary layer thickness through the cascade.

A special exit rake consisting of a cone probe and a radiation-shielded total temperature probe was constructed to perform the exit flow surveys in this program. The exit probe was carried on a computer-controlled, three degree-of-freedom traverse system. The probe first was aligned with the nominal exit air angle and then was traversed, covering about 20–50 points in the blade-to-blade direction and 8–10 stations from midspan to the endwall. The traverse was programmed to concentrate the data gathering in the viscous wake and near-endwall regions.

Representative Data

In summary then, the cascade instrumentation provides a definition of the inlet velocity and temperature field, the static pressure distribution on the vane and endwalls, the endwall surface temperature, the endwall heat flux, the endwall adiabatic temperatures, and the exit flow field. These raw data amount to about 2000 data items per run condition. Additional derived variables such as Stanton numbers or loss coefficients increase a complete data report for one test run to about 80 pages. A set of summary results for one run are presented here to make the content of the data base more clear.

Figure 12 shows examples of the inlet profile for normal and tripped inlet boundary layer runs. The normal boundary layer thickness is about 0.250 in. (6.35 mm) compared to a half-span of 1.500 in. (3.810 cm).

Figure 13 shows the vane surface static pressure distribution
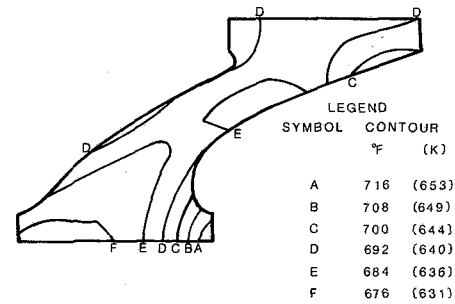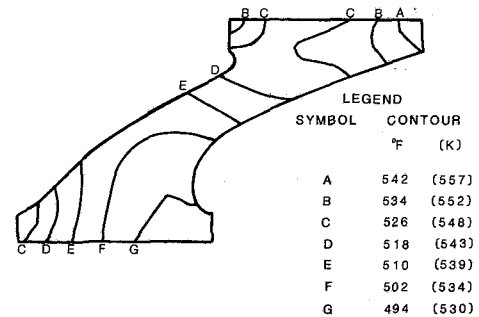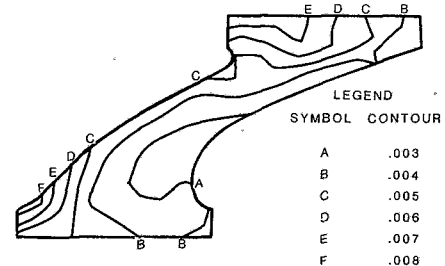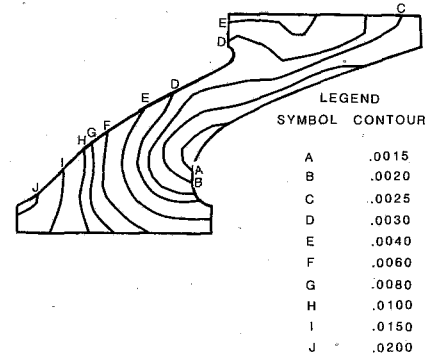
for one run. The data for all three spanwise stations are in general concurrence giving no indication of suction surface-endwall corner stall as in [4]. Figure 14 shows the endwall static pressure distribution in the form of a contour plot. The strong acceleration leading to the throat and the pressure minimum at midchord on the suction surface are as expected fron strictly two-dimensional analysis, also suggesting that no strong endwall interaction is taking place.

Figures 15–17 present typical endwall thermal results. The adiabatic temperature contours of Fig. 15 give evidence of the effects of the horseshoe vortex in the curvature of the isotherms around the suction surface leading edge and in the

Table 1 Linear cascade run conditions

Run No.	Inlet conditions					Exit conditions		
	Gas total temperature (°F)	Total pressure (psia)	Static pressure (psia)	Mach number	Reynolds number × 10^{-6}	Mach number	Reynolds number × 10^{-6}	Expansion ratio
57	197	21.4	20.9	0.19	0.43	0.71	1.34	1.40
61	196	37.5	36.5	0.20	0.81	1.10	2.76	2.13
67	225	15.5	15.3	0.14	0.23	0.30	0.46	1.06
86	814	21.4	21.0	0.18	0.19	0.70	0.59	1.37
87	614	21.6	21.1	0.18	0.23	0.71	0.74	1.39
89	785	15.4	15.3	0.09	0.07	0.27	0.20	1.05
91	817	51.7	50.3	0.20	0.50	1.10	1.68	2.11
94	1078	15.5	15.4	0.10	0.06	0.28	0.17	1.05
98	1017	55.7	54.4	0.19	0.43	1.09	1.52	2.07
99	782	21.8	21.2	0.19	0.17	0.69	0.52	1.36
105	213	21.5	20.9	0.20	0.46	0.71	1.31	1.40
107	197	38.2	36.8	0.23	0.94	1.10	2.83	2.13
108	228	15.9	15.8	0.11	0.18	0.31	0.48	1.07
109	799	55.2	53.3	0.23	0.60	1.12	1.82	2.11
111	807	21.3	20.8	0.20	0.20	0.68	0.59	1.36
112	606	22.3	21.7	0.20	0.27	0.72	0.78	1.40
113	1000	22.4	21.8	0.21	0.19	0.72	0.54	1.40
114	776	15.5	15.4	0.10	0.08	0.28	0.21	1.05
116	815	43.4	42.3	0.19	0.40	0.70	1.20	1.37
118	799	34.6	33.9	0.18	0.31	0.69	0.96	1.36
122	769	59.8	58.4	0.19	0.57	0.71	1.74	1.39
123	770	32.0	31.3	0.18	0.30	0.69	0.92	1.36
124	885	37.4	37.0	0.12	0.21	0.30	0.50	1.06
131	757	64.4	64.0	0.10	0.32	0.30	0.96	1.06
132	822	34.7	33.9	0.18	0.31	0.69	0.95	1.36
133	819	34.0	33.3	0.18	0.30	0.69	0.94	1.37
149	799	32.7	31.7	0.21	0.34	0.69	0.91	1.36
150	795	34.6	34.4	0.09	0.16	0.28	0.48	1.06
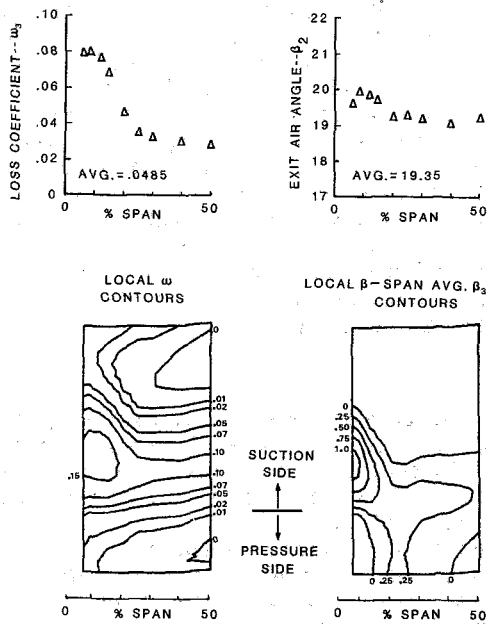
Fig. 19 Exit aerodynamic survey results

penetration of the isotherms into the passage entrance region. These patterns have been observed to systematically shift in response to the operating point of the cascade. Figure 16 presents a contour plot of surface temperature on the heat transfer (nonadiabatic) endwall. These patterns usually show isotherms which curve around the pressure surface leading edge. Figure 17 presents endwall heat flux results non-dimensionalized on inlet free-stream $\rho V c_p$. These patterns also systematically respond to changes in the cascade operating point.

Finally, Fig. 18 shows the corresponding contour plot of local Stanton number. The preceding four contour plots have distinctive features in only certain regions where strong gradients of the respective variable occur, for instance: the

pressure gradient in the central passage, the isotherms which curve around the suction surface leading edge on the adiabatic contours, and the similarly curved isoheat flux lines around the pressure surface leading edge. These features tend to be collected in the local Stanton number contours, resulting in the very representative patterns in Fig. 18.

Typical results of the exit surveys are shown in the composite Fig. 19. This figure shows the exit loss contours and exit air angle contours, the latter referenced from the average midspan value to better show regions of local over- or underturning. A blade-to-blade integration of these contours gives the spanwise distribution of loss and turning also shown in Fig. 18. These contour results are strongly similar in magnitude and structure to those of [3].

Experimental Program

The experimental program was organized to span the principal factors expected to influence vane endwall heat transfer and associated passage aerodynamics, except for radial pressure gradient effects. The test conditions for which data exist are given in Table 1. These tests were conducted in six series intended to separate the effects of the prime independent variables: Reynolds number, exit Mach number, inlet turbulence level, inlet boundary layer thickness, and T_w : T_g ratio.

Series I – "Cold Flow" Baseline Aerodynamics. The inlet and exit aerodynamic data of the cascade were acquired at nominal exit Mach numbers of 0.3, 0.7, and 1.1 for a flow with an inlet total temperature of about 200°F (365 K). This series of runs was accomplished with the burner inoperative, so that the aerodynamic data are characteristic of low inlet turbulence conditions. The purpose of this test was to provide baseline loss data for use in comparisons with other effects present. All baseline data, both hot and cold, were taken with the facility exhaust valve removed, in order to acquire the baseline data at as low an exit Reynolds number as could be achieved in the facility. The absence of exhaust pressure control resulted in the exit Reynolds number varying with exit Mach number.

Table 2 Baseline test run numbers

	Exit Mach number		
	0.3	0.7	1.1
"Cold"	67	57	61
"Hot"	89	86	91

Table 3 Mach and Reynolds number variation runs

Nominal Reynolds no.	Exit Mach number		
	0.3	0.7	1.1
0.25×10^6	89		
0.50×10^6	124	86	
1.00×10^6	131	123	
1.25×10^6		116	
1.75×10^6		122	91

Table 4 Turbulence level variation runs

Gas temperature	Turbulence intensity	0.3	0.7	1.1
1000°F (810 K)	9.35 ± .47	94	99	98
800°F (700 K)	7.95 ± .40	89	86	91
600°F (590 K)	7.90 ± .40		87	

Table 5 Tripped boundary layer runs

Nominal Reynolds no.	Exit Mach Number		
	0.3	0.7	1.1
0.25	114		
0.50	150	111	
0.75		112	
1.00		149	
1.75			109

Series II – Baseline Heat Transfer and Hot Aerodynamics.

This series of tests was intended to provide heat transfer and exit aerodynamic data at a nominal gas temperature of 800°F (700 K) at a low Reynolds number condition to serve as a baseline for determining the effects of the prime variables. Three runs were made in this series, at exit Mach numbers identical to those for the cold baseline aerodynamic runs as shown in Table 2. Exit Reynolds numbers were different due to the effect of gas temperature on the Reynolds number.

Series III – Reynolds Number Variation.

To account for the effects of both exit Mach and Reynolds numbers on heat transfer and aerodynamic performance, a set of runs was made at conditions as divergent as facility limits would allow. Table 3 shows the run numbers that can be used to separate these effects. A 4.6:1 variation in exit Reynolds number was obtained at a constant value of $M_2 = 0.3$, and a range of 2.9:1 at $M_2 = 0.7$. Three pairs of exit Mach numbers variations at constant Reynolds number are available as shown in Table 3.

Series IV – Inlet Turbulence Level Variation.

One of the variables which might be expected to affect endwall heat transfer, as it has been shown to alter heat transfer to the airfoils proper, is free-stream turbulence. The turbulence level in the ACF was varied by varying the burner operating point, i.e., changing gas temperature, while keeping exit Reynolds number at baseline conditions. Table 4 shows runs available and the associated turbulence intensities to examine this variable.

Series V – Tripped Inlet Boundary Layer.

This series was intended to provide data with inlet boundary layer conditions different from those that existed during the previous series of tests. The inlet boundary layer was altered for this series of tests by installing 3/8-in. (9.53-mm) dia tubes on both endwalls upstream of the cascade. These resulted in a significant change in the inlet velocity profile, as seen in Fig. 12.

The tests in this series duplicated the operating points of many of those in the previous series in order to adequately evaluate the effects of the change in the inlet profile. A series of runs (Nos. 108, 105, and 107) was made at cold baseline conditions similar to those run previously in Series I. Similarly, heat transfer runs were made at conditions nearly identical to several of those in Series II and III. This series includes two runs at gas temeratures other than 800°F (700 K). While not duplicating all the runs made with the normal inlet boundary layer, this series with the tripped inlet does provide several runs for comparison as shown in Table 5.

Series VI – Wall-to-Gas Temperature Ratio Variation.

A test series was conducted to provide data for the effect of wall-to-gas temperature ratio in the range of conditions encountered in engines, nominally 0.7 to 0.8. This was accomplished at a constant inlet total temperature condition, 800°F (700 K), to suppress effects associated with burner performance. Four values of wall-to-gas temperature ratio were included. These are runs 133, 118, 123, and 132.

Computer Data Base

The specific objective of the program was to provide a broad base of endwall heat transfer data for comparison with predicted results as they become available. The resulting data base is very large because it contains numerous types of data at numerous spatial observation points and at numerous run conditions. One can also anticipate that the specific data items recorded in the data base and those reported by a predictive computer program will not always be similarly scaled or in the same units. In addition, the numerical computation grid is sure to be different from the grid of experimental data.

Therefore, in order to facilitate such comparisons, the reported data and all pertinent geometry have been organized into a computerized data base. This data base includes software for listing all, or portions of, the data: for editing the data; for recalling specific data sets or items; and for interpolating within the data. Volume III of the final report [17] constitutes a user's manual.

Closure

The experimental program described above has generated a substantial base of data on endwall aerodynamics and heat transfer. These data are now available for use by the technical community and provision has been made for their transfer via a computerized data base.

The majority of the work was performed in a linear turbine vane cascade as described briefly above. Due to space limitations, the work on distorted inlet conditions done in the linear cascade and a companion effort conducted in a full annular cascade with a different vane profile were not reported here but are included in [17].

Besides use as a data base for comparison with new analyses, the data base contains valuable trend information relative to the effects of Reynolds number, expansion ratio (exit Mach number), etc. The data are currently being examined in detail to identify trends and develop useful correlations. This effort will be the subject of a future paper.

Acknowledgments

References

1 Sjolander, S. A., "The Endwall Boundary Layer in an Annular Cascade of Turbine Nozzle Guide Vanes," Report No. ME/A 75-4, Department of Mechanical and Aeronautical Engineering, Carleton University, Dec. 1975.

2 Waterman, W. F., and Tall, W. A., "Measurement and Prediction of Three-Dimensional Viscous Flows in Low-Aspect-Ratio Turbine Nozzles," ASME Paper No. 76-GT-73, 1976.

3 Marchal, Ph., and Sieverding, D. H., "Secondary Flows Within Turbomachinery Bladings," *Secondary Flows in Turbomachines*, AGARD CP 214, Mar. 1977.

4 Langston, L. S., Nice, M. L., and Hooper, R. M., "Three-Dimensional Flow Within A Turbine Cascade Passage," ASME JOURNAL OF ENGINEERING FOR POWER, Vol. 99, Jan. 1977, pp. 21–28.

5 Liu, H. C., Booth, T. C., and Tall, W. A., "An Application of Three-Dimensional Viscous Flow Analysis to the Design of a Low-Aspect-Ratio Turbine," ASME Paper No. 79-GT-53.

6 Bailey, D. A., "Study of Mean- and Turbulent- Velocity Fields in a Large-Scale Turbine-Vane Passage," ASME Paper No. 79-GT-33.

7 Blair, M. F., "An Experimental Study of Heat Transfer and Film Cooling on Large-Scale Turbine Endwalls," ASME Paper No. 74-GT-33.

8 Gaugler, R. E., and Russell, L. M., "Streaklike Flow Visualization Study of a Horseshoe Vortex in a Large-Scale, Two-Dimensional Turbine Stator Cascade," ASME Paper No. 80-GT-4, 1980.

9 Langston, L. S., "Crossflows in a Turbine Cascade Passage," ASME Paper No. 80-GT-5, 1980.

10 Sieverding, C. H., and Wilputte, Ph., "Influence of Mach Number and End Wall Cooling on Secondary Flows in a Straight Nozzle Cascade," ASME Paper No. 80-GT-52, 1980.

11 Carrick, H. B., "Secondary Flow and Losses in Turbine Cascades With Inlet Skew," *Secondary Flows in Turbomachines*, AGARD CP 214, 1977.

12 Bindon, J. P., "The Effects of Hub Inlet Boundary Layer Skewing on the Endwall Shear Flow in an Annular Turbine Cascade," ASME Paper No. 79-GT-13.

13 Dunn, M. G., and Stoddard, F. J., "Measurement of Heat-Transfer Rate to a Gas Turbine Stator," ASME JOURNAL OF ENGINEERING FOR POWER, Vol. 101, No. 2, Apr. 1979.

14 Dunn, M. G., and Hause, A., "Measurement of Heat Flux and Pressure in a Turbine Stage," ASME Paper 81-GT-88, 1981.

15 Georgiou, D. P., Godard, M. E., and Richards, B. E., "Experimental Study of the Iso-Heat-Transfer-Rate Lines on the End-Wall of a Turbine Cascade," ASME Paper No. 79-GT-20, 1979.

16 Graziani, R. A., Blair, M. F., Taylor, J. R., and Mayle, R. E., "An Experimental Study of Endwall and Airfoil Surface Heat Transfer in a Large Scale Turbine Blade Cascade," ASME Paper No. 79-GT-99, 1979.

17 Hylton, L. D., Mihelc, M. S., Turner, E. R., and York, R. E., "Experimental Investigation of Turbine Endwall Heat Transfer," AFWAL-TR-81-2077, 1981.

18 Gladden, H. J., and Livingood, J. N. B., "Procedure for Scaling of Experimental Vane Airfoil Temperatures from Low to High Gas Temperatures," NASA TN D-6510, 1971.

19 York, R. E., Hylton, L. D., Fox, R. G. Jr., and Simonich, J. C., "An Experimental Investigation of the Heat Transfer to a Turbine Vane at Simulated Engine Conditions," ASME Paper No. 79-GT-23, 1979.

20 Turner, A. B., "Local Heat Transfer Measurements on a Gas Turbine Blade," *J. Mech. Eng. Sci.*, Vol. 13, 1971.

21 Kohler, H., Hennecke, D. K., Pfaff, K., and Eggebrecht, R., "Hot Cascade Test Results of Cooled Turbine Blades and Their Application to Actual Engine Conditions," AGARD CP 229, 1977.

22 Turner, A. B., "Heat Transfer Instrumentation," *High Temperature Turbines*, AGARD-CP-73-71, 1971.

23 Kline, S. J., and McClintock, F. A., "Describing Uncertainties in Single-Sample Experiments," *Mechanical Engineering*, Vol. 75, Jan. 1953, p. 3.

R. E. Gaugler
Aerospace Engineer.
Mem. ASME

L. M. Russell
Aerospace Engineer.

National Aeronautics and
Space Administration,
Lewis Research Center,
Cleveland, Ohio 44135

Comparison of Visualized Turbine Endwall Secondary Flows and Measured Heat Transfer Patterns

Various flow visualization techniques were used to define the secondary flows near the endwall in a large scale turbine vane cascade. The cascade was scaled up from one used to generate endwall heat transfer data under a joint NASA-USAF contract. A comparison of the visualized flow patterns and the measured Stanton number distributions was made for cases where the inlet Reynolds number and exit Mach number were matched. Flows were visualized by using neutrally buoyant helium-filled soap bubbles, by using smoke from oil soaked cigars, and by a new technique using permanent marker pen ink dots and synthetic wintergreen oil. For the first time, details of the horseshoe vortex and secondary flows can be directly compared with heat transfer distributions. Near the cascade entrance, there is an obvious correlation between the two sets of data, but well into the passage the effect of secondary flow is not as obvious.

Introduction

In order to design efficient cooling configurations for the endwall surfaces between the vanes in a gas turbine, a detailed description of the heat transfer from the hot gas is required. However, the convective heat flux distribution on the endwall is highly nonuniform as the result of the complex secondary flows present. The mainstream flow is subjected to turning and acceleration as it passes between the vanes, producing pressure gradients across the flow passage. As the endwall inlet boundary layer approaches the row of vanes it is strongly influenced by these pressure gradients. A horseshoe vortex results from the endwall inlet boundary layer interacting with the blunt leading edge of a vane. The boundary layer rolls up into a vortex near the stagnation point. The vortex then wraps around the vane leading edge and is convected downstream. The leg of the vortex on the suction side of the passage stays close to the vane as it is swept downstream, but the pressure side leg is driven across the passage by the pressure difference, becoming part of the passage vortex. The passage vortex results from the boundary layer within the passage being driven across the passage by the pressure gradients and rolling up when it encounters the suction surface of the vane.

Aerodynamic investigations of the secondary flow patterns have been the object of flow visualization studies for some time. Using smoke, Herzig et al. [1] observed the roll-up of the endwall boundary layer into a passage vortex. They showed very clearly that the deflection of the boundary layer flow from pressure side to suction side varies strongly with distance from the endwall, with the fluid nearer the wall being affected the most. However, due to the relatively sharp

leading edge on their vane, they did not observe the horseshoe vortex. Langston et al. [2], and Langston [3] reported detailed aerodynamic measurements in a large-scale turbine rotor cascade, including endwall flow visualization and smoke addition to the boundary layer. They observed the streamlines on the endwall associated with the leading edge horseshoe vortex, and noted that all of the smoke introduced into the endwall inlet boundary layer ended up in the passage vortex. Marchal and Sieverding [4] used smoke and laser light sheet to visualize a cross section normal to the flow near the leading edge for both a turbine rotor cascade and a turbine stator cascade. With this technique, they obtained a view of the flow pattern in a plane at an instant in time, but did not show the spatial development of the vortex. They did note that the location of the horseshoe vortex core at the cascade exit moved from about midpassage for the stator to close to the suction surface for the rotor. Gaugler and Russell [5] presented flow visualization studies of the horseshoe vortex by photographing neutrally buoyant helium-filled soap bubbles in the vortex. This allowed the path followed by a single element of fluid to be followed as it was entrained in the vortex.

In addition to the visualization studies of the secondary flow patterns, a number of studies have been reported where the heat transfer to a turbine endwall was investigated. Blair [6] simulated the passage between two vanes on a large scale and found the endwall heat transfer to be strongly influenced by the existence of the passage vortex near the vane suction surface-endwall corner, particularly in the trailing edge region. He also tested passages with both rounded and sharp leading edges to isolate the effect of the leading edge horseshoe vortex on the endwall heat transfer and found significant variations near the leading edge.

Graziani et al. [7] studied the endwall and blade surface

BUBBLE INJECTION SLOT

END-WALL STATIC PRESSURE TAPS (5)

TAILBOARDS TO ASSURE PERIODICITY

LIGHT SOURCE
0.69 m (27 in.)

ALTITUDE EXHAUST

108°

1.52 m (60 in.)

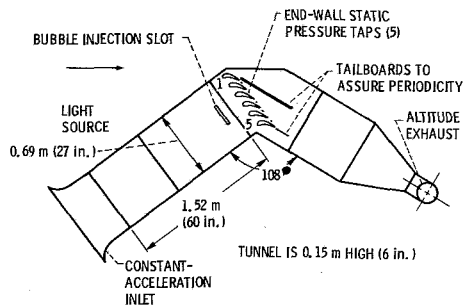TUNNEL IS 0.15 m HIGH (6 in.)

CONSTANT-ACCELERATION INLET

Fig. 1 Schematic plan view—flow visualization rig

heat transfer in a large scale cascade of blades and observed that passage secondary flows greatly influenced the heat transfer. They noted that the endwall inlet boundary layer thickness also had a significant effect on the endwall heat transfer, particularly near the vane leading edge where the horseshoe vortex manifests itself most strongly.

Georgiou et al. [8] conducted endwall heat transfer tests in a facility that permitted simulation of turbine Mach number, Reynolds number, and temperature ratio. They concluded that changes in the inlet boundary layer thickness only influenced the heat transfer in the vicinity of the leading edge.

The most complete set of endwall heat transfer data currently available has been reported by Hylton et al. [9]. Under joint NASA-U.S. Air Force sponsorship, measurements were made of endwall Stanton numbers over a range of conditions that included typical engine operating conditions. The results of that work have been summarized by York et al. [10].

In this secondary flow visualization study, the cascade used was scaled directly from that used by Hylton et al. [9] for endwall heat transfer. Reynolds number and Mach number in the flow visualization cascade matched selected run conditions in [9]. For the first time, details of the horseshoe vortex and secondary flows were directly compared with heat transfer distributions. Flows were visualized by using neutrally buoyant helium-filled soap bubbles, by using smoke from oil soaked cigars, and by a new technique, developed by Langston and Boyle [11], using permanent marker pen ink dots and synthetic wintergreen oil. Direct comparisons were made between endwall contour plots of Stanton number and the paths taken by bubbles in the horseshoe vortex. The surface flow visualization features were also compared with the heat transfer data.

Apparatus and Procedure

Cascade. The facility used in this study was the same as that used by Gaugler and Russell [5], with the exception of the test vanes. For this work, the six vanes used were scaled up by a factor of 1.9 from the profile used by Hylton et al. [9] for the endwall heat transfer tests. The pertinent cascade parameters were: axial chord, 9.75 cm (3.84 in.); chord/axial chord, 1.78; pitch/axial chord, 1.29; aspect ratio (span/axial chord), 1.56; air inlet angle, 0 deg (axial); air exit angle, 72 deg.

Air flow through the cascade was drawn in from an atmospheric inlet and exhausted to the laboratory central exhaust system. The wind tunnel built to hold the cascade is shown schematically in Fig. 1. The inlet nozzle was designed for constant acceleration of the flow through it, as described in [12]. At the end of the inlet nozzle the flow enters a duct, 68.6-cm (27-in.) wide by 15.2-cm (6-in.) high by 152.4-cm (60-in.) long. This duct was long enough to ensure a turbulent endwall boundary layer, which was confirmed by profile measurement.

The tunnel boundary layer profile was measured at a point 21.6 cm (8.5 in.) upstream of the vanes. The cascade of six

vanes was located at the end of the inlet duct. The end vanes had adjustable tailboards to assure periodicity of the flow through the cascade. One of the vanes in the center of the cascade was instrumented with static pressure taps around the vane at midspan. The cascade inlet Reynolds number, based on true chord, ranged from 0.7 × 10^5 to 3.2 × 10^5 for the tests described. From the cascade, the flow was ducted to the laboratory central exhaust system. The vanes were fabricated from wood and painted black to provide contrast in the pictures. The rest of the cascade was built of clear acrylic plastic with the bottom endwall painted black.

Flow Visualization Techniques. There is a slot in the endwall located about 21 cm (8.25 in.) upstream of the vane leading edges, shown in Fig. 1. The helium bubbles used for flow visualization are injected into the boundary layer from a plenum beneath this slot. The bubble generating system is described in detail by Hale et al. [13], and its use in this facility is described in [5]. The desired bubble size and neutral buoyancy are achieved by proper adjustment of air, bubble solution, and helium flow rates. As many as 300 bubbles per second are formed in this device. For these tests the bubble diameter was about 1.5 mm (0.06 in.). The bubble generator head was placed through a grommet in the wall of the plenum beneath the injection slot shown in Fig. 1.

The light source for bubble illumination consisted of a 300-W quartz arc lamp, a rectangular aperture, and a 300-mm lens. The light source was located upstream and to one side of the tunnel and projected a beam through the tunnel wall into the cascade. The image of the aperture was focused in the cascade, and its vertical location was adjustable to illuminate either the boundary layer or the free stream. When viewed from above, or from the side, the bubbles showed up very brightly when they were in the light beam. Photographs of the bubbles were taken from two locations, directly above the cascade, providing a plan view of the flow, and upstream of the cascade, looking through the tunnel sidewall into the cascade, providing an oblique view of the flow. At either location, a motion picture camera, running at 3 frames per second, was used to record the bubble traces. The motion picture camera was merely a convenient way to acquire the data. Since the time of flight of the bubbles through the field of view was much shorter than the open time of the shutter, each frame was an independent data record. The bubbles appear as streaklines on the film, and adjacent frames of the film can never show the same bubble. The movies were viewed one frame at a time, and 35-mm copies were made of the most interesting frames.

A second technique used to visualize the flow was to inject smoke into the stream through a probe. A smoke generator was constructed, similar to that described in [1], and used also in [5]. The source of the smoke was a burning, oil-soaked cigar. A regulated air supply provided combustion air, and the smoke was carried through a trap to allow large oil droplets to settle out, then it was ducted to the test section. The same lighting and camera system was used for the smoke as was used for the bubbles. The smoke had the advantage that it could be precisely placed where desired, but the disadvantage was that it diffused, and being a continuous source, tended to average out temporal variations in the flow. This means that local details of the horseshoe vortex cannot be observed with smoke, but it does a good job of delineating regions of the flow and showing gross fluid motions.

Perhaps the most spectacular flow visualization pictures resulted from use of the ink dot technique developed by Langston and Boyle [11]. For this procedure, a regular array of ink dots was laid down on a sheet of drafting film, using a permanent ink marker pen. The sheet was then rubber-cemented to the endwall surface, and a uniform layer of synthetic wintergreen oil was sprayed on the film. Then the
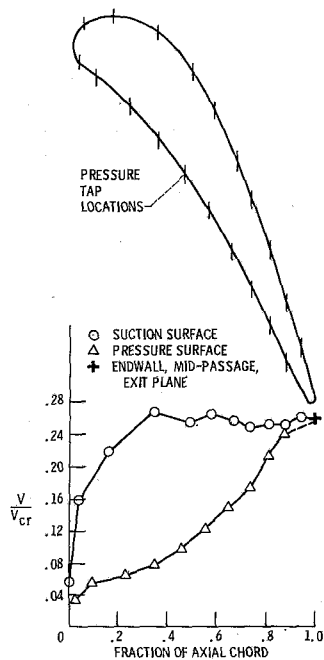
Fig. 2 Measured velocity distribution around the vane
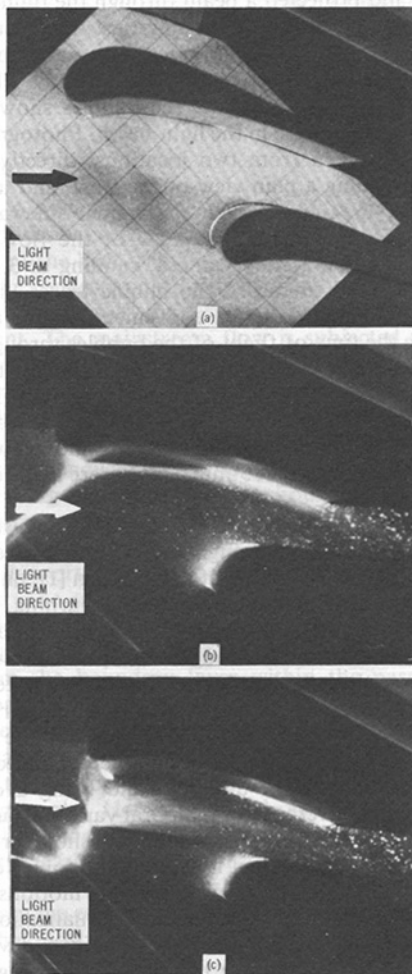
Fig. 3 Smoke flow visualization, plan view: (a) endwall scale, 2.54-cm (1-in.) grid; (b) smoke on stagnation streamline, but in the free stream, out of the endwall boundary layer; (c) smoke on stagnation streamline, but in the outer part of the endwall boundary layer
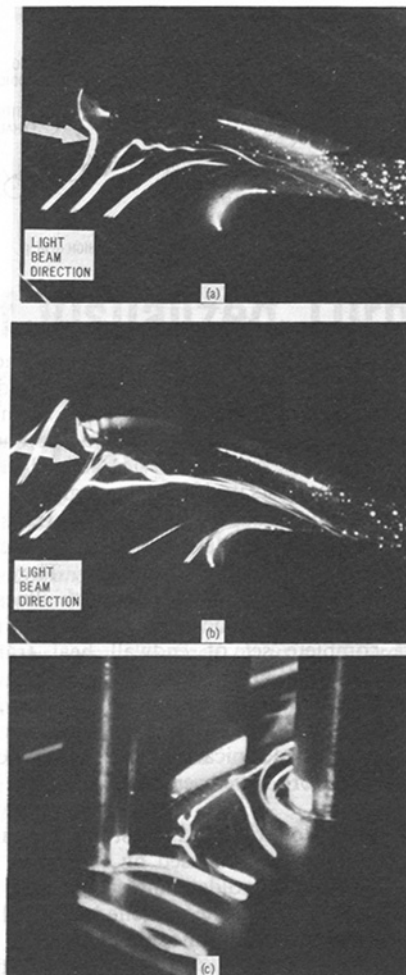
Fig. 4 Neutrally-buoyant, helium-filled, soap bubble traces in the endwall boundary layer: (a) plan view; (b) plan view; (c) oblique view
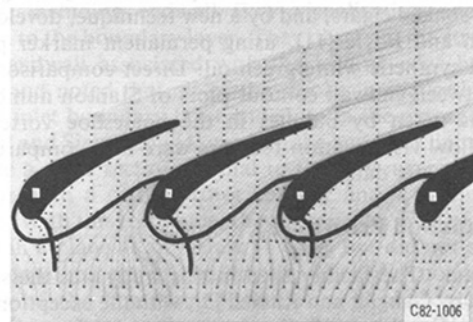
Fig. 5 Ink dot flow visualization of the endwall surface secondary flows. Solid lines illustrate the location of the three-dimensional separation line and stagnation streamline.

facility flow was started and continued until the oil had all been dragged downstream and/or evaporated. What remained on the sheet was the array of dots, with tails originating from each dot, pointing in the direction of the local wall shear stress.

Additionally, some endwall surface flow visualization data were taken by placing small drops of light mineral oil mixed with a yellow pigment on the surface and recording on movie film the flow of the oil drops when air flow was established in the cascade. Comparison of the distance moved by different drops over the same number of movie frames gave an indication of the difference in wall shear stress at different points.

The four flow visualization techniques used can be put into two general catagories. The bubble and smoke methods show
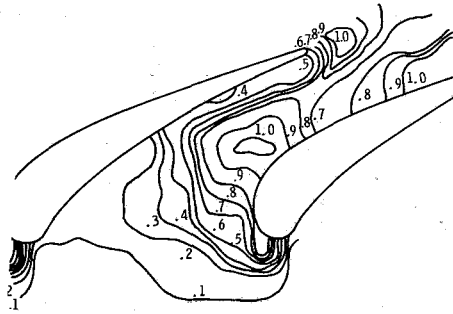
Fig. 6 Endwall contours of lines of constant nondimensional wall shear stress

the motion of fluid "particles," while the ink dot and oil drop techniques delimit shear stress directions at the wall.

Results and Discussion

Aerodynamic Qualification. The initial work done in the facility served to qualify the rig and define the flow conditions.

The cascade periodicity was set by adjusting the tailboards until the variation in exit pressure difference (total pressure minus static pressure) between passages was minimized. At the final setting of the tailboards with the cascade operating at an inlet Reynolds number based on true chord of about 2.75 $\times$ 10^5, there was a variation of less then ± 1 percent in the exit pressure difference between the five passages.

The pressure distribution around one of the vanes was measured and the results are shown in Fig. 2 as the ratio of local velocity to inlet critical velocity versus fraction of axial chord. A comparison of these data with the results presented in [9] shows good agreement, indicating that the vane profile used for the flow visualization tests is correctly scaled from the vanes in [9].

The cascade inlet boundary layer profile was measured at a point 21.6-cm upstream of the vanes using a Pitot-static probe. Profiles were taken at two flow conditions at nominal inlet Reynolds numbers of 2.3 $\times$ 10^5 and 1.6 $\times$ 10^5. The profile data were reduced to nondimensional form and compared with the universal turbulent boundary layer profile. The good agreement observed indicated that a fully developed turbulent boundary layer existed upstream of the vanes. For the two flow conditions, boundary layer thicknesses were about 1.9 (0.75) and 2.2 cm (0.85 in.), respectively. These values are comparable, when scaled, with the inlet boundary layer thicknesses reported in [9].

Free-stream turbulence intensity was measured at the same location as the boundary layer profiles, for the same two inlet Reynolds numbers. The results were 0.031 and 0.037, respectively. This is roughly half the turbulence level reported in [9].

**Flow Visualization.** Over the range of operating conditions available for the cascade it was observed that the flow visualization results were essentially independent of inlet conditions. There was no noticeable difference in bubble traces between the highest and lowest inlet Reynolds number cases. The same was true for the smoke and the ink dot traces. Thus, in the descriptions to follow, specific flow conditions will not be discussed, rather, the best visual data available will be used regardless of flow conditions.
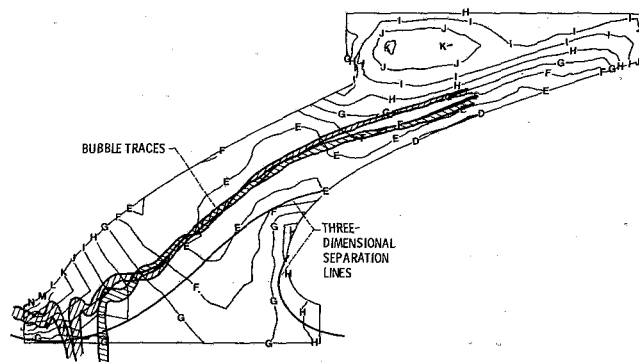
The results of using smoke to visualize the flow are presented in Fig. 3. Figure 3(a) is a plan view photograph of a grid on the cascade endwall. The grid squares are 2.54 cm (1.0 in.) on a side. Figure 3(b) shows smoke put in along a free-stream stagnation line. In this case, the smoke is far enough from the wall to be out of the endwall boundary layer, and shows very little spreading. The straight line seen near the pressure surface is the edge of the shadow of the vane leading edge falling on the smoke. The smoke did actually extend all the way to the pressure surface. For this picture, the light beam was grazing the endwall surface and had a thickness of about 4.8 cm. The picture shows bright highlights where the beam illuminates the vane surfaces, near the leading edge and the last half of the pressure surface. The bright spots on the endwall surface are light reflections from oil and dust particles on the surface. Figure 3(c) shows the smoke injected into the endwall boundary layer, but still off the wall. Here the path of the smoke spreads very widely and a large region is filled with smoke. In this case, the smoke has been caught in the horseshoe vortex system.
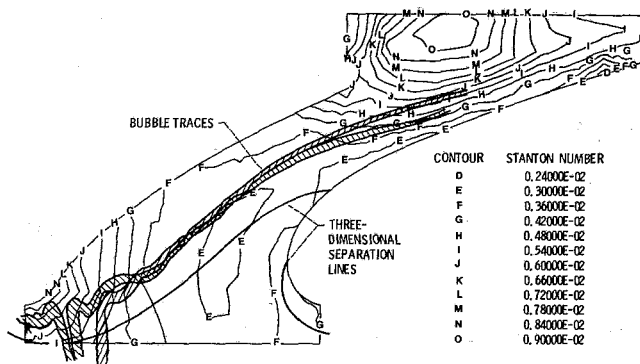
Figure 4 shows photographs of bubbles streaking through the cascade in the endwall boundary layer. For these pictures, the light beam was grazing the endwall surface and had a thickness of about 1 cm. Parts (a) and (b) show a plan view of the cascade (refer to Fig. 3(a) for the endwall scale). The wavy paths shown are actually plan views of corkscrewlike paths followed by bubbles that are caught in the horseshoe vortex. The core of the horseshoe vortex on the pressure side leg moves across the passage as it moves downstream, and analysis of the films at the trailing edge plane shows the location of the vortex to be centered at about two-thirds of the way from pressure to suction sides of the passage. Part (c) is an oblique view looking into the cascade at an angle with the inlet in the foreground. The corkscrewlike path of a bubble in the horseshoe vortex is more clearly seen in this view. Note also the extent of the light beam where it strikes the vane surfaces. The height of the beam was about 1 cm.

The different regions of flow on the endwall were most sharply outlined by use of the ink dot technique. Figure 5 shows typical results from using this method. The stagnation streamlines and three-dimensional separation lines are apparent and have been highlighted in the figure for clarity. A detailed description of the significance of these features has been presented by Langston et al. [2]. The stagnation streamline separates flow between the suction and the pressure sides of the vane. The three-dimensional separation line divides the flow field adjacent to the endwall into distinct three-dimensional flow zones. Upstream of the three-dimensional separation, endwall flow is channeled toward the vane suction surface. The horseshoe vortex is located downstream of this line, and endwall flow is from the pressure side toward the separation line, leaving the surface at that point. The result shown in Fig. 5 is a black-and-white print of the actual data. In the actual test, two different colors of ink were used, one color in regions upstream of the three-dimensional separations, and another color downstream. The separation of the two regions is dramatically illustrated in this manner. In Fig. 5, the heavy black line has been added to show the location of the three-dimensional separation line. From the results of Fig. 5, it is apparent that all of the fluid entering the cascade very close to the endwall ends up on the suction surface of the vane. However, the smoke and bubble pictures show that most of the inlet boundary layer fluid ends up on the downstream side of the three-dimensional separation and leaves the cascade in the vortex. Langston et al. [2] noted this same effect when they put smoke in the upstream boundary layer. A full color view of this figure was given to Langston and Boyle and has been published by them in [11] to demonstrate an application of the ink dot method.

The endwall flow visualization traces in Fig. 5 show the direction of the local wall shear stresses, but do not include any information about the magnitude. An attempt was made to gain information about the relative magnitude of the wall shear stress at different points on the endwall by an analysis of the motion picture of the flow of oil drops on the surface. It was assumed that for a given time interval, the length of the path followed by a given oil drop is proportional to the local wall shear stress. A justification of this assumption is

(a) Run 124, inlet Reynolds number = 0.208 × 10⁶ (reference [9]).

CONTOUR	STANTON NUMBER
D	0.24000E-02
E	0.30000E-02
F	0.36000E-02
G	0.42000E-02
H	0.48000E-02
I	0.54000E-02
J	0.60000E-02
K	0.66000E-02
L	0.72000E-02
M	0.78000E-02
N	0.84000E-02
O	0.90000E-02

(b) Run 131, inlet Reynolds number = 0.296 × 10⁶ (reference [9]).

Fig. 7 Comparison of endwall Stanton number contours and visualized secondary flows

presented by Atraghji [14]. A number of drops were compared over a fixed number of movie frames, and their relative path lengths tabulated. Contours of constant relative motion were then sketched by hand, and the result is shown in Fig. 6. The higher numbers on the contours correspond to regions of higher shear stress.

Heat Transfer Comparison. Figure 7 shows measured Stanton number contours overlaid with flow visualization information for two of the runs reported by Hylton et al. [9]. For these runs the exit Mach number and inlet Reynolds number were in the range tested in the flow visualization cascade. Two prominent peaks in Stanton number stand out, one near the vane leading edge on the pressure side, and one downstream of the trailing edge. A smaller peak occurs near the vane suction side, at about one-fourth of the axial chord into the passage. A region of relatively low Stanton number covers a large part of the first half of the midpassage area.

The most obvious correlation between the flow visualization data and the Stanton number contours in Fig. 7 is in the leading edge region, on the pressure side. The large gradient in Stanton number, leading to a peak in that area, coincides with the region of most intense vortex action, as shown by the smoke in Fig. 3 and the bubble traces in Fig. 4. The smaller peak in Stanton number, near the suction surface, coincides with the region where the three-dimensional separation line reaches the suction surface. It is in this area where the oil on the endwall ahead of the separation line was observed to begin to climb onto the suction surface of the vane.

The large peak in Stanton number seen downstream of the vane trailing edge does not appear to be directly related to any of the horseshoe vortex features shown by the bubble traces, but the endwall ink dot traces in Fig. 5 show a diverging flow

pattern on the endwall in this region. This would indicate that there is a flow of fluid toward the endwall in the vane wake, resulting in a high heat transfer coefficient. Comparing the midchannel region upstream and downstream of the three-dimensional separation line in Fig. 5 with the Stanton number contours in Fig. 7 shows that this is a region of relatively uniform, low Stanton number. Interestingly, there is nothing obvious in the Stanton number data that correlates with the location of the separation line.

Summary and Conclusions

Various flow visualization techniques were used to define the secondary flows near the endwall in a large scale turbine vane cascade. The cascade was scaled up by a factor of 1.9 from one used to generate endwall heat transfer data under a joint NASA-USAF contract. A comparison of the visualized flow patterns and the measured Stanton number distributions was made for cases where the inlet Reynolds number and exit Mach number were matched. Flows were visualized by using neutrally buoyant helium-filled soap bubbles, by using smoke from oil soaked cigars, and by a technique using permanent marker pen ink dots and synthetic wintergreen oil.

From this investigation it can be concluded that:

1 The only obvious correlation between the horseshoe vortex and the endwall heat transfer is near the vane leading edge, where a local peak in heat transfer occurs and the initial vortex rollup begins.

2 The three-dimensional separation line on the endwall does not correlate with any endwall heat transfer features.

3 The large peak in Stanton number seen downstream of the vanes is not related to the horseshoe vortex, but appears to be related to downflow in the vane wake.

4 The ink dot surface flow visualization technique correlates well with boundary layer flow visualized by means of neutrally buoyant bubbles.

References

1 Herzig, H. Z., Hansen, A. G., and Costello, G. R., "A Visualization Study of Secondary Flows in Cascades," NACA Report 1163, 1953.

2 Langston, L. S., Nice, M. L., and Hooper, R. M., "Three-Dimensional Flow Within a Turbine Cascade Passage," ASME JOURNAL OF ENGINEERING FOR POWER, Vol. 99, No. 1, Jan. 1977, pp. 21-28.

3 Langston, L. S., "Crossflows in a Turbine Cascade Passage," ASME JOURNAL OF ENGINEERING FOR POWER, Vol. 102, No. 4, 1980, pp. 866-874.

4 Marchal, Ph., and Sieverding, C. H., "Secondary Flows Within Turbomachinery Bladings," AGARD CP-214, Advisory Group for Aerospace Research and Development, Paris, France, 1977, Paper 11.

5 Gaugler, R. E., and Russell, L. M., "Flow Visualization Study of the Horseshoe Vortex in a Turbine Stator Cascade," NASA TP-1884, 1982.

6 Blair, M. F., "An Experimental Study of Heat Transfer and Film Cooling on Large-Scale Turbine Endwalls," ASME *Journal of Heat Transfer*, Nov. 1974, pp. 524-529.

7 Graziani, R. A., Blair, M. F., Taylor, J. R., and Mayle, R. E., "An Experimental Study of Endwall and Airfoil Surface Heat Transfer in a Large Scale Turbine Blade Cascade," ASME JOURNAL OF ENGINEERING FOR POWER, Vol. 102, No. 2, 1980, pp. 257-267.

8 Georgiou, D. P., Godard, M., and Richards, B. E., "Experimental Study of the Iso-Heat-Transfer-Rate Lines on the End-Wall of a Turbine Cascade," ASME Paper No. 79-GT-20, Mar. 1979.

9 Hylton, L. D., Mihelc, M. S., Turner, E. R., and York, R. E., "Experimental Investigation of Turbine Endwall Heat Transfer," AFWAL-TR-81-2077, 3 Volumes, 1981.

10 York, R. E., Hylton, L. D., and Mihelc, M. S., "An Experimental Investigation of Endwall Heat Transfer and Aerodynamics in a Linear Vane Cascade," proposed for presentation, ASME Paper No. 83-GT-52, March 1983.

11 Langston, L. S., and Boyle, M. T., "A New Surface Streamline Flow Visualization Technique," *Journal of Fluid Mechanics*, Vol. 125, Dec. 1982, pp. 53-57.

12 Yuska, J. A., Diedrich, J. H., and Clough, N., "Lewis 9- by 15-Foot V/STOL Wind Tunnel," NASA TM X-2305, 1971.

13 Hale, R. W., Tan, P., Stowell, R. C., and Ordway, D. E., "Development of an Integrated System for Flow Visualization in Air Using Neutrally Buoyant Bubbles," SAI-RR 7107, SAGE ACTION, Inc., Ithaca, N.Y., Dec. 1971. (AD-756691)

14 Atraghji, E., "More Than Meets the Eye: The Oil Dot Technique," *International Symposium on Flow Visualization*, Bochum, Sept. 1980, pp. 67-68.

Heat Transfer Optimized Turbine Rotor Blades—An Experimental Study Using Transient Techniques

J. H. Nicholson

A. E. Forest

Rolls-Royce Ltd.,
Derby, England

M. L. G. Oldfield

D. L. Schultz

Department of Engineering Science,
University of Oxford,
Oxford OX2 3PJ, England

Conventionally, high-pressure turbine blading is optimized for aerodynamic performance without any film cooling applied to the surfaces of the blades. It is considered that modern boundary layer prediction technqiues are now sufficiently accurate to allow the heat transfer to be considered at the profile design stage. Two turbine rotor profiles were designed, each with a heat transfer optimized pressure surface, and a detailed experimental study using transient techniques in the Oxford cascade tunnel was made. The results show that significant reductions in pressure surface heat transfer can be achieved by boundary layer optimization without compromising the aerodynamic efficiency of the blades. A description of the profiles is given, together with transfer rate measurements, pressure distribution, and aerodynamic loss measurements (a technique devleoped to measure aerodynamic loss in a transient cascade is described) and flow visualization photographs.

Introduction

The high operating temperatures and pressures of current and future high-pressure gas turbine aeroengines demand that turbine stator and rotor blades are cooled. Without cooling, the blade metal temperature would be beyond the material capability, and with inadequate cooling the blade life would be unacceptably short. First stage high-pressure turbine blading of modern engines requires film cooling and the addition of a layer of cooling air over the surface results in a reduction in turbine efficiency. To minimize the loss of efficiency due to film cooling it is necessary to be able to predict accurately the external heat transfer coefficient during the aerofoil design. Stepka [1] showed that the greatest improvements in the accuracy of metal temperature—and hence blade life—prediction can be achieved by improving the prediction of the external heat transfer coefficient.

In addition to reducing the turbine efficiency, the use of cooling air reduces the overall engine efficiency, and thus any reduction in the total amount of cooling air required will reduce the engine fuel consumption. This paper is concerned with a design philosophy in which the heat transfer to the blades is minimized during the design by pressure surface boundary layer control. A heat transfer optimized turbine design results in minimum blade cooling air requirement and hence maximum engine efficiency.

An understanding of the boundary layer development around turbine blade profiles is of prime importance to the designer since it directly affects the heat transfer to the blade.

The main factors governing boundary layer growth are: Re, Reynolds number; $\partial P / \partial x$, pressure gradient; $1/R$, surface curvature; Tu, freestream turbulence level; M, local Mach number. A more detailed study of the factors which govern the heat transfer to blades was given by Graham [2].

The boundary layer can be visualized as an insulating blanket around the blade, and for a given profile the heat transfer to the blade will reduce as the boundary layer thickens. In addition, the heat transfer to a blade through a turbulent boundary layer is higher than that through a laminar boundary layer.

The concave curvature of the pressure surface may lead to the generation of longitudinal Goertler vortices which promote early transition and increase the heat transfer rate to the entire surface. These longitudinal vortices are not well understood, and a review of the current knowledge was given by Martin and Brown [3].

The normal design procedure for a turbine blade is to consider only aerodynamic efficiency. It is considered that modern boundary layer prediction techniques are sufficiently accurate to justify estimates of the blade heat transfer to be made during the profile design. It was expected that, by designing the profile aerodynamics to control the boundary layer to minimize the heat transfer to the uncooled profile, a significant reduction in the amount of film cooling required would be made. Two profiles were designed, each minimizing the pressure surface heat transfer by using different methods of boundary layer control. One of the blades achieved minimum pressure surface heat transfer by relaminarization of the boundary layer, whilst the other was designed to have a fully turbulent and thick boundary layer over as much of the surface as possible. The suction surface was designed for

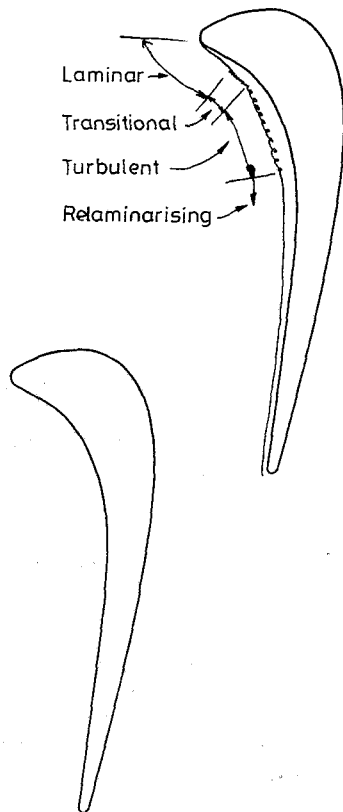Fig. 1 HS profile and design boundary layer

Fig. 2 LS profile and design boundary layer

aerodynamic performance and was not optimized to minimize heat transfer rates.

Description of Profiles

The two profiles are referred to as the High Stagger (HS) and Low Stagger (LS) profiles throughout the remainder of this paper. The profiles are representative of a two-stage, high-pressure turbine for a high bypass ratio civil transport engine.

The HS profile is shown in Fig. 1, and the designed pressure surface boundary layer is shown schematically on the uppermost blade. The pressure surface boundary layer was designed to undergo a transition between 10 and 20 percent of the surface length. Soon after transition, the pressure surface flow is subjected to a high acceleration over the remainder of the surface. This high acceleration, coupled with a flat blade profile from about 50 percent surface length on the pressure surface was designed to relaminarize the boundary layer.

The LS profile with its designed pressure surface boundary layer illustrated is shown in Fig. 2. The pressure surface pressure gradients and acceleration parameters are maintained at low levels over as much of the surface length as
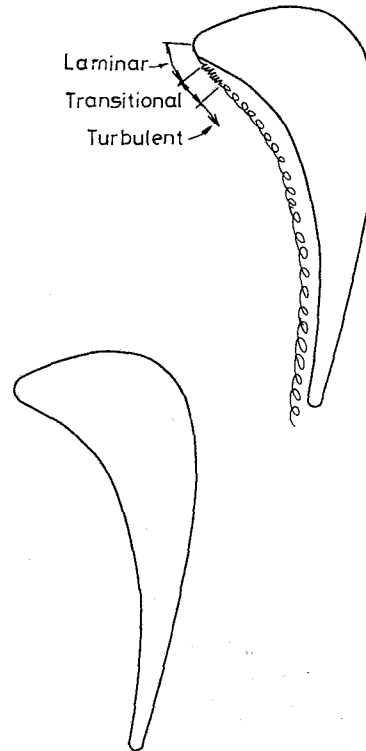
possible. An early boundary layer transition occurs and the boundary layer thickens rapidly because of the low accelerations. The pressure surface flow must, of course, at some point, accelerate to the correct value of exit Mach number. The resulting high value of acceleration parameter over the rear of the blade will not relaminarize the boundary layer because of (a) the high momentum thickness Reynolds number and (b) the concave surface curvature of the pressure surface.

Coordinates of each profile are given in the Appendix, and other relevant geometrical details are given later in this paper.

The two profiles are shown with their leading edge circle centres superimposed in Fig. 3. They are designed to function with equal work ouptut, and the study can be regarded as a study of the effect of blade stagger angle on aerodynamic and thermal performance. The HS profile represents the maximum practical stagger angle, limited by manufacturing considerations of long thin aerofoil sections. The lower limit of stagger angle, represented by the LS profile, is fixed by a maximum allowable suction surface diffusion rate. It was found during the design of the two profiles that the heat transfer rates over the suction surface could not be significantly decreased without incurring heavy aerodynamic penalties. The suction surfaces were therefore designed using conventional aerodynamic restraints.

─────── **Nomenclature** ───────

C_1	=	pressure loss coefficient	Tu	=	turbulence level	
C_2	=	primary loss coefficient	t	=	time	
h	=	specific enthalpy	V	=	velocity	
M	=	Mach number	x/C_{ax}	=	axial distance/axial chord from leading edge	
P	=	pressure				
$\dot{q}$	=	heat transfer rate	x/s	=	surface distance/surface length from leading to trailing edge	
R	=	surface curvature				
Re	=	Reynolds number				
s	=	surface length	β	=	relative flow angle	
T	=	temperature	η	=	efficiency	
			ρ	=	density	

Ω = axial velocity-density ratio
ν = kinematic viscosity

Subscripts

g = mainstream gas
o = total conditions
s = isentropic process
w = wall conditions
prim = primary
1 = inlet to rotor
2 = exit of rotor

Fig. 3 Comparison of HS and LS profiles with LE circle centers superimposed

Fig. 4 Cascade dimensions (HS blades shown)

Fig. 5 HS and LS operating conditions

Experimental Arrangements

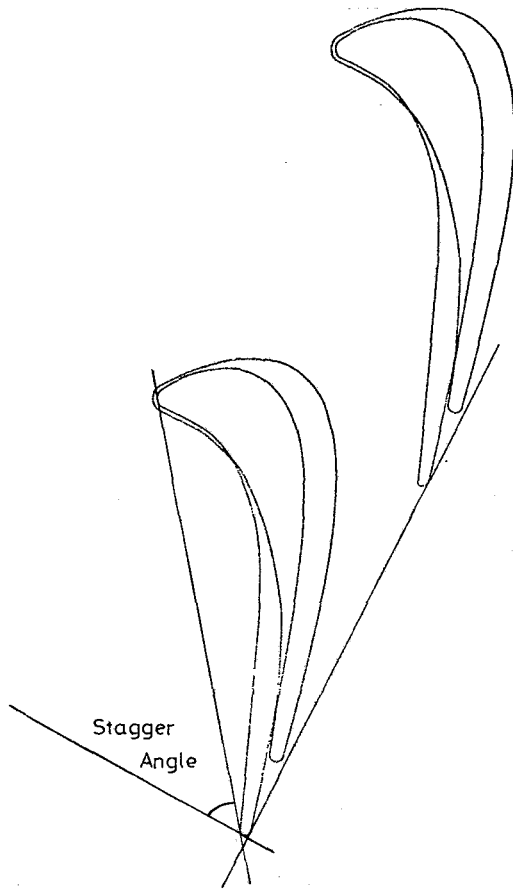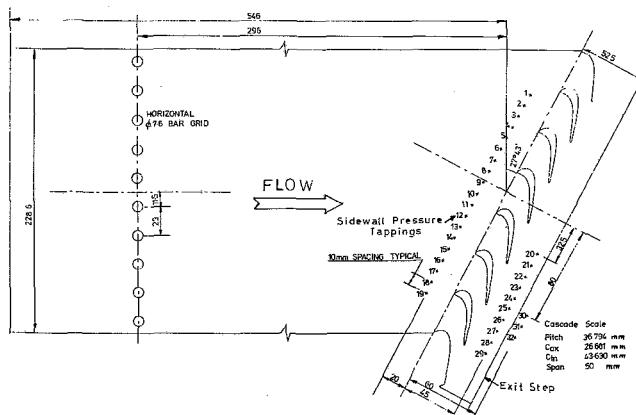The Oxford cascade tunnel [4, 5, 7] is an isotropic light piston tunnel which generates a flow having a stagnation temperature of 430 K over a cascade of blades at 290 K. Full-scale Reynolds and Mach numbers, and flow-to-wall temperature ratios, are achieved for flow durations of between 0.3 and 1 s. The operating pressures, blade pressure distributions, heat transfer rate, and aerodynamic loss were monitored using appropriate transducers, and a dedicated minicomputer. Data from the transducers were collected and analyzed using the data acquisition system described by Oldfield et al. [7]. Both profiles were designed for the same turbine application and, because of the many common dimensions, could be tested in the same cascade configuration. A seven passage cascade was used and the general arrangement is shown in Fig. 4. To give a parallel inlet duct at the inlet angle of 27.43 deg the cascade pitch was fixed at 36.794 mm. The blade span was 50 mm and an inlet span reducing contraction, 70-mm long, was positioned 380 mm upstream of the cascade. A turbulence generating grid, used to increase the inherently low (< 0.2 percent) level of ILPT flow, consisting of eight bars each, of 7.6-mm dia, at a spacing of 23 mm, was positioned with the bar centers 296 mm upstream of the cascade. This distance is sufficient to ensure homogeneity and isotropy of the turbulent flow at the working section. To ensure periodic flow through the cascade an exit step expansion was positioned 26.88 mm (one axial chord) downstream of the blade trailing edges.

The cascade sidewall was instrumented with 32 static pressure tappings (Fig. 4). The inlet total pressure was measured using a total pressure probe built into the bottom blade or by a conventional pitot probe protruding into the flow at the centre of the instrumented passage.

Two models for each cascade were used to measure the pressure distribution, one instrumented with thirteen static pressure tappings on the pressure surface and the other with an equal number on the suction surface. For heat transfer measurements, two full-span machineable glass ceramic blades for each cascade were manufactured. The thin film gauges were painted over the centre 10 mm of the span.

The Reynolds number, isentropic exit Mach number, and gas-to-wall temperature ratio of the profiles at their design condition are: $Re = 1.113 \times 10^6$; $M_{exit} = 0.78$; $T_g/T_w = 1.5$, where the Reynolds number is based on the isentropic Mach number and blade axial chord.

It is important to understand the relative importance of Reynolds number, Mach number, and free-stream turbulence level on the profile aerodynamic and thermal performance. One of the advantages of using transient techniques is the ease with which the operating condition can be varied. The range of conditions selected to provide the most useful data whilst minimizing the cost of the experiment is shown in Fig. 5. The heat transfer to the blades is greatly affected by changes in Reynolds and exit Mach numbers and by changes in free-
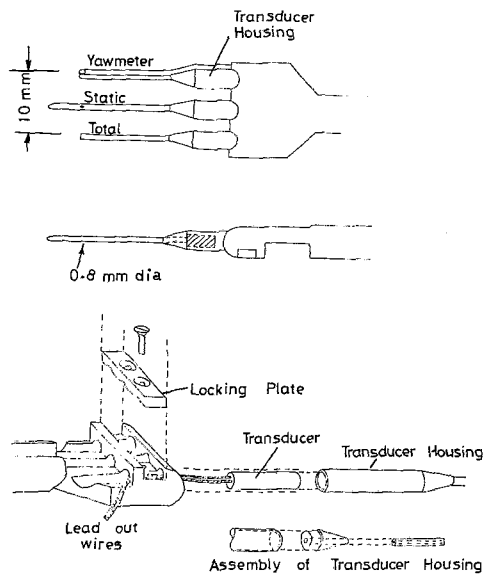
Fig 6 Schematic arrangement of Neptune probe for cascade loss measurements
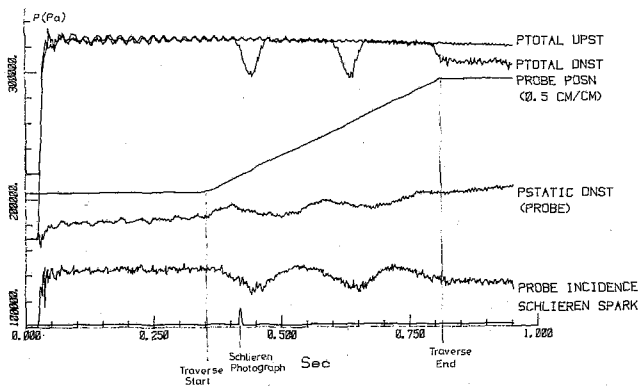
Fig. 7 Downstream traverse timing during tunnel run

Re	M$_{exit}$	Tu	Knife edge
1.113 x 10^6	0.96	4%	H

Fig. 8(a) HS profile Schlieren photograph showing downstream traverse probe in motion

stream turbulence level whereas the pressure distribution is changed most significantly by changes in the flow exit Mach number. For these reasons, the heat transfer to the blades was measured at all five conditions with (Tu = 4 percent) and without (Tu < 0.2 percent) the turbulence grid fitted, whilst the pressure distribution was measured at the three exit Mach numbers (plus one additional value for the HS profile) at the design Reynolds number with the turbulence grid fitted. Loss measurements were taken over a range of exit Mach numbers at the design Reynolds number but, except during runs to demonstrate the effect of heat transfer on loss, with cold (228 K) flow.

Description of Probe Used for Aerodynamic Loss Measurements

A scaled version of the "Neptune" probe used by Kiock [8] was used for measuring the aerodynamic loss of the cascades. This type of probe is particularly suitable for measurements downstream of a row of cascade blades because each sensing head is in the same plane, permitting high accuracy measurements in regions of high-pressure gradient such as in a blade wake. It is particularly suitable for use in a transient tunnel where relatively short response times are required.

The probe is shown schematically in Fig. 6. It consists of three hypodermic tubing sensing heads to measure the flow total pressure, static pressure, and flow direction. A probe support quadrant and arm, connected to a variable speed pneumatic actuating mechanism, allowed independent ad-

Re	M$_{exit}$	Tu	Knife edge
1.13 x 10^6	0.96	4%	H

Fig. 8(b) LS profile Schlieren photograph showing downstream traverse probe in motion
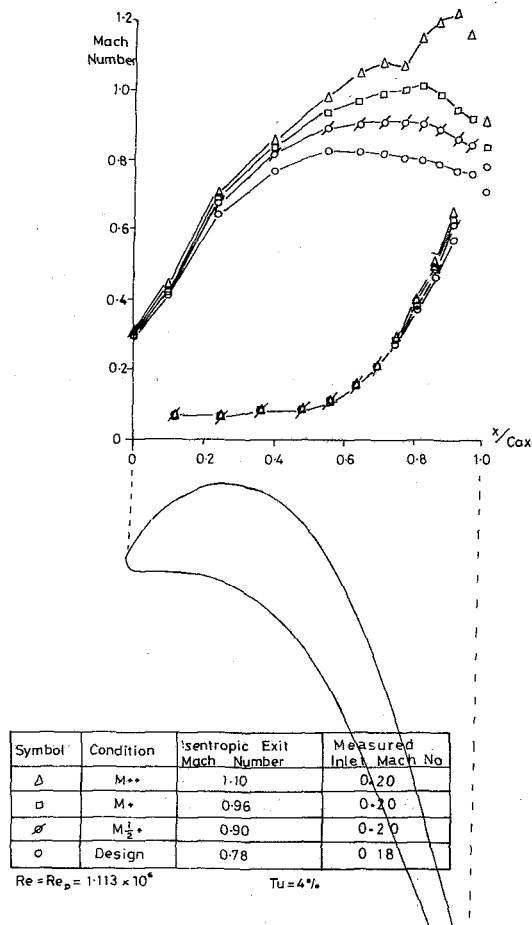
Fig. 9 HS profile: effect of exit Mach number on Mach number distribution

Symbol	Condition	Isentropic Exit Mach Number	Measured Inlet Mach No
Δ	M++	1·10	0·20
□	M+	0·96	0·20
∅	M½+	0·90	0·20
○	Design	0·78	0·18

Re = Re$_D$ = 1·113 × 10^6 Tu = 4%

Fig. 10 LS profile: effect of exit Mach number on Mach number distribution

Symbol	Condition	Isentropic Exit Mach Number	Measured Inlet Mach No
Δ	M++	1·10	0·21
□	M+	0·96	0·21
○	Design	0·78	0·19

Re = Re$_D$ = 1·113 × 10^6 Tu = 4%

justment of the probe angle and position. The probe was constructed of 0.8-mm-dia tubing spaced 5 mm apart; Kiock's probe used 1.5-mm-dia tubing spaced 30 mm apart.

A traverse was initiated electrically during a tunnel run and the timing of a typical traverse is shown in Fig. 7. For this run the traverse mechanism was triggered approximately 0.3 s after the flow started and lasted for about 0.45 s. The oscillations in downstream total pressure follow those in upstream pressure and the two measured wakes are clearly shown. At the end of the traverse ($t \approx 0.75$ s) the Neptune probe is in a third wake, and the measured downstream total pressure remains at the low value for the remainder of the run. A Schlieren photograph for the run down in Fig. 7 was taken about 0.4 s after the flow commenced, about 0.1 s after the traverse started. A typical Schlieren photograph taken with the probe in motion is shown in Fig. 8 and shows that the probe produces a negligible disturbance to the flow field. For each run the probe angle relative to the axial direction was measured from a Schlieren photograph.

The probe was calibrated in a 9 × 3 in. working section continuous wind tunnel over a range of Mach numbers and incidence angles. The results obtai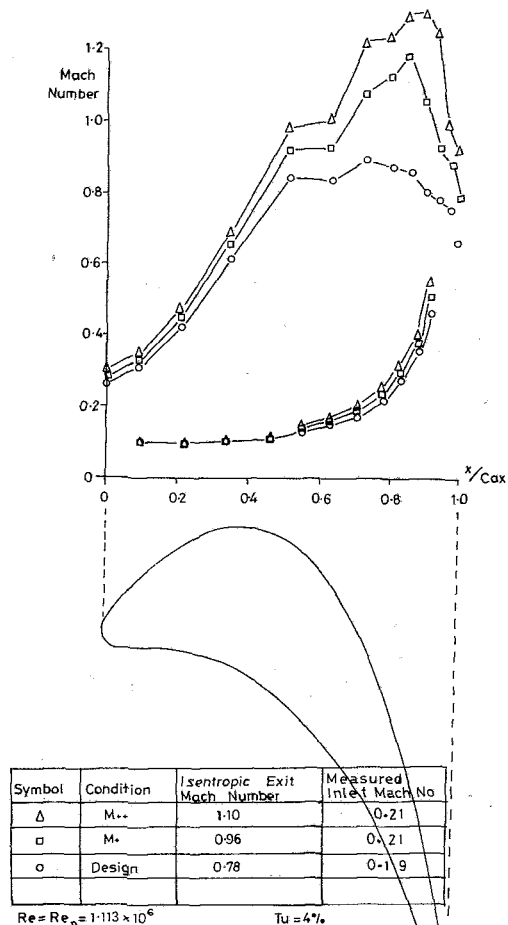ned were similar to those given by Kiock [8]. The total pressure probe had a negligible error, whilst the static pressure probe had an essentially constant error of about 1 percent of the dynamic head over the calibration range. The yawmeter calibration was linear over an incidence range of ± 8 deg.

The data from each traverse was stored on magnetic disks and analyzed using a suite of computer programs described by Nicholson [6]. The method used for the analysis was based on that of Amecke [9] but extended to include the energy

equation. The inclusion of the energy equation allows flow with a variation in total temperature (such as would occur in a cascade of film cooled blades) to be correctly analyzed. The analysis of the traverse results yields the following parameters:

(*i*) Total pressure loss coefficient

$$C_1 = \frac{P_{01} - P_{02}}{P_{02} - P_2}$$

(*ii*) Primary efficiency

$$\eta_{\text{prim}} = \frac{\text{Actual kinetic energy leaving cascade}}{\text{Ideal kinetic energy leaving cascade}}$$
$$= \frac{h_{01} - h_2}{h_{02} - h_{2s}}$$

(*iii*) Primary loss coefficient $C_2 = 1 - \eta_{\text{prim}}$

(*iv*) Mixed out exit angle β_2

(*v*) Axial velocity density ratio

$\Omega = \rho_2 V_2 \cos\beta_2 / \rho_1 V_1 \cos\beta_1$ (ideally $\Omega = 1.0$)

An experimental error investigation showed there to be an accuracy of about ± 4 percent on the calculated loss coefficient, and this is of the same magnitude as would be expected from measurements in continuous running cascades.

A series of diagnostic experiments was performed to demonstrate that the probe gave constant and repeatable results. The results of these runs showed that:

1 Loss coefficients calculated from either of the two measured wakes or from both of them were equal.

2 The measured wakes were one pitch apart.
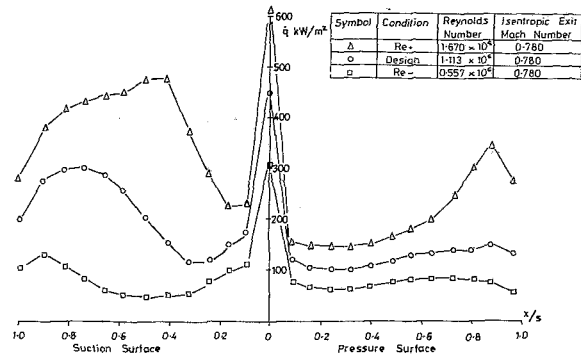
3 The midpassage total pressure loss was zero.

Symbol	Condition	Reynolds Number	Isentropic Exit Mach Number
△	Re +	1·670 × 10⁶	0·780
○	Design	1·113 × 10⁶	0·780
□	Re -	0·557 × 10⁶	0·780

Fig. 11 HS profile: effect of Reynolds number on heat transfer, 4 percent Tu

Symbol	Condition	Reynolds Number	Isentropic Exit Mach Number
○	Design	1·113 × 10⁶	0·780
□	M +	1·113 × 10⁶	0·960
△	M + +	1·113 × 10⁶	1·100

Fig. 12 HS profile: effect of exit Mach number on heat transfer, 4 percent Tu

Symbol	Condition	Reynolds Number	Isentropic Exit Mach Number
△	Re +	1·670 × 10⁶	0·780
○	Design	1·113 × 10⁶	0·780
□	Re -	0·557 × 10⁶	0·780

Fig. 13 HS profile: effect of Reynolds number on heat transfer, < 0.2 percent Tu

Symbol	Condition	Reynolds Number	Isentropic Exit Mach Number
○	Design	1·113 × 10⁶	0·780
□	M +	1·113 × 10⁶	0·960
△	M + +	1·113 × 10⁶	1·100

Fig. 14 HS profile: effect of exit Mach number on heat transfer, < 0.2 percent Tu

Symbol	Condition	Reynolds Number	Isentropic Exit Mach Number
△	Re +	1·670 × 10⁶	0·780
○	Design	1·113 × 10⁶	0·780
□	Re -	0·557 × 10⁶	0·780

Fig. 15 LS profile: effect of Reynolds number on heat transfer, 4 percent Tu

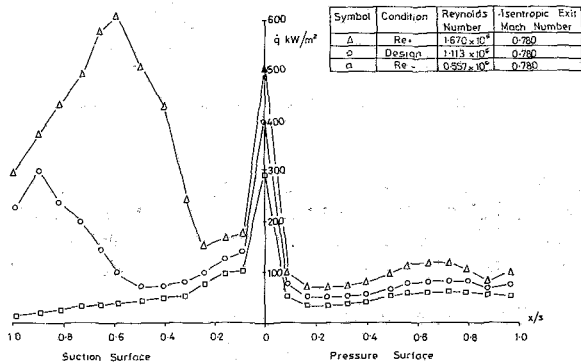| Symbol	Condition	Reynolds Number	Isentropic Exit Mach Number
○	Design	1·113 × 10⁶	0·780
□	M +	1·113 × 10⁶	0·960
△	M + +	1·113 × 10⁶	1·100

Fig. 16 LS profile: effect of exit Mach number on heat transfer, 4 percent Tu

4 The computed loss coefficients were independent of the direction and speed of the traverse.

5 The signal noise did not change the value of the computed data, and this value was equal to that from smooth traces more typical of continuous cascade data.

Pressure Distribution Results

The measured Mach number distributions around the HS profile at four exit Mach numbers are shown in Fig. 9. At all conditions the pressure surface flow undergoes a strong acceleration commencing at 60 percent axial chord. The suction surface flow is entirely subsonic at the design exit Mach number and at an exit Mach number of 0.9. At an exit Mach number of 0.96 the flow is just sonic over a portion of the suction surface. The data at an exit Mach number of 1.1 show a peak suction surface Mach number of 1.2, followed by a shock wave which reduces the flow Mach number to the correct value to satisfy the exit conditions. In general, the Mach number distribution around the HS profile is aerodynamically acceptable at all conditions in that it agrees well with the design predictions.
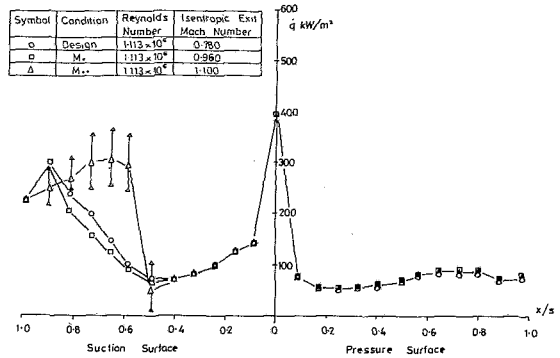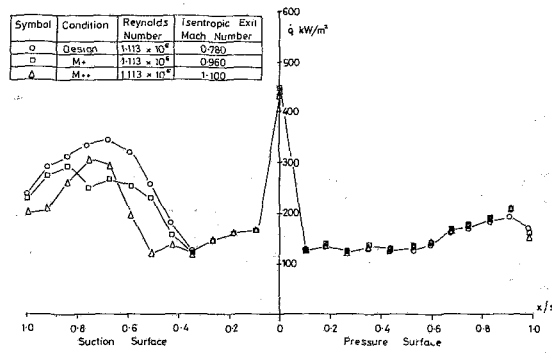
The measured Mach number distributions around the LS profile at three exit Mach numbers are shown in Fig. 10. The Mach number along the pressure surface is low until about 80 percent axial chord, when it is rapidly accelerated to the correct value for the exit Mach number. At the design exit Mach number the suction surface flow is diffused from about 80 percent axial chord although no flow separation has occurred. At an exit Mach number of 0.96 a peak suction surface Mach number of 1.2 is reached (cf. HS peak suction surface Mach number of 1.0 at this condition), followed by a rapid compression through a shock wave at approximately 85 percent axial chord. At an exit Mach number of 1.1, the peak suction surface Mach number rises to 1.3 at about 90 percent axial chord, also followed by rapid shock wave compression. In general, the Mach number distribution around this profile is aerodynamically undesirable because of the high suction surface diffusion rates imposed on the flow.

Schlieren photographs of both profiles are shown in Fig. 8 at an exit Mach number of 0.96. The moving probe, seen at

Table 1 HS profile heat transfer rate observations

	Suction surface	Pressure surface
Boundary layer transiton	A transition from laminar to turbulent heat transfer rates is clear at all except one condition, the lowest Reynolds number at low free-stream turbulence, when the boundary layer remains laminar over the entire surface.	A transition is not clearly evident at any condition except perhaps at the highest Reynolds number with the turbulence grid fitted.
Effect of Reynolds number	The mean heat transfer rate in both the laminar and turbulent regions is increased. The transition point moves forward as the Reynolds number is increased.	The mean transfer rate is increased as the Reynolds number increases, and there is a possible transition at the highest Reynolds number.
Effect of Mach number	Principal effect is observed at the highest exit Mach number, with a change in the location and length of transition. The effect of the shock waves is to produce large fluctuations on the heat transfer signals which are represented by the error bars on the data.	Negligible effect.
Effect of free-stream turbulence level	The heat transfer to the blade in the region of a laminar boundary layer is significantly increased at the high freestream turbulence level. The transition point moves forward at the higher turbulence level but the effect on the heat transfer with a turbulent boundary layer is insignificant.	The mean heat transfer rate is significantly increased (by a factor of approximately 2) for all conditions at the high freestream turbulence level. The data at the highest Reynolds number indicate a strong dependence of pressure surface transition on free-stream turbulence level.

Table 2 LS profile heat transfer rate observations

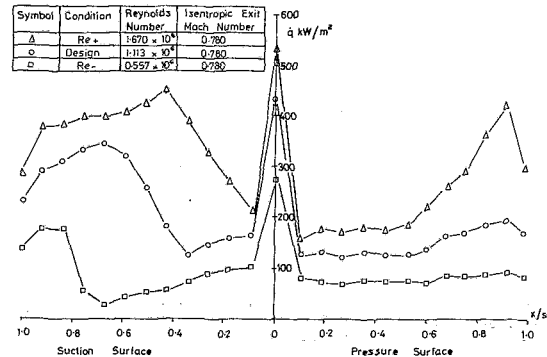|	Suction surface	Pressure surface
Boundary layer transiton	At all conditions, a boundary layer transition is evident when the heat transfer rate rises sharply.	The only clear pressure surface transition occurs at the highest Reynolds number, low free-stream turbulence condition. The identification of the type of pressure surface boundary layer is difficult to determine from the heat transfer data.
Effect of Reynolds number	Heat transfer rates increased and transition point moved forward as the Reynolds number is increased.	The heat transfer rate is increased as the Reynolds number increases. No changes in the point at which the heat transfer starts to rise are observed and thus the transition point cannot be located.
Effect of Mach number	There is no change in the heat transfer rate in the laminar part of the boundary layer. At an exit Mach number of 0.96 there is a reduction in the heat transfer rate at 75 percent surface length, probably caused by the shock wave observed from the Schlieren photographs at this condition. As the exit Mach number is further increased to a value of 1.1, the transition point is changed markedly.	There is an increase of heat transfer rate with Mach number and such an effect has not previously been observed. The Mach number distribution on the pressure surface changed significantly, thus increasing the accelerations of the flow. It is thought that the higher accelerations are thinning the turbulent boundary layer, hence increasing the heat transfer.
Effect of free-stream turbulence	The heat transfer is the laminar boundary layer region is increased, the transition point brought forward and the length of transition increased as the turbulence level is increased. The increase in transition length is probably due to the change in pressure gradient (due to transition movement) rather than the change in free-stream turbulence.	The heat transfer rate is increased at all conditions as the freestream turbulence level is increased.

Fig. 17 LS profile: effect of Reynolds number on heat transfer, < 0.2 percent Tu

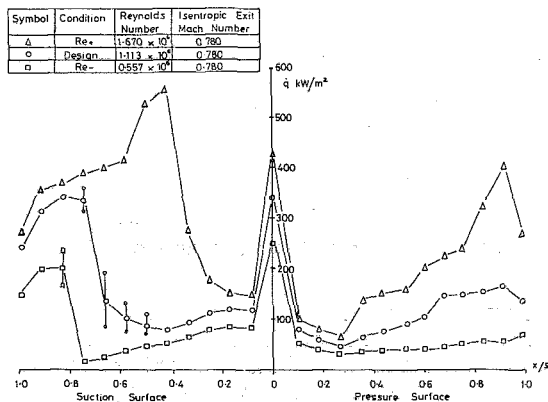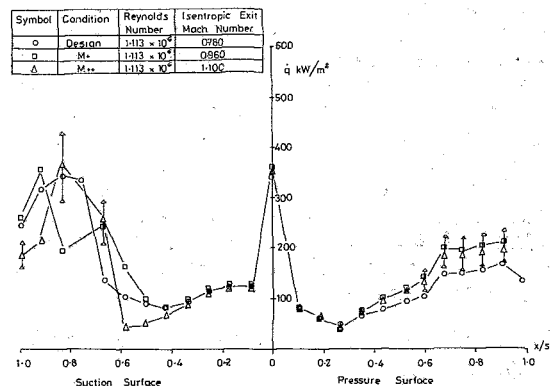Fig. 18 LS profile: effect of exit Mach number on heat transfer, < 0.2 percent Tu

Table 3 HS profile loss at two turbulence levels

	Turbulence level	$\dfrac{\Delta P}{P_{02}-P_2} \times 100\%$
Bottom wake		2.4
	<0.2%	
Top wake		2.2
Bottom wake		3.1
	4%	
Top wake		3.0

the bottom of the photograph, causes only minor disturbance to the flow, and the flow field was similar on photographs taken without the probe.

Heat Transfer Results

The effects of Reynolds and Mach number variations on the heat transfer rate to the HS blade at 4 percent free-stream turbulence level are shown in Fig. 11 and Fig. 12, respectively. The corresponding effects at low free-stream turbulence are shown in Figs. 13 and 14. The measured data are discussed in Table 1.

Boundary layer transitions were inferred from rapid increases of mean heat transfer rate along the blade and from the increase of heat transfer fluctuations in the transition region.

The effects of Reynolds and Mach number variations on the heat transfer rate to the LS blade at 4 percent turbulence are shown in Fig. 15 and Fig. 16, respectively. The corresponding effects at low free-stream turbulence are shown in Fig. 17 and Fig. 18. The data are summarized in Table 2.

Aerodynamic Loss Results

The loss coefficients measured for the two profiles with 4 percent upstream turbulence and cold flow are shown in Fig. 19. The coefficients are similar for both profiles over a wide range of exit Mach numbers. For the LS profile the loss, up to an exit Mach number of about 0.88, is slightly less than the HS profile. At this exit Mach number the loss of the LS profile increases rapidly due to onset of the suction surface separation. The loss of the HS profile remains low until an exit Mach number of 0.93 is reached, when the effects of shock wave boundary layer interaction become significant. The exit flow angle, β_2, of both profiles displays the expected trends. The axial velocity density ratio Ω is close to unity for all conditions.

Effect of Freestream Turbulence Level on Aerodynamic Loss

The loss of the HS profile was measured at two turbulence levels, 4 percent and < 0.2 percent, at design conditions Re and M. The results are shown in Table 3. An increase in free-stream turbulence level has increased the loss of this profile significantly. Other data, not shown here, taken on different cascades showed that the loss was not changed by an increase in free-stream turbulence. Consideration of the heat transfer data showed that the aerodynamic loss changed with turbulence level when the suction surface heat transfer rate changed. In the case of the HS profile data we have shown that at low free-stream turbulence levels the suction surface boundary layer has a late transition and is therefore thin and turbulent as it leaves the blade, whereas at 4 percent free-stream turbulence an early transition occurs, producing a thick-turbulent boundary layer as it leaves the blade.

Effect of Gas/Wall Temperature Ratio on Aerodynamic Loss

The downstream pressures and flow angles were measured with a hot (432 K) flow over both cascades. The
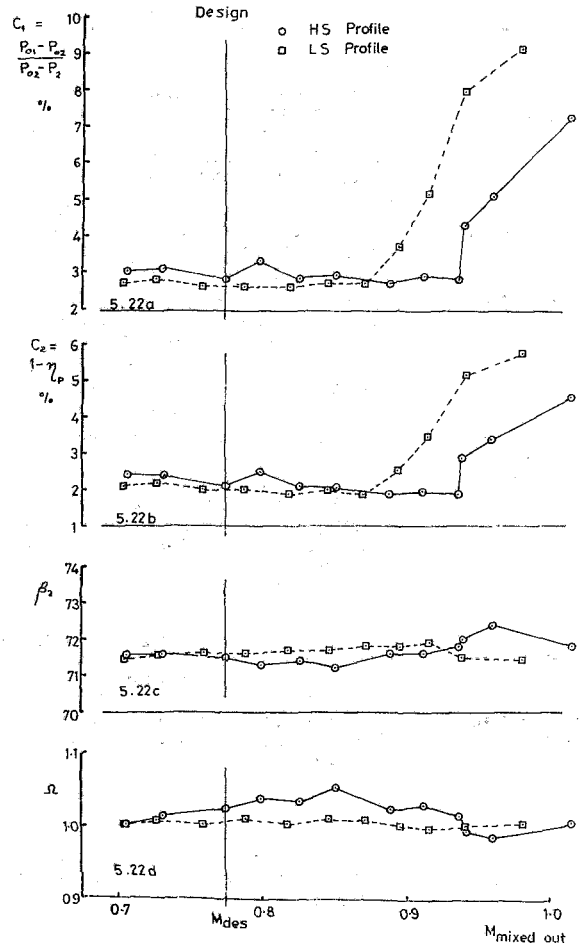
Fig. 19 Profile loss coefficient data, Tu = 4 percent, cold flow
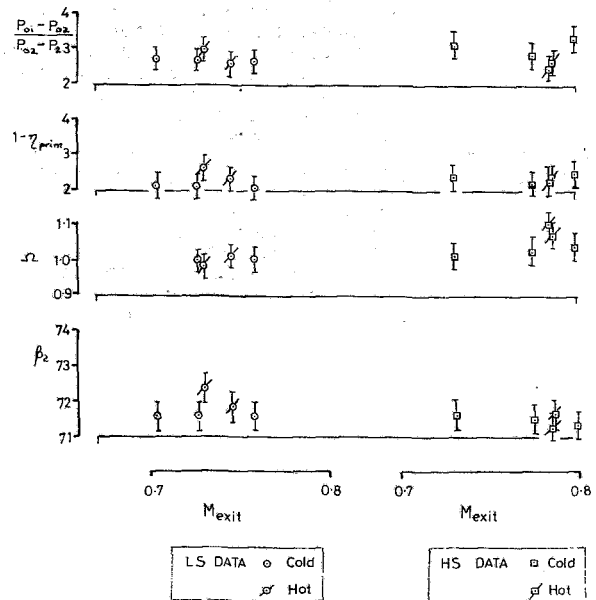

Fig. 20 Effect of heat transfer on loss coefficients

measurements were performed at an exit Mach number close to the design value and with the turbulence grid fitted. The results are compared with those obtained for cold (288 K) flow in Fig. 20. Within the experimental error the data points from both profiles lie on the curve formed by the cold data points.
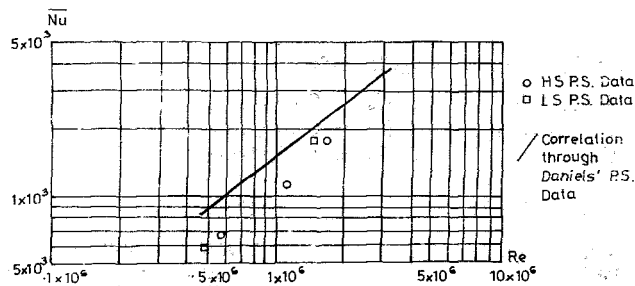
Fig. 21 Comparison of measured mean pressure surface Nusselt number of rotor profiles with Daniels's data

Discussion

A correlation between Nusselt number based on the mean pressure surface heat transfer coefficient and Reynolds number based on the mean of inlet and exit flow conditions and the blade true chord, derived from the data given by Daniels [10], is

$$Nu = 0.0308\, Re^{0.781} \text{ for } 5 \times 10^5 < Re < 2 \times 10^6$$

This type of correlation has been shown to be reasonable by comparison with other unpublished data and the above correlation is applicable to aerofoils designed using conventional aerodynamic data.

The data for the two profiles discussed here are compared with the correlation in Fig. 21. At the design Reynolds number a reduction in Nusselt number based on the mean pressure surface heat transfer coefficient of about 20 percent has been achieved by the optimized designs. This magnitude of reduction in the total pressure surface heat load would result in a significant reduction of blade metal temperature which would in turn be rewarded by an increase in blade life or a reduction in cooling air requirements. It is encouraging that the aerodynamic loss of the heat transfer optimized designs is low since any reduction in uncooled efficiency is undesirable.

As the suction surface design was not optimized for minimum heat transfer, no conclusions can be drawn for this surface.

Although both profiles show a significant reduction in pressure surface heat transfer it must be noted that the pressure surface boundary layer remained laminar over the entire surface of the HS profile. It is thought unlikely that this situation could occur in an actual high-pressure turbine. It is therefore not possible to conclude whether or not a practical heat transfer optimized design can be achieved by designing high-stagger aerofoils. A series of experiments to demonstrate whether or not relaminarization will occur on the HS cascade is to be performed to test the validity of the hypothesis.

Conclusions

1 A technique to measure aerodynamic loss in a transient cascade has been developed and diagnostic experiments have shown that the data obtained using the technique are of high quality.

2 The technique has been used to measure the aerodynamic loss of two heat transfer optimized turbine rotor aerofoils. The measurements show that aerodynamic efficiency is not compromised by a heat transfer optimized design.

3 The technique has been used to show that, for non-film-cooled profiles, the effects of heat transfer to the blade on aerodynamic loss are negligible but that free-stream turbulence can change the loss significantly.

4 A comprehensive set of heat transfer and aerodynamic data relating to modern high-pressure gas turbine rotors have been collected.

5 The heat transfer data show that a significant reduction in heat transfer to the pressure surface of rotor blades can be made by heat transfer optimization during the profile design.

6 The heat transfer optimization is essentially a study of the effect of blade stagger angle on pressure surface heat transfer. A short amount of further testing is to be made in an attempt to demonstrate boundary layer relaminarization. The results from this testing will permit the formulation of a general turbine design rule for high or low stagger blading for minimum pressure surface heat tranfer.

7 The experimental data published, together with detailed blade coordinates and cascade geometry, will help to fulfill the requirement for experimental data to enable prediction accuracy to be improved.

Acknowledgments

References

1 Stepka, F. S., "Uncertainties in Predicting Turbine Blade Metal Temperatures," *Proceedings of ASME/AIChE National Heat Transfer Conference*, Orlando, Florida, Paper 80-MT-23, 1980.

2 Graham, R. W., "Fundamental Mechanisms That Influence the Estimate of Heat Transfer to Gas Turbine Blades," NASA TM79128, 1979.

3 Martin, B. W., and Brown, A., "Factors Influencing Heat Tranfer to the Pressure Surface of Gas Turbine Blades," *International Journal of Heat and Fluid Flow*, Vol. 1, No. 3, 1979.

4 Schultz, D. L., Jones, T. V., Oldfield, M. L. G. and Daniels, L. C., "A New Transient Facility for the Measurement of Heat Transfer Rates," *Proceedings of AGARD Symposium*, Ankara, Turkey, CP229, 1977.

5 Jones, T. V., Schultz, D. L., and Hendley, A. D., "On the Flow in an Isentropic Light Piston Tunnel," MOD(PE)R and M 3I731, 1973.

6 Nicholson, J. H., "Experimental and Theoretical Studies of the Aerodynamic and Thermal Performance of Modern Gas Turbine Blades," D.Phil. thesis, Oxford University, 1981.

7 Oldfield, M. L. G., Jones, T. V., and Schultz, D. L., "On-Line Computer for Transient Turbine Cascade Instrumentation," *Transactions IEEE Aerospace Electronic Systems*, Vol. AES-14, No. 5, 1978, pp. 738-749.

8 Kiock, R., "Description of a Probe for Measurements of Two-Dimensional Wake Flow Properties," DFVLR, Braunschweig IB151-74/2, 1974.

9 Amecke, J., "Anwendung der transsonichen Ahnlichkietsregel auf die Stromung durchebene Schaufelgitter, Gottingen, 1968.

10 Daniels, L. C., "Film Cooling of Gas Turbine Blades," D.Phil. thesis, Oxford University, 1979.

APPENDIX 1

Coordinates of HS cascade blade

Axial chord	CAX = 26.681 mm
Tangent chord	CTN = 43.630 mm
Pitch	PCH = 36.794 mm

X MM.	Y MM.	X MM.	Y MM.
0.000	33.303	25.857	0.168
0.028	33.531	25.771	0.260
0.110	33.746	25.710	0.371
0.967	35.106	24.912	2.393
1.823	36.126	24.115	4.398
2.680	36.936	23.317	6.380
3.537	37.591	22.519	8.347
4.393	38.146	21.721	10.304
5.250	38.594	20.923	12.255
6.106	38.880	20.125	14.182
6.963	39.014	19.327	16.099
7.820	39.028	18.529	18.024
8.676	38.926	17.731	19.831
9.533	38.694	16.933	21.491
10.389	38.344	16.135	23.058
11.246	37.882	15.337	24.434
12.103	37.267	14.539	25.627
12.959	36.521	13.741	26.701
13.816	35.614	12.943	27.643
14.673	34.495	12.145	28.469
15.529	33.228	11.347	29.206
16.386	31.743	10.549	29.858
17.242	30.023	9.752	30.443
18.099	28.165	8.954	30.960
18.956	26.065	8.156	31.388
19.812	23.788	7.358	31.741
20.669	21.390	6.560	32.023
21.526	18.806	5.762	32.219
22.382	16.099	4.964	32.310
23.239	13.234	4.166	32.338
24.095	10.231	3.368	32.358
24.952	7.152	2.570	32.375
25.809	3.976	1.772	32.375
26.665	0.679	0.974	32.359
26.681	0.555	0.807	32.369
26.666	0.430	0.643	32.408
26.619	0.313	0.489	32.475
26.545	0.211	0.350	32.569
26.448	0.130	0.230	32.686
26.333	0.077	0.132	32.822
26.209	0.053	0.059	32.974
26.084	0.061	0.015	33.136
25.964	0.100	0.000	33.303

Coordinates of LS cascade blade

Axial chord	CAX = 26.681 mm
Tangent chord	CTN = 37.503 mm
Pitch	PCH = 36.794 mm

X MM.	Y MM.	X MM.	Y MM.
0.000	25.759	25.699	0.079
0.027	26.029	25.559	0.179
0.108	26.288	25.450	0.311
0.239	26.526	25.378	0.467
1.091	27.680	24.603	2.788
1.944	28.698	23.829	4.884
2.796	29.607	23.054	6.807
3.649	30.424	22.280	8.574
4.501	31.185	21.505	10.238
5.354	31.848	20.731	11.817
6.207	32.383	19.956	13.209
7.059	32.825	19.182	14.381
7.912	33.173	18.407	15.418
8.764	33.453	17.633	16.385
9.617	33.637	16.858	17.321
10.469	33.678	16.084	18.216
11.322	33.587	15.309	19.054
12.175	33.393	14.535	19.840
13.027	33.101	13.760	20.585
13.880	32.688	12.986	21.257
14.732	32.109	12.211	21.851
15.585	31.291	11.437	22.389
16.438	30.347	10.662	22.845
17.290	29.243	9.887	23.201
18.143	27.945	9.113	23.478
18.995	26.478	8.338	23.716
19.848	24.783	7.564	23.946
20.700	22.739	6.789	24.155
21.553	20.445	6.015	24.314
22.406	17.908	5.240	24.398
23.258	14.967	4.466	24.415
24.111	11.779	3.691	24.412
24.963	8.454	2.917	24.419
25.816	4.824	2.142	24.420
26.669	0.797	1.368	24.413
26.681	0.667	1.102	24.434
26.659	0.497	0.846	24.509
26.595	0.338	0.609	24.632
26.492	0.201	0.402	24.799
26.357	0.095	0.231	25.004
26.200	0.026	0.105	25.239
26.030	0.000	0.026	25.494
25.859	0.018	0.000	25.759

Full-Coverage Discrete Hole Wall Cooling: Discharge Coefficients

G. E. Andrews

M. C. Mkpadi

Department of Fuel and Energy,
University of Leeds,
Leeds LS2 9JT,
United Kingdom

Factors influencing the design of full coverage drilled plate wall cooling systems for gas turbine combustors are studied. It is shown that the large number of small diameter holes required result in a low Reynolds number operating regime. The physical features giving rise to the hole pressure loss are examined, and it is shown that under hot conditions heat transfer within the hole can appreciably alter the hole mass flow for a fixed pressure loss. It is shown that this effect may be used to estimate the hole outlet temperature and the results show that the heat transfer within the combustor wall may be very significant. The rise in coolant temperature within the wall appreciably alters the blowing rate and hence influences the hot gas side convective heat transfer to the plate. The influence of an impingement plate on hole discharge coefficients is also investigated and shown to be small.

Introduction

To satisfy the growing interest in the increase in both compressor outlet and turbine entry temperatures, either the properties of metal-alloys employed in gas turbine components, particularly the combustor wall and turbine blades, or the methods of cooling them must be improved. There is little hope of a dramatic improvement in material properties, apart from the development of high-temperature ceramic components; thus, techniques to cool metal walls efficiently are required. Almost all current gas turbine engines employ the film cooling technique for combustion chamber wall cooling. Film cooling requires approximately 40 percent of the total air to produce a combustor chamber exit gas temperatures of about 1500 K. If this technique is to be used for the future aero and industrial engines, where compressor delivery temperatures could be in the range of 700–1000 K and the desired combustor outlet temperatures could be in the range of 1700–2000 K, then combustor wall coolant air will have to be increased to approximately 60–70 percent of the total air [1] if film cooling is used. Thus, very little air would be left for combustion which would be highly unacceptable, especially for low calorific value fuels where a large proportion of the air is required to sustain combustion.

To overcome this future problem, the transpiration cooling technique has been proposed and recognized as a potential means of cooling gas turbine components with considerably less coolant air [2]. However, this technique is associated with some problems, namely, manufacture of the components, their mechanical strength, working temperature, oxidation and blockage of pores. The only known commercial gas turbine application of transpiration cooling is the use of finely woven wire mesh materials in turbine blades by the Curtiss-Wright Corporation [3]. Approximately 10 mm wide strips of the transpiration material were supported by fins along the length of the blade, each fin passage being fed with a metered coolant air supply. The application of this constructional technique to combustion chamber walls would be very difficult. In an attempt to overcome these problems, complex wall materials have been developed that attempt to simulate the heat transfer characteristics of porous materials whilst improving the mechanical reliability. Two such materials are Lammilloy, developed by Detroit Diesel Allison [4] and Transply, developed by Rolls Royce [5]. Both these materials involve a complex manufacturing process that creates internal flow passages longitudinally within the wall material thickness. These passages are fed by discrete holes on the inlet and exhaust side. These materials are not generally available, and it is not certain that they can achieve a satisfactory mechanical life, for industrial gas turbine applications.

For many years discrete hole cooling (sweat cooling or effusion cooling are other descriptions applied to the same process) has been used for cooling local hot spots in gas turbine combustion chamber walls. However, the flow rates used have been such that if applied to the whole flame tube area they would, in many cases, require an air flow in excess of that delivered by the compressor. It has been extensively used for local cooling as it permits a flame tube to be modified with minimal mechanical construction changes during a development programme. Very little published work exists whereby the potential of this relatively simple cooling technique can be assessed for full coverage flame tube wall cooling. Much of the data that does exist [6–8] refers to idealized test conditions with low mainstream turbulence and in most cases does not take into account the convective cooling that occurs within the walls.

The work reported here represents the first stages of a comprehensive evaluation of the full coverage effusion cooling technique. This initial work is aimed at a single-skin wall construction. This necessarily involves the full flame tube pressure loss being applied across the effusion cooling holes.

In this situation the pressure loss characteristics of the effusion cooling holes are important as these will determine the air split between the combustion and wall cooling system which encounter the same pressure loss. In this respect, the heating of the coolant as it passes through the wall acts as a throttle on the coolant air and will direct air from the effusion cooling to the combustor. Thus less air will be used for cooling than was designed for and wall overheating may result. This phenomena, the significance of which has not previously been realized, is examined and the theoretical predictions of the discharge coefficients are used to predict the mass flow changes. The phenomena are also shown to be useful to examine the heat transfer within the plate. For a constant mass flow, it is shown that the temperature rise of the coolant air within the plate may be predicted from the measured change in wall pressure loss.

Design Requirements

To select the hole geometries applicable to the full coverage combustion chamber wall cooling situation, it is necessary to know the required coolant mass flow per unit surface area. To enable realistic geometries to be selected, a survey of coolant flows per unit surface areas for a range of aero and industrial gas turbines was carried out. The results are shown in Table 1; the data were obtained by dividing the engine mass flow by the operating pressure and the flame tube surface area. The latter parameter was only evaluated approximately by taking combustion chambers as simple cylinders or annular rings; however, the resultant G values are reasonably reliable (± 10 percent) for the purposes of design evaluation. A typical proportion of the mass flow used for cooling in a conventional engine is approximately 40 percent. Table 1 indicates that a range of G values from 0.9 to 1.5 kg/sm^2 bar is representative of current cooling techniques. If the proportion of air used for wall cooling is to be reduced, then G values in the range 0.2–0.4 are required. This represents coolant flow in the range 10–20 percent of the total flow rate, which is a substantial reduction on conventional techniques.

Future high-temperature industrial gas turbines present a particularly formidable problem as the flame tube involves a much larger surface area than for aero engines. This is principally due to the very long transition ducts used between the combustor and the turbine, necessitated by the much lower pattern factor requirements for longer life. At present, many industrial gas turbines operate at temperatures that do not require the transition duct to be cooled. However, the high temperatures of future engines, particularly those operating with low calorific-value fuels derived from the gasification of coal, necessitate cooling of the transition duct, and this will approximately double the surface area to be cooled. For these types of industrial engines, a G value of 0.2 kg/sm^2 may be a minimum requirement for a coolant flow of 20 percent of the total air flow.

Coolant mass flow per square meter of wall area, G, is related to the total coolant flow area per square meter of wall

Table 1 Coolant air flow at 1 bar per unit surface area, G-kg/sm^2, for a range of gas turbines A–H

C%	A	B	C	D	E	F	G	H
10	0.22	0.14	0.24	0.20	0.23	0.33	0.10	0.30
20	0.45	0.28	0.47	0.41	0.47	0.67	0.20	0.60
30	0.67	0.43	0.71	0.61	0.70	0.99	0.30	0.90
40	0.90	0.57	0.95	0.82	0.93	1.32	0.40	1.20
50	1.12	0.71	1.18	1.02	1.16	1.65	0.50	1.50

area, A, and the combustor wall pressure loss, ΔP, by equation (1).

$$G = C_D A (2\rho \Delta P)^{0.5} \tag{1}$$

where C_D is the discharge coefficient of the coolant holes. The determination of this discharge coefficient is not straightforward, as the hole sizes are small and the metal thickness significant; this results in hole length to diameter (t/d) generally of at least 2 and for thick walls could easily be as high as 10. This paper discusses the determination of C_D and the factors that influence it.

Equation (1) may also be expressed as in equation (2)

$$G = C_D A P \left(\frac{2}{RT} \frac{\Delta P}{P} \right)^{0.5} \tag{2}$$

A coolant flow parameter, G_p, results from equation (2) which is independent of the combustor operating pressure, P.

$$G_p = \frac{G}{P} = \frac{uA}{RT} = C_D A \left(\frac{2}{RT} \frac{\Delta P}{P} \right)^{0.5} \tag{3}$$

For a fixed geometry and coolant pressure loss, G_p is only dependent on the operating temperature. G_p also essentially determines the coolant hole velocity, u, as shown by equation (4).

$$u = \frac{G}{\rho A} = \frac{G_p RT}{A} = C_D \left(2RT \frac{\Delta P}{P} \right)^{0.5} = C_D \left(2 \frac{\Delta P}{\rho} \right)^{0.5} \tag{4}$$

The present results are obtained at a nominal pressure of 1 bar. Equation (3) shows that for a constant G_p an equivalent 1 bar operational condition can be obtained by dividing G by the operating pressure in bars.

The coolant injection pressure loss for the single skin wall cooling systems considered here is set by the overall flame tube pressure loss. For design purposes, a pressure loss of 3 percent of the upstream pressure was chosen as a typical value for gas turbines. The influence of the wall pressure loss will be studied in future work. The specification of the pressure loss, discharge coefficient and coolant temperature allows the total coolant flow area per unit surface area to be derived from equation (3) for a specified G_p value. The precise hole geometry used to achieve this total area depends on the number of holes per square meter, n. The hole diameter, d, is given by equation (5) and the hole pitch, x, for a square array by equation (6).

$$d = \left(\frac{4}{\pi} \frac{A}{n} \right)^{0.5} \tag{5}$$

——————— **Nomenclature** ———————

A = total hole area per unit surface area (dimensionless)
C_c = contraction to coefficient
C_D = discharge coefficient
C_v = velocity coefficient
d = mean hole diameter, mm
e = surface roughness, mm
F_c = friction factor
G = coolant mass flow rate per unit surface area, kg/sm^2

G_p = G per bar, kg/sm^2 bar
K = hole dynamic pressure, Pa
M = hole Mach number
n = number of holes per unit surface area, m^{-2}
P = static pressure, bar (10^{5}Pa)
R = gas constant, 287.04 J/kgk
Re = Reynolds number $\rho ud/\mu$
t = plate thickness, mm
T = coolant temperature, k

u = mean coolant velocity in hole, m/s
x = hole pitch, mm
ΔP = static pressure loss across the plate, Pa
ρ = coolant density, kg/m^3
μ = coolant viscosity, kg/ms
γ = ratio of specific heats
ϵ = expansibility factor

$$x = n^{-0.5} \qquad (6)$$

Combining equations (5) and (6) gives equation (7) for the pitch to diameter ratio which is independent of the number of holes.

$$\frac{x}{d} = \left(\frac{\pi}{4A}\right)^{0.5} \qquad (7)$$

It may be shown that the hole Reynolds number, which is the major factor influencing the convective heat transfer coefficient within the plate, is given by equation (8)

$$Re = \left(\frac{4}{\pi A n}\right)^{0.5} \frac{G}{\mu} \qquad (8)$$

where μ is the coolant viscosity. Table 2 summarizes the influence of the number of holes and total hole area per square meter of wall for an assumed C_D of 0.8 and static pressure loss of 3 percent. Table 2 shows that, for low G values with the full flame tube pressure loss, x/d values of 10 or more are required. This is larger than most available data on effusion systems as most published results refer to the turbine blade cooling situation where the surface area to be cooled is much lower. Table 2 also shows that the hole Reynolds numbers are relatively low. In actual engines these will be higher in direct proportion to the pressure, but for large values of n will still be quite close to the transition regime for laminar to turbulent flow. Hole pressure loss and discharge coefficient, C_D, are strongly dependent on Reynolds number. For incompressible flow, Lichtarowicz et al. [9] have shown that for single holes the C_D is only independent of the hole Reynolds numbers, Re, for values greater than approximately 5000.

In the present work, C_D data were obtained at a pressure of 1 bar. For the same hole velocity and Mach number as under pressure conditions, the Reynolds numbers will be proportionately lower. To establish C_D values at Reynolds numbers of 5000 or higher for use in engine designs, tests have to be carried out at higher G values, which entail high plate pressure losses. Unfortunately, compressibility effects become important and a constant incompressible flow C_D is not obtained for the hole sizes in Table 2.

It may be shown using equation (4) that the hole Mach number, M, is given by equation (9).

$$M = \frac{u}{(\gamma RT)^{0.5}} = \frac{G}{PA}\left(\frac{RT}{\gamma}\right)^{0.5} = C_D \left(\frac{2}{\gamma} \frac{\Delta P}{P}\right)^{0.5} \qquad (9)$$

For a flame pressure loss of 3 percent and a C_D of 0.8, equation (9) gives a Mach number of 0.17. Compressible flow effects would not normally be significant at this value of Mach number. However, if to increase the hole Reynolds number, G is increased then the Mach number will increase in proportion as shown by equation (9). For many of the hole diameters in Table 2, choking flow conditions will occur before a high Reynolds number can be achieved as the increase in G can only be a factor of 5.9 before sonic flow in the holes occurs. Thus the testing of plates with a high value of n at high Reynolds numbers is not possible. To maximize the test Reynolds numbers the present work was carried out at ambient coolant temperatures as preheating the coolant only reduces the Reynolds number range.

Test Geometries

For industrial gas turbine applications, combustor weight is not an important factor. To maximize internal wall cooling effects, it was considered that a relatively thick wall would be advantageous and a thickness of 6.3 mm was chosen. Pressure loss data is reported for four test geometries as shown in Table 3. The range of n studied spans the values in Table 2. A test area of 152-mm square was used and this corresponds to

Table 2 Influence of number of holes on various design parameters for a C_D of 0.8 and 3 percent pressure loss

n m^{-2}	A	d mm	$\dfrac{x}{d}$	G kg/sm^2 300K	700K	Re (1 bar) 300K	700K
40,000	.001	0.20	24.9	0.07	0.04	743	253
	.005	0.45	11.1	0.34	0.22	1668	566
	.010	0.64	7.8	0.68	0.45	2362	802
	.030	0.98	5.1	2.04	1.35	4091	1389
20,000	.001	0.29	24.9	0.07	0.04	1057	359
	.005	0.64	11.1	0.34	0.22	2362	801
	.010	0.90	7.8	0.68	0.45	3337	1132
	.030	1.38	5.1	2.04	1.35	5780	1961
10,000	.001	0.40	24.9	0.07	0.04	1494	507
	.005	0.90	11.1	0.34	0.22	3337	1132
	.010	1.27	7.8	0.68	0.45	4721	1602
	.030	1.95	5.1	2.04	1.35	8177	2775
5000	.001	0.57	24.9	0.07	1.04	2110	716
	.005	1.27	11.1	0.34	0.22	4721	1602
	.010	1.80	7.8	0.68	0.45	6675	2265
	.030	2.76	5.1	2.04	1.35	11561	3923
2500	.001	0.80	24.9	0.07	0.04	2967	1007
	.005	1.80	11.1	0.34	0.22	6675	2265
	.010	2.55	7.8	0.68	0.45	9441	3204
	.030	3.91	5.1	2.04	1.35	16325	5549

Table 3 Test geometries

Hole manufacture	n	t mm	d mm	x mm	$\dfrac{x}{d}$	$\dfrac{t}{d}$
A (drilled)	4306	6.35	1.42	15.2	10.7	4.50
B (spark eroded)	4306	6.35	1.38	15.2	11.0	4.60
C (drilled)	4306	3.18	1.31	15.2	11.6	2.43
D (spark eroded)	26910	6.35	0.64	6.1	9.5	9.92

100 holes on a 10 × 10 square array for test plates A, B and C and 625 holes on a 25 × 25 array for test configuration D.

These two basic hole configurations were used as they enable the relative merits of a high hole number density to be explored. A large number of small diameter jets are likely to offer a better cooling film coverage with a lower coolant jet penetration than for designs with a smaller number of holes. The three test plates, A, B and C, with the same number of holes were designed to investigate wall thickness effects and method of hole manufacture.

The measurement of a mean hole size of each test plate presented a major problem. Commercially available calibrated tapered hole gauges were found to be the most suitable method as they measured the minimum inside hole diameter. Agreement with data using a travelling microscope was good; this method is time consuming and measures the surface hole diameter which may not necessarily be the minimum diameter. All holes were found to be square edged under microscope examination.

Experimental Arrangement

The coolant air supply to the test section was supplied by a small compressor, metered, and then fed to a plenum chamber on which was bolted the test 152-mm square section. This air could be electrically heated upstream of the plenum chamber. The plenum chamber had a drilled plate flow distributor mounted approximately 400 mm upstream of the test plate. A plenum chamber type of air feed is common in many industrial gas turbines. A static pressure ring was mounted 100 mm upstream of the test plate to monitor the pressure loss. For most of the pressure loss work, the air was discharged to atmosphere and no downstream static pressure tapping was necessary. However, some work was also carried out under crossflow conditions on the discharge side. For this
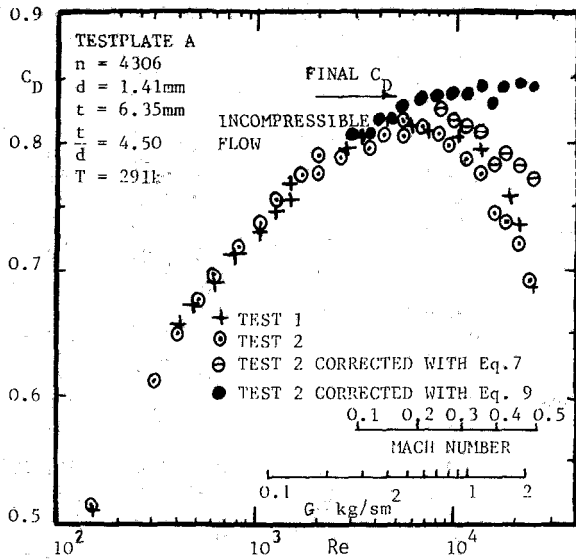
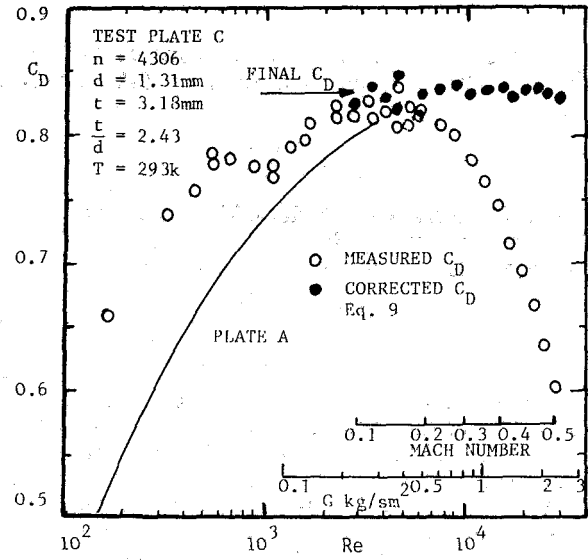Fig. 1 C_D as a function of Re for plate A

Fig. 3 C_D as a function of Re for plate C
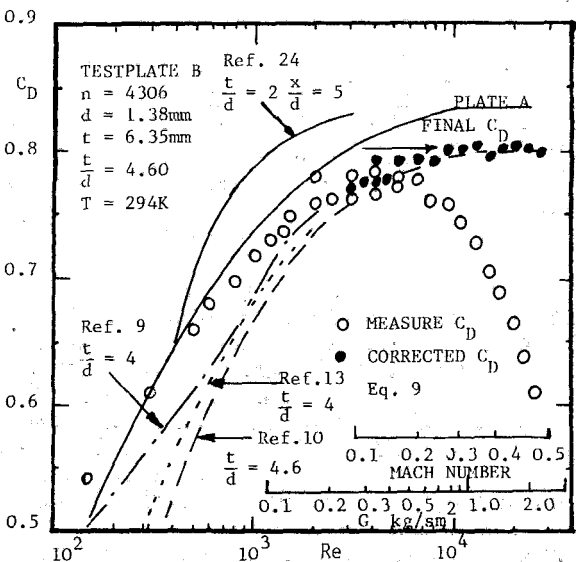

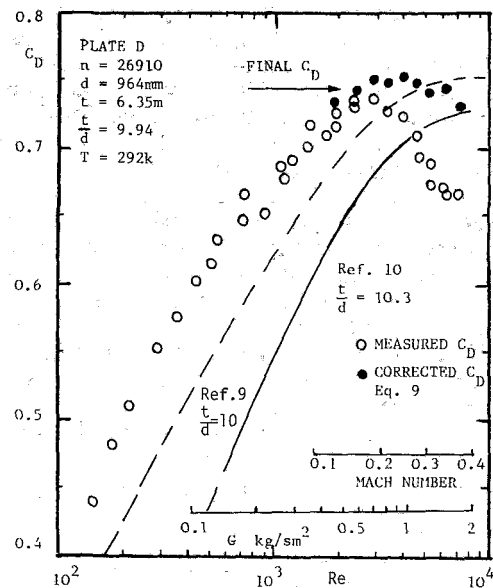Fig. 2 C_D as a function of Re for plate B

Fig. 4 C_D as a function of Re for plate D

the plenum chamber was mounted in the complete heat transfer rig. This need not be described in detail here, but essentially consisted of a 152 × 76 mm duct through which air flowed at a temperature controlled by upstream preheaters. This rig was used to heat the plates to study the influence of plate temperature on pressure loss.

Discharge Coefficient Results

Free Discharge. The discharge coefficient, C_D, under free discharge conditions, calculated according to equation (1), are shown as a function of Reynolds number, Re, in Figs. 1–4, for the four test plates. An error analysis of the measurements required by equation (1) showed an error of ±0.02 on C_D. Flow metering and hole diameter uncertainties were the principal contributors to the error; pressure loss was monitored using an electronic micromonometer with a resolution better than 1 percent of the reading. For the type A plate, two separate tests were carried out on separate occasions with the test plate removed from the plenum chamber

between the tests. The repeatability was good as shown in Fig. 1. All the figures show similar shaped curves with an increase in C_D with Re until a peak value is reached. This remains constant for further increase in Re but decreases at high Re. The dual scale of hole Mach number shows that this occurs at a Mach number above approximately 0.2 and is caused by compressibility effects within the hole. For the 100 hole plates (A, B, and C) this occurs at a hole Reynolds number of approximately 6000 compared with 3000 for the 625 hole plate. As the Re at which the C_D becomes independent of Re is only approximately 2000 in both cases, the reliable determination of this incompressible flow final C_D value is difficult.

Compressible Flow Effects. To correct the measured results for compressible flow effects an expansibility factor, ϵ, is required. This is defined as the ratio of the actual mass flow to the equivalent incompressible mass flow at the same pressure loss. The physical factors giving rise to the observed discharge coefficients will be shown later to consist of both flow separation and a vena contraction flow at the hole inlet

followed by nozzle flow after reattachment. Consequently, the nature of the expansibility correction was uncertain. Nakayama [10, 11] has presented C_D data for a single hole for incompressible flow using water and for compressible flow using air. The ratio of these gave an expansibility factor. All their results apply to the present situation where the approach flow area is very much larger than the hole area. It may be shown that their results for a sharp edged orifice, rounded nozzle, and cylindrical nozzle are given by equations (10-12), respectively.

$$\epsilon = 1 - .293\frac{\Delta P}{P} \qquad (10)$$

$$\epsilon = 1 - .598\frac{\Delta P}{P} \qquad (11)$$

$$\epsilon = 1 - .590\frac{\Delta P}{P} + .0107\frac{t}{d}\frac{\Delta P}{P} \qquad (12)$$

$$\text{for } 1.5 < \frac{t}{d} < 10$$

Equations (10) and (11) agree with the standard flow metering data for orifice plates and nozzles [12], consequently equation (12) for the present geometry may be considered to be reliable.

The t/d term in equation (12) is quite a small influence in the present situation. The maximum $\Delta P/P$ and t/d are approximately 0.3 and 10, respectively, giving a maximum value of approximately 0.03 for this term. Consequently, it may be concluded that the compressible flow effects are dominated by the reattached nozzle flow and not by vena contraction effects at the inlet. This is somewhat surprising as the Mach number would be locally much higher at the vena contraction.

Equations (10) and (12) have been applied to the measured results for the Type A test plate to illustrate the relative magnitudes of the two corrections. The results are shown in Fig. 1 and show that equation (12) produces a better correction with more of the data, falling on a constant incompressible flow C_D line at high Re. Equation (12) has been applied to the other results in Figs. 2-4, and they all show a good correction to a constant incompressible flow C_D value at high Reynolds numbers.

Final Incompressible Flow C_D. Figures 1-4 show that at high Re the incompressible flow C_D is independent of Re. These final C_D values together with the Reynolds number below which C_D starts to fall are listed in Table 4. Comparison of Test Plates A, C, and D give an indication of the influence of t/d. Over the range 2.4 to 4.5 t/d has no influence on C_D, as found by Asihmin [13] but for larger t/d there is a significant reduction in C_D as has been found by other workers [9, 10]. It is not intended to discuss the t/d effect in detail here, as more results are being obtained on a wide range of test plates, which will allow this effect to be determined more precisely.

Comparison of Test Plates A and B shows that the method of hole manufacture may have a significant influence on C_D. This can influence the hole entry profile and the internal hole surface roughness. The difference in C_D between Plates A and B could be due to higher surface roughness and hence higher wall frictional pressure loss for the spark eroded Test Plate B. However, the lack of influence of t/d on C_D for a range of t/d 2.5-4.5 indicates that wall friction effects may not be important in this region. Hence, differences in hole inlet geometry, with a possible slight rounding of the hole inlet is the likely cause of the differences between Plates A and B.

Comparison With Previous C_D Data. The Reynolds number at which the final C_D value is established is quite low and close to the laminar to turbulent transition region. The present results show a lower limit Re than for some other workers using single hole geometries [9, 10, 13]. The low Reynolds number region has higher C_D values than for previous single hole measurements as shown in Figs. 2 and 4. The reason for this is uncertain but could be an influence of the multihole geometry compared to single holes.

For the final C_D values, Table 5 lists a wide range of previous results for both single and multihole arrangements with a test t/d in the range 1-5. This shows that the present results are in very good agreement with previous measurements. The agreement between single hole and multihole data indicates that at high Reynolds number the present geometries, with an x/d of approximately 10, produce a situation where each hole is aerodynamically independent of its neighbor. This makes the low Re C_D results difficult to explain.

Table 4 Final incompressible flow C_D values

Test plate	$\frac{t}{d}$	Final C_D	Limit Re
A	4.47	0.83	5000
B	4.60	0.80	5000
C	2.43	0.83	2000
D	9.92	0.74	2000

Table 5

Ref.	Hole dia. mm	$\frac{t}{d}$	No. holes	Fluid	Final C_D
[14]	4.79	5.30	1	Air	0.83
[15]	1.59	1	1	Air	0.83
	0.79	1	1	Air	0.75-0.84
[11]	0.3-1.2	1.5-17	1	Air & Water	0.78(t/d=4.5)
[16]	1.57	2	1	Kerosine	0.80
	1.57	1	1	Kerosine	0.76
[13]	1.5-4	2-5	1	Water	.802(t/d=4.4)
[13]		3.33	1		0.814
[13]		3.0	1		0.82
[17]	12.7	2	1	Air	0.82
[18]	28	2.86	1	Water	0.82
				Gas Oil	0.822
[19]	1.57	4.0	1	Air	0.84
[20]	2.87	2.21	1/in^2	Air	0.822
[21]	0.48	1.84	1225	Air	0.84
[22]	3.2-6.4	1-2	Multi	Water & Air	0.85-0.87
[23]	0.38-1.9	1	Multi	Air	0.78
[24]	1.59-6.35	0.2-3.0	Multi	Air	0.774(t/d=3)
[9]	1.96-12.8	0.5-10	1	Water & Oil	.79(t/d=4.5)

Influence of Crossflow. Tests on the Type A plate under varying crossflow conditions, typical of those experienced in combustion chambers, showed that there was no influence of the crossflow on C_D for hole Reynolds numbers of approximately 5000. Dewey [25] has shown that the influence of crossflow on C_D is not significant until the ratio of hole outlet velocity to free stream velocity is less than 0.7. For a combustion chamber application this would only occur for hole velocities below approximately 30 m/s. This corresponds to the low Reynolds number regime in Figs. 1-4, below the constant C_D region.

Influence of Coolant Temperature on C_D. It was found that passing the coolant through a heated plate significantly influenced the C_D values. This effect will be discussed in detail later, but to establish that coolant temperature did not influence the C_D some tests were carried out on Plate A in the high Re region at various coolant temperatures. The coolant was electrically preheated. Figure 5 shows no significant influence on the final C_D value.

Impingement Discharge. Future work in this program involves the study of combined impingement and effusion systems. Impingement cooling systems are widely used in turbine blade cooling, but little information has been published on the pressure loss characteristics of such systems. The influence of an impingement plate on the final C_D value was studied for plate A. The impingement plate was positioned a distance z from the drilled plate and the air had an unobstructed discharge at the plate perimeter.

The results are shown in Fig. 6. They show that the impingement plate has no influence on C_D unless z/d is less than unity. As this situation is rarely used, it may be concluded that free discharge C_D values may be used for impinging jet applications. The reason for this result will be discussed later.

Prediction of C_D

The aerodynamic features influencing the pressure loss for flow through a long hole is summarized in Fig. 7. For the present range of hole sizes shown in Table 2 and the low G values, all practical designs involve hole length to diameter, ratios, t/d, greater than 1. The hole aerodynamics are such that the flow reattaches to the wall at a t/d of approximately 0.8 [26]. Thus, for all hole geometries of interest in the present applications flow reattachment will contribute to the pressure loss as summarized in Fig. 7.

Inlet and Exit Pressure Loss at High Re. The hole discharge is to a much larger area and hence the exit pressure loss will be one hole dynamic head, provided the velocity profile is uniform. At the hole inlet flow, separation occurs at the sharp edge and a vena contraction occurs as shown in Fig. 7. Flow expansion from the vena contraction to the reattachment point then creates a pressure loss. Wall friction losses are expected to be small in comparison with this inlet loss for small t/d.

Application of the Momentum and Energy Equations to the inlet flow gives equation (13) for the inlet pressure loss, K_1, in terms of hole dynamic heads.

$$K_1 = \frac{\Delta P}{\frac{1}{2}\rho u^2} = \left(\frac{1}{C_c} - 1\right)^2 \qquad (13)$$

A value of C_c of 0.61 has been found theoretically and experimentally to apply for a sharp edged orifice in a pipe whose area is much larger than that of the orifice [27]. No data exist for contraction coefficients in a pipe of downstream area of the same size of the orifice. However, it is usually found that it is the upstream area ratio that influences C_c. Taking the orifice plate C_c value of 0.61 gives the inlet pressure loss K_1 as 0.41. Although this is close to some experimental results [28],
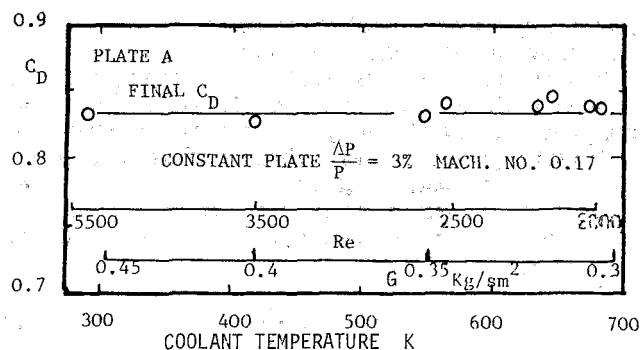
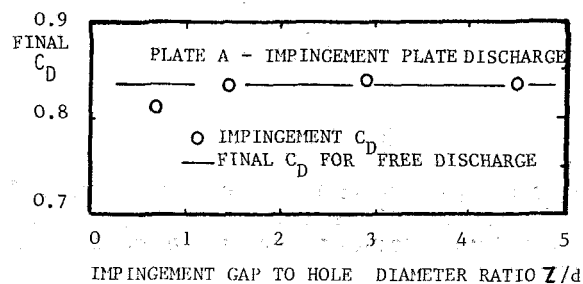

Fig. 5 Variation of C_D with coolant temperature
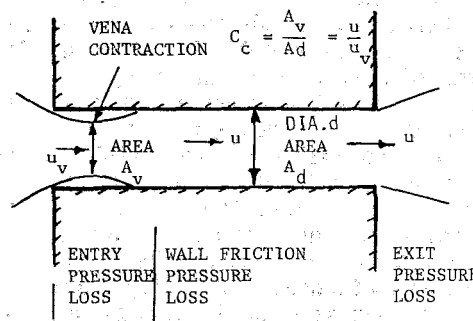

Fig. 6 Effect of impingement on C_D

Fig. 7 Hole aerodynamics

Table 6 Predicted values of C_D

K_1	C_D
0.41	0.842
0.50	0.816
0.58	0.796

an empirical value of 0.5 is often taken in the literature [29]. However, Benedict et al. [29] have reported a value for K_1 of 0.58, well above other data, and this has been recommended as reliable [30].

It may be shown using the mass continuity equation and equation (1) that the total pressure loss factor K_T is related to C_D by equation (14).

$$K_T = \frac{1}{C_D^2} \qquad (14)$$

For a short cylindrical tube the total pressure loss, K_T, is the sum of the inlet and exit pressure loss

$$K_T = K_1 + 1 \qquad (15)$$

Combining equations (14) and (15) gives a prediction for C_D, which is entirely dependent on the hole inlet loss K_1 provided the exit velocity profile is uniform. Table 6 shows the values of C_D predicted by the three values of K_1 discussed above.

The simple theory based on equation (13) gives good

agreement with the measured C_D for plates A and C, although plate B gives a value coincident with that based on a K_1 of 0.58. A factor ignored in the simple theory is the influence of upstream hole inlet frictional effects which cause the velocity distribution at the vena contraction to be nonuniform. This effect can be taken into account by the use of a velocity coefficient, C_V. This is defined as the ratio of the actual mean velocity to the ideal uniform velocity at the vena contraction. Application of the momentum and energy equations to the flow gives a modified equation of K_1.

$$K_1 = \left(\frac{1}{C_v C_c} - 1\right)^2 \tag{16}$$

For an inlet loss K_1 of 0.58 [29] and a C_c of 0.61 equation (16) gives a value for C_v of 0.93. This is unusually low, well below any of the values measured by Weisbach [29]. For the measured C_D of 0.83, a K_1 of 0.45 is required for which equation (13) predicts a C_v of 0.98. For a C_D of 0.82, K_1 is 0.49 and C_v is .965. Both these C_v values are reasonable [29], and it is therefore unlikely that the exit velocity profile deviates significantly from the uniform assumption.

Reynolds Number Effects. The influence of Re on C_D may be predicted by summating the inlet [30] and exit [31] pressure losses as a function of Re. Figure 3 shows that this gives a C_D prediction well below the observed results for Re < 2000 where laminar flow has been assumed. The final Reynolds number is based on the K_1 value of 0.58 of Benedict [29, 30]. For laminar flow a fully developed flow is assumed in [31] upstream of the exit. In the present situation the hole lengths are not sufficiently long for fully developed flow to be established [32]. A uniform exit velocity profile may be a more realistic assumption at all Re; Fig. 8 shows this gives a better agreement with the observed C_D values at low Re; however, it still predicts a sudden jump in the C_D values at the laminar to turbulent transition, which is not observed.

For the laminar region an inlet pressure loss of just over one dynamic head is given [30]. This arises as a pressure loss necessary to establish the velocity profiles of fully developed laminar flow and is clearly inappropriate in the present circumstances. Flow separation under laminar flow inlet conditions is not generally a feature considered in most classical theoretical predictions of inlet pressure loss [32]. However, there is experimental evidence [33, 34] that this does occur for Reynolds numbers higher than approximately 200. A gradual development of inlet flow separation with Re is compatible with the present results showing only a gradual steady increase in C_D with Re.

Wall Friction Effects. Wall friction effects may be predicted by including a frictional pressure loss, K_f, in equation (15).

$$K_f = 4F_c \frac{t}{d} \tag{17}$$

where the friction factor, F_c, depends on the hole surface roughness to diameter ratio (e/d) and Re [35]. For a t/d of 4.5 and a Re of 15,000, it may be shown that the effect of friction is to reduce C_D by 0.03 for a smooth hole and by .06 for an e/d of .02. Considering the very small hole diameters, an e/d of .02 is fairly realistic. The ability of the simple theory of inlet and exit losses to predict C_D without including friction losses indicates that for a t/d of 4.5 friction losses are likely to be negligible. This is due to the inlet aerodynamics of flow separation and reattachment occupying the bulk of the hole length. These considerations have important consequences for heat transfer within the wall, as this is likely to be dominated by inlet effects and to be much higher than for fully developed flow heat transfer.

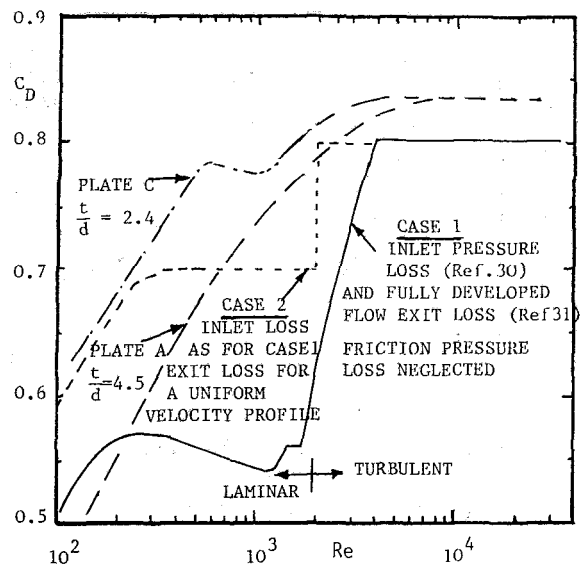For larger holes, wall friction effects are likely to be more

Fig. 8 Prediction of C_D

important. If it is assumed that wall friction only applies beyond a t/d of 4.5, then the Type D test plate results may be predicted. Using an inlet pressure loss K_1, of 0.45, a one dynamic head exit loss, and an e/d ratio of approximately 0.03, the observed C_D value of 0.74 is predicted. The surface roughness is 0.02 mm which is a reasonable value for a spark eroded hole.

Impingement Plate Effects. With an impingement plate the hole exit can no longer be considered a free discharge. The impingement plate forces the jets to turn through 90 deg at the hole exit. For a 90 deg bend with the downstream area larger than the upstream, the dynamic head loss at the bend varies from 1.1 for an area ratio of unity to 1.0 for an area ratio of 0.2 or less [36]. This means that the influence of the impingement plate on C_D should be negligible for all impingement gaps, z, except very small values. For small z values a hole exit bend loss of 1.1 dynamic heads is more appropriate. This coupled with an inlet pressure loss, K_1, of 0.45 gives a C_D of 0.80. The measured results in Fig. 6 support these considerations and show that free discharge coefficient data may be reliably applied to the impingement situation.

Heat Transfer Effects

It has been noted above that the presence of flow separation at the hole inlet, over a wide range of Re, including the laminar range, will result in very high heat transfer coefficients in the inlet region. In the present application with the wall temperature higher than the coolant there must be a temperature rise of the coolant as it passes through the wall. The hole pressure loss and C_D values are a function of the hole dynamic head as shown by equations (13–15). If the coolant density is altered by heat transfer then there must be an associated change in the dynamic head and hence an influence on the pressure loss.

Observed Influence of Wall Temperature. With the test plate mounted to simulate a section from a combustion chamber with a crossflow of hot gases, the plate is heated by these gases and cooled by the coolant air passing through it. Eventually an equilibrium plate temperature is reached. It is not intended here to discuss these plate temperatures and associated cooling effectiveness values. However, the influence of the heated plate and internal heat transfer was found to significantly alter the plate pressure loss.
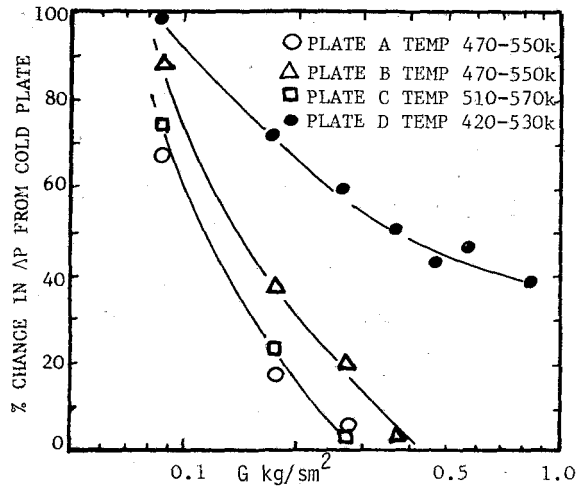
Fig. 9 Change in ΔP at low plate temperatures

Fig. 10 Change in ΔP at high plate temperatures

Fig. 11 Reduction in design G for high plate temperatures

For a constant coolant mass flow it was found that increasing the plate temperature, by increasing the crossflow gas temperature, resulted in an increase in the plate pressure loss. Also, if the plate pressure loss was maintained constant, as in the combustor situation, then the coolant mass flow decreased as the plate temperature increased. Typical examples of these pressure loss changes are shown in Figs. 9 and 10 for a range of plate temperatures and coolant flow rates.

The pressure loss is interdependent on both the wall temperature and the coolant flow rate. Even for the 3.2-mm thick Test Plate C the effect is significant. For a practical combustor wall temperature of approximately 1000 K the change in coolant flow rate, from a base design assuming cold flow pressure loss data, is very significant, as shown in Fig. 11. At low design coolant flow rates the reduction in flow rate can be as high as 30 percent. For designs with greater internal plate heat transfer the effect is more significant, as shown in Fig. 11. Consequently, it is considered that for a combustor wall with the full flame tube pressure loss, the full coverage effusion design should take into account this throttling effect of the wall when it is hot. The effect will also have a significant influence on the hot gas side film cooling process due to changes in blowing rate.

Prediction of Hole Outlet Temperature. Andrews et al. [33] have shown that the heat transfer processes with arrays of short holes in a heated plate are not well established. The basic process is generally assumed to consist of short tube heat transfer and a convective heat transfer equation proposed by McAdams [38]. Andrews et al. [33] have shown that this equation underestimates the heat transfer in sharp edge tube entries. Also, no account is taken of the heat transfer to the coolant as it passes over the backside of the plate prior to entry in the holes. This effect was found to be very significant and to form a major part of the plate heat transfer process which was independent of the plate thickness. However, uncertainties in the heat transfer process remain and the effect of heat transfer on pressure loss was considered to be a useful method of checking the reliability of the heat transfer model.

For a situation where the coolant temperature may change from the hole inlet to the outlet the dynamic head will be different for each term in equation (15). However, it is unrealistic to calculate the inlet dynamic head based on the coolant density as there is considerable air preheat prior to the hole entry as discussed above. If the change in pressure due to heating within the hole is only allowed for in the change in exit dynamic head, then hole outlet temperatures are overpredicted and may be higher than the plate temperature which
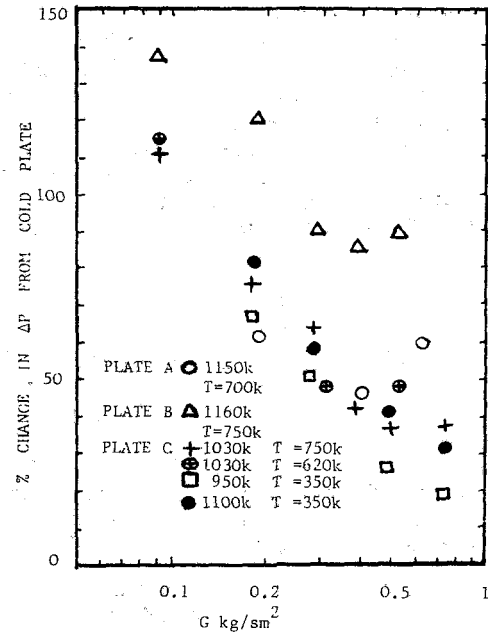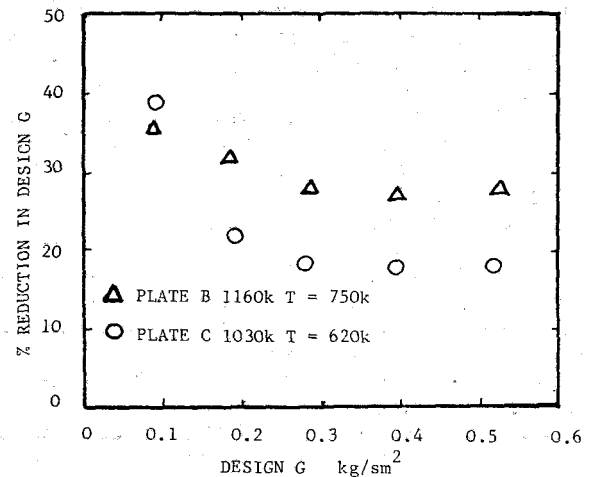
is impossible. These initial calculations led to the conclusion that it was more realistic to ascribe both the inlet and exit pressure loss to the outlet gas density. This will underestimate the outlet temperature, but will be much closer to reality than taking the inlet density at the coolant temperature.

The change in temperature resulting from the observed pressure loss change may be predicted using equation (1). The discharge coefficient has been shown to be independent of temperature and hence may be taken to be unaffected by the heat transfer process. The hole area A changes slightly due to expansion, but this effect is only of the order of 1–2 percent. For a constant coolant flow rate or G value, equation (1) shows that the observed pressure loss, ΔP_2, with heating by the plate may be used to predict the gas temperature within the hole, T_2. The relationship is given by equation (18), where T_1 is the coolant temperature at which the "cold" flow pressure loss, ΔP_1, was obtained.

$$T_2 = T_1 \frac{\Delta P_2}{\Delta P_1} \qquad (18)$$

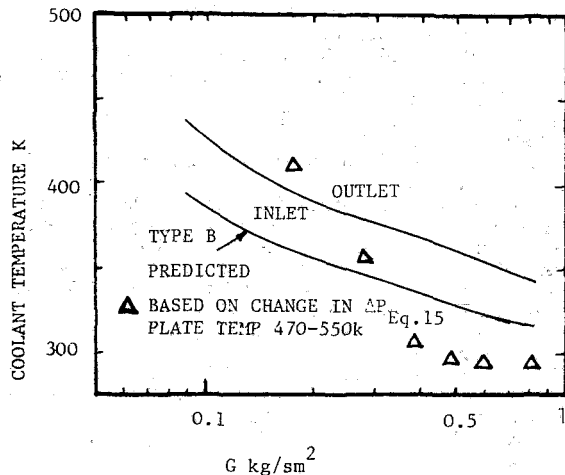This simple theory has been applied to some of the present

Fig. 12 Predicted coolant temperature rise for low plate temperatures
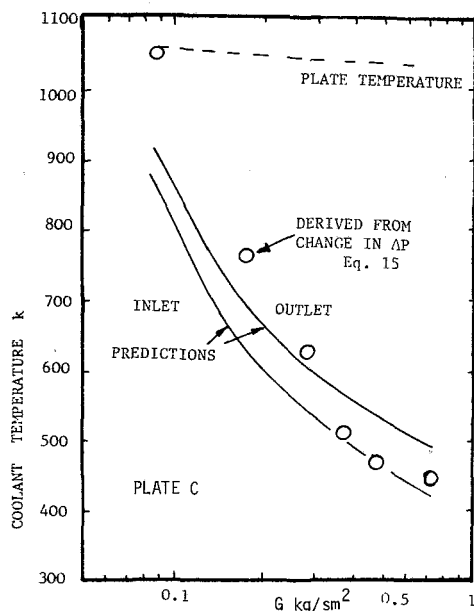

Fig. 13 Predicted coolant temperature rise for high plate temperatures

test plates, and the predicted outlet temperatures are shown in Figs. 12 and 13. The figures give data for relatively low and high crossflow gas temperatures. The results in Fig. 13 are close to practical gas turbine temperature conditions. Also shown in Figs. 12 and 13 are the heat transfer predictions of Andrews et al. [33] based on convective heat transfer correlations of the two main heat transfer processes within the plate. The hole inlet temperature predictions [37] are shown to demonstrate the importance of the backside heat transfer effect. The results based on equation (15) are in reasonable agreement with the heat transfer predictions. They are lower because of the assumption of a constant temperature throughout.

Conclusions

Factors influencing the discharge coefficients, C_D, of full coverage discrete hole cooling systems for gas turbine combustion chamber wall cooling applications have been investigated. Hole t/d effects have been shown to be significant only for $t/d > 4.5$, provided the hole was sufficiently long for reattached flow to be established. The Re range of interest in combustion is the low Re range from 500

up to 20000. At low Re it has been shown that flow separation occurs, and this results in a gradual increase in C_D with Re to reach a final value at an Re of approximately 2000. There is no evidence of any unstable transition region. The influence of inlet temperature and an impingement plate on C_D have both been shown to be negligible.

For practical applications where the wall is heated by the combustion gases the heat transfer processes within the wall have been found to significantly influence the pressure loss. This can result in a significant reduction in coolant air flow at a constant flame tube pressure loss across the effusion cooling system. This effect has also been shown to be capable of approximately predicting the hole outlet temperature. The associated change in blowing rate due to this internal wall heating influence can significantly influence the film cooling heat transfer.

References

1 Jackson, S. R., and Odgers, J., "Factors Influencing Heat Release in Combustion Chambers," *Combustion in Advanced Gas Turbine Systems*, Cranfield, 1968, Pergamon Press.

2 Bayley, F. J., Carnforth, J. W., and Turner, A. B., "Experiments on a Transpiration Cooled Combustion Chamber," *Proc. I. Mech. E.*, Vol. 187, 1973, p. 158.

3 Wolf, J. C., Moskowitz, S., and Manning, G. R., "Development of a High Temperature Turbine for Operation on Coal-Derived Fuel," ASME Paper No. 80-GT-188.

4 Nealy, D. A., and Reider, S. R., "Evaluation of Laminated Porous Wall Materials for Combustor Liner Cooling," ASME Paper No. 79-GT-100.

5 Wassell, A. B., and Bhangu, K., "The Development and Application of Improved Combustor Wall Cooling Techniques," ASME Paper No. 80-GT-66.

6 Le Brocq, P. V., Saunder, B. E., and Priddin, C. H., "Discrete Hole Injection as a Means of Transpiration Cooling—An Experimental Study," *Proc. I. Mech. E.*, Vol. 187, 1973, p. 149.

7 Kasagi, N., Hirati, M., and Kumaha, M., "Studies of Full Coverage Film Cooling Part 1: Cooling Effectiveness of Thermally Conductive Wall," ASME Paper No. 81-GT-37.

8 Metzger, P. E., Takeuchi, D. I., and Kyenstler, P. A., "Effectiveness and Heat Transfer With Full Coverage Film Cooling," ASME JOURNAL OF ENGINEERING FOR POWER, July 1973, p. 180.

9 Lichtarowicz, A., Duggins, R. K., and Markland, E., "Discharge Coefficients for Incompressible Iron-Cavitating Flow Through Long Orifices," *J. Mech. Eng. Sci.*, Vol. 7, 1965, p. 210.

10 Nakayama, Y., "Action of the Fluid in the Air Micrometer, I," *Bull. JSME*, Vol. 4, 1961, pp. 507–515.

11 Nakayama, Y., "Action of the Fluid in the Air Micrometer, II," *Bull. JSME*, Vol. 4, 1961, pp. 516–524.

12 Bean, H. S., ed., *Fluid Meters*, ASME, 6th ed., 1971.

13 Asihmin, V. I., et al., "Discharge of a Real Fluid from Cylindrical Orifices," *Oil Ind.*, Moscow, Vol. 9, 1961, p. 55.

14 Jackson, R. A., "The Compressible Discharge of Air Through Small Thick Plate Orifices," *App. Sci. Res.*, Vol. A13, 1963, p. 241.

15 Grace, H. P., and Lapple, C. E., "Discharge Coefficients of Small Diameter Orifices and Flow Nozzles," ASME *Transactions*, Vol. 73, 1951, p. 639.

16 Spikes, R. H., and Pennington, G. A., "Discharge Coefficients of Small Submerged Orifices," ASME *Transactions*, Vol. 173, 1959, p. 661.

17 Deckker, R. E. L., and Chang, Y. F., "An Investigation of Steady Compressible Flow Through Thick Orifices," *Proc. I. Mech. E.*, Vol. 180, 1965, p. 321.

18 Koennecke, W., "New Nozzle Shapes for Low and Medium Reynolds Numbers," *Forch Auf Dem Geleif Des Ingenieur Wesens*, Vol. 9, 1938, p. 109.

19 Rhode, J. E., Richards, H. T., and Metger, G. W., "Discharge Coef-

ficients for Thick Plate Orifices with Approach Flow Perpendicular and Inclined to the Orifice Axis,'' NASA TN 5467, 1969.

20 Dannenberg, R. E., Gambucci, B. J., and Weiberg, S. A., "Perforated Sheets as a Porous Material for Distributed Suction and Injection," NACA TN 3669, 1956.

21 Stokes, G. M., Davis, D. D., and Sellers, T. B., "An Experimental Study of Porosity Characteristics of Perforated Materials in Normal and Parallel Flow," NACA TN 3085, 1954.

22 Mayfield, F. D., et al., "Perforated Plate Distillution Columns," *I/EC*, Sept. 1952, p. 2238.

23 Damerow, W. P., et al., "Experimental and Analytical Investigations of the Coolant Flow Characteristics in Cooled Turbine Aerofoils," NASA CR 120883, 1972.

24 Smith, P. L., and Van Winkle, M., "Discharge Coefficients Through Perforated Plates," *JAIChE*, Vol. 4, 1958, p. 266.

25 Dewey, P. E., "A Preliminary Investigation of Small Inclined Air Outlets at Transonic Mach Numbers," NACA TN 3442, 1955.

26 Ward-Smith, A. J., *Pressure Losses in Ducted Flows*, Butterworths, 1971.

27 Rouse, H., and Abdul-Fetoug, A. H., "Characteristics of Irrational Flow Through Axially Symmetric Orifices," ASME *Transactions*, Vol. 72, 1950, pp. 421–426.

28 Osborne, W. C., and Turner, C. G., eds., *Woods Practical Guide to Fan Engineering*, 2d ed., 1961, Woods of Colchester, p. 119.

29 Benedict, R. P., Carlucci, N. A., and Swetz, S. D., "Flow Loses in Abrupt Enlargements and Contractions," ASME JOURNAL OF ENGINEERING FOR POWER, Vol. 88, 1966, pp. 23–81.

30 ESDU, "Pressure Losses in Flow Through a Sudden Contraction of Duct Area," ESDU 78007, Dec. 1977.

31 ESDU, "Flow Through a Sudden Enlargement of Area in a Duct," ESDU 72011, June 1972.

32 Ward-Smith, A. J., *Internal Fluid Flow*, Clarendon Press, Oxford, 1980.

33 Astarita, G., and Greco, G., "Excess Pressure Drops in Laminar Flow Through a Sudden Contraction," *I/EC Fundamentals*, Vol. 7, 1968, p. 27.

34 Barozzi, G. S., Dumas, A., and Pompoli, R., "The Influence of an Abrupt Convergence on Heat Transfer in Circular Ducts," *International Journal of Heat Fluid Flow*, Vol. 3, 1982, pp. 45–51.

35 ESDU, "Friction Losses for Fully Developed Flow in Straight Pipes," ESDU 66027, Sept. 1966.

36 Kazantsev, E. I., *Industrial Furnaces*, MIR Publishers, Moscow, 1977.

37 Andrews, G. E., Gupta, M. L., and Mkpadi, M. C., "Heat Transfer Within Arrays of Short Holes in a Heated Plate," to be published.

38 McAdams, *Heat Transmission*, McGraw-Hill, Kogatusha, 3d ed., 1954, pp. 224–226, 239.

S. L. K. Wittig

Professor.
Mem. ASME

O. M. F. Elbahar[1]

Lecturer.

B. E. Noll

Research Assistant.

Lehrstuhl und Institut für
Thermische Strömungsmaschinen,
Universität Karlsruhe,
D-7500 Karlsruhe, 1, West Germany

Temperature Profile Development in Turbulent Mixing of Coolant Jets With a Confined Hot Crossflow

The mixing of coolant air jets with the hot gas exiting the primary zone is of major importance to the combustor exit temperature profile. Geometry and momentum flux ratios are the dominant parameters. A theoretical and experimental study of single as well as opposite-wall jet injection into a hot crossflow reveals the applicability and limitations of existing correlations. Modified correlations are presented for opposite-wall injection with jets of different momentum flux ratios. The advantages in applying field methods for describing the flow are discussed.

Introduction

Operation at elevated turbine inlet temperatures imposes stringent limitations on the quality of the combustor exit temperature profiles, which should be matched carefully to the blade stress levels in order to maintain extended lifetime and ensure reliability.

The temperature profile at the combustor exit depends decisively on the mixing of the cooling air jets with the combustion products in the dilution zone [1, 2, 3]. Prediction methods are here of cardinal importance not only due to the number of parameters involved but also because of the increasing costs of experimental investigations. The penetration and mixing characteristics of rows of cooling jets injected into a hot confined crossflow therefore have been the subject to several experimental studies [4, 5]. The experimental results of Walker and Kors [4] of the mixing of a row of jets with a confined, plane, hot crossflow (see Fig. 1) have been used extensively in developing empirical correlations of the scaling parameters [2, 6, 7] to predict the temperature distribution.

These correlations are applicable only for single-wall injection, as shown in Fig. 1(a). However, for opposite-wall injection, which is of high importance for the design of annular combustors, Cox [3] suggested that the correlations for the single-wall injection could be used with some modification. For the particular case of two, directly opposite rows of jets, Fig. 1(b), experiments show (e.g., [8]) that the plane of symmetry between the two rows acts almost like a wall. Cox utilized this fact to define an "equivalent duct height" for each row of jets, which depends on the ratio of their momentum fluxes. In considering annular combustors, he also made suggestions concerning the case of opposite-

Table 1 Parameter variation for single-wall injection

No.	S/D_j	H/D_j	J	T_∞	T_j	u_∞
1	5	15.15	64.9	556.0	316.0	18.8
2	2.5	12.5	26.4	547.4	313.9	18.4
3	2.5	12.5	56.1	428.1	311.5	14.3
4	2.5	12.5	53.6	553.9	315.9	18.5

wall, staggered jet injection. However, additional tests are required in supporting their applicability.

The present work represents an experimental and theoretical study of the mixing process between rows of jets and a hot confined crossflow. Single-wall as well as opposite-wall injection with equal and with different momentum flux ratios of each row of jets have been investigated.

With the aid of the experimental results, the applicability and limitations of the empirical multiple jet correlations (e.g., [2, 7]) for the case of double wall, directly opposite jets have been demonstrated.

Prediction methods based on the numerical solution of the time-averaged conservation equations of mass, momentum, and energy are also applied to compute the temperature profiles in mixing processes. Various aspects of the numerical procedure are described elsewhere [9, 10].

Experimental Facility

The experimental facility is shown schematically in Fig. 2. Air from the compressor is subdivided into the primary and the mixing jet flow. Adjustable valves and standard orifice meters facilitate accurate control and volumetric flow measurements within the three ducts, respectively. The primary air flows through an electric heater ($\Delta T \approx 350$ °C) into a settling chamber fitted with turbulence grids. It enters the test section of 300-mm × 100-mm cross-sectional area through a nozzle with a contraction factor of 20.8. The
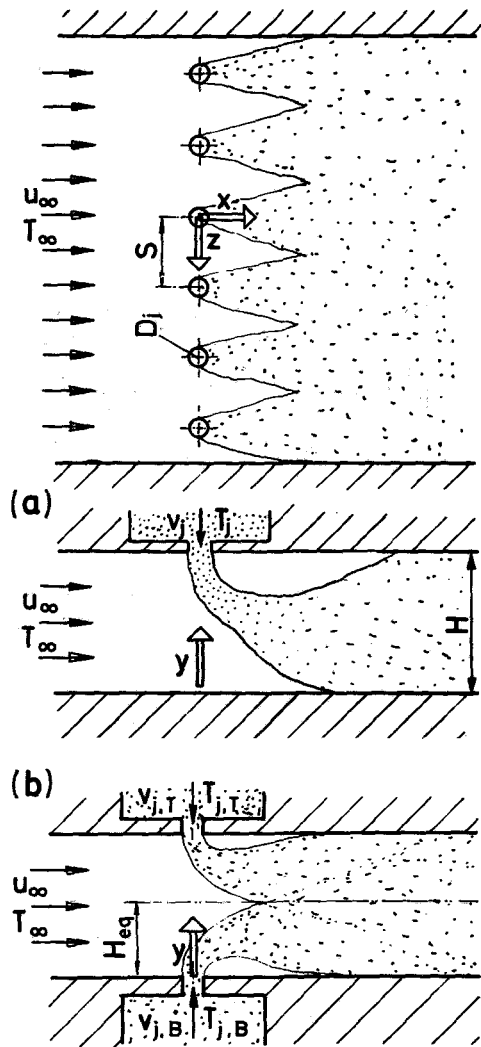
Fig. 1 Mixing of cooling air jets with hot main flow: (a) single-wall cooling air injection; (b) opposite-wall cooling air injection

mixing air is led into the secondary air chambers, where the flow is stabilized before it is injected into the test section through exchangeable orifice plates mounted in the top and bottom walls of the test section. The gases are exhausted into a suction nozzle at the exit of the test section as shown in Fig. 2. The temperature profile at the entry of the test section was found to be uniform within $\pm$ 1 percent. The field measurements of the temperature were accomplished by means of a rake consisting of 13 total temperature/total pressure probes. The temperature distribution at the walls has been also recorded by means of calibrated NiCr-Ni thermocouples. Due to the symmetry of the flow, it is sufficient to measure between the two planes of symmetry only, i.e., Z/S = 0 and Z/S = 0.5 (Fig. 1).

Computer-assisted data acquistion is necessary as a large matrix of data is obtained and has to be analyzed. The results presented here are concerned with temperature measurement only. Simultaneous temperature and velocity field measurements have been made as well.

Results and Discussion

Single-Wall Injection. In a first attempt to clarify the accuracy of the numerical calculations and to provide a comparison with the existing corrrelations, a sequence of tests was initiated with single-wall injection. Table 1 illustrates the variation of the relevant parameters, such as jet and duct geometry, momentum flux ratio, and respective temperatures.

As shown in Figs. 3(a) and 3(b) for the conditions of test No. 2 (Table 1), the agreement of the measurements in the central plane (Z/S = 0) as well as those for Z/S = 0.4 at X/H = 0.25, with the correlations especially by Holdeman and Walker [7], are quite satisfactory. It should be noted that the measurements were taken at Z/S = 0.4 (not at Z/S = 0.5) due to the specific design of the probe rake. Also, three-dimensional calculations [10] reveal a slight shift of the temperature minimum towards the injection wall of the duct, whereas the earlier correlations [2, 3] can lead to an overprediction of the temperature at the jet-opposed wall (Z/S = 0.4) with $T > T_\infty$, which is physically impossible, and an underprediction towards Y/H = 0.8. It should be noted here, that in applying the correlations, conservation laws are not
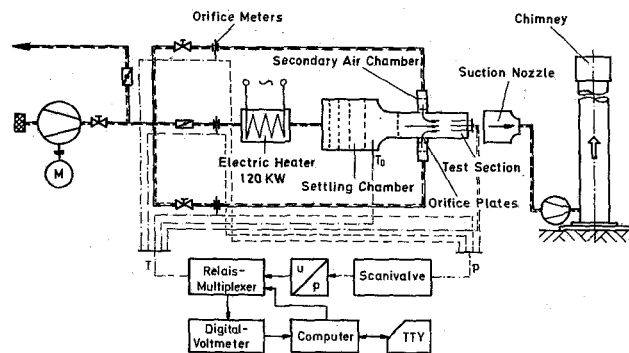

Fig. 2 Experimental facility

Nomenclature

A = area
D = diameter
H = duct height
J = momentum flux ratio
S = spacing between centerlines of adjacent orifices
T = temperature [K]
u = velocity [m/s]
X = distance in flow direction

Y = distance in direction perpendicular to X
Z = distance in direction perpendicular to both X and Y
θ = dimensionless temperature ratio

Subscripts

B = bottom wall
eq = equivalent

id = energy-balance state
j = jet
min = minimum value
T = top wall
∞ = mainstream

Superscripts

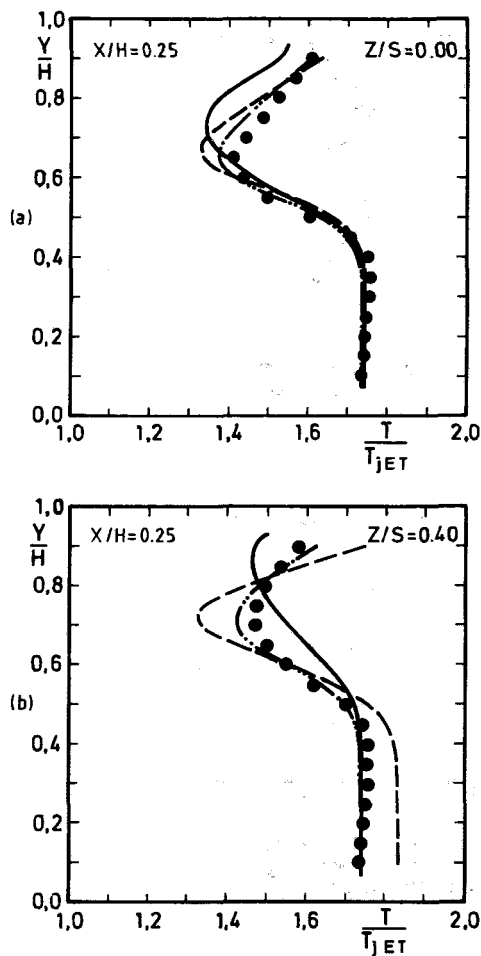$+$ = plus side or side away from jet entrance wall

Fig. 3 Temperature profile development with single-wall injection (Test No. 2, Table 1): ____ three-dimensional calculation, present paper; - - - Cox; - - - Holdeman and Walker; ● experiment, present paper
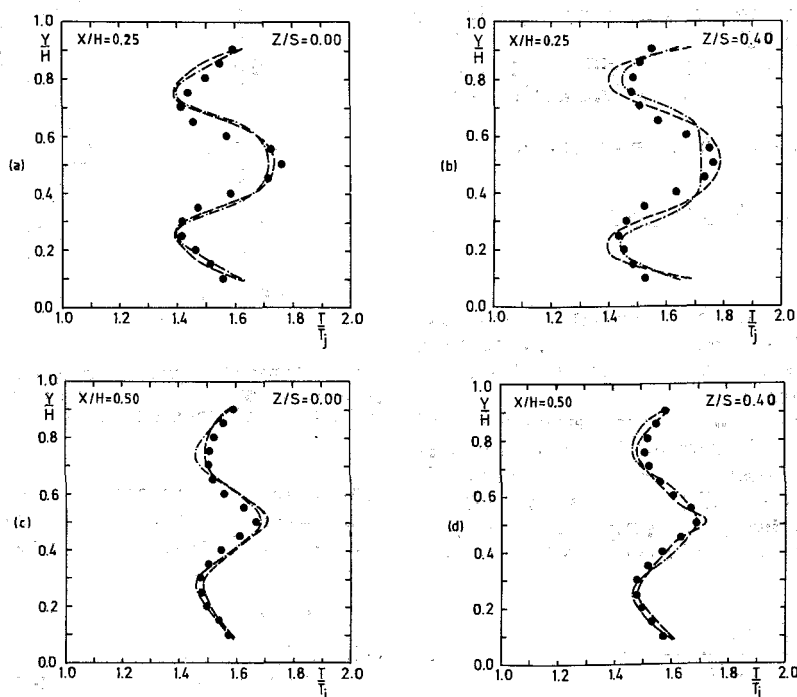
Table 2 Parameters combination for opposite-wall injection

No.	J_T	J_B	T_∞	T_j	u_∞	S/D_j
5	25.0	24.0	554.4	316.3	18.4	2.5
6	54.1	56.6	434.4	310.5	14.3	2.5
7	18.2	33.3	433.0	309.1	14.4	2.5
8	10.3	46.1	430.8	310.9	14.4	2.5
9	8.9	38.7	554.6	316.4	18.5	2.5
10	57.8	60.24	558.4	318.7	18.5	2.5

always strictly observed. In general, however, in predicting temperature profiles, good agreement is obtained between the various calculations and the measurements.

Opposite-Wall Injection. In extending the results from single-wall injection to conditions found in combustor application, i.e., opposite-wall injection with differing momentum flux ratios as experienced in annular combustors, a sequence of experiments with directly opposite jets (see Fig. 1(b)) was initiated. Typical test conditions are shown in Table 2.

Cox [3] suggests that in applying his correlations, a symmetry plane, which is observed with directly opposite jets, can be assumed representing a solid (fictitious) wall. The temperature distribution, therefore, can be obtained from the superposition of two separate profiles [3]. In positioning the plane of symmetry, the following equation has been suggested by Cox to determine an equivalent height H_{eq} (see Fig. 1(b))

$$H_{eq} = \frac{A_{j,B} J_B}{A_{j,B} J_B + A_{j,T} J_T} \cdot H \tag{1}$$

The temperature is calculated from

$$\theta(H_{eq}) = \frac{\theta^+_{min,T} + \theta^+_{min,B}}{2} \tag{2}$$

For details, see the analysis presented by Cox [3]. In comparing the profiles obtained using the correlations with the experimental data, good agreement was observed only for identical and small momentum flux ratios as shown in Figs. 4(a) to 4(d).
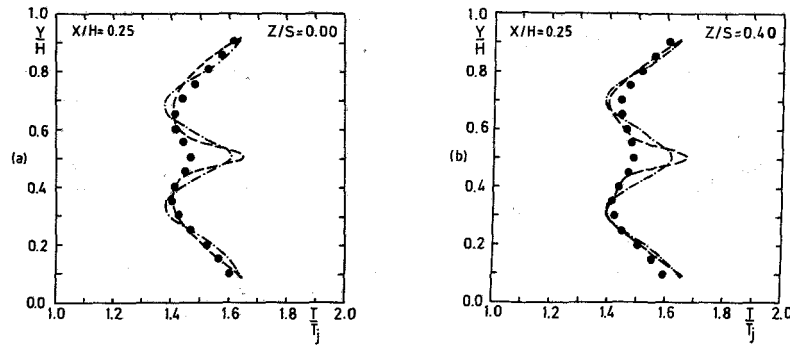

Fig. 4 Temperature profile development with double-wall injection (Test No. 5, Table 2): - - - Cox; - - - Holdeman and Walker; ● experiment, present paper

Fig. 5 Temperature profile development with double-wall injection (Test No. 10, Table 2):· · · Cox;· · · Holdeman and Walker;● experiment, present paper
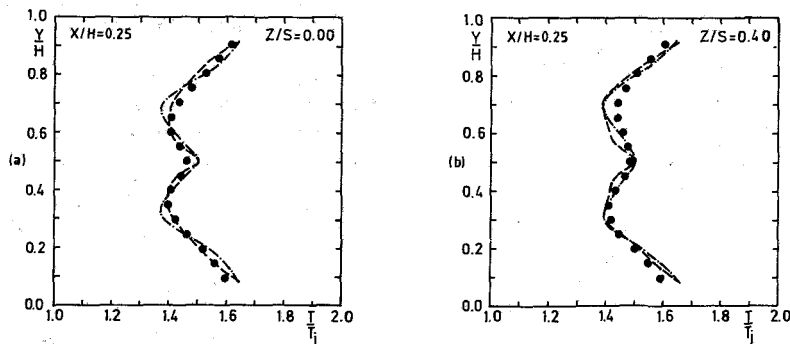

Fig. 6 Temperature profile development with double-wall injection (Test No. 10, Table 2):· · · modified correlation (equation (3) Cox), $\theta(H_{eq})$ = θ_{id};· · · modified correlation (equation (3) Holdeman and Walker), ● experiment, present paper

As expected, the corrrelations will not hold as soon as higher momentum flux ratios are required, i.e., whenever the jets will combine in the meridional plane ($Y/H \simeq 0.5$). A typical example is shown in Fig. 5, where the calculated temperatures are shown to be excessively high in the meridional plane ($Y/H \simeq 0.5$).

Measurements indicate that for this specific case $\theta(H_{eq}) \simeq \theta_{id}$ (see Fig. 6), where θ_{id} is the ideal dimenionless mixing temperature.

In generalizing, therefore, it is necessary to expand equation (2) as shown

$$\theta(H_{eq}) = \alpha \cdot \theta_{id} + \beta \cdot \frac{\theta_{min,T}^+ + \theta_{min,B}^+}{2} \qquad (3)$$

with α, $\beta = f(J_T, J_B)$

where α and β again have to be determined by correlating available experimental data. α and β will vary between 0 and 1. In a first approximation for modest momentum flux ratios, however, α and β may be set to 0.5.

Large deviations were found between experiment and correlations for higher differences in the momentum flux ratios for opposite jet injection. This is illustrated in Fig. 7. One reason for the underprediction of the temperature maximum is because equations (1) and (2) give $\theta_{id,T} \neq \theta_{id,B}$.

Significant improvement is found calculating H_{eq} from the following new relation

$$H_{eq} = \frac{A_{j,B}\sqrt{J_B}}{A_{j,B}\sqrt{J_B} + A_{j,T}\sqrt{J_T}} \cdot H \qquad (4)$$

With this assumption, we find $\theta_{id,T} = \theta_{id,B}$. Figure 8 shows considerably better agreement between this correlating
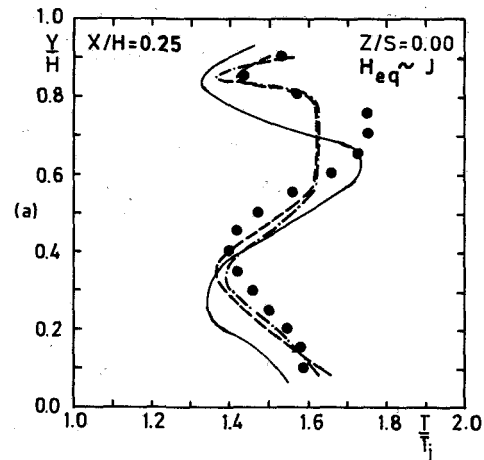

Fig. 7 Temperature profile development with double-wall injection (Test No. 9, Table 2):_____ three-dimensional calculation, present paper;· · · Cox;· · · Holdeman and Walker; ● experiment, present paper

equation and the experimental results. The advantage of using three-dimensional-field method is evident from Fig. 7, where the numerical results are compared with the original correlations and the experiment.

Conclusions

In applying existing correlations derived from single wall jet injection for the determination of the temperature profile in a hot gas crossflow to opposite-wall injection, good agreement is obtained for low momentum flux ratios. Modified correlations are presented. Their general ap-
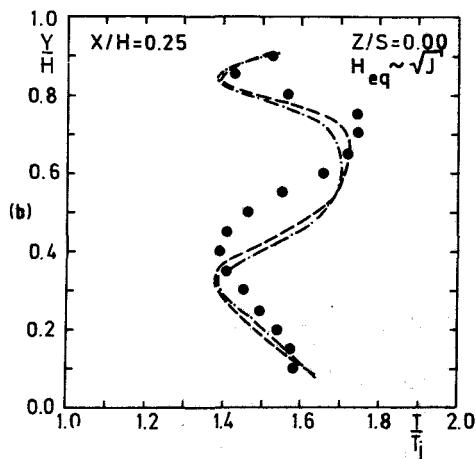
Fig. 8 Temperature profile development with double-wall injection (Test No. 9, Table 2): · · · **modified correlation (equation (4) Cox)** $H_{eq} \sim \sqrt{J}$; · · · **modified correlation (equation (4) Holdeman & Walker)** $H_{eq} \sim \sqrt{J}$; • **experiment, present paper**

plicability, however, should be tested under an extended range of determining parameters. For example, up to now the influence of staggered, oblique injection and converging duct geometry has not been analyzed. Furthermore, it is quite questionable whether the correlations can be applied for combustor flow with profiled mixing zone entrance conditions, i.e., temperature and velocity profiles.

As indicated earlier, the application of numerical solutions, i.e., the utilization of field methods in solving the time-averaged basic equations, seems to be a more promising approach. Despite an unquestionably higher effort required,

field methods are capable of incorporating a broad range of boundary conditions and providing solutions for all flow parameters, i.e., temperature, pressure, velocity, etc., in the whole flow field under consideration. We, therefore, at present are testing a newly developed program for describing mixing zone flow. Extended correlations, however, will be useful for the designer in the first stage of a combustor development and under relatively simplified conditions.

Acknowledgments

References

1 Lefebvre, A. H., and Norster, E. R., "The Design of Tubular Gas Turbine Combustion Chambers for Optimum Mixing Performance," *Proc. Instn. of Mechn. Engrs.*, Vol. 183, 1968, p. 158.

2 Cox, J. B., Jr., "Multiple Jet Correlations for Gas Turbine Engine Combustor Design," ASME Paper No. 75-GT-45, 1975.

3 Cox, J. B., Jr., "An Analytical Model for Predicting Exit Temperature Profile From Gas Turbine Annular Combustors," AIAA Paper No. l75-1307, 1975.

4 Norgren, C. T., and Humenik, F. M., "Dilution Jet Mixing Study for Gas Turbine Combustors," NASA TN D-4695, 1968.

5 Walker, R. E., and Kors, D. L., "Multiple Jet Study," NASA CR-12 12 17, 1973.

6 Walker, R. E., and Eberhardt, R. G., "Multiple Jet Study Data Correlations, NASA CR-13 47 95, 1975.

7 Holdeman, J. D., and Walker, R. E., "Mixing of a Row of Jets with a Confined Cross Flow," *AIAA Journal*, Vol. 15, 1977, p. 243.

8 Kamotani, Y., and Greber, I., "Experiments on Confined Turbulent Jets in Crossflow," NASA CR-23 92, 1974.

9 Elbahar, O. M. F., und Wittig, S. L. K., "Zur Berechnung der Temperaturprofile am Austritt von Ring- und Rohrbrennkammern," Sammelband VGB, *Forschung in der Kraftwerkstechnik 1980*," 1980, S. 220–227.

10 Elbahar, O. M. F., "Zum Einfluß von Kühlluftrahlen und Mishzonengeometrie auf die Temperaturprofilentwicklung in Gasturbinenbrennkammern," Ph.D. dissertation, Lehrstuhl und Institut für Thermische Strömungsmaschinen, Universität Karlsruhe, 1982.

Aerodynamic Loss Penalty Produced by Film Cooling Transonic Turbine Blades

B. R. Haller

Senior Turbine Engineer,
Rolls-Royce Limited,
Derby, England

J-J Camus

Senior Research Associate,
Whittle Laboratory,
University of Cambridge,
England

Aerodynamic loss measurements are presented for a state-of-the-art film cooled transonic gas turbine rotor blade tested in a two-dimensional cascade. A mixture of carbon dioxide and air, which correctly simulated engine coolant-to-mainstream density ratio and blowing rate, was ejected from each of five individual cooling hole rows in the aerofoil suction surface. The temperature of the coolant was equal to the cascade inlet stagnation temperature. The dependence of blade row efficiency and turning on outlet Mach number, blowing rate, and coolant-to-mainstream density ratio was investigated. Measured surface static pressure distributions were compared with time-marching predictions for both the datum aerofoil and film cooled blades. Detailed suction surface boundary layer measurements both upstream and downstream of a cooling film were compared with available differential calculation procedures. Unexpectedly, films downstream of the throat, even at blowing rates near unity, did not generate significantly higher losses compared to prethroat suction surface films on this aerofoil.

1 Introduction

Low specific fuel consumption (s.f.c.) of an aircraft gas turbine in cruise requires a combination of both high thermal efficiency and high propulsive efficiency. Higher thermal efficiency may be achieved by increasing turbine entry temperature (T.E.T.) and cycle pressure ratio. The maximum practical T.E.T. is limited by the capability of materials to withstand high gas temperatures and is dependent upon effective cooling design.

A progressive improvement in materials technology initially permitted increases in T.E.T., but since 1960 the introduction of air cooled turbines has increased the rate of improvement with time.

Rapid increases in oil costs and depletion of fuel resources make it essential that future aircraft gas turbines operate at the highest possible efficiency. In order to maximize component efficiencies, practical turbine cooling systems and flows in blade passages and ducts need to be studied in depth. Of particular interest is the interaction between blade passage flows and cooling flows injected into the mainstream from various points on the aerofoil surface. To minimize engine initial cost, weight, and complexity, advanced high-pressure (HP) turbines may use highly loaded blading which operates at high relative outlet Mach numbers. The design of an advanced high-efficiency, single-stage transonic HP turbine represents a significant challenge due to higher loading and additional shock losses compared with an equivalent two-stage subsonic unit. In the past, single-stage turbines have been proposed for engine applications where overall weight and simplicity is more important than high component efficiency. Turbine rig tests however, including Okapuu [1] and Liu et al. [2], suggest that acceptable efficiency levels may be achieved for blading with relative outlet Mach numbers up to 1.3 for commercial engines. This cascade test program was initiated in order to study the loss penalty introduced by film cooling a typical transonic turbine blade. The main objectives were:

(*a*) To evaluate the thermodynamic efficiency penalty associated with different suction surface fan-shaped cooling hole configurations at varying cascade outlet Mach number and film blowing rate

(*b*) To compare the performance of fan-shaped and cylindrical cooling hole geometries, and to determine the variation of cascade efficiency with coolant-to-mainstream density ratio

(*c*) To provide a detailed data base of boundary layer mean velocity profile development on transonic film cooled aerofoils. This data enables the turbulence, shock/boundary layer interaction and coolant ejection models in the differential calculation to be checked.

(*d*) To extend further the interactive transonic aerofoil design process by including the effects of boundary layer growth and coolant blowing in the time marching prediction technique

2 Test Facility

The aerodynamic measurements presented in this paper were obtained using the Whittle Laboratory transonic cascade
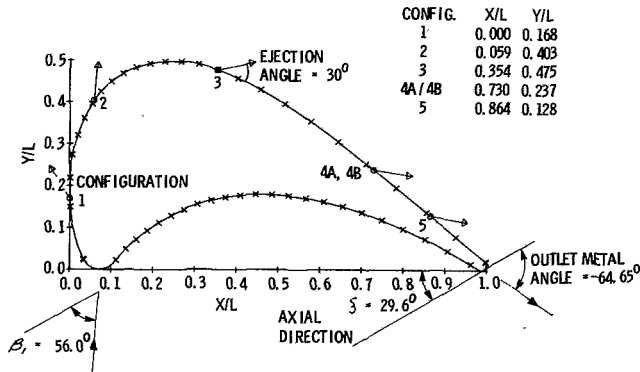
Fig. 1 Suction surface film-cooled rotor profile

test facility at Cambridge University, England [3]. The closed circuit variable density tunnel is supplied with air from a 1000-hp (746-KW) three-stage centrifugal Reavell compressor. A fraction of the tunnel airflow may be passed through two driers containing a water absorbent chemical. The tank pressure level may be controlled by either venting parts of the tunnel to atmosphere or by pressurizing with auxiliary blowers, thus enabling the Reynolds number to be varied independently. The tunnel can generate Mach numbers up to 1.25 in a cascade of 80-cm^2 throat area. Cascade inlet angle is variable within the range +70 to −40 deg using a rotating turntable and movable upper and lower inlet sidewalls.

Film cooled cascade blades could be supplied with a carbon dioxide/air mixture using an auxiliary blowing system. The use of carbon dioxide premixed with air correctly simulated nondimensional coolant-to-mainstream density ratio (ρ_c/ρ_L) and blowing rate $B = (\rho u)_c/(\rho u)_L$ compatible with hot engine conditions. Also, the acoustic speed ratio (a_L/a_c) is comparable with engine conditions and thus shock formations are modeled accurately. The blades were supplied with carbon dioxide from a bulk storage vessel, precharged using liquid CO_2 syphon cylinders, at a maximum rate of 0.04 kg/s with a pressure up to 170 KN/m^2 absolute. The auxiliary air supply was taken from a 7.5KW isothermal compressor with a maximum delivery of 0.023 kg/s. Mass flow rates of CO_2 and air in individual lines were measured using orifice plates and the two gas streams premixed and fed into a plenum chamber and then into the blades. The final coolant plenum supply
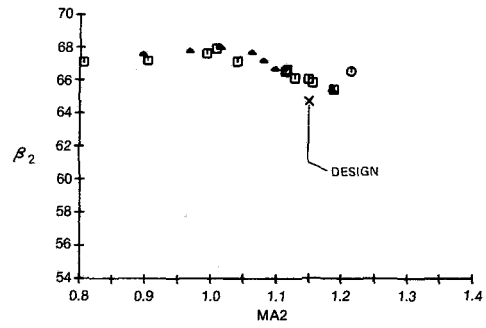

Fig. 2 Variation of blade loss and mixed-out gas exit angle with exit Mach number

temperature was near the cascade inlet stagnation temperature ($\simeq 296$K).

3 Test Program and Measuring Techniques

The blade profile tested was the midheight section of a high-pressure rotor blade intended for high work capacity transonic operation with a design outlet Mach number of 1.15, and as such is typical of coolable state-of-the-art blading. A plot of the aerofoil (design surface coordinates tabulated in [4]) is shown in Fig. 1. Design cascade geometry is given below

blade true chord, L	41.7 mm	aspect ratio, h/L	2.4
blade span, h	101.6 mm	pitch/chord ratio, t/L	0.842

--- Nomenclature ---

B = blowing rate, $(\rho U)c/(\rho U)_L$

H = compressible shape factor, δ^*/θ

MA = Mach number

P_o, P = stagnation, static pressure

S/S_o = nondimensional surface length

Tu = percentage turbulence level, $100\sqrt{\overline{u'^2}}/\overline{u_1}$

u = boundary layer velocity component parallel to wall

v = boundary layer velocity component normal to wall

XM = axial distance of traverse plane from blade trailing edge

y = coolant mass fraction, $\dot{m}_c/\dot{m}_g$

β = gas angle (measured from the axial direction)

$\delta_{0.995}$ = boundary layer thickness

δ^* = compressible displacement thickness

η_{th} = thermodynamic efficiency,

$$\frac{\left(1 + \frac{\dot{m}_c}{\dot{m}_g} \frac{c_{pc}}{c_{pg}} \frac{T_{0c}}{T_{01}}\right)[1 - (P_2/P_{02})^{\gamma_2 - 1/\gamma_2}]}{1 - (P_2/P_{01})^{\gamma_g - 1/\gamma_g} + \frac{\dot{m}_c}{\dot{m}_g} \frac{c_{pc}}{c_{pg}} \frac{T_{0c}}{T_{01}} [1 - (P_2/(P_{0c})^{\gamma_c - 1/\gamma_c}]}$$

θ = compressible momentum thickness

ρ = density

Subscripts

0 = stagnation value

1 = mixed inlet flow

2 = mixed outlet flow

C = coolant

K = tank

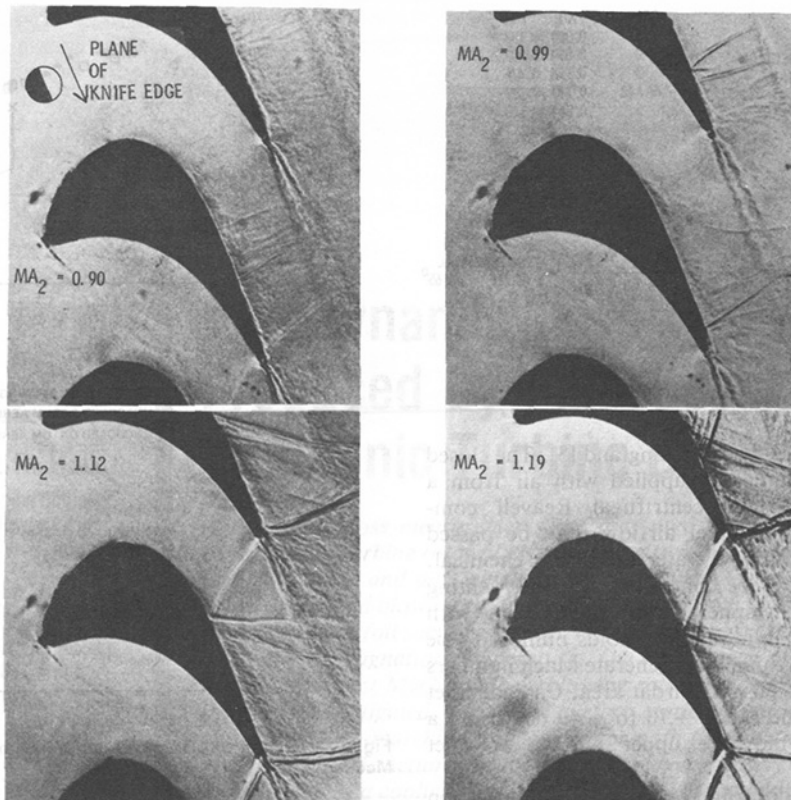L = local conditions along the profile surface

e = edge of boundary layer

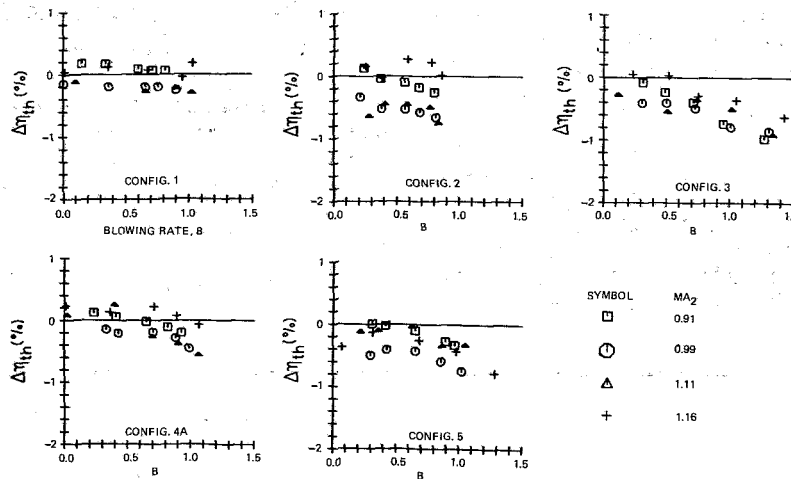Fig. 3 Development of datum cascade shock structure as back pressure is reduced

Fig. 4 Effect of coolant blowing rate, outlet Mach number, and film position upon thermodynamic efficiency penalty

blade pitch, t	35.1 mm	arccos (o/t)	67.5°
throat width, o	13.4 mm	stagger angle, ξ	29.6°
		nominal inlet flow angle, β_1	56.0°

The cascade was located between two plane circular disks. For double-pass Schlieren photography, a glass disk and an optionally ground and polished reflecting stainless steel plate were used to locate the aerofoils. No tailboards were used downstream of the trailing edge plane so the outlet flow was allowed to determine its direction freely. For these tests the tunnel inlet turbulence level and outlet Reynolds number based upon true chord were 0.5 percent and 8.5×10^5, respectively.

In addition to testing with the uncooled datum aerofoil six further film cooled configurations were manufactured (see table on page 201).

Suction surface cooling films were positioned on either side of the geometric throat at 42 percent true chord. Configurations 1 and 2 were placed in a region of rapid acceleration, whilst configuration 3 was just upstream of the throat. Configurations 4 and 5 were designed to reveal the behavior of a cooling film in a diffusing flow field.

Flow cooled cascade configurations consisted of six blades and the four central blades were supplied with coolant. The cooling film spanned the central half of each blade corresponding to the region of two-dimensional flow.

Configuration	1	2	3	4A	4B	5
Position of cooling holes (X/L) %	0.0	5.9	35.4	73.0	73.0	86.4
Hole shape	⊢——— flared ———⊣				cyl[1]	flared
Hole diameter d (mm)	0.51	0.51	0.51	0.51	0.51	0.51
Hole spacing s (mm)	2.03	2.03	2.03	2.03	2.03	2.03
Hole spanwise included flare angle	25°	25°	25°	25°	0°	25°
Inclination of hole centre line with blade surface	30°	30°	30°	30°	30°	30°

[1] Cylindrical

For aerodynamic loss measurements, wake traverses were performed in a plane 40 percent of a true chord downstream of the cascade using a five-hole wedge probe. From the inhomogenous flow data in the traverse plane, the properties of fully mixed-out exit flow were determined by applying the equations of conservation of mass, momentum, and energy [5]. Aerofoil midheight static pressure distributions were measured using 11 pressure surface and 24 suction surface tappings. For black and white Schlieren photographs, a flash source of approximately ⅓ μs duration from an argon jet light source was used. Suction and pressure surface mean stagnation pressure profile boundary layer traverses were obtained using a flattened pitot probe of height 0.083 mm and width 1.219 mm.

4 Discussion of Results

4.1 Uncooled Datum Efficiency and Deflection. The efficiency characteristics and gas deflection of the uncooled datum profile are presented in Fig. 2. For the datum aerofoil at an outlet Mach number of 1.21 an additional traverse was performed at 80 percent of a true chord downstream of the blade row, and good agreement was found for measured loss, although β_2 was 1.1 deg higher. A higher measured outlet angle further downstream is surprising since the cascade wall boundary layer growth would produce a lower value for β_2. Use of Schlieren photography to examine transonic cascade flow behavior combined with detailed wake traverse results and measured aerofoil surface pressure distributions assist the interpretation of the loss characteristic shown in the figure. For this profile, the blade loss varied from only 2.2 to 2.4 percent for subsonic outlet Mach numbers between 0.805 and 0.99, respectively. Here the loss consisted mainly of aerofoil boundary layer growth and trailing edge blockage. As the outlet Mach number was increased above unity, a rapid increase in loss may be detected rising to 5.0 percent at $MA_2 \approx 1.15$. The rapid decrease in efficiency is due to an increase in trailing edge shock wave strength and wake mixing loss. Figure 3 shows the development of the cascade shock structure as the back pressure is reduced. The main points to note are as follows:

(a) For $MA_2 = 0.90$, a series of weak normal shocks may be observed downstream of the throat on the suction surface, and a thick boundary layer ($\approx$ 1-mm thickness just upstream of the trailing edge) produced by back surface diffusion is clearly visible.

(b) At an outlet Mach number near unity, the cascade chokes and a normal shock may be seen extending across the channel passage.
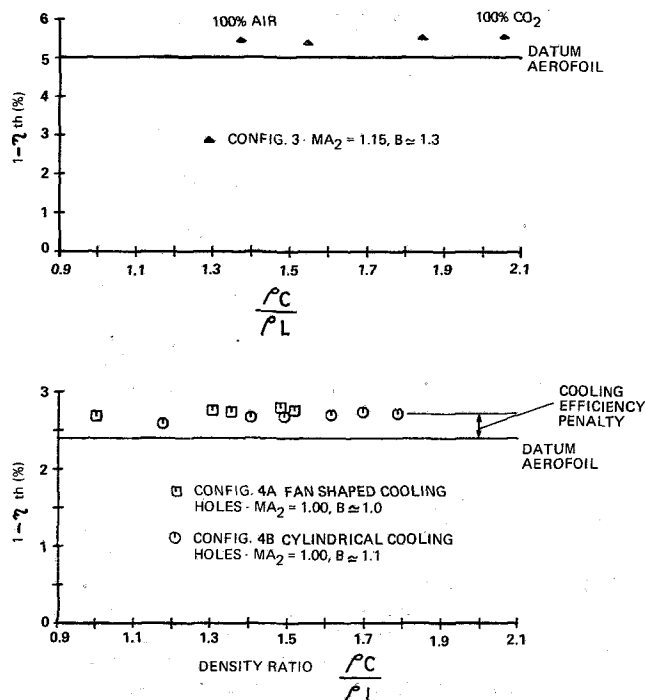

Fig. 5 Effect of coolant-to-free-stream density ratio and hole shape upon blade thermodynamic loss
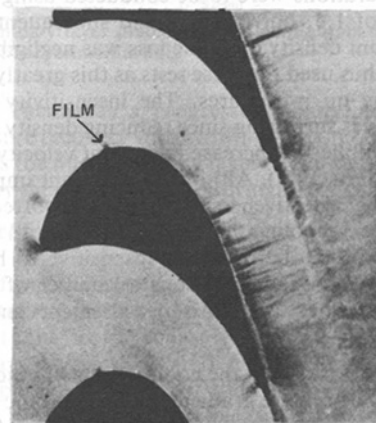

Fig. 6 Configuration 2, $MA_2 = 0.91, B = 0.68$

(c) Increase of the outlet Mach number above unity results in supersonic expansion of the flow downstream of the throat. Local overexpansion occurs around the trailing edge and this is followed by recompression when the separated pressure and suction surface boundary layers mix to form the wake. The compression shocks formed downstream of the trailing edge combine with the two "lip" shocks generated by separation of the boundary layers. The combined oblique pressure surface trailing edge shock crosses the passage and interacts with the suction surface boundary layer.

Referring to Fig. 2, attention is drawn to the higher subsonic loss relative to datum for configuration 3 with coolant off due to the recirculation bubble in the cooling hole producing transition of the laminar boundary layer. The turbulent layer downstream of the hole generates more skin friction and mixing loss at subsonic outlet conditions.

Loss measurements for the five fan shaped cooling hole configurations were taken at four outlet Mach numbers from $MA_2 = 0.90 \rightarrow 1.17$ over a range of blowing rate. The datum efficiency losses $(1 - \eta_{DATUM})$ for the uncooled aerofoil are 2.4 percent (for $MA_2 = 0.90, 0.99$), 4.6 percent ($MA_2 = 1.12$) and 5.0 percent ($MA_2 = 1.17$).
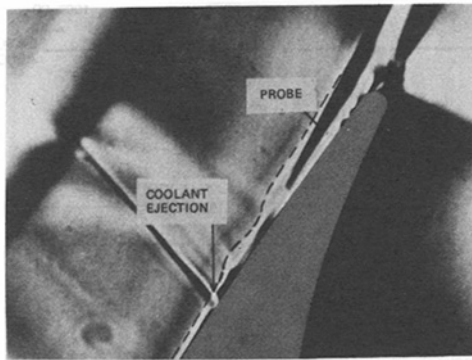
Fig. 7 Shock/expansion wave pattern for configuration 4A (approximate edge of boundary layer is shown by discontinuous line)

4.2 Film Cooled Blading Performance. The thermodynamic efficiency penalty $(\Delta\eta_{th} = \eta_{th} - \eta_{DATUM})$ produced by coolant ejection is shown in Fig. 4. For all configurations changes of efficiency were restricted to a maximum of approximately -1 percent. The additional entropy sources with blowing arise from mixing of coolant and mainstream flows, friction and shock losses within the convergent-divergent cooling hole, and increased skin friction/turbulent boundary layer mixing downstream of the injection region. Originally, wake traverses for the five film cooled configurations were to be conducted using a constant density ratio of 1.5, but it was found subsequently that the effect of coolant density on blade loss was negligible (Fig. 5). Air only was thus used for these tests as this greatly simplified cascade setting up procedures. The insensitivity of loss to coolant density is surprising since reducing density at constant blowing rate implies an increase in coolant velocity and hence mixing loss (Hartsel [6]). Although significant improvements in film cooling effectiveness have been reported for convergent-divergent cooling holes [7], the overall blade row efficiency appears to be relatively insensitive to hole shape. For the film cooled configurations a number of significant features were revealed by the loss measurements and Schlieren photography:

(a) For configuration 1, the cooling film was ejected into a highly favorable pressure gradient with a subsonic freestream Mach number of ≈ 0.67, and only small changes of blade row efficiency were measured.

(b) A thick turbulent boundary layer was observed on the blade back suction surface for configuration 2 at an outlet Mach number of 0.91, due to the cooling film tripping the laminar boundary layer (Fig. 6). In the coolant ejection region $(MA_L \approx 0.92)$, the flow may expand to supersonic conditions at high blowing rates with diffusion downstream of the film thickening the surface boundary layer. The reduction in thermodynamic efficiency was restricted to a maximum of 0.8 percent (Fig. 4).

(c) A local compression shock was generated upstream of the cooling film for configuration 3, together with a turning stock downstream. The disturbance to the mainstream flow extended over approximately 20 percent throat width (see [4] for Schlieren photographs and laser holographic interferometry).

(d) For configurations 4 and 5 an additional compression shock was generated across the passage at the coolant ejection position (Fig. 7). In addition to the compression shock, just ahead of the cooling film a further shock was produced as the flow turned back towards the blade surface. The presence of this additional shock implied that the separated cooling film was forced back onto the blade surface. Significantly higher losses were expected for post-throat suction surface ejection
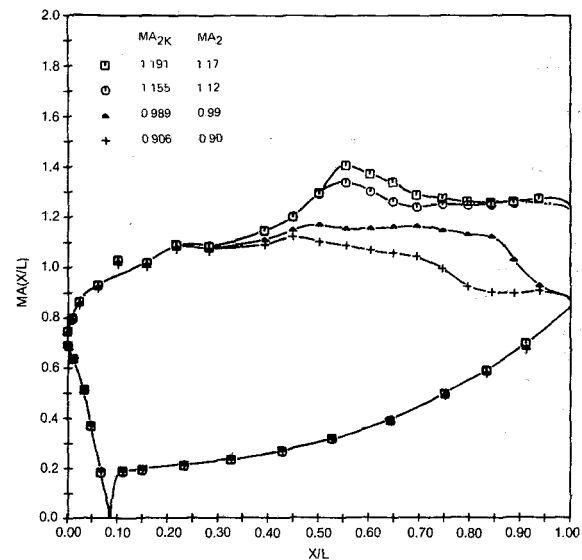

Fig. 8 Measured surface Mach number distributions for datum aerofoil
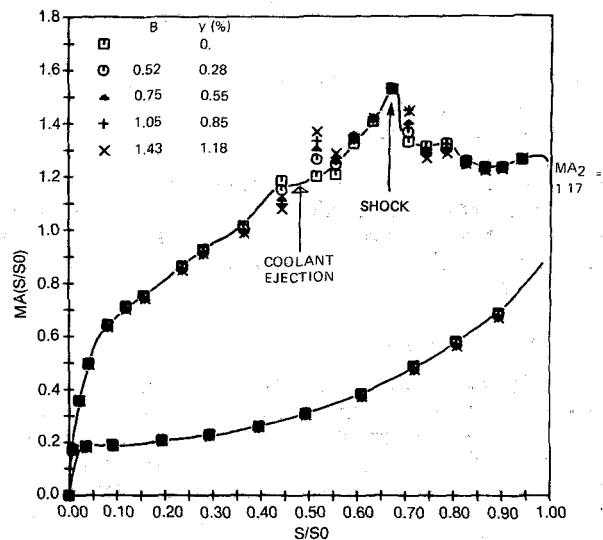

Fig. 9 Measured surface Mach number distribution with air blowing (configuration 3)

but reattachment of the film resulted in losses comparable to prethroat films (Fig. 4).

4.3 Surface Static Pressure Distributions. The aerofoil surface static pressure data was converted into isentropic local Mach numbers using the measured value of cascade inlet stagnation pressure. The resultant surface Mach number distributions for the uncooled datum aerofoil are shown in Fig. 8.

At an outlet Mach number of 0.90, the flow accelerates rapidly on the suction surface and then more gradually towards the throat at $X/L = 0.42$. This is followed by deceleration due to back surface deflection. Increasing the outlet Mach number increases local Mach numbers downstream of the throat and more supersonic flow develops. For an outlet Mach number near unity a shock approximately normal to the suction surface may be observed at $X/L \approx 0.85$ (Fig. 3), with rapid diffusion and consequential thickening of the boundary layer. As the back pressure is reduced further, the trailing edge shock strength increases with the shock angle becoming more oblique (Fig. 3). The position where the trailing edge pressure surface shock meets the suction surface of the adjacent blade moves downstream as the outlet Mach number is increased.
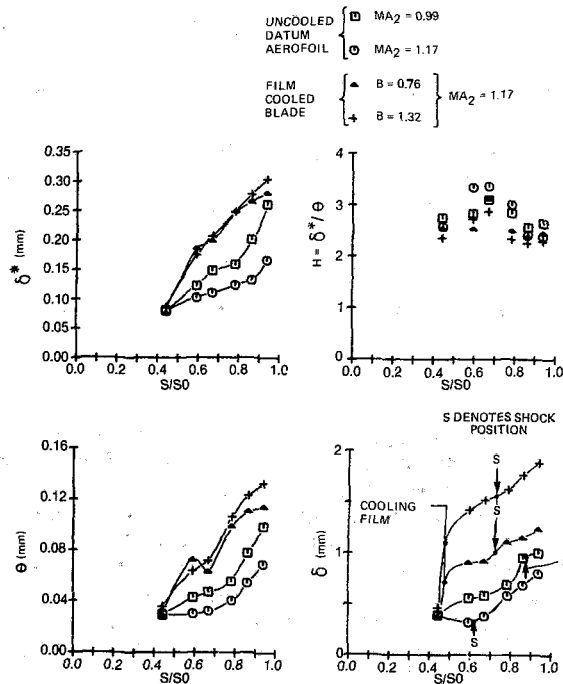
Fig. 10 Variation of boundary layer parameters, θ, H, δ^*, and $\delta_{0.995}$, along suction surface perimeter (configuration 3)
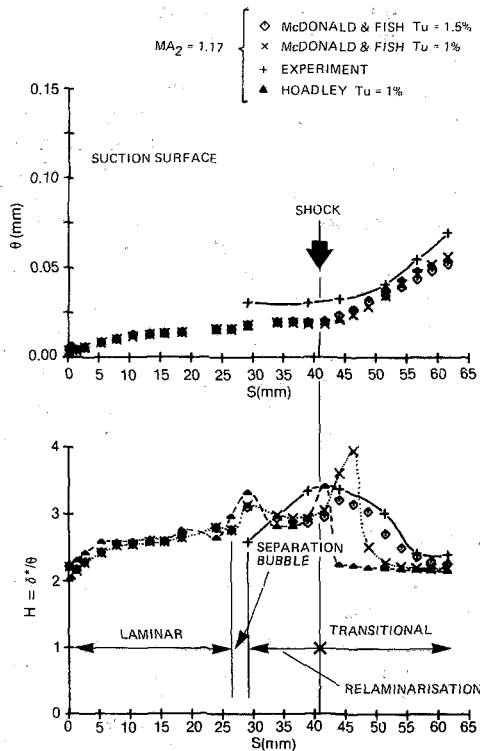

Fig. 11 Comparison of measured and predicted boundary layer growth (datum aerofoil)

Fig. 12 Boundary layer predictions for configuration 3 (coolant on) compared with experimental data

The measured surface Mach number distributions for configuration 3 with blowing at near design conditions (MA_2 = 1.17) are shown in Fig. 9. A progressive deceleration ahead of the film and acceleration through the blowing region may be detected with increasing blowing rate. In addition to the compression shock ahead of the film at high blowing rates, a further shock may be generated downstream where the flow turns back towards the blade surface. For this particular film cooling geometry the major effects of the perturbation extend over approximately 25 percent surface perimeter and wash out
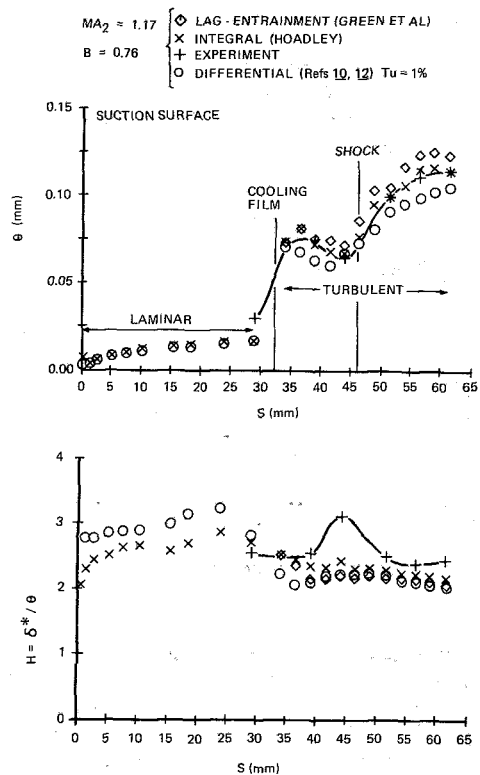
thereafter. There was a progressive change in the passage shock pressure recovery with blowing. Recompression became less rapid as the inlet boundary layer to the passage shock was thickened by the effects of the blowing.

4.4 Aerofoil Boundary Layer Measurement and Prediction. The velocity within the boundary layer was calculated from the measured stagnation pressure assuming constant static pressure and stagnation temperature perpendicular to the profile contour. The static pressure through the boundary layer was found from a local blade surface pressure tapping. Variation of the parameters θ, H, δ^*, and $\delta_{0.995}$ along the suction surface perimeter for both the datum aerofoil and configuration 3 are shown in Fig. 10.

Errors associated with the boundary layer measurements are described in [4]. For the datum blade the boundary layer is thinner at the higher outlet Mach number of 1.17 with θ and δ reaching maximum values of 0.070 mm and 0.80 mm near the trailing edge. The dramatic effects of coolant ejection upon the boundary layer growth for configuration 3 may be seen from the figure. Physically, the boundary layer appears thicker at the higher blowing rate with δ reaching a value of 1.9 mm near the trailing edge, compared to 1.2 mm for a blowing rate of 0.76. For both blowing rates a rapid increase in δ across the cooling film may be detected. At the high blowing rate of 1.32 ($y \simeq 1.2$ percent) the coolant jet within the boundary layer velocity profile was clearly visible just downstream of the film [4] and gradually mixed out, although traces of the jet were still present near the trailing edge.

A number of prediction methods were used for comparison with the boundary layer data for both the datum and film cooled aerofoils:

(a) For the datum aerofoil (MA_2 = 1.17, Fig. 11) a method based upon the McDonald and Fish [8] model of transitional boundary layer flow was used, together with the integral method of Hoadley [9].

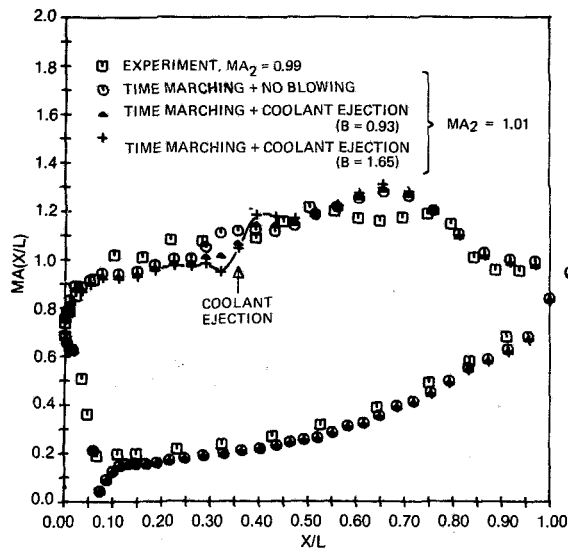The integral method predicted a short laminar separation

Fig. 13 Prediction of blade surface Mach number near blowing region (configuration 3)

bubble at the shock position due to the rapid pressure rise with reattachment as a fully turbulent boundary layer. The Mc-Donald and Fish based method run at a turbulence level of 1 percent yielded a slightly later transition point with laminar shape factors approaching 4. At a higher turbulence level of 1.5 percent, transition was found to be more gradual, and good agreement with experimental results was found for shape factor. As separation is avoided in this calculation, θ downstream of the shock is slightly lower at 1.5 percent turbulence than at 1 percent. It should be noted that θ was underpredicted by all calculations at the first measurement station. A possible explanation for this discrepancy was found during surface flow visualization studies [4]. At 43 percent surface perimeter on the suction surface a laminar separation/bubble region was detected produced by slight deceleration (Fig. 8). Although the presence of this bubble results in an increase in local turbulence, it is likely that the combination of rapid acceleration and the stabilizing effect of blade convex curvature produced relaminarization of the transitional boundary layer.

(b) The differential boundary layer calculation [10], based upon the GENMIX IV code of Patankar and Spalding [11], has been developed to include the effects of coolant ejection and also now deals with regions of separation [12]. The theoretical predictions using the differential and integral [9, 13] methods showed good agreement for θ with the data (Fig. 12), but slightly lower shape factors were calculated.

For the integral and lag entrainment methods, "jump" conditions (obtained by integrating the momentum integral equation across the injection region) were applied using the method described in [4]. Before the shock, θ is reduced by a large streamwise acceleration but then increases rapidly due to a steep adverse pressure gradient through the shock interaction region.

4.5 Two-Dimensional Transonic Flow Field Analysis. The development of efficient time marching prediction methods [14] enables mixed subsonic, transonic, and supersonic flows to be calculated without any prior knowledge of shock strength or position. Viscous effects were included in the Denton computation using two alternative methods [4].

(a) "Surface Transpiration" Method. The second-order matching relationship between the inviscid normal velocity and boundary layer normal velocity is

$$(\rho v)_{\text{inviscid}}(x,0) = \frac{d}{dx}(\rho_e u_e \delta^*) \qquad (1)$$

This result implies mass transfer at the wall and forms the basis of the method.

(b) Solid Displacement" Model. The conventional method for solving for the inviscid flow is over a streamline surface, $h(x)$, through which no mass flows, i.e.,

$$\frac{d}{dx}\int_0^h \rho u\, dy = 0 \qquad (2)$$

In this case the matching relationship is

$$h(x) = \delta^*(x) \qquad (3)$$

The boundary layer growth is governed by the static pressure distribution at the edge of the layer. The blade-to-blade passage flow however depends upon boundary layer blockage effects and thus an iterative calculation must be used. The blade profile was modified in the iteration by an amount equal to the local displacement thickness and the inviscid flow calculated within a "virtual" passage.

The comparison between measured and calculated blade surface Mach number distributions is fully reported in [4] and will not be repeated here.

Coolant ejection from holes or slots in the blade surface was included in the Denton time-marching calculation by the addition of a source of mass, momentum, and energy to the control volume adjacent to the ejection location. The comparison between an experimentally measured Mach number distribution for configuration 3 (cooling holes open, no blowing, $MA_2 = 0.99$) and calculations at blowing rates of 0, 0.93, and 1.65 is shown in Fig. 13. With secondary flow ejection the calculation predicts a Mach number distribution near the equivalent cooling slot which is altered considerably compared with the no blowing case. A sharp increase in pressure upstream of the film produced by local turning of the mainstream flow is followed by an overexpansion, and further turning as the two flows mix. Comparison with a no blowing calculation may be achieved easily by equating the cooling hole equivalent slot width to zero, and results predict virtually constant static pressure near the holes. Computationally, mixing of mainstream and coolant flows in the streamwise direction occurs within 20 percent of the blade true chord.

5 Conclusions

The following specific conclusions may be drawn as a result of the present investigation:

(a) Surprisingly, ejection downstream of the throat even at high blowing rates ($B \simeq 1.3$) did not generate significantly higher losses compared to prethroat suction surface films. This is an important result as post-throat suction surface ejection may provide an ideal method for cooling the thin trailing edges on transonic turbines.

(b) The cooling efficiency penalty was insensitive to hole shape and also surprisingly unaffected by changes in coolant density at constant blowing rate. Shaped cooling holes offer significant improvements in film cooling effectiveness, without any additional aerodynamic loss penalty.

(c) The boundary layer data base presented in this paper enables the turbulence, shock/boundary layer interaction and coolant ejection models in the differential calculation to be checked in detail.

(d) The Denton time-marching calculation, suitable for transonic aerofoil design, has been extended by including the effects of boundary layer growth and film cooling ejection.

6 Acknowledgments

The cascade test program at Cambridge University was supported by Rolls-Royce Limited and the Ministry of Defence (Procurement Executive). The authors gratefully acknowledge the permission of Rolls-Royce Ltd. to publish this work and their continued support, advice, and encouragement during the project. The authors also wish to thank J. D. Denton for his contribution to the work.

References

1 Okapuu, U., "Some Results From Tests on a High Work Axial Gas Generator Turbine," ASME Paper No. 74-GT-81.

2 Liu, H. C., Booth, T. C., and Tall, W. A., "An Application of Three-Dimensional Viscous Flow Analysis to the Design of a Low-Aspect-Ratio-Turbine," ASME Paper No. 79-GT-53, Mar. 1979.

3 Gostelow, J. P., and Watson, P. J., "Closed Circuit Variable Density Air Supply for Turbomachinery Research," ASME Paper No. 76-GT-62.

4 Haller, B. R., "The Effect of Film Cooling Upon the Aerodynamic Performance of Transonic Turbine Blades," Ph.D. thesis, University of Cambridge, 1980.

5 Amecke, J., "Anwendung der Transsonischen Ahnlichkeitsregel auf die Strömung durch ebene Schaufelgitter," VDI Forshungscheft Nr. 540, 1970, pp. 16–28.

6 Hartsel, J. E., "Prediction of Effects of Mass-Transfer Cooling on the Blade-Row Efficiency of Turbine Air-foils," AIAA Paper No. 72-11.

7 Goldstein, R. J., Eckert, E. R. G., and Burggraf, F., "Effects of Hole Geometry and Density on Three-Dimensional Film Cooling," International Journal of Heat and Mass Transfer, Vol. 17, 1974, pp. 595–607.

8 McDonald, H., and Fish, R. W., "Practical Calculations of Transitional Boundary Layers," International Journal of Heat and Mass Transfer, Vol. 16, 1973, pp. 1729–1744.

9 Hoadley, D., "An Integral Method for Calculating Compressible Two-Dimensional Boundary Layers," C.E.G.B. Report R/M/N632.

10 Forest, A. E., "Engineering Predictions of Transitional Boundary Layers," Laminar-Turbulent Transition, AGARD-CP-224, Paper 22, 1977.

11 Patankar, S. V., and Spalding, D. B., Heat and Mass Transfer in Boundary Layers, Intertext Books, London, 1970.

12 Forest, A. E., private communication, Apr. 1982.

13 Green, J. E., Weeks, D. J., and Brooman, J. W. F., "Prediction of Turbulent Boundary Layers and Wakes in Compressible Flow by a Lag-Entrainment Method," RAE Technical Report 72231.

14 Denton, J. D., "A Time Marching Method for Two and Three-Dimensional Blade to Blade Flows," ARC R & M 3775.

Analysis of Film Cooling and Full-Coverage Film Cooling of Gas Turbine Blades

E. R. G. Eckert

University of Minnesota,
Department of Mechanical Engineering,
Minneapolis, Minn. 55455

Film cooling has become a standard method for the protection of the skin of gas turbine blades against the influence of the hot gas stream. The cooling air is usually injected into the boundary layer covering the skin through one or two rows of holes. A calculation method to predict heat transfer to the skin of a film cooled wall based on two parameters—the film effectiveness and a heat transfer coefficient defined with the adiabatic wall temperature—has been widely accepted. More recently, those sections of a turbine blade skin requiring intensive cooling are covered over its entire area with holes through which cooling air is ejected. A different method to predict the temperature of this section by this "full coverage film cooling" has been proposed which is based on two different parameters θ and K. The air used for the cooling of the perforated section of the skin also provides protection to a solid section located downstream in the normal film cooling process. The two methods are reviewed, and it is discussed under what conditions and in which way results obtained with one method can be transformed to the parameters used in the other one. Published data [8, 9] are used to calculate film cooling effectiveness values and Stanton numbers based on the adiabatic wall temperature for a perforated wall and a solid surface downstream of 11 rows of holes with coolant injection. The results demonstrate the advantage of this method which has been shown in previous experiments with ejection through one or two rows of holes, for film cooling of a solid surface. For full-coverage film cooling, there is still the advantage that a heat transfer coefficient defined with the adiabatic wall temperature is independent of temperature difference within the restrictions imposed by the superposition model.

Introduction

Film cooling has become a standard method to protect the skin of gas turbine blades against the influence of the hot gas stream. The cooling air is usually injected into the boundary layer covering the skin through rows of holes inclined in a downstream direction to generate a cool film downstream of the holes. One or two rows are mostly used. In a newer development, called "full-coverage film cooling," a part of the whole area of the skin is covered by a pattern of holes through which the cooling air is ejected. Figure 1 shows the area around the leading edge of the blade protected in this way. The cooling air also provides protection to the area downstream of the one covered by the holes as in the normal film cooling.

Two methods have been developed to predict the cooling effect. They are in both cases based on the assumption that the fluid properties involved can be considered as constant and equal for the main stream fluid and the coolant so that the energy equation becomes linear and superposition of temperature fields is possible. The calculation method which

is widely used in film cooling redefines the heat transfer coefficient with an adiabatic wall temperature [1, 2], whereas the method proposed in [3, 4] for full coverage film cooling used the definition of the heat transfer coefficient which is standard in convective cooling and is also used in transpiration cooling. The full-coverage method incorporates the effect of the coolant injection by an adjustment of the heat transfer coefficient. Experimental results are available in the literature using either one of the sets of parameters occurring in the two methods. It is, therefore, important for design calculations to know how far and in which way the results obtained with one method can be transformed into the parameters used in the other one. The present paper addresses itself to this subject.

Prediction of Gas Turbine Blade Temperatures

Figure 1 presents the cross section through a typical high-performance, gas turbine blade. The skin of the blade is heated by the hot gas stream forming a boundary layer along the outer surface. It is cooled by the ejection of cooling air through rows of holes, as shown near the nose of the blade, or through interrupted slots, as used at its downstream end. It is also cooled internally by impingement cooling in the nose
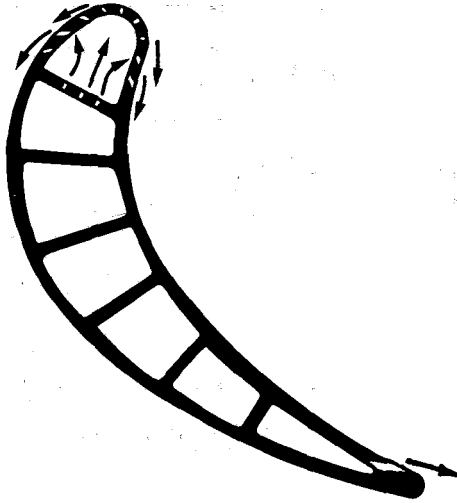
Fig. 1 Cross section of a blade for a high-performance gas turbine. Film cooling is used on the outside, impingement and convection cooling on the inside of the blade. Full coverage film cooling and impingement cooling protect the nose, film cooling and internal convection cooling protect the center part of the blade and film cooling is also used to cool the trailing edge.

Fig. 2 Notation for the film cooling process

Fig. 3 Temperature profiles in the boundary layer of a film cooled surface. t_i shows the boundary layer temperature for isoenergetic film cooling. t_a shows the boundary layer temperature for the adiabatic wall condition. The boundary layer temperature, t, for a general situation is obtained by superposition of the temperatures t_i and t_a.

region and by convection cooling with air flowing through internal passages normal to the plane of drawing. All of these processes determine the blade temperature in an involved way. The gas flow over the blade surface arrives with a turbulence, the intensity and characteristics of which are poorly known. The flow is also unsteady because the rotating blades periodically pass the wakes of the stationary blades and vice versa. Flow velocities are usually high and sometimes transonic so that large density variations occur and shock formation complicates the boundary layer development. Internal friction modifies the temperature within the boundary layer. Radiation may also be contributing to heat transfer.

The large number of parameters influencing the film cooling process makes it necessary to study first one parameter at a time, with the hope of later on establishing their mutual interference. In basic film cooling studies, the flow and heat transfer process is usually idealized by considering the flow as steady and the velocities and temperature variations as sufficiently small so that the fluid properties can be considered as constant. These are also postulated identical for the main stream fluid and the coolant. Even with this simplification, the problem to predict the skin temperature of turbine blades is still formidable. It is, in a strict sense, a situation which has recently been termed "conjugated." This means the film cooling process interacts with the impingement and internal cooling and all of them have to be analyzed simultaneously. When the blade skin temperature at a specific location is calculated with local heat transfer coefficients on
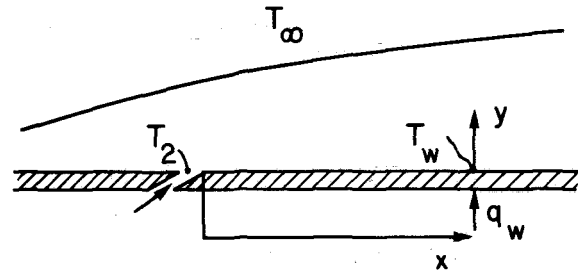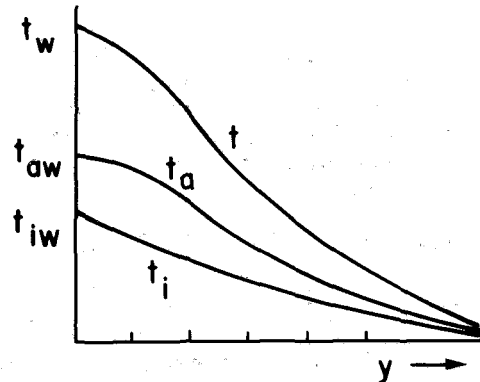
the outside and inside of the skin, it is found that these coefficients are affected by the way in which the skin temperature varies upstream of the point under consideration (assuming that no backward flow is caused by separation). The effect of such an upstream variation of the surface temperature on local convective heat transfer has been studied in the past. Two standard cases are usually selected for experimental work. Either a wall temperature that is constant along the surface or a constant heat flux that leads to a locally nonuniform surface temperature is prescribed. Calculation methods have also been developed to determine the influence of an arbitrary wall temperature variation on local convective heat transfer [5, 6]. Fortunately, it has been found that the temperature variation has only a minor influence on convective local heat transfer in a turbulent boundary layer as long as the temperature gradients are not too strong in a close vicinity of the location at which heat transfer is considered. The effects, however, are larger in a laminar boundary layer, and insufficient knowledge is available on this effect in film cooling arrangements.

Nomenclature

c_p = specific heat
D = diameter of film cooling holes
h_o = heat transfer coefficient defined by equation (7)
h' = heat transfer coefficient defined by equation (10)
K = parameter defined by equation (13)
k = thermal conductivity
M = blowing parameter, ratio of mass flow rate of coolant to that of the main stream
n = number of lateral rows of film cooling holes

P = distance between film cooling holes
Pr = Prandtl number
Re = Reynolds number, $u_\infty x/\nu$
T = temperature
s = slot width
t = temperature counted from T_∞
u,v,w = velocity components
x,y,z = coordinates

Subscripts

a = adiabatic

i = isoenergetic
w = at the wall surface
2 = coolant exit
∞ = in the free stream

Greek Symbols

α = thermal diffusivity
ϵ_H = turbulent diffusivity for heat
η_f = film cooling effectiveness
θ = parameter defined by equation (11)
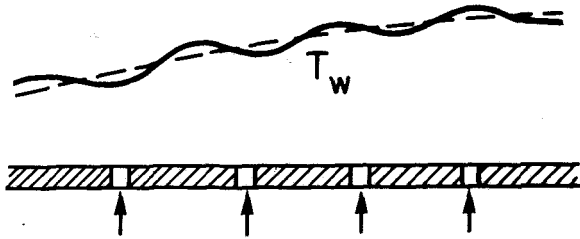ν = kinematic viscosity
ρ = density

Fig. 4 Wall temperature variation for full coverage film cooling. The wall temperature, T_w, exhibits periodic fluctuations due to the local ejection superimposed on a gradual variation.

This situation has a bearing on the comparison of the two calculation methods for film cooling, because the skin temperature of a blade is seldom constant, and it is an important task to predict the temperature gradients along the blade which arise in steady operation or in start up and shut down of the engine.

Calculation Method "A" for Film Cooling

Film cooling is considered for a surface as shown in Fig. 2. A fluid flowing along the surface generates a turbulent layer. The temperature in the stream outside of the boundary layer is T_∞. A coolant with the same properties as the main flow is ejected through one or several rows of holes with the temperature of the jets leaving the holes being T_2. Steady-state conditions, constant properties, and a negligible effect of aerodynamic heating are assumed. A heat flux of magnitude, q_w, per unit time and area leaves the surface along the length, x. The temperature field in the boundary layer downstream of the holes is described by the energy equation

$$u \frac{\partial t}{\partial x} + v \frac{\partial t}{\partial z} + w \frac{\partial t}{\partial z} = (\alpha + \epsilon_H) \frac{\partial^2 t}{\partial x^2} \qquad (1)$$

in which the temperature, t, is counted from the free stream temperature T_∞

$$t = T - T_\infty$$

The boundary conditions are

$$x = 0, y = 0 : t = t_2, t_2 = T_2 - T_\infty$$
$$y = 0 \qquad : q = q_w \qquad (2)$$
$$y = \infty \qquad : t = 0$$

Along the transverse coordinate, z, the temperature varies periodically. For constant fluid properties, the velocity field is independent of the temperature field so that the velocity components u, v, w can be considered as prescribed.

Equation (1) is, therefore, linear in the temperature, t. Solutions to the temperature field and the wall temperature, t_w, can then be obtained by superposition of two specific solutions. Figure 3 presents boundary layer profiles at an arbitrary location, x.

The following boundary conditions are considered.

(a) The fluid is ejected at a temperature, t_2, and the heat flux, q_w along x is zero.

$$q_w = 0 \qquad (3)$$

The temperature in the boundary layer in Fig. 3 is t_a, the wall temperature for this situation is denoted t_{aw} and called "adiabatic wall temperature."

(b) A finite heat flux is prescribed along x, but the ejection temperature of the coolant is equal to the main stream temperature

$$t_2 = 0 \qquad (4)$$

The temperature in the boundary layer is t_i in Fig. 3, and the wall temperature in this case is referred to as "isoenergetic

St DATA AT P/D = 5
Fig. 5

St DATA AT P/D = 10
Fig. 6
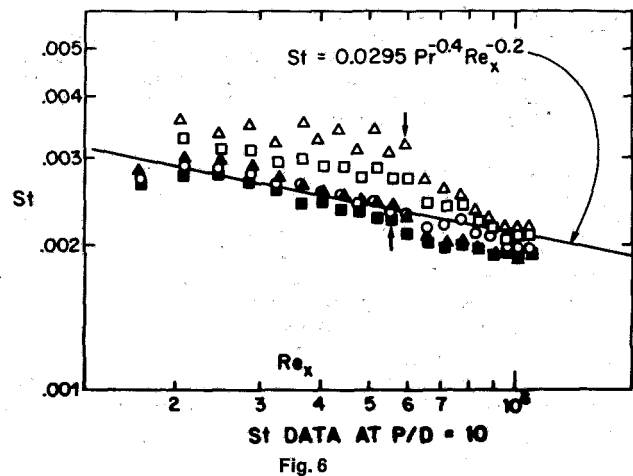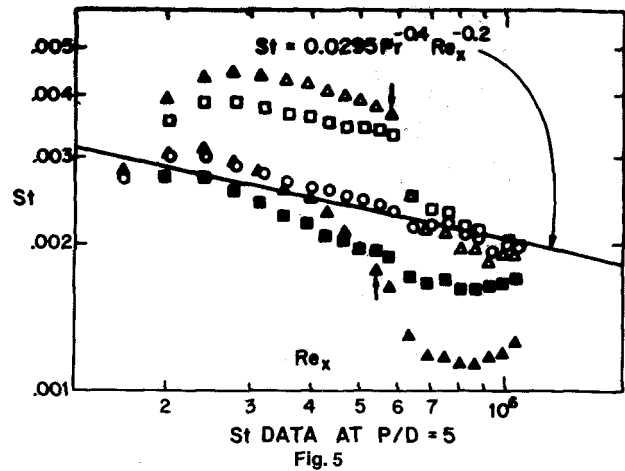
Figs. 5 and 6 Stanton numbers defined in method "B" for $P/D = 5$ and $P/D = 10$ (after H. Choe, W. M. Kays, and R. J. Moffat [8])

temperature," t_{iw}. A heat transfer coefficient is defined by the equation

$$q_w = h_o t_{iw} \qquad (5)$$

The temperature field for a general situation in which the coolant entry temperature is different from the main stream temperature and the heat flux is finite can now be obtained by superposition of the situation (a) and (b) resulting in the temperature profile $t = t_a + t_i$ and the wall temperature

$$t_w = t_{aw} + t_{iw} \qquad (6)$$

The coolant entry temperature is $t_2 + 0 = t_2$ as required. The heat flux in this case is again described by equation (5). With equation (6) it reads

$$q_w = h_o t_{iw} = h_o (t_w - t_{aw}) \qquad (7)$$

This method has several advantages. It ensures that the heat flux is zero when the temperature difference goes to zero. The heat transfer coefficient varies then in a continuous way with $t_w - t_{aw}$, and for a constant property fluid, is independent of this temperature difference. Any other temperature difference will have the effect that the heat flux and the temperature difference do not go to zero simultaneously. The heat transfer coefficient then assumes the value zero when the heat flux is zero and jumps from minus infinity to plus infinity when the temperature difference moves through zero. The heat transfer coefficient also has values close to those for no injection but otherwise identical boundary conditions when a region close
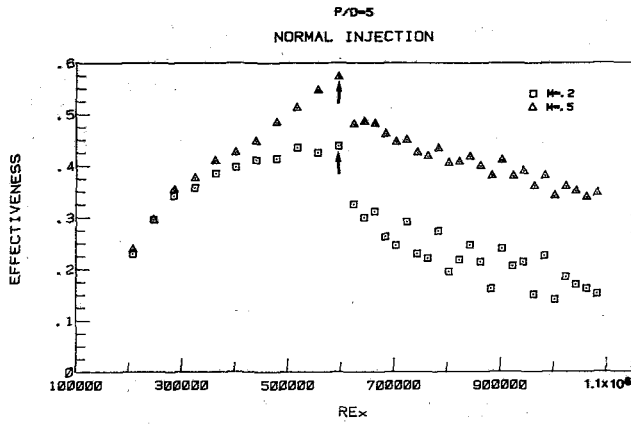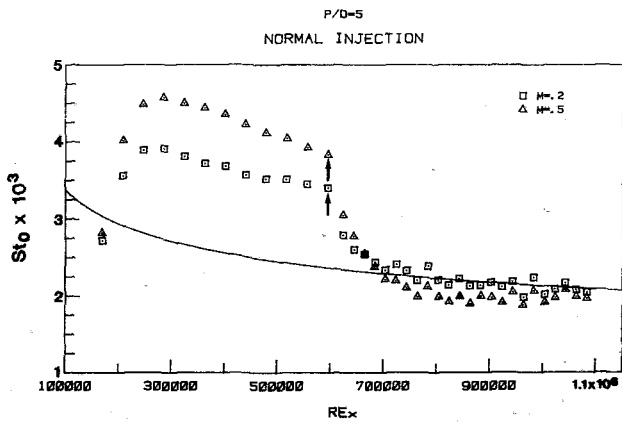
Fig. 7

Fig. 8

Figs. 7 and 8 Film cooling effectiveness and Stanton numbers respectively defined in method "A" for $P/D = 5$ and normal injection through 11 rows of holes for two blowing parameters, M

Fig. 9

Fig. 10

Figs. 9 and 10 Film cooling effectiveness and Stanton numbers respectively for normal injection through 11 rows of holes with $P/D = 10$ for two blowing parameters, M

to the location of injection is excluded. This has been demonstrated by experiments and can be derived from superposition when the ejection of coolant is approximated by a heat source or sink [1].

The flow and energy exchange processes are rather involved so that relations for the two situations (a) and (b) are generally obtained by experiments. The adiabatic wall temperature in case (a) is conveniently expressed in the form of a dimensionless parameter called film effectiveness

$$\eta_f = \frac{t_{aw}}{t_2} = \frac{T_{aw} - T_\infty}{T_2 - T_\infty} \qquad (8)$$

and the heat transfer coefficient, defined by equation (7), is reported in the form of a Nusselt or Stanton number (St), for instance

$$St_o = \frac{h_o}{\rho c_p u_\infty} f(M, Re, Pr) \qquad (9)$$

in which M denotes the blowing parameter.

In principle, the superposition can be used for any prescribed distribution of the heat flux q along x. Conveniently, however, experiments are performed for a uniform heat flux and the results are used to also describe approximately situations with non-uniform heat flux making use of the finding that the upstream history within a boundary layer does not effect turbulent local heat transfer strongly as long as the variation along x close to the point where the heat flux is considered is not too rapid.

The effect of aerodynamic heating as it becomes important in high velocity flow or for a fluid with a large Prandtl number has been discussed in [2] and will not be repeated here.
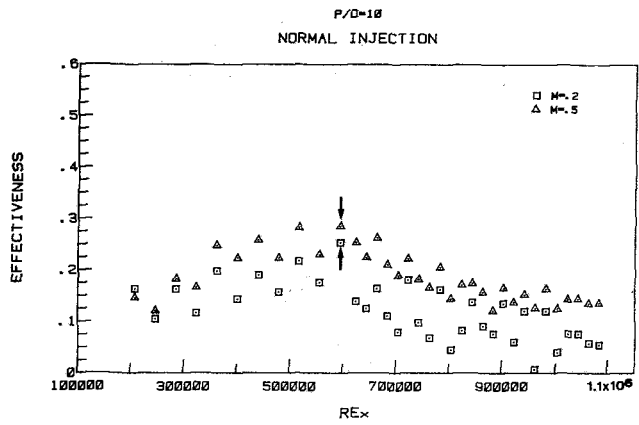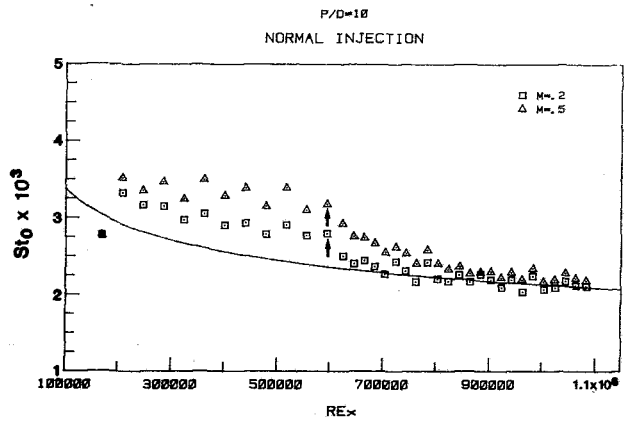
Calculation Method "B" for Full Coverage Film Cooling

Steady-state, constant properties and negligible effect of aerodynamic heating are again considered. The notation in Fig. 2 will again be used. In this method [4] the heat flux, q_w, is defined by the equation

$$q_w = h'(T_w - T_\infty) \qquad (10)$$

and a dimensionless parameter, θ, is used

$$\theta = \frac{t_2}{t_w} = \frac{T_2 - T_\infty}{T_w - T_\infty} \qquad (11)$$

The effect of film cooling is now incorporated in the heat transfer coefficient, h', and the ratio of the heat transfer coefficient, h', with an arbitrary temperature, T, to the heat transfer coefficient, h'_o, for the situation that T_2 is equal to T_∞ or $\theta = 0$ is

$$\frac{h'}{h'_o} = 1 + K\theta \qquad (12)$$

The constant, K, is

$$K = \frac{h'_1 - h'_o}{h'_o} \qquad (13)$$

The heat transfer coefficient h'_1 is describing the situation when $\theta = 1$ or the coolant ejection temperature, T_2, is equal to the wall temperature, T_w. The heat transfer coefficients are for situations with the same velocity and temperature boundary conditions. Equations (12) and (13) are again obtained by superposition of the temperature fields [3].
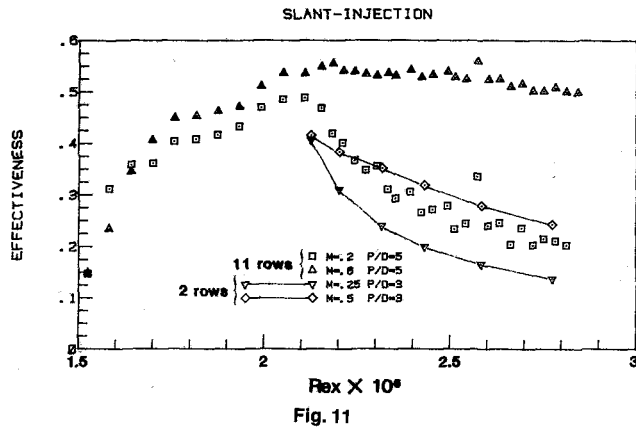
Fig. 11

Fig. 13 Laterally averaged film cooling effectiveness values as function of the parameter, ξ, for injection through two rows of inclined holes with $P/D = 3$ (after R. J. Goldstein, E. R. G. Eckert, H. D. Chiang, and E. Elovic [10])
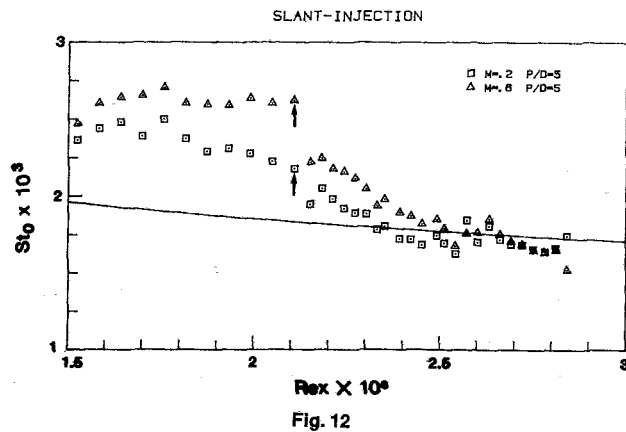

Fig. 12

Figs. 11 and 12   Film cooling effectiveness and Stanton numbers for injection through 11 rows of inclined holes with $P/D = 5$ for two blowing parameters, M

Fig. 14

Two sets of experiments are conveniently used in this method: (a) The coolant ejection temperature is equal to the main stream temperature, $T_2 = T_\infty$ ($\theta = 0$). (b) The coolant ejection temperature is equal to the wall temperature, $T_2 = T_w$ ($\theta = 1$). The method is based on superposition of temperature fields and holds in principle for any variation of T_w along x. It is, however, especially convenient for situations where the wall temperature is uniform along x.

It has been pointed out that the heat transfer coefficient can go to infinity when it is defined by equation (10). This happens, where T_2 is different from T_∞, but when the wall temperature is made equal to T_∞ by a proper positive or negative heat flux. It happens, for instance, when the wall surface receives more heat by radiation then is removed by internal cooling. This is rare for gas turbine blade cooling, but can occur in other applications.

Comparison of the Two Methods

The temperature field in full coverage film cooling (even the one averaged across the coordinate z) varies in the way sketched in Fig. 4. It exhibits more or less periodic fluctuations with a wavelength equal to the distance of the rows of cooling holes and in addition in general also a more gradual variation along x. The magnitude of the periodic variations depends on the conductivity of the film cooled wall, and it can have a considerable effect on the heat transfer coefficients as shown in [7]. It is, however, expected that the gradual variation has a smaller effect. Values of the heat transfer coefficient h_o' and of K obtained on an isothermal surface then can be used as an approximation to calculate heat transfer for a surface on which the periodic fluctuations are expected to be small.
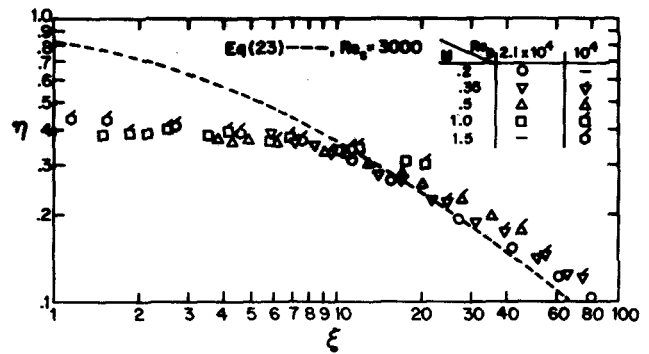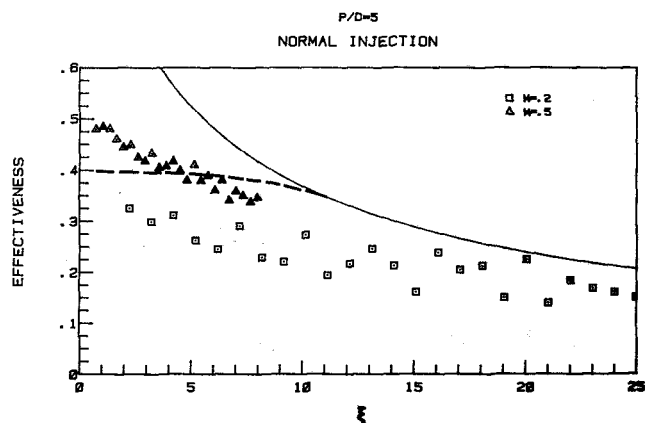
In this case, the parameters on which the two methods are based can be converted into each other. The heat transfer coefficient, h_o, of method "A" defined by equation (7) is then identical to the heat transfer coefficient, h_o', in method "B."

$$h_o = h_o' \tag{14}$$

The heat flux can then be written, considering equation (10) and (12)

$$q_w = h' \, (T_w - T_\infty) = h_o' \, (1 + K\theta) \, (T_w - T_\infty) \tag{15}$$

which can be transformed to

$$q_w = h_o' \, (T_w - T_\infty + KT_2 - KT_\infty) \tag{16}$$

Comparison of this equation with equation (7) results in

$$T_{aw} = T_\infty - K(T_2 - T_\infty) \tag{17}$$

The film effectiveness as defined by equation (8) becomes

$$\eta_f = \frac{T_{aw} - T_\infty}{T_2 - T_\infty} = -K \tag{18}$$

The parameters h_o and η_f required for the calculation method "A" are therefore connected with the parameters h' and K of method "B" by equations (14) and (18).

Extensive experiments have been performed at Stanford University on full coverage film cooling of an isothermal plane plate in a uniform mainflow of air with a velocity of approximately 10 to 15 m/s, producing a turbulent boundary layer. Part of the plate (the perforated section) had 11 rows of holes for ejection of cooling air. There was also a (solid) downstream portion which had no holes. The plate was electrically heated. The imposed temperature differences were about 15°C. The studies, therefore, covered full coverage film
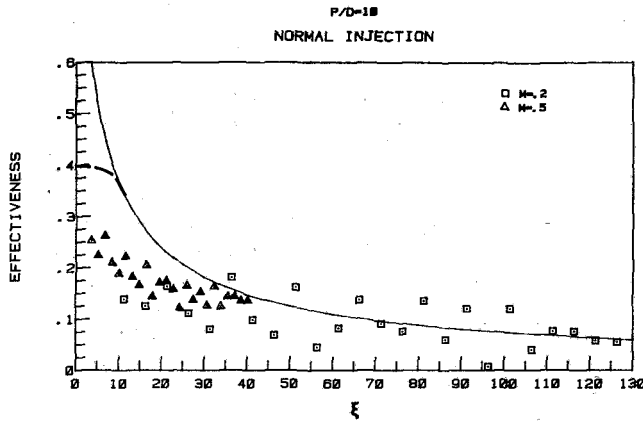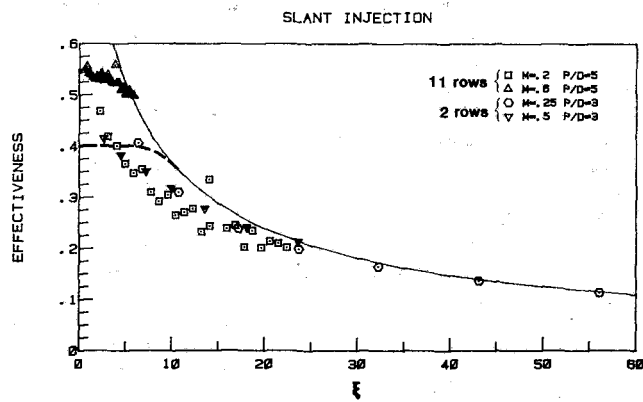
P/D=10
NORMAL INJECTION

□ M=.2
△ M=.5

Fig. 15

SLANT INJECTION

11 rows { □ M=.2 P/D=5
         { △ M=.5 P/D=5
2 rows { ○ M=.25 P/D=3
        { ▽ M=.5 P/D=3

Fig. 16

Figs. 14, 15 and 16 Film cooling effectiveness values as a function of the parameter, ξ, for normal injection through eleven rows of holes with P/D = 5 and P/D = 10 and for slant injection through eleven and two rows of holes, for two blowing parameters, M. The full line represents values for injection through a slot and the dashed line correlates values for injection through two rows of inclined holes.

cooling on the perforated section of the plate and film cooling on the solid downstream portion. Interesting observations can be made on the results published in [3] and reproduced in Figs. 5 and 6.

The Stanton numbers St = $h'/\rho c_p u_\infty$ as dimensionless parameters describing the heat transfer coefficient, h', are plotted over the Reynolds number $Re_x = u_\infty x/\nu$ determining the longitudinal position along the plate. The film cooled surface on which the results in Fig. 5 were obtained had 11 rows of holes with their axis normal to the plane surface in a staggered arrangement with a ratio of the distance, P, to the diameter, D, of the holes equal to 5 in x- and z-directions. For Fig. 6, the ratio P/D is 10. The open symbols are for the boundary condition which has the ejection temperature equal to the mainstream temperature or $\theta = 0$. The full symbols are for an ejection temperature equal to the wall temperature ($\theta = 1$). A line in the figures represents the Stanton number on a plane surface with a turbulent boundary layer and no injection. The first 11 experimental points encountered in flow direction represent measurements on the surface equipped with holes. The end of this section is indicated by arrows in this and subsequent figures. The points further downstream were obtained on the solid part of the plane wall on which film cooling occurs. It can be observed that the (laterally averaged) Stanton numbers for the condition $\theta = 0$ on that part of the surface are quite close to the Stanton numbers without injection, if values close to the last row of holes are

excluded. In those regions, the Stanton number with injection is up to about 25 percent higher than the Stanton number without injection. The situation $\theta = 0$ corresponds closely to the isoenergetic situation described in section 1, with the exception that in Figs. 5 and 6 a constant wall temperature was prescribed whereas most of the experiments performed for the isoenergetic situation dealt with a constant heat flux. The conclusions that the laterally averaged Stanton number in the film cooled region approaches closely the Stanton number for no ejection for the downstream region and is larger close to the ejection applies, therefore, equally to constant wall temperature and constant heat flux condition.

It is interesting to note that, for the full coverage film cooling portion, the experimental points for the condition which has the ejection temperature equal to the wall temperature ($\theta = 1$) are closer to the line representing no ejection. These are the full symbols in Figs. 5 and 6. This is an indication that the cooling process for full-coverage film cooling is different from that for film cooling and is closer to transpiration cooling, as has been pointed out in [3].

Film Cooling of a Surface Downstream of a Region With Injection Through 11 Rows of Holes

The experiments shown in Figs. 5 and 6 provide results not only for the full coverage portion but also for the solid wall located downstream. The data have also been reported in detail in [8] and additional results for the same geometry, except that the holes are inclined under an angle of 30 deg in downstream direction, are described in [9]. We have used these data to calculate film effectiveness values and heat transfer coefficients as defined in method "A." The results are presented in the following figures in which a linear scale is chosen for the abscissa because the film cooled region is compressed to a narrow range in the logarithmic scale used in Figs. 5 and 6.

Figures 7 and 8 present the film effectiveness as defined by equation (8) and the Stanton number defined by equation (9) for a geometry with a ratio P/D = 5. The Reynolds number used on the abscissa is based on the distance from the upstream end of the perforated test section. The blowing parameter is

$$M = \frac{\rho_2 v_2}{\rho_\infty u_\infty} \qquad (19)$$

Air was used for the mainstream and as coolant. The experiments were close to room temperature with a temperature difference of approximately 15°C. The results are, therefore, for Prandtl number Pr = 0.72.

The perforated section is provided with 11 rows of cooling holes and extends in the figures from the left to the value of Re_x indicated by an arrow. The points on the right-hand side of the arrows present the effectiveness along the solid section of the test plate. These effectiveness values are, therefore, for film cooling with injection of coolant through 11 rows of holes. Figure 8 presents the Stanton number described by equation (9). The heat transfer coefficient, h_o, is set equal to h_o' according to section 5. The line in the figure presents Stanton numbers for convective cooling of a turbulent boundary layer on a flat surface according to the equation

$$St = 0.0295 Re_x^{-0.2} Pr^{-0.4} \qquad (20)$$

It can be observed that the Stanton numbers measured for film cooling of the downstream solid portion of the surface are represented well by this equation except for a region close to the starting line of this section indicated by the arrows.

Film cooling effectiveness values and Stanton numbers are shown in Figs. 9 and 10 for the geometry with P/D = 10. Figure 10 demonstrates again that the Stanton numbers for the solid film cooled region are well presented by equation

(20), except for the region close to the starting point of this surface.

The same presentation of the effectiveness and the Stanton number for the geometry with holes inclined by 30 deg. and for a ratio $P/D = 5$ are presented in Figs. 11 and 12 for two values of the blowing parameter, M, the ratio of the specific mass flow leaving the holes to that of the main stream. Figure 11 also contains the laterally averaged effectiveness values obtained in our laboratory [10] for film cooling with injection of cooling air into a turbulent boundary layer of air along a plane surface through two rows of holes with a ratio $P/D = 3$ and inclined by 35 deg in flow direction. In comparing the blowing rates, M, for the two curves with the ones used in the experiments with 11 rows of holes, one has to keep in mind that $P/D = 3$ for injection through two rows, but $P/D = 5$ for injection through 11 rows of holes. Another comparison of results obtained with the two cooling methods will be made in the next paragraph. The Stanton numbers presented in Fig. 12 are again quite well represented by equation (20) in the downstream range and have higher values close to the start of the film cooled section.

Jabbari and Goldstein [11] were able to correlate laterally averaged film cooling effectiveness values for injection of air as coolant through two rows of holes into a turbulent boundary layer of air using a parameter ξ, which has been developed to correlate film cooling with injection through a slot. X in this parameter denotes the distance from the slot measured in downstream direction

$$\xi = \frac{(X + 1.909D)}{Ms} \left(\frac{\mu_2}{\mu_\infty} \text{Re}_s \right)^{-1/4} \tag{21}$$

M is the blowing parameter, s denotes the slot width, and the Reynolds number, Re_s, is defined with the mean exit velocity of the coolant from the slot and with the slot width. The ratio μ_2/μ_∞ is the ratio of the viscosity of the coolant to that of the main flow.

Jabbari and Goldstein defined an effective slot width for injection through holes that required the coolant flow per unit span have the same value when leaving the slot with the effective width as the one leaving the holes. This results in the equation

$$s = \frac{n\pi D^2}{4P} \tag{22}$$

for the effective slot width. The experimental points in Fig. 13 present the laterally averaged effectiveness as a function of the parameter ξ. It can be observed that experimental results for various values of the blowing parameter, M, and for two Reynolds numbers correlate quite well around one curve. For these experiments, $n = 2$ and $P/D = 3$. A dashed line is also inserted in the figure which presents the equation

$$\eta = (1 + 0.249\xi)^{-0.8} \tag{23}$$

derived by S. S. Kutateladze and A. I. Leontiév [2], which approximates well experimental data obtained in film cooling with injection through a slot. It can be observed that, for values of the parameter ξ larger than 10, the experimental points for film cooling with injection through two rows of holes agree fairly well with the effectiveness values for injection through a slot whereas, for smaller values of ξ, the film cooling parameter for injection through a slot is higher.

Figures 7, 9, and 11 were replotted using this parameter. The results are shown in Figs. 14, 15, and 16. The dashed line in these figures holds for injection through two rows of holes (Fig. 13). Experimental points for injection through two rows of holes are also included in Fig. 16. Obviously, use of the parameter ξ provides only a small improvement in the correlation of the data obtained with injection through 11 rows of holes as compared with Figs. 7–10.

Full Coverage Film Cooling Calculated With Method "A"

Figures 7–12 can also be used to calculate full coverage film cooling with method "A." The isoenergetic Stanton number is in this case not approximated by the relation for convection cooling but has to be taken from Figs. 8, 10, and 12. Method "A" still has the advantage that the heat transfer coefficient used in equation (7) is independent of temperature for a constant property situation, whereas the heat transfer coefficient or the Stanton number changes drastically and jumps from minus to plus infinity at a certain combination of the prescribed boundary temperatures in method "B" or in any other definition of the heat transfer coefficient. This combination probably does not occur in film cooling of turbine blades but film cooling is used for other applications and even in gas turbines at other places, for instance, for de-icing (as film heating). It is, therefore, of advantage to have a definition of the heat transfer coefficient which avoids this irregularity. The adiabatic condition ($q_w = 0$) on which the film cooling effectiveness is based applies locally only when a constant wall temperature is prescribed, and it is difficult to set up an experiment to determine the film effectiveness η because part of the surface has to be heated and part has to be cooled in order to create the adiabatic condition at the location x for which the effectiveness is desired. Film effectiveness can, however, be calculated from experiments discussed in section 4, where the coolant injection temperature, T_2, is made equal to the wall temperature, T_w, in one set and equal to the mainstream, T_∞, in the other set of experiments. Such measurements can conveniently be performed using the heat/mass transfer analogy with naphthalene ablation [6]. The effectiveness is then calculated with equations (13) and (18).

Mayle and Camarata reported the results of experiments on multihole cooling film effectiveness and heat transfer [12]. The film covered a flat surface with a turbulent boundary layer. A triangular pattern of holes with 2.5-mm dia and P/D ratios of 8, 10, and 14 covered the perforated part of the plate which had a length of 180 mm. The plate downstream of the perforated part was solid and had the same length. The holes were inclined by 30 deg toward the surface in main flow direction and by 45 deg sidewise. Experiments were carried out in a flow channel with 23 m/s mainstream velocity and a temperature difference of 27°C between the main and coolant air. Experiments were performed at values 0.5, 1.0, 1.5, and 2 of the blowing parameter, M. The experiments were evaluated using the film effectiveness method "A."

The spanwise-averaged film effectiveness is presented as a function of the downstream distance in Fig. 4 of [12]. Values at $M = 0.5$ and $P/D = 10$ can be compared with Fig. 9 of this paper. The effectiveness curve in Fig. 4 increases along the perforated part of the surface with decreasing rate in flow direction and finally reaches a flat plateau. Downstream of the perforated part, the effectiveness values decrease in downstream direction quite rapidly at first and at diminishing rate at larger downstream distances. This character of the effectiveness curve compares quite well with the corresponding values in Fig. 9 of this paper and even the numerical values exhibit reasonable agreement.

Stanton numbers evaluated with the film effectiveness method are presented in Fig. 5 of [12]. The values for $M = 0.5$ and $P/D = 10$ can again be compared with the corresponding values of Fig. 10 in this paper. In the far downstream solid portion of Fig. 5, the Stanton numbers agree well with values for a flat surface with a turbulent boundary layer but without film cooling. The film effectiveness values increase beyond those without film cooling at an increasing rate as the junction between the perforated and the solid part is approached in an upstream direction. In

the perforated part, the Stanton numbers with film cooling are larger than those without film cooling up to approximately 40 percent. All these factors agree again quite well with those exhibited in Fig. 10 of this paper. One can, therefore, conclude that inclining the holes in sidewise direction had little effect on the film cooling effectiveness and the Stanton numbers at $M = 0.5$ and $P/D = 10$.

Summary

Two calculation methods, "A" and "B," for the prediction of heat transfer in film cooling have been presented and compared. Both are based on the principle of superposition of solutions of the temperature fields for a constant property fluid. The method "A" based on film cooling effectiveness and isoenergetic heat transfer coefficients has been widely used for the presentation of results obtained in film cooling with injection through slots and a porous section as well as through one or two rows of holes. This method has the advantage that laterally arranged heat transfer coefficients or Stanton numbers defined in this way are independent of the imposed temperature differences for a constant property situation and are close to values for convective film cooling for the region some distance downstream of injection. For the region close to injection, they increase with decreasing distance to values which are up to 25 percent higher than those for convection cooling. This fact has been established in the past for injection through slots, porous sections, and one or two rows of holes and has been reaffirmed in the present paper for film cooling with injection through 11 rows of holes. The main experimental effort can, therefore, concentrate on a determination of the film cooling effectiveness.

Figures 7, 9, and 11 can be applied to design calculations considering injection of a coolant through 11 rows of holes with $P/D = 5$ or 10, and Figs. 14–16 may be useful for interpolation when information on other hole arrangements is required.

For full-coverage film cooling describing the situation in the region which is provided with injection holes, method "B" has been introduced in [3] which is based on the parameters θ and K. This method has the basic disadvantage that the heat transfer coefficient or the Stanton number vary in an irregular way with the temperature difference $T_w - T_\infty$ as defined in equation (10). This can be avoided when the film cooling process for the perforated section is also calculated with method "A."

References

1 Eckert, E. R. G., "Transpiration and Film Cooling," *Heat Transfer Symposium*, University of Michigan, University of Michigan Press, 1953.

2 Goldstein, R. J., "Film Cooling," *Advances in Heat Tranfer*, Vol. 7, Academic Press, New York, 1971, pp. 321–379.

3 Metzger, D. E., Carper, H. J., and Swank, L. R., "Heat Transfer With Film Cooling near Nontangential Injection Slots," ASME JOURNAL OF ENGINEERING FOR POWER, Vol. 90, 1968, p. 157.

4 Choe, H., Kays, W. M., and Moffat, R. J., "The Superposition Approach to Film Cooling," ASME Paper No. 74-WA/HT-27, New York, 1974.

5 Tribus, M., and Klein, J., "Forced Convection from Nonisothermal Surfaces," Heat Transfer Symposium, University of Michigan Press, 1953, pp. 211–235.

6 Eckert, E. R. G., Hartnett, J. P., and Birkebak, R., "Simplified Equations for Calculating Local and Total Heat Flux to Nonisothermal Surfaces," *Journal of Aeronautical Sciences*, Vol. 24, No. 7, July, 1957, pp. 549–550.

7 Hirata, M., Kasagi, N., and Kumada, M., "Studies in Full-Coverage Film Cooling," Reports of Special Project Research under Grant in Aid of Scientific Research of the Ministry of Education Science and Culture Japan, *Research on Effective Use of Energy*, Vol. 1, 1982, pp. 127–134.

8 Choe, H., Kays, W. M., and Moffat, R. J., "The Turbulent Boundary Layer on a Full-Coverage Film Cooled Surface: An Experimental Heat Transfer Study with Normal Injection," Report HMT-22, Stanford University, Department of Mechanical Engineering, Stanford, Calif.

9 Crawford, M. E., Kays, W. M., and Moffat, R. J., "Full-Coverage Film Cooling on Flat, Isothermal Surfaces; A Summary Report on Data and Predictions," Report HMT-30, Stanford Unversity, Department of Mechanical Engineering, Stanford, Calif.

10 To be published, submitted for presentation at the 1984 International Gas Turbine Conference.

11 Jabbari, M. Y., and Goldstein, R. J., "Adiabatic Wall Temperature and Heat Transfer Through Two Rows of Holes," ASME JOURNAL OF ENGINEERING FOR POWER, Vol. 100, No. 2, Apr., 1978, pp. 303–307.

12 Mayle, R. E., and Camarata, F. J., "Multihole Cooling Film Effectiveness and Heat Transfer," AMSE *Journal of Heat Transfer*, Vol. 97, No. 4, November, 1975, pp. 534–538.

Cooling Airflow Studies at the Leading Edge of a Film-Cooled Airfoil

E. S. Tillman

Mechanical Engineering Department,
University of Bridgeport,
Bridgeport, Conn. 06601

H. F. Jen

Heat Transfer Department,
Avco-Lycoming Division,
Stratford, Conn. 06497

An experimental flow study on cooling holes in cylindrical models simulating the leading edge of a typical turbine airfoil is presented. The effect of external flow around the cylinder on the coolant discharge through a single hole is represented as a function of the momentum ratio of the cooling jet to the local external flow. A similar correlation was found for the effect of internal axial flow. The ability to separate the entrance and exit effects on the hole is due to the fact that the hole is a long orifice. The entrance and exit effects on the coolant flow are expressed as loss coefficients analogous to traditional loss coefficients in pipe flow. The loss coefficients for single holes were used to predict the total and individual flows through an array of holes in the presence of an external flow field. The total flow is predicted accurately as compared to the results of tests on arrays of holes. It can be concluded that the interaction between adjacent cooling holes is slight. The physical model can be used for coolant optimization studies.

Introduction

The demand for improved gas turbine cycle efficiencies has resulted in progressively higher turbine inlet temperatures. One of the most challenging tasks facing turbine design engineers is the thermal protection of the hot section in order to achieve acceptable component life. Film cooling, often augmented by internal impingement cooling, is the most commonly used method for turbine blade thermal protection. It has been found that film cooling provides protection in two ways, first by forced convection cooling of the metal as the coolant passes through the cooling holes and second, by forming a protective film of cool gas over the outer surface of the blades.

When the film cooling air is injected through rows of holes in the leading edge of a turbine vane or blade, the method is frequently referred to as "showerhead" cooling. In this method, which is described by Taylor [1], the accurate prediction of the flow from individual holes and the local convection heat transfer coefficients are essential if the cooling holes are to be located in a pattern which will make optimum use of the available coolant supply. The study discussed in this paper was concerned with investigating the flow from holes on the leading edge of a simulated airfoil. The major objective of this research was to develop an analytical method for the prediction of flow from arrays of leading edge cooling holes.

When showerhead cooling is used for a turbine vane or blade, the flow from individual holes is influenced by several factors. The location of the holes relative to the forward stagnation region will have a strong effect on the coolant flow rate. Holes near the stagnation point will be injecting into a region with a local pressure equivalent to the main stream stagnation pressure. However, holes a short circumferential distance from the stagnation region will experience a local pressure much lower than the stagnation pressure because of the rapid flow acceleration around the cylindrical leading edge. The angle of the external flow relative to the injected jet also changes around the leading-edge. For injection from a normal hole at the stagnation region, the main flow is in opposition to the jet flow. At a location 90 deg from the leading edge the free stream flow would be perpendicular to the injected fluid.

In a typical turbine vane or blade, the cooling air is supplied to the cooling holes through passages within the leading edge region. The internal velocity along the blade decreases as the air escapes through the holes. Thus, each hole in an array can be subjected to a different combination of internal and external velocity and flow environments with the result that coolant flow rate may vary significantly from hole to hole.

The discharge of cooling air from a hole in the leading edge of a turbine blade represents an extremely complex three-dimensional type of flow. Even with existing computer codes for three-dimensional flow, an exact solution of the problem is not possible. The major difficulty is that the modeling of flow separation and turbulent jet mixing are not yet available. Thus, an empirical approach was undertaken to develop a working method for the calculation of flow from multiple hole arrays.

Literature Review

The flow through cooling holes is related to flow through a thick plate orifice. The discharge coefficients of long orifices

have been studied by Lichtarowicz et al., [2] who compiled the results of several investigations. Their study concentrated on flows normal to the orifice plate and covered plate thickness to hole diameter ratios of 0.5 to 4.0.

In a gas turbine blade, the flow often approaches the cooling holes in a spanwise direction. This condition was studied by Rohde and Richards, [3] in a series of experiments on a single cooling hole machined through the wall of a tube with a 6.4-mm i.d. The experiments were performed at approaching Mach numbers between 0.02 to 0.65. Their results showed that the coefficient of discharge of the hole was very sensitive to the approaching velocity. As the tube approach velocity increased, a significant drop in the coefficient of discharge was measured.

The effect of both upstream and downstream flow on the discharge coefficient of an orifice has been studied by Hay et al., [4]. Most of their results are presented in theses by Mellor [5] and Cornfield [6]. Their apparatus consisted of a flat plate with four orifices mounted between two wind tunnels. The velocities past the entrance and the exit of holes could be controlled. The flow rate through the orifices was deduced from the flow rates in the tunnels. The wind tunnels could be arranged for either parallel or cross flow. Data were presented for several combinations of flow rates. No analytical model was reported, but a comparison was made to the "lid model" of Rogers and Hersh [7]. This model is based on momentum exchange and pressure forces between the jet and the free stream flowing past the orifice. The model predicts discharge coefficients which are higher than experimental values.

Discharge from a hole in a cylinder in crossflow was studied by Saski et al., [8]. Their tests were performed on a 20-mm-o.d. cylinder with various single test holes and on multiple hole cylinders. The results were plotted as an additive loss coefficient versus a momentum flux ratio. The additive loss coefficient is a term which represents the flow interaction with mainstream air at the hole exit. Using this type of correlation, the authors were able to present data for various hole locations, relative to the stagnation point, by a simple correlation.

A detailed study of the interaction between a jet discharging from a single normal hole in a flat plate and an external cross flow was made by Bergeles, Gosman and Launder [9]. They took extensive velocity measurements which showed that the jet distortion by the cross flowing free stream extended as far as one half diameter into the hole.

A recent paper by Jen and Sobanik [10] presents a numerical method for the calculation of cooling air flow through gas turbine components. Their method requires that the entire flow path be subdivided into a series of simple flow elements. A flow parameter, which includes the pressure loss coefficient due to irreversible effects and a factor due to area change, must be determined for each element. The results of the flow studies discussed in this paper could be used to establish physical models of the showerhead cooling holes for the prediction of injected coolant flow rate.

Experimental Program

The experimental phase of this study consisted of two test series. The first series involved the study of flow from single holes machined in 10.16-cm (4.00-in.) dia cylinders. These tests were used to establish coefficients of discharge and entrance and exit loss coefficients for individual holes. The second series consisted of tests with arrays of holes drilled into 5.08-cm (2.00-in.) dia cylinders. The multiple hole cylinders represented approximately 10:1 scale models of the leading-edge of a small gas turbine blade. The large scale models were used for the single hole tests to give more room for pressure taps and velocity measuring instruments.

For the single hole experiments, standard thick wall aluminum tubing was machined to 10.16-cm (4.00-in.) o.d. with a 2.03-cm (0.80-in.) wall thickness. Two 10.6-cm (4.00-in.)-long test cylinders were fabricated: one with 5.08-mm (0.20-in.)-dia test holes and one with 10.16-mm (0.40-in.)-dia test holes which correspond to length to diameter ratios of 4 and 2, respectively. Each cylinder had three test holes spaced 120 deg apart: one drilled at 90 deg to the cylinder axis, one drilled at 45 deg to the cylinder, and one drilled at 30 deg to the cylinder axis. Each test hole has three evenly spaced pressure tap holes along its length. Surface pressure taps were also located around the cylinder spaced 20 deg apart.

Each test cylinder was mounted in a low-speed wind tunnel with a 0.43-m (17-in.)-wide by 0.30-m (12-in.)-high test section (Fig. 1). All tests holes and pressure tap holes, except those under study, were blocked off with tape. A support cylinder with flange was fitted onto each end of the test cylinder to form a single 0.71-m (28-in.)-long cylinder which was mounted across the center of the wind tunnel test section to insure two-dimensional flow. The cylinder could be rotated about its axis so that the test hole could be oriented at the stagnation point or up to 90 deg away from the stagnation point. The stagnation point was assumed to exist at the 0 deg angular orientation measured from the horizontal. A tapered wooden blockage device was mounted behind the cylinder to prevent vortex shedding and provide flow stability.

Air supplied to the test cylinder through a commercial grade rotometer and hand operated control valve. Various flow meters were used depending on the flow range. All

---

Nomenclature

A_j = flow area of single cooling hole

A_T = cross-sectional flow area inside cylinder

C_D = coefficient of discharge

C'_D = coefficient of discharge based on ΔP

d = test hole diameter

D = tube outside diameter

K_i = internal momentum ratio, $K_i = \rho_j V_j^2 / \rho_T V_T^2$

K_0 = external momentum ratio, $K_0 = \rho_j V_j^2 / \rho_\infty V_s^2$

L = test hole length

M = blowing velocity ratio, V_j / V_∞

N = number of cooling hole rows

ΔP_e = exit pressure correction, Pe

ΔP_i = inside pressure correction

ΔP = effective pressure difference for flow $P = P_T - P_S - \Delta P_e - \Delta P_i$

P_p = plenum static pressure

P_s = surface static pressure at hole location

P_T = total pressure inside cylinder

P_∞ = wind tunnel static pressure

Q = volume flow rate through test hole, $Q = V_j A_j$

Re_d = Reynolds number based on hole diameter and hole flow

Re_D = Reynolds number based on outside tube diameter and external flow

Re_T = Reynolds number based on inside tube diameter and internal flow

V_j = hole velocity

V_s = surface velocity

V_T = tube axial velocity

V_∞ = wind tunnel velocity

β = area ratio for orifice, A_j / A_T

δ_0 = external additive loss coefficient

δ_i = internal loss coefficient

θ = hole orientation relative to stagnation point

ϕ = spanwise hole angle

ρ_j = air density in coolant jet

ρ_∞ = air density in wind tunnel
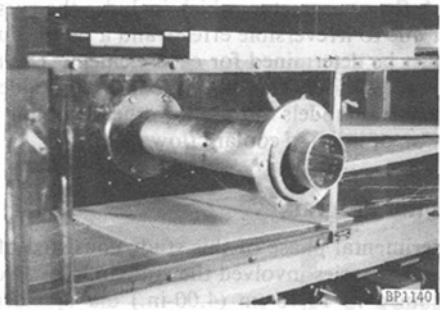
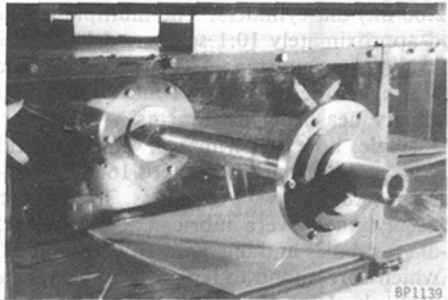
Fig. 1 Large test cylinder with a single hole

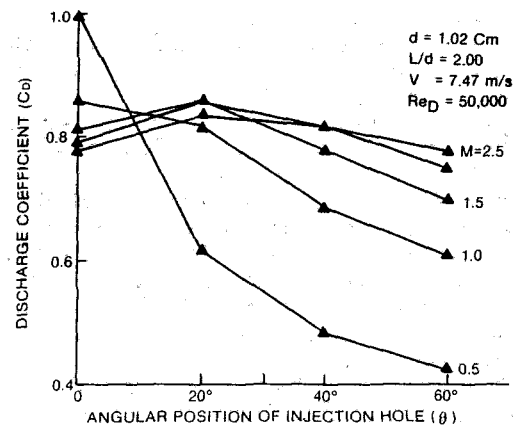Fig. 2 Test cylinder with multiply rows of holes

Fig. 3 Angular dependence of coefficient of discharge, 90 deg hole
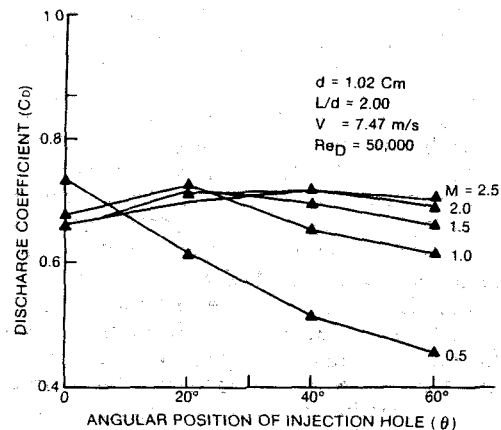

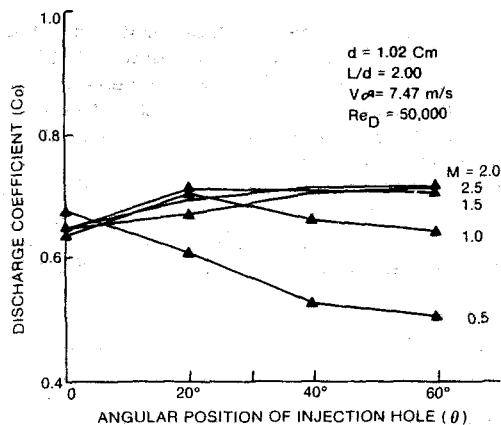Fig. 4 Angular dependence of coefficient of discharge, 45 deg hole

Fig. 5 Angular dependene of coefficient of discharge, 30 deg hole

meters were manufactured by Fischer and Porter Co. and were accurate to ±2 percent of full flow. The air supply tube was mounted coaxially to the support tube. Its inside diameter was similar to the inside diameter of the test cylinder so that there would be no disturbance of the inside air flow as it approached the test hole. All pressure tap leads passed from the wind tunnel through the support tube at the opposite end to the air inlet.

All air pressures were measured with a Setra Systems Inc., Model No. 239 precision pressure transducer connected to a digital pressure indicator. This system measured differential pressures from 0 to 13.8 KPa in increments of 0.7 Pa. The system was checked against a laboratory grade micromanometer and found to be accurate within 0.3 percent over the range of pressures used in these tests. All pressure taps were connected through a valved manifold to the pressure transducer. For the wind tunnel experiments the static pressure, P_∞, located 0.3-m upstream of the test cylinder was used as a reference pressure. The wind tunnel velocity was measured by a built-in meter and checked with a pitot tube and laboratory grade manometer. It is estimated that the air velocity is accurate to within 5 percent. The air temperatures were measured with thermocouples connected to a digital temperature indicator with 1 °F subdivision. All testing was performed at low subsonic velocities, maximum V_∞ approximately 15 m/s, and room air temperature of approximately 24°C.

Two types of testing were performed in the single hole experiments: wind tunnel testing with negligible velocity inside the cylinder and bench testing with varying internal velocity. During wind tunnel testing the end of the test cylinder was sealed off so all air discharged through the test hole. During the bench testing the end cap was removed and a damper device installed to control airflow. Since there was no direct way to measure the flow through the hole during the bench testing, a plenum was attached over the hole and the flow rate measured after discharge.

In multiple hole testing, standard 5.08-cm (2.00-in.)-dia aluminum tubing with a 9.5-mm (0.375-in.) wall thickness was used. The test cylinders were 20.32-cm (8.0-in.)-long with holes drilled over the middle 15.24-cm (6.00-in.) section. Six

cylinders were fabricated: three with 2.54-mm (0.10-in.)-dia holes and three with 5.08-mm (0.20-in.)-dia holes. For the first and fourth cylinders the holes were drilled perpendicular to the cylinder axis, for the second and fifth cylinders the holes were oriented at 45 deg from the axis, while for the third and sixth cylinders the holes were oriented at 30 deg from the axis. For all test cylinders the rows of holes were arranged in a staggered array with hole to hole and row to row spacings of 2.5-hole diameters.

Each test cylinder and support cylinder was mounted in the low-speed wind tunnel in a manner similar to the single hole models (Fig. 2). Support flange adapters were made for each
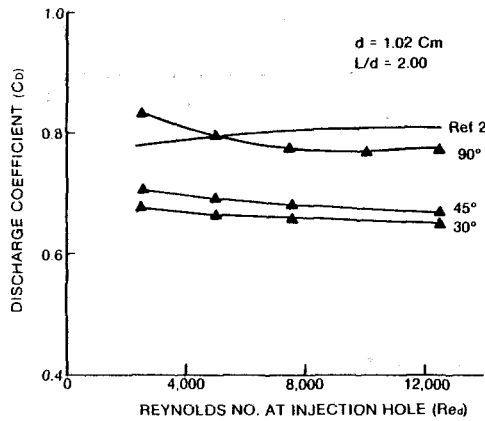
Fig. 6 Coefficient of discharge with zero free-stream velocity and low approach velocity
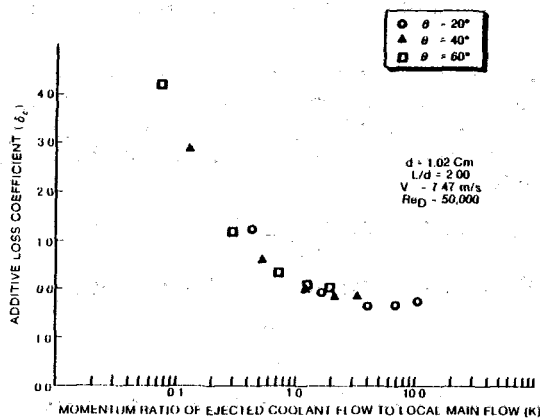

Fig. 8 Additive loss coefficient for 45 deg hole

Fig. 7 Additive loss coefficient for 90 deg hole
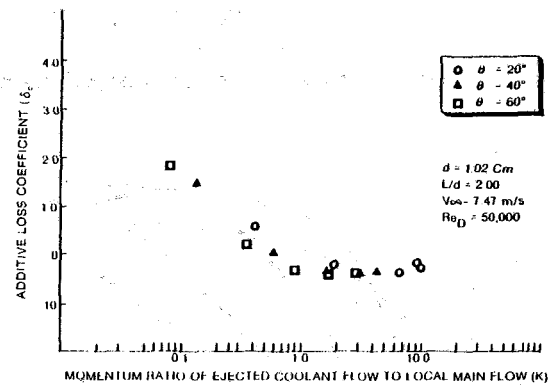
Fig. 9 Additive loss coefficient for 30 deg hole

end so that the test cylinder could be turned on its axis. As in the single hole experiments, air was supplied through a flow meter and hand control valve. Various meters were used depending upon the flow range desired. All pressures were measured with the same pressure transducer and digital pressure indicator used in the single hole tests. The test cylinders were instrumented with static pressure taps to give values of internal and external static pressures. A single pressure tap at the closed end of each cylinder indicated the supply total pressure.

Experimental Results

The first group of single hole tests was run with the 10.16-mm (0.40-in.)-dia test holes, $L/d = 2$. Tests were run with various jet to free-stream velocity ratios. The wind tunnel velocity was adjusted to give a cylinder Reynolds number of 50,000, typical of turbine blade operating conditions. The test hole was adjusted to angular orientations of 0, 20, 40, and 60 deg from the stagnation point. A coefficient of discharge defined as

$$C_D = \frac{Q_j}{A_j \sqrt{2(P_T - P_S)/\rho_j}} \tag{1}$$

was calculated for each test point. Plots of C_D versus angle are shown in Figs. 3, 4, and 5 for various blowing ratios, M. Referring to Fig. 3 for the 90-deg hole, it can be seen that for high blowing ratios, M, the value of C_D reaches a maximum at an orientation of 20 deg. However, for the lower blowing ratios, the maximum value of C_D is reached at the stagnation point. This phenomenon had been discussed in [8] and was attributed to the spreading action of the incoming free stream
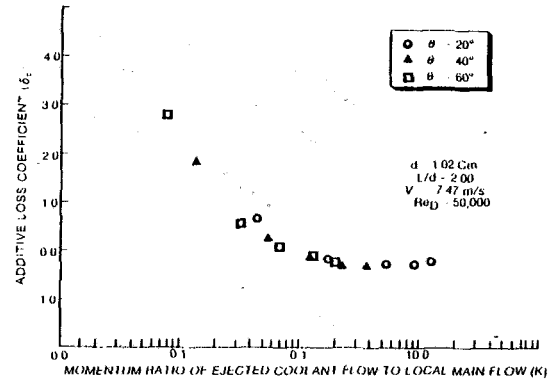
near the stagnation point. A similar but less pronounced effect can be seen in Fig. 4 for the 45-deg hole and Fig. 5 for the 30-deg hole.

The coefficient of discharge with zero free-stream velocity was also measured for each test hole. These results are presented in Fig. 6. The results of [2] are also presented in Fig. 6 for comparison for the 90-deg hole only. A close correlation between the results can be noted. The slight deviation at low flow could be due to wall curvature effects. Also, it should be noted that in this Reynolds number range, the data of [2] shows some instability which makes it difficult to determine whether the slope is positive or negative.

The test points of Fig. 3 can be correlated by the method of Saski et al., [8] in which an additive loss coefficient, δ_0, was defined as

$$\delta_0 = \frac{(P_T - P_S)_{V_\infty} - (P_T - P_S)_{V_\infty = 0}}{\rho_j V^2/2} \tag{2}$$

where $(P_T - P_S)_{V_\infty}$ is the pressure difference across the test hole with wind tunnel flow and $(P_T - P_S)_{V_\infty} = 0$ is the pressure difference across the test hole, at the same hole flow rate, with no wind tunnel flow. The values of δ_0 can be correlated against a local momentum ratio, K_0 where

$$K_0 = \frac{\rho_j V_j^2}{\rho_\infty V_s^2} \tag{3}$$

When the data of Fig. 3 is plotted on a $K_0 - \delta_0$ coordinate system as Fig. 7, the data falls essentially on a single curve. The stagnation point data cannot be correlated in this manner since the momentum ratio become infinite. Figures 8 and 9 show similar correlations for the 45 and 30 deg holes. Similar tests on the 5.08-mm (0.20-in.)-dia holes, $L/d = 4.0$, produced almost identical results showing that the effect of L/d on the coefficient of discharge is very weak. These
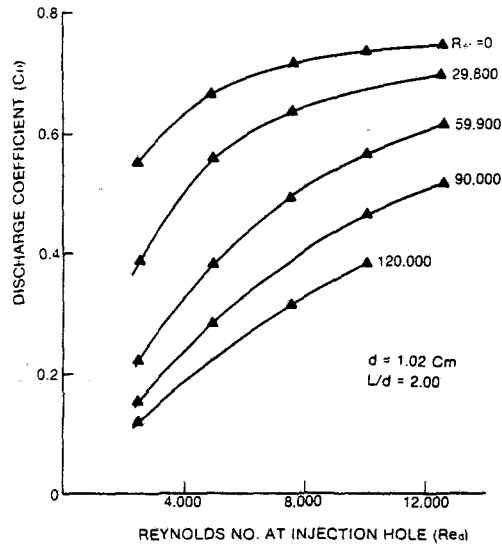
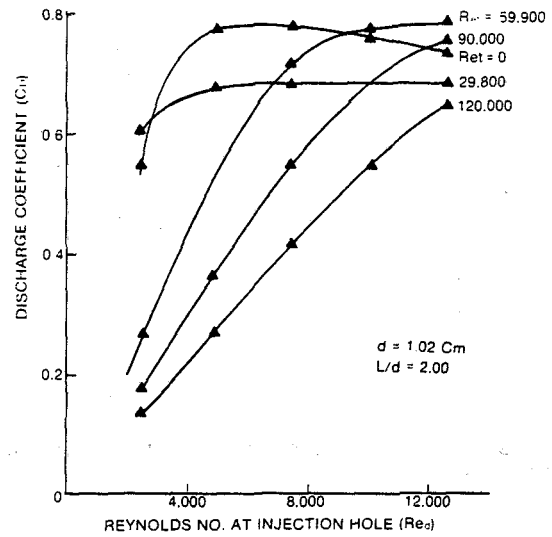Fig. 10 Effect of internal flow on coefficient of discharge, 90 deg hole

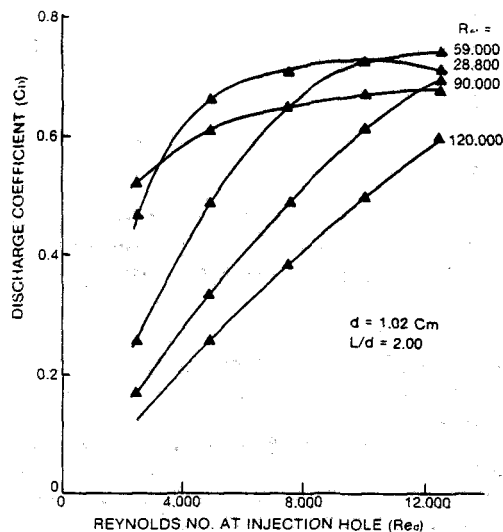Fig. 12 Effect of internal flow on coefficient of discharge, 30 deg hole

Fig. 11 Effect of internal flow on coefficient of discharge, 45 deg hole

correlations are not presented in this paper for reasons of brevity. However, they are used in the analytical results discussed in the next section.

The next sets of curves show the effect of internal flow on the coefficient of discharge in the bench testing condition. In these experiments a controlled amount of flow bypassed the hole and escaped through an end damper. The velocity past the inside end of the hole was measured by pitot tube. The flow through the hole was captured in a small plenum and discharged to atmosphere through a flowmeter. Figure 10 shows coefficients of discharge plotted versus hole Reynolds number for various values of internal Reynolds number. For these curves, P_S was replaced by P_P in equation (1). The top curve represents the case of zero axial flow. This coefficient of discharge is less than that shown in Fig. 6 for the hole discharging into the open air. The difference is due to interference effects of the small plenum mounted over the hole. Since the primary interest is on the effect of tube axial velocities, the values of C_D at various values of Re_T are compared to the values of C_D at $Re_T = 0$. Thus, the plenum inteference effects tend to cancel out. The most significant point seen in this figure is the large decrease in the coefficient of discharge as the tube velocity increases for a fixed hole flow rate. Similar effects are shown in Figs. 11 and 12 for 45- and

30-deg holes, respectively. The experimental values used to develop these curves can be plotted as a loss coefficient, δ_i, versus a momentum ratio, K_i, in a manner similar to the data for the exit condition. The internal loss coefficient, δ_i, is defined as

$$\delta_i = \frac{(P_T - P_P)_{\text{Tube flow}} - (P_T - P_P)_{\text{Tube flow}=0}}{\rho_j V^2 / 2} \qquad (4)$$

while the internal momentum ratio, K_i, is defined as

$$K_i = \frac{\rho_j V_j^2}{\rho_T V_T^2} \qquad (5)$$

For low subsonic velocities, $\rho_j = \rho_T$ so K_i can be represented by $(V_j / V_T)^2$. These correlations are shown in Figs. 13, 14, and 15. It can be seen that most of the points fall into a well-defined curve. One point of interest is that the loss coefficients became negative for the 45- and 30-deg holes when the tube and hole velocities are the same magnitude. This is due to the fact that the air approaches the hole with significant momentum in the axial direction of the hole which increases flow above that which would occur with low tube velocities. Similar results not presented in this paper, were obtained for the small hole test cylinders, [4]. This shows that the influence of the L/d ratio is weak for the internal loss coefficients.

It is not possible to measure the coolant flow through the hole when internal axial flow and exterior flow occurred simultaneously. This is because the hole coolant flow would have to be determined by subtracting the measured values of the total coolant flow and the bypassed axial flow, both of which are large compared to the hole flow. An effort was made to use the hole pressure taps to indicated flow rate. This proved unsuccessful because of two problems. First, a high degree of fluctuation was experienced in those pressure measurements so accurate reading was impossible. Second, under certain flow conditions the pressure increased in the flow direction due to jet reattachment, and in other cases the pressure decreased. Thus, no consistent pattern of pressure gradient versus hole flow could be developed.

The final tests were run with the six 5.08-cm (2.00-in.)-dia multiple hole cylinders. In these tests the total flow rate through all the holes was measured and the pressure differential, $P_T - P_\infty$ was measured for each flow rate. These tests were run to give a basis of comparison for the analytical method discussed in the next section. Four test conditions were run for each cylinder. The entire array of holes was tested at Reynolds numbers, based on the outside cylinder diameter, of 20,000 and 50,000. Then alternate rows of holes
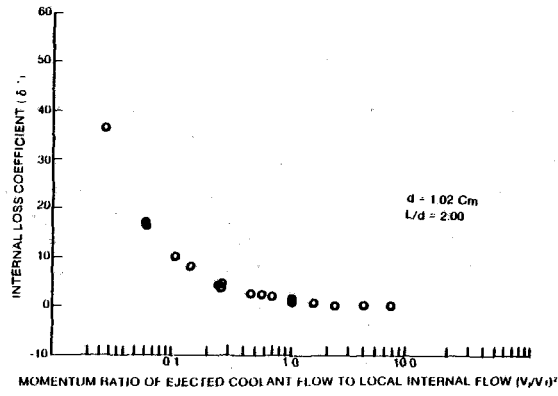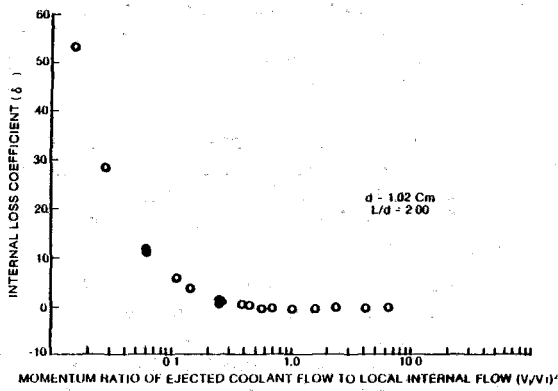
Fig. 13 Internal loss coefficient, 90 deg hole

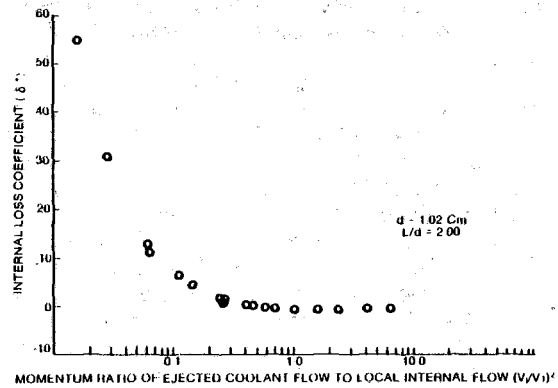Fig. 14 Internal loss coefficient, 45 deg hole

Fig. 15 Internal loss coefficient, 30 deg hole

Table 1 Experimental (Q) and calculated (Q') total flow for multiple hole cylinders

$$L/d = 1.875$$

N	φ	M_{avg}	Re$_D$ = 20,000 Q (L/s)	P Pa	Q' (L/s)	Re$_D$ = 50,000 Q (L/s)	P a	Q' (L/s)
5	90°	0.5	3.92	23.46	4.58	9.86	137.42	11.19
		1.0	7.88	63.20	7.69	19.68	374.42	18.83
		1.5	11.80	135.98	11.33	29.50	837.90	28.27
		2.0	15.72	249.93	15.38	36.81	1355.01	35.87
		2.5	19.68	397.88	19.49			
		3.0	23.60	584.14	23.55			
3	90°	1.0				6.56	224.58	6.65
		1.5	3.92	82.83	3.93	9.82	493.17	9.72
		2.0	5.24	149.39	5.24	13.1	871.42	12.70
		2.5	6.56	228.39	6.51	16.37	1369.38	15.67
		3.0	7.88	331.81	7.83	19.68	2025.34	18.83
5	45°	0.5	3.92	22.98	5.66	9.86	135.98	14.06
		1.0	7.88	50.27	8.54	19.68	289.68	21.00
		1.5	11.80	100.07	11.89	29.50	574.56	29.02
		2.0	15.72	170.45	15.10	36.81	876.21	34.17
		2.5	19.68	261.91	18.55			
		3.0	23.60	379.21	22.18			
3	45°	1.0				6.56	239.40	7.69
		1.5	3.92	90.49	4.47	9.82	507.53	10.81
		2.0	5.24	158.00	5.85	13.12	885.78	13.83
		2.5	6.56	242.75	7.36	16.38	1378.95	16.80
		3.0	7.88	350.96	8.73	19.68	2078.00	20.15
5	30°	0.5	3.92	22.98	6.04	9.86	139.33	15.24
		1.0	7.88	50.27	8.97	19.68	300.69	22.13
		1.5	11.80	96.72	12.27	29.50	579.35	29.83
		2.0	15.72	162.79	15.29	36.81	861.84	35.68
		2.5	19.68	245.63	18.03			
		3.0	23.60	355.75	21.57			
3	30°	1.0				6.56	232.22	8.02
		1.5	3.92	84.75	4.51	9.82	497.95	11.32
		2.0	5.24	158.00	6.04	13.12	871.42	14.35
		2.5	6.56	245.63	7.65	16.38	1388.53	17.60
		3.0	7.88	354.31	9.06	19.68	2044.49	20.95

Table 2 Experimental (Q) and calculated (Q') total flow for multiple hole cylinders

$$L/d = 1.875$$

N	φ	M_{avg}	Re$_D$ = 20,000 Q (L/s)	P Pa	Q' (L/s)	Re$_D$ = 50,000 Q (L/s)	P a	Q' (L/s)
9	90°	0.5				8.50	152.26	10.38
		1.0	6.80	67.03	6.94	16.99	383.52	11.89
		1.5	10.19	139.81	10.62	25.49	804.39	26.24
		2.0	13.59	241.80	14.30	33.98	1412.47	34.83
5	90°	1.0				4.91	285.37	5.47
		1.5				7.36	598.50	7.88
		2.0	3.92	173.81	4.24	9.82	1048.58	10.43
		2.5	4.91	272.92	5.29	12.32	1642.29	13.03
		3.0	5.90	398.36	6.37	14.77	2403.59	15.72
9	45°	0.5	3.40	23.94	3.85	8.50	140.77	11.09
		1.0	6.80	53.15	6.56	16.99	272.92	17.46
		1.5	10.19	92.89	9.39	25.49	502.74	24.73
		2.0	13.59	149.87	13.03	33.98	837.90	32.38
		2.5	16.99	222.10	16.57			
		3.0	20.39	308.35	19.63			
5	45°	1.0				4.91	266.21	5.47
		1.5				7.36	545.83	7.88
		2.0	3.94	174.28	4.34	9.82	785.24	9.39
		2.5	4.91	265.26	5.43	12.32	1465.14	12.74
		3.0	5.90	382.08	6.47	14.77	2092.37	15.20
9	30°	0.5	3.40	26.81	4.12	8.50	148.91	11.23
		1.0	6.80	61.29	6.98	16.99	327.02	19.35
		1.5	10.19	113.96	10.38	33.98	627.23	27.14
		2.0	13.59	182.90	14.35			
		2.5	16.99	278.66	18.03			
		3.0	20.39	385.44	21.19			
5	30°	1.0				4.91	310.74	5.19
		1.5				7.36	651.17	7.41
		2.0	3.94	199.18	3.97	9.82	1139.55	9.77
		2.5	4.91	314.57	5.14	12.32	1867.33	12.81
		3.0	5.90	453.43	6.14	14.77	2662.14	14.87

and alternate holes in each remaining row were blocked off with tape to give a square array spaced 5-hole dia apart. Each modified cylinder was tested at the same two Reynolds numbers as before. For each cylinder, the flow was adjusted so that the average velocity through the holes gave values of the velocity ratio, M, ranging from 0.5 to 3.0 in increments of 0.5.

The results of the four tests for each of the six test cylinders are presented in Tables 1 and 2.

Analytical Method

As stated in the introduction, the major objective of this study was the development of an analytical method for the prediction of flow from arrays of holes in the leading edge of a turbine blade. The empirical curves developed from the single hole tests were used to calculate the entrance and exit losses at each hole. The coolant flow of multiple holes could

then be calculated from known orifice discharge coefficients and entrance and exit loss coefficients. The analytical method for obtaining multiple hole flow is detailed below.

Discharge Coefficient. Flow through an orifice is usually calculated by use of empirically determined coefficient of discharge defined through the following equation by White [11]

$$Q = C_D A_j \left[\frac{2(P_1 - P_2)/\rho}{1 - \beta^4} \right]^{1/2} \qquad (6)$$

where P_1 and P_2 are static pressures upstream and downstream of the orifice. The exact location of these pressure measurements will influence the value of C_D. For the present model the diameter ratio, β, is effectively very small so that the term β^4 is negligible. Also, since the velocity field inside a multiple hole tube is complex, it is convenient to redefine C_D by the following equation for flow from each individual hole

$$Q = C_D' A_j [2(P_{T(\text{eff})} - P_{S(\text{eff})})/\rho]^{1/2} \qquad (7)$$

where $P_{T(\text{eff})}$ is the effective internal total pressure at the hole, and $P_{S(\text{eff})}$ is the effective static pressure at the hole exit. It should be noted that the single hole experiments were performed with such a low velocity inside the cylinder that the total pressure was essentially equal to the inside static pressure. Thus, the values of coefficient of discharge presented in Fig. 6 can be used directly in equation (7).

External Loss Coefficient. When external flow passes over the cylinder the jets of air from the holes are distorted. In general, this distortion causes a decrease in the flow rate for a given differential pressure except near the stagnation point. In the stagnation region the external flow forces the jets to fill more of the hole cross section which increases the flow rate. The effect of external flow was expressed as a loss coefficient, defined by equation (2). The effective loss, or gain, of pressure at the exit of an orifice can be expressed by rearranging equation (2) as

$$\Delta P_e = P_{S_{(V_\infty = 0)}} - P_{S_{(V_\infty)}} = \delta_0 \frac{\rho_j V_j 2}{2} \qquad (8)$$

The measured values of δ_0 were correlated by a least-square curve fitting routine and entered into the computer program as a function of the local value of K. The value of δ_0 at high K values was assumed to be valid at the stagnation point.

Internal Loss Coefficient. Internally the air supplied at one end of the cylinder and feeds along the tube to the various cooling holes. This means that holes near the inlet end are exposed to a high axial velocity while at the opposite end the axial velocity is essentially zero. As with the external loss coefficient, the high axial velocity causes an irreversible loss which can be expressed in terms of a loss coefficient defined by equation (4). The pressure loss (or gain) at the hole inlet can be expressed by rearranging equation (4) as

$$\Delta P_i = P_{T(\text{Tube flow})} - P_{T(\text{Tube flow} = 0)} = \delta_i \frac{\rho_j V_j^2}{2} \qquad (9)$$

The experimental values shown in Figs. 13, 14, and 15 were correlated by a least-squares curve fitting routine and entered into the program as a function of the local velocity ratio $(V_j/V_t)^2$.

Calculation of Hole Flow. When the local internal and external velocities are known at a given hole location, the values of δ_0 and δ_i could be found if the velocity through the hole was known. Since this velocity is a function of δ_0 and δ_i an iterative method according to James [12] was programed to find δ_0 and δ_i from assumed values of the hole flow rate. The hole flow rate can be expressed as

$$Q = C_D' A_j [2\Delta P/\rho]^{1/2} \qquad (10)$$

where ΔP is expressed as

$$\Delta P = P_T - P_S - \Delta P_e - \Delta P_i = P_{T(\text{eff})} - P_{S(\text{eff})} \qquad (11)$$

The average internal velocity at any axial location is equal to the flow from all the holes downstream of that location divided by the inside cross-sectional area of the cylinder. Thus, if the calculation procedure is started at the blanked-off end of the cylinder where the internal velocity is zero, the flow from the first holes can be calculated if the external velocity is known. The external velocity over the leading edge of a cylinder in crossflow can be approximated closely by the potential flow solution.

$$V_s = 2 V_\infty \sin\theta \qquad (12)$$

This expression was used in the present calculation method. A more exact expression could be programed if compressibility or blockage effects were to be included.

Since this study was conducted at low subsonic velocities compressibility effects were negligible. The problem of blockage is discussed by Farell et al. [13] for a cylinder operating under similar conditions to those of this study. Their results show that blockage effects on the pressure coefficient were small over the leading edge region of the cylinder. Also, pressure measurements taken as part of this study on the 5.08-cm (2.00-in.)-dia cylinders confirmed that the potential flow equation gives accurate pressures over the forward leading edge region.

Computer Program. The calculation procedure outlined above was programed for solution. The required input includes correlation constants for δ_i, δ_0 and C_D'. In addition, air properties and geometric parameters are entered as data. The overall pressure difference $P_T - P_\infty$ and the free-stream velocity are entered as independent variables. For a first calculation step the average flow through the first hole was estimated from an assumed overall coefficient of discharge, $C_D = 0.79$ and the overall pressure difference $P_T - P_\infty$. This flow was then divided by a large number, usually 100 or 1000, to give the iteration step size. The first calculation was performed by using this small assumed flow and the known values of external and internal flows at the hole locations to calculated δ_i, δ_0 and C_D'. The values were substituted into equations (11) and (10) to calculate the actual hole flow. If the calculated flow did not match the assumed flow rate within a specified tolerance, the assumed flow was increased by one step size and the process repeated. Once the solution was found approximately, the step size was successively decreased by factors of 10 until the desired accuracy of the answer was established. The method is relatively slow but worked well with the rapidly changing exponential type functions used to represent δ_i and δ_0. Once all the holes at one axial location have been analyzed the total internal flow is calculated and internal velocities past the next row of holes are calculated. This procedure is repeated until the entire array has been analyzed. The individual hole flow rates and the total flow are printed as the output.

Analytical Results

The test conditions of Tables 1 and 2 were entered into the computer program, and the total flow was calculated for each test point. These analytical values of flow are also presented in the tables. A comparison to the experimental values shows excellent overall agreement for 90- and 45-deg holes and poorer agreement for 30-deg holes, $L/d = 1.875$. In the 90- and 45-deg holes, the only values with excessive error are those for the lowest flow rates. It should be noted that the low flow rates are probably the least accurate experimental values because the measurements were made at the low end of the flowmeter and the differential pressures were low relative to the accuracy of the pressure measurement system. Thus, the

Table 3 Calculated individual note flow rates
$L/d = 1.875$, $d = 0.508$ Cm, $v_\infty = 14.93$ m/s, $\Delta P = 374.4$ Pa (individual flow rates in L/S

Cm from end	$\theta = 0°$	$\theta = 28°$	$\theta = 57.3°$
0	0.31489	0.37103	0.45723
1.27	0.31489	0.37103	0.45723
2.54	0.30988	0.37103	0.45723
3.81	0.29847	0.36949	0.45723
5.08	0.27256	0.34744	0.45008
6.35	0.23995	0.32011	0.42810
7.62	0.20130	0.28261	0.40372
8.85	0.15772	0.24769	0.37759
10.16	0.11109	0.21069	0.35055
11.43	0.06771	0.17315	0.32367
12.7	0.00000	0.13702	0.29246
13.97	0.00000	0.10608	0.26956
15.24	0.00000	0.07959	0.24801

Total flow = 18.82 L/s
Mavg = 1.0
Measured flow = 19.68 L/s

Table 3(b)
$L/d = 3.75$, $d = 0.254$ in., $v_\infty = 14.93$ m/s, $\Delta P = 383.5$ Pa (individual flow rates in L/S)

Cm from end	$\theta=0°$	$\theta=14.3°$	$\theta=28.6°$	$\theta=42.9°$	$\theta=57.3°$
0	0.07712	0.08144	0.09131	0.10340	0.11440
.635	0.07712	0.08144	0.09131	0.10340	0.11440
1.27	0.07712	0.08144	0.09131	0.10340	0.11440
1.91	0.07712	0.08144	0.09131	0.10340	0.11440
2.54	0.07712	0.08144	0.09131	0.10340	0.11440
3.18	0.07712	0.08144	0.09131	0.10340	0.11440
3.81	0.07644	0.08127	0.09131	0.10340	0.11440
4.45	0.07462	0.07951	0.09067	0.10340	0.11440
5.08	0.07257	0.07754	0.08884	0.10256	0.11440
5.72	0.07032	0.07537	0.08693	0.10080	0.11326
6.35	0.06788	0.07302	0.08481	0.09891	0.11152
6.99	0.06526	0.07050	0.08255	0.09689	0.10968
7.62	0.06200	0.06784	0.08017	0.09477	0.10774
8.26	0.05927	0.06503	0.07767	0.09255	0.10572
8.85	0.05541	0.06211	0.07507	0.09025	0.10362
9.53	0.05157	0.05868	0.07239	0.08788	0.10148
10.16	0.04778	0.05479	0.06964	0.08546	0.09929
10.80	0.04407	0.05099	0.06684	0.08301	0.09707
11.43	0.04045	0.04729	0.06401	0.08053	0.09484
12.07	0.03699	0.04371	0.06116	0.07805	0.09260
12.7	0.03362	0.04027	0.05773	0.07556	0.09037
13.34	0.03044	0.03698	0.05426	0.07308	0.08815
13.97	0.02744	0.03386	0.05094	0.07063	0.08596
14.61	0.02464	0.03092	0.04778	0.06821	0.08379
15.24	0.02206	0.02816	0.04478	0.06583	0.08167

Total flow = 17.89 L/s
Mavg = 1.0
Measured flow = 16.99 L/s

larger error may not be due entirely to inaccuracy in the analytical method. In 30-deg holes the reason for error is not quite clear yet and it may be due to internal and external interferences of the coolant jets since the jets may reach to the adjacent holes to alter the pressure field.

A printout of the flows from a complete hole array is given for cylinders Number 1 and 4 in Table 3. The large hole-to-hole deviation from average flow should be of interest to designers. The low flow at the stagnation region holes near the entrance end should be noted.

Conclusions

A study was performed to acquire the coolant flow loss data of film cooling holes around the leading edge of a typical turbine airfoil and to establish an analytical model for predicting the individual coolant flow through the cooling holes. It can be concluded from this study that:

1 The discharge coefficient of the leading edge holes changes under the influence of the external main stream flow and internal passage axial flow. The study found that the entrance and exit effects for the cooling holes can be considered separable.

2 The analytical model of the leading edge holes consists of three parts: the flow orifice without internal and external flow effects, the additive hole entrance loss coefficient due to the internal axial flow, and the additive hole exit loss coefficient due to the external loss coefficient.

3 The additive exit loss coefficient can be expressed as a function of momentum ratios between the jet and main stream. A similar correlation exists for the additive entrance loss coefficient. The test data for hole $L/d = 2$ and 4 shows that at the entrance and exit loss coefficients are essentially independent of the L/d ratio.

4 The total flow data for multiple hole cylinders shows good agreement with the analytical results based on the flow model of the single hole.

5 Nonuniform individual coolant flow distribution occurs at the multiple holes of the test cylinders along the cylinder axial direction. Therefore, the turbine heat transfer designers should be careful in sizing and orienting the cooling holes of the turbine airfoils.

Acknowledgments

References

1 Taylor, J. R., "Heat Transfer Phenomena in Gas Turbines," ASME Paper No. 80-GT-172.

2 Lichtarowicz, A., Duggins, R., and Markland, E., "Discharge Coefficients for Incompressible Non-Cavitating Flow Through Long Orifices," Journal of Mechanical Engineering Science, Vol. 7, No., 2, 1965, p. 210–219.

3 Rohde, J. E., and Richards, H. T., "Discharge Coefficients for Thick Plate Orifices with Approach Flow Perpendicular and Inclined to the Orifice Axis," NASA Technical Note, TN D5467, Oct. 1969.

4 Hay, N., Lampard, D., and Bermansour, S., "Effect of Crossflows on the Discharge Coefficient Film Cooling Holes," ASME Paper 82-GT-147, Apr. 1981.

5 Mellor, B. V., "Discharge Coefficient of Film Cooling Holes," Third year project thesis, University of Nottingham, Mechanical Engineering Department, 1978.

6 Cornfield, C. T., "Discharge Coefficient of Film Cooling Holes," Third year project thesis, University of Nottingham, Mechanical Engineering Department 1979.

7 Rogers, T., and Hersh, A. S., "The Effect of Grazing Flow on the Steady State Resistance of Square-Edged Orifices," AIAA Paper No. 75-493, Mar. 1975.

8 Saski, M., Takahara, K., Sakata, K., and Kumagai, T., "Study on Film Cooling of Turbine Blades," Bulletin of JSME, Vol. 19, No. 137, Nov. 1976, p. 1344–1352.

9 Bergeles, G., Gosman, A. D., and Launder, B. E., "The Near-Field Character of a Jet Discharged Normal to a Main Stream," ASME JOURNAL OF HEAT TRANSFER, Aug. 1976, p. 373–378.

10 Jen, H. F., and Sobanik, J. B., "Cooling Air Flow Characteristics in Gas Turbine Components," ASME Paper No. 81-GT-76.

11 White, F. M., Fluid Mechanics, McGraw-Hill, New York, 1979.

12 James, M. L., Smith, G. M., and Wolford, J. C., Applied Numerical Methods, International Textbook Co., Scranton, Pa. 1967.

13 Farell, C., Carrasquel, S., Guven, O., and Patel, V. C., "Effect of Wind-Tunnel Walls on the Flow Past Circular Cylinders and Cooling Tower Models," ASME Journal of Fluids Engineering, Vol. 99, No. 3, pp. 470–479.

Effect of an Oscillating Flow Direction on Leading Edge Heat Transfer

M. L. Marziale

Research Engineer,
Westvaco, Covington, Va

R. E. Mayle

Associate Professor,
Rensselaer Polytechnic Institute,
Troy, N.Y., 12181

An experimental investigation was conducted to examine the effect of a periodic variation in the angle of attack on heat transfer at the leading edge of a gas turbine blade. A circular cylinder was used as a large-scale model of the leading edge region. The cylinder was placed in a wind tunnel and was oscillated rotationally about its axis. The incident flow Reynolds number and the Strouhal number of oscillation were chosen to model an actual turbine condition. Incident turbulence levels up to 4.9 percent were produced by grids placed upstream of the cylinder. The transfer rate was measured using a mass transfer technique and heat transfer rates inferred from the results. A direct comparison of the unsteady and steady results indicate that the effect is dependent on the Strouhal number, turbulence level, and the turbulence length scale, but that the largest observed effect was only a 10 percent augmentation at the nominal stagnation position.

Introduction

Current axial gas turbine designs are usually based upon steady, two-dimensional modeling of the gas flow around the airfoils even though it is unsteady and three dimensional. At most, a quasi-steady or quasi-two-dimensional analysis is used to account for "slow" transients and certain three-dimensional effects. The necessity of including three-dimensional effects in the next generation design system has been recognized and both theoretical and experimental research in this area has begun. Only a few experimenters, however, have begun to examine the effects of unsteady flows on turbine heat transfer, and then only in actual or near engine configurations (e.g., [1, 2]). As a result, only very limited information is currently available to the designer for the prediction of these effects.

In order for a turbine to extract work, the flow viewed from a fixed reference must be unsteady. Present design systems account for this unsteadiness by assuming that the flow leaves a blade row in a steady manner with velocity and exit angles independent of the azimuthal direction. Under these assumptions, the inlet velocity and angle of attack relative to the following blade row are constant and a steady flow analysis relative to each blade row may be performed.

In reality, however, the flow leaving a blade row is neither steady nor uniform. A number of factors contribute to the unsteadiness as seen in the relative frame of reference. These include the effects of the passage vortex, leakage flows, together with the fluctuations originating in the burner, and random turbulence; however, probably the most significant type of unsteadiness is that created by the wakes behind the individual airfoils. The variations of velocity and temperature

---

Contributed by the Gas Turbine Division presented at the 1983 Tokyo International Gas Turbine Congress, Tokyo, Japan, October 24 - 28, 1983. Manuscript received by the Gas Turbine Division May 13, 1983. Paper No. 83-GTJ-3.
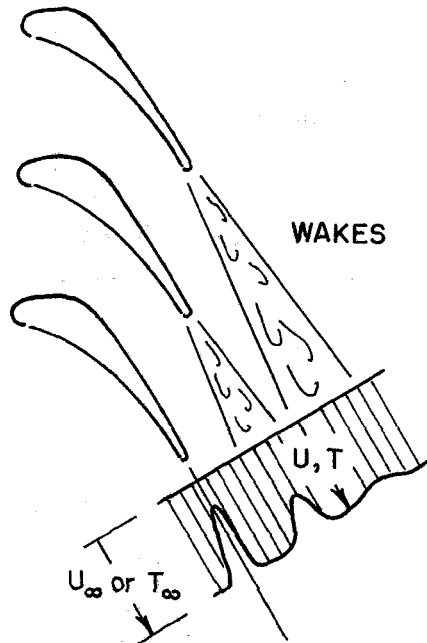
in these wakes cause the inlet flow relative to the following row to fluctuate in a regular periodic manner. This is shown schematically in Figs. 1 and 2. In Fig. 1, typical wake velocity and temperature profiles are shown as they would appear at various distances downstream of the airfoils and in the same reference frame as the airfoils. The relative velocity vectors which result when the wheel speed is added have been drawn in Fig. 2 for several positions within the wake. Since the second blade experiences this set of velocity vectors as inlet conditions, the inlet flow is unsteady with fluctuations in both its angle of attack and magnitude. In addition, the inlet temperature fluctuates and, incidently, since the turbulence in the wake is different than that of the mainstream, so does the inlet turbulence.

As part of an ongoing basic investigation into these unsteady effects, the current effort examined the effect of a periodic variation in the angle of attack upon the local transfer rate in the leading edge region of a turbine blade. The effect of unsteadiness is of particular importance in this region since leading edge cooling schemes are severely limited by geometrical constraints and the heat load per unit area is usually a maximum there. As a consequence, blade life critically depends upon the leading edge design. Currently, the uncertainty of these designs is on the order of 50 percent, and the degree of inaccuracy due to unsteady flow effects is, as yet, unknown. The intent of the present work is to partly fill this void.

To investigate this problem, the set of basic experiments shown in Fig. 3 were performed. Since the leading edge region in most blade designs is formed by a cylindrical surface, a circular cylinder was used as a large scale model of the leading edge region. In all of the experiments a nominally uniform steady flow with a superimposed level of turbulence was established as the inlet flow and the periodic variation in the

Fig. 1 Airfoil wakes

Fig. 2 Velocity triangles at an interrow position
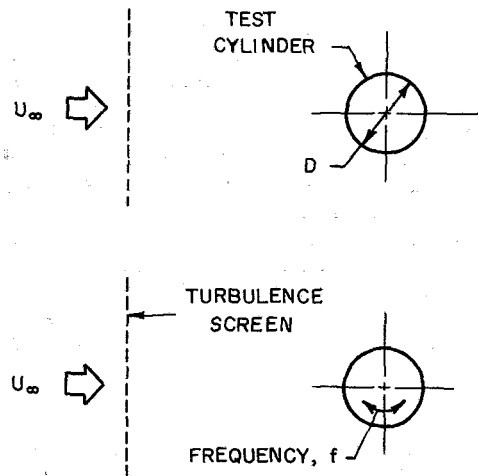
Fig. 3 Schematic of experimental modeling

angle of attack modeled by oscillating the cylinder about its axis. This experimentally isolated the effect of an oscillating flow direction from those caused by temporal variations in the flow's magnitude and turbulence. In the first part of the investigation, a stationary cylinder was used and the transfer rate measured as a function of position around the leading edge for various Reynolds numbers and turbulence conditions. In the second part, identical flow conditions were established but the cylinder was oscillated at Strouhal numbers modeling typical blade passing frequencies in a gas turbine. A direct comparison of the two results, with and without oscillation, provided the effect of a periodic variation in flow direction on the transfer rate at the leading edge.

A Brief Review of the Work on Cylinders

Numerous investigations, both theoretical and experimental have been conducted to determine the heat transfer rate from a cylinder in a steady, high Reynolds number crossflow. The usual theoretical treatment, first used by Frossling [3], is to use a laminar boundary layer analysis together with an experimentally determined free-stream velocity distribution to yield the local transfer rate over the forward portion of the cylinder up to separation. At stagnation, the resulting expression for the Nusselt number has the form

$$Nu \propto Re^{1/2} Pr^n \qquad (1)$$

where Re is the Reynolds number based on the cylinder's diameter and incident flow velocity, Pr is the Prandtl number, and n is an exponent which depends on the Prandtl number range of interest.

Early experiments to determine the rate of heat and mass transfer from cylinders in crossflow were for the most part incompatible with each other and with the developed laminar theory. This discord was somewhat clarified by subsequent investigations, namely those by Kestin, Maeder, and Sogin [4] and Kestin and Wood [5], which showed that the incident turbulence level had a substantial effect on the transfer rate. A number of recent studies, notably those of Yardi and Sukhatme [6] and Traci and Wilcox [7], suggest that not only

is the turbulence level important but also its scale. In particular, it appears that the maximum effect of turbulence occurs when its integral length scale is on the order of ten times the boundary layer thickness. Unfortunately, the results from transfer rate measurements in turbulent fields are too widely scattered and the methods used to measure and report turbulence are too varied to provide a precise empirical relation. Nevertheless, the data suggests that, when the turbulent length scale is kept constant, the Nusselt number at stagnation has the form

$$Nu/Re^{1/2} = fnc(TuRe^{1/2}) \qquad (2)$$

where Tu is the turbulent intensity.

A number of theoretical investigations have been performed in an attempt to evaluate the effects of periodic unsteadiness in the flow incident to a stagnation zone. Lighthill [8] presented a general theory to model the response of a laminar boundary layer to periodic fluctuations in the magnitude of the external flow field and applied the theory to stagnation flows. Rott [9] and Glauert [10] derived exact solutions for the case of stagnating flow on a plate which oscillates in its own plane. In this case the flow fluctuates not only in magnitude but also in direction. Recently, Childs [11] considered the problem of a circular cylinder oscillating rotationally in a steady incident stream, bringing into consideration the effects of advection normal to the surface. In this case, the flow relative to the cylinder fluctuates in direction only. Expressions for the unsteady laminar skin friction and local heat transfer rate were obtained. These results indicate that even though the skin friction can vary significantly, the time-averaged, local transfer rate is decreased rather then increased over the forward portion of the cylinder with the maximum discrepancy from steady state being less than 4 percent. To date, the importance of incident turbulence to the effects of periodic unsteadiness in the flow field has not been theoretically or experimentally investigated.

Experimental Apparatus and Procedure

The cylinder's oscillation and the large number of cycles involved in any one of the tests made the use of a conventional heat transfer measurement technique impractical. Therefore, a mass transfer technique, similar to that used by Sogin and Subramanian [12], which used napthalene as the sublimating substance was developed for the program. Using the heat and mass transfer analogy, the heat transfer rate can be obtained from the mass transfer results.

The experiments were performed in a low-speed, open-circuit wind tunnel. A centrifugal fan provided the air flow. After passing through a plenum, the air accelerated through a two-dimensional, two-to-one contraction nozzle into a rectangular duct 46-cm high by 76-cm wide. Turbulence grids could be inserted at any of three locations in the first part of the duct to provide a variety of incident turbulence levels and scales. The test cylinder was placed downstream of the turbulence generating section in a vertical position as shown in Fig. 4. Air leaving the duct entered the room, mixed with the surrounding air and circulated back to the fan's inlet. An air conditioner in the room with its sensor placed in the tunnel automatically controlled the air temperature to within 1°C.

The test cylinder had a 7.6-cm radius and passed through the top and bottom walls of the duct. As shown in Fig. 5, the cylinder was constructed in three sections, two end cans and a central test section containing the naphthalene, which were held together by an axial tension rod. Bearings fastened to the top and bottom walls supported the end cans along a common axis. With the tension rod removed, the upper can was free to slide vertically through its mount, allowing quick removal of the central test section. The cylinder was oscillated rotationally about its axis using a direct link driving
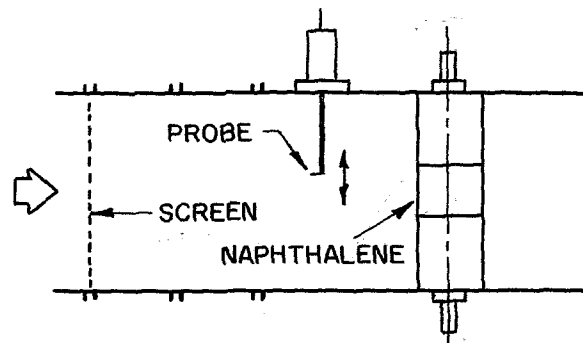

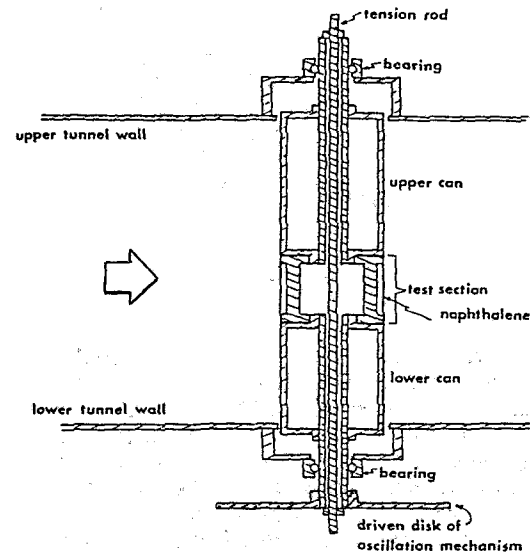Fig. 4 Schematic of the test section
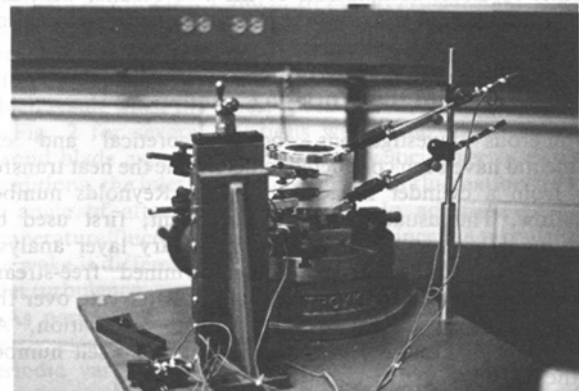

Fig. 5 Sectioned view of test cylinder

Fig. 6 Photograph of the measuring apparatus with the cylinder installed

mechanism mounted to the tunnel and attached to the lower can. This provided an oscillation which was within 2 percent of a true sinusoid.

The test section was made of stainless steel, was 10-cm long and had a 6.4-mm thick, 7.6-cm wide naphthalene band cast into its circumference (see Fig. 6). The band was bordered on each edge by a stainless steel rim, which was employed as a reference for all surface measurements. To cast the naphthalene into the test cylinder, a cylindrical stainless steel sleeve was slip fitted over the rims to form a mold cavity. After the naphthalene solidified and the mold cooled down, the sleeve was knocked off leaving a smooth, glasslike test surface. A new insert was cast for each mass transfer test.

Profile measurements of the naphthalene surface were made using the apparatus shown in Fig. 6. The section with the naphthalene insert was held to a rotary milling machine head by a fixture such that their axes coincided and the surface measured by displacement transducers. The lever type transducers could measure to within 1 μm using approximately 2.5 gms of gaging pressure. The two outermost gages were mounted to the same table as the rotary head and contacted the steel rims of the test section. The two inner gages contacted the naphthalene surface and were mounted to a vertical cross slide which in turn was fixed to the table. Initial adjustments of the transducer supports were made to position all of the transducer's contact points along a common line parallel to the axis of the test section. For each circumferential position, the outputs of the two reference gages were combined with those from the gages on the naphthalene to give the depth of the naphthalene surface relative to the rims. Depth measurements before each run were subtracted from those after to yield the local mass loss. This measurement technique was carefully developed to eliminate sources of random error. The repeatability of the experiment and measurement procedure was found to be ± 2 percent. Further details of the mass transfer technique and data reduction procedures, together with information on the casting technique, may be found in [13].

Mean velocity and turbulent measurements were made using a Thermo-Systems 1051 hot-wire anemometer system. All incident flow traverses were made by slowly moving the velocity probe across the flow using an automatic traverse device attached to the upper wall and recording the outputs on a strip chart recorder. Particular care was taken to assure that the incident flow was uniform in both velocity and turbulence. As recently shown by Mayle and Marziale [14], nonuniformities in the incident flow as small as 1 percent can increase the transfer rate on a blunt body by 30 percent. Two separate hot-wire probes placed along a vertical line in the stagnation plane of the cylinder were used to measure the actual turbulence levels. This was done to eliminate correlated tunnel noise from the measurements. Turbulent length scales were obtained from measurements of the turbulence energy spectrum compensated for the frequency response of the hot wire. The reported turbulence levels and length scales were all measured with the cylinder removed from the tunnel at a location corresponding to the leading edge position of the cylinder.

Initial mass transfer tests were performed at the base turbulence level of the tunnel and at Reynolds numbers Re of 75,000, 110,000, and 125,000. The turbulence level based on the streamwise component was 0.52 percent. Most other experiments were performed at a nominal Reynolds number of 110,000. Turbulence grids having mesh to diameter ratios of about five produced turbulence levels of 0.34 percent to 4.9 percent with integral length scale-to-cylinder diameter ratios of .028 to 0.19. The highest turbulence level was produced by a grid placed in the plenum upstream of the contraction nozzle rather than in the test section as all of the others. This was necessary to provide sufficient entry length for the production of a uniform, high-turbulence incident flow. An oscillation amplitude of ± 6 deg was used for most of the tests and Strouhal numbers were varied between 0.007 and 0.146. Due to excessive vibration at high oscillation frequencies, the highest Strouhal number could only be reached at a correspondingly lower Reynolds number. The maximum oscillation amplitude tested was ± 12 deg.

Both the mass transfer tests and surface measurements were conducted at a temperature of 19 $\pm 1^\circ$ C. During the test, temperatures were measured at 1 min intervals by a thermocouple placed in the incident flow. The density of the naphthalene vapor at the surface, ρ_v, was determined using the expression given by Sogin [15]. These were then averaged
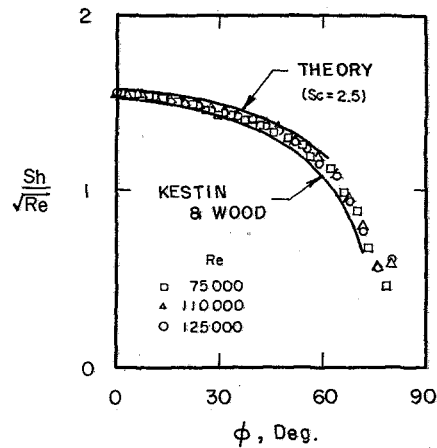

Fig. 7 Mass transfer results without a turbulence grid in the test section

for the test interval and used to determine the mass transfer coefficient and Sherwood number, Sh. Calculations of the naphthalene buildup in the incident flow indicated that the maximum concentration during the test was less than 0.5 percent of that at the surface and could be neglected.

The Sherwood number was determined from

$$\text{Sh} = \frac{\rho_s}{\rho_v} \frac{(\Delta y - \delta y)d}{\tau D}$$

where ρ_s is the density of solid naphthalene, Δy is the measured sublimation depth, τ is the test duration time, and d is the cylinder's diameter. Typical values for Δy and τ are 0.15 mm and 9 hrs. The quantity, δy, is a correction for the evaporation loss during the measurement interval and was determined by repeating measurements at specific points on the surface. Typically δy was about 2 percent of Δy. The diffusion coefficient of naphthalene in air D was obtained from the Schmidt number, Sc, using the kinematic viscosity of air, ν, at the temperature and pressure of the tunnel, i.e., $D = \nu/\text{Sc}$. A Schmidt number of 2.5 was used. This value was established by Sogin and has been used by many other investigators.

Results

The free-stream velocity around the cylinder, U, was obtained from surface static pressure measurements using a separate test cylinder. The best fit to the velocity distribution is given by

$$U/U_\infty = 1.915\varphi - 0.320\varphi^3 - 0.0526\varphi^5 \qquad (3)$$

for $\varphi < 1.2$, where φ is the angle in radians measured from stagnation, and U_∞ is the incident velocity.

The measured distribution of mass transfer around the forward portion of the cylinder is shown in Fig. 7 for tests conducted without a turbulence generating grid at three different Reynolds numbers. In this figure the local Sherwood number scaled by $\text{Re}^{1/2}$ is plotted against the angular distance from stagnation in degrees. No spanwise variation of mass transfer could be discerned for these tests nor for any of those whose results are presented herein. Because of symmetry, only the data from one side are shown. In agreement with the relation given in equation (1) and the heat-mass transfer analogy (see equation (4)), the data for all three Reynolds numbers correlate quite well on this plot. The maximum deviation from the average is about 2 percent. Compared to the results of tests conducted under similar conditions by Kestin and Wood a good agreement is seen. The theoretical result was obtained by a series solution to the boundary layer equations similar to Frossling's but using a Schmidt number
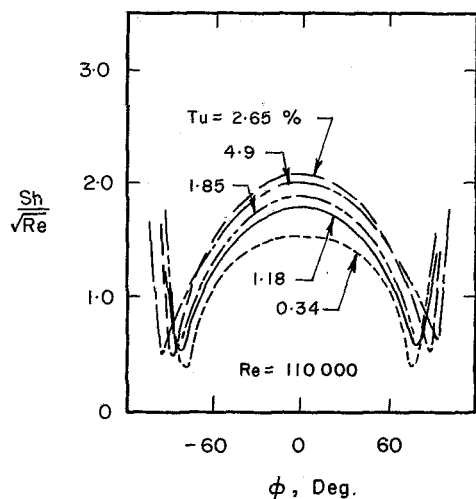
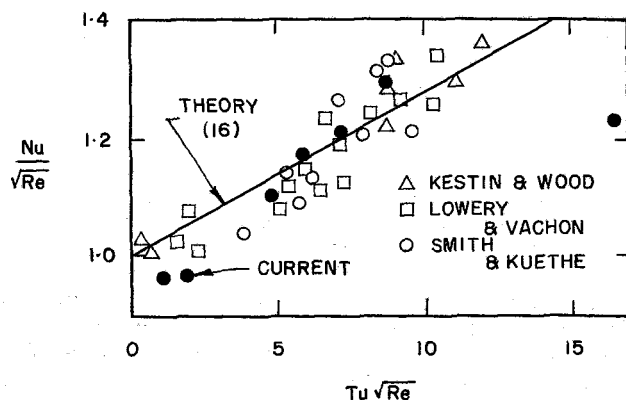Fig. 8 Mass transfer distributions at various turbulence conditions, Re = 110,000

Table 1

	Tu = .52% L/D = .087	= .34% = .028	= 1.18% = .050	= 1.80% = .038	= 2.65% = .030	= 4.9% = .188
Re = 110,000						
St = .0071					Yes	No
St = .0213					Yes	No
St = .0355					Yes	No
St = .0497					Yes	No
St = .0639	No	No	No	Yes	Yes	No
St = .0781					Yes	
$\varphi_o = 12°$ St = .0213					Yes	
Re = 75,000						
St = .0417					Yes	
St = .1041					Yes	
Re = 50,000						
St = .1460					Yes	

Fig. 9 Comparison of results at stagnation with those of other investigators

of 2.5 and the velocity distribution in equation (3). The slight discrepancy between theory and data is presently attributed to inaccuracies in the Schmidt number and vapor density. If the error is assumed to be caused only by the uncertainty in the Schmidt number, a value of 2.55 is required to make the theory and experiment correspond. This is within the error of experimentally determined values.

An additional low turbulence test was conducted where the whole surface of the cylinder was coated with naphthalene in contrast to most tests, where only the central 7.6 cm portion was covered. In this case, the results were found to be identical over the forward portion of the cylinder up to separation and different only within the cylinder's wake as might be expected because of the large scale transport by the turbulent eddies in the wake. The difference was an 8 percent decrease along the rear stagnation line for the fully covered test.

The results of the steady-state experiments performed behind turbulence generating grids for Re = 110,000 are presented in Fig. 8. For clarity, only a best fit curve to each data set is shown. The well-known effects of turbulence are readily evident where, in the stagnation region, the mass transfer rate is substantially higher at the higher turbulence levels. An augmentation as high as 30 percent is demonstrated by the current results. The maximum, however, is not produced by the highest incident turbulence level used in the test. This behavior is attributed to the effect that turbulent length scale has on the transfer rate and is in agreement with the results of Yardi and Sukhatma.

In Fig. 9, the steady-state results at stagnation are plotted as a function of $TuRe^{1/2}$. In order to compare with the heat transfer measurements of other investigators and the theory of Smith and Kueth [16], equivalent Nusselt numbers have been calculated from the mass transfer results using the heat/mass transfer analogy. For the case at hand, this becomes

$$Nu = Sh\left(\frac{Sc}{Pr}\right)^n \qquad (4)$$

where the results of a laminar analyses for Sc = 2.5 and Pr = 0.7 using equation (3) indicated that n = 0.38 was appropriate. Due to the large discrepancies in the methods used to measure and report turbulence levels, this figure should be viewed only as an indication of general trends and not as a basis for the establishment of precise empirical correlations. The figure does, however, demonstrate that the current results are well within the band of scatter of the data from other investigations, although they appear somewhat low at low turbulence levels. This may be caused by either the inaccuracies in the Schmidt number and vapor pressure relation, or the ambient tunnel noise which made the measurement of low turbulence levels more prone to error.

For each unsteady test, the effects of rotational oscillation on the transfer rate were evaluated by comparing the unsteady result to a "quasi-steady" curve calculated from the steady-state results obtained with an identical flow. Physically, the quasi-steady distributions represent the results which would be obtained from a cylinder oscillating at an infinitely small frequency. In this situation, the surface velocity of the cylinder is negligible and the effect of oscillation is a simple averaging of the transfer rates seen by a particular point on the surface at particular times, i.e.,

$$Sh_{quasisteady}(\varphi) = \frac{1}{2\pi}\int_{-\pi}^{\pi} Sh_{steady}(\varphi + \varphi_o \sin\theta)d\theta$$

where φ_0 is the amplitude of oscillation. The quasi-steady curves thus establish the "no effect" level for the oscillation tests. It should be noted that since the oscillation amplitudes used in these experiments are small, the quasi-steady curves is virtually identical to the steady-state distribution everywhere in the region of interest.

A summary of the oscillation tests and their results are given in Table 1. For each test, the table provides information on the incident turbulence level, Tu, length scale to diameter ratio, L/d, Reynolds number, oscillation amplitude, φ_o, and the Strouhal number, St. All the cases marked "No"
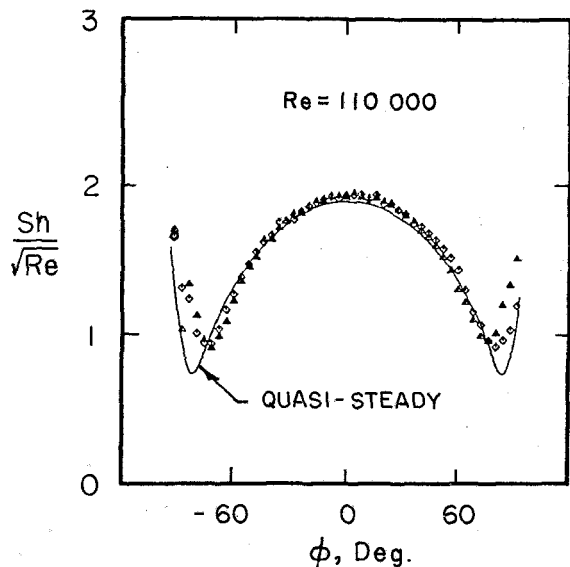
Fig. 10 Mass transfer distribution at the turbulence condition of Tu = 1.80 percent with $L/d = 0.04$, Re = 110,000 φ_o = 6 deg and St = 0.064

demonstrated no measurable effect of oscillation over the forward portion of the cylinder within the limits of experimental error and are essentially the same as the quasisteady result. For these, as in all oscillation tests, deviations were found only in the regions around separation. It should be noted that one of the tests which produced no effect was the test conducted without any turbulence grids. This was confirmed by repeating the experiment a number of times as was done for most of the reported tests.

On the other hand, those tests marked "Yes" in the table did produce a measurable effect of oscillation. As is shown, however, these corresponded to only two of the incident turbulence conditions tested. The result obtained with Tu = 1.8 percent and $L/d = 0.04$ at the Strouhal number of 0.064 is shown in Fig. 10. In this case a small effect of oscillation is noticeable with the mass transfer rate at stagnation about 3 percent higher than the quasisteady curve. This is barely above the 2 percent limit of experimental repeatability. The difference seen near separation ($\varphi = 80$ deg) is typical of all results.

A composite plot of the mass transfer distributions at the higher turbulence level is presented in Fig. 11 for various Strouhal numbers. The amplitude of oscillation and the Reynolds number are respectively ±6 deg and 110,000 for each of these results. In each case the mass transfer is increased above the quasi-steady curve, but only by an amount of 3 to 10 percent. The augmentation ratio at stagnation, that is the unsteady mass transfer rate divided by the quasisteady mass transfer rate for similar incident flow conditions, is plotted as a function of Strouhal number in Fig. 12. The data at the highest values of Strouhal number, fd/U, was obtained by lowering the incident flow velocity. Although this changes the Reynolds number, a test conducted at a lower frequency (Strouhal number) shows that the Reynolds number effect on the augmentation ratio is small. The augmentation in mass transfer caused by oscillation is seen to initially increase with Strouhal number, reaching a maximum value of 1.1 at about St = 0.06, and then decreases, apparently in an asymptotic fashion back to 1.0, the no-effect level. A similar result should be expected for heat transfer from a rotationally oscillating cylinder.

The augmentation in transfer rate at the higher oscillation amplitude $\varphi_o = 12$ deg is also shown in Fig. 12. This test was conducted at Re = 110,000 and Tu = 2.65 percent with a
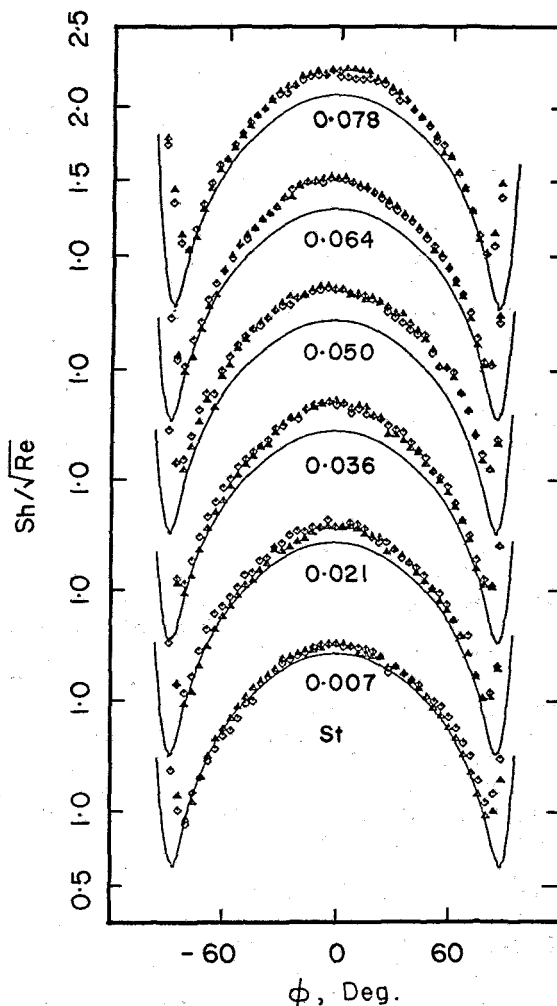

Fig. 11 Composite of mass transfer distributions for various Strouhal numbers: Tu = 2.65 percent, $L/d = 0.03$, Re = 110,000 and φ_o = 6 deg
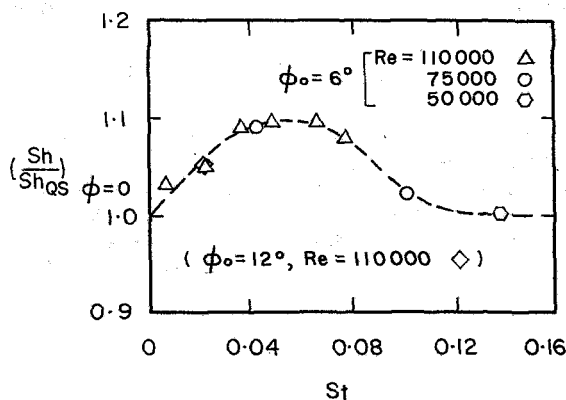

Fig. 12 Augmentation of mass transfer through oscillation; Tu = 2.65 percent and $L/d = 0.03$

Strouhal number of 0.021. Again the augmentation is small, being about 5 percent, but interestingly, it is approximately equal to that measured at the smaller amplitude.

Conclusions

For the range of parameters considered in these experiments, the effect of rotational oscillation on the distribution of the local transfer rate over the forward portion of a cylinder is small. The largest observed effect was a 10

percent augmentation at stagnation. Since the range of parameters used was chosen to model an actual turbine condition, the results suggest that the heat load in the leading edge region of a turbine is not significantly affected by the variation in angle of attack of the incident flow generated by airfoil wakes. The implication of the measurements is that, for the Strouhal number range of interest, the period associated with the oscillation is too long, compared to the residence time of a fluid particle passing over the surface, to have an effect on the mass transfer. This would further suggest that not only are the effects of flow angle oscillations small, but also the effects of unsteadiness in the flow's magnitude since the mechanism for transfer is basically the same and the Strouhal number is identical for both. Hence, the uncertainty in leading edge heat load predictions due to the unsteady mean flow effects is estimated to be only on the order of 10 percent, whereas increases at least as large as 30–40 percent can be attributed to turbulence in the incident flow.

The magnitude of the oscillation effects is intimately connected to the level and scale of the incident turbulence. For the range of St and Re used in the investigation and for turbulence scales on the order of $L/d \approx 0.03$, the effect seems to increase with turbulence level. Turbulence levels below 1.5 percent produced no effect while increasing the level to 1.8 and 2.6 percent gave an increase at stagnation of 3 and 7 percent, respectively. However, a larger length scale of $L/d = 0.19$, produced no effect even though the turbulence level was higher, Tu = 4.9 percent, indicating the importance of the scale to the observed results. Interestingly, the length scale at which significant effects are evident is about eight boundary layer thicknesses and of the order of the value which produces the maximum transfer rate for steady flow according to Yardi and Sukhatme.

At the incident turbulence conditions that demonstrated a significant effect of oscillation, Tu = 2.6 percent $L/d = 0.03$, the magnitude of the augmentation initially increases with Strouhal number reaching a maximum at St ≈ 0.06 after which the effect decreases. This would suggest that some type of interaction between the turbulent eddies and the oscillating flow occurs for a narrow range of the characteristic turnover frequency of a turbulent eddy to the oscillation frequency, i.e.,

$$R_T = \left(\frac{Tu U_\infty}{L} \right) \Big/ \left(\frac{St U_\infty}{d} \right)$$

The maximum effect occurs at $R_T \approx 16$. This value is, however, significant only when the turbulence scale is of the proper order, viz., $L/d \approx 0.03$. Since the scale of a turbulent eddy changes as the stagnation point is approached, in accord to Helmholtz' law, this may be the incident eddy size which generates eddies at stagnation of a scale on the order of the boundary layer thickness.

As a final comment, the effects of a uniform, unsteady incident flow on heat transfer to the leading edge of a turbine blade seem to be of little importance when compared to either the effects of turbulence or the effects arising from small nonuniformities in the flow.

Acknowledgment

References

1 Dunn, M. G., and Hause, A., "Measurements of Heat Flux and Pressure in a Turbine Stage," ASME Paper No. 81-GT-88, presented at the International Gas Turbine Conference, Houston 1981.

2 Dring, R. P., Joslyn, H. D., Hardin, L. W., and Wagner, J. H., "Turbine Rotor-Stator Interaction," ASME JOURNAL OF ENGINEERING FOR POWER, Vol. 104, 1982. pp. 729–742.

3 Frossling, N., "Verdunstung Warmeülbertragung und Geschwindigkeitsverteilung bei Zweidimensionaler und Rotationssymmetrischer Grenzschichtströmung," Acta Univ. Jund, Vol. 2, No. 4, 1940, p. 36. (see also NACA TM 1432).

4 Kestin, J., Maeder, P. F., and Sogin, H., "The Influence of Turbulence on the Heat Transfer from Cylinders Near the Stagnation Point," Z. Agnew, Math. Phys., Vol. 12, 1969, pp. 115–132.

5 Kestin, J., and Wood, R., "The Influence of Turbulence on the Mass Transfer from Cylinders," ASME Journal of Heat Transfer, Vol. 93, 1971, pp. 321–327.

6 Yardi, N. R., and Sukhatma, S. P., "Effects of Turbulence Intensity and Integral Length Scale of a Turbulent Free Stream on Forced Convection Heat Transfer from a Circular Cylinder in Cross Flow," Proc. of the Sixth Int. Heat Transfer Conf., Toronto, Canada, Vol. 5 FC(b)-29, 1978, pp. 347–352.

7 Traci, R. M., and Willcox, D. C., "Free-Stream Turbulence Effects on Stagnation Point Heat Transfer," AIAA Journal, Vol. 13, 1965, pp. 890–896.

8 Lighthill, M. J., "The Response of Laminar Skin Friction and Heat Transfer to Fluctuations in the Stream Velocity," Proc. Roy. Soc., Vol. A224, 1954, pp. 1–23.

9 Rott, M., "Unsteady Viscous Flow in the Vicinity of a Stagnation Point," Quart. Appl. Math., Vol. 13, 1956, pp. 444–451.

10 Glauert, M. B., "The Laminar Boundary Layer on Oscillating Plates and Cylinders," Journal of Fluid Mechanics, Vol. 1, 1956, pp. 97–110.

11 Childs, E. P., Jr., "Analysis of the Response of Laminar Skin Friction and Heat Transfer to the Rotational Oscillation of a Circular Cylinder in a Steady Stream," Master's thesis, Rensselaer Polytechnic Institute, 1980; to be published in IJHMT, 1983.

12 Sogin, H. H., and Subramanian, V. S., "Local Mass Transfer from Circular Cylinders in Cross Flow," ASME Journal of Heat Tranfser, 1961, pp. 483–493.

13 Marziale, M. L., "Mass Transfer from a Circular Cylinder—Effect of Flow Unsteadiness and 'Slight Nonuniformities'," Ph.D. thesis, Rensselaer Polytechnic Institute, 1982.

14 Mayle, R. E., and Marziale, M. L., "Spanwise Mass Transfer Variations on a Cylinder in 'Nominally' Uniform Crossflow," Proc. Seventh Int. Heat Transfer Conf., Munich, F. D. R., Vol. 3, FC15, 1982, pp. 87–92.

15 Sogin, H., "Sublimation from Disks to Air Streams Flowing Normal to Their Surface," Trans. ASME, Vol. 80, 1958, p. 61.

16 Smith, M., and Kuethe, A., "Effects of Turbulence on Laminar Skin Friction and Heat Transfer," Physics Fluids, Vol. 9, 1966, pp. 2337–2344.

17 Lowery, G. W., and Vachon, R. I., "The Effect of Turbulence on Heat Transfer from Heated Cylinders," Int. J. Heat Mass Transfer, Vol. 18, 1975, pp. 1229–1242.

Measurement and Analyses of Heat Flux Data in a Turbine Stage: Part I—Description of Experimental Apparatus and Data Analysis

M. G. Dunn

W. J. Rae

Aerodynamic Research Department,
Calspan Advanced Technology Center,
Buffalo, N.Y. 14225

J. L. Holt

Air Force Wright Aeronautical
Laboratories,
Aero Propulsion Laboratory,
Wright-Patterson AFB, Ohio 45433

Parts I and II of this paper report the measurements and analysis of detailed heat flux distributions obtained on the nozzle guide vane (NGV), rotor, and shroud of the full-stage rotating turbine of the Garrett TFE 731-2 engine. Part I includes a description of the experimental apparatus, a discussion of the measurements performed and a discussion of the data analysis procedure. Part II is composed of a presentation of experimental conditions, a discussion of results, and comparison of these results with predictions obtained using a flat-plate technique and with predictions obtained using STAN5. The essential features of the measurement program are that a shock tube is used as a short-duration source of heated air and miniature thin-film heat-flux gages are used to obtain detailed measurements on the component parts. The gasdynamic and physical parameters of the experiment are representative of typical engine operating conditions.

Introduction

The efficiency of aircraft gas turbine engines is affected very strongly by the maximum allowable turbine inlet temperature, and the performance improvements that can be achieved by increases in this parameter are substantial. Such increases are limited by heat transfer considerations. For this reason, many contemporary research efforts are aimed at better understanding of the flow and heat transfer in the turbine components.

One such program is being carried out at Calspan, the major emphasis being placed on making accurate measurements of heat flux distributions in a full-scale rotating turbine stage. The experimental technique being used is the short-duration, shock-tunnel approach, in which fast-response, thin-film thermometers are used to measure the surface temperature histories at prescribed positions on the various component parts. Heat transfer rates are then inferred from the temperature histories, using standard data reduction procedures. Previous results of this measurement program were reported as they became available. The first of these [1] described the flow-establishment process within the model containing the turbine hardware and the results of total temperature and pressure measurements, which confirmed that the gasdynamic behavior of the flow within the model was as designed. The second [2] reported detailed heat flux

results obtained at many locations within the nozzle guide vane. The geometry used in [2] was a 180 deg sector of inlet guidevanes (NGV's), but without a downstream rotor. Turning vanes were placed downstream of the nozzles to remove a substantial portion of the flow turning introduced by the nozzles. The third paper in this series [3] included heat flux measurements for a full 360 deg section of NGV's and the associate downstream rotor in order to obtain full-stage data. The full-stage heat flux results for the inlet nozzle were used to calculate a Stanton number and the results were compared with the previous [2] measurements obtained with an inlet nozzle in the absence of the rotor. The comparisons presented in [3] suggested that the rotor can have an upstream influence on the boundary-layer development on the NGV airfoil.

In [4] the initial 180 deg-sector data were compared with the predictions obtained using a flat-plate correlation, a two-dimensional parabolic boundary layer code (STAN5), and a three-dimensional viscous code (NANCY I). The measurements obtained for the rotor blades were later compared [5] with the predictions of [4]. In addition, the comparisons earlier presented in [4] were updated to correct the heat flux data for temperature variations in the thermal properties of the substrate.

Since publication of [1–5], a considerable amount of detailed heat flux data have been obtained for the nozzle guide vane (endwall and airfoil), the rotor blade, the rotor tip, the rotor platform, and the shroud. In addition, an array of heat flux gages was placed at the stagnation point on a cylinder located just ahead of the nozzle guide vane so that the

Fig. 1 Schematic of experimental apparatus

* NUMBERS IN CIRCLES DENOTE LOCATION
OF PRESSURE TRANSDUCERS

Fig. 2 Schematic of test-section apparatus for full-stage turbine experiments
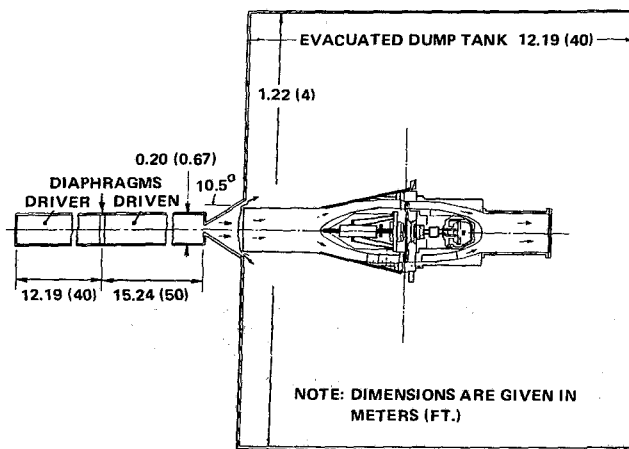

Fig. 3 Photograph of heat transfer gage taken through Leitz microscope

spanwise variation of the inlet flow and an estimate of the freestream turbulence could be obtained for each experimental condition. With the instrumentation just described, a measurement program was completed in order to obtain detailed Stanton number distributions for which: (a) the rotor speed and flow function were selected to be values representative of typical engine operating conditions, and (b) the ratio of wall temperature to gas total temperature, T_w/T_0, was set at values of approximately 0.21, 0.33, and 0.53.

Predictions made by using two different analytical techniques have been compared with the data presented here. The results of these predictions are discussed in Part II of the paper. The technique applied most extensively has been the Turbine Design System (TDS) [6] in use at the Air Force Aero Propulsion Laboratory. This system incorporates an axisymmetric throughflow solution, a blade-to-blade solution found by a streamline-curvature method, and a flat-plate prediction of the heat transfer rate based on the local pressure and velocity conditions. These conditions were also used as inputs to the Gaugler modification of the STAN code [7], to generate heat transfer rate predictions. In addition, a brief attempt was made to improve on the blade-to-blade solutions by using the full-potential code CAS2D developed by Dulikravich [8].

Many different facilities are currently being used to perform turbine related studies. These include the long run-time cascade facilities, such as those used by Blair [9], Graziani et al. [10], and Hylton et al. [11], and the low-speed rotating rig of Dring [12]. Other groups have used short-duration facilities similar to that used in the present study. Louis [13, 14] has used thin-film, heat transfer gages to obtain heat flux measurements on turbine components with a blow-down facility as the source of test gas. Jones, Schultz et al. at Oxford University [15–18] have also used thin-film heat transfer gage techniques, with a light piston technique as the supply of test gas.

The shock-tunnel facility provides a clean, uniform, and well-known gasdynamic condition at the inlet to the stationary nozzle. The experimental technique is not intended to duplicate every known parameter important to turbine heat transfer studies, but the intent is to have the flow conditions sufficiently well defined and enough parameters duplicated so
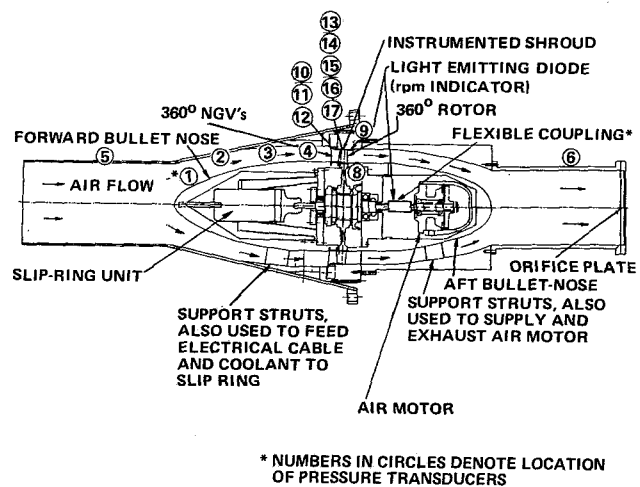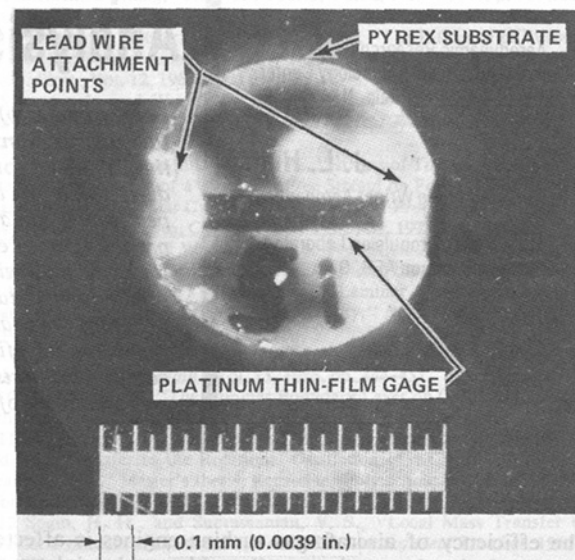
that the measured heat flux distributions can be used to validate and improve confidence in the accuracy of full-stage design data and predictive techniques under development.

Experimental Apparatus

The experimental apparatus sketched in Fig. 1 consists of an 0.20-m (8-in.) i.d. helium-driven shock tube with a 12.2-m (40-ft) long driver tube and a 15.2-m (50-ft) long driven tube, as a short-duration source of heated air, driving the test-section device mounted near the exit of the primary shock tunnel nozzle. The receiver tank is initially evacuated to a pressure of approximately 8 torr in order to minimize the starting air load on the turbine wheel and to improve the flow-establishment characteristics of the model. The test-section device sketched in Fig. 2 consists of a forward transition section with a circular opening facing the supersonic primary

——— Nomenclature ———

c = specific heat of pyrex
k = thermal conductivity
$T = T_w + \Delta T$
T_0 = total temperature

T_w = initial wall temperature
X = defined on Fig. 5
x = distance into pyrex substrate

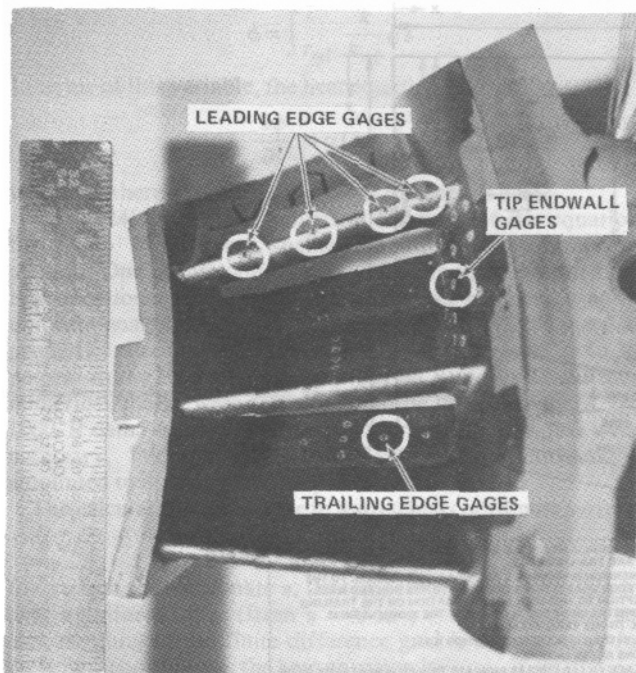α = thermal diffusivity
ρ = pyrex density

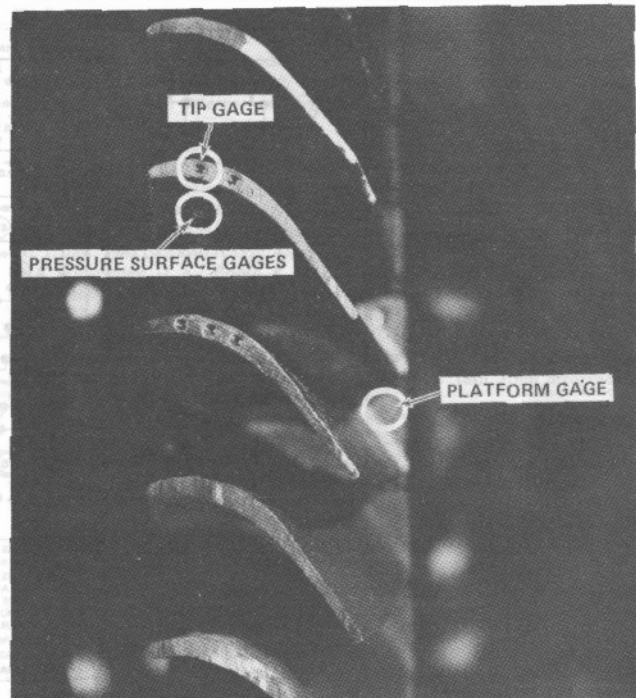Fig. 4 Photograph of NGV pressure surface instrumentation

Fig. 5 Photograph of rotor tip and pressure surface instrumentation

nozzle flow. The circular opening is followed by a complete 360 deg annular passage containing the nozzle guidevanes, the rotor, and the shroud as sketched in Fig. 2. For these experiments, the rotor/shroud clearance when the wheel is operating at 27,000 rpm is on the order of 3.0×10^{-4}-m (0.012-in.). The orifice plate located at the tail end of the model is used to set the weight flow through the device and thus to set the exit Mach number of the stator nozzle. This particular stator vane is designed to operate with a subsonic exit Mach number.

Static pressure measurements were obtained at 17 locations within the model as noted by the circled numbers on Fig. 2. Five of these pressure transducers were located in the forward transition section from the inlet to just ahead of the NGV's, 3 more were located at the exit of the NGV's, 6 more were located in the shroud above the rotor blade, 2 were located downstream of the rotor (1 in the hub wall and 1 in the tip wall), and the remaining pressure transducer was located in the exit section approximately one diameter ahead of the orifice plate. These pressure measurements were used to define the flow-establishment time within the model and to measure the overall pressure change through the stage. The flow-establishment process and typical pressure histories throughout the model have previously been shown in [3] for test conditions similar to those used here and thus will not be repeated. However, the measured pressure change across the full stage will be reported in Table 1 of Part II.

A cylinder of 0.0041-m (0.160-in.) diameter with eight thin-film gages located on a stagnation line was placed across the flow channel at 0.046-m (1.8-in.) upstream of the NGV for the primary purpose of measuring the uniformity of the flow across the channel for each experiment. The cylinder was not directly upstream of the instrumented NGV but rather was offset circumferentially by approximately 60 deg. A secondary use of these rake data was to infer the freestream turbulence level in the flow entering the NGV's in a manner to be described in Part II of this paper.

A photograph of one of the heat-flux gages used in this work was taken through a Leitz microscope and is shown in Fig. 3. The thin-film gages are made of platinum (~ 1000 Å thick) and are painted on a pyrex substrate [9.7×10^{-4}-m

(0.04-in.) in diameter] in the form of a strip approximately 1.0×10^{-4}-m (0.004-in.) wide by about 5.1×10^{-4}-m (0.02-in) long. In building these gages, the intent is to obtain a gage with a room temperature resistance on the order of 50 to 100Ω. The thickness of the pyrex substrate depends upon the gage location. Those gages located in the NGV trailing edge and near the rotor blade trailing edge are approximately 3.8×10^{-4}-m (0.015-in.) thick but gages at other locations are 7.1×10^{-4}-m (0.03-in.) thick. The response time of these heat transfer elements can be shown to be on the order of 10^{-8} s. A coating of magnesium fluoride (~ 1200 Å thick) is vapor deposited over the gage to protect the platinum element against abrasion.

The thin-film gages constructed in the manner described above were installed in the turbine stage at the following locations: (a) 26 gages on the NGV tip endwall, (b) 20 gages on the NGV suction surface, (c) 21 gages on the NGV pressure surface, (d) 4 gages on the NGV airfoil leading edge, (e) 3 gages on the rotor blade platform, (f) 5 gages on the rotor blade suction surface, (g) 11 gages on the rotor blade pressure surface, (h) 5 gages in the rotor blade tip and (i) 10 gages in the shroud above the rotor, for a total of 106 measurement locations on the stage for each run. An additional 8 gages were located on the stagnation rake as described earlier. Figure 4 is a photograph of the NGV pressure surface instrumentation showing the leading edge gages and the airfoil gage coverage. Figure 5 is a similar photograph for the rotor illustrating the tip and pressure surface gage locations. Detailed descriptions of the gage locations can be found in [19]. Figure 6 is typical of the plots appearing in that reference that will provide the detailed location of each gage on a particular component. As described on this figure, the y-dimension is measured in the plane tangent to the leading and trailing edge. The x-dimension is measured along a line parallel to the leading edge that is perpendicular to the hub endwall. The exception to this is the gage location on the trailing edge downstream of the slot where the x-dimension is parallel to the trailing edge. The data plotted in Part II are given as percent of airfoil chord where the chord is as defined above. It is important to note that this value is very nearly equal to percent axial chord.
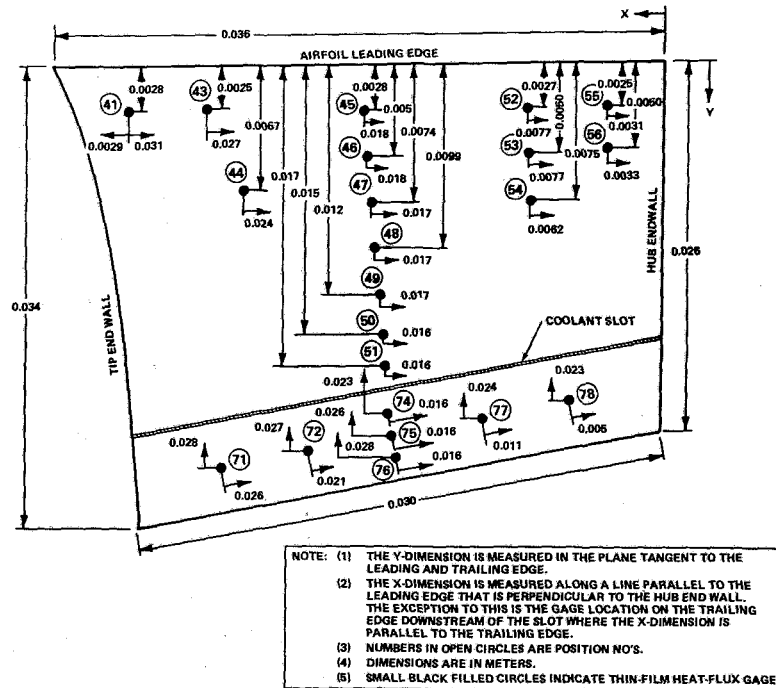
Fig. 6 Sketch of heat flux gage locations on airfoil pressure surface of NGV

The temperature versus time histories of the thin-film gages were recorded directly on a digital data acquisition system (DDAS) [20]. This data system contains 128 channels that can be sampled and digitized with 10-bit resolution at a sampling rate of 50 μs per sample. The software system performs two major functions, (i) data reduction and calibration, and (ii) data display. The data reduction task generates a sorted, calibrated reduced data file from the DDAS raw data file. This reduced data file contains a digitized time history of each channel calibrated in engineering units. A later section will describe the technique used to obtain heat flux values from the temperature-time histories. The second task permits the system to plot, list and generate strip charts for each channel on the reduced data file. All of the data are recorded on magnetic tape for permanent file. The instrumentation amplifiers used in the data recording system have a bandwidth in excess of 20 KHz.

The temperature versus time histories obtained from the thin-film gages located on the rotating component are transferred to the DDAS by use of a slip-ring system. Each heat transfer gage is a separate circuit with the power supply for the entire array located in the tunnel control room. During the experiments, a constant current of 1 mA was passed through each gage via the slip rings. The resulting $i^2 R$ heating of the gage produced less than 0.1 percent of the gage ΔT experienced during an experiment. The slip ring contact noise is on the order of 25 μ volts compared to a heat transfer gage output in the tens of millivolt range. During the experiment, a freon-oil mixture is flowed through the slip-ring unit in order to provide the proper cooling and lubrication for the rings. These rotor data were processed on the DDAS in the manner discussed above in order to obtain the desired heat flux histories.

Discussion of Data Analysis

The range of heat transfer rates and test times used in this measurement program produced pyrex-substrate surface-temperature rises of 100°F or more for several gage locations at the high T_0 (see Table 1 of Part II, Runs 40–42) test condition and at a few gage locations at the intermediate T_0

(Runs 35–39) condition. At the low total temperature test condition (Runs 26–34), the substrate temperature rise was generally less than 100°F. The temperature of the metal surface adjacent to the gages is estimated to have risen less than 5°F in all cases. This fact raises two issues concerning the heat transfer rates inferred from the temperatures measured at the substrate surfaces:

1 What is the influence, on the flow, of the spatial distribution of surface temperature? 2 How are the inferred rates affected by the temperature dependence of the thermal properties of the substrate? The first question is virtually impossible to answer in a quantitative way, except for two-dimensional situations, where a solution for the flow over a discontinuity in surface temperature offers some guidance [21, Section 7]. The present situation is not two-dimensional, however. The gages presumably act as miniature heat islands in the boundary layer, but solutions covering the appropriate range are not available. The approach taken in these tests has been to minimize the ratio of the gage diameter to the chord length, but a quantitative measure of the degree to which the flow is perturbed is not known. However, the experimental results presented later in this paper suggest that the spatial temperature distribution does not significantly influence the heat transfer results.

The second question can be answered quantitatively, by carrying out numerical solutions of the one-dimensional heat conduction equation

$$\rho c \frac{\partial T}{\partial \tau} = \frac{\partial}{\partial x}\left(\frac{k \partial T}{\partial x} \right)$$

where $T(x,t)$ is the temperature, x measures distance into the pyrex, and k, ρ, and c are the thermal conductivity, density, and specific heat of the pyrex. When the latter properties are constant, the heat transfer rate can be written as a convolution of the surface temperature with the appropriate influence function [22].

If the thermal properties are not constant, the heat equation is nonlinear and numerical solutions must be used. These are facilitated by use of the Kirchoff transformation [23]

$$\phi = \int_{T_{\mathrm{ref}}}^{T} \frac{k}{k_{\mathrm{ref}}}\, dT$$

In terms of this variable, the heat equation becomes

$$\frac{\partial \phi}{\partial t} = \alpha(\phi)\, \frac{\partial^2 \phi}{\partial x^2}$$

where the thermal diffusivity $\alpha = k/\rho c$ depends on ϕ.

Cook [24] carried out numerical solutions of this equation for Code 7740 Pyrex, using an explicit time-marching method. One of his solutions, in which the surface value of ϕ is proportional to the square root of time, has been used in our data analysis to correct for the effect of variable thermal properties. Because these corrections were as large as 25 to 30 percent in the case of some locations on Runs 40–42, further numerical checks were run. It should be noted for the $T_0 = 1000°R$ data, very small corrections to the recorded data were necessary. For the $T_0 = 1600°R$ data, the corrections amounted to approximately 8 percent.

The calculations were done in a stretched coordinate system

$$\tau = t, \eta = x/2\sqrt{\alpha_{\mathrm{ref}}t}$$

In terms of the coordinate η, the temperature variations occur over a uniform range (from $\eta = 0$ to $\eta = 3$) at all times, so that rezoning of the finite-difference grid is unnecessary. In these new coordinates, the heat equation is

$$\frac{\alpha}{\alpha_{\mathrm{ref}}}\, \frac{\partial^2 \phi}{\partial \eta^2} + 2\eta\, \frac{\partial \phi}{\partial \eta} = 4\tau\, \frac{\partial \phi}{\partial \tau}$$

Numerical solutions of this equation were carried out for selected cases, using an implicit Crank-Nicholson finite-difference scheme, with surface boundary conditions given by the measured surface-temperature rise. These spot checks suggested correction factors that were within 5 percent of those which had been applied.

Conclusions

The experimental apparatus, the measurements performed, and the data analysis procedure used to obtain detailed heat flux data for a full-stage rotating turbine have been described. The comparisons with theoretical results, given in Part II, plus the continuing refinements in data acquisition and reduction procedures, indicate that the short-duration testing technique is capable of providing an important data base so necessary for improving the turbine heat transfer predictive capability.

Acknowledgments

References

1 Dunn, M. G., and Stoddard, F. J., "Application of Shock-Tube Technology to the Measurement of Heat-Transfer Rate to Gas Turbine Components," 11th International Symposium on Shock Tubes and Waves, July 1977.

2 Dunn, M. G., and Stoddard, F. J., "Measurement of Heat-Transfer Rate to a Gas Turbine Stator," ASME JOURNAL OF ENGINEERING FOR POWER, Vol. 101, No. 2, Apr. 1979 (also see ASME Paper No. 78-GT-119).

3 Dunn, M. G., and Hause, A., "Measurement of Heat Flux and Pressure in a Turbine Stage,"ASME JOURNAL OF ENGINEERING FOR POWER, Vol. 104, No. 1, Jan. 1982 (see also ASME Paper No. 81-GT-88).

4 Winstanley, D. K., Booth, T. C., and Dunn, M. G., "The Predictability of Turbine Vane Convection Heat Transfer," Paper accepted for presentation at the AIAA/SAE/ASME 17th Joint Propulsion Conference, July 27–30, 1981, Colorado Springs, CO.

5 Dunn, M. G., and Holt, J. L., "The Turbine Stage Heat Flux Measurements," Paper No. 82-1289, AIAA/ASME 18th Joint Propulsion Conference, 21–23 June 1982, Cleveland, Ohio.

6 Wysong, R. R., et al., "Turbine Design System," AFAPL-TR-78-92, Nov. 1978.

7 Gaugler, R. E., "Some Modifications to, and Operating Experiences with, the Two-Dimensional Finite-Difference, Boundary-Layer Code, STAN5," ASME Paper 81-GT-89 (Mar. 1981).

8 Dulkravich, D. S., "CAS2D - FORTRAN Program for Nonrotating Blade-to-Blade, Steady, Potential Transonic Cascade Flows," NASA TP 1705, July 1980.

9 Blair, M. F., "An Experimental Study of Heat Transfer and Film Cooling on Large-Scale Turbine Endwalls," ASME Journal of Heat Transfer, Vol. 96, Nov. 1974, pp. 524–529.

10 Graziani, R. A., et al., "An Experimental Study of Endwall and Airfoil Surface Heat Transfer in a Large Scale Turbine Blade Cascade," ASME JOURNAL OF ENGINEERING FOR POWER, Vol. 102, Apr. 1980, pp. 257–267.

11 Hylton, L. D., Mihelc, M. S., Turner, E. R., and York, R. E., "Experimental Investigation of Turbine Endwall Heat Transfer," Vols. I, II, and III, AFWAL-TR-81-2077, Aug. 1981.

12 Dring, R. P., et al., "An Expeirmental Investigation of Film Cooling on a Turbine Rotor Blade," ASME JOURNAL OF ENGINEERING FOR POWER, Vol. 102, Jan. 1980, pp. 81–87.

13 Louis, J. F., "Investigation of Factors Affecting Heat Transfer to Turbine End Walls," Air Force Aero-Propulsion Laboratory, TR-73-93, Oct. 1973.

14 Louis, J. F., "Heat Transfer in Turbines," Air Force Aero-Propulsion Laboratory TR-75-107, Sept. 1975.

15 Jones, T. V., and Schultz, D. L., "A Study of Film Cooling Related to Gas Turbines Using Transient Techniques," University of Oxford Report No. 1121/70, 1970.

16 Jones, T. V., et al., "Measurement of the Heat Transfer Rate to Turbine Blades and NGV's in the Transient Cascade," 6th International Heat Transfer Conference, Toronto, Canada, Paper EC-12, 1978.

17 Schultz, D. L., et al., "A New Transient Facility for the Measurement of Heat Transfer Rates," Conference Proceedings No. 229, High Temperature Problems in Gas Turbine Engines, Sept. 1977, pp. 31-1 to 31-27.

18 Smith, M. R., "A Study of Film Cooling Effectiveness with Discrete Holes and Slots," University of Oxford Report No. 1100/74, 1974.

19 Dunn, M. G., and Rae, W. J., "Measurement and Analysis of Heat-Flux Data," Final Report for Contract No. F33615-81-C-2017, Calspan Rept. No. 6897-A-1, Sept. 1982.

20 Wittliff, C. E., Pflueger, P. G., and Donovan, P. J., "A High-Speed Digital Data Acquisition System for Short-Duration Test Facilities," International Congress on Instrumentation in Aerospace Simulation Facilities, ICASF Record-97, Sept. 1979, Monterey, CA.

21 Schultz, D. L., and Jones, T. V., "Heat-Transfer Measurements in Short-Duration Hypersonic Facilities," Agardograph No. 165, Feb. 1973.

22 Vidal, R. J., "Model Instrumentation Techniques for Heat Transfer and Force Measurements in a Hypersonic Shock Tunnel," Calspan Rept. No. AD-917-A-1, Feb. 1956.

23 Carslaw, H. S., and Jaeger, J. C., Conduction of Heat in Solids, 2nd Ed., Clarendon Press, Section 2.16.

24 Cook, W. J., "Determination of Heat-Transfer Rates from Transient Surface Temperature Measurements," AIAA Journal, Vol. 8, 1970, pp. 1366–1368.

Measurement and Analyses of Heat Flux Data in a Turbine Stage: Part II—Discussion of Results and Comparison With Predictions

M. G. Dunn

W. J. Rae

Aerodynamic Research Department,
Calspan Advanced
Technology Center,
Buffalo, N.Y. 14225

J. L. Holt

Air Force Wright Aeronautical
Laboratories,
Aero Propulsion Laboratory,
Wright-Patterson AFB, Ohio 45433

Parts I and II of this paper report the measurement and analysis of detailed heat flux distributions obtained on the nozzle guide vane (NGV), rotor, and shroud of the full-stage rotating turbine of the Garrett TFE 731-2 engine. Part I is devoted to a description of the experimental apparatus and the data analysis procedure. Part II is concerned with the experimental results and their comparison with predictions obtained using a flat-plate technique and with predictions obtained using STAN5. Measurements were performed for values of the ratio of wall temperature to total temperature equal to 0.21, 0.33, and 0.53. For the NGV airfoil and rotor blade, the influence of wall temperature ratio on the Stanton number is shown to be generally 10 percent or less. For the NGV airfoil, and the rotor blade pressure surface, the flat-plate turbulent-flow prediction provides a reasonably good comparison with the data. With the rotor operating, the state of the boundary layer generally appears to be turbulent for both the NGV airfoil and the rotor blade. Predictions obtained using STAN5 confirm that boundary layer transition occurs at a value of Re_θ substantially less than 200.

Experimental Conditions

Table 1 gives the experimental conditions at which heat flux measurements were performed. This table includes the following quantities: (a) the stator inlet temperature, T_0, determined from the shock-tube conditions, (b) the measured model wall temperature, T_w, (c) the weight flow, $\dot{w}$, calculated knowing the area of the exit channel, the orifice area, the turbine work extraction, and the inlet total temperature, (d) the measured rotor speed, (e) the stator inlet Reynolds number based on midchord, C_s, (f) the total pressure at the NGV inlet calculated from the measured static pressure and the calculated inlet Mach number, (g) the total pressure ratio across the turbine stage calculated from the measured upstream and downstream static pressures and the calculated inlet and outlet Mach numbers, and (h) the flow function calculated from the relation F.F. $= (\dot{w} \sqrt{T_0/518.7}) / [P_T)_{NGV)_{IN}}/14.696]$. As indicated by Table 1, 17 separate experiments were performed. For most of these experiments, approximately 114 heat flux measurements and 16 pressure measurements were obtained. The individual experiments can be grouped in order to ascertain the influence of temperature ratio, T_w/T_0, speed, and flow function. Accordingly, the separate experiments have been grouped as follows: (a) Run 26, (b) Runs 27–29, (c) Runs 30–31, (d) Run 32, (e) Runs 33–34, (f) Runs 35–39, and (g) Runs 40–42.

The shock-tunnel apparatus described in Part I has the capability of duplicating the stagnation pressures and temperatures typical of turbine inlets. However, the wall temperature remains essentially at its room-temperature value during the twenty-millisecond test duration, and the question arises as to how strongly the data are affected by this parameter.

It should first be pointed out that one of the uses to which the data from this program are to be put is the validation of computer codes; for this purpose, the duplication of flight-hardware conditions is not critical. As long as the experimental conditions are carefully defined, they can serve as valid checks on the capabilities of computer codes. On the other hand, if the data are to be used directly, as a basis for estimating the heat loads on operating engines, then the effects of wall temperature must be known.

The primary effect, of course, is contained in the driving temperature difference $T_0 - T_w$; this effect is removed by presenting the data in terms of the Stanton number, but then it must be asked whether there is any residual effect of wall temperature on the Stanton number. It is possible to postulate many physical mechanisms which might have such an effect (the influence of cooling on transition and the response of thinner boundary layers to centrifugal and Coriolis forces are two examples), but it is difficult to quantify these effects.

Table 1 Summary of experimental conditions

RUN NO.	STATOR INLET T_0 °R	T_w °R	WEIGHT FLOW lb/sec	PHYSICAL SPEED rpm	RE)C_s	$P_T)NGV)_{in}$ psi	$\frac{P_T)NGV)_{in}}{P_T)rotor)_{out}}$	FLOW FUNCTION
26	1006	534	22.8	22,050	3.7^5	102.3	1.80	4.55
27	1006	534	22.5	20,105	3.7^5	102.8	1.80	4.47
28	1009	534	22.8	20,590	3.7^5	103.9	1.78	4.49
29	1013	535	22.8	21,350	3.7^5	103.3	1.76	4.53
30	1013	534	22.5	18,050	3.6^5	103.3	1.78	4.47
31	1013	534	22.2	18,350	3.6^5	101.7	1.79	4.47
32	1013	534	23.6	20,810	3.6^5	102.1	-	4.75
33	1007	533	21.5	20,360	3.4^5	104.9	1.48	4.20
34	1015	534	21.5	20,890	3.3^5	106.6	1.49	4.14
35	1624	534	29.1	23,840	3.2^5	165.1	1.75	4.58
36	1650	535	29.0	25,100	3.1^5	167.9	1.75	4.53
37	1629	533	28.2	24,260	3.1^5	160.2	1.75	4.59
38	1630	533	28.8	22,710	3.1^5	168.5	1.75	4.43
39	1624	532	28.9	23,030	3.1^5	168.3	1.75	4.43
40	2485	533	29.5	25,215	2.5^5	206.5	1.52	4.83
41	2467	532	30.7	24,810	2.6^5	206.7	1.42	4.79
42	2504	533	30.7	24,540	2.6^5	207.2	1.45	4.80

Accordingly, the present set of experiments was designed to investigate the effect of wall temperature.

The approach used was to test at values of the appropriate dimensionless ratios, rather than attempting to duplicate all of the conditions on the flight environment. Accordingly, a given set of corrected conditions on the turbine operating map was held fixed through a series of measurements, while the stagnation temperature was varied, so as to cover a range of values of T_w/T_0. For the purposes of comparing the experimental results with the results of our analysis, Runs 27–29 will be considered to be representative of $T_w/T_0 = 0.53$, Runs 35–39 representative of $T_w/T_0 = 0.33$ and Runs 40–42 representative of $T_w/T_0 = 0.21$.

Experimental Results and Predictions

In this part of the paper, the experimental results are presented in detail and, where possible, the measurements are comared with predictions obtained using the Wright-Patterson AFB *Turbine Design System (TDS) computer code* [1]. In addition, predictions obtained using a modified STAN5 code [2] are also presented.

Table 2 Summary of conditions for comparison

RUN NO.	T_w/T_0	N)$_{PHY}$	$\frac{P_T)NGV)_{IN}}{P_T)_{rotor)out}}$	F.F.	Re_{C_s}
27-29	0.53	20,680	1.78	4.50	3.7^5
35-39	0.33	23,790	1.75	4.51	3.1^5
40-42	0.21	24,860	1.46	4.74	2.6^5

Reference [3] presents a summary of the mean Stanton numbers ± the standard deviation tabulated for the specific engine component and the heat-flux gage position number. A detailed description of the relative locations of the gages can also be found in [3] as noted in Part I. The Stanton number used in this work is based on conditions at the NGV inlet and was evaluated using the relationship

$$St.No._{INLET} = \frac{\dot{q}(T)}{(\dot{w}/A)[H_0 - H(T)]}$$

The standard deviation was computed [4] for each group of

Nomenclature

A = stator inlet area

C = specific heat of pyrex

C_s = stator midannular chord length

C_r = rotor midannular chord length

Flow Function = $\dot{w}\sqrt{T_0/518.7}/[P_{T)NGV)_{IN}}/14.696]$

H_0 = total enthalpy

$H_w(T)$ = wall enthalpy

k = thermal conductivity

k_m = thermal conductivity evaluated at $(T_0 + T)/2$

N_{phy} = physical rotor speed

N_{corr} = corrected rotor speed, $N_{corr} = N_{phy}/\sqrt{T_0/518.7}$

Nu)$_D$ = Nusselt number, $\dfrac{\dot{q}_{s.p.}D}{k_m(T_0 - T)}$

P_T = total pressure

$\dot{q}$ = measured heat flux corrected for variable thermal properties of the pyrex substrate

$\dot{q}_{s.p}$ = measured stagnation point heat flux

Re)c_r = Reynolds number based on rotor mid-chord, $\dfrac{\rho V C_r}{\mu_0}$

Re)c_s = Reynolds number based on stator mid-chord, $\dfrac{\rho V C_s}{\mu_0}$

Re)$_D$ = Reynolds number based on cylinder Diameter, $\dfrac{(\dot{w})}{A}\dfrac{(D)}{\mu_m}$

Stanton No.)$_{INLET}$ = $\dfrac{\dot{q}(T)}{(\dot{w}/A)[H_o - H_w(T)]}$

$T = T_w + \Delta T$

T_w = initial wall temperature

ΔT = measured temperature rise of pyrex substrate

T_0 = total temperature

Tu = turbulence level

$\dot{w}$ = physical weight-flow rate

μ_0 = dynamic viscosity evaluated at T_0

x = distance measured into pyrex

α = thermal diffusivity

V = obtained from $(\dot{w}/A)$

X = defined in Fig. 5

Y = spanwise distance, see Fig. 5

ρ = pyrex density or gas density

Fig. 2 Distribution of Stanton number for NGV airfoil midspan

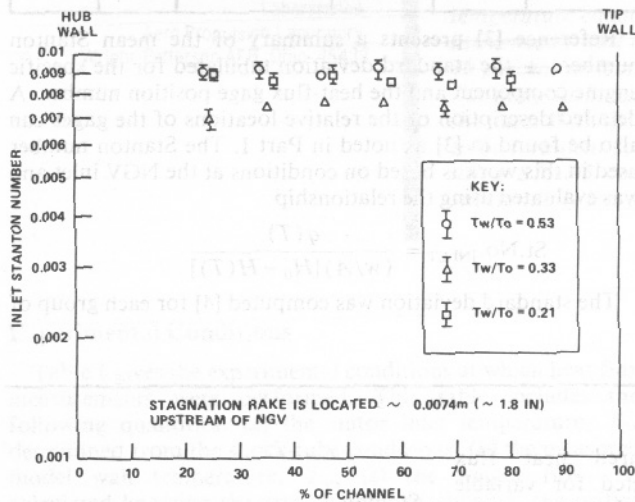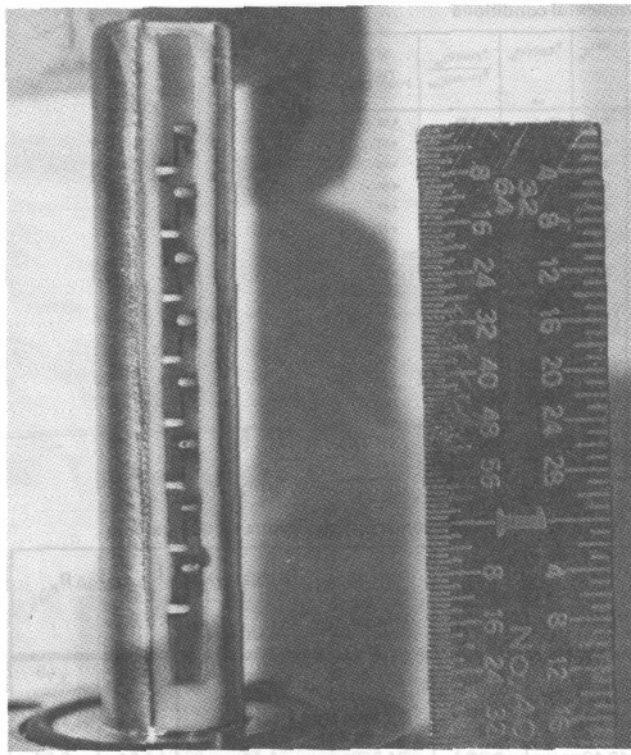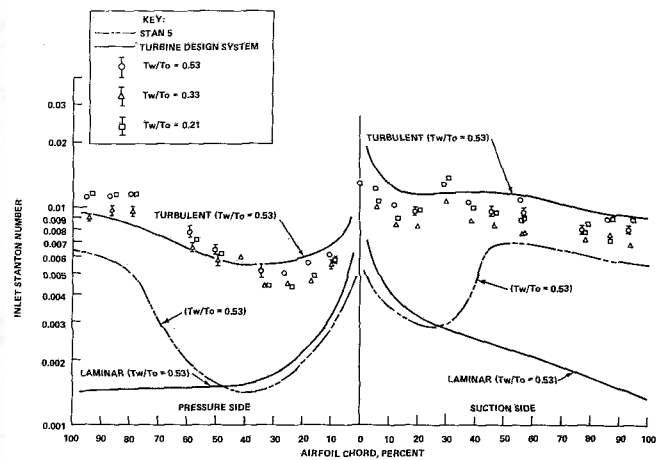Fig. 3 Local Mach number distributions for stator pitch section

Fig. 1 Stanton number distribution at stagnation point on cylinder in flow channel

Table 3 Freestream turbulence level estimated from cylinder data

T_w/T_0	Nu_D	Re_D	$\sqrt{Re_D}$	$Nu_D/\sqrt{Re_D}$	TRACI/WILCOX		LOWERY/VACHON	
					$Tu\sqrt{Re_D}$	Tu	$Tu\sqrt{Re_D}$	Tu
-	-	-	-	-	-	%	-	%
0.53	299.4	5.3×10^4	229.3	1.31	12	5.2	13.2	5.7
0.33	260.7	5.2×10^4	227.0	1.15	6	2.6	6	2.6
0.21	270.1	4.3×10^4	206.4	1.31	12	5.8	13.2	6.4

runs at a given test condition and is tabulated along with the mean Stanton number. The experimental reproducibility can be seen to be generally within ±5 percent for most locations within the stage.

In order to present comparisons between the measurements and predictions, the following discussion will concentrate on three groups of data taken from Table 1 as described in Table 2.

The uniformity of the flow just upstream of the NGV inlet is illustrated by the Stanton number distributions presented in Fig. 1. The insert on Fig. 1 is a photograph of the rake used here. The pyrex cylinder is 0.0041-m (0.160-in.) diameter and is backed by a metal support. This configuration was later changed to a uniform diameter pyrex rod, but the results were essentially the same. The symbol indicates the mean value and the bar the standard deviation. The absence of a bar indicates that the standard deviation was within the symbol. The results presented in Fig. 1 illustrate that the flow conditions are uniform across the channel ahead of the NGV inlet. Previous measurements [5] of the total temperature profile across the channel also suggested a uniform inlet flow for this model configuration.

Note that the data obtained at $T_w/T_0 = 0.33$ were approximately 10 percent below the other two test conditions. Theoretical expressions for the stagnation-line heat transfer rate to a cylinder would suggest a monotonic variation between the three conditions of Table 2.[1] The results of Cohen [8], as quoted in [9] (see equation (258)), show that the Stanton number should vary as the -0.5 power of the Reynolds number, with a small additional variation due to transport properties. Evaluation of this formula shows that the Stanton numbers for the three conditions of Table 2 should be in the ratio 1.0/1.05/1.17 for $T_w/T_0 = 0.53, 0.33,$ and 0.21. The data for the first and third values of T_w/T_0 conform to these ratios, but the second one is low. This lower value of Stanton number is felt to be due to a lower turbulence level associated with the $T_w/T_0 = 0.33$ test condition. The cylinder stagnation gages were used to estimate the relative turbulence level of the flow upstream of the NGV inlet. Traci and Wilcox [6] and Lowery and Vachon [7] provide correlations from which the free-stream turbulence can be

_____
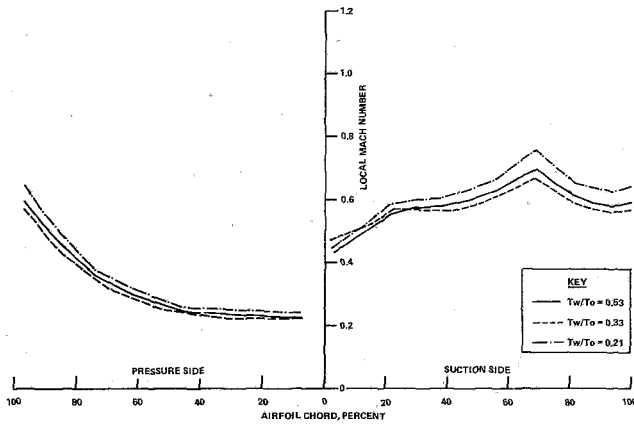[1] The authors are indebted to the reviewers for suggesting this discussion.

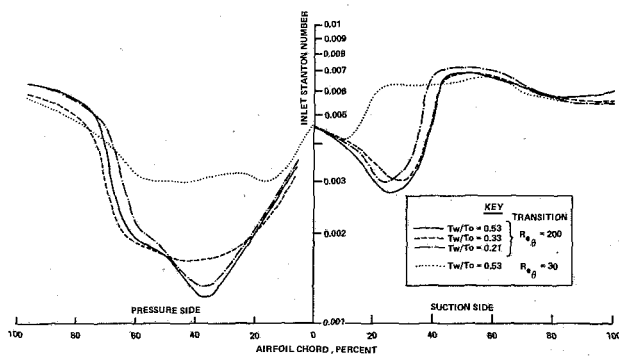**Fig. 4 Local Mach number distributions for rotor pitch section**

Fig. 6 Distribution of Stanton number for NGV airfoil near hub end-wall

Fig. 5 Influence of wall temperature ratio on STAN5 predictions for NGV airfoil midspan

Fig. 7 Distribution of Stanton number for NGV airfoil near tip endwall

inferred using the measured parameters. In both papers, correlations of the parameter $Nu_D \sqrt{Re_D}$ against $TU \sqrt{Re_D}$ are presented. Table 3 is a summary of the inferred turbulence levels for the test conditions used here obtained using the measured heat flux and wall temperature values. The thermal conductivity and viscosity were evaluated at a mean temperature, $(T_0 + T)/2$.

We are not suggesting that the absolute value of the turbulence is accurate, but we do believe that the relative turbulence levels are reasonably good. Accepting the relative values, it can then be argued that the reason for the lower stagnation point Stanton number values measured at $T_w/T_0 \approx 0.33$ is associated with the free-stream turbulence level. Further investigation will be required, in order to resolve this question.

The measured and predicted distributions of Stanton number are compared on Fig. 2 for the NGV airfoil midspan. The numbers in circles are heat flux gage locations (see [3]) and the data are presented for all three values of T_w/T_0. On both the pressure and suction surface, data were obtained from the leading edge to approximately 94 percent chord. Gage positions (67) and (35) are essentially duplicate chord positions on two different airfoils. The resulting Stanton numbers suggest the absence of any significant gasdynamic differences between adjoining flow paths as should be anticipated. The solid and dashed lines on Fig. 2 are the predicted distributions using TDS and STAN5, respectively. Figures 3 and 4 show the Mach number distributions on which the STAN5 calculations were based. The TDS predictions are insensitive to the ratio T_w/T_0 and thus only the 0.53 results are presented. The TDS calculations assume that the boundary layers either fully turbulent or fully laminar. However, the STAN5 predictions have been performed for a transition Reynolds number, Re_θ, of either 30 or 200. As noted above, the STAN5 prediction was performed for three values of T_w/T_0 and the results are compared on Fig. 5. The
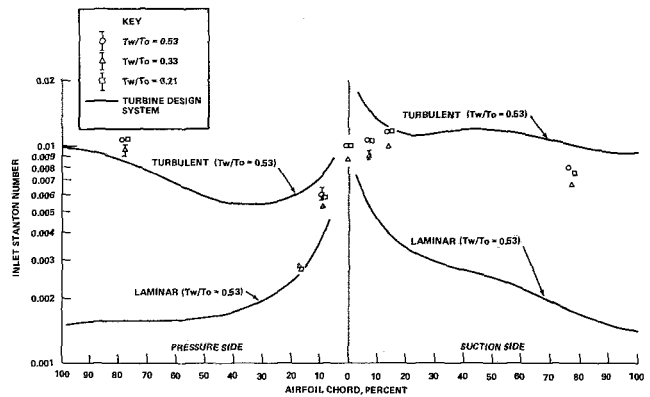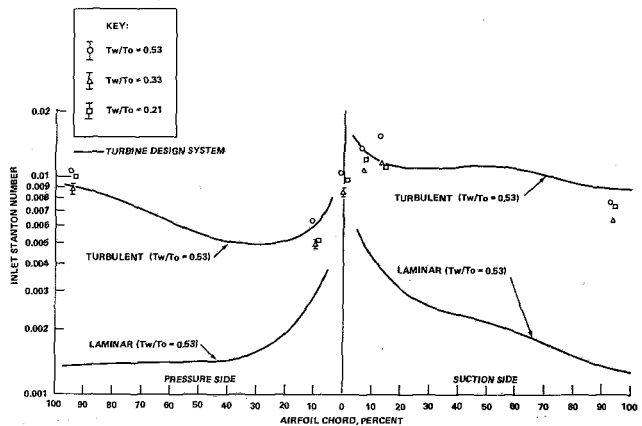
STAN5 predictions do illustrate an influence of T_w/T_0 over the range of interest, the magnitude of the effect depending upon the particular surface and chord position. The largest influence is shown to occur on the pressure surface in the vicinity of 70 percent chord. Inclusion of all three predictions on the data figures unnecessarily complicates the comparison. Therefore, the prediction obtained for $T_w/T_0 = 0.53$ was considered to be representative and will be included on the comparison given in Fig. 2. The important observation from Fig. 2 is that on the suction surface, transition occurs much earlier than $Re_\theta = 200$. With a value of $Re_\theta = 200$, the STAN5 code significantly underpredicts the data at chord positions less than 30 percent and underpredicts the data by approximately 30 percent for chord positions beyond 50 percent. By contrast, the turbulent flat-plate prediction overpredicts the data at chord locations less than 10 percent but at greater chord positions, the prediction is on the order of 20 percent above the data. Considering the degree of sophistication of the flat-plate prediction, the correlation is reasonably good. The suction-surface laminar flat-plate prediction is clearly far below the data and is only included for completeness. For the same NGV airfoil operated in the absence of a downstream rotor (10) for the $T_w/T_0 = 0.21$ test condition, a laminar flow region appeared to be present on the suction surface with transition occurring in the vicinity of 15 to 20 percent chord. As was previously observed in [10], the presence of the rotor tends to move transition forward on the airfoil and increase the level of the Stanton number. On the pressure surface, the turbulent flat-plate prediction overpredicts the data at less than 30 percent chord, is in reasonable agreement between 30 and 60 percent chord, and underpredicts towards the trailing edge. The STAN5 prediction significantly underpredicts the pressure surface data presumably because of the assumed laminar flow region
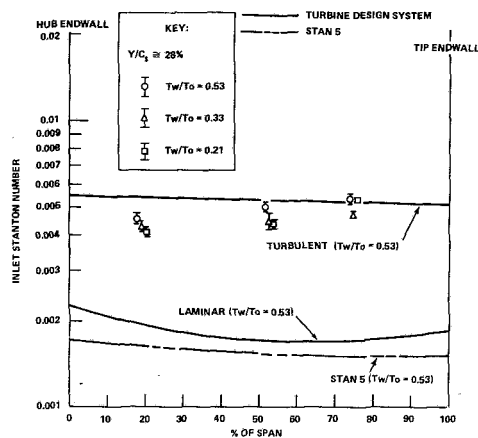
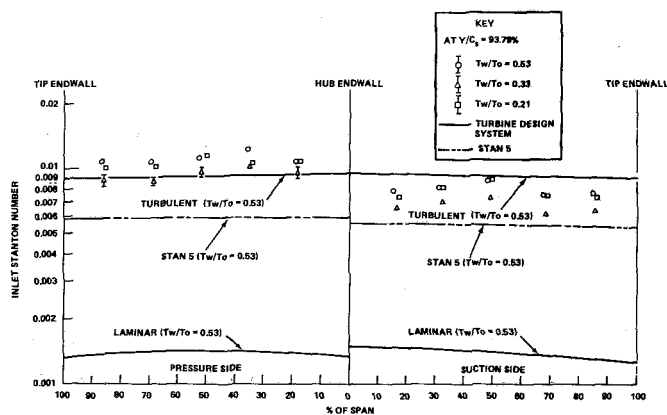**Fig. 8 NGV spanwise pressure surface distribution of Stanton number at $Y/C_S \cong 28$ percent**

Fig. 9 Spanwise distribution of Stanton number on trailing edge of NGV at $Y/C_S \cong 93.8$ percent

from the leading edge up to $Re_\theta = 200$. This same trend continued with the STAN5 comparisons; thus only a limited number of additional comparisons is shown.

The flat-plate predictions are compared to the data in Figs. 6 and 7 for the NGV airfoil near the hub and tip endwall, respectively. Figure 6 illustrates a comparison between the experimental results and the predictions suggesting that the suction surface flat-plate turbulent prediction exceeds the data by somewhat more than was found at the midchord region, while the pressure surface predictions suggest a region of laminar flow up to a chord position of about 20 percent. The pressure side flat-plate turbulent prediction underpredicts the data near the 80 percent chord position by about 15 percent. Near the tip endwall, the suction surface comparison between the data and predictions is compatible with what was observed at the midspan and the pressure side turbulent flat-plate prediction is a reasonably good approximation to the data.

Plots of spanwise Stanton number distribution at fixed chord positions have also been constructed from the data and are compared with both the TDS and STAN5 predictions at 28 and 93.8 percent chord. Figure 8 is a comparison of measured versus predicted spanwise pressure surface Stanton number distribution at $Y/c_s = 28$ percent. The results are plotted so that the hub endwall is on the left and the tip endwall on the right. The turbulent flat-plate prediction is shown to be a reasonably good approximation to the data. Once again, use of the STAN5 code with $Re_\theta = 200$ results in a significant underprediction of the data as shown.

Figure 9 is a comparison of the spanwise data with the flat-

plate and STAN5 predictions for the NGV airfoil at $Y/c_s = 93.8$ percent. Both the suction and pressure surface results are shown and the figure is constructed so that the hub endwall is in the center and the tip endwall at the outer edges. Both predictions suggest that the boundary layer was turbulent at this chord position. On the suction surface, the flat-plate prediction is above the data by approximately the same amount that the STAN5 prediction is below the data. For the pressure surface, the flat-plate prediction is in relatively good agreement with the measurements and the STAN5 prediction is approximately 30 percent low.

As noted in an earlier section, detailed Stanton number distributions were also obtained for the tip endwall and the results of these measurements are presented on Fig. 10 for $T_w/T_0 = 0.53$. The relative locations of these endwall thin-film gages can be found in (Fig. 3) and the experimentally determined Stanton numbers for the other two values of T_w/T_0 can be found in [3]. The largest endwall Stanton number values were found near the pressure surface close to the NGV exit (position numbers ⑨⑥ , ⑨⑧ , and ⑩⑤) and near the suction surface at about one-third of the axial channel (position numbers ⑧⑧ , ⑨③ , and ⑨⑤).

A significant amount of rotor blade (pressure and suction surface, tip and platform locations) and shroud data were also obtained. The measured distribution of Stanton numbers on the blade pressure and suction surfaces are compared with the TDS and STAN5 predictions on Fig. 11. This figure is plotted so that the tip is in the center and the platform is on each edge. The majority of the measurements were performed for chord positions in the range of 19 to 45 percent. One data point is presented for the 71 percent chord position near the tip. The respective predictions bounding the 19 and 45 percent chord positions are thus included on the plot. Note that the Stanton numbers deduced from the thin-film gages mounted in the tip are shown at the center of this figure and those obtained for the platform gages are shown on the left outer edge. Neither the flat plate nor the STAN5 predictions give a good comparison on the rotor blade suction surface. The laminar predictions are far below the data while the turbulent flat-plate prediction is above the data. At the 45 percent midchord position, the STAN5 prediction approaches the measured value as the platform is approached. For the pressure surface, the turbulent flat-plate predictions is in good agreement with the measurement. However, the predictions made here with the STAN5 code significantly underpredict the measurements. Detailed heat flux measurements obtained for a rotor blade in a linear cascade [11], but for a significantly different blade geometry and test condition, would suggest that the pressure surface boundary layer up to approximately 45 percent chord may have been expected to be laminar. However, added to the already noted differences between the present experiment and the one described in [11] is a major one attributed to the rotating of the rotor used here.

The rotor tip data are plotted on Fig. 12 as a function of midchord position. Again, the detailed locations of the gages can be found in [3] but the relative locations can be seen on the photographs given in Part I. The tip region Stanton number can be seen to increase from the 10 percent chord position to the 30 percent chord position which is the limit of the data. The tip Stanton numbers are large, being on the same order as those obtained at or near the NGV airfoil leading edge.

Figure 13 presents the Stanton number results obtained on the rotor blade platform. On this plot, the Stanton number appears to be relatively uniform along the platform and the results are indicative of the general trend. However, review of the gage positions relative to the pressure and suction surfaces suggests that better gage coverage would be desirable.
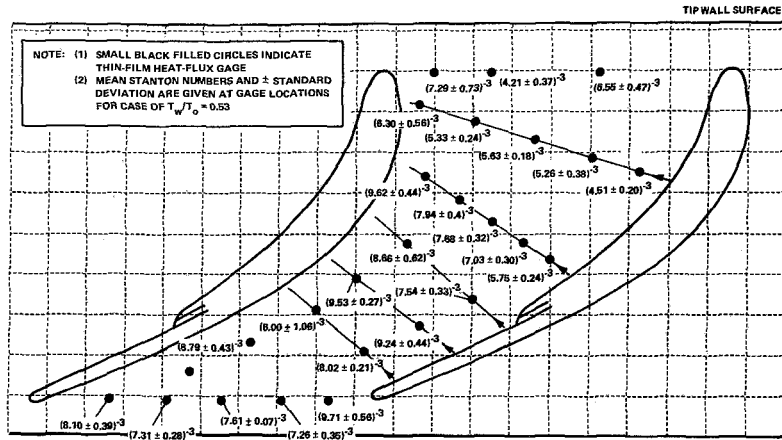
Detailed heat flux measurements were performed for the

Fig. 10 Distribution of Stanton number on NGV tip endwall for T_w/T_0 = 0.53

shroud region and the Stanton number results based on inlet conditions are shown in Fig. 14 as a function of rotor mid-chord position with data included from 13 to 105 percent. It was previously noted in [3] that the Stanton number values showed a steady decrease from the 13 percent position to the 75 percent midchord position. In this regard, it is important to note that the Stanton numbers reported here are based on inlet conditions, i.e., $H_o - H_w$ where H_0 is constant as a function of axial position. However, because of work extraction by the rotor, H_0 will decrease and the term $(H_0 - H_w)$ will become smaller with increasing axial distance. If the Stanton number were plotted against local H_0 values, then the trend would appear different. The local variation of H_0 with axial distance is not readily available and thus the results were based on inlet

conditions. For this series of measurements, positions ⑪⑧ and ⑪⑨ were added to complete the distributions. As can be seen from Fig. 14, the Stanton number continues to decrease in the axial direction. It is of interest to compare the tip data in the 10 to 30 percent midchord region with the shroud data in the 13 to 30 percent region. In this region of comparison, the measured Stanton numbers indicate that the shroud value was about 12 percent higher at the 13 percent location and the tip value was about 20 percent higher at the 30 percent location.

The influence of rotor speed on the measured Stanton numbers can be seen on Fig. 15 which presents a comparison of the results of Run 26 with those of Runs 27–29 and with those of Runs 30–31. These three groups of runs were performed at nearly the same flow function and Reynolds number. However, the rotor speed was varied by approximately ±10 percent about 20,000 rpm. The comparison shown in Fig. 15 suggests that for the NGV midspan, a variation of ±10 percent of the rotor speed did not have a significant influence on the resulting Stanton number.

Figure 16 illustrates the influence of the flow function (Reynolds number) on the NGV midspan Stanton number. This plot was constructed by comparing the results of Runs 27–29 with those of runs 33–34. The rotor speed and the T_w/T_0 ratio for the two sets of data were approximately the same. The results are essentially uninfluenced by the flow function from the leading edge to the 60 percent chord location on both the suction and pressure side. Near the trailing edge on both surfaces the reduced flow function (lower Reynolds number) data are about 10 percent higher than the data obtained at the higher flow function value.

Conclusions
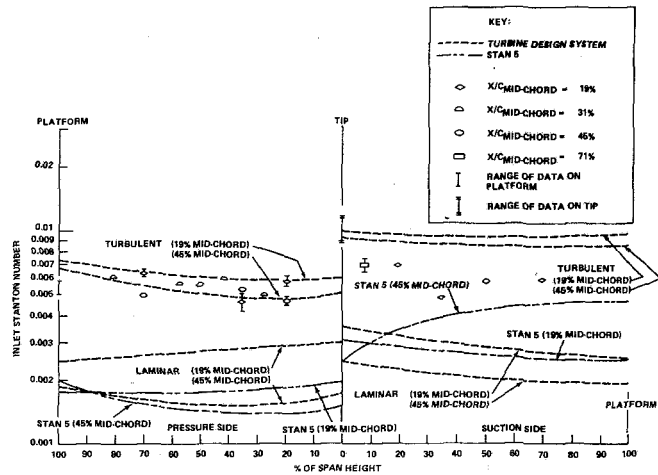
Full-stage turbine heat flux data have been obtained for

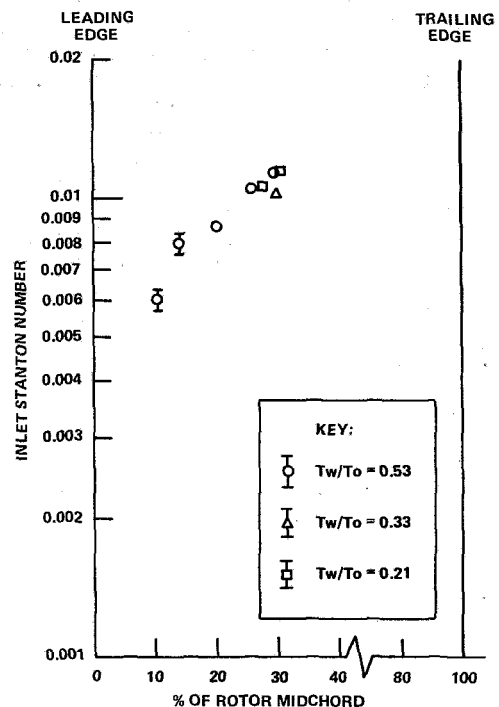**Fig. 11** Distribution of Stanton number on rotor blade for T_w/T_0 = 0.53

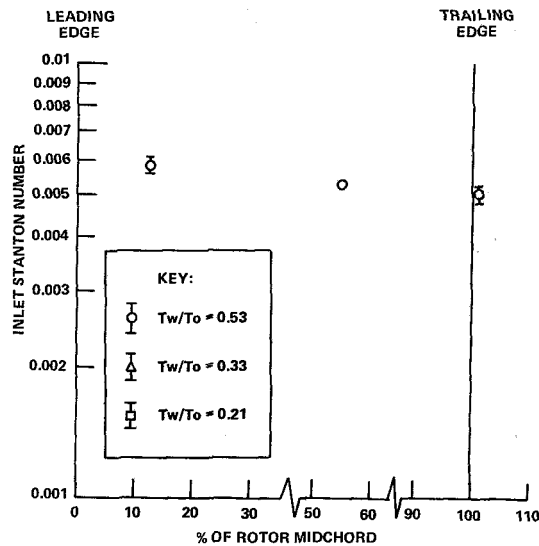**Fig. 12** Distribution of Stanton number at rotor blade tip

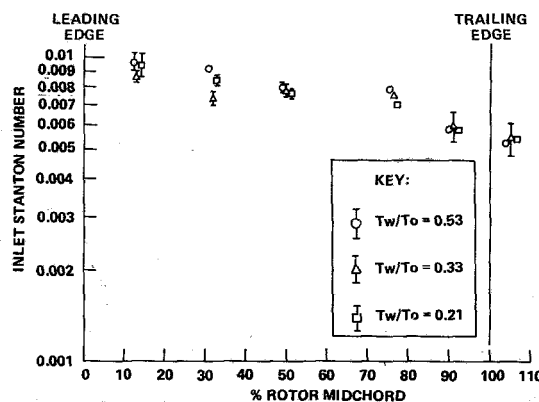**Fig. 13 Distribution of Stanton number on rotor blade platform for $T_w/T_0 = 0.53$**

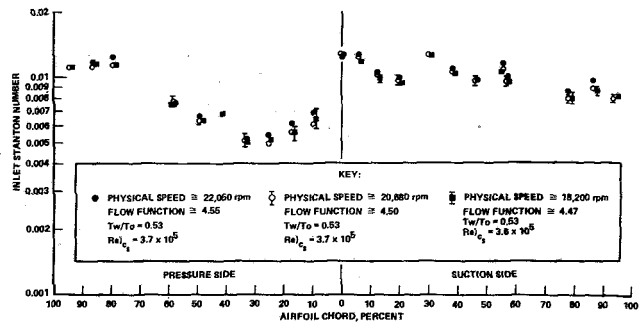**Fig. 14 Axial distribution of Stanton number for shroud**

Fig. 15 Influence of rotor speed on NGV midspan Stanton number distribution
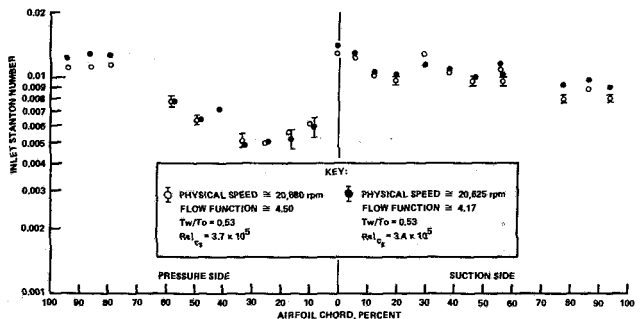
Fig. 16 Influence of flow function on NGV midspan Stanton number

representative operating conditions. For the NGV airfoil and rotor blade, the influence of wall temperature ratio on the Stanton number is shown to be generally 10 percent or less over the range of 0.53 to 0.21. The results suggest that the boundary layer transition occurred very early on the NGV suction surface and that the flow was generally turbulent on the rotor blade pressure and suction surface. The AFAPL Turbine Design System (TDS) was used to obtain satisfactory correlation with the NGV airfoil data and with the rotor pressure surface data. The TDS correlation obtained for the rotor blade suction surface was not particularly good. The predictions made here with the STAN5 code generally underpredicted the data both on the NGV airfoil and on the rotor blade because of the assumption of a substantial laminar flow region.

Acknowledgments

References

1 Wysong, R. R., et al., "Turbine Design System," AFAPL-TR-78-92, Nov. 1978.

2 Gaugler, R. E., "Some Modifications to, and Operating Experiences with, the Two-Dimensional Finite-Difference, Boundary-Layer Code, STAN5," ASME Paper 81-GT-89 (Mar. 1981).

3 Dunn, M. G., and Rae, W. J., "Measurement and Analysis of Heat-Flux Data," Final Report for Contract No. F33615-81-C-2017, Calspan Rept. No. 6897-A-1, Sept. 1982.

4 Bevington, P. R., *Data Reduction and Error Analysis for the Physical Sciences*, McGraw-Hill, 1969.

5 Dunn, M. G., and Stoddard, F. J., "Application of Shock-Tube Technology to the Measurement of Heat-Transfer Rate to Gas Turbine Components," 11th International Symposium on Shock Tubes and Waves, July 1977.

6 Traci, R. M., and Wilcox, D. C., "Freestream Turbulence Effects on Stagnation Point Heat Transfer," *AIAA Journal*, Vol. 13, No. 7, July 1975, pp. 890–896.

7 Lowery, G. W., and Vachon, R. I., "The Effect of Turbulence on Heat Transfer from Heater Cylinders," *International Journal of Heat and Mass Transfer*, Vol. 18, 1975, pp. 1229–1242.

8 Cohen, N. B., "Boundary-Layer Similar Solutions and Correlation Equations for Laminar Heat Transfer Distribution in Equilibrium Air at Velocities up to 41,000 Feet per Second," NASA Report R-118, 1961.

9 Rubesin, M. W., and Inouye, M., "Forced Convection, External Flows," Section 8 of *Handbook of Heat Transfer*, ed. by W. M. Rohsenow and J. P. Hartnett, McGraw-Hill, New York, 1973.

10 Dunn, M. G., and Hause, A., "Measurement of Heat Flux and Presure in a Turbine Stage," ASME JOURNAL OF ENGINEERING FOR POWER, Vol. 104, No. 1, Jan. 1982 (see also ASME Paper No. 81-GT-88).

11 Cosigny, H., and Richards, B. E., "Short Duration Measurements of Heat-Transfer Rate to a Gas Turbine Rotor Blade," ASME JOURNAL OF ENGINEERING FOR POWER, Vol. 104, 1982.

Length to Diameter Ratio and Row Number Effects in Short Pin Fin Heat Transfer

B. A. Brigham

G. J. VanFossen

National Aeronautics and Space
Administration,
Lewis Research Center,
Cleveland, Ohio 44135

Recently, several experiments concerning heat transfer from short pin fins have been conducted with the results indicating lower heat transfer from short pin fins than from longer pin fins found in tube banks and other similar configurations. Assessments of the effect of the number of pin rows and row geometry have also been made. It was felt that there was a need to determine the relative contribution of pin length to diameter ratio and pin row geometry on the heat transfer. Array-averaged heat transfer coefficients on pin and endwall surfaces were measured for two configurations of staggered arrays of short pin fins (length to diameter ratio of 4). One configuration contained eight streamwise rows of pins, while the other contained only four rows. Results showed that both the eight-row and the four-row configurations for an L_p/D of 4 exhibit higher heat transfer than in similar tests on shorter pin fins (L_p/D of 1/2 and 2). It was also found that for this L_p/D ratio the array-averaged heat transfer was slightly higher with eight rows of staggered pins than with only four rows.

Introduction

For the maximum possible efficiency, modern commercial and military gas turbines operate at pressures and temperatures that require the hot section parts to be cooled. The demand for increased turbine blade reliability and durability has led to a desire for a more thorough understanding of the heat transfer and fluid flow phenomena involved in the various cooling geometries. One of the many possible cooling schemes used for turbine blades is to cast pin fins into the interior of the blade. Casting technology limits the diameter of the pin fins, requiring that they have a small length to diameter ratio as compared to the type of fins found in compact heat exchangers.

Due to a lack of data in the literature on heat transfer to short pin fins, an experimental program was initiated at NASA-Lewis Research Center with the objective of developing a better understanding of the heat transfer in pin fin passages. Initial results of the program are reported in [1] in which two geometries were tested. Both of these geometries were four-row (streamwise) staggered arrays of pins set on an equilateral triangular spacing. One array had pins 2-dia long spaced 4 dia apart. The other array had pins 1/2-dia long spaced 2 dia apart. Array-averaged heat transfer for these two sets of short pin fins was found to be considerably lower than for arrays containing more rows of longer pins (about 8-dia long, endwalls included, [2]). The data for both configurations tested in [1] fell on a single correlating line. In a separate test using wood pins it was found that the heat

transfer coefficient on the endwall surface was approximately 35 percent lower than the heat transfer coefficient on the pin fin surface.

A second set of experiments was carried out to find out the effect of position within an array on the heat transfer to a single pin fin [3]. The addition of one or more rows of pins in an inline pattern upstream of the measuring pin increased the heat transfer by about 50 percent, independent of the number of upstream rows. The addition of one, two, or three rows of pins in a staggered pattern upstream of the measuring pin increased the local heat transfer 21, 64, 58 percent, respectively. It was shown that the addition of four or more rows of pins resulted in a 46 percent increase in local heat transfer. Measurement of turbulence intensity profiles in the channel ahead of the measuring pin helped to explain the heat transfer behavior. The results of this study showed that the average channel velocity should be used as the reference velocity in the Reynolds number rather than the maximum velocity based on the minimum flow area. Heat transfer to the endwalls was not included.

In work carried on concurrently in Japan [4], array-averaged heat transfer coefficients were measured for a ten-row (streamwise) array of staggered pin fins that were 1-dia long. The pins were set in a square array pattern with a 3-dia spacing in both the streamwise and transverse directions. The array averaged heat transfer results fall slightly below the correlation derived from the data of [1].

Another experimental effort concurrent with the present work was conducted at the Arizona State University. Results of that program have been reported in [5-7]. In [5] and [6], the heat transfer was measured from pins arranged in ten-row (streamwise) staggered array patterns. In both cases, the pin

---

length to diameter ratio was 1 with transverse by streamwise pin spacings of 2.5 by 2.5 and 2.5 by 1.5, respectively. The heat transfer to each row of pins was measured with trends similar to those of [3]; however [5] and [6] report average heat transfer to both pin and endwall, while [3] reports only heat transfer to the pin. This work, as well as the work done in Japan, is covered further in the discussion of results.

The work of [1] made clear the fact that heat transfer from arrays of short pin fins was considerably lower than for that of data available for longer pins from heat exchanger work, while the work of [3] showed that the number of streamwise rows also had an effect on the level of heat transfer. One question remaining to be answered was which of these effects played the more dominant role in the heat transfer in short pin fins. The purpose of this paper is to present the results of a test designed to answer this question.

A test section was fabricated which had pins that were 4-dia long. The pins were spaced 4 dia apart in an equilateral triangular array with eight rows of pins in the streamwise direction. Heat transfer results on this model were obtained using the same inlet and flow path as in [1]. Array average heat transfer coefficients on both the pin and endwall surfaces were obtained using this test section. The model was then cut in half, with the upstream half retained to give a configuration with only four rows in the streamwise direction. Heat transfer results are presented in the form of Nusselt numbers over a range of Reynolds numbers that cover those of interest for the turbine cooling application. The results are compared to those of [1] and [2].

Description of Experiment

Test Section and Flow Apparatus. A schematic of the rig used for the pin fin experiment is shown in Fig. 1. Room air was drawn through a constant acceleration inlet, into the test section and then through either an orifice flow meter (large flow rates) or through a venturi flow meter (low flow rates). The air passes through the respective flow control valves and then on into the laboratory altitude exhaust system. Air temperatures were measured at the test section inlet, test section outlet, and flow meters. Air density at the flow meters was calculated using the ideal gas law. The data was collected and converted to engineering units using the laboratory data collection system [8].

Figure 2 shows a schematic of the two test sections used, illustrating the channel geometry. For ths particular test, X_T was 4, X_s was 4, and D_o was 0.318-cm (0.125-in). The flow channel was made of two 0.635-cm (0.250-in.) thick copper plates in which holes were drilled for the insertion of the pins.
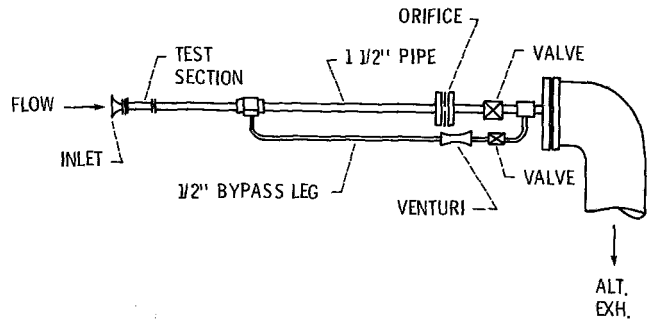

Fig. 1 Pin fin heat transfer rig

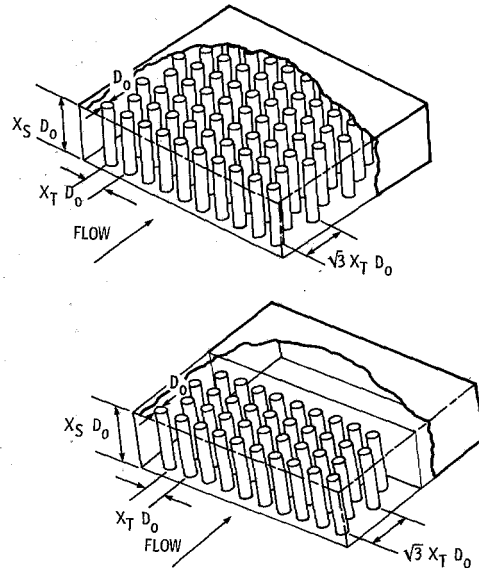$X_S = 4, X_L = X_T = 4, D_o = 0.318 \, cm \, (0.125 \, in.)$

Fig. 2 Test section schematic

The pins, which extended completely through the endwall plates, were then soldered into place. The dimensions of the flow channel were 9.58-cm long by 12.7-cm wide by 1.27-cm high (3.77-in. by 5.0-in. by 0.50-in.).

The test section was heated with commercially available electric foil resistance heaters attached to the endwalls with pressure sensitive adhesive. The streamwise centerline temperatures of the endwalls were measured by thermocouples inserted in holes drilled along the edge of each endwall plate.

Nomenclature

$\bar{A}$ = average flow area, V/L

A_p = pin cross-sectional area, $\pi D_o^2/4$

A_w = endwall area, $(\sqrt{3}/2)(X_T D_o)^2$

D' = characteristic length

D_o = pin diameter

h' = average heat transfer coefficient in pin fin test section

h_{eff} = effective heat transfer coefficient

h_p' = average heat transfer coefficient on pin surface

h_w' = average heat transfer coefficient on endwall surface

k_a = thermal conductivity of air

k_p = thermal conductivity of pin material

l = pin half length

L = test section streamwise length

L_p/D = pin length to diameter ratio

m = fin parameter, $\sqrt{h'P/k_p A_p}$

Nu = Nusselt number, $h'D'/k_a$

P = pin perimeter, πD_o

Q = heat dissipated in electric heater

Re = Reynolds number, $(w/\bar{A})D'/\mu$

S = total heat transfer surface area

T_{aw} = adiabatic wall temperature

T_r = Eckert reference temperature

T_s = static temperature

T_w = endwall temperature

V = flow channel volume minus pin volume

w = mass flow rate

X_L = ratio of pin spacing to pin diameter, streamwise direction

X_s = ratio of pin height to pin diameter (same as L_p/D)

X_T = ratio of pin spacing to pin diameter, transverse direction

μ = viscosity of air

Figure 2 illustrates how the original test section (with eight rows in the streamwise direction) was modified to give a four-row configuration. The removed pin section was replaced with heated copper plates separated from the downstream edge of the four-row configuration with an insulating layer of epoxy. During runs, these plates were kept at the same temperature as the test section.

Test Procedure. In order to account for heat losses, a set of calibrations were made with no air flow through the test section. By measuring the endwall temperatures, the ambient air temperature, and the total heat flux, an overall heat loss coefficient could be determined. This was done after the test section had reached a steady-state condition, which was normally overnight. The next day a data run was made by adjusting the power level to the heaters in order to maintain a constant plate temperature for the desired flow rate.

Data Analysis. The theoretical model used as the basis for the data analysis is shown in Fig. 3. The total heat flux for the pin and endwall surfaces is the sum of the heat flux through the endwall and the heat flux through the pin. The average heat transfer coefficients on the pin surface and endwall surface are h_p' and h_w', respectively. The heat lost by the pin fin surface (endwalls included) is equated to the heat lost by a plain surface with heat transfer coefficient h_{eff}. For the purpose of this work, the average heat transfer coefficient on the pin, h_p', was assumed to be equal to the heat transfer coefficient on the endwalls, h_w', and is denoted by h'. The data analysis from here on is identical to that of [1] and shall be omitted.

The data was put in dimensionless form of Reynolds number and Nusselt number for purposes of comparison. The Reynolds number is defined as

$$Re = (w/\bar{A})D'/\mu \qquad (1)$$

where

$$D' = 4V/S \qquad (2)$$

$$\bar{A} = V/L \qquad (3)$$

and μ is the viscosity of air. The Nusselt number is defined as

$$Nu = h'D'/k_a \qquad (4)$$

where k_a is the thermal conductivity of air. Both μ and k_a were found from curve fits of data from [9] and were evaluated at the Eckert reference temperature [10] defined as

$$T_r = 0.5T_w + 0.28T_s + 0.22T_{aw} \qquad (5)$$

Based on other experiments that have been done using the same type of experimental setup as was used in this work, the estimated level of uncertainty in this work is about 5 percent.

Results and Discussion

Dimensionless heat transfer coefficients averaged over the pin and endwall surfaces were found over a range of Reynolds numbers for both the eight and four row configurations. Figure 4 is a comparison of the heat transfer data from the current work with the data of [1] and [2] and shows two important results. First, Fig. 4 shows the current data plotted against the correlation derived in [1]. It can be seen that the pin fins that were 4-dia in length had higher heat transfer coefficients than the pin fins of 1/2 and 2-dia in length of [1]. The second result is the array-averaged heat transfer coefficients for the eight row configuration were slightly higher than the heat transfer coefficients for the four-row configuration. Reference [3] showed that the heat transfer to a single pin in a staggered array of pin fins increased for the first two rows added upstream of the measuring pin. For three or more rows added upstream, the heat transfer decreased slightly and then remained constant regardless of the number
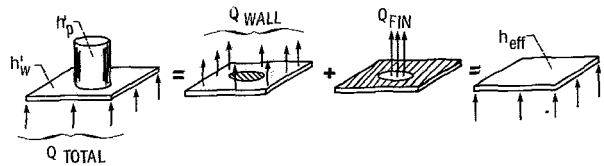
$$Q_{TOTAL} = Q_{WALL} + Q_{FIN}$$

$$Q_{TOTAL} = h'_w(A_w - A_p)(T_w - T_{aw}) + \sqrt{Ph_p'k_pA_p}\ tanh\ (ml)\ (T_w - T_{aw})$$

$$Q_{TOTAL} = h_{eff}A_w(T_w - T_{aw})$$
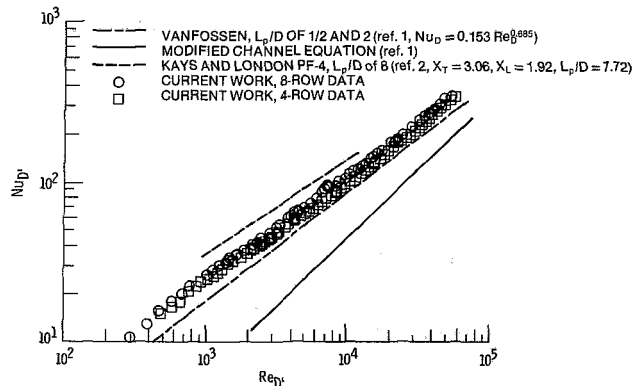
Fig. 3   Theoretical model

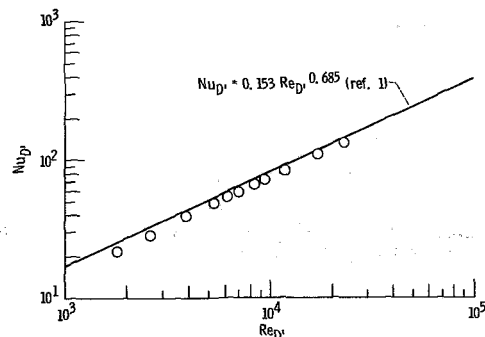**Fig. 4   Current data plotted against results of [1] and [2]**

Fig. 5   Comparison of the heat transfer data of Morishita et al. [4] with the correlation of [1]

of rows upstream. The same results were found in [5] and [6]. From these results it can be expected that array-averaged heat transfer for an eight-row array of staggered pin fins would have higher heat transfer coefficients than would a four-row array, as was found in the current work.

Figure 4 also shows that the heat transfer from the 4-dia long pin fins was lower than the heat transfer from the 8-dia long configuration, PF-4, of [2]. This indicates that the pin fins 4-dia in length did not give quite as high heat transfer coefficients as some of the configurations commonly used in compact heat exchanger design. Also shown in Fig. 4 is the correlation for the channel with no pins used in [1] for comparison purposes.

Figure 4 suggests that the number of streamwise rows and the pin length to diameter ratio both have an influence on short pin fin heat transfer. However, Fig. 4 tends to indicate that, while the number of streamwise rows has a small effect on short pin fin heat transfer, the dominant effect on the overall level of heat transfer is the pin length to diameter ratio.

Figure 5 shows the work of Morishita et al. [4], plotted against the correlation derived in [1]. It can be seen that these
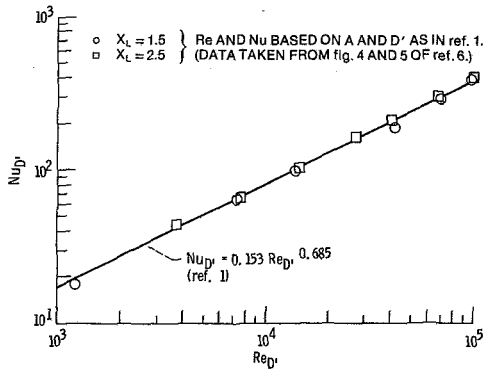
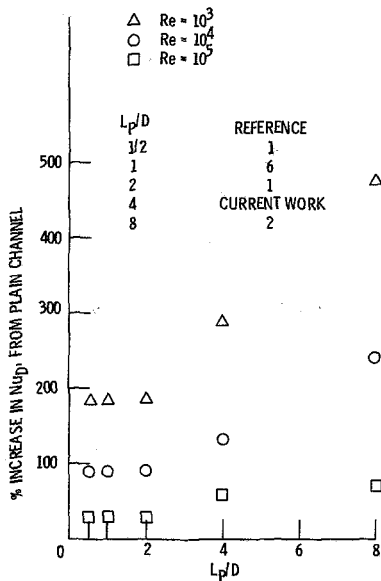**Fig. 6 Comparison of heat transfer data from [1] and array-averaged data from [6]**

Fig. 7 Percent increase in Nu_D' from plain channel equation versus L_p/D for staggered arrays of short pin fins

Summary of Results

In short pin fin heat transfer over a range of Reynolds numbers applicable to the turbine cooling problem, the results of tests on a staggered array of 4-dia long pin fins are as follows:

1 The pin length to diameter ratio is the dominant factor in the level of array-averaged heat transfer coefficients for short pin fins (endwalls included).

2 The number of streamwise rows in the staggered array has a slight effect on heat transfer, with array-averaged heat transfer coefficients increasing with the addition of rows in the streamwise direction.

3 For an L_p/D less than 2, the Nusselt number is a function of Reynolds number only. For an L_p/D greater than 2, the Nusselt number is a function the length to diameter ratio as well as the Reynolds number.

References

1 VanFossen, G. J., "Heat Transfer Coefficients for Staggered Arrays of Short Pin Fins," ASME JOURNAL OF ENGINEERING FOR POWER, Vol. 104, No. 2, Apr. 1982, pp. 268–274.

2 Kays, W. M., and London, A. L., Compact Heat Exchangers, National Press, Palo Alto, California, 1955.

3 Simoneau, R. J., and VanFossen, G. J., "Effect of Location in an Array on Heat Transfer to a Cylinder in Crossflow," Symposium on Tube Bundle Thermal Hydraulics, ASME, New York, 1982, pp. 1–8.

4 Morishita, Teruo, et al., "Heat Transfer and Pressure Loss of Internal Cooling Passages for Marine Gas Turbines," Proceedings of the 9th Annual Gas Turbine Meeting, June 1981.

5 Metzger, D. E., Berry, R. A., and Bronson, J. P., "Developing Heat Transfer in Rectangular Ducts with Arrays of Short Pin Fins," ASME Paper No. 81-WA/HT-6, Nov. 1981.

6 Metzger, D. E., and Haley, S. W., "Heat Transfer Experiments and Flow Visualization for Arrays of Short Pin Fins," ASME Paper No. 82-GT-138, Apr. 1982.

7 Metzger, D. E., Fan, Z. X., and Shepard, W. B., "Pressure Loss and Heat Transfer Through Multiple Rows of Short Pin Fins," ASME Paper No. 82-IHTC-31, Sept. 1982.

8 Miller, R. L., "ESCORT: A Data Acquisition and Display System to Support Research Testing," NASA TM-78909, May 1978.

9 Hilsenrath, J., Tables of Thermal Properties of Gases, NSB-Circ-564, National Bureau of Standards, Washington, D.C., 1955.

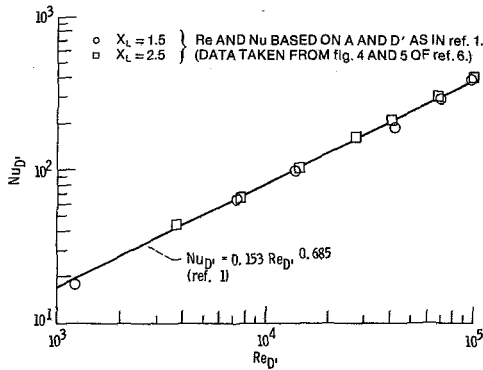10 Eckert, E. R. G., and Drake, R. M., Heat and Mass Transfer, 2d. ed., McGraw-Hill, New York, 1959, p. 270.

results fall slightly below the work of [1]. In [4], the heat flux was calculated from the air flow rate and the temperature difference between the inlet and outlet cooling air. Small errors of nonuniformities in temperature could lead to large errors in calculated heat flux.

Figure 6 shows the array-averaged heat transfer coefficients of [5] and [6] compared with equation (16) of [1]. When the Nusselt and Reynolds numbers of [5] are converted to the definitions used herein, the data and correlation agree very well. This confirms the correlation found in [1] and indicates that the pin length is the dominant controlling factor in short pin fin heat transfer.

Figure 7 shows the percent increase of the Nusselt number, with the plain channel correlation as the base reference, plotted against the length to diameter ratio for three different Reynolds numbers. It can be seen that for an L_p/D less than 2, the percent increase in the Nusselt number remains constant for each Reynolds number. For an L_p/D greater than 2, the percent increase in the Nusselt number rises sharply. This rise in Nusselt number is also a function of the Reynolds number, with the percent increase in Nusselt number decreasing as Reynolds number increases. Thus at lower Reynolds numbers the effect of the length to diameter ratio is much stronger than at higher Reynolds numbers. This data was taken from Fig. 4, extrapolating the curves for the highest Reynolds numbers.
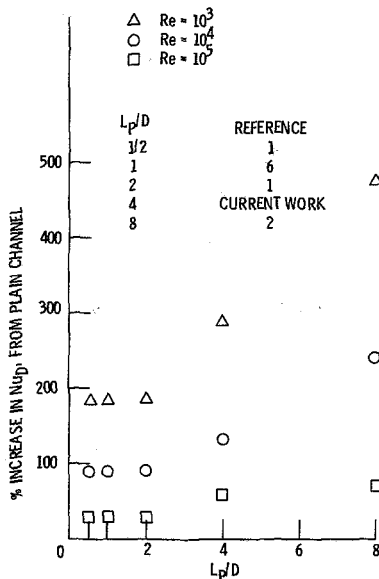
Fig. 7 Percent increase in Nu_D' from plain channel equation versus L_p/D for staggered arrays of short pin fins

Summary of Results

In short pin fin heat transfer over a range of Reynolds numbers applicable to the turbine cooling problem, the results of tests on a staggered array of 4-dia long pin fins are as follows:

1 The pin length to diameter ratio is the dominant factor in the level of array-averaged heat transfer coefficients for short pin fins (endwalls included).

2 The number of streamwise rows in the staggered array has a slight effect on heat transfer, with array-averaged heat transfer coefficients increasing with the addition of rows in the streamwise direction.

3 For an L_p/D less than 2, the Nusselt number is a function of Reynolds number only. For an L_p/D greater than 2, the Nusselt number is a function of the length to diameter ratio as well as the Reynolds number.

References

1 VanFossen, G. J., "Heat Transfer Coefficients for Staggered Arrays of Short Pin Fins," ASME JOURNAL OF ENGINEERING FOR POWER, Vol. 104, No. 2, Apr. 1982, pp. 268–274.

2 Kays, W. M., and London, A. L., Compact Heat Exchangers, National Press, Palo Alto, California, 1955.

3 Simoneau, R. J., and VanFossen, G. J., "Effect of Location in an Array on Heat Transfer to a Cylinder in Crossflow," Symposium on Tube Bundle Thermal Hydraulics, ASME, New York, 1982, pp. 1–8.

4 Morishita, Teruo, et al., "Heat Transfer and Pressure Loss of Internal Cooling Passages for Marine Gas Turbines," Proceedings of the 9th Annual Gas Turbine Meeting, June 1981.

5 Metzger, D. E., Berry, R. A., and Bronson, J. P., "Developing Heat Transfer in Rectangular Ducts with Arrays of Short Pin Fins," ASME Paper No. 81-WA/HT-6, Nov. 1981.

6 Metzger, D. E., and Haley, S. W., "Heat Transfer Experiments and Flow Visualization for Arrays of Short Pin Fins," ASME Paper No. 82-GT-138, Apr. 1982.

7 Metzger, D. E., Fan, Z. X., and Shepard, W. B., "Pressure Loss and Heat Transfer Through Multiple Rows of Short Pin Fins," ASME Paper No. 82-IHTC-31, Sept. 1982.

8 Miller, R. L., "ESCORT: A Data Acquisition and Display System to Support Research Testing," NASA TM-78909, May 1978.

9 Hilsenrath, J., Tables of Thermal Properties of Gases, NSB-Circ-564, National Bureau of Standards, Washington, D.C., 1955.

10 Eckert, E. R. G., and Drake, R. M., Heat and Mass Transfer, 2d. ed., McGraw-Hill, New York, 1959, p. 270.

results fall slightly below the work of [1]. In [4], the heat flux was calculated from the air flow rate and the temperature difference between the inlet and outlet cooling air. Small errors of nonuniformities in temperature could lead to large errors in calculated heat flux.

Figure 6 shows the array-averaged heat transfer coefficients of [5] and [6] compared with equation (16) of [1]. When the Nusselt and Reynolds numbers of [5] are converted to the definitions used herein, the data and correlation agree very well. This confirms the correlation found in [1] and indicates that the pin length is the dominant controlling factor in short pin fin heat transfer.

Figure 7 shows the percent increase of the Nusselt number, with the plain channel correlation as the base reference, plotted against the length to diameter ratio for three different Reynolds numbers. It can be seen that for an L_p/D less than 2, the percent increase in the Nusselt number remains constant for each Reynolds number. For an L_p/D greater than 2, the percent increase in the Nusselt number rises sharply. This rise in Nusselt number is also a function of the Reynolds number, with the percent increase in Nusselt number decreasing as Reynolds number increases. Thus at lower Reynolds numbers the effect of the length to diameter ratio is much stronger than at higher Reynolds numbers. This data was taken from Fig. 4, extrapolating the curves for the highest Reynolds numbers.

DISCUSSION

A. S. Mujumdar[1]

The authors are to be complimented for presenting very useful results in an area of continually growing interest. The objective of this communication is primarily to seek clarification that will make the paper clearer to a wider readership.

First, could the authors elaborate on the choice of the length scale (D') in the definition of the Reynolds and Nusselt numbers? This is crucially important if the results are to be scaled to other dimensions of pins and channels. Good agreement with prior work perhaps justifies the authors' choice, but an explanation based on the fundamentals of the flow processes involved is still warranted.

Second, the writer is surprised by the authors' conclusion number 3. The L_p/D ratio would be expected to be more important at smaller L_p/D values rather than at larger ones, owing to the edge effects. Since the heat transfer coefficient here is defined very differently than that for single cylinders (where transfer is considered only from the cylinder surface and not the endwalls), the conclusions may well be quite

[1]Department of Chemical Engineering, McGill University, Montreal, Quebec, Canada, Mem. ASME

different. It would be enlightening if the authors could separate for each row the contribution of the endwalls to the total heat transfer in the given row. Further, how is this relative contribution influenced by the stream Reynolds number and the L_p/D ratio? The cylinder (pin) contribution could then be compared with well-established data for cylinder heat transfer in crossflow.

Finally, a flow visualization study, which can shed some light on the flow patterns in bundles of small aspect ratio tubes, would be very helpful in elucidating the heat transfer results that are becoming available at an accelerating pace. Are the authors aware of any studies in this direction?

Closure

When correlating the data, the authors tried several different definitions for the characteristic length (D'). The normal definition for hydraulic diameter assumes that the cross section is constant throughout the flow channel. In this work, the cross section varies due to the staggered pin placement. Therefore, the definition chosen in [1] is based on channel volume rather than cross-sectional area. This definition is the only one that caused all the data to collapse to a single line. Previous tests reported in [1] were made on two separate test sections which were different in size by a factor of four. Therefore, it would appear that any necessary scaling is taken care of simply by using this definition of characteristic length (D').

Regarding the comment on length to diameter ratio, at small L_p/D ratios, the pin length is so small that there really is no increase in surface area due to the pins. At small L_p/D ratios, the pins merely serve to make the flow turbulent. As the L_p/D increases, the additional pin surface area begins to have an effect. Eventually, as the L_p/D becomes large, the heat transfer approaches the data for cylinders in crossflow. The facility used for collecting this data is not set up to do row by row heat transfer measurements. In [1], a test was made using copper endwalls and wooden pins. For this test, it was found that the average heat transfer coefficient on the pin surface was 35 percent higher than that on the endwall surface.

A flow visualization program is not within the scope of the present work.

Heat Transfer and Friction Loss Characteristics of Pin Fin Cooling Configurations

Yao Peng

Avco Lycoming Division,
Stratford, Conn. 06497

Pin fin or full cross pin cooling configurations have long been of interest to the turbine cooling designer because of their potentially high heat transfer characteristics and high surface area density, as well as their structural and castability advantages. The pin fin cooling configurations consist of flow channels with circular pins extending from the walls into the channel flow. The pin fins function as turbulators to produce high heat transfer rate; however, their geometric arrangement must be optimized to avoid high friction loss. Experimental tests have been conducted to investigate the effects of pin heights, spacings, and channel height to length ratios to the heat transfer and friction loss characteristics of the pin fin cooling configurations. The test results indicate that the pin fin configuration provides a means to reduce the flow friction loss and yet to maintain a reasonably high heat transfer rate as compared to the cross pin configuration. The pin spacing in the test range shows less effects on the pin fin performance than the pin height.

Introduction

Air cooled turbine blades have made possible the high cycle temperatures and resulting high specific power achieved in the modern gas turbine engines of today. In the immediate future, it is most likely that air cooled turbine blades will continue to be the solution for handling the higher turbine inlet temperatures with optimization of the design being necessary.

Pin fins or full cross pins (similar to banked tubes normal to the flow) have long been of interest to the turbine cooling designer because of their potentially high heat transfer characteristics and surface area density, as well as their structural and castability advantages. However, accurate data on pin fins, particularly in the small sizes and short flow lengths that are typical with cooled turbine blades, is limited. It is the purpose of this investigation to obtain such data by test. The heat transfer and friction flow data will allow an optimized cooled turbine to be designed, and will determine which is better: full cross pins, long or short pin fins, high density or low density arrangements. The competitive position of pin fins compared to other convective cooled designs can also be more readily resolved.

The pin fin configuration consists of a cooled air flow passage with many pins of cylindrical rod form built onto the passage wall. These pins protrude from the passage wall and do not cross over the entire width of the flow passage (Fig. 1). In heat exchanger designs, crossflow tubes or pins (extending from wall to wall) have been used to increase both the turbulence level in the flow and the total heat transfer area. These cross tube or pin configurations possess very high heat transfer ability, but also demonstrate the characteristics of
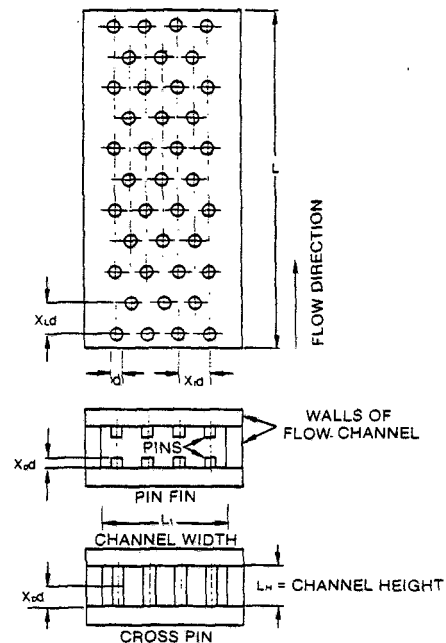

Fig. 1 Geometry of pin fin test cores

very high pressure loss. The high pressure loss is undesirable if the pressure head available in the channel flow is limited. Therefore, reducing the pressure loss while maintaining the high heat transfer ability in the channel flow would be desirable. The pin fin configuration may fulfill these requirements. Because of the short length of the pin fin, the center core of the passage is open, causing no obstruction to the flow, and therefore less pressure loss. On the other hand,

Table 1 Characteristic dimension of tested configurations

Code no.	X_L	X_T	$L_{t/LH}$	X_P	N_R	A_F	Amin	S_{tot}	$\dfrac{S_{pin}}{S_{tot}}$	D_H	$L/_{D_H}$
							in²	in²	in/²in²	in	
221*	2	2	2	1	16	1.125	.9375	27.539	.3921	.572	7.34
222*	2	2		2			.750	36.179	.5372	.348	12.06
223**	2	2		3			.5625	42.658	.6076	.221	18.96
321*	3	3		1	11		1.00	23.404	.2045	.744	5.85
322*	3	3		2			.875	27.233	.3163	.559	7.78
323**	3	3		3			.750	30.104	.3816	.433	10.03
421*	4	4		1	8		1.031	20.863	.1176	.830	5.06
422*	4	4		2			.9375	22.827	.1935	.690	6.09
423**	4	4		3			.844	24.300	.2424	.583	7.20
231*	2	2	3	1	16	.750	.562	25.439	.4245	.371	11.30
232**	2	2		2			.375	31.919	.5413	.197	21.28
331*	3	3		1	11		.625	21.229	.2254	.512	8.49
332**	3	3		2			.500	24.100	.3177	.361	12.05
431*	4	4		1	8		.656	18.764	.1307	.587	7.14
432**	4	4		2			.5625	20.236	.1941	.467	8.99

Note: * pin fin configuration
** cross pin configuration

the pin fins will increase the turbulence level in the flow adjacent to the passage wall where the actual heat transfer takes place. The pin height, the spacing between pins, and the flow channel dimensions will affect the heat transfer and friction loss performances of the pin fin configuration.

In the open literature, considerable experimental data were found for cross pin heat transfer and friction loss coefficients [1, 2, 4, 9, 11, 12]. Reports of the pin fin or noncross pin configuration, however, is not available. Therefore, an experimental evaluation of pin fins was carried out. The tests include measurement of both the heat transfer rate and pressure loss for the pin fin configurations.

A total of nine pin fin and six cross pin configurations were tested. The test cores were built with length to diameter ratios

similar to that used in convective cooled turbine blades. In the test, steam was used for the heating medium and air was used for the cooling medium. The test results are correlated by the nondimensional parameters of j-factor, friction coefficient, and Reynolds number. Comparisons between the present test results with the cross pins and banked tubes from other sources, the cross pins and the pin fins of the present test, and the pin fins with different pin height and spacing are discussed.

Apparatus and Test Procedure

The pin fin test cores were built in rectangular channel form with staggered pins installed on the pair of wide channel walls (Fig. 1). The test cores consisted of two channel heights, 0.75

Nomenclature

A_F = frontal cross-sectional area of test core ($L_t \times L_H$ on Fig. 1) – in.² (cm²)

A_{min} = minimum free flow area of test core – in.² (cm²)

A_{pin} = pin fin cross-section area – in.² (cm²)

C_P = specific heat-Btu/lbm °F (kg-cal/kg°C)

D_H = hydraulic diameter, 4 A_{min} L/S-in. (cm)

D = hydraulic diameter, 4 V_{flow}/S-in. (cm)

d = pin or tube outside diameter-in. (cm)

G_{max} = mass velocity = W/A_{min} – lbm/in.² s (Kg/cm², s)

G' = mass velocity = $W L/V_{flow}$ – lbm/in.² s (kg/cm², s)

g_c = conversion factor – 32.2 lbm-ft/lbf-s² (1 kgm/N.s²)

h = heat transfer coefficient-Btu/hr ft²°F (kg-cal/hr.m² °C)

k = heat conductivity-Btu/hr ft °F (kg-cal/hr m² °C/m)

K_c = contraction pressure loss coefficient

K_e = expansion pressure loss coefficient

l = length of pins-in. (cm)

L = channel length-in. (cm)

N = number of pin rows

Pr = Prandtl number = (Cp /k)

P = perimeter of pin cross-sectional area-in. (cm)

ΔP = pressure differential-static

Re = Reynolds number

S = heat transfer surface area – in.² (cm²)

t = temperature °F(°C)

V = volume – in³ (cm³)

W = air flow rate – lbm/s. (Kg/s)

X = pitch-diameter ratio-nondimensional

δ = wall thickness of test core-in. (cm)

η = efficiency – dimensionless

λ = $((f_{cross} - f_{pin})/f_{cross})/$ $((j_{cross} - j_{pin})/j_{cross})$

μ = air viscosity – lb/ft hr (kg/m, hr)

ρ = air density – lbm/ft³ (kg/m³)

σ = core free flow area/area of inlet or exit duct-in.²/in.² (cm²/cm²)

Subscripts

1 = inlet
2 = exit
cross = cross pin
flow = free flow
LMTD = Logarithmic mean temperature difference
m = mean
max = maximum
min = minimum
pin = pin fin
ref = reference condition
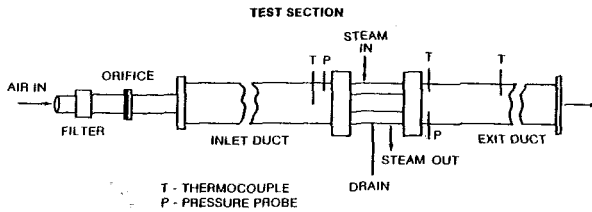s = static
std = standard
tot = total
w = wall

TEST SECTION

Fig. 2 Schematic of test rig

T - THERMOCOUPLE
P - PRESSURE PROBE

and 0.5 in. (1.905 and 1.270 cm), and two channel lengths, 4.0 in. (10.160 cm) for pin pitch of 2d and 4d and 4.15 in. (10.540 cm) for pin pitch of 3d. The channel width of 1.5 in. (3.810 cm) and the pin diameter of 0.125 in. (0.318 cm) are the same for all the test cores. Three pin heights of 1d, 2d, and 3d, and three pitches of 2d, 3d, and 4d in both the transverse and parallel directions to the flow were used in the test. The pin height of the full cross pins is considered as half of the channel height. The sizes of the test cores were chosen to be similar in length to hydraulic diameter ratio typical for turbine blade cooling passages. The detail dimensions of the test core are given in Table 1.

The walls of the test core are made of 0.25-in. (0.635 cm) thick copper plate with drilled holes. Copper pins of selected lengths are located in the holes and brazed to the plate with low temperature silver solder. The silver solder has approximately the same heat conductivity as copper giving essentially no resistance to heat flow between the pins and plate.

The test rig as shown in Fig. 2, has the following three main sections: the air inlet, test, and exit sections.

Air Inlet Section. The air inlet section consists of an air filter, a regulator, an orifice, and a duct. The inlet duct is 24 in. (60.96 cm) long and has a double wall for insulation. The outside wall was made from stainless steel and the inside wall was made from plastic tubing. The space between the wall is a stagnant air pocket. A turbulator was installed at the entrance of the inlet duct to produce uniform velocity and temperature profiles in the duct.

Test Section. The test section includes a steam jacket and the test core. The steam jacket which envelopes the test core has a cylindrical form. Two steam inlet and outlet ports positioned at 180 deg apart are used to minimize the steam temperature variation. Baffle plates were installed in the steam jacket to improve the spread of the steam in the jacket for uniform heating of the test core. Between the test section and the inlet and outlet ducts teflon plates were installed for heat insulation.

Exit Section. The exit duct is similar to the inlet duct: a double wall with outside steel shell, inside plastic tube, and a turbulator at the entrance. The space between the double wall contains a small airflow bypassed from the main air stream. The small airflow is introduced to the space between the walls at the entrance of the exit duct. Because the bypassed airflow has a temperature approximately equal to the main air stream in the exit duct the heat loss through the inner plastic wall is limited. Additional insulation materials of plastic foam and cotton fiber were wrapped around the outside surface of the exit duct to further insure heat insulation.

Instrumentations for both pressure and temperature measurements were installed. At the airflow orifice meter, upstream static pressure and static pressure differential across the orifice are recorded. At the test core, static pressures are recorded in the inlet and exit ducts at a distance of 1 in. from both the entrance and exit of the test core. Water and mercury manometers are used for pressure readings. Air temperature is measured by nine thermocouples each in the inlet and exit

ducts. The nine thermocouples are positioned in one place perpendicular to the airflow direction with each thermocouple covering an equal flow area. The thermocouple plane in the inlet duct is 2 in. (5.08 cm) upstream from the test core and in the exit duct 8 in. (20.32 cm) downstream from the test core. By measurement, the air temperature upstream of the orifice meter showed no difference from the air temperature in the inlet duct. Therefore, the air temperature measured in the inlet duct was used for airflow computation. In the exit duct four additional thermocouples for air temperature measurement are place 1 in. (2.54 cm) downstream from the test core. These four thermocouples serve to indicate the air temperature profile at the core exit and to detect for heat loss in the exit manifold. All the thermocouple serve to indicate the air temperature measurement are shielded to measure only total air temperature. In addition, thermocouples were installed on the plastic tube in the exit duct at distances of 1, 4.5, and 6.5 in. (2.54, 11.43, and 16.51 cm) downstream from the test core measure heat loss.

In the present tests, the core surface temperature instead of the steam temperature was measured. The use of core surface temperature to calculate heat input to the airflow simplified the evaluation process by eliminating the calculations of the steam heat transfer coefficients at the core outside surface. A total of 24 thermocouples were installed on the first core. However, the wall temperature was found quite uniform with a maximum of $1°F$ ($.6°C$) temperature difference between the core inlet and exit. Therefore, the number of thermocouples for the subsequent cores was reduced to 12 with three installed on each of the four channel surfaces along its centerline parallel to the flow direction. The thermocouples were made of 30-gage iron-constantan and were imbedded in the outside copper surface of the test core. Steady-state data were used for evaluating the heat transfer parameters.

The range of the test variables are

w	0.0029 lb/s – .076 lb/s
t_w	211°F – 219°F
T_1	76°F – 87°F
T_2	94°F – 197°F
P	8.2 psi – 45 psi

Data Reduction and Correlation Parameters

Reynolds Number. Three Reynolds numbers were used to correlate the experimental results. The three Reynolds numbers are different in the definition of their respective mass velocity and hydraulic diameters.

$$\mathrm{Re} = D_H G_{\max}/\mu \qquad (1)$$

$$\mathrm{Re}d = d\, G_{\max}/\mu \qquad (2)$$

$$\mathrm{Re}' = D'G'/\mu \qquad (3)$$

The test results seem best correlated by the Reynolds number of equation (1). The viscosity of air in the Reynolds number is evaluated based on the logarithmic mean temperature difference.

$$t = t_w - \frac{(t_w - t_1) - (t_w - t_2)}{l_n\left(\dfrac{t_w - t_1}{t_w - t_2}\right)} \qquad (4)$$

The air properties of specific heat, heat conductivity, and viscosity are from [5].

Colburn Factor.

$$j = \frac{h}{G_{\max} C_P}\mathrm{Pr}^{2/3} \qquad (5)$$

The heat transfer coefficient h in the Colburn factor is the overall average value in the test core. With the known wall
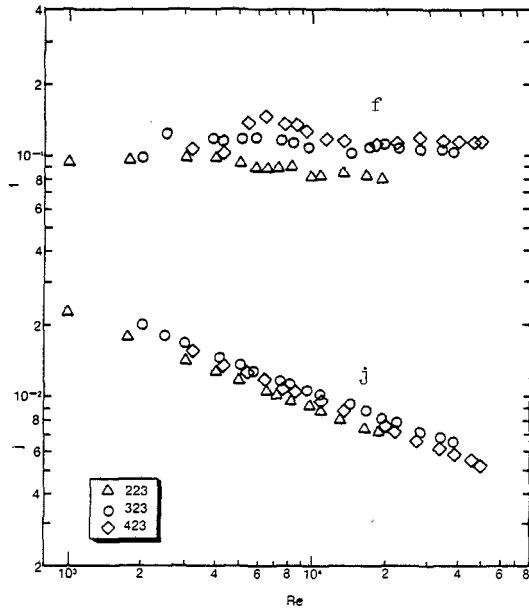
Fig. 3 Heat transfer and friction characteristics of cross pin configurations 223, 323, 423
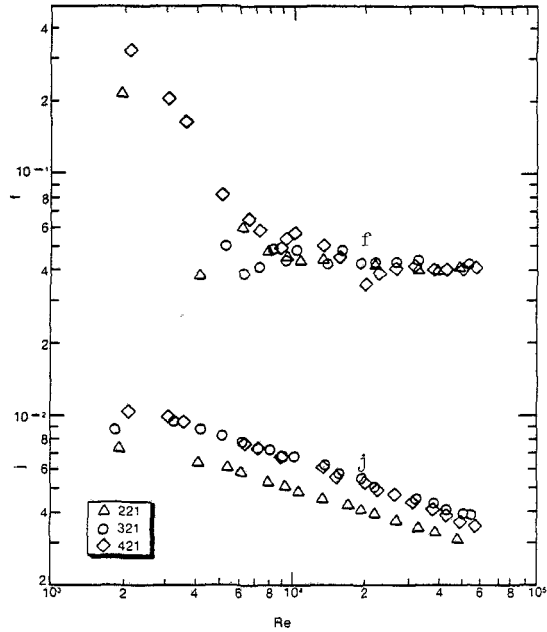

Fig. 5 Heat transfer and friction characteristics of pin fin configurations 221, 321, 421
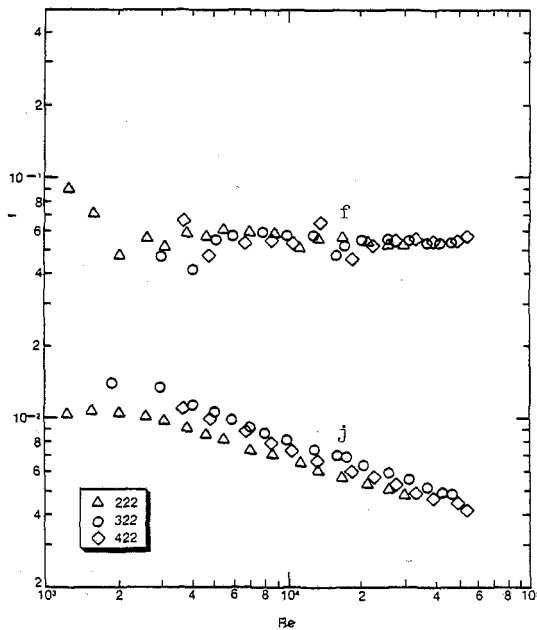

Fig. 4 Heat transfer and friction characteristics of pin fin configurations 222, 322, 422
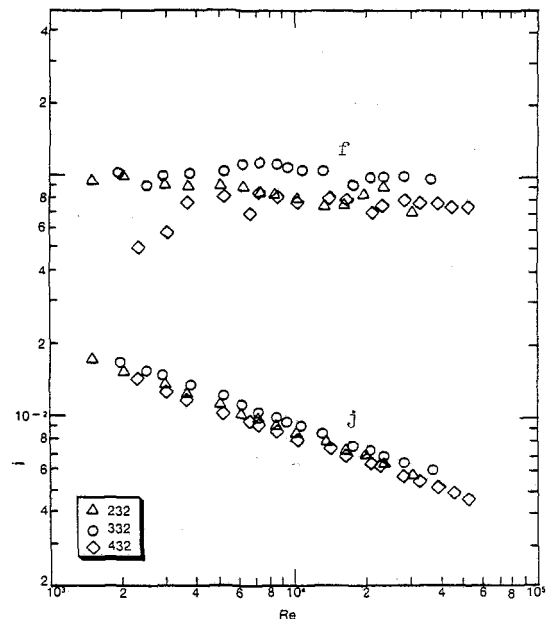

Fig. 6 Heat transfer and friction characteristics of cross pin configurations 232, 332, 432

resistance and pin fin efficiency, h can be determined from the measurements of t_w, t_1, and t_2. That is

$$h = \cfrac{1}{\eta \left[\cfrac{S_{tot}}{WC_p l_n \left(\cfrac{t_w - t_1}{t_w - t_2} \right)} - \cfrac{S_{tot} \delta_w}{S_w k_w} \right]} \quad (6)$$

The efficiency in equation (6) is the overall efficiency of the total heat transfer surface area defined as

$$\eta = 1 - \frac{S_{pin}}{S_{tot}} (1 - \eta_{pin}) \quad (7)$$

where the pin efficiency η_{pin} is defined by

$$\eta_{pin} = \cfrac{1}{m \left(\cfrac{d}{4} + 1 \right) \mathrm{Cosh}(ml) + \cfrac{h}{km} \mathrm{Sinh}(ml)} \cdot \cfrac{\mathrm{Sinh}(ml) + \cfrac{h}{mk} \mathrm{Cosh}(ml)}{} \quad ;$$

$$m = \sqrt{\frac{hp}{kA_{pin}}} \quad (8)$$

Equation (7) assumes equal heat transfer coefficients for the pins and the channel surfaces. A constant value of 210 Btu/hr. ft² °F/ft (1025,2 kg-cal/hr. m² °C/m) is assumed for the heat conductivity of copper.

Friction Factor. The pressure drop through the test section is divided into three components: the pressure drop
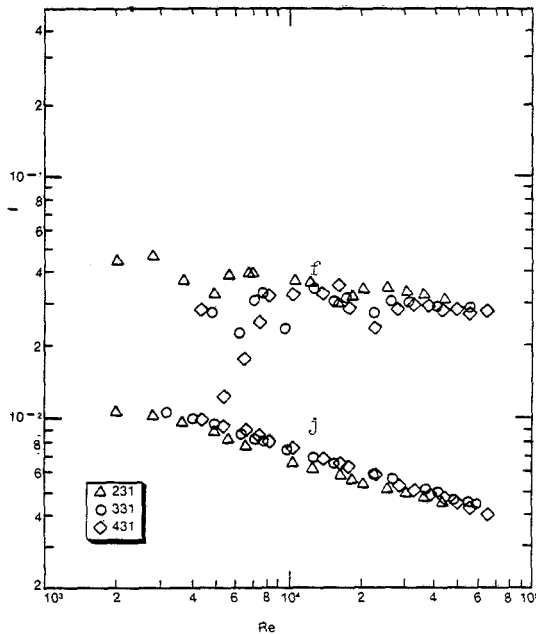
Fig. 7 Heat transfer and friction characteristics of pin fin configurations 231, 331, 431
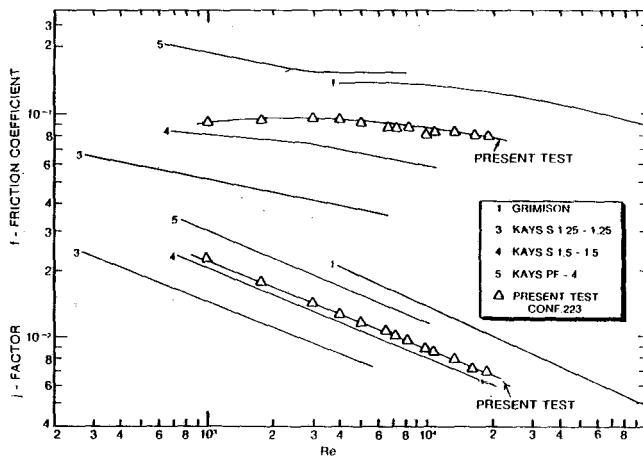

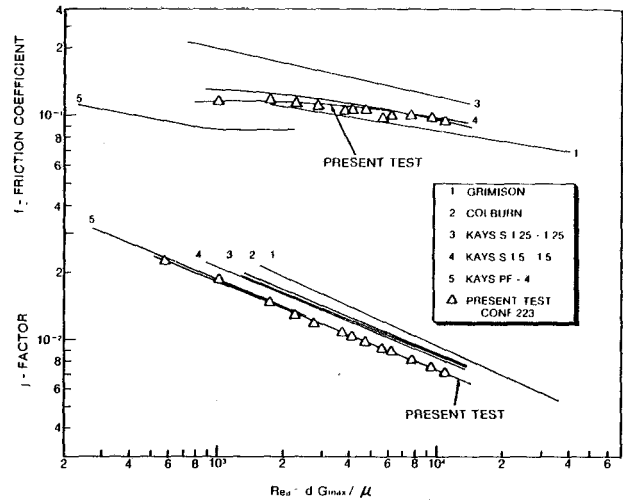Fig. 8 Comparison of heat transfer and friction characteristics with Kays and Grimison's results

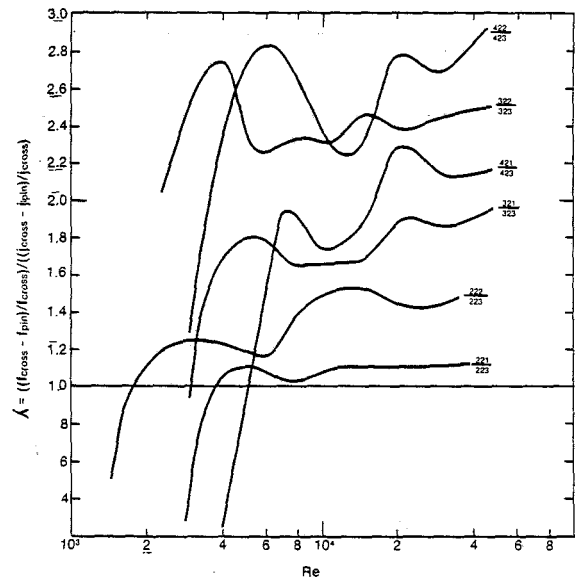Fig. 9 Comparison of cross pin configuration 223 with Kays, Grimisom and Colburn

Fig. 10 The ratio of relative increases of friction coefficient and j-factor between the pin fin and cross pin configurations

due to entrance contraction, the pressure drop in the core, and the pressure drop due to expansion at exit. Therefore, the friction factor of the test core can be obtained by subtracting the pressure drops due to entrance contraction and exit expansion from the measured overall pressure loss. The formulation of the friction factor is

$$f = \frac{D_H}{4L} \rho m \left\{ \frac{\Delta P}{G^2 2gc} - 2\left(\frac{1}{\rho_2} - \frac{1}{\rho_1}\right) - \frac{1}{\rho_1}(K_c + 1 - \sigma_1^2) \right.$$
$$\left. + \frac{1}{\rho_2}(1 - \sigma_2^2 - K_e) \right\} \tag{9}$$

The application of equation (9) requires, in addition to the measured flow, pressure and temperature, also the knowledge of the contraction and expansion pressure loss coefficients K_c and K_e. For the cross pin configuration, the flow through each pin row has a contraction and an expansion, and the friction behavior is no different between the entrance and exit portions and the interior of the channel. Therefore, determination of the friction coefficients for the cross pin configurations in the present tests has been made by assuming both K_c and K_e = 0. The pin fin configuration resemble more or less the interrupted fin configuration. Therefore, the en-

trance contraction and exit expansion loss coefficients K_c and K_e at Re = ∞ for the multiple square tubes from [4] were used.

The probable uncertainty of the test results was analyzed based on instrument uncertainty, uncertainties in the transport properties, viscosity and thermal conductivities, and in the determination of the test core dimensions. The uncertainties of Re is about ±3.0 percent, j-factor is about ±6.0 percent, and f is ±6.5 percent.

Discussion of Results

Although great caution was exercised in heat insulation of the exit duct, the temperature measurements at the test core exit by the four thermocouples and further downstream by the nine thermocouples indicates that some heat loss exists at low flow rates particularly for the cross pin configurations. The heat loss is evident by the following symptoms: (i) the temperatures registered by the four thermocouples for the cross pin configuration indicate quite a uniform temperature distribution in the duct, and yet, the temperatures from the downstream nine thermocouples show a profile of high temperature at the center line and low temperature at the wall

of the duct; (*ii*) the average temperature from the nine thermocouples is lower than the average temperature from the four thermocouples. The maximum measured temperature difference is about 2 percent.

The heat loss in the exit duct for the pin fin configuration is less evident than the cross pin configuration, however, in this configuration temperature profiles were observed from the four thermocouples at the test core exit. These temperature profiles have low temperatures at the center and high temperatures at the wall of the duct, and are more pronounced for the test core with shorter pins. The temperature profile shows that the airflow in the pin fin test core may not mix well.

Figures 3 through 7 give both the *j*-factor and friction coefficient and for the 15 test cores plotted against the Reynolds number. The *j*-factor, friction coefficient, and Reynolds number are defined respectively, by equations, (5), (9), and (1). An examination of Figs. 3 through 7 reveals several interesting points. (*i*) A turbulent flow exists through the test range for each of the cross pin configurations. (*ii*) The *j*-factor lines for the pin fin core have a shallower slope than that of the cross pin cores and flatten or dip at low flow rates. The dip of the *j*-factor line at low flow rate indicates that transition from turbulent to laminar flow starts. (*iii*) The *j*-factors for the pin fin configuration 221 have much lower value than the configuration 421, though the former has more heat transfer surface area than the latter. Both configurations have the same pin height except the pin spacing in 221 is much closer than in 421. The low *j*-factor of 221 shows that the closely spaced pins give less flow turbulence, forcing most of the airflow through the center core. (*iv*) The friction coefficients for the cross pin core are rather constant at different Reynolds numbers. The friction coefficient lines vary with the pin height. For the short pins, configuration 221, 421, the friction lines closely resemble that of plain channels (Fig. 5) which is expected. (*v*) The cross pin core 232 shows a friction increase at high flow rates which corresponds to the intense whistling sound heard during the test.

A comparison of the cross pin core 223 test results to those reported by Kays, Grimisom, and Colburn [1,2,7] for banked tubes and cross pins are given in Figs. 8 and 9. In Fig. 8, the *j*-factor line from the present test shows the same slope as Kays and slightly flatter than Grimisom's. The friction coefficient line from the present test shows, on the other hand, a similar shape as Grimisom's and a little flatter than Kays. The magnitude of the *j*-factor and friction coefficient are rather scattered between the various sources. A close correlation between these results is obtained however, if the *j*-factor, friction coefficient, and Reynolds number are defined on the pin or tube outside diameters. This correlation is shown in Fig. 9. In Fig. 9, the *j*-factor line from the present cross pin configuration coincides with the cross pin results from Kays. Figure 9 shows also that the *j*-factor lines from banked tubes by Kays, Grimisom, and Colburn are generally higher than the cross pins. The higher heat transfer performance of the banked tubes compared to the cross pins is considered as due to the difference between the heat transfer flux of the two configurations. The heat transfer surface of the banked tube, such as in the transient tests by Kays, includes the tube surface only. In the cross pin tests, the heat transfer surfaces include both the surface of the pins and the surface of the channel wall. Because of the impingement effect, the heat transfer flux on the tube or pin surface is larger than on the channel wall.

The friction coefficients in Fig. 9 correlate less than the *j*-factors.

The cross pins have both *j*-factor and friction coefficient higher than the pin fins, the increase of friction coefficient of the cross pin over the pin fin is more than the increase of the *j*-factor. This is evident from the plot of the ratio of the relative increase of friction coefficients to the relative increase of *j*-

factor, $= ((f_{\text{cross}} - f_{\text{pin}})/f_{\text{cross}})/((j_{\text{cross}} - j_{\text{pin}})/j_{\text{cross}})$, in Fig. 10. Figure 10 indicates also: (*i*) The benefit from using pin fin configuration is reduced with decreasing pin height; (*ii*) Large pitch of pin spacing gives relatively large friction loss reduction. However, the application of Fig. 10 is in a relative sense only. The pin fin configuration 422 with the highest value of λ in Fig. 10 does not imply that it is the optimum design. Though configuration 422 may have the least friction loss, its heat transfer rate may be too low for efficient turbine cooling.

Conclusions

The experimental heat transfer results of the staggered six cross pin and nine pin fin flow configurations provided an understanding of their heat transfer and friction loss characteristics. The pin fin configuration provides a means to reduce the flow friction loss and yet to maintain a reasonable high heat transfer rate in the channel flow. The pitch of pin spacing in the test range shows less effects on the pin fin configuration performance than the pin height. Very short pins are undesirable. The heat transfer gain from very short and closely spaced pins is only slightly better than plain channel.

The application of either the cross pin or the pin fin configuration to turbine blade cooling depends on the amount of cooling air and the pressure differential available across the turbine blade. In general, cross flow pins give somewhat more heat transfer but give also greater pressure losses. Each cooled blade design in a specific case must be evaluated. The data presented in this report will allow for optimization of a cooling design and will allow comparisons between competing designs.

References

1 Grimisom, E. D., "Correlation and Utilization of New Data on Flow Resistance and Heat Transfer for Cross Flow of Gases Over Tube Banks," ASME *Transactions*, Vol. 59, 1937, pp. 583–594.

2 Huge, E. C., "Experimental Investigation of Effects of Equipment Size on Heat Transfer and Flow Resistance in Cross Flow Tube Banks," ASME *Transactions*, Vol. 59, 1937, pp. 573–581.

3 Hilding, W. E., and Coogan, C. H., "Heat Transfer and Pressure Loss Measurements in Internally Finned Tubes," Symposium on Air-Cooled Heat Exchangers, ASME, pp. 57–58, Aug. 1964.

4 Kays, W. M., and London, A. L., *Compact Heat Exchangers*, McGraw-Hill, 1964.

5 Keenan, J. H., and Kaye, J., *Gas Tables*, Wiley, 1957.

6 Kreith, F., *Principles of Heat Transfer*, International Textbook Company, 1958.

7 McAdams, William H., *Heat Transmission*, 3rd ed., McGraw-Hill, 1954.

8 Norris, R., "Calibration and Operating Procedure for G.P. Multiple Orifice Flow Meters," Report RD3-g-068-66, Lycoming, Avco. Dec. 1966.

9 Pierson, O. L., "Experimental Investigation of the Influence of Tube Arrangement on Convection Heat Transfer and Flow Resistance in Cross Flow Gases Over Tube Banks," ASME *Transactions*, Vol. 59, 1937 pp. 563–572.

10 Shah, R. K., "Data Reduction Procedures for the Determination of Convective Surface Heat Transfer and Flow Friction Characteristics—Steam-to-Air Test Cores," T.R. No. 64, Dept. of Mechanical Engineering, Stanford University, Stanford, California, June 1967.

11 Theoclitus, G., "Heat Transfer and Flow Friction Characteristics of Nine Pin-Fin Surfaces" 6-HT-56, ASME/AIChE Heat Transfer Conference and Exhibit, Los Angeles, Calif., Aug. 1965.

12 Van Fossen, G. J., "Heat Transfer Coefficients for Staggered Arrays of Short Pin Fins," 81-GT-75, ASME Gas Turbine Conference & Products Show, Houston, Texas, Mar. 1981.

Effects of Pin Shape and Array Orientation on Heat Transfer and Pressure Loss in Pin Fin Arrays

D. E. Metzger

C. S. Fan

S. W. Haley

Mechanical and Aerospace
Engineering Department,
Arizona State University,
Tempe, Ariz. 85287

Modern high-performance gas turbine engines operate at high turbine inlet temperatures and require internal convection cooling of many of the components exposed to the hot gas flow. Cooling air is supplied from the engine compressor at a cost to cycle performance and a design goal is to provide necessary cooling with the minimum required cooling air flow. In conjunction with this objective, two families of pin fin array geometries which have potential for improving airfoil internal cooling performance were studied experimentally. One family utilizes pins of a circular cross section with various orientations of the array with respect to the mean flow direction. The second family utilizes pins with an oblong cross section with various pin orientations with respect to the mean flow direction. Both heat transfer and pressure loss characteristics are presented. The results indicate that the use of circular pins with array orientation between staggered and inline can in some cases increase heat transfer while decreasing pressure loss. The use of elongated pins increases heat transfer, but at a high cost of increased pressure loss. In conjunction with the present measurements, previously published results were reexamined in order to estimate the magnitude of heat transfer coefficients on the pin surfaces relative to those of the endwall surfaces. The estimate indicates that the pin surface coefficients are approximately double the endwall values.

Introduction

One of the most common heat transfer augmentation schemes for gas turbine airfoil internal cooling flows is an array of pin fins. Such arrays are especially useful in the narrow trailing edge region as shown in Fig. 1, where they serve both a structural and a heat transfer role. The airfoil dimensions and manufacturing constraints usually dictate that the individual pin length, from pressure to suction side of the airfoil internal passage, is the order of the pin diameter. This pin length has posed special problems for designers in predicting heat transfer and pressure drop characteristics. There are two extensive sets of information available in the literature for arrays of circular cylinders in crossflow, one for very long cylinders, the other for cylinders much shorter than one diameter.

The long cylinder information is applicable to and stimulated by crossflow heat exchanger applications. In these applications virtually all of the heat transfer area is on the cylindrical surfaces of the tube banks. The heat transfer rates on the bounding duct walls (endwalls) and the endwall effects on the tube surface heat transfer adjacent to the walls are of minor importance. References [1–3] are representative of this body of literature. Reference [3] in particular is a comprehensive summary of the long tube array literature.
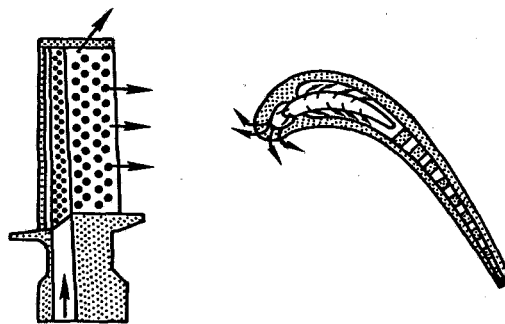
Fig. 1 Cooled turbine airfoil with pin fins

For cylinder arrays much shorter than one diameter, extensive heat transfer and pressure drop information has been obtained as part of studies on the plate-fin type of compact heat exchanger surfaces. In these situations flow normal to tube arrays is constrained between closely spaced thin plates attached to the tubes. The tube lengths exposed between adjacent plates are generally from one-tenth to no more than one-half the tube diameter. Most of the heat transfer area is thus on the plates, rather than on the tubes themselves. References [4–8] are representative of the published information in this case. Reference [4] in particular is a comprehensive summary.

There are significant differences in the heat transfer characteristics between the very short tube and long tube

Table 1 Array geometries

No.	Shape	α(0)	γ(0)	D(in)	(S/D,	X/D,	H/D)	A/D	B/D
1	circular	0	n.a.	0.167	(2.5,	1.5,	1.0)	0.5	1.5
2	circular	13	n.a.	0.167	(2.5,	1.5,	1.0)	0.5	1.5
3	circular	26	n.a.	0.167	(2.5,	1.5,	1.0)	0.5	1.5
4	circular	40	n.a.	0.167	(2.5,	1.5,	1.0)	0.5	1.5
5	circular	0	n.a.	0.200	(2.5,	2.5,	1.0)	1.5	1.5
6	oblong	0	0	0.200	(3.5,	2.5,	1.0)	1.5	1.5
7	oblong	0	30	0.200	(3.23,	2.5,	1.0)	1.5	1.5
8	oblong	0	±30	0.200	(3.23,	2.5,	1.0)	1.5	1.5
9	oblong	0	45	0.200	(2.91,	2.91,	1.0)	1.5	1.5
10	oblong	0	±45	0.200	(2.91,	2.91,	1.0)	1.5	1.5
11	oblong	0	90	0.200	(2.5,	3.5,	1.0)	1.5	1.5

array cases. In the long tube case, row-averaged heat transfer coefficients increase in the streamwise (longitudinal) direction from the first through the third to fifth rows and then remain constant thereafter. In the very short tube case, row-averaged heat transfer coefficients are lower than for the long tube case and display various streamwise development trends depending on the Reynolds number.

The array geometries used in internal airfoil cooling represent an intermediate case where both the endwall and pin surfaces contribute significantly to the total heat transfer surface area. Until recently, this case had not been studied, but the airfoil cooling application has stimulated several investigations [9–15]. All of these latter studies have involved pins of circular cross section placed in regular staggered arrays. It is by no means clear that either the circular cross-section pin shape or the regular staggered array pattern is best.

In general, the airfoil cooling designer would like to identify those array geometries which give the highest heat transfer coefficients for either a given coolant flowrate or a given available pressure drop across the array. The present study was initiated to examine two families of array geometries that deviate from those previously investigated.

One family studied retains the circular pin cross section but skews the array orientation at various angles α as shown in Fig. 2. This geometry variation was suggested by the results of [16] which indicate, for long cylinder tube banks, that increases in array-averaged heat transfer coefficients can be obtained by orienting the tube banks with α ≠ 0.

A second geometry examined in the present study contains oblong rather than circular cross-section pins. Each pin has semicircular ends and a cross-section length along the major axis of twice the end diameter, as shown in Fig. 3. Pins in each streamwise row are all oriented the same, at an angle, γ, to the mean flow direction. Pins in adjacent streamwise rows can either be oriented the same or in opposite (± γ)-directions.
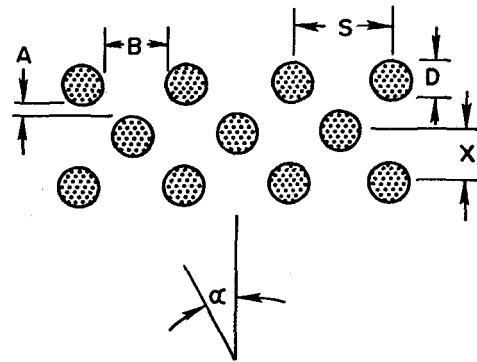

Fig. 2 Skewed circular pin array geometry

The arrays with α ≠ 0 are all based on the α = 0 staggered array pattern with S/D = 2.5 and X/D = 1.5 (No. 1 in Table 1). Those with oblong pins all have constant values of the clearances A/D = B/D = 1.5. These clearance values correspond to those of circular cross-section pin arrays for the case S/D = X/D = 2.5 (No. 5 in Table 1). The eleven array configurations fabricated and tested for the present study are listed in Table 1.

Apparatus and Procedure

Previous investigations into the effect of array configurations for pin lengths of interest in airfoil cooling have been limited by time and expense associated with fabrication of the test models. In [11], for example, extreme care was taken during fabrication to assure that good thermal contact between pins and duct walls was achieved and that the assembled duct had very smooth end walls. These test sections have fixed geometry and any changes in array pattern require fabrication of entirely new hardware.

_____ Nomenclature _____

A = pedestal streamwise clearance, heat transfer area

a = pin cross sectional area

B = pedestal spanwise clearance

C = ratio of pin and endwall heat transfer coefficients

D = pedestal diameter

f = pressure loss coefficient = $\Delta P/(2\rho V_{max}^2 N)$

h = array average convective heat transfer coefficient

H = pedestal height, channel height

m = pin parameter = $(h_p P/\kappa a)^{1/2}$

N = number of pedestal rows in streamwise direction ($=10$)

Nu = array average Nusselt number = $h D/k$

P = pin perimeter

$\dot{q}$ = heat transfer rate

ΔP = pressure drop across array

Re = Reynolds number = $\rho V_{max} D/\mu$

Δt = bulk fluid to surface temperature difference

S = pedestal spacing in spanwise direction

V_{max} = mean streamwise velocity in the minimum flow area

X = pedestal spacing in streamwise direction

α = array row orientation

γ = elongated pedestal orientation

κ = pin thermal conductivity

μ = fluid dynamic viscosity

ρ = fluid density

Subscripts

e = quantity associated with endwall surface area

p = quantity associated with pin surface area

t = quantity associated with total surface area

Fig. 3 Oblong pin array geometry

Fig. 4 Baseline results, $S/D = 2.5, X/D = 1.5, H/D = 1.0$

Fig. 5 Baseline results, $S/D = 2.5, X/D = 2.5, H/D = 1.0$
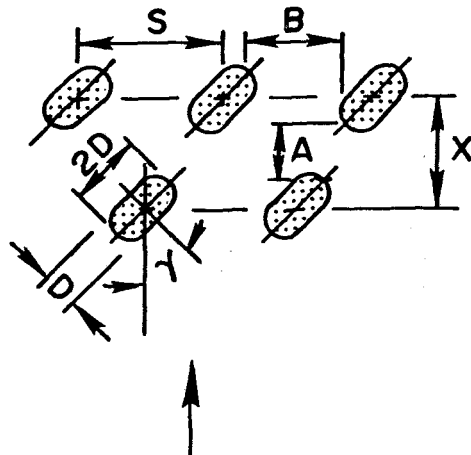
This situation has hindered systematic examination of the effects of array geometry on performance. Reference [12] reports on the use of a more flexible test method utilizing low conductivity wood pins that are easily set in different patterns and easily replaced. Two array geometries matching these used in [11] were fabricated in this manner and compared with the conducting pin results. Array average Nusselt numbers were based on the uncovered duct wall heat transfer area in contrast to the conducting pin cases where Nusselt numbers were based on the total duct wall and pin wetted area. Over the range $5,000 \leq Re \leq 50,000$, which encompasses most turbine applications, the two sets of results were found to agree to within 10 percent. On the basis of this correspondence, the low conductivity pin testing has proceeded as a means of screening a wide variety of array geometries. It would be preferable to retest promising geometries with high conductivity pins, but such is not always feasible in practice. In response to this situation, the present study further elaborates on the use of low conductivity pin test results to predict performance in actual applications with high conductivity pins and utilizes this test method to explore performance of the geometries listed in Table 1.

The apparatus has been described in detail in [11] and [12], only a brief review will be presented here. The test section consists of a rectangular duct of constant cross section. The upper and lower duct walls are of segmented copper construction with each segment provided with a separate electric resistance heater, thermocouples, and suitable control and measuring equipment. The channel side walls are interchangeable plastic spacers which allow different pin heights to be used. The test surface width in the transverse, or spanwise, direction is 12.7 cm. This results in duct aspect ratios for the present test series of either 24.9 or 30.2. The test surface length in the flow direction is also 12.7 cm. Entrance and exit duct sections extend the test section duct height (H) and width (12.7 cm) and additional 12.7-cm upstream and 7.62 cm downstream of the test section. The flow approaching the first pin row is thus characterized by an essentially fully developed velocity profile for all geometries tested.

The material used for the pins in the present tests is balsa wood. The pin stock is machined for cross-section accuracy and uniformity, and cut to length on a special jig. The individual pins are selected for use based on surface smoothness and are waxed on their exposed surfaces to fill any exposed pores. The finished pins can be placed in any desired pattern between the upper and lower walls. Accurate placement in a specific pattern is accomplished through use of a perforated plate machined for that pattern and pin-positioned on the lower end wall. A small drop of adhesive is placed on the
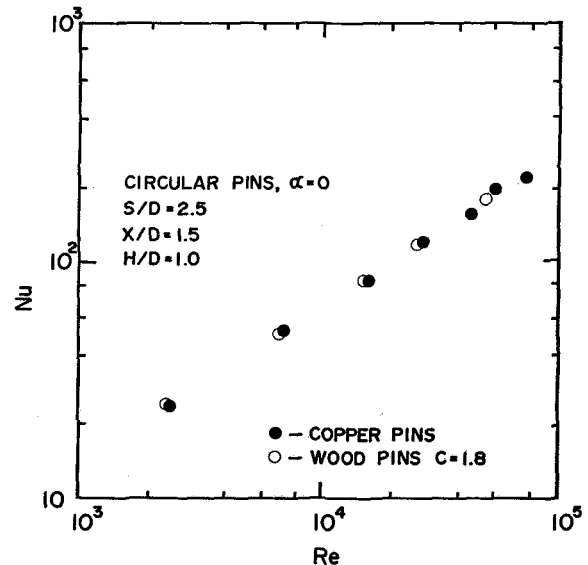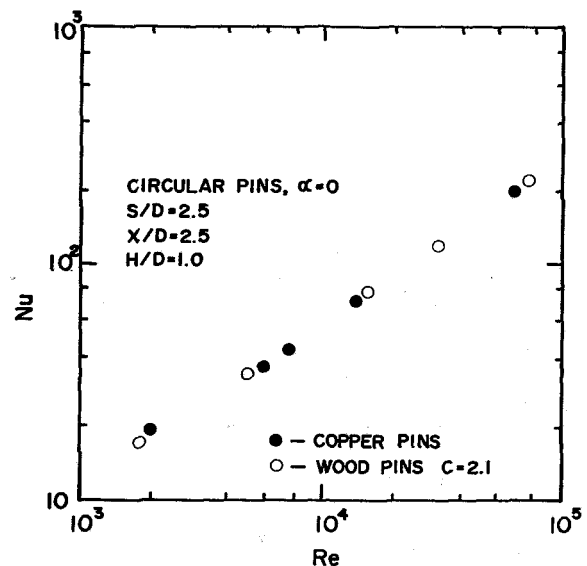
bottom and top of each pin, the template is removed, and the upper end wall is placed on top of the array. Only a very small amount of adhesive is used since the pins are cut slightly longer than the duct height and are primarily held in place mechanically after the test section is assembled. To avoid the use of excess adhesive that would change the effective pin conductivity, a new set of pins must be fabricated for each different array. Nevertheless, the time and expense involved in changing array patterns is relatively very small in comparison with a fixed geometry conducting pin apparatus.

All testing is carried out at steady-state conditions and utilizes the heater power measurements to determine average convective heat transfer rates over the ten rows of pins in the flow direction. In all cases an isothermal wall boundary condition is used where the individually controlled heaters are adjusted to equalize the end wall segment temperatures. In a typical test, steady isothermal conditions are achieved on all segments to within ± 0.1 C. Convective heat transfer coefficients are based on the differences between the wall surface temperatures and the local streamwise bulk average fluid temperatures. Fluid properties are evaluated locally at the
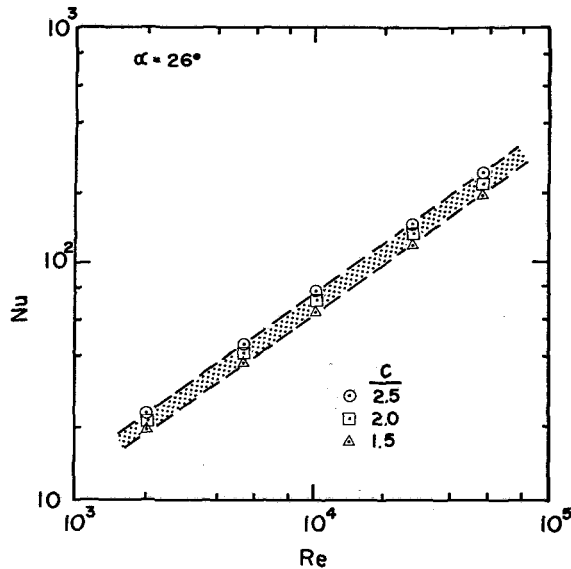
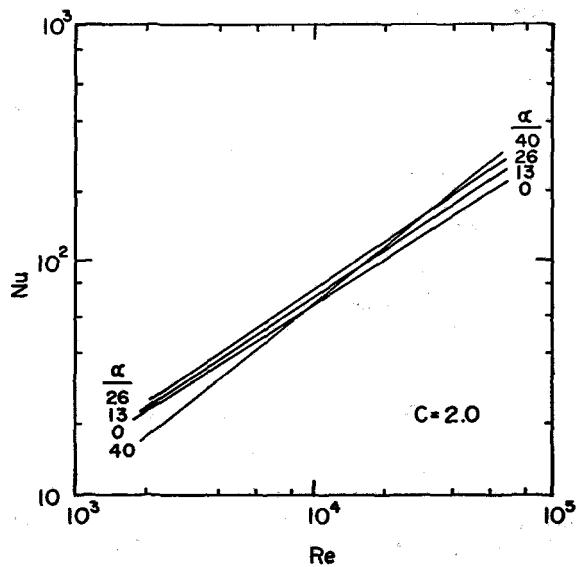Fig. 6 Effect of C on Nusselt No., $\alpha = 26$ deg

Fig. 8 Nusselt number comparison with [16]

Fig. 7 Effect of α on Nusselt number

Fig. 9 Effect of C on Nusselt number, $\gamma = \pm 30$ deg

Fig. 10 Effect of γ on Nusselt number

average of the surface and bulk temperatures. Additional details of the experimental apparatus and data acquisition and reduction procedures are given in [11] and [12].

Results and Discussion

Correspondence Between Low and High Conductivity Pin Results. As part of the present study, previously obtained circular pin array results with $\alpha = 0$ were reexamined, taking into account the small conductivity (0.1 W/m·K) of the wooden pins. The measured heat transfer rate per degree temperature difference is expressed as the sum of endwall and pin surface contributions with the pin modeled as a fin with symmetrical temperature profile between the top and bottom endwalls

$$\dot{q}/\Delta t = h_e A_e + \tanh(mH/2)(h_p P \kappa a)^{1/2} \qquad (1)$$

In general, $h_e \neq h_p$, and solution of equation (1) requires an additional relationship regarding their relative values. Here that relationship is arbitrarily taken to be a simple proportionality
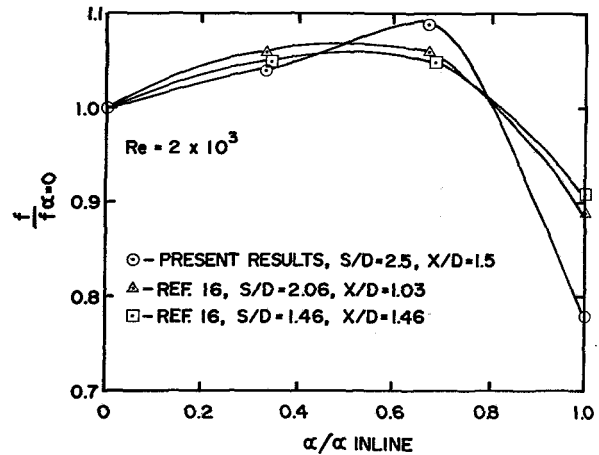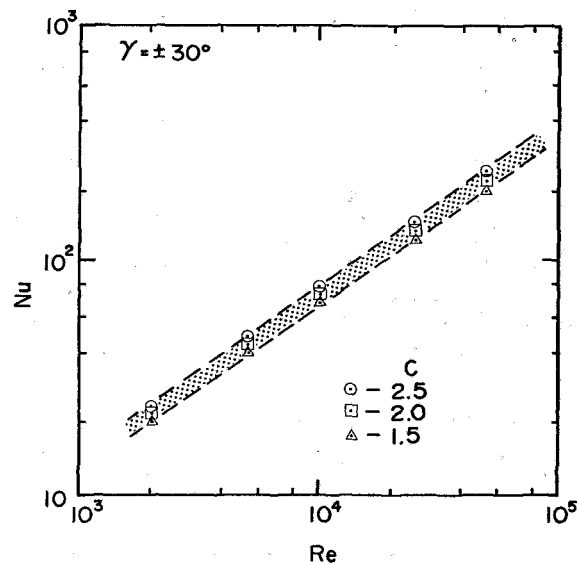
Fig. 11 Effect of α on pressure loss coefficients
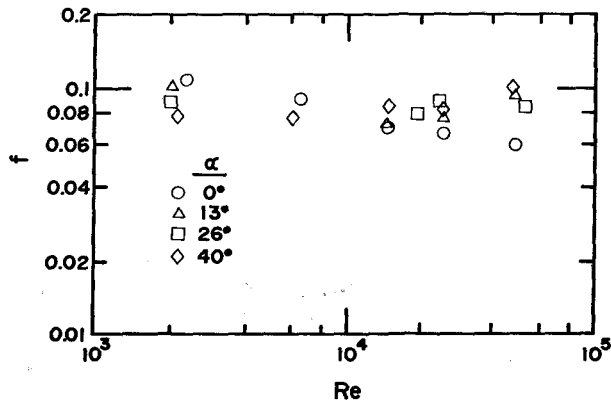

Fig. 12 Pressure loss comparison with Reference 16

Fig. 13 Effect of γ on pessure loss coefficients

$$h_p = C\,h_e \tag{2}$$

Assumption of a value of the ratio, C, allows calculation of h_e and h_p from equation (1) and also calculation of the corresponding overall (pins + endwall) heat transfer coefficient for a geometrically identical array with high conductivity pins

$$h_t = h_e\,(A_e/A_t) + h_p\,(A_p/A_t) \tag{3}$$

These calculations have been repeated with various values of C until good correspondence with the measured high conductivity pin results from [11] is achieved. Figures 4 and 5 show the best correspondence for the baseline cases (2.5, 1.5, 1.0) and (2.5, 2.5, 1.0), respectively. Experimental uncertainties in Nu, not including uncertainties associated with the ratio C, have been estimated to be ± 5 percent, based on the methods of [17]. The good agreement shown between low and high conductivity pin results was achieved with pin-to-endwall heat transfer coefficient ratios of 1.8 and 2.1, respectively. Thus this ratio appears to increase as the pin density decreases. This appears plausible since the endwall heat transfer is less influenced by the cylinder presence as the pin spacing becomes more sparse.

Effect of α on Heat Transfer. Figure 6 shows average array heat transfer results for the $\alpha = 26$ deg array. The Nusselt numbers as shown are based on h_t from equation (3). This requires data reduction using equations (1) and (2) and in particular, an assumption regarding the value of C, the ratio of pin to endwall heat transfer coefficients. Three sets of data reduction results are shown for assumed values of $C = 1.5$, 2.0, and 2.5. This appears to be a reasonable range of expected values of C based on the $\alpha = 0$ results in Figs. 4 and 5. The band defined by the upper and lower lines on Fig. 6 thus represents an additional uncertainty associated with the nature of the test method utilizing low conductivity pins. This uncertainty, about ± 9 percent, remains the same for the results obtained at other values of α. Figure 7 shows similar results for the remaining arrays where, for clarity, only the midband lines, $C = 2$, are shown.

The relative heat transfer performance as a function of the array orientation with respect to mean flow direction shows a slight improvement as the orientation moves from staggered toward in-line pins. The $\alpha = 40$ deg case is essentially an in-line arrangement. (The actual tested angle is 40.4 deg, the in-line angle is 39.8 deg). The latter orientation yields lower heat transfer coefficients than $\alpha = 0$ for Re $< 10^4$, and higher for Re $> 10^4$. The results of [16] were obtained in the range 2.8 $\times\ 10^3 \le$ Re $\le 10^4$, and are very similar in both trend and magnitude to those of the present study. Figure 8 summarizes the similarity at Re $= 2000$ in terms of $Nu/Nu_{\alpha=0}$ versus the fraction of angular orientation toward the in-line arrangement.
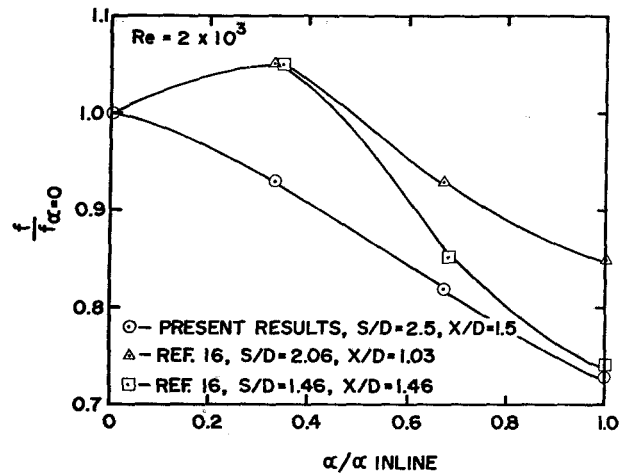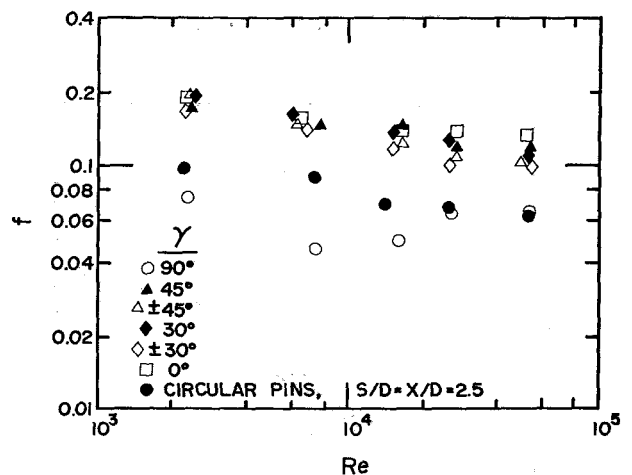
Effect of γ on Oblong Pin Heat Transfer. Figure 9 shows average array heat transfer results for the $\gamma = \pm\ 30$ deg array of oblong pins. Again, the Nusselt numbers shown are based on h_t from equation (3). Again, three sets of data reduction results are shown for assumed values of $C = 1.5$, 2.0, and 2.5. These define an uncertainty band associated with the use of low conductivity pins. Figure 10 shows similar results for the remaining arrays in this family of geometries. Again, for clarity, the individual data points have been left out and only the midband lines, $C = 2$, are shown. The dashed line is the baseline circular pin array behavior for comparison. All of the angles less than 90 deg yield higher Nusselt numbers, although the increase is slight. The $\gamma = \pm\ 30$ deg array has the highest Nusselt numbers, some 20 percent higher than the circular pin array on the average. The $\gamma = 90$ deg array yields significantly lower Nusselt numbers, especially toward the lower end of the Reynolds number range.

Pressure Loss Coefficients. Pressure loss coefficients were determined for all the tested arrays by measuring the streamwise static pressure distributions in both the entrance and exit ducts upstream and downstream of the test section. These distributions are extrapolated to points $X/2$ upstream of the first pin row and $X/2$ downstream of the last pin row. The resulting pressure difference across the array was used to determine the overall array pressure loss coefficient.

Figure 11 shows a summary of these results for the effect of α. The general trend of the $\alpha = 0$ results is a decreasing

coefficient with increasing Reynolds number. The $\alpha > 0$ results show less dependence on Reynolds number, with lower values than the $\alpha = 0$ case at low Reynolds numbers and higher values at high Reynolds numbers. These trends are again similar to those reported in [16], as shown in Fig. 12 for Re = 2000.

Figure 13 shows a summary of the pressure loss coefficients for the oblong pins at various values of γ. With the exception of $\gamma = 90$ deg, the pressure drop for the oblong pin arrays is substantially higher than the baseline circular pin array over the entire Reynolds number range. This is undoubtedly associated with the turning of the flow that takes place at every row when $\gamma < 90$ deg. At low Reynolds numbers, and particularly at intermediate Re ≈ 7000, the pressure drop for the $\gamma = 90$ arrangement is lower than the circular pin array.

Summary and Conclusions

Heat transfer and pressure loss were investigated for two families of short pin fin array configurations which deviate from the regular staggered patterns of circular cross section pins previously studied. The principal conclusions derived from the investigation are as follows.

For the circular cross section pin array, the array orientation with respect to the mean flow direction has a small but possibly significant effect on both heat transfer and pressure loss. With this array rotated two-thirds of the way toward an inline orientation from a staggered orientation, a 9 percent increase in heat transfer and an 18 percent decrease in pressure loss was observed.

For the oblong pin arrays, heat transfer increases of approximately 20 percent over the corresponding circular pin array were measured. These increases are offset by increases in pressure loss of approximately 100 percent.

For both array geometries investigated, the complex, highly three-dimensional separated flow precludes a simple physical explanation for the observed results. Flow visualization and/or velocity field measurements would be required to form a basis for such explanation.

A secondary, but important conclusion of the present study is the indication that pin surface heat transfer coefficients are approximately twice as large as those acting on the endwalls. The evidence, although persuasive, is nevertheless indirect.

The designer is urged to exercise caution in the use of this conclusion until direct measurements of separate pin and endwall surface heat transfer coefficients are made. Such measurements are strongly recommended for future work.

References

1 Jacob, M., "Heat Transfer and Flow Resistance in Crossflow of Gases over Tube Banks," *ASME Transactions*, Vol. 60, 1938, pp. 384–386.

2 Grimison, E. D., "Correlation and Utilization of New Data on Flow Resistance and Heat Transfer for Crossflow of Gases over Tube Banks," *ASME Transactions*, Vol. 59, 1937, pp. 583–594.

3 Zukauskas, A., "Heat Transfer from Tubes in Crossflow," *Advances in Heat Transfer*, Vol. 8, 1972, pp. 93–160.

4 Webb, R. L., "Air-Side Heat Transfer in Finned Tube Heat Exchangers," *Heat Transfer Engineering*, Vol. 1, 1980, pp. 33–49.

5 Rich, D. G., "The Effects of Fin Spacing on the Heat Transfer and Friction Performance of Multirow, Smooth Plate Fin-and-Tube Heat Transfer," *ASHRAE Transactions*, Vol. 79, pt. 2, 1973, pp. 137–145.

6 Rich, D. G., "The Effect of the Number of Tube Rows on Heat Transfer Performance of Smooth Plate-Fin-Tube Heat Exchangers," *ASHRAE Transactions*, Vol. 81, pt. 1, 1975, pp. 307–317.

7 Saboya, F. F. M., and Sparrow, E. M., "Local and Average Heat Transfer Coefficients for One-Row Plate Fin and Tube Heat Exchanger Configurations," ASME JOURNAL OF HEAT TRANSFER, Vol. 96, 1974, pp. 265–272.

8 Saboya, F. F. M., and Sparrow, E. M., "Transfer Characteristics of Two-Row Plate Fin and Tube Heat Exchanger Configurations," *International Journal of Heat and Mass Transfer*, Vol. 19, 1976, pp. 41–49.

9 VanFossen, G. J., "Heat Transfer Coefficients for Staggered Arrays of Short Pin Fins," ASME Paper No. 81-GT-75, 1981.

10 Brown, A., Mandjikas, B., and Mudyiwa, J. M., "Blade Trailing Edge Heat Transfer," ASME Paper No. 80-GT-45, 1980.

11 Metzger, D. E., Berry, R. A., and Bronson, J. P., "Developing Heat Transfer in Rectangular Ducts with Staggered Arrays of Short Pin Fins," ASME JOURNAL OF HEAT TRANSFER, Vol. 104, 1982, pp. 700–706.

12 Metzger, D. E., and Haley, S. W., "Heat Transfer Experiments and Flow Visualization for Arrays of Short Pin Fins," ASME Paper No. 82-GT-138, 1982.

13 Bringham, B. A., and VanFossen, G. J., "Length to Diameter Ratio and Row Number Effects in Short Pin Fin Heat Transfer," ASME Paper No. 83-GT-54, 1983.

14 Peng, Y., "Heat Transfer and Friction Loss Characteristics of Pin Fin Cooling Configuration," ASME Paper No. 83-GT-123, 1983.

15 Arora, S. C., and Abdel Messeh, W., "Heat Transfer Experiments in High Aspect Ratio Rectangular Channel with Epoxied Short Pin Fins," ASME Paper No. 83-GT-57, 1983.

16 Evenko, V. I., and Anisin, A. K., "Increasing Efficiency of Heat Transfer by Bundles of Tubes in Transverse Flow," *Teploenergetika*, Vol. 23, 1976, pp. 21–24.

17 Kline, S. J., and McKlintock, F. A., "Describing Uncertainties in Single Sample Experiments," *Mechanical Engineering*, Vol. 75, Jan. 1953.